Structural Chemistry of Inorganic Actinide Compounds

Editors: Sergey V. Krivovichev,
Peter C. Burns and Ivan G. Tananaev

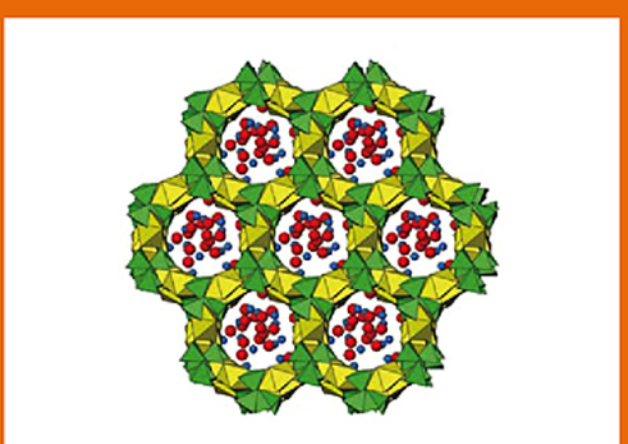

STRUCTURAL CHEMISTRY OF INORGANIC ACTINIDE COMPOUNDS

This page intentionally left blank

STRUCTURAL CHEMISTRY OF INORGANIC ACTINIDE COMPOUNDS

edited by

SERGEY V. KRIVOVICHEV
Department of Crystallography
St. Petersburg State University
St. Petersburg, Russia

PETER C. BURNS
Department of Civil Engineering and
Geological Sciences
University of Notre Dame
Notre Dame, Indiana, U.S.A.

IVAN G. TANANAEV
Frumkin Institute of Physical Chemistry
and Electrochemistry
Russian Academy of Sciences
Moscow, Russia

ELSEVIER

Amsterdam – Boston – Heidelberg – London – New York – Oxford – Paris
San Diego – San Francisco – Singapore – Sydney – Tokyo

Elsevier
Radarweg 29, PO Box 211, 1000 AE Amsterdam, The Netherlands
The Boulevard, Langford Lane, Kidlington, Oxford OX5 1GB, UK

First edition 2007

Library of Congress Cataloging-in-Publication Data
A catalog record for this book is available from the Library of Congress

British Library Cataloguing in Publication Data
A catalogue record for this book is available from the British Library

ISBN-13: 978-0-444-52111-8
ISBN-10: 0-444-52111-9

Printed and bound in The Netherlands

07 08 09 10 11 10 9 8 7 6 5 4 3 2 1

Table of Contents

Foreword

This book is a series of reviews of recent results on the state-of-art of structural and crystal chemistry of uranium and transuranium element compounds.

Investigations into crystal structures of neptunium and plutonium compounds were already of great importance at the time of the Second World War. In the 1950s, these studies were extended to include americium, curium and berkelium as well. The first structure determinations of compounds of the new-born elements were carried out at a time when their worldwide quantities were only at the level of micrograms which caused many problems, in particular, in the interpretation of powder X-ray diffraction patterns. Much easier were experiments with uranium and thorium which were in good supply. Despite all the difficulties, the investigations into solid compounds of uranium and transuranium elements were extremely important for the emerging technologies of nuclear fuels reprocessing, the determination of speciation of actinides in the environment, the search for new radioactive waste forms, etc. As a consequence, a large number of reports, papers, reviews and monographs have been published in the field of crystal chemistry of actinide elements. The modern state of science and, in particular, the essential amount of experimental data and development of new methods of structural characterization, allows for the large-scale development of crystal chemistry of actinide compounds. However, not so many books have been published in this area; for instance, the last monograph of this kind in Russia was published more than 20 years ago by M.P. Mefod'eva and N.N. Krot ('Compounds of Transuranium Elements', Moscow, Nauka, 1984). There is no doubt that the enormous amount of accumulated data needs serious systematization and analysis. This book is intended to fulfill this purpose, at least partially. Due to the extensive participation of Russian authors, the book contains many ideas and approaches traditional in Russian science but less well known in the West.

I hope that this book will be another example of a productive and successful international collaboration that transcends the borders of the present world.

Academician Prof. B.F. Myasoedov
Moscow

This page intentionally left blank

Preface

This book is a collection of reviews concerning the structural and coordination chemistry of actinide compounds. Over the past decade, these compounds have attracted considerable attention because of their importance for radioactive waste management, catalysis, ion-exchange and absorption applications, and various other applications. Synthetic and natural actinide compounds form as a result of alteration of spent nuclear fuel and radioactive waste under Earth surface conditions, during burn-up of nuclear fuel in reactors, and as oxidation products of uranium mines and mine tailings. Soils and sediments contaminated by actinides often contain such phases as well. Actinide compounds are also of considerable interest to materials scientists owing to the unique electronic properties of actinides which give rise to interesting physical properties that are controlled by the structural architecture of the respective compounds.

The structural chemistry of actinides is very diverse due to the possibility of different oxidation states and the richness of actinide coordination geometries. Whereas actinides in lower oxidation states sometimes mimic rare earth elements, actinides in higher oxidation states possess unique coordination chemistry, due to the tendency to form linear actinyl ions. The reviews in this book are written by specialists in their fields and the subjects range from low-valence actinide compounds to actinide-based metal-organic frameworks. The active participation of Russian authors provides overviews of some activities undertaken by scientists in the former Soviet Union. Their results are sometimes not well known to 'western' readers because of the relatively closed nature of works in this field during the Cold War years.

The book begins with two chapters (by Burns and Serezhkin) concerning the basic structural chemical features of uranium oxocompounds, as these are the most studied actinide compounds in general. Chapter 3, written by Tananaev, describes research results on hydrated oxides, hydroxides and peroxides of transuranium elements and contains some instances of infrared structural features for poorly crystallized compounds from spectroscopic data. The next five chapters are devoted to particular classes of actinide compounds that are characterized by specific structural principles. Krivovichev and Burns (Chapter 4) review structures of over 300 actinide compounds containing hexavalent cations of the VI group elements (S, Se, Mo, Cr, W). In Chapter 5, Sykora, Shvareva and Albrecht-Schmitt describe structural trends observed for actinide compounds with heavy oxoanions containing a stereochemically active lone-pair of electrons (e.g., those formed by Sb(III), Bi(III), Se(IV), Te(IV), Br(V), and I(V)). Chapter 6, written by Locock, provides an overview of actinide phosphates and arsenates that are of great mineralogical and environmental importance. Chapter 7 by Abraham and Obbade presents a systematic overview of the structural diversity of uranyl vanadates. Chemistry and structural chemistry of anhydrous tri- and tetravalent actinide orthophosphates is the topic of Chapter 8 by Orlova. In Chapter 9, Pope describes actinide complexes of polymolybdates and polytungstates, and also discusses solution studies of equilibria between actinide cations and polyoxometalate anions.

Grigory Andreev, Nina Budantseva and Alexander Fedoseev review the current state of the art in research on the interaction of the transuranium elements (TRUE) with N-donor ligands (Chapter 10). Chapter 11 is devoted to a 'hot' topic: U(VI)-containing metal-organic frameworks and coordination polymers and is written by Christopher Cahill and Lauren Borkowski. A short introduction concerning nanostructured actinide compounds is provided in Chapter 12. Finally, Chapter 13, written by Sergey Yudintsev, Sergey Stefanovsky and Rodney Ewing, examines actinide host phases as radioactive waste forms.

In total, the book provides an overview of the structural features of more than two thousand actinide compounds and contains about fifteen hundred references. We are well aware that the reviews gathered in this book do not cover all aspects of research concerning the structures of inorganic actinide compounds. However, we hope that it will be useful for those seeking detailed and updated basic research data concerning actinide compounds as well as those who are seeking a clue in the solution of some important practical problems such as immobilization of radionuclides, utilization of depleted uranium, and safe disposal of nuclear waste.

Sergey V. Krivovichev
Peter C. Burns
Ivan G. Tananaev
May 2006
St. Petersburg – Notre Dame – Moscow

Structural Chemistry of Inorganic Actinide Compounds
S.V. Krivovichev, P.C. Burns & I.G. Tananaev (Editors)

Chapter 1

Crystal chemistry of uranium oxocompounds: an overview

Peter C. Burns

Department of Civil Engineering and Geological Sciences, University of Notre Dame, Notre Dame, IN 46556 U.S.A.
Chemistry Division, Argonne National Laboratory, Argonne, IL, U.S.A.

1. Introduction

Crystals containing U^{6+} have been the focus of considerable research over several decades. The introduction of CCD-based detectors of X-rays and their application to crystal structure analysis [1] helped facilitate recent studies that have revealed many novel and fascinating crystal structures. A decade ago, the structures of about 180 inorganic compounds containing U^{6+} were known [2], and by 2006 the number of known structures has more than doubled [3]. The majority of these structures correspond to synthetic compounds, but about 90 are for minerals, the special subset of inorganic compounds that are stable for geological times, and that are consistent with geochemical conditions.

Current research concerning the crystal chemistry of U^{6+} oxocompounds is driven by the search for novel solids with important materials properties [4-10], as well as the importance of U^{6+} compounds in the environment [11-16], in geological U deposits [17], and in nuclear waste disposal [18]. The quantity of new structures becoming available is dramatically impacting the state of knowledge of the crystal chemistry of U^{6+}. Relative to a decade ago, dramatically more is known about the structures of uranyl molybdates, sulfates, selenates, selenites, iodates, phosphates, arsenates, oxyhydrates, and peroxides, and significant advances have also been made in the cases of uranyl carbonates, chromates, and silicates. Many of the newer structures follow earlier-established trends, such as the dominance of layered structures, but recent

research has also revealed the remarkable ability of U^{6+} structures to adopt curvature, resulting in nano-scale tubules and spheres [8-10].

The purpose of this chapter is to discuss the specifics of U^{6+} crystal chemistry in terms of the geometries of the coordination polyhedra and their linkages into extended structures. Approaches to understanding and classifying structures containing U^{6+} are examined. Specific coverage is provided for the structures of uranyl oxyhydrates, uranyl silicates, and uranyl carbonates. U^{6+} compounds containing iodate, selenite and tellurite are examined in Chapter 6, sulfates, selenates, molybdates, chromates, and tungstates are in Chapter 7, phosphates and arsenates are in Chapter 8, and uranyl vanadates are covered in Chapter 10.

2. Coordination Polyhedra and Polyhedral Linkages

Actinide cations in higher oxidation states (V and VI) almost invariably form two double bonds to two atoms of oxygen, resulting in an O=*An*=O (*An*: actinide cation) ion that is linear or nearly so. The U^{6+} cation conforms to this trend, forming a $(UO_2)^{2+}$ ion in most cases. The U^{6+}-O bond lengths are short because of the double bond, and are typically in the range of 1.78 to 1.82 Å. These short bonds come close to satisfying the bonding requirement of the O atoms, and correspond to about 1.6 to 1.7 valence units [19].

The formal valence of the uranyl ion is 2+, and the ion is always coordinated by multiple ligands in a crystal structure. These ligands are usually located within or near a plane oriented perpendicular to the uranyl ion, passing through the U^{6+} cation. In the case of oxocompounds, four, five or six O, OH or H_2O ligands coordinate the uranyl ion, and are located in the equatorial positions of square, pentagonal and hexagonal bipyramids. In each case, the O atoms of the uranyl ions are located at the two apical positions of the bipyramids (Fig. 1).

The distribution of bond lengths about U^{6+} cations in well-refined structures, as summarized by Burns [3], is presented in Figure 2. The distributions for both pentagonal bipyramids and hexagonal bipyramids are completely bimodal, reflecting the presence of a uranyl ion in each of these polyhedra. The average U-O bond lengths in the uranyl ion are 1.793(35) and 1.783(30) Å for pentagonal and hexagonal bipyramids, respectively. Bond lengths to the equatorial ligands are significantly longer, and show more dispersion: 2.368(100) and 2.460(107) Å for pentagonal and hexagonal bipyramids, respectively.

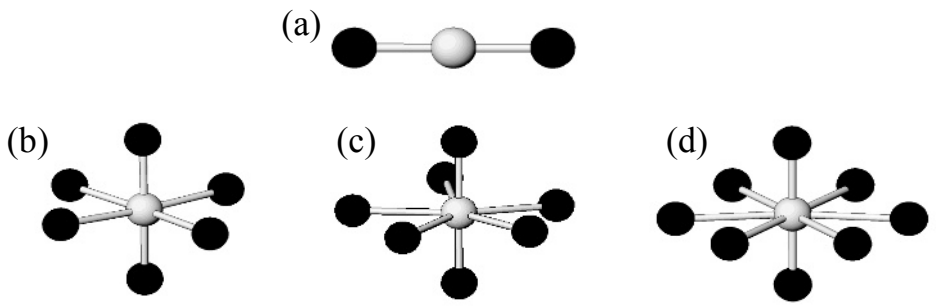

Figure 1. U^{6+} coordination polyhedra. (a) uranyl ion, (b) square bipyramid, (c) pentagonal bipyramid, (d) hexagonal bipyramid.

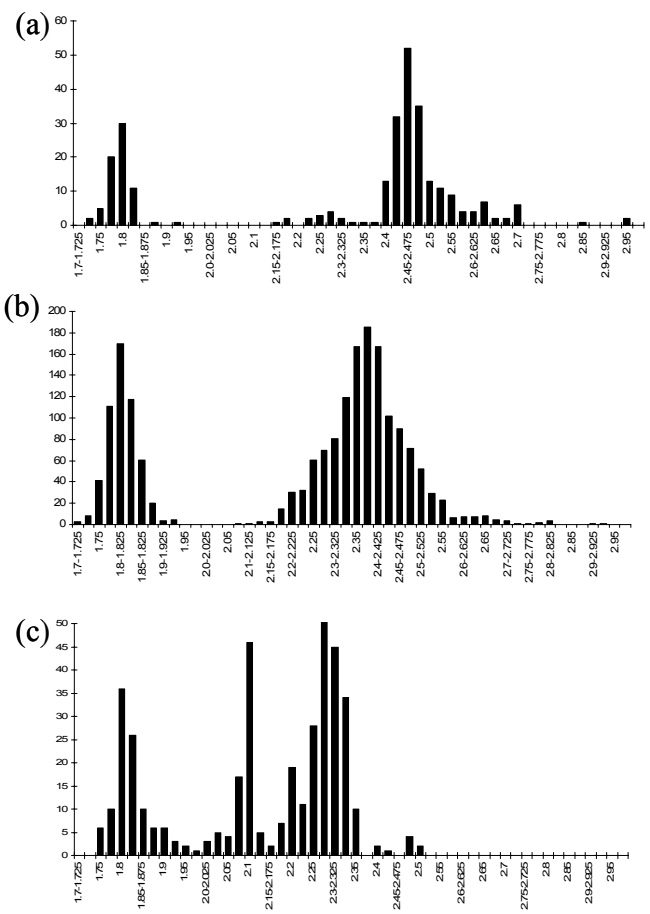

Figure 2. Bond-length distribution for polyhedra containing U^{6+}. (a) hexagonal bipyramids, (b) pentagonal bipyramids, (c) square bipyramids. From [3], reproduced with permission.

Only some of the structures that contain U^{6+} coordinated by six atoms of O exhibit uranyl ions. In the others, the U^{6+} cation is at the center of an octahedron, with a bond-length of about 2.08 Å. It is also interesting to note that various coordination polyhedra intermediate between uranyl square bipyramids and holosymmetric octahedra are present in structures. Where a uranyl ion is present in a square bipyramidal polyhedron, the average uranyl ion and equatorial bond lengths are 1.816(50) and 2.264(64) Å, respectively.

The uranyl ion bond length is weakly dependent upon the number of coordinating ligands, with the shortest bond lengths occurring for hexagonal bipyramids and the longest for square bipyramids. The bond lengths to the equatorial ligands are 0.2 Å longer in the hexagonal bipyramid than in the square bipyramid, and those of the pentagonal bipyramid are intermediate in this range. The corresponding bond-valences associated with the bonds from the U^{6+} cation to the equatorial ligands are 0.71 valence units for the square bipyramid, 0.53 valence units for the pentagonal bipyramid, and 0.44 valence units for the hexagonal bipyramid. Satisfaction of the remaining bond-valence requirements must be achieved if a stable structure is to result. Where H_2O coordinates the uranyl ion, the O atom of the H_2O does not require additional bonds, as the H atoms contribute the required bond valance. Although it may be common in solution, coordination of uranyl ions by H_2O groups is rare in crystal structures, and of the uranyl minerals, is only observed in a few species such as soddyite [20] and uranopilite [21].

Where the equatorial ligands of uranyl bipyramids are O or OH, these O atoms must participate in significant additional bonding to form a stable structure. To meet these bonding requirements, the uranyl polyhedra share equatorial vertices or edges with other polyhedra containing higher-valence cations. Often, such linkages are only between uranyl polyhedra. In these cases, O or OH groups are shared between uranyl ions and the sharing of equatorial edges is common between the polyhedra. As these linkages are almost invariably between equatorial ligands, sheets of uranyl polyhedra are the result. In such sheets, O atoms are almost always bonded to three uranyl ions, but OH groups can bond to either two or three uranyl ions. Where the OH group is linked to three uranyl ions, the bond length is about 0.2 Å longer than the case where O is bonded to three uranyl ions.

It is also common for uranyl polyhedra to share their equatorial vertices with polyhedra containing other types of cations of higher valence. Where this is the case, the types of linkage are dependent upon both the size of the second polyhedron, and the charge of the central cation. For example, borate and

carbonate triangles that are small and contain trivalent or quadravalent cations usually share edges with uranyl hexagonal bipyramids, which presents the shortest equatorial edge length of any of the three types of uranyl bipyramids. In comparison, tetrahedra containing hexavalent cations usually share single vertices with uranyl polyhedra, so as to minimize the repulsion between the cations. Tetrahedra containing pentavalent cations, such as phosphate or arsenate, link to uranyl polyhedra both by sharing edges and only vertices, in roughly equal proportions.

3. Structural Hierarchy of Inorganic Uranyl Compounds

With the substantial growth in the number of known structures containing uranyl polyhedra, a hierarchical arrangement of structures that facilitates comparison and that highlights underlying structural relationships is desirable. The goal of a structural hierarchy is to organize a wealth of complex and diverse structures into a cohesive framework. Structural hierarchies are usually based upon the connectivity of polyhedra in the structures, and thus carry a great deal of information concerning the crystal chemistry of the target group. The intent is to recognize structural trends within large groups of compounds, as such trends are usually obscured by the complexity of individual structures.

Burns et al. [2] developed a detailed structural hierarchy for inorganic uranyl compounds, and included both minerals and synthetic phases. At that time, 180 structures were available for inclusion. Burns [22] expanded the structural hierarchy and updated it in the case of minerals only. Burns [3] further developed the entire hierarchy and included coverage of 368 mineral and synthetic phases. The structural hierarchy is based upon the linkages of those polyhedra that contain higher-valence cations. In every case this includes polyhedra with U^{6+}, and often it includes one or more other types of cation polyhedra. For the purposes of the hierarchy, bonds to low-valence cations and H bonds are ignored (although these bonds are important for the stability of the entire structure).

Structures containing U^{6+} fall into five categories corresponding to isolated polyhedra (8), finite clusters of polyhedra (43), chains of polyhedra (57), sheets of polyhedra (204), and frameworks of polyhedra (56). The numbers in parenthesis indicate the frequency of each type of structure in Burns [3]. Note that linkages through equatorial vertices of uranyl bipyramids results in dominance of sheets of polyhedra, which account for about 55% of known structures.

Burns [3] adopted two different approaches to arranging the structures within the structural classes. In the cases of finite clusters of polyhedra, chains of polyhedra, and sheets of polyhedra that are dominated by the sharing of polyhedra vertices rather than edges, a graphical representation of the structural units was adopted.

Graphical representations are powerful because they reduce the structural complexity and allow recognition of underlying relationships amongst groups of structures. The graph is obtained from a structure by representing each distinct type of polyhedron with a colored circle, and the number of vertices shared between adjacent polyhedra are shown by connectors between the colored circles. Consider for example the clusters and their graphs shown in Figure 3. The graph corresponding to the cluster in Figure 3a has two black circles and eight white circles, the number of uranyl polyhedra and tetrahedra in the cluster. There are two types of white circles; those that are connected to two black circles, and those that are linked to only one. These two types of white circles correspond to the two- and one-connected tetrahedra of the cluster, respectively. The graph also indicates that all linkages in the cluster are by the sharing of vertices, without any sharing of edges that would have been shown by double connectors in the graph. This may be compared to the graph shown in Figure 3b, which has three types of white circles; those that are connected to a single black circle by a single connector, those that are connected to two black circles by single connectors, and those that are connected to a single black circle by two connectors. In the latter case, the two connectors extending between the black and white circle indicate that an edge is shared between the uranyl polyhedron and the corresponding tetrahedron.

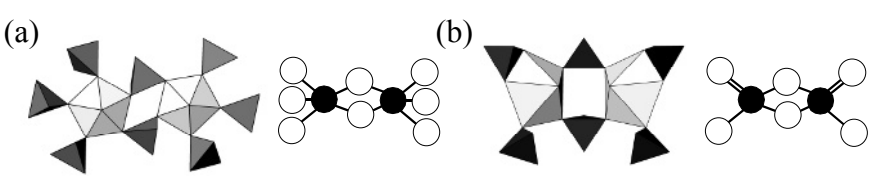

Figure 3. Examples of clusters of uranyl polyhedra and tetrahahedra and their corresponding graphs.

Krivovichev & Burns [23] developed a graphical approach for the analysis of sheets that are dominated by the sharing of vertices, Krivovichev [24] greatly expanded this approach, and Burns (2005) analyzed such structures in the same way. This approach is especially powerful because it permits recognition of parent graphs from which many other graphs may be derived. Chapter 7

presents uranyl structures containing sulfate, molybdate, chromate, and selenate using this approach.

Where linkages between polyhedra of higher bond valence within sheets are largely through the sharing of edges, the topological arrangement of anions within the sheets are a powerful means of arranging the structures [2, 3, 22]. In this approach, the connectivity of the sheet of polyhedra is analyzed and only those anions that are bonded to two or more cations within the sheet are considered. Those that are separated by less than about 3.5 Å are connected by lines, all atoms are removed from further consideration, and the resulting representation is projected onto a plane. The resulting two-dimensional tiling of space represents the topological arrangement of anions within the sheet, and is designated the sheet anion-topology. The utility of this approach is that sheets of polyhedra with little obvious resemblance often have the same underlying sheet anion-topology. As shown by Miller et al. [25] and Burns [22], it is possible to create most of the sheet anion-topologies by stacking a small number of distinct chains of polygons. These chains, and their corresponding designations, are presented in Figure 4. This provides a useful means of further comparing sheet anion-topologies, as well as a simple shorthand notation for the topologies. As shown by Miller et al. [25], this also permits derivation of as-yet unknown topologies. Burns [26, 27] showed that it is possible to use this approach to demonstrate that extraordinarily complex sheets in some minerals are composed of modules of simpler sheets found in other minerals or synthetic compounds.

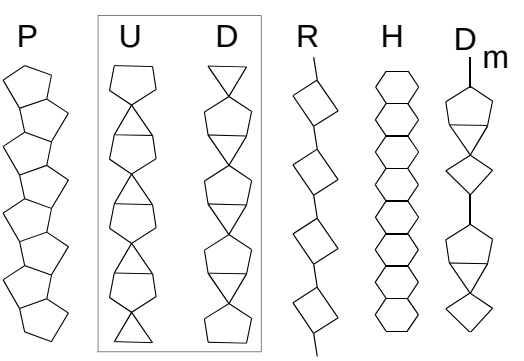

Figure 4. Chains of polygons used to generate sheet anion-topologies.

4. Bond-Valence Approach to Uranyl Structures

The bond-valence approach [28] has proven to be a powerful tool for the prediction and interpretation of bond lengths in solids. Burns et al. [19] presented revised bond-valence parameters derived from uranyl polyhedra in well-refined structures. These parameters facilitate calculations in the case of U^{6+}, as previously proposed parameters generally performed poorly. Burns et al. [19] provided bond valence parameters that were optimized over all uranyl polyhedra, as well as those that are coordination specific. The coordination specific parameters for six-coordinated U^{6+} are R_{ij} = 2.074 Å, b = 0.554 Å; for seven-coordinated U^{6+} R_{ij} = 2.045 Å, b = 0.510 Å; for eight-coordinated U^{6+} R_{ij} = 2.042 Å, b = 0.506 Å. Optimal parameters for all types of U^{6+} polyhedra are R_{ij} = 2.051 Å, b = 0.519 Å.

Schindler and Hawthorne [29] presented novel insights into the chemical composition and occurrence of uranyl oxide hydrates using a combined binary representation and bond-valence approach. In essence, this approach looks for conditions of overlap of the bonding requirements emanating from the structural unit and interstitial components. The outcome is a series of predicted compositions and mineral stabilities.

5. Uranyl Oxide Hydrates

The most recent compilation of uranyl structures [3] included 29 uranyl oxide hydrates. These structures contain uranyl bipyramids that are invariably linked by the sharing of their equatorial vertices or edges. Most contain interstitial H_2O, and all but six contain low-valence cations that provide linkages between the structural units. Of the 29 uranyl oxide hydrates that have known structures, 17 are minerals. These minerals often form as alteration products of uraninite, UO_{2+x}, in the oxidized portions of U deposits [30]. They are typically the first uranyl minerals to form at the onset of alteration, and although they can persist for geologically significant times. Continued alteration often results in their replacement by other uranyl minerals such as uranyl silicates or phosphates. Uranyl oxide hydrates have also received considerable attention because they form when spent nuclear fuel is altered in a moist, oxidizing environment [31, 32]. It has been suggested that these phases may significantly impact the future fate of a variety of radionuclides during evolution of the repository, as they may incorporate radionuclides such as Cs, Sr, and Np upon crystallization [16].

The linkage of uranyl bipyramids through their equatorial vertices results in the dominance of sheets of polyhedra within this structural class: of the 29 known

structures, 27 contain sheets of polyhedra and the other two are frameworks of polyhedra in which there is a significant layered character.

The uranyl oxide hydrates for which there are known crystal structures are listed in Table 1. The structures that are based upon sheets are arranged according to the topological arrangements of the anions within the sheets. Structures with identical sheet anion-topologies are grouped in the Table. There are 13 sheet anion-topologies that are the basis of the 27 sheets in uranyl oxide hydrates. It is important to note that several of these anion topologies are also the basis of sheets containing uranyl polyhedra and other polyhedra of higher bond-valence, and these structures are not included in the current discussion. Some structures, such as those of the minerals vandendiescheiite [26] and wölsendorfite [27] possess sheets with tremendous complexity, despite their relative chemical simplicity.

The autunite anion-topology is a simple array of squares located such that their corners correspond (Fig. 5). Two uranyl oxide hydrates, γ-$[(UO_2)(OH)_2]$ [33] and β-$[(UO_2)(OH)_2]$ [34], contain sheets with this anion topology. The topologically identical sheets in these two structures contain only uranyl square bipyramids that are located in half of the squares of the underlying anion topology. Each square bipyramid shares all four of its equatorial vertices with four different uranyl square bipyramids, thus each is four-connected and all of the connections within the sheet involve only the sharing of vertices. The sheets in these structures are electroneutral, there are no interlayer constituents, and the sheets are linked directly by H bonds.

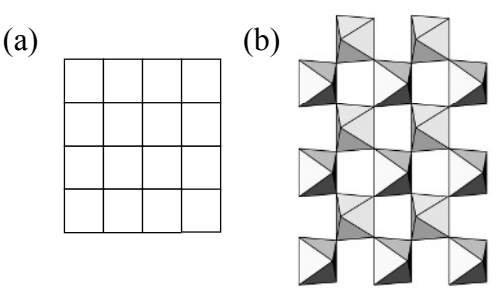

Figure 5. The autunite sheet anion-topology (a) and corresponding sheet of vertex-sharing uranyl square bipyramids from the structures of β and γ $[(UO_2)(OH)_2]$ (b).

Table 1. Uranyl Oxide Hydrates

Name	Formula	S. Gr.	*a* (Å)	*b* (Å)	*c* (Å)	Ref.
	Autunite anion-topology					
	γ-$[(UO_2)(OH)_2]$	$P2_1/c$	5.560	5.522	6.416	33
	β-$[(UO_2)(OH)_2]$	*Pbca*	5.6438	6.2867	9.9372	34
	Protasite anion-topology					
Protasite	$Ba[(UO_2)_3O_3(OH)_2](H_2O)_3$	*Pn*	12.2949	7.2206	6.9558	37
Billietite	$Ba[(UO_2)_3O_2(OH)_3]_2(H_2O)_4$	$Pbn2_1$	12.0720	30.167	7.1455	37
Becquerelite	$Ca[(UO_2)_3O_2(OH)_3]_2(H_2O)_8$	$Pn2_1a$	13.8527	12.3929	14.9297	35
	$Sr_{1.27}[(UO_2)_3O_{3.54}(OH)_{1.46}](H_2O)_3$	*P*3	7.020		6.992	35
	$Cs_3[(UO_2)_{12}O_7(OH)_{13}](H_2O)_3$	*R*3	14.124		22.407	90
	$Na_2[(UO_2)_3O_3(OH)_2]$	$P2_1/n$	7.0476	11.4126	12.0274	67
Richetite	$(Fe,Mg)_xPb_{8.57}[(UO_2)_{18}O_{18}(OH)_{12}]_2(H_2O)_{41}$	*P*1	20.939	12.100	16.345	38
Agrinierite	$K_2(Ca_{0.65}Sr_{0.35})[(UO_2)_3O_3(OH)_2]_2(H_2O)_5$	*F2mm*	14.094	14.127	24.106	40
Masuyite	$Pb[(UO_2)_3O_3(OH)_2](H_2O)_3$	*Pn*	12.241	7.008	6.983	39
Compreignacite	$K_2[(UO_2)_3O_2(OH)_3]_2(H_2O)_7$	*Pnnm*	14.859	7.175	12.187	36
	Fourmarierite anion-topology					
Fourmarierite	$Pb[(UO_2)_4O_3(OH)_4](H_2O)_4$	$Bb2_1m$	13.986	16.400	14.293	41
Metaschoepite	$[(UO_2)_4O(OH)_6](H_2O)_5$	*Pbcm*	14.6861	13.9799	16.7063	42
Schoepite	$[(UO_2)_8O_2(OH)_{12}](H_2O)_{12}$	$P2_1ca$	14.337	16.813	14.731	43
	Vandendriesscheite anion-topology					
Vandendriesscheite	$Pb_{1.57}[(UO_2)_{10}O_6(OH)_{11}](H_2O)_{11}$	*Pbca*	14.116	41.378	14.535	26
	β-U_3O_8 anion-topology					
Ianthinite	$[U_2^{4+}(UO_2)_4O_6(OH)_4(H_2O)_4](H_2O)_5$	$P2_1ca$	7.178	11.473	30.39	45
Spriggite	$Pb_3[(UO_2)_6O_8(OH)_2](H_2O)_3$	*C*2/*c*	28.355	11.990	13.998	44
	Curite anion-topology					
	$Sr_{2.82}(H_2O)_2[(UO_2)_4O_{3.82}(OH)_{3.18}]_2$	*Pnam*	12.314	12.961	8.404	47
Curite	$Pb_3[(UO_2)_8O_8(OH)_6](H_2O)_3$	*Pnam*	12.551	13.003	8.390	46
	Sayrite anion-topology					
Sayrite	$Pb_2[(UO_2)_5O_6(OH)_2](H_2O)_4$	$P2_1/c$	10.704	6.960	14.533	48
	Wölsendorfite anion-topology					
Wölsendorfite	$Pb_{6.16}Ba_{0.36}[(UO_2)_{14}O_{19}(OH)_4](H_2O)_{12}$	*Cmcm*	14.131	13.885	55.969	27

	Vandenbrandeite anion-topology					
Vandenbrandeite	$[(UO_2)Cu(OH)_4]$	$P\bar{1}$	7.855	5.449	6.089	50
	$Na[(UO_2)_4O_2(OH)_5](H_2O)_2$ anion-topology					
	$Na[(UO_2)_4O_2(OH)_5](H_2O)_2$	$P\bar{1}$	8.0746	8.4633	11.2181	51
	$K_5[(UO_2)_{10}O_8(OH)_9](H_2O)$ anion-topology					
	$K_5[(UO_2)_{10}O_8(OH)_9](H_2O)$	*Pn*	13.179	20.895	13.431	52
	$Ca[(UO_2)_4O_3(OH)_4](H_2O)_2$ anion-topology					
	$Ca[(UO_2)_4O_3(OH)_4](H_2O)_2$	$P\bar{1}$	8.0556	8.4214	10.958	53
	α-$[(UO_2)(OH)_2]$ anion-topology					
	α-$[(UO_2)(OH)_2]$	*Cmca*	4.242	10.302	6.868	54
	Frameworks					
	$(NH_4)_3(H_2O)_2\{[(UO_2)_{10}O_{10}(OH)]$	*C2/c*	11.627	21.161	14.706	55
	$[(UO_4)(H_2O)_2]\}$					
	$Pb_2(H_2O)[(UO_2)_{10}UO_{12}(OH)_6(H_2O)_6]$	*C2/c*	13.281	10.223	26.10	56

The protasite anion-topology is the basis for sheets of uranyl pentagonal bipyramids in ten structures. This is a relatively simple topology that contains only triangles and pentagons (Fig. 6). The anion topology is composed of **P** and **D** chains, with the stacking sequence being **PDPD**… Each of the pentagons in the anion topology is populated by a uranyl ion, giving a sheet of edge-sharing uranyl pentagonal bipyramids with the uranyl ions oriented approximately perpendicular to the plane of the sheet. In all cases the sheets of uranyl polyhedra bear a negative charge, but there are multiple versions of the sheet that differ in terms of the number and distribution of OH groups at the equatorial positions of the bipyramids. For example, the sheet compositions in becquerelite [35], billietite [37] and compreignacite [36] are all $[(UO_2)_3O_2(OH)_3]^{-1}$. All of the corners of all of the triangles in the anion topologies corresponding to these sheets are occupied by OH. The sheets in masuyite and protasite have the composition $[(UO_2)_3O_3(OH)_2]^{-2}$, and only two of the vertices of each of the triangles in the anion topology are occupied by OH. The sheet in richetite [38] has the same formula as masuyite [39], but the distribution of OH groups within the anion topology is different. The interlayers of nine of the structures that contain sheets based upon the protasite anion topology contain H_2O. All of the interlayers contain either monovalent or divalent cations, and the structure of agrinierite [40] contains both.

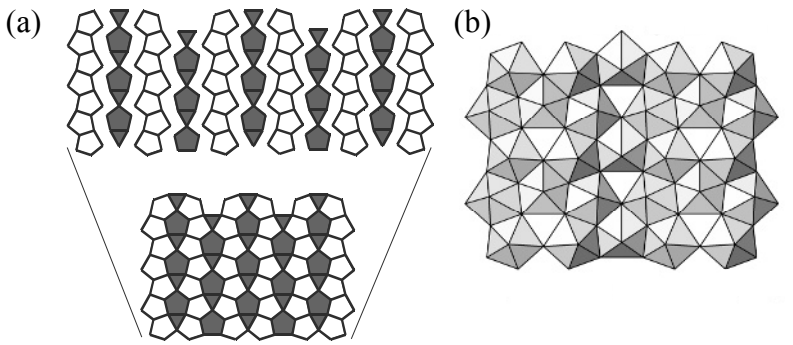

Figure 6. The protasite sheet anion-topology generated by stacking chains (a), and the sheet of uranyl pentagonal bipyramids that occurs in 10 structures (b).

The fourmarierite anion-topology (Fig. 7) is the basis for topologically identical sheets that occur in the structures of fourmarierite [41], schoepite [42] and meta-schoepite [43]. This topology contains only pentagons and triangles, and is created using the **P**, **D** and **U** chains with the stacking sequence **DUPUDPDU**… In each case all of the pentagons of the anion topology are populated by uranyl ions, giving sheets of edge-sharing uranyl pentagonal bipyramids. In fourmarierite, the sheets have a net negative charge that is balanced by Pb cations in the interlayer. Li & Burns [41] studied the structures of multiple fourmarierite crystals, and determined that the occupancies of the two Pb sites in the interlayer are not constant, and that variation of the amount of Pb in the structure is correlated with substitution of O for OH groups at equatorial positions of uranyl pentagonal bipyramids in the sheets. One synthetic crystal showed a composition that was midway between that of fourmarierite and schoepite. In schoepite and meta-schoepite the sheets are electroneutral, H_2O is in the interlayer, and only H bonds link the sheets through the interlayer constituents.

The structure of vandendriesscheite [26] contains the remarkably complex sheet of uranyl pentagonal bipyramids illustrated in Figure 8. To date, this sheet is only known from vandendriesscheite, and synthesis of crystals containing this sheet has not been reported. The corresponding anion topology is shown in Figure 8a, and contains only pentagons and triangles, which is remarkable given the complexity of the topology. Construction of the anion topology requires only the **P**, **D** and **U** chains, and the stacking sequence is **PDUPUPUPUDPDPDPDUPUPU**…. The structure has a primitive repeat length of more than 41 Å owing to the complexity of the sheet. The interlayer of the structure contains only Pb and H_2O, and the Pb^{2+} coordination polyhedra are distorted because of the presence of a stereoactive lone-electron pair.

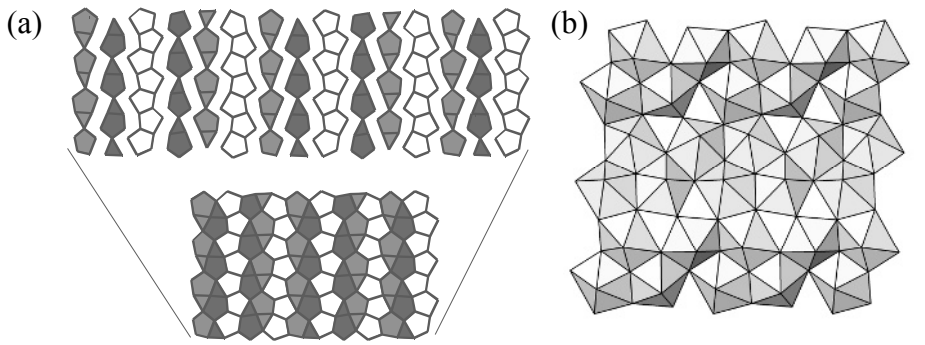

Figure 7. The fourmarierite sheet anion-topology generated by stacking chains (a), and the sheet of uranyl pentagonal bipyramids that occurs in fourmarierite, schoepite and meta-schoepite (b).

The β-U_3O_8 anion topology contains chains of edge-sharing pentagons, as well as chains of edge-sharing triangles and squares arranged such that the pentagons of adjacent chains share vertices (Fig. 9). The anion topology is best described using the **U**, **D** and **R** chains, with the sequence **DRUDRU**… The structures of spriggite [44] and ianthinite [45] contain sheets that are based upon this anion topology. In the spriggite sheet, the pentagons and squares of the anion topology are both occupied by uranyl ions, resulting in sheets of uranyl square and pentagonal bipyramids. The Pb cations and H_2O groups are located in the interlayer. The ianthinite sheet is obtained from the anion topology by population of the pentagons with uranyl ions, and the squares with U^{4+} cations. The resulting sheet is electroneutral, and linkages between the sheets are through H bonds involving H_2O groups in the interlayer.

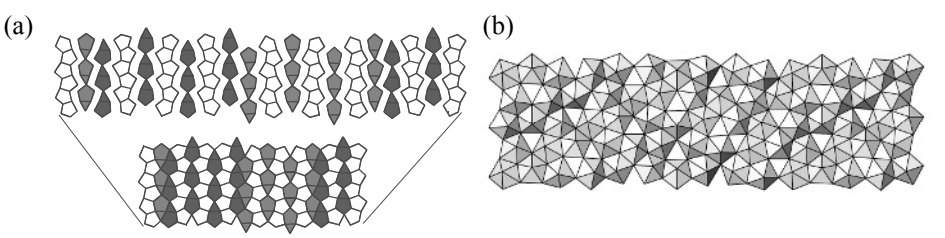

Figure 8. The vandendriesscheite sheet anion-topology generated by stacking chains (a), and the sheet of uranyl pentagonal bipyramids that occurs in vandendriesscheite (b).

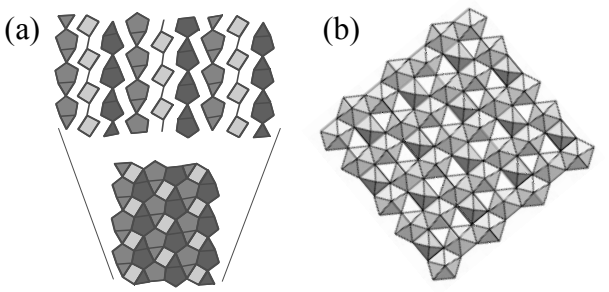

Figure 9. The β-U_3O_8 sheet anion-topology generated by stacking chains (a), and the sheet of uranyl square and pentagonal bipyramids that occurs in spriggite and ianthinite (b).

The curite anion-topology, which contains pentagons, distorted squares, and triangles is shown in Figure 10. Creation of this anion topology using chains of polygons requires the **D** and $\mathbf{U^M}$ chains with the stacking sequence $\mathbf{DU^MDU^M}$… It is the basis of the sheet found in curite [46], as well as its isostructural Sr analogue [47]. The pentagons and squares of the anion topology are populated by uranyl ions, resulting in a sheet that contains uranyl pentagonal bipyramids and strongly distorted square bipyramids (Fig. 10). Similarly distorted uranyl square bipyramids occur in at least three other uranyl oxide hydrates. The interlayer of the structure contains Pb cations and H_2O groups. The existence of the isostructural Sr analogue demonstrates that the unusual sheet in the structure of curite is not a result of the highly distorted coordination polyhedra that are typical of Pb cations in the interlayer.

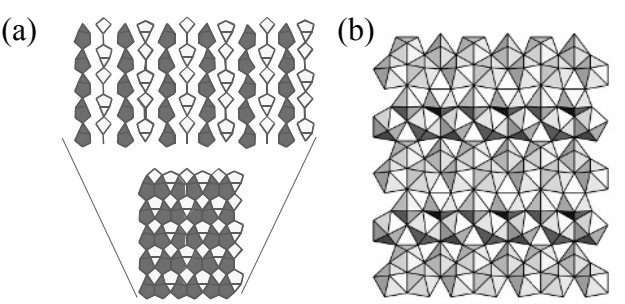

Figure 10. The curite sheet anion-topology generated by stacking chains (a), and the sheet of uranyl square and pentagonal bipyramids that occurs in curite and its Sr analogue (b).

Sheets in the structure of the rare Pb uranyl oxide hydrate mineral sayrite [48] are based upon the anion topology shown in Figure 11. The topology contains the **P**, **R**, **U** and **D** chains with the sequence **RUPURDPDRUPU**… The

squares and the pentagons of the anion topology are each populated by uranyl ions, giving a sheet of uranyl square and pentagonal bipyramids (Fig. 11). The sheets are linked through bonds to Pb and through H bonding to H_2O groups, both of which are located in the interlayer. This sheet has also been observed in the synthetic anhydrous phase $K_2[(UO_2)_5O_8](UO_2)_2$ [49], where the interlayer contains uranyl ions.

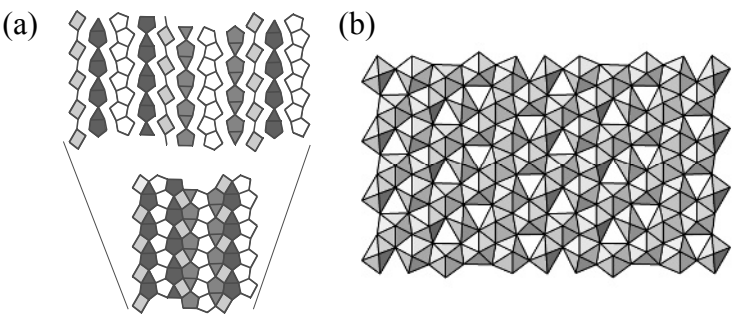

Figure 11. The sayrite sheet anion-topology generated by stacking chains (a), and the sheet of uranyl square and pentagonal bipyramids that occurs in sayrite (b).

The structure of wölsendorfite [27] contains the most complex sheet of uranyl polyhedra known (Fig. 12). The corresponding anion topology is composed of pentagons, squares, and triangles, and has a primitive repeat distance of 56 Å. The topology contains **P**, **R**, **U** and **D** chains with the sequence **DRUDRUDRUPDPDRUDRUDRUPDP**… The pentagons and squares of the anion topology are occupied by uranyl ions, giving sheets of uranyl square and pentagonal bipyramids. The interlayer of the structure contains Pb and some Ba, as well as H_2O groups. Burns [27] demonstrated that the wölsendorfite anion topology, as well as the sheet of polyhedra, is composed of modules of the protasite and β-U_3O_8 topologies. In particular, the sequence of chains **DRUDRUDRU** is identical to that of the β-U_3O_8 topology, and the **PDP** sequence occurs in the protasite anion topology.

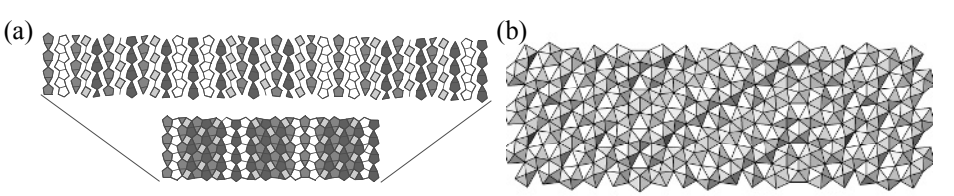

Figure 12. The wölsendorfite sheet anion-topology generated by stacking chains (a), and the sheet of uranyl square and pentagonal bipyramids that occurs in wölsendorfite (b).

The structure of vandenbrandeite [50] contains unique sheets of uranyl pentagonal bipyramids and Cu^{2+} square bipyramids (Fig. 13). The corresponding anion topology contains pentagons, squares and triangles, and is composed of the **D**, **U** and **R** chains with the sequence **DRURRRDRURRR**… The pentagons of the anion topology contain uranyl ions, giving uranyl pentagonal bipyramids, and the squares correspond to the bases of the Cu^{2+} square bipyramids. The Cu^{2+} square bipyramids share an edge along their base, giving dimers in which the apical ligands of the two bipyramids extend in opposite directions. Apical ligands of the Cu^{2+} square bipyramids correspond to O_{Ur} atoms of adjacent sheets.

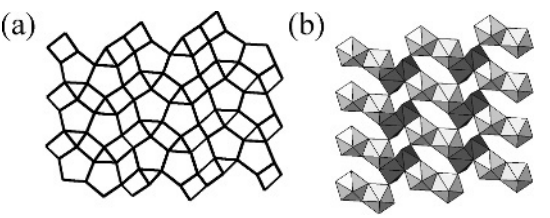

Figure 13. The vandenbrandeite sheet anion-topology (a), and the sheet of uranyl pentagonal bipyramids and Cu square pyramids that occurs in vandenbrandeite (b).

The structure of $Na[(UO_2)_4O_2(OH)_5](H_2O)_2$ [51] contains a sheet of edge-sharing uranyl pentagonal bipyramids (Fig. 14), and has the underling anion topology shown in Figure 14a. This anion topology contains only pentagons and triangles, yet it is distinct from the protasite anion topology. Construction of the anion topology requires the **U**, **D** and **P** chains, with the stacking sequence **UPDUPD**… This differs from that of the protasite anion topology only in the orientation of the **U** chains. Reversing the directional sense of the **U** chains results in **D** chains and the protasite anion topology.

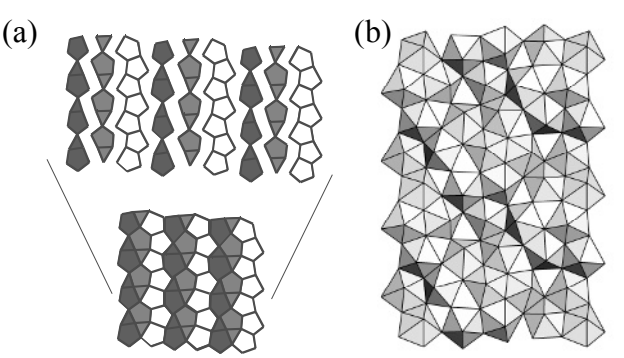

Figure 14. The $Na[(UO_2)_4O_2(OH)_5](H_2O)_2$ sheet anion-topology generated by stacking chains (a), and the sheet of uranyl pentagonal bipyramids that occurs in $Na[(UO_2)_4O_2(OH)_5](H_2O)_2$ (b).

The structure of $K_5[(UO_2)_{10}O_8(OH)_9](H_2O)$ was determined for a synthetic crystal grown under mild hydrothermal conditions [52]. The structural sheet contains uranyl pentagonal bipyramids and strongly distorted uranyl square bipyramids, similar to those in the curite sheet. The K and H_2O group are located in the interlayer, and provide linkages between the sheets. The sheet of uranyl polyhedra (Fig. 15) contains double-wide chains of bipyramids that share equatorial edges, and adjacent chains are connected by the sharing of vertices and edges between bipyramids. The anion topology is shown in Figure 15a, and contains pentagons, squares and triangles. It contains the **P**, **D**, **U** and **R** chains with the stacking sequence **DUPDPUDRDUPDPUDR**…. To date, this is the only sheet anion topology known for a uranyl compound in which a **P** chain is flanked by both a **D** and a **U** chain. In all other cases where **P** chains are flanked by **D** or **U** chains, both of the flanking chains have the same directional sense.

The structure of $Ca[(UO_2)_4O_3(OH)_4](H_2O)_2$ [53] has an unusual sheet of uranyl pentagonal bipyramids and strongly distorted square bipyramids (Fig. 16). The sheet anion topology contains pentagons, squares and triangles (Fig. 16a). The sheet has two distinct double-wide chains of bipyramids, one composed of only pentagonal bipyramids, and one that contains both square and pentagonal bipyramids. These two double-wide chains are linked into a sheet by the sharing of equatorial vertices only. The resulting sheet is closely related to the sheet in $Na[(UO_2)_4O_2(OH)_5](H_2O)_2$, and these sheets differ only in the position of a single anion, which differs by about 0.6 Å in the two structures.

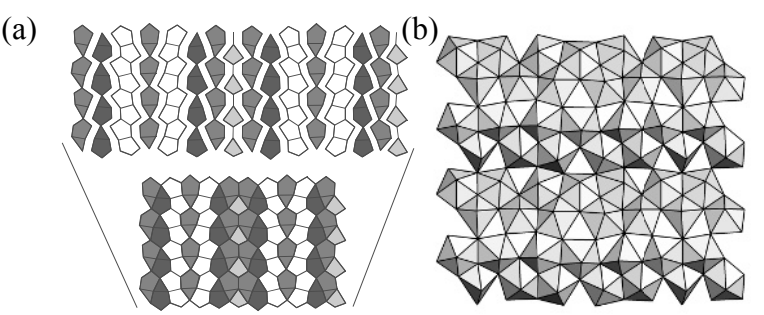

Figure 15. The $K_5[(UO_2)_{10}O_8(OH)_9](H_2O)$ sheet anion-topology generated by stacking chains (a), and the sheet of uranyl square and pentagonal bipyramids that occurs in $K_5[(UO_2)_{10}O_8(OH)_9](H_2O)$ (b).

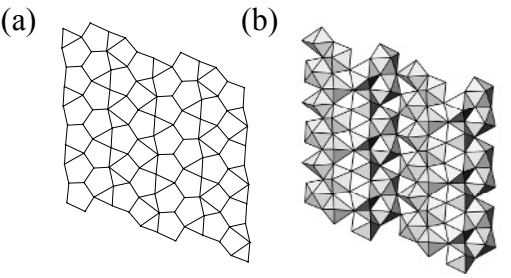

Figure 16. The $Ca[(UO_2)_4O_3(OH)_4](H_2O)_2$ sheet anion-topology (a), and the sheet of uranyl square and pentagonal bipyramids that occurs in $Ca[(UO_2)_4O_3(OH)_4](H_2O)_2$ (b).

Consider the sheets that contain only uranyl pentagonal bipyramids and their corresponding anion topologies. All of these contain chains of edge-sharing pentagons, and the anion topologies differ mostly in the positions of the triangles. Note that these triangles are vacant in each of the sheets that are based upon these anion topologies. In the protasite anion topology, each of the triangles are isolated from each other, and each points in the same direction (Fig. 6). In the $Na[(UO_2)_4O_2(OH)_5](H_2O)_2$ anion topology, the triangles occur as pairs that share a vertex, resembling bowties, and there are two distinct orientations of the bowties (Fig. 14). The fourmarierite anion topology also has pairs of triangles resembling bowties, but each are oriented in the same direction (Fig. 7). In the vandendriesscheite anion topology, some triangles are isolated and some are linked into pairs resembling bowties (Fig. 8). The isolated triangles point in two different directions, as do the bowties.

The structure of α-$[(UO_2)(OH)_2]$ [54] contains sheets of uranyl hexagonal bipyramids (Fig. 17), and the sheet anion topology consists only of hexagons. This is the only uranyl oxide hydrate that contains hexagonal bipyramids, although this coordination type is common in uranyl carbonates, uranyl nitrates, and uranyl phosphates of the phosphuranylite group.

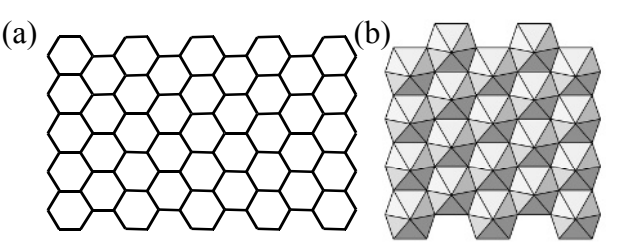

Figure 17. The α-$[(UO_2)(OH)_2]$ sheet anion-topology (a), and the sheet of uranyl hexagonal bipyramids that occurs in α-$[(UO_2)(OH)_2]$ (b).

The structures of $(NH_3)_3(H_2O)_2\{[(UO_2)_{10}O_{10}(OH)][(UO_4)(H_2O)_2]$ (Fig. 18a) [55] and $Pb(H_2O)[(UO_2)_{10}UO_{12}(OH)_6(H_2O)_6]$ (Fig. 18b) [56] are the only uranyl oxide hydrates with frameworks of uranyl polyhedra. In the case of $(NH_3)_3(H_2O)_2\{[(UO_2)_{10}O_{10}(OH)][(UO_4)(H_2O)_2]$, there are five uranyl square or pentagonal bipyramids and one distorted octahedron containing U^{6+}. The structure is dominated by sheets that are based upon the β-U_3O_8 anion topology that are topologically indistinguishable from the sheets in spriggite and ianthinite. The square sites of the anion topology are occupied by both uranyl square bipyramids and the distorted octahedra. Two additional uranyl pentagonal bipyramids share an edge, giving a dimer that is located in the interlayer between the sheets, and that provides direct linkages of the sheets into the framework structure. The NH_3 and H_2O groups are located in channels that extend through the framework parallel to the sheet of polyhedra.

The structure of $Pb(H_2O)[(UO_2)_{10}UO_{12}(OH)_6(H_2O)_6]$ is the only known Pb uranyl oxide hydrate with a framework structure. It was prepared by mild hydrothermal synthesis and has not yet been reported as a mineral species. It has both uranyl square and pentagonal bipyramids, as well as one U^{6+} site that is in a distorted octahedral coordination environment. The structure contains complex ribbons of vertex and edge-sharing uranium polyhedra that are closely related to those found linked into two dimensions in the curite sheet. However, in $Pb(H_2O)[(UO_2)_{10}UO_{12}(OH)_6(H_2O)_6]$ the ribbons are oriented with their widths in opposing directions, and they are connected into a framework. Channels extending through the framework contain the Pb cations as well as a H_2O group.

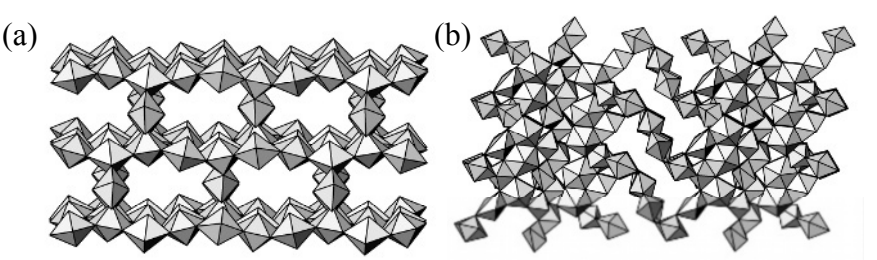

Figure 18. The frameworks of uranyl polyhedra that occur in the structures of $(NH_3)_3(H_2O)_2\{[(UO_2)_{10}O_{10}(OH)][(UO_4)(H_2O)_2]$ (a) and $Pb(H_2O)[(UO_2)_{10}UO_{12}(OH)_6(H_2O)_6]$ (b).

6. Uranyl Silicates

Uranyl silicates are an important group of minerals in the altered zones of many uranium deposits, and uranophane, the most common member of this group, is

the most abundant uranyl mineral in many occurrences [30]. Uranyl silicates have also received attention because they form when spent nuclear fuel interacts with water containing silicon under oxidizing conditions, such as those expected in the proposed repository for nuclear waste in Yucca Mountain, Nevada [32]. The structures are currently known for 15 uranyl silicates, of which ten are minerals (Table 2).

The most significant group of uranyl silicates is the uranophane group. The structures are known for seven members of this group, and in all cases they contain sheets of uranyl pentagonal bipyramids and silicate tetrahedra with the uranophane anion-topology. This anion topology (Fig. 19) contains pentagons, triangles and squares and is elegant in its simplicity. It contains chains of edge-sharing pentagons that are separated by chains of edge-sharing triangles and squares. The uranyl silicate sheet is derived from the anion topology by populating each of the pentagons with uranyl ions, giving uranyl pentagonal bipyramids, and each of the triangles correspond to the face of a silicate tetrahedron. It is important to note that the uranophane anion-topology is the basis for many sheets in addition to uranyl silicates [3].

Although members of the uranophane group of minerals all contain uranyl silicate sheets based upon the same anion topology, there are three different types of sheets that differ in the orientation of the silicate tetrahedra. α-uranophane [57], boltwoodite [58], cuprosklodowskite [59], sklodowskite [60] and kasolite [61] are contain sheets with the same orientations of silicate tetrahedra (Fig. 19b). All of these but kasolite contain acid silicate groups. Consider the chains of edge-sharing triangles and squares in the underlying anion topology. In this particular sheet, the tetrahedra alternate up and down along the chains of triangles and squares. Going along the length of any chain of edge-sharing pentagonal bipyramids in the sheet, all of the tetrahedra attached to one side of the chain point in one direction, while those on the opposite side of the chain point in the other direction. The sheet that occurs in oursinite [62] is different because all of the silicate tetrahedra attached to any chain of uranyl pentagonal bipyramids point in the same direction, even though the tetrahedra alternate up and down along the length of the chain of edge-sharing triangles and squares in the anion topology (Fig. 19c). The third type of sheet occurs in β-uranophane [63] (Fig. 19d). Along the chain of edge-sharing triangles and squares in the underlying anion topology, pairs of tetrahedra are oriented in the same direction, such that are two pointing up, followed by two pointing down. Tetrahedra attached to one side of the chains of uranyl pentagonal bipyramids alternate up and down along the chain length.

Table 2. Uranyl Silicates

Name	Formula	S. Gr.	*a* (Å)	*b* (Å)	*c* (Å)	Ref.
	Uranophane anion-topology					
α-uranophane	$Ca[(UO_2)(SiO_3OH)]_2(H_2O)_5$	$P2_1$	15.909	7.002	6.665	57
Boltwoodite	$(K_{0.56}Na_{0.42})[(UO_2)(SiO_3OH)](H_2O)_{1.5}$	$P2_1/m$	7.077	7.060	6.648	58
	$Cs[(UO_2)(SiO_3OH)]_2$	$P2_1/m$	7.4038	7.0774	6.6566	91
Cuprosklodowskite	$Cu[(UO_2)(SiO_3OH)]_2(H_2O)_6$	$P\bar{1}$	7.052	9.267	6.655	59
Sklodowskite	$Mg[(UO_2)(SiO_3OH)]_2(H_2O)_6$	$C2/m$	17.382	7.047	6.610	60
Kasolite	$Pb[(UO_2)(SiO_4)](H_2O)$	$P2_1/c$	6.704	6.932	13.252	61
Oursinite	$Co[(UO_2)(SiO_3OH)]_2(H_2O)_6$	$Cmca$	7.0494	17.550	12.734	62
β-uranophane	$Ca[(UO_2)(SiO_3OH)]_2(H_2O)_5$	$P2_1/a$	13.966	15.443	6.632	63
	Haiweeite anion-topology					
Haiweeite	$Ca[(UO_2)_2Si_5O_{12}(OH)_2](H_2O)_3$	$Cmcm$	7.125	17.937	18.342	64
	Frameworks					
Weeksite	$K_{1.26}Ba_{0.25}Ca_{0.12}[(UO_2)_2(Si_5O_{13})]H_2O$	$Cmmb$	14.209	14.248	35.869	65
Soddyite	$(UO_2)_2(SiO_4)(H_2O)_2$	$Fddd$	8.334	11.212	18.668	21
	$KNa_3(UO_2)_2(Si_4O_{10})_2(H_2O)_4$	$C2$	12.782	13.654	8.268	14
	$Na_4(UO_2)_2(Si_4O_{10})_2(H_2O)_4$	$C2/m$	12.770	13.610	8.2440	67
	$Na_2(UO_2)(SiO_4)$	$I4_1/acd$	12.718		13.376	68
	$RbNa(UO_2)(Si_2O_6).H_2O$	$P\bar{1}$	7.3668	7.8691	8.1766	69

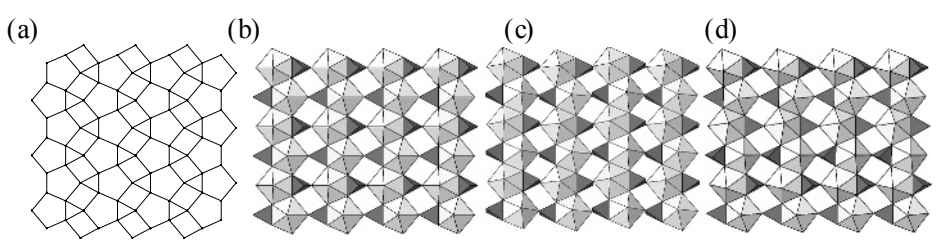

Figure 19. The uranophane anion-topology (a) and uranyl silicate sheets based upon this anion topology (b-d) which differ only in the orientations of the silicate tetrahedra.

The uranyl silicate minerals haiweeite [64] and weeksite [65] both contain the sheet of uranyl pentagonal bipyramids and silicate tetrahedra shown in Figure 20. Note that it contains the same chain of edge-sharing uranyl pentagonal bipyramids as the uranophane group of minerals, and that silicate tetrahedra are also attached to either side of this chain by sharing edges with the bipyramids. However, the haiweeite sheet contains more silicate tetrahedra, and the uranophane-type chains are not linked directly as in the uranophane group, but rather are linked through a crankshaft-like chain of linked silicate tetrahedra that extends parallel to the sheet. In haiweeite, the uranyl silicate sheets are connected through Ca sites in the interlayer, as well as through H bonds originating from H_2O groups in the interlayer. In weeksite, the sheets are actually connected through the sharing of vertices between silicate tetrahedra of the crankshaft-like chains in adjacent sheets, and the structure of weeksite is therefore a framework of polyhedra. Voids in the framework contains K, Ba and Ca cations, as well as H_2O groups.

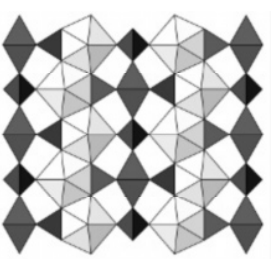

Figure 20. The sheet of uranyl pentagonal bipyramids and silicate tetrahedra that occurs in haiweeite and weeksite.

Soddyite [21] and the isostructural compound $[(UO_2)_2(GeO_4)(H_2O)]$ [66] contain uranyl pentagonal bipyramids that share equatorial edges, forming chains (Fig. 21). Each of the bipyramids also shares an edge with a tetrahedron. One of the equatorial vertices of each bipyramid in occupied by H_2O, and this vertex is not shared with another polyhedron. Each tetrahedron shares two of its edges with bipyramids on either side, and this links the chains of bipyramids into a framework. Additional linkages are provided by H bonds.

The compound $KNa_3[(UO_2)_2(Si_4O_{10})_2](H_2O)_4$ was found as an alteration phase on actinide-bearing borosilicate glass that had been treated under mild hydrothermal conditions [14]. $Na_4[(UO_2)_2(Si_4O_{10})_2](H_2O)_4$ was later synthesized [67], and the two compounds have identical uranyl silicate frameworks. There are sheets of vertex-sharing silicate tetrahedra that contain both four and eight-membered rings (Fig. 22). Adjacent silicate sheets are

linked through uranyl square bipyramids that have their uranyl ions aligned parallel to the silicate sheet. All four of the equatorial vertices of the bipyramids are also apical ligands of silicate tetrahedra from the sheets on either side. The K and Na cations, as well as the H_2O groups, are located in channels that pass through the structure.

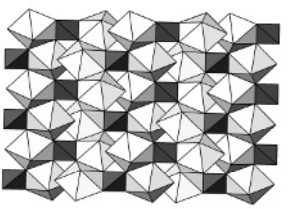

Figure 21. The framework of uranyl pentagonal bipyramids and silicate tetrahedra that occurs in soddyite.

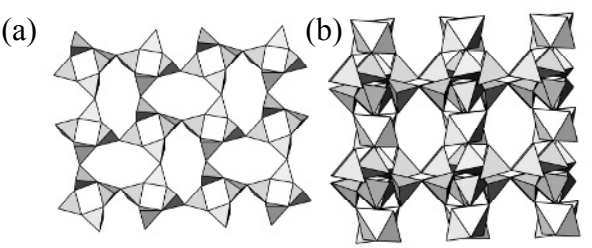

Figure 22. The sheet of silicate tetrahedra (a) connected into a framework (b) in the structures of $KNa_3[(UO_2)_2(Si_4O_{10})_2](H_2O)_4$ and $Na_4[(UO_2)_2(Si_4O_{10})_2](H_2O)_4$.

The structure of $Na_2[(UO_2)(SiO_4)]$ [68] contains U^{6+} in an unusual distorted octahedral coordination, with four short bonds (~2 Å) and two longer (~ 2.3 Å) bond lengths. Each octahedron shares four of its vertices with silicate tetrahedra, and the silicate tetrahedra are linked into four-membered rings. The Na cations are located in voids within the framework (Fig. 23a).

The compound $RbNa[(UO_2)(Si_2O_6)](H_2O)$ [69] has rings of four linked silicate tetrahedra, and these rings are linked into sheets that are parallel to (001) by sharing vertices with uranyl square bipyramids (Fig. 23b). Each of the equatorial ligands of any specific square bipyramid is shared with a tetrahedron from a different ring. The uranyl silicate sheets are linked into a framework through additional uranyl square bipyramids, such that the four vertices of the silicate tetrahedra are shared with two tetrahedra within the ring, and two

bipyramids. The Rb and Na cations and the H_2O group are located in relatively large voids within the framework.

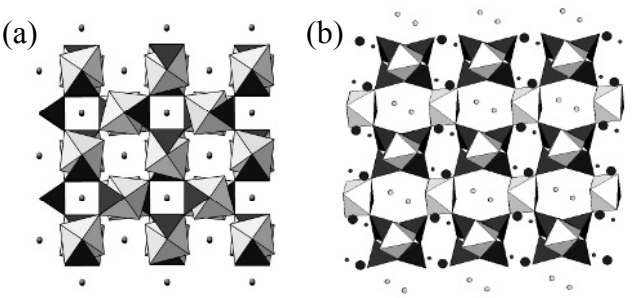

Figure 23. The uranyl silicate framework structures in $Na_2[(UO_2)(SiO_4)]$ (a) and $RbNa[(UO_2)(Si_2O_6)](H_2O)$ (b).

7. Uranyl Carbonates

Uranyl carbonate minerals are common in the altered zones of uranium deposits, and tend to be amongst the most soluble of the uranyl minerals. Currently, there are 22 known structures of uranyl carbonates, of which 12 correspond to minerals (Table 3). In slightly alkaline to alkaline groundwater the uranyl tricarbonate cluster, with formula $[(UO_2)(CO_3)_3]^{4-}$ is the dominant species, and uranyl minerals that form from such solutions contain the uranyl tricarbonate group as an isolated cluster.

Seventeen uranyl carbonates contain the isolated uranyl tricarbonate cluster shown in Figure 24. The cluster is composed of a uranyl hexagonal bipyramid that shares three equatorial edges with carbonate triangles, such that each equatorial vertex is shared between the uranyl polyhedron and one carbonate triangle. Most minerals that contain this cluster have relatively simple structures in which the uranyl tricarbonate clusters are linked through bonds to lower-valence cations, as well as by hydrogen bonds. The structure of schröckingerite [70] is more complex in that it also contains sulfate tetrahedra, and the tetrahedra and uranyl carbonate clusters are linked through an array of bonds to Na and Ca.

Five uranyl carbonate minerals are known that contain sheets of uranyl polyhedra and carbonate triangles. These minerals probably form from circum-neutral to somewhat acidic solutions where the uranyl tricarbonate cluster does not dominate. Each of the uranyl carbonate sheets are shown in Figure 25-29.

Wyartite is the only mineral known to contain pentavalent uranium, although several synthetic compounds are known to contain uranium in this valence state

Table 3. Uranyl Carbonates

Name	Formula	S. Gr.	*a* (Å)	*b* (Å)	*c* (Å)	Ref
	Uranyl tricarbonate cluster					
Liebigite	$Ca_2[(UO_2)(CO_3)_3](H_2O)_{11}$	*Bba*2	16.699	17.557	13.697	76
Schröckingerite	$NaCa_3[(UO)_2(CO_3)_3](SO_4)F(H_2O)_{10}$	$P\bar{1}$	9.634	9.635	14.391	70
Bayleyite	$Mg_2[(UO_2)(CO_3)_3](H_2O)_{18}$	$P2_1/a$	26.560	15.256	6.505	77
Swartzite	$CaMg[(UO_2)(CO_3)_3](H_2O)_{12}$	$P2_1/m$	11.080	14.634	6.439	78
Andersonite	$Na_2Ca[(UO_2)(CO_3)_3](H_2O)_5$	$R\bar{3}m$	17.904		23.753	79
Grimselite	$K_3Na[(UO_2)(CO_3)_3](H_2O)$	*P*-62*c*	9.302		8.260	80
Čejkaite	$Na_4[(UO_2)(CO_3)_3]$	$P\bar{1}$	9.291	9.292	12.895	81
	$Rb_6Na_2[(UO_2)(CO_3)_3]_2(H_2O)$	*P*-62*c*	9.4316		8.3595	82
	$Cs_4[(UO_2)(CO_3)_3](H_2O)_6$	$P2_1/n$	18.723	9.647	11.297	83
	$Sr_2[(UO_2)(CO_3)_3](H_2O)_8$	$P2_1/c$	11.379	11.446	25.653	84
	$(NH_4)_4[(UO_2)(CO_3)_3]$	*C*2/*c*	10.679	9.373	12.850	85
	$Na_4[(UO_2)(CO_3)_3]$	$P\bar{3}c1$	9.342		12.824	86
	$Ca_5[(UO_2)(CO_3)_3]_2(NO_3)_2(H_2O)_{10}$	$P2_1/n$	6.5729	16.517	15.195	87
	$Ca_6[(UO_2)(CO_3)_3]_2Cl_4(H_2O)_{19}$	*P4/mbm*	16.744		8.136	87
	$Ca_{12}[(UO_2)(CO_3)_3]_4Cl_8(H_2O)_{47}$	$Fd\bar{3}$	27.489			87
	$Cs_4[(UO_2)(CO_3)_3]$	*C*2/*c*	11.513	9.6037	12.9177	88
	$K_2Ca_3[(UO_2)(CO_3)_3]_2(H_2O)_6$	*Pnnm*	17.015	18.048	18.394	89
	Miscellaneous sheets					
Wyartite	$CaU^{5+}(UO_2)_2(CO_3)O_4(OH)(H_2O)_7$	$P2_12_12_1$	11.271	7.105	20.807	71
Fontanite	$Ca[(UO_2)_3(CO_3)_2O_2](H_2O)_6$	$P2_1/n$	6.968	17.276	15.377	72
Roubaultite	$[Cu_2(UO_2)_3(CO_3)_2O_2(OH)_2](H_2O)_4$	$P\bar{1}$	7.767	6.924	7.850	73
Rutherfordine	$[UO_2CO_3]$	*Imm*2	4.840	9.273	4.298	74
Bijvoetite	$[M^{3+}(H_2O)_{25}(UO_2)_{16}O_8(OH)_8(CO_3)_{16}](H_2O)_{14}$	*B*12$_1$1	21.234	12.958	44.911	75

[71]. The sheet in the structure of wyartite contains square and pentagonal bipyramids that are occupied by U^{6+}, pentagonal bipyramids that contain U^{5+}, and carbonate triangles (Fig. 25). The sheets are closely related to those with the β-U_3O_8 sheet anion-topology found in the structures of spriggite and

ianthinite. One of the pentagonal bipyramids of the sheet of polyhedra contains U^{5+}, and this polyhedron shares an edge with the carbonate triangle, which extends into the interlayer. Linkage between the sheets is provided by Ca and H_2O in the interlayer.

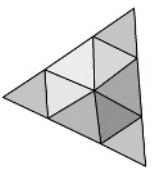

Figure 24. The $(UO_2)(CO_3)_3$ cluster that occurs in 17 uranyl carbonates.

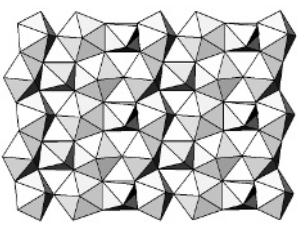

Figure 25. The uranyl carbonate sheet that occurs in the structure of wyartite. The carbonate triangles are shown in black, and are almost perpendicular to the page.

The structure of fontanite [72] contains the novel sheet of uranyl pentagonal and hexagonal bipyramids and carbonate triangles shown in Figure 26. This sheet is based upon the well-known phosphuranylite anion-topology that is the basis for several uranyl phosphate and uranyl selenite mineral structures. However, fontanite represents the only example of a uranyl carbonate sheet with this topology. Both the pentagons and the hexagons of the anion topology are populated by uranyl ions, which gives chains containing edge-sharing dimers of pentagonal bipyramids that are linked through the hexagonal bipyramids. The carbonate triangles are located in the triangles of the anion topology, where they share an edge with a uranyl hexagonal bipyramid and the other vertex with a uranyl pentagonal bipyramid of an adjacent chain of bipyramids. The sheets are linked through bonds to Ca atoms located in the interlayer, as well as through H bonds to H_2O groups in the interlayer.

Roubaultite [73] contains the sheet illustrated in Figure 27b, and its underlying anion-topology is shown in Figure 27a. This sheet is rather similar to the fontanite sheet. Both contain the same chain of uranyl pentagonal and hexagonal bipyramids, and CO_3 triangles. In the fontanite sheet, these chains

are linked directly through the carbonate triangle. The roubaultite sheet also contains chains formed by the sharing of edges between octahedra containing Cu^{2+}, and the uranyl carbonate chains are separated by and linked through these chains of octahedra on either side. Linkages between the sheets are though H bonds from H_2O groups located in the interlayer.

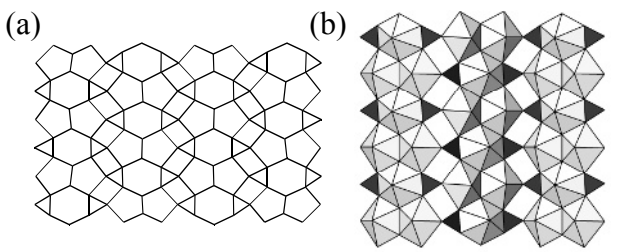

Figure 26. The uranyl carbonate sheet from the structure of fontanite (b), which is based upon the phosphuranylite anion-topology (a).

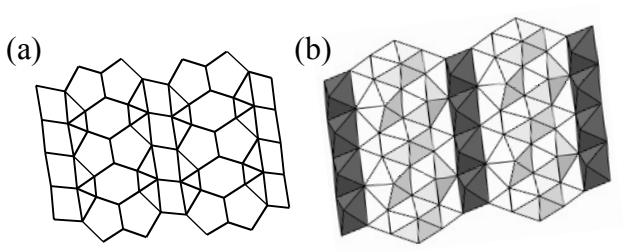

Figure 27. The uranyl carbonate sheet from the structure of roubaultite, which incorporates chains of edge-sharing Cu polyhedra (b), and its underlying sheet anion-topology (a).

Rutherfordine [74] contains the sheet of uranyl hexagonal bipyramids and carbonate triangles shown in Figure 28b, with the corresponding sheet anion-topology shown in Figure 28a. The anion topology contains chains of edge-sharing hexagons that are connected in the second dimension by the sharing of vertices, with adjacent chains separated by triangles. Each of the hexagons in the anion topology is populated by a uranyl ion, giving hexagonal bipyramids. Triangles in the anion topology occur as pairs with a common edge, and only one of the triangles of each of these pairs contains a carbonate triangle. The interlayer in rutherfordine is empty.

Bijvoetite [75] possesses the most complex uranyl carbonate sheet (Fig. 29). The sheet contains both uranyl pentagonal and hexagonal bipyramids. Dimers

of hexagonal bipyramids result from the sharing of an equatorial edge, and these dimers are oriented perpendicular to a chain formed by the linkage of the dimers through sharing edges with pentagonal bipyramids. Carbonate triangles are attached to either side of this chain by sharing edges with the hexagonal bipyramids, resulting in a novel uranyl carbonate chain. These chains are linked into sheets through irregular coordination polyhedra about trivalent cations, which correspond to Y and various rare earth elements.

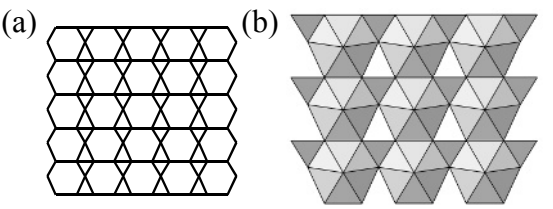

Figure 28. The uranyl carbonate sheet in the structure of rutherfordine (b) and its sheet anion topology (a).

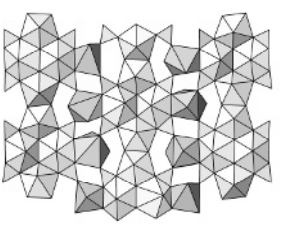

Figure 29. The uranyl carbonate sheet, which also contains Y^{3+} polyhedra, in the structure of bijvoetite.

References

1. P.C. Burns, Can. Mineral., 36 (1998) 847.
2. P.C. Burns, M.L. Miller and R.C. Ewing, R.C., Can. Mineral., 34 (1996) 845-880.
3. P.C. Burns, Can. Mineral. (2005, in press).
4. A.J. Locock and P.C. Burns, J. Solid State Chem., 163 (2002) 275.
5. S.V. Krivovichev, C.L. Cahill and P.C. Burns, Inorg. Chem., 41 (2002) 34.
6. S.V. Krivovichev and P.C. Burns, J. Solid State Chem., 168 (2002) 245.
7. P.M. Almond, M.K. McKee and T.E. Albrecht-Schmitt, Angew. Chem. Int. Ed., 41 (2002), 3426.
8. P.C. Burns, K.A. Hughes Kubatko, G. Sigmon, B.J. Fryer, J.E. Gagnon, M.R. Antonio and L. Soderholm, Angew. Chem. Int. Ed, 44 (2005) 2135.
9. S.V. Krivovichev, V. Kahlenberg, I.G. Tananaev, R. Kaindl, E. Mersdorf and B.F. Myasoedov, J. Amer. Chem. Soc., 127 (2005) 1072.
10. S.V. Krivovichev, V. Kahlenberg, R. Kaindl, E. Mersdorf, I.G. Tananaev and B.F. Myasoedov, Angew. Chem. Int. Ed., 44 (2005) 1134.

11. E.C. Buck, N.R. Brown amd N.L. Dietz, Env. Sci. Technol., 30 (1996) 81.
12. Y. Roh, S.R. Lee, S.K. Choi, M.P. Elles and S.Y. Lee, Soil Sed. Contam., 9 (2000) 463.
13. Y. Li and P.C. Burns, J. Nucl. Mater., 299 (2001) 219-226.
14. P.C. Burns, R.A. Olson, R.J. Finch, J.M. Hanchar and Y. Thibault, Y., J. Nucl. Mater., 278 (2000) 290.
15. K.A.Hughes Kubatko, K.B. Helean, A. Navrotsky and P.C. Burns, Science, 302 (2003) 1191.
16. P.C. Burns, K.M. Deely and S. Skanthakumar, Radiochim. Acta, 92 (2004) 151.
17. C. Frondel, Systematic mineralogy of uranium and thorium. U.S. Geological Survey Bulletin, 1064, 1958.
18. D.J. Wronkiewicz, J.K. Bates, S.F. Wolf and E.C. Buck, J. Nucl. Mater., 238 (1996) 78.
19. P.C. Burns, R.C. Ewing and F.C. Hawthorne, Can. Mineral., 35 (1997) 1551.
20. P.C. Burns, Can. Mineral., 39 (2001) 1139.
21. F. Demartin, C.M. Gramaccioli and T. Pilati, Acta Crystallogr., C48 (1992) 1.
22. P.C. Burns, Rev. Mineral., 38 (1999) 23.
23. S.V. Krivovichev and P.C. Burns, Zeit. fur Kristallogr., 218 (2003) 725-752.
24. S.V. Krivovichev, Crystallogr. Rev., 10 (2004) 185.
25. M.L. Miller, R.J. Finch, P.C. Burns and R.C. Ewing, J. Mater. Res., 11 (1996) 3048.
26. P.C. Burns, Amer. Mineral., 82 (1997) 1176.
27. P.C. Burns, Amer. Mineral., 84 (1999) 1661.
28. I.D. Brown, The bond-valence method: an empirical approach to chemical structure and bonding. In Structure and Bonding in Crystals II (M. O'Keeffe and A. Navrotsky, eds.), Academic Press, New York, 1981.
29. M. Schindler and F.C. Hawthorne, Can. Mineral., 42 (2004) 1601.
30. R.J. Finch and R.C. Ewing, J. Nucl. Mater., 190 (1992) 133.
31. P.A. Finn, J.C. Hoh, S.F. Wolf, S.A. Slater and J.K. Bates, Radiochim. Acta, 74 (1996) 65.
32. R.J. Finch, E.C. Buck, P.A. Finn and J.K. Bates, Materials Research Society Symposium Proceedings, 556 (1999) 431.
33. S. Siegel, H. Hoekstra and E. Gebert, Acta Crystallogr., B28 (1972) 3469.
34. J.C. Taylor amd M.J. Bannister, Acta Crystallogr., B28 (1972) 2995.
35. P.C. Burns and Y. Li, Amer. Mineral., 87 (2002) 550.
36. P.C. Burns, Can. Mineral., 36 (1998) 1061.
37. M.K. Pagoaga, D.E. Appleman and J.M. Stewart, Am. Mineral., 72 (1987) 1230.
38. P.C. Burns, Can. Mineral., 36 (1998) 187.
39. P.C. Burns and J.M. Hanchar, Can. Mineral., 37 (1999) 1483.
40. C.L. Cahill and P.C. Burns, Amer. Mineral., 85 (2000) 1294.
41. Y. Li and P.C. Burns, Can. Mineral., 38 (2000) 737.
42. R.J. Finch, M.A. Cooper, F.C. Hawthorne and R.C. Ewing, Can. Mineral., 34 (1996) 1071.
43. M.T. Weller, M.E. Light and T. Gelbrich, Acta Crystallogr., B56 (2000) 577.
44. J. Brugger, S.V. Krivovichev, P. Berlepsch, N. Meisser, S. Ansermet and T. Armbruster, Am. Mineral., 89 (2004) 339.
45. P.C. Burns, R.J. Finch, F.C. Hawthorne, M.L. Miller and R.C. Ewing, J. Nucl. Mater., 249 (1997) 199-206.
46. Y. Li and P.C. Burns, Can. Mineral., 38 (2000) 727.
47. P.C. Burns and F.C. Hill, Can. Mineral., 38 (2000) 175.
48. P. Piret, M. Deliens, J. Piret-Meunier and G. Germain, Bull. Minéral., 106 (1983) 299.
49. L.M. Kovba, Sh. Struk. Khim., 13 (1972) 256.
50. A. Rosenzweig and R.R. Ryan, Cryst. Struct. Commun., 6 (1977) 53.
51. P.C. Burrns and K.M. Deely, Can. Mineral., 40 (2002) 1579.
52. P.C. Burns and F.C. Hill, Can. Mineral., 38 (2000) 163.
53. R.E. Glatz, Y. Li, K.A. Hughes,C.L. Cahill and P.C. Burns, Can. Mineral., 40 (2002) 217.

54. J.C. Taylor, Acta Crystallogr., B27 (1971) 10881.
55. C.L. Cahill and P.C. Burns, Chem. Mater., 13 (2001) 4026.
56. Y. Li and P.C. Burns, Can. Mineral., 38 (2000) 1433.
57. D. Ginderow, Acta Crystallogr., C44 (1988) 421.
58. P.C. Burns, Can. Mineral., 36 (1998) 1069.
59. A. Rosenzweig and R.R. Ryan, Am. Mineral., 60 (1975) 448.
60. R.R. Ryan and A. Rosenzweig, Cryst. Struct. Commun., 6 (1977) 611.
61. A. Rosenzweig and R.R. Ryan, Cryst. Struct. Commun., 6 (1977) 617.
62. K.A. Kubatko and P.C. Burns, Amer. Mineral., 91 (2006) 333.
63. K. Viswanathan and O. Harneit, Am. Mineral., 71 (1986) 1489.
64. P.C. Burns, Can. Mineral., 39 (2001) 1153.
65. J.M. Jackson and P.C. Burns, Can. Mineral., 39 (2001) 187.
66. J.P. Legros and Y. Jeannin, Acta Crystallogr., B31 (1975) 1140.
67. Y. Li and P.C. Burns, J. Nucl. Mater., 299 (2001) 219.
68. D.P. Shashkin, E.A. Lur'e and N.V. Belov, Kristallografiya, 19 (1974) 958.
69. X. Wang, J. Huang, L. Liu and A.J. Jacobson, J. Mater. Chem., 12 (2002) 406.
70. K. Mereiter, Tschermaks Mineral. Petrogr. Mitt., 35 (1986) 1.
71. P.C. Burns and R.J. Finch, Amer. Mineral., 84 (1999) 1456-1460.
72. K.A. Hughes and P.C. Burns, Amer. Mineral., 88 (2003) 962.
73. D. Ginderow and F. Cesbron, Acta Crystallogr., C41 (1985) 654.
74. R.J. Finch, M.A. Cooper, F.C. Hawthorne and R.C. Ewing, Can. Mineral., 37 (1999) 929.
75. Y. Li, P.C. Burns and R.A. Gault, Can. Mineral., 38 (2000) 153.
76. K. Mereiter, Tschermaks Mineral. Petrogr. Mitt., 30 (1982) 277.
77. H. Mayer and K. Mereiter, Tschermaks Mineral. Petrogr. Mitt., 35 (1986) 133.
78. K. Mereiter, Tschermaks Mineral. Petrogr. Mitt., 30 (1982) 129.
79. K. Mereiter, Akad. Wiss. Math.-Naturwiss. Kl., 3 (1986) 39.
80. Y. Li and P.C. Burns, Can. Mineral., 39 (2001) 1147.
81. P. Ondrus, R. Skala, F. Veselovsky, J. Sejkora and C. Vitti, Am. Mineral., 88 (2003) 686.
82. K.A. Hughes and P.C. Burns, Acta Crystallogr., C60 (2003) i25.
83. K. Mereiter, Acta Crystallogr., C44 (1988) 1175.
84. K. Mereiter, Acta Crystallogr., C42 (1986) 1678.
85. V.N. Serezhkin, M.A. Soldatkina and N.V. Boiko, J. St. Chem., 24 (1983) 770.
86. Y. Li, S.V. Krivovichev and P.C. Burns, Mineral. Mag., 65 (2001) 285.
87. Y. Li and P.C. Burns, J. Solid State Chem., 166 (2002) 219.
88. S.V. Krivovichev and P.C. Burns, Radiochem., 46 (2004) 12.
89. S.V. Krivovichev and P.C. Burns, Radiochem., 46 (2004) 16.
90. F.C. Hill and P.C. Burns, Can. Mineral., 37 (1999) 1283.
91. P.C. Burns, J. Nucl. Mater., 265 (1999) 218.

Structural Chemistry of Inorganic Actinide Compounds
S.V. Krivovichev, P.C. Burns & I.G. Tananaev (Editors)

Chapter 2

Some features of stereochemistry of U(VI)

Victor N. Serezhkin

Department of Chemistry, Samara State University, Ac. Pavlov Street 1, 443011 Samara, Russia

1. Introduction

The stereochemistry and crystal chemistry of uranium was born in 1927 when Goldschmidt and Thomassen [1] published experimental data on the structure of UO_2, which was the first structurally characterized uranium compound. However, systematic structural studies of uranium compounds started later, during the process of exploitation of nuclear energy. Structure data accumulated in this period were published only in 1948 and served as the basis for subsequent crystal chemical investigations. At the present day, structures of more than 3000 uranium compounds are known, including minerals, inorganic, coordination, and organometallic compounds. Our analysis of the information extracted from structure databases [2, 3] indicates (Fig. 1) that, since 1950, structural data on uranium compounds are accumulating with an increasing speed. Every year, more than 100 uranium minerals and inorganic compounds are structurally characterized.

As is well-known, the electronic structure of the U valence electron shell is $5f^3 6d^1 7s^2$, which allows uranium to possess the II, III, IV, V, and VI formal oxidation states. The latter is the most stable under atmospheric conditions and has been realized in many compounds that contain approximately linear uranyl ions, UO_2^{2+}. Thus it is not surprising that most of structurally characterized uranium compounds contain uranyl ions.

At the present time, it is generally acknowledged that, in uranyl ions, uranium-oxygen bonds have a strong covalent character and are interpreted as double bonds in a classical model and as triple bonds in a quantum chemical model of interatomic interaction. The structure of the uranyl ion is almost linear, - in contrast to other known dioxocations such as MoO_2^{2+} or WO_2^{2+}, for which

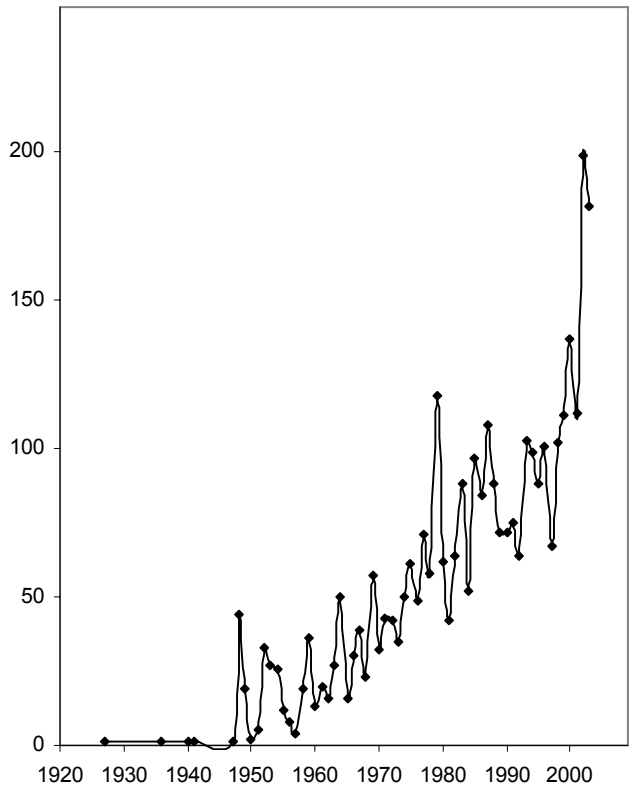

Figure 1. Number of crystal-structure determinations of U compounds (N) versus the year of publication.

O-*A*-O ≈ 102-114° (*A* = Mo, W). This is generally explained on the basis of quantum mechanical calculations. According to these results, electronic configuration of U atoms in uranyl ions is either $5f^{2,6}6d^{0,8}$ [4] or $5f^{2,4}6d^{1,2}$ [5] and is essentially the same as electronic configuration of the ground state of the U^{2+} ion ($5f^{3}6d^{1}$). Thus the linear structure of the uranyl ion is energetically favorable and involves *fd*-hybridization of uranium electronic orbitals. In contrast, for the MoO_2^{2+} and WO_2^{2+} ions, the A^{2+} ions have their ground states as $(n\text{-}1)d^4$ and the first excited state as $(n\text{-}1)d^3ns^1$, which determines the angular structure of the dioxocations due to the *ds*-hybridization of the electronic orbitals [6]. The main alternative view on the structure of the uranyl ion has been recently suggested in [7]. Using the Walsh diagrams constructed on the basis of extended Hückel method calculations, these authors determined that the increase of the O-U-O angle in the uranyl ion from 100 to 180° decreases the

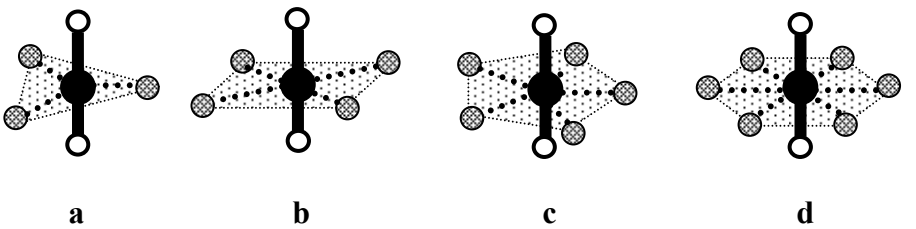

Figure 2. Schemes of the UO_2X_n coordination polyhedra with n = 3 (a), 4 (b), 5 (c) and 6 (d). Legend: U atoms are black circles; O atoms of the uranyl ions are white circles; equatorial X atoms are grey circles. The coordination U-X bonds and equatorial planes perpendicular to the O=U=O lines are dotted.

energy of the highest occupied molecular orbital (HOMO) dramatically (by 0.9 eV), whereas the total energy of all other orbitals increases by 0.3 eV only.

The valence requirements of the U(VI) atoms are not satisfied by the formation of the uranyl ions. Thus the U(VI) atoms are able to form from 3 to 6 additional bonds to the *X* atoms of various inorganic or organic ligands. Without regard to the number and chemical nature of the *X* atoms, they have their positions in the plane perpendicular to the linear uranyl ions. In U(VI) stereochemistry, this plane is regarded as equatorial and the *X* atoms as equatorial ligands. With addition of the equatorial ligands, the U(VI) atoms have coordination of either trigonal (UO_2X_3), square (UO_2X_4), pentagonal (UO_2X_5), or hexagonal (UO_2X_6) bipyramids, which are flattened along the apical axes (Fig. 2). The *X* anions may be represented by the F, Cl, Br, O, S, Se, N, or C atoms. However, in most known U(VI) compounds, the uranyl ions are coordinated by O atoms. Since the U(VI) oxocompounds are the main object of this chapter, we shall define the uranium-oxygen bonds within the uranyl ions as r(U=O), and the equatorial bonds as r(U-O).

With respect to the crystal chemical role of equatorial O atoms in uranyl bipyramids, the U(VI) compounds can be subdivided into two groups. In the first group, the O atoms can be considered as O^{2-} anions bonded to metal atoms only (including the U(VI) atoms). These compounds are either simple (such as UO_3) or mixed oxides such as Na_2UO_4, Na_4UO_5, $Cs_2U_2O_7$, and $Cs_4U_5O_{17}$. The other group consists of complex or coordination uranyl compounds, where equatorial O atoms of uranyl bipyramids form strong covalent bonds to non-metal atoms (C, N, S, H, etc.) and therefore constitute parts of polyatomic acido- (e.g. CO_3^{2-}, NO_3^-, SO_4^{2-}, OH^-) or electroneutral (e.g. carbamide, acetamide, H_2O) ligands.

In mixed oxides, which are usually called uranates, the U(VI) atoms constitute parts of some oxoanions such as UO_4^{2-}, UO_5^{4-}, $U_2O_7^{2-}$, etc. In most of these anions (that, as a rule, have a polymeric structure), one can formally subdivide

uranyl cations. For instance, in the structure of Na_2UO_4 {79423: here and in the following we give in brackets the Inorganic Crystal Structure Database (ICSD) or Cambridge Structure Database (CSD) registration numbers of the compound under discussion}, the U(VI) atoms have a coordination number (*CN*) of 6 and form two short (1.90 Å) and four long (2.19 Å) U-O bonds. However, there are uranates in which coordination of the U(VI) atoms can be characterized as 'anti-uranyl'. For example, the structure of Na_4UO_5 {68360} contains the U(VI) atom with *CN* = 6 and coordination consisting of four short (2.03 Å) and two long (2.32 Å) U-O bonds. Other uranates are known with the U(VI) coordination without clear uranyl ions. Some examples are α-Li_6UO_6 {48209}, α-Ca_3UO_6 {35457} and Cr_2UO_6 {15133}, where each U(VI) atom forms six equal bonds with r(U-O) ≈ 2.07(1) Å. As a result, the UO_6 polyhedron has a configuration of almost a regular octahedron and not of a flattened square UO_2O_4 bipyramid.

In the structures of U(VI) coordination compounds, uranium is usually present in the form of uranyl ions UO_2^{2+}, which is reflected in the accepted formulas of these compounds, e.g. $UO_2(NO_3)_2.6H_2O$, $UO_2SO_4.2{,}5H_2O$, $K_2UO_2(SO_4)_2.2H_2O$, etc. In general, the composition of coordination compounds can be described by the formula $R_c[(UO_2)_d\sum_i L_i]\cdot nL_j$, where R are outer sphere cations; L_i are ligands in the first coordination sphere; L_j are acidic or electroneutral ligands of the outer sphere; c, d, and n are stoichiometric indices. As a rule, uranyl compounds are described in terms of the $[(UO_2)_d\sum_i L_i]^{z\pm}$ complexes. Depending upon nature and numbers of the L_i ligands, these complexes can be either electroneutral (e.g. $[UO_2SO_4(H_2O)_2]$) or positively charged (e.g. $[UO_2(H_2O)_5]^{2+}$). In most coordination compounds, there are well-defined uranyl ions. However, in some compounds it is impossible to clearly identify uranyl ions. For instance, in the structure of hexakis(neopentoxy)uranium(VI) {XEBVOP}, uranium atoms have sixfold coordination consisting of six equivalent bonds with r(U-O) = 2.00 Å.

Depending upon number and chemical nature of oxygen-containing ligands, the equatorial r(U-O) bond lengths in the UO_n bipyramids are in the range of 2.1 – 2.6 Å [8] and are significantly longer than the r(U=O) bonds, which are usually in the range from 1.7 to 1.9 Å. According to existing knowledge, the difference between the U=O and U-O bond lengths within the UO_n polyhedra is due to the fact that, in addition to the electrostatic interactions, there are complementary donor-acceptor interactions between the uranyl ions and the equatorial O atoms (i.e. interactions between lone electron pairs on the O atoms and vacant orbitals of the U atoms). Since O atoms of the uranyl ions also have lone electron pairs, they compete with equatorial O atoms in interactions via a donor-acceptor mechanism. The differing ability of uranyl and equatorial O atoms to interact

with uranium determines observed variations in the U-O bond lengths within the UO_n polyhedra.

The influence of the electron-donor properties of equatorial ligands L upon the strength of the U-L and U=O bonds mentioned above helps to interpret the scheme of ligand replacement in the uranyl coordination sphere. This scheme is also known as the Chernyaev-Schelokov row [8, 9]. In this row, part of which is shown in scheme (1), relative position of ligands is determined by the formation constants of uranyl complexes in aqueous solutions. According to [9, 10], ligands on the left side of the row form stronger U-L bonds. Thus, ligands on the left side will replace ligands on the right side from the equatorial plane of the uranyl ions.

$$\begin{aligned} &O_2^{2-} \geq CO_3^{2-} \geq OH^- \geq F^- \geq C_2O_4^{2-} \geq CH_3COO^- \geq SO_4^{2-} \\ &\geq NCS^- \geq NO_3^- \geq Cl^- \geq Br^- \geq I^- \\ &OC(NH_2)_2 \geq OS(CH_3)_2 \geq \ldots\ldots \geq H_2O \end{aligned} \qquad (1)$$

In the framework of the covalent model of uranyl complexes [11, 12], the difference between the U=O and U-O bonds is explained by their multiplicity (n_{UO}), which in turn depends upon force constant of the interaction between U and O (K). The K value can be determined from vibrational spectra. The n_{UO} parameter can be calculated from the equation:

$$n_{UO} = 0.303\ K + 0.18\ . \qquad (2)$$

In accord with [11, 12], the calculated n_{UO} values for different ligands can be used to estimate electron-donor properties of ligands. If one arranges ligands according to the decreasing n_{UO} value, the resulting row is in almost perfect agreement with the Chernyaev-Schelokov row. The row of the electron-donor ability of ligands in coordination uranyl compounds has been obtained from the infra-red (IR) vibrational spectra for CN_U = 7 and 8 (Suglobov row) and is shown in schemes (3) and (4).

$$КЧ_U=8 \qquad O_2^{2-} > CO_3^{2-} > CH_3COO^- > NO_3^- > ClO_4^- > BF_4^- \qquad (3)$$

$$КЧ_U=7 \qquad OH^- > F^- > Py > SO_4^{2-} > PyNO > DMFA > NCS^- > H_2O\ . \qquad (4)$$

It is worthy to note that the Chernyaev-Schelokov and Suglobov rows can be used not only in classification of experimental data but also in prediction of the interplay between composition and structure for many different uranyl complexes. However, as to our knowledge, there were no attempts made in understanding chemical factors that determine coordination number of uranium in uranyl complexes (i.e. 5, 6, 7, or 8). However, this question is of primary importance for us and was considered in detail in [13, 14]. In these works, we have used a new stereoatomic model of crystal structures which we shall briefly outline in the following section.

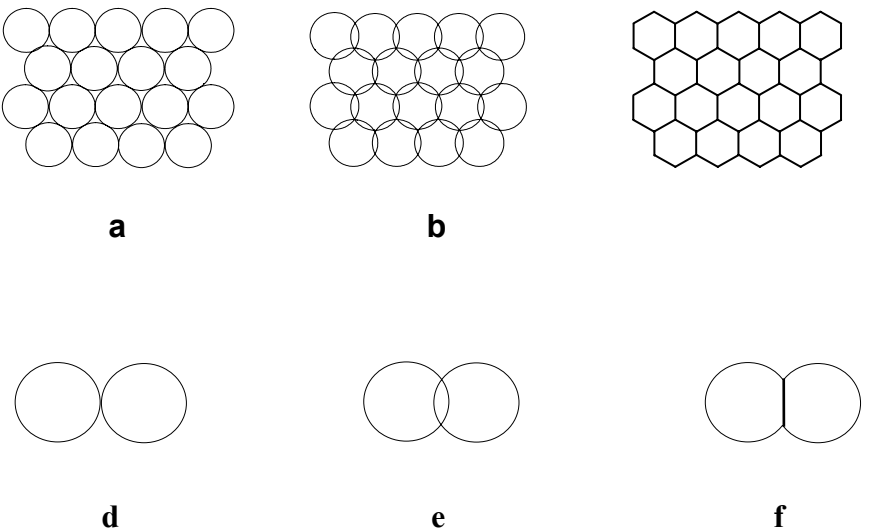

Figure 3. 2D crystal lattice considered as a closest sphere packing (a), plane covering by equal circles (b) and corresponding Voronoi-Dirichlet partition (c). During the formation of closest packing, two adjacent 'hard-sphere' atoms can touch each other only (d), whereas in formation of covering and partition they overlap (e) and deform (f), respectively.

2. Basic principles of stereoatomic model of crystal structures

In one of the theoretical models of classical crystal chemistry, atoms are considered as rigid spheres with radius depending upon chemical nature of atoms and the nature of the chemical bonds they form (covalent, ionic, van der Waals, etc.). In accordance with the principle of maximal filling of space, crystal structure can be modeled as periodic packing of rigid spheres that do not overlap (Fig. 3a). In stereoatomic model of crystals [13-24], their structure is considered as partition of the 3D space (Fig. 3c) where geometrical images of atoms are their Voronoi-Dirichlet (VD) polyhedron. The VD polyhedron of a given atom A is defined as follows. At first, the atom is linked to its neighbors by line segments. Then planes perpendicular to these segments are constructed which intersect the segments at the middle points. A convex polyhedron formed by these planes is a VD polyhedron. Each crystallographically independent atom in a structure has its own strictly defined VD polyhedron. Since each point of space belongs to at least one VD polyhedron, the structure can be considered as a covering of space by VD polyhedra. The difference between packing, covering and partition is demonstrated in Fig. 3 using a hexagonal 2D lattice as

an example. In general, the VD polyhedron of atom A has the composition AX_nZ_m, where X are atoms that form chemical bonds to A, and Z are atoms with VD polyhedra having common faces with the VD polyhedron of A but no chemical bonds to A (these contacts will be denoted as A/Z). Thus the total number of faces of the VD polyhedron (N_f) is equal to n + m, where n is the coordination number of A, and m is the number of non-bonding A/Z contacts. The number of faces, form and volume (V_{VDP}) of the VD polyhedron is uniquely determined by its position in the structure. As a linear parameter that characterizes dimensions of atoms in the structure, we shall use radius of the sphere, R_{SD}, with its volume equal to V_{VDP}. Each face of the VD polyhedron corresponds to a certain kind of interatomic interaction. In classical crystal chemistry, interactions between A and its neighbors Y are quantitatively studied using the interatomic distances r(A-Y_i). The use of VD polyhedra allows one to characterize each A-Y_i interaction by three additional parameters: area of the common face (S_i) between the A and Y_i VD polyhedra; solid angle (Ω_i) corresponding to the common face; volume of the bipyramid with apical vertices in A and Y_i and equatorial vertices being the vertices of the common face. The sum of the Ω_i values for all faces is equal to 4π. In the following, we shall express the Ω_i values not in steradians but in percents from 4π.

Thus, in contrast to the usual geometrical models of the crystal structure (e.g. packing of rigid spheres), the A-Y chemical bond has a 3D image and can be described by the above mentioned bipyramid with A and Y being its apical vertices [13-14, 19]. Basic characteristics of this bipyramid are its height which is equal to the interatomic distance r(A-Y), and the Ω_i solid angle.

It is essential that the stereoatomic model take into account not only the first but also the second coordination sphere of an atom. To subdivide the interatomic interactions of the A atom into bonding (A-X) and non-bonding (A/Z), the method of intersecting spheres has been employed [15]. Using this approach, each atom in the structure is approximated by two spheres centred at A and having radii R_{SD} and r_S. The A(R_{SD}) sphere characterizes the chemically bonded atom (its radius is defined as above), whereas the A(r_S) sphere corresponds to the isolated (not bonded) atom. The radius r_S is constant for a given element and is equal to its Slater quasi-orbital radius. According to [15], two atoms are chemically bonded when two (Π_2), three (Π_3) or four (Π_4) of their spheres intersect (Fig. 4). Overlap of the outer spheres (Π_1) or the absence of any overlap (Π_0) are considered as van der Waals bonds and are not taken into account when calculating the coordination number of the interacting atoms. Table 1 provides results of analysis of U(VI) coordination in some structures using the method of intersecting spheres. The VD polyhedra of the U atoms in these structures are shown in Fig. 5.

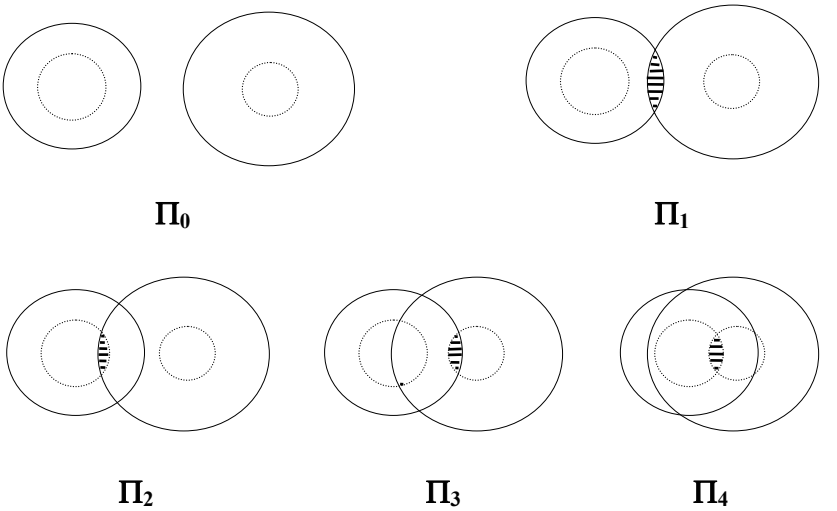

Figure 4. Schematic representation of five possible type of overlap (intersection) of bispheric 'atoms' [15]. The overlap fields are lined. The subscript indices show the sum of overlaps which can vary from 0 (type Π_0) to 4 (type Π_4).

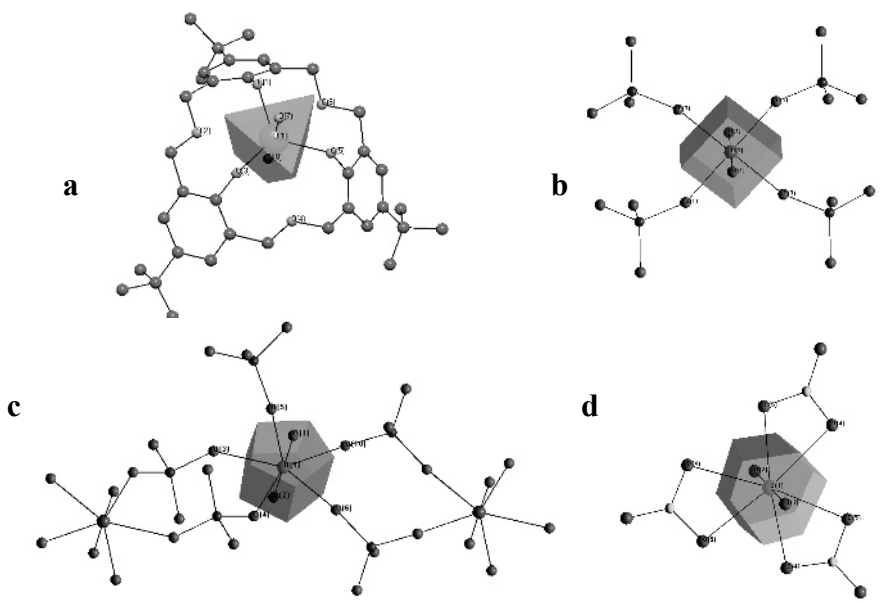

Figure 5. VD polyhedra of the U(VI) atoms with CN = 5, 6, 7, and 8 in $\{NH(C_2H_5)_3\}[UO_2(C_{36}H_{45}O_6)].3H_2O$ {BINKIS} (a), $K_8[UO_2(CrO_4)_4](NO_3)_2$ {98718} (b), $Na_4[UO_2(CrO_4)_3]$ {98653} (c) and $Na_4[UO_2(CO_3)_3]$ {93968} (d), respectively.

Table 1. Analysis of U(VI) coordination in some U compounds using the method of intersecting spheres

Characteristics of the VDP			Overlap volume (Å^3) *				Overlap type
Atoms	r(U-O), Å	Ω(U-O), %	$r_S \times r_S$	$r_S \times R_{SD}$	$R_{SD} \times r_S$	$R_{SD} \times R_{SD}$	
{NH(C_2H_5)$_3$}[UO_2($C_{36}H_{45}O_6$)].3H_2O {BINKIS} CN_U = 5							
O(7)	1.782	21.14	0.360	5.783	0.032	2.862	Π_4
O(8)	1.787	21.57	0.355	5.365	0.030	2.615	Π_4
O(3)	2.152	16.32	0.052	2.851	0	1.048	Π_3
O(5)	2.203	15.97	0.029	2.524	0	0.864	Π_3
O(1)	2.223	15.35	0.022	2.350	0	0.771	Π_3
O(2)	3.069	3.45	0	0.002	0	0	Π_1
O(6)	3.075	3.63	0	<0.001	0	0	Π_1
O(4)	3.158	2.58	0	0	0	0	Π_0
K_8[UO_2(CrO_4)$_4$](NO_3)$_2$ {98718} CN_U = 6							
O(4)	1.808 (×2)	20.81 (×2)	0.332	6.342	0.011	2.911	Π_4 (×2)
O(3)	2.245 (×2)	14.67(×2)	0.015	2.765	0	0.847	Π_3 (×2)
O(1)	2.259 (×2)	14.51 (×2)	0.011	2.675	0	0.801	Π_3 (×2)
Na_4[UO_2(CrO_4)$_3$] {98653} CN_U = 7							
O(1)	1.780	21.01	0.361	5.528	0.016	2.444	Π_4
O(2)	1.782	21.38	0.359	5.509	0.015	2.433	Π_4
O(6)	2.334	12.17	<0.001	1.951	0	0.445	Π_3
O(5)	2.337	11.45	<0.001	2.139	0	0.524	Π_3
O(3)	2.338	11.77	<0.001	2.074	0	0.496	Π_3
O(10)	2.395	11.05	0	2.012	0	0.459	Π_2
O(4)	2.398	11.18	0	1.911	0	0.417	Π_2
Na_4[UO_2(CO_3)$_3$] {93968} CN_U = 8							
O(2)	1.807	20.95	0.333	4.741	0.010	2.026	Π_4
O(1)	1.815	20.67	0.325	4.557	0.009	1.923	Π_4
O(5)	2.385 (×3)	10.05 (×3)	0	1.632	0	0.316	Π_2 (×3)
O(4)	2.427 (×3)	9.41 (×3)	0	1.548	0	0.278	Π_2 (×3)

* first and second radii are of the U and O atoms, respectively.

The VD polyhedra model also allows one to introduce two important parameters describing distortion of the atomic coordination [16, 17]. The first of these is the D_A vector that originates in the A atom and ends in the centroid of the VD polyhedron. According to [18], length of the D_A vector is proportional to the gradient of the local electric field created by the atoms surrounding the A atom in the structure. The second parameter is the second moment of inertia, $\mathbf{G_3}$, which describes the deviation of the VD polyhedron from an ideal sphere and characterizes uniformity of distribution of the X and Z atoms around A. For an ideal sphere, $G_3 = 0.077$, whereas for an ideal AX_6 octahedron (which correspond to a cubic VD polyhedron), $G_3 = 0.0833$ [17].
The above mentioned parameters and some other parameters of the VD polyhedra can be determined using the software package TOPOS [16]. As input data, this software employs space group, unit-cell dimensions and atomic coordinates.

3. Voronoi-Dirichlet polyhedra of the U(VI) atoms in oxygen-containing compounds

Using the U oxocompounds, we have demonstrated (Serezhkin 1995) that the volumes of the VD polyhedra of atoms A that form complexes AX_n depend upon the chemical nature of the A and X atoms and the A oxidation state only [20-24]. It is essential that, within the accuracy of the experimental structure determination, the volume of the VD polyhedron of the A atoms practically does not depend on the coordination number of A. More recently this hypothesis has been confirmed for many chemically different coordination centres, including metals from Li to Bk and non-metals as well.
Since first data concerning structures of uranyl compounds with *CN*(U(VI)) = 5 appeared in 1999, it is of great interest to include these structures into the analysis of the characteristics of the U(VI) VD polyhedra. Initial crystal structure information was extracted from the known structure databases [2, 3] and analyzed using the TOPOS software [16]. Structures were included into consideration under conditions that crystallographic agreement index (R_1) is less than 0.10 and that there is no disorder in the U or O sites in the UO_n polyhedra. In total, 908 compounds were considered that contained 1465 crystallographically independent U(VI) atoms. From these atoms, 15, 306, 906, and 238 have coordination numbers of 5, 6, 7, and 8, respectively.
In most cases, the coordination polyhedra and VD polyhedra of the U(VI) atoms were distorted. The primary reason for this is obviously their low site symmetry. There are 19 different site symmetries of the U sites observed. However, by far the most prevalent site symmetry is a complete asymmetry - C_1 (1017 from 1465 sites). Site symmetries C_s, C_i and C_2 are relatively frequent and have been observed 138, 129 and 71 times, respectively. Other site-

symmetry groups have been encountered less than 20 times. It is noteworthy that oxygen atoms in the compounds analysed also occupy low-symmetry sites. Of 11113 O atoms, 9973 (≈90%) occupy asymmetrical positions C_1, 809 and 124 have site symmetries C_s and C_2, respectively, whereas 15 different site symmetries have been found in amounts from 1 to 59.

The $\mathbf{G}_3$ parameter that characterizes sphericity of coordination polyhedra varies from 0.081 to 0.092. As for other AX_n complexes, the $\mathbf{G}_3$ value decreases with the increase of the CN (Table 2). For most of the U atoms, $G_3 > 0.082$. According to [17], this means that the U-O bonds have basically covalent character.

The 1465 different VD polyhedra of the U atoms in the structures under consideration have in total 10871 faces. Our analysis [15] indicated that 10157 faces correspond to U=O and U-O bonds. The 714 non-bonding U/Z contacts correspond mostly to Z = O or H (381 and 243 faces, respectively). The remaining 90 faces correpond to 14 other elements, including non-metals (C, N, Se, Cl), and metals (Li, Na, Cs, Sr, Ba, etc.)

As expected, the distribution of faces versus interatomic U-O distances shows some well-defined maxima (Fig. 6). The first maximum corresponds to the U=O bonds (1.7-1.8 Å), whereas maxima within 2.1-2.6 Å correspond to the equatorial U-O bonds. It should be noted that non-bonding U/O contacts are present for all CNs of the U(VI) atoms. With the decrease of the CN from 8 to 7, 6, and 5, the number of non-bonding U/O contacts per one uranium-oxygen chemical bond increases to 0.002, 0.008, 0.150, and 0.600, respectively. It is the presence of non-bonding U/O contacts that is responsible for the poorly defined maxima at 2.8-3.7 Å (CN = 5) and 2.9-3.8 Å (CN = 6) (Figs. 6a and 6b, respectively). Fig. 7 shows the distribution of faces of the VD polyhedra versus Ω solid angles. The U=O uranyl bonds corrrespond to the faces with Ω = 20-23%, whereas equatorial U-O bonds determine faces with Ω = 8-17%. Non-bonding U/O interactions are most abundant for CN = 5 and 6 and have Ω < 8% (Figs. 7a, b).

Despite the differences in the CNs of the U atoms and the diversity of their coordination polyhedra in terms of shape and symmetry, both bonding and non-bonding uranium-oxygen interactions can be characterized by the same linear equation:

$$\Omega(\text{U-O}) = 44.26(9) - 13.51(4) \cdot r(\text{U-O}) \quad (5)$$

The correlation coefficient ρ = -0.957 for all 10538 faces corresponding to the U=O, U-O, and U/O contacts (Fig. 8a). For comparison, Fig. 8b shows fragment of the graph in Fig. 8a that provides the (Ω, r) distribution for the U(VI) atoms with CN = 5 only. As can be seen, the latter distribution possess three non-intersecting domains (see Figs. 6a and 7a for comparison), which is in contrast to the whole distribution (Fig. 8a), which is rather uniform.

Table 2. Characteristics of the Voronoi-Dirichlet polyhedra (VDP) of oxygen-coordinated U(VI) atoms*

CN	No. of U atoms	N_f	N_{nb}	V_{VDP}, Å^3	$S_{VDP,}$ Å^2	$R_{SD,}$ Å	D_A, Å	G_3	Bond lengths in UO_n polyhedra, Å			
									range	mean	Δ	μ
5	15	9.7	0.94	10.2 (2)	28.3 (4)	1.343(8)	0.02 (1)	0.089(1)	1.75-2.27	2.05 (22)	0.52	75
6	306	7.6	0.27	9.4 (5)	27(1)	1.309(23)	0.03 (4)	0.086(2)	1.61-2.50	2.12 (21)	0.89	1836
7	906	7.1	0.01	9.2 (3)	25.8 (6)	1.299 (14)	0.03 (2)	0.084(1)	1.51-2.86	2.21 (28)	1.35	6342
8	238	8.2	0.03	9.3 (3)	25.7(5)	1.306 (13)	0.02 (2)	0.084(1)	1.60-2.80	2.29 (31)	1.20	1904
5-8	1465	7.4	0.07	9.3 (4)	26.0 (8)	1.303 (17)	0.03 (3)	0.084(1)	1.51-2.86	2.21 (28)	1.35	10157

* The following parameters are given for each type of U(VI) atoms:
CN – coordination number; N_f – average number of faces of the VDPs; N_{nb} – average number of non-bonding contacts per one U-O bond; V_{VDP} – volume of the VD polyhedron; S_{VDP} – total area of faces of the VDP; R_{SD} – radius of the sphere with volume equal to that of the VDP; D_A - vector that originates in the U atom and ends in the centroid of the VD polyhedron; G_3 - the second moment of inertia, which describes deviation of the VD polyhedron from ideal sphere; Δ - difference between the shortest and the longest bonds in the coordination polyhedron; μ - total number of faces. Standard deviations are given in parentheses.

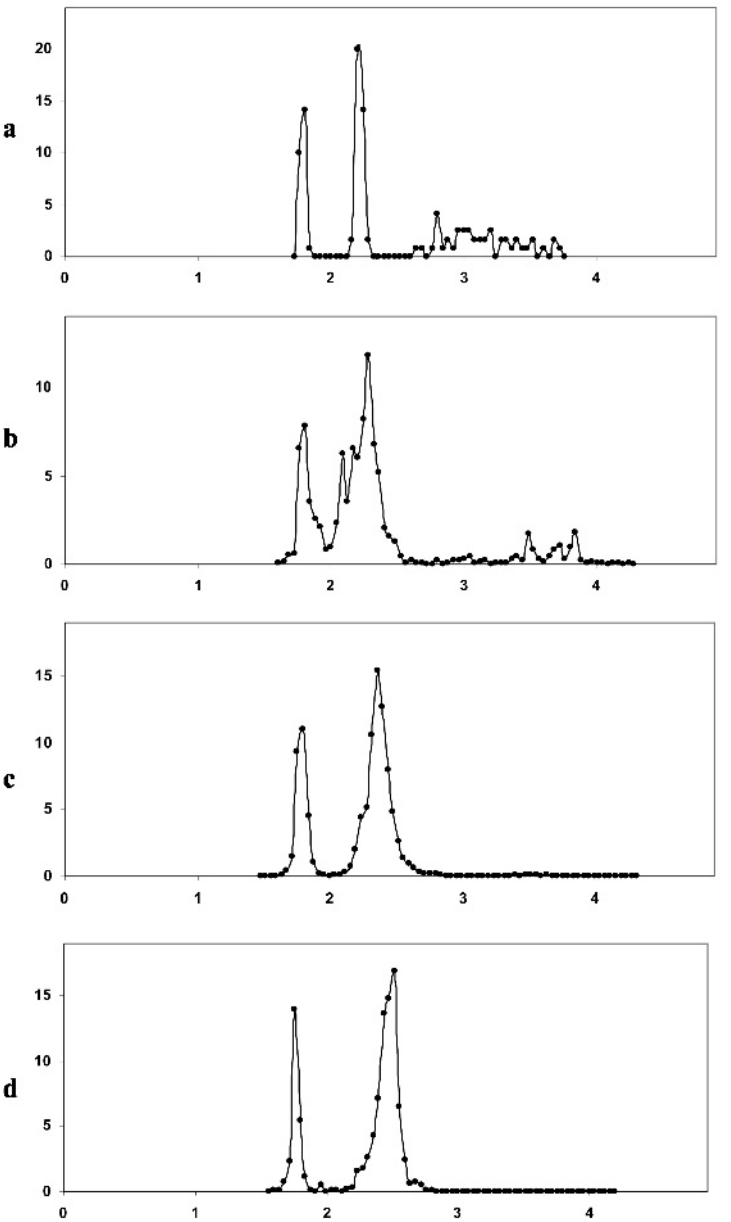

Figure 6. Distribution of the number of U-O contacts versus U-O distances: (a) trigonal bipyramids (120 U-O contacts, including 75 bonds); (b) tetragonal bipyramids (2118 U-O contacts, including 1836 bonds); (c) pentagonal bipyramids (6392 U-O contacts, including 6342 bonds); (d) hexagonal bipyramids (1908 U-O contacts, including 1904 bonds).

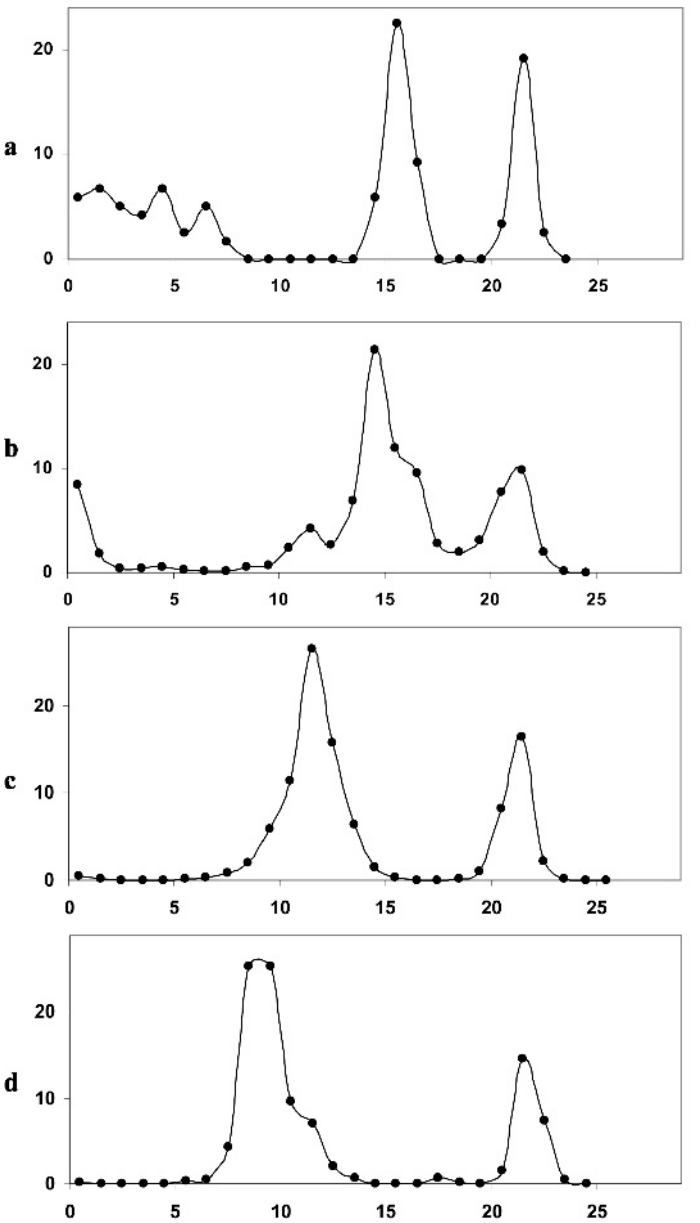

Figure 7. Distribution of the number of VDP faces versus the value of Ω(U-O) solid angles: (a) trigonal bipyramids (120 U-O contacts, including 75 bonds); (b) tetragonal bipyramids (2118 U-O contacts, including 1836 bonds); (c) pentagonal bipyramids (6392 U-O contacts, including 6342 bonds); (d) hexagonal bipyramids (1908 U-O contacts, including 1904 bonds).

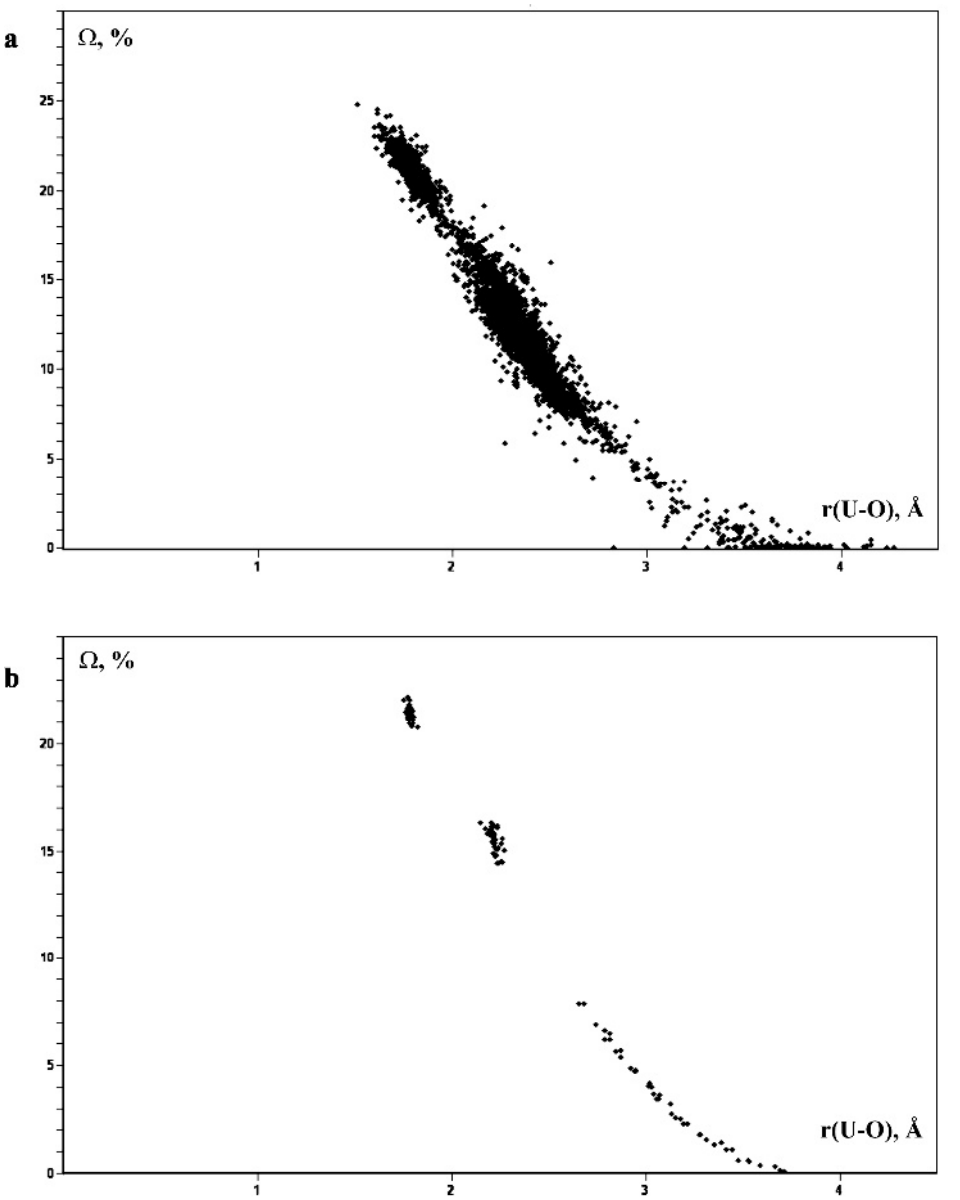

Figure 8. Values of the Ω solid angles (expressed in % from 4π) of the VDP faces of U(VI) atoms versus corresponding U-O distances: (a) 10538 faces of the U=O, U-O or U/O types of the VD polyhedra of the 1465 U atoms with CN = 5, 6, 7 and 8; (b) 120 faces of the U=O, U-O or U/O types of the VD polyhedra of the 15 U atoms with CN = 5.

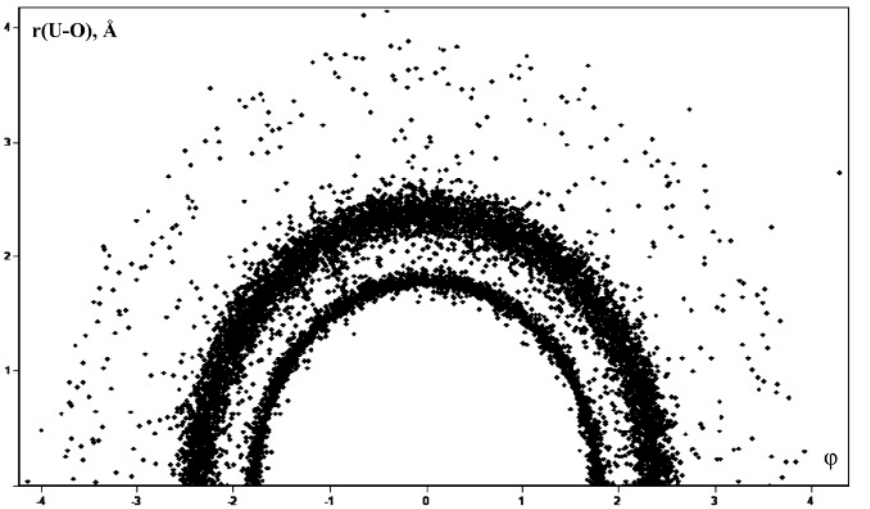

Figure 9. The (r, φ) distribution for the 1465 U(VI) atoms with the UO_n coordination. See text for details

According to the data listed in Table 2, the average volume of the VD polyhedra of the U atoms is 9.3(4) Å^3. This is in general agreement with the previously determined value of 9.2(3) Å^3 calculated for 354 independent U atoms [21-23]. However, for CN = 5, the V_{VDP} is by 1 Å^3 larger than for CN = 6, 7, and 8. This effect (enlargement of V_{VDP} for CN < 6) has been observed by us for atoms of *d*- and *f*-elements in the environments of halogen and chalcogen ions. In all cases, the enlargement of V_{VDP} for CN < 6 is accompanied by the sharp increase in the number of non-bonding A/Z contacts per one A-X bond (N_{nb}). For instance, for the U atoms with CN = 8, 7, 6, and 5, N_{nb} = 0.03, 0.01, 0.27, and 0.94, respectively. In this regard, it is worthy to mention that, for any VD polyhedron AX_nZ_m, the following equation should be fulfilled:

$$\Omega = \Omega^{A\text{-}X} + \Omega^{A/Z}, \quad (6)$$

where Ω is equal to 4π steradian or 100%, $\Omega^{A\text{-}X}$ is a sum of the solid angles corresponding to the A-X bonds, $\Omega^{A/Z}$ is a sum of the solid angles corresponding to the non-bonding A/Z contacts. The ratio between $\Omega^{A\text{-}X}$ and $\Omega^{A/Z}$ depends upon the chemical nature and CN of the A atom. For the U(VI) compounds under consideration, CN = 8, 7, 6, and 5 corresponds to $\Omega^{A/Z}$ = 0.05, 0.07, 1.96, and 10.47%, respectively.

The use of VD polyhedra allows one to characterize specific properties of the coordination spheres of cations by means of the (r, φ) distributions [24]. In Figure 9, each point corresponds to the VD polyhedron with a given r(U=O), r(U-O), or r(U/O) bond length and the φ angle between the $\mathbf{D_A}$ vector and the direction of the corresponding uranium-oxygen bond (we remind the reader that

the $\mathbf{D_A}$ vector originates in the site of the A atom and ends in the centroid of the VD polyhedron). The nuclei of the U atoms are at the origin of a polar system of coordinates, with the $\mathbf{D_A}$ vector directed to the right along the horizontal axis. As can be seen, the points in the graph form half-circles. The closest half-circle has a radius of $R_1 \approx 1.78(4)$ Å and corresponds to the U=O bonds in the uranyl ions. The second half-circle has $R_1 \approx 2.4(1)$ Å and reflects equatorial U-O bonds, whereas points with $R_1 > 2.9$ Å correspond to the non-bonding U/O interactions. This type of (r, φ) distribution is typical for quasi-spherical electron density distributions around complex-forming cations with $\mathbf{D_A} \approx 0$ (for the 1465 U(VI) atoms, $D_A = 0.03(3)$ Å, see Table 2).

In general, the data analyzed indicate that the volume of the VD polyhedron practically does not depend on the CN of the U atoms. Thus, the $\boldsymbol{R}_{\mathbf{SD}}$ radius is almost always close to 1.30(2) Å, whereas the U-O bonds within the UO_n polyhedra vary by more than 1 Å. The $\sigma(\boldsymbol{R}_{\mathbf{SD}})$ standard deviation is comparable with the bond length standard deviation in modern structure analysis.

The approximately constant value of the volumes of the VD polyhedra allows us to consider atoms as soft (easy-to-deform) spheres of constant volumes. Approaching of the two atoms due to their chemical interaction is accompanied by mutual deformations of their spheres (Fig. 3f), which, in the end, leads to the transformation of the spheres into VD polyhedra. The shapes of the VD polyhedra are controlled by the arrangement of atoms in the structure that can thus be considered as a close packing of soft spheres.

4. The 18-electron rule for the U(VI) oxocompounds

According to present concepts, interatomic interactions that lead to the formation of inorganic and coordination compounds are controlled by the tendency of atoms to have stable electronic configurations by means of electron transfer. The 'octet' and 18-electron rules are the most important rules that can be successfully applied to a large variety of molecules and compounds [25]. Following these general ideas, we consider the fact that U(VI) atoms have CN-independent permanent volumes of their VD polyhedra as a consequence of the formation of stable electronic configurations [13, 14]. For the sake of convenience, we shall use the following postulates:

1. In all compounds under consideration, all U atoms exist as U^{6+} ions that accept electrons from the O atoms. In turn, O atoms act as donors of electrons to the U atoms.
2. Through interactions with O atoms, the U atoms form a stable N-electron valence shell. Within the UO_n polyhedra, the electron acceptor properties of the U atoms are distributed between the U-O_i bonds in proportion to the value of the Ω_i(U-O_i) solid angles. Since the full solid angle (4π or 100%) corresponds

to the N-electron valence shell, each Ω_i(U-O_i) solid angle is proportional to the number of electrons, E_i, that the U atom receives from the atom O_i.

3. As a first approximation, we suggest that the U(VI) atoms tend to form 18-electron stable electronic configurations. Therefore, if the Ω_i are expressed in percentages,

$$E_i = 0.18 \cdot \Omega_i . \quad (7)$$

The model proposed has been verified using several groups of uranyl compounds, in particular, sulfates [13] and nitrates [14]. More than 200 crystallographically independent U atoms were taken into account. For each U-O_i bond, the E_i values have been calculated using the equation (7). Table 3 provides the most typical coordination characteristics of various ligands (using the notation proposed in [26]), the total number of the U-O bonds formed by each ligand ($\mathbf{N_b}$), and the average number of such bonds (calculated as $\mathbf{N_b/D}$, where D is a dentate number of the ligand). In addition, Table 3 gives average statistical values E_i and E_L, as well as the number of observations (μ). The μ values for E_i and E_L indicate the number of crystallographically independent U-O bonds and number of ligands of a certain type. Here and in the following, $\mathbf{E_L}$ is an average value of electron donor ability of the ligand which is determined using the equation:

$$E_L = E_O \cdot D = E_i \cdot N_b . \quad (8)$$

Analysis of the obtained results (Table 3) allows one to conclude that the electron donor ability of a ligand is determined by its coordination type and does not depend on the CN of U. This is most clearly seen for the uranyl ions, where each U=O bonds receives 3.9(1) electrons, without regard to the coordination number of the U atoms. This is in a good agreement with the general ideas that each U=O is formed by means of two electron pairs, i.e. 4 electrons. In the following, we shall write the ligand coordination type [26] after its chemical formula separated by two slashes, «//». For instance, the notation $O^{2-}//M^1$ defines uranyl O atoms, whereas $O^{2-}//M^2$ and $O^{2-}//M^3$ correspond to the equatorial O atoms that are bonded to two (M^1) or three (M^2) U atoms. Table 3 also takes into account the very rarely observed situation when the same O atom belongs to uranyl ion of one and equatorial plane of another U atom. To distinguish this case from the usual $O^{2-}//M^2$ coordination, it is denoted as $UO_2^{2+}//M^1$.

Our discussion of the factors that control the coordination number of U in inorganic structures will be based on the following assumptions.

1. In aqeous systems, containing uranyl ions, there are either mono- or polynuclear $[UO_2(L)_n]^{z\pm}$ complexes with compositions determined by the chemical nature and concentration of acidic or/and electroneutral ligands L, their electron donor characteristics and their possible types of coordination to the U atoms.

Table 3. Electron-donor characteristics of some ligands in the structures of uranyl compounds

Ligand	Coord. mode	N_b	N_b/D	E_i	μ *	$E_L=E_i \cdot N_b$	μ *
O^{2-}	M^1	1	1	3.87(11)	347	3.9(1)	347
O^{2-}	M^3	3	3	2.25(11)	30	6.7(1)	10
OH^-	M^3	3	3	1.90(8)	15	5.7(1)	5
	M^2	2	2	2.04(6)	34	4.1(1)	17
	M^1	1	1	2.25	1	2.25	1
H_2O	M^1	1	1	1.88(10)	78	1.9(1)	78
NO_3^-	B^{01}	2	1	1.54(6)	158	3.1(1)	79
CO_3^{2-}	B^{01}	2	1	1.72(4)	76	3.44(5)	38
SO_4^{2-}	M^1	1	1	2.22(14)	12	2.2(1)	14
	B^2	2	1	2.13(9)	88	4.25(15)	44
	B^{01}	2	1	1.77(5)	22	3.5(1)	11
	T^3	3	1	2.09(9)	132	6.3(2)	44
	T^{11}	3	1	1.9(2)	21	5.7(1)	7
	K^4	4	1	2.04(17)	40	8.2(3)	10
SeO_4^{2-}	B^2	2	1	2.14(19)	4	4.3(3)	2
	T^3	3	1	2.07(7)	18	6.2(1)	6
	K^4	4	1	2.15(8)	4	8.6	1
CrO_4^{2-}	B^2	2	1	2.22(10)	2	4.4	1
	T^3	3	1	2.11(6)	27	6.3(1)	9
MoO_4^{2-}	B^2	2	1	2.11(6)	3	4.2(1)	3
	T^3	3	1	2.09(10)	23	6.2(1)	8
	K^4	4	1	2.08(9)	76	8.3(2)	20
PO_4^{3-}	T^{31}	5	1.67	1.85(36)	45	9.2(1)	9
	K^4	4	1	2.57(14)	27	10.3(2)	9
SiO_4^{4-}	T^{31}	5	1.67	2.09(30)	50	10.5(1)	10
	K^{42}	8	2	2.05(20)	2	16.4	1
UO_2^{2+}	M^1	1	1	1.73(5)	3	1.73(5)	3
Urea	M^1	1	1	2.07(8)	27	2.07(8)	27

* μ - number of bonds taken into account. In all cases, only crystallographically different U···O bonds have been considered.

2. Electron donor characteristics determined on the basis of crystal structure data (Table 3) correspond to ligands with a certain composition and coordination type in both crystals and aqueous solutions.
3. The most stable $[UO_2(L)_n]^{z\pm}$ complexes are those, in which U atoms form stable 18-electron valence shell configurations.
4. The total number of electrons in the valence shell of the U atom (N_e) is determined by the equation:

$$N_e=\sum_{i}^{n} \nu_{L(i)}\cdot E_{L(i)}\,, \qquad (9)$$

where the ν_L are stoichiometric coefficients that indicate the number of L_i ligands with the same number E_L per one U atom in the complex. Since for the uranyl ion, $O^{2-}//M^1$ E_L = 3.9 e^-, two uranyl O atoms transfer to the U atom in total 7.8 e^-. Therefore, the equation (9) can be transformed into:

$$N_e = 7.8 + \sum_{i}^{n} \nu_{L(i)}\cdot E_{L(i)}\,, \qquad (10)$$

where the ν_L are stoichiometric coefficients that indicate the number of L_i ligands with the same number E_L per one uranyl ion in the complex.
5. Since the E_L values listed in Table 3 are determined with errors $\sigma(E_L)$, we postulate that stable uranyl complexes possess $N_e = 18.0 \pm 0.3$ e^- or

$$\Delta N_e = |18 - N_e| \le 0.3 \qquad (11)$$

6. The $[UO_2(L)_n]^{z\pm}$ complexes with N_e <<18 are electron-deficient. For them, chemical reactions should be typical that increase the N_e value to 18. In addition, for these complexes, replacement reactions according to the Chernyaev-Schelokov row should be observed with replacement of ligands by others with higher E_i value. The uranyl complexes with N_e >>18 are electron-excessive. They should be characterized by chemical reactions that lower the N_e values to 18.
7. Complex-forming processes are considered as many-stage processes. Each stage is characterized by its own equilibrium constant. We postulate that replacement, association, and dissociation reactions take place only when the resulting complex is characterized by the smaller ΔN_e value than the initial complex.

5. Uranyl aqua-complexes

In order to demonstrate the practical importance of the 18-electron rules, we consider formation complexes in aqueous salt systems. Since many uranyl compounds can be synthesized by crystallization from aqueous solutions, let us first discuss the coordination of uranyl ions by water molecules in aqueous

solutions. For this, we consider the $UO_2(ClO_4)_2$ - H_2O, in which uranyl ions coexist with perchlorate anions and water molecules. It is worthy to mention that perchlorate ions have the lowest electron donor ability in crystal structures [13-14]. Thus, we suppose that they do not associate with uranyl ions. In relation to uranyl ions, the water molecules can only be monodentate ligands with E_L = 1.9 e^- (Table 3). Therefore, for the $[UO_2(H_2O)_n]^{2+}$ complexes, equation (10) can be transformed into:

$$N_e = 7.8 + n \cdot 1.9 \quad (12)$$

where n is a number of water molecules coordinating one uranyl ion. Formation of the uranyl aqua-complexes can be described by the following scheme (here UO_2 =A):

$$[A]^{2+} \rightarrow [A(H_2O)]^{2+} \rightarrow [A(H_2O)_2]^{2+} \rightarrow [A(H_2O)_3]^{2+} \rightarrow [A(H_2O)_4]^{2+} \rightarrow [A(H_2O)_5]^{2+} \leftarrow [A(H_2O)_6]^{2+} \quad (13)$$

7.8		9.7		11.6		13.5		15.4		17.3		19.2	
10.2	→	8.3	→	6.4	→	4.5	→	2.6	→	0.7	←	1.2	

Here each complex is characterized (in the second row) by the N_e value calculated using the equation (12). The third row provides the ΔN_e values (equation (11)). The arrows point into direction with the decreasing ΔN_e. It can be seen that the first five stages of the uranyl ion hydration are accompanied by the decrease of ΔN_e and end up in the formation of the $[UO_2(H_2O)_5]^{2+}$ complex with minimal ΔN_e value. Thus only these stages will be energetically favorable, whereas sixth one will be not. Therefore, the $[UO_2(H_2O)_5]^{2+}$ complex with pentagonal bipyramidal coordination of the U atom is the most stable and should be present in U compounds crystallizing from aqueous solutions. This is in agreement with the recently reported results of quantum chemical calculations [27]. In addition, all U(VI) compounds containing 'pure' uranyl aqua-complexes consist of the $[UO_2(H_2O)_5]^{2+}$ pentagonal bipyramids (e.g. $[UO_2(H_2O)_5](ClO_4)_2.2H_2O$ {412809}, $[UO_2(H_2O)_5](ClO_4)_2$ {412808}, and $[UO_2(H_2O)_5]B_{12}H_{12}.6H_2O$ {201402}).

However, the uranyl pentaaquacomplexes are rare in the structures of U compounds, despite the fact that the H_2O:UO_2 ratio can be as high as 18 (e.g., in the structure of $Mg_2[UO_2(CO_3)_3].18H_2O$ {32101}). This is because the $[UO_2(H_2O)_5]^{2+}$ are relatively unstable and have N_e = 17.3 < 18 e^-, i.e. are electron-deficient.

Since for the $[UO_2(H_2O)_n]^{2+}$ complexes with n = 5 and 6, the N_e values are equal to 17.3 and 19.2 e^-, respectively, they are more or less symmetrical relative to the stability value of N_e = 18±0.3 e^-. In our opinion, this means that there is a dynamic equilibrium:

$$[UO_2(H_2O)_5]^{2+} + H_2O \leftrightarrow [UO_2(H_2O)_6]^{2+}. \quad (14)$$

That is, the only way to increase the N_e value for the $[UO_2(H_2O)_5]^{2+}$ complex is to attract additional H_2O molecule but this leads to the $[UO_2(H_2O)_6]^{2+}$ electron-excessive complex, which is therefore (also? PAG) unstable ($N_e = 19.2 > 18\ e^-$). Another alternative for the $[UO_2(H_2O)_5]^{2+}$ complex to receive 18 electrons is to attract an O atom from the adjacent uranyl ion ($E_L(UO_2^{2+})//M^1 = 1.73\ e^-$) (Table 3), but this is unfavorable because water molecules are stronger donors than uranyl ions and will replace them from the resulting configuration.

Since both complexes in the equation (14) have $\Delta N_e > 0.3\ e^-$, they are unstable and may participate in the reactions of the type:

$$[UO_2(H_2O)_n]^{2+} + L \leftrightarrow [UO_2(H_2O)_{n-y}L]^{2+} + yH_2O\ , \qquad (15)$$

if the $[UO_2(H_2O)_{n-y}L]^{2+}$ complex will have smaller ΔN_e.

In our opinion, it is the fact that all uranyl aqua-complexes have $\Delta N_e > 0$, which is responsible for chemical ability of uranyl ions to form complexes with a large diversity of ligands in aqueous solutions.

6. Carbonate and nitrate uranyl complexes

The UO_2^{2+} - XO_3^{z-} - H_2O (X= C or N) systems have been chosen for analysis for two reasons. First, they are well studied experimentally, since carbonate and nitrate uranyl complexes are important from technological standpoints. Second, the isoelectronic anions XO_3^{z-} have the same planar structure (symmetry D_{3h}) and form bidentate coordination around uranyl ions (the B^{01} type). However, their electron-donor characteristics are different: E_L = 3.1 and 3.4 for the NO_3^- and CO_3^{2-} ions, respectively. From this viewpoint, it would be of interest to understand how the difference in the electron-donor properties influences complex formation in the UO_2^{2+} - XO_3^{z-} - H_2O systems. As in the case of aqua-complexes, we shall use the 18-electron rule to obtain answers to the following questions: (a) what is the composition of stable complexes in aqueous solutions containing carbonate or nitrate uranyl complexes; (b) what is the coordination number of U(VI) in these complexes.

To simplify our task, we assume that the aqueous solution contains $[UO_2(H_2O)_5]^{2+}$ and $[UO_2(H_2O)_6]^{2+}$ complexes (CN_U = 7 and 8, respectively), which are in equilibrium according to equation (14). Let the concentration of the XO_3^{z-} anions (X = C and N) increase continuously, and the nature of the outer-sphere R cations does not influence complex formation. The triangular ions can link to uranyl ions only in a bidentate cyclic fashion: as a result, coordination of the uranyl ion by an XO_3^{z-} anion is through the replacement of two H_2O molecules of the uranyl-water complexes.

The resulting complexes will have the composition $[UO_2(XO_3)_m(H_2O)_n]^{z\pm}$. Equation (10) transforms into:

$$N_e = 7.8 + m\cdot E_L(XO_3^{z-}) + n\cdot E_L(H_2O)\ . \qquad (16)$$

Taking of the E_L values from Table 3, this equation will transform into the equations (17) and (18) for the carbonate and nitrate complexes, respectively:

$N_e = 7.8 + m \cdot 3.4 + n \cdot 1.9$. (17)

$N_e = 7.8 + m \cdot 3.1 + n \cdot 1.9$. (18)

Thus complex formation in the systems can be described by the following schemes:

$$[UO_2(H_2O)_6]^{2+} \rightarrow [UO_2(CO_3)(H_2O)_4] \rightarrow [UO_2(CO_3)_2(H_2O)_2]^{2-} \rightarrow [UO_2(CO_3)_3]^{4-} \quad (19)$$

I, 19.2 — 1.2 → II, 18.8 — 0.8 → III, 18.4 — 0.4 → IV, 18.0 — 0.0

$$[UO_2(H_2O)_5]^{2+} \leftarrow [UO_2(CO_3)(H_2O)_3] \leftarrow [UO_2(CO_3)_2(H_2O)]^{2-} \quad (20)$$

V, 17.3 — 0.7 ← VI, 16.9 — 1.1 ← VII, 16.5 — 1.5

$$[UO_2(H_2O)_6]^{2+} \rightarrow [UO_2(NO_3)(H_2O)_4]^{+} \rightarrow [UO_2(NO_3)_2(H_2O)_2] \leftarrow [UO_2(NO_3)_3]^{-} \quad (21)$$

I, 19.2 — 1.2 → VIII, 18.5 — 0.5 → IX, 17.8 — 0.2 ← X, 17.1 — 0.9

$$[UO_2(H_2O)_5]^{2+} \leftarrow [UO_2(NO_3)(H_2O)_3]^{+} \leftarrow [UO_2(NO_3)_2(H_2O)] \quad (22)$$

V, 17.3 — 0.7 ← XI, 16.6 — 1.4 ← XII, 15.9 — 2.1

For each of the 12 complexes considered in equations (19)-(22), the next row provides assigned numbers given in Roman numerals and the N_e values calculated according to the equations (17) and (18). The next row provides the ΔN_e values for these complexes and arrows pointing towards the more stable complexes.

Analysis of the data obtained indicates that, under equilibria described by the equations (20) and (22), replacement of H_2O molecules in the complexes V by carbonate and nitrate ions is accompanied by the decrease in the N_e parameter (it was already less than 18 for the $[UO_2(H_2O)_5]^{2+}$ complex). In other words, the increase of the XO_3^{z-} : UO_2^{2+} ratio in the complexes VI, VII, XI, and XII (schemes (20) and (22)) is accompanied by the increase of ΔN_e from 0.7 to 1.5 and 2.1 for X = C and N, respectively. From the viewpoint of the 18-electron rule (the most stable complexes have $N_e = 18 \pm 0.3$ e^-), the reactions (20) and (22) are energetically unfavorable. That is, the reactions (20) and (22) will deliberately occur only from the right to the left, since the aqua-complexes V are more stable than their acid derivatives VI, VII, XI, and XII.

In two other equilibria (schemes (19) and (21)), replacement of water molecules in the $[UO_2(H_2O)_6]^{2+}$ complexes by acid ligands is accompanied by the decrease

of the N_e parameter from its initial value of 19.2 e^-. In the carbonate system (eq. 19), all three stages of the replacement reactions correspond to the decrease of ΔN_e (from 1.2 to 0.8, 0.4, and 0 for the complexes I, II, III, and IV, respectively). Taking this into account, we conclude that, in the UO_2^{2+} - CO_3^{2-} - H_2O system, transformations described by the scheme (19) will result in the formation of very stable ($\Delta N_e = 0$) complexes $[UO_2(CO_3)_3]^{4-}$ with $CN_U = 8$. This conclusion is in a perfect agreement with experimental data on carbonate-containing systems [9] and is supported by the existence of numerous minerals and synthetic compounds containing the $[UO_2(CO_3)_3]^{4-}$ complexes. Since triuranylcarbonate complexes have $\Delta N_U = 0$, the $R^I_4[UO_2(CO_3)_3]$ or $R^{II}_2[UO_2(CO_3)_3]$ compounds can easily be crystallized from aqueous solutions, where these complexes should be very stable (in fact, they were detected even in seawater).

It should be noted that despite the fact that in the nitrate system (21) the NO_3:UO_2 ratio increases from left to right, whereas the N_e value is decreasing as in the equation (19), the situation is different. The point is that the change in the ΔN_e parameter is not monotonic. Thus, for the complexes I, VIII, IX, X (21), that have NO_3:UO_2 = 0, 1, 2, and 3, respectively, ΔN_e = 1.2, 0.5, 0.2 and 0.9 e^-, respectively. Therefore, in the UO_2^{2+} - NO_3^- - H_2O system, the most stable complex should be IX ($\Delta N_e = 0.2$ e^- and $N_e = 17.8$ e^-). Thus, the reactions that will take place in the scheme (21) should result in the formation of the complex IX (since I→VIII→IX←X). Indeed, the electroneutral complexes IX, which have the composition $[UO_2(NO_3)_2(H_2O)_2]$, have been observed in the structures of all known uranyl nitrate hydrates and their derivatives. Since the NO_3 : UO_2 in the most stable complexes IX is the same as for uranyl nitrate, it might be concluded that, under standard thermodynamic conditions, in the R^INO_3 (or $R^{II}(NO_3)_2$) - $UO_2(NO_3)_2$ - H_2O) systems, there should be no complex formation at all. In other words, these systems should be simple eutonic ones, and their solubility isotherms must contain crystallization fields of R^INO_3 (or $R^{II}(NO_3)_2$) and uranyl nitrate only. Moreover, one may point out that all attempts to re-crystallize the $R^I[UO_2(NO_3)_3]$ compounds (that can be obtained under specific conditions only [9]) from aqueous solutions will result in their decomposition into binary nitrates. We emphasize that the conclusions mentioned above are in agreement with numerous crystal structure investigations and experimental data [9], which, however, were not interpreted from a common perspective until now. At the same time, in $UO_2(NO_3)_2$ – H_2O – L systems, where L is an electroneutral ligand with electron-donor characteristics E_i higher than for nitrate ions and water molecules, formation of polyligand complexes can be observed.

Let us consider the $UO_2(NO_3)_2$ – $CO(NH_2)_2$ – H_2O system as an example. Here $CO(NH_2)_2$ is a carbamide (urea), that has E_L = 2.1 e^- for urea//M^1. At present

time, formation of nine compounds have been established in this system. Among them, three [$UO_2(NO_3)_2$.2urea (**XIII**), $UO_2(NO_3)_2$.4urea.H_2O (**XIV**) and $UO_2(NO_3)_2$.5urea.H_2O (**XV**)] have their crystallization fields on the solubility isotherm in the $UO_2(NO_3)_2$ - urea - H_2O system, whereas six others have been obtained from non-aqueous systems or by solid-state reactions [28]. Taking into account equation (10) and Table 3, for polyligand complexes with composition $[UO_2(NO_3)_m(Urea)_u(H_2O)_n]^{Z+}$ crystallized from aqueous solutions, one may obtain: (23)

$N_e = 7.8 + m \cdot E_L(NO_3^-) + u \cdot E_L(urea^-) + n \cdot E_L(H_2O) = 7.8 + m \cdot 3.1 + u \cdot 2.1 + n \cdot 1.9.$

Assuming that all nitrate ions are crystal chemically equivalent and can be either intrasphere ligands (m = 2) or outer sphere ligands (m = 0), the formulas of the compounds should be written as $[UO_2(NO_3)_2(urea)_2]$ (XIII), $[UO_2(urea)_4(H_2O)](NO_3)_2$ (XIV) and $[UO_2(urea)_5](NO_3)_2.H_2O$ (XV). This is in complete agreement with the crystal structures determined for these compounds. The decrease in the coordination number of U from 8 to 7 that occurs with the increase of the urea : $UO_2(NO_3)_2$ ratio in the $UO_2(NO_3)_2$ - urea - H_2O system can be described by the scheme:

$$[UO_2(NO_3)_2(H_2O)_2] \leftrightarrow [UO_2(NO_3)_2(Urea)_2] \leftrightarrow [UO_2(Urea)_4(H_2O)]^{2+} \leftrightarrow [UO_2(Urea)_5]^{2+} \quad (24)$$

IX, $КЧ_U$=8	XIII, $КЧ_U$=8	XIV, $КЧ_U$=7	XV, $КЧ_U$=7
N_e=17.8	N_e=18.2	N_e=18.1	N_e=18.3

This scheme is supported by the crystal structure data on these complexes and should be considered as the result of exclusively electronic and not steric effects.

7. Sulfate uranyl complexes

According to the existing data, sulfate ions may have six different coordination types in relation to the uranyl ions (Fig. 10). Like carbonate and nitrate ions, sulfate ions may have bidentate cyclic coordination to U(VI) atoms. However, the most common coordination is bidentate bridging that has $E_L = 4.25\ e^-$ (Table 3). Therefore theoretical analysis of complex formation in the UO_2^{2+} - SO_4^{2-} - H_2O system with bidentate bridging sulfate ions forming the $[UO_2(SO_4)_m(H_2O)_n]^{z\pm}$ complexes should be based upon the equation:

$N_e = 7.8 + m \cdot E_L(SO_4^{2-}) + n \cdot E_L(H_2O) = 7.8 + m \cdot 4.25 + n \cdot 1.9$. (25)

As for carbonate and nitrate compounds, inclusion of one bidentate sulfate ion into uranyl complex must be accompanied by the exclusion of two water molecules. Therefore the interactions present in the system can be described by the following schemes:

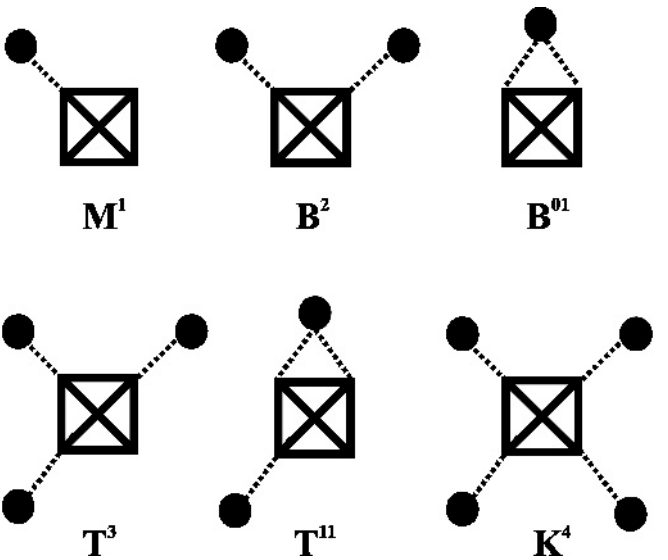

Figure 10. Schematic representations of all known types of sulfate coordination by U(VI) atoms (shown as black circles). Dotted lines denote U-O coordination bonds.

$$[UO_2(H_2O)_6]^{2+} \leftarrow [UO_2(SO_4)(H_2O)_4] \leftarrow [UO_2(SO_4)_2(H_2O)_2]^{2-} \leftarrow [UO_2(SO_4)_3]^{4-} \quad (26)$$

I, 19.2 — XVI, 19.65 — XVII, 20.1 — XVIII, 20.55

1.2 ← 1.65 ← 2.1 ← 2.55

$$[UO_2(H_2O)_5]^{2+} \rightarrow [UO_2(SO_4)(H_2O)_3] \rightarrow [UO_2(SO_4)_2(H_2O)]^{2-} \quad (27)$$

V, 17.3 — XIX, 17.75 — XX, 18.2

0.7 → 0.25 → 0.2

As can be derived from the schemes (26) and (27), the reactions of complex formation will take place in the direction XVIII→XVII→XVI→I→V→XIX→XX. In the end, they must lead to the formation of the $[UO_2(SO_4)_2(H_2O)]^{2-}$ complex, which is the most stable and the most abundant complex in uranyl sulfates. It is of interest that it was a uranyl disulfate $K_2[UO_2(SO_4)_2(H_2O)].H_2O$, a complex of the XX type, which was used by Becquerel in his discovery of radioactivity. In the structures of the XX complexes, the U atoms have CN = 7. We note that, according to the scheme (27), the most stable complexes should the electroneutral complexes XIX for which $\Delta N_e = 0.25$ and $CN_U = 7$. Indeed, there are some data in the literature that provide some evidence concerning the existence of such complexes in crystals.

However, it should be noted that, for UO_2^{2+} : $SO_4^{2-} \approx 1$, the most characteristic coordination of sulfate ions relative to the uranyl ions is not bidentate bridging (B^2, Fig. 10) but tridentate bridging (T^3, Fig. 10). Due to the inclusion of third O atom into the coordination, electron-donor ability of sulfate ions increases significantly: they have $E_L = 3E_i = 6.3e$. For this reason, the most stable electroneutral complexes have the composition $[UO_2(SO_4)(H_2O)_2]$, since for them $N_e = 7.8 + 6.3 + 2 \cdot 1.9 = 17.9\ e^-$, and $\Delta N_e = 0.1\ e^-$, i.e. less than for the complexes XIX. This explains why the $[UO_2(SO_4)(H_2O)_2]$ complexes occur in crystal structures more frequently than the $[UO_2(SO_4)(H_2O)_3]$ complexes.

In relation to the U(VI) centers, bidentate sulfate ions may occur not only as bridging (B^2), but also as cyclic (B^{01}, Fig. 10) ligands. The data known indicate that the electron-donor ability of bidentate sulfate ions depends upon their coordination type. This is caused by the significant shortening of the U-S contact for $SO_4^{2-}//B^{01}$ (≈ 3.1 Å) in comparison to $SO_4^{2-}//B^2$ (≈ 3.6 Å). The mutual repulsion of the U(VI) and S(VI) centers in the U-O-S-O-U cycle that forms owing to the bidentate cyclic coordination is stronger and leads to the decrease of the O-S-O angle from ideal tetrahedral (109.5^0) to 102^0 and to the elongation of the U-O bonds. As a result, the solid angle corresponding to the U-O bond at bidentate cyclic coordination constitutes 9.8(3)% of the total 4π only, whereas it is equal to 11.9(6)% for a bidentate bridging coordination. As a consequence, the E_L value for $SO_4^{2-}//B^{01}$ is essentially lower than for $SO_4^{2-}//B^2$ (3.5 and 4.25 e^-, respectively). Therefore, in the case of bidentate cyclic coordination, the stability calculations for sulfate-containing uranyl complexes given in (26) and (27) should be carried out according to the equation:

$$N_e = 7.8 + m \cdot E_L(SO_4^{2-}) + n \cdot E_L(H_2O) = 7.8 + m \cdot 3.5 + n \cdot 1.9 \ . \qquad (28)$$

Analysis shows that, if all sulfate ions are coordinated by uranyl ions in a bidentate cyclic fashion, the most stable among the complexes XVI-XX given in (26) and (27) must be the complex $[UO_2(SO_4)_3]^{4-}$ (XVIII). This complex has $N_e = 18.3\ e^-$, whereas others have $\Delta N_e > 0.6\ e^-$. This is confirmed by the recent data on the structure of $(C_5H_{14}N_2)_2[UO_2(SO_4)_3]$ {IPUKOT}, which is the only known example of uranyl trisulfate with $CN_U = 8$ (Fig. 11a). In this regard, it is worthy to note that, in other known uranyl trisulfates $[K_4[UO_2(SO_4)_3]$ {14062}, $(C_4H_{14}N_2)_2[UO_2(SO_4)_3].2H_2O$ {IKUDAT} and $\{NH(C_2H_7N)_3\}[UO_2(SO_4)_3].0{,}5H_2O$ {LABGOL}], the U(VI) atoms have CN = 7. Because of the simultaneous presence of monodentate (M^1), bidentate bridging (B^2) and bidentate cyclic (B^{01}) sulfate ions, the trisulfate complexes have a binuclear structure (Fig. 11b). Taking into account data listed in Table 3, we note that, from the viewpoint of the 18-electron rule, the binuclear complexes $[UO_2(SO_4)_3]^{4-}$ with $N_e = 7.8 + E_L(SO_4^{2-}//B^{01}) + E_L(SO_4^{2-}//B^2) + E_L(SO_4^{2-}//M^1) = 7.8 + 3.5 + 4.25 + 2.2 = 17.75\ e^-$ are more stable than

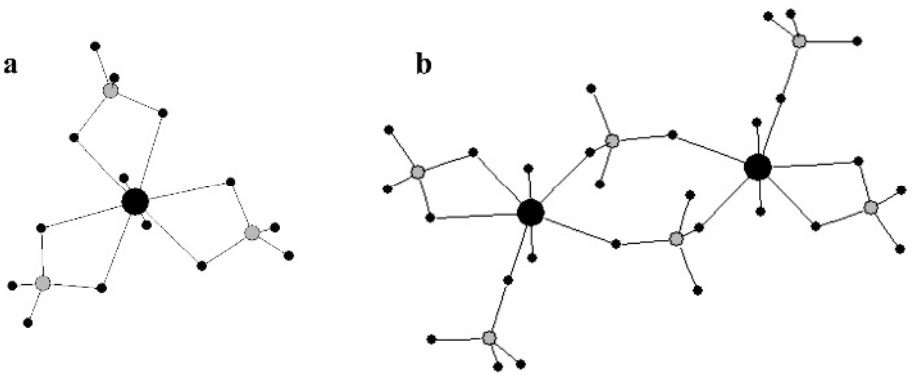

Figure 11. Structure of the $[UO_2(SO_4)_3]^{4-}$ complexes (large circles: U; medium circles: S; small circles: O): (a) mononuclear complex with $CN_U = 8$ in the structure of $(C_5H_{14}N_2)_2[UO_2(SO_4)_3]$ {IPUKOT}; b) binuclear complex with $CN_U = 7$ in the structure of $(C_4H_{14}N_2)_2[UO_2(SO_4)_3].2H_2O$ {IKUDAT}.

mononuclear ones. However, the existence of two $[UO_2(SO_4)_3]^{4-}$ isomers provides the evidence that, for close ΔN_e values (0.3 and 0.25 e^- for mono- and binuclear complexes, Fig. 11), the 'choice' of coordination of the U(VI) atoms (8 or 7) is controlled by the difference in the packing energy of uranyl complexes and outer sphere cations and molecules. Thus, in the structure of $(C_5H_{14}N_2)_2[UO_2(SO_4)_3]$ {IPUKOT} with $CN_U = 8$ (Fig. 11a), the ratio of outer-sphere H atoms able to form hydrogen bonds to the number of terminal O atoms of the sulfate ions, hereafter H:O, is equal to 1.3. If this structure contained dimers (Fig. 11b), then the H:O ratio would be equal to 1.1 due to the increase of the number of the terminal O atoms. In the case of the binuclear complexes $(C_4N_2H_{14})_2[UO_2(SO_4)_3].2H_2O$ {IKUDAT} and $\{NH(C_2H_7N)_3\}[UO_2(SO_4)_3].0{,}5H_2O$ {LABGOL} with $CN_U = 7$, and H:O ≈ 1.5 and 1.8, respectively, formation of mononuclear complexes would lead to H:O = 1.7 and 2.0, respectively. We may conclude that the mononuclear complexes with $CN_U = 8$ are stable at H:O < 1.4, whereas binuclear complexes with $CN_U = 7$ are stable at H:O > 1.4.

As an example of predictive power of stereoatomic model in combination with the 18-electron rule, let us find an answer to the following question:

'What is the coordination number of U(VI) in $[UO_2(SO_4)_4]^{6-}$ complexes?'

Let us consider all possible structures of uranyl tetrasulfates that satisfy the following conditions:

(a) in the $[UO_2(SO_4)_4]^{6-}$ complexes, all U(VI) atoms are equivalent and may have the coordination numbers equal to 5, 6, 7, and 8;

(b) the coordination type of the sulfate ions might be one of the six types possible in uranyl compounds (M^1, B^2, B^{01}, T^3, T^{11} or K^4);

Table 4. Crystal chemical formulas of theoretically possible complexes $[UO_2(SO_4)_4]^{6-}$

№	Crystal chemical formula of the complex *	CN_U	N_e (e^-)	ΔN_e (e^-)
1	$AM^1{}_4 = AM_{4/1}$	6	16.6	1.4
2	$AB^2M^1{}_3 = AB_{2/2}M_{3/1}$	7	18.65	0.65
3	$AB^{01}M^1{}_3 = AB^2{}_{1/1}M_{3/1}$	7	17.9	0.1
4	$AT^3M^1{}_3 = AT_{3/3}M_{3/1}$	8	20.7	2.7
5	$AT^{11}M^1{}_3 = A(T^2{}_{1/1}T_{1/1})M_{3/1}$	8	20.1	2.1
6	$AB^2{}_2M^1{}_2 = AB_{4/2}M_{2/1}$	8	20.7	2.7
7	$AB^{01}{}_2M^1{}_2 = AB^2{}_{2/1}M_{2/1}$	8	19.2	1.2
8	$AB^2B^{01}M^1{}_2 = AB_{2/2}B^2{}_{1/1}M_{2/1}$	8	19.95	1.95

* For all formulas written according to [26], $A \equiv UO_2^{2+}$.

(c) uranyl ions might be linked to each other through bridging sulfate ions only. The results of the analysis are presented in Table 4 and show that the conditions (a-c) are satisfied for 8 possible complexes, which are different in the CNs of U(VI) and crystal-chemical role of sulfate ions. According to the 18-electron rule, only one out of eight complexes (# 3 in Table 4) has $\Delta N_e = 0.1$ and therefore is stable, whereas $\Delta N_e >> 0$ (from 0.65 to 2.7) for all other complexes. In this stable complex, uranyl ion coordinates one bidentate cyclic and three monodentate sulfate ions. It is this very complex that has been observed in the only known uranyl tetrasulfate $Na_6[UO_2(SO_4)_4].2H_2O$ {51751} (Fig. 12).

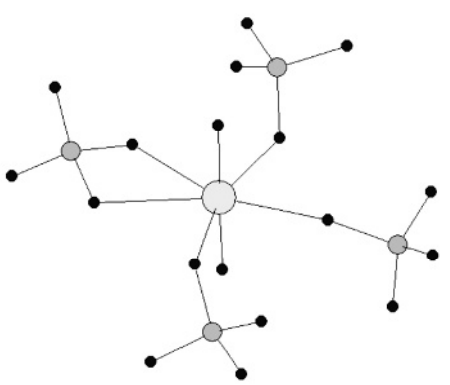

Figure 12. Structure of the $[UO_2(SO_4)_4]^{6-}$ complex with CNU = 7 in $Na_6[UO_2(SO_4)_4].2H_2O$ {51751}.

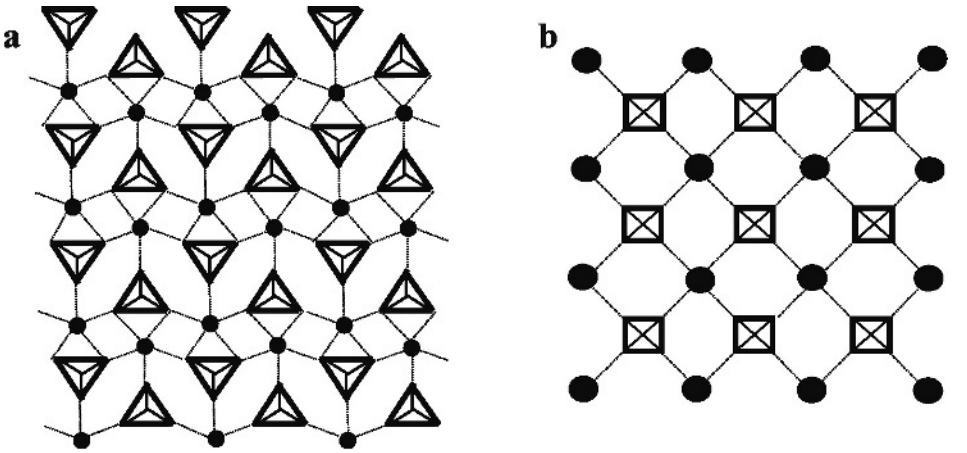

Figure 13. Schemes illustrating structures of layered complexes $[UO_2SiO_4]^{2-}$ (a) and $[UO_2PO_4]^{-}$ (b). Black circles are U atoms, dotted lines are the U-O coordination bonds.

8. Structure of the $[UO_2XO_4]^{z-}$ complexes (X= Si, P или S)

As an additional example of the practical utility of the 18-electron rule for the analysis of relationships between composition, structure and properties of uranyl compounds, let us discuss the problem of influence of tetrahedral cations of the XO_4^{z-} anions (X = Si, P, S) upon the structure of $[UO_2XO_4]^{z-}$ complexes. In particular, we look to the answers to the following questions.

1. 'Why do stoichiometrically identical complexes $[UO_2SiO_4]^{2-}$ (**XXI**) and $[UO_2PO_4]^{-}$ (**XXII**) have different structures?' Indeed, in the structure of XXI, there are uranophane-type sheets with $CN_U = 7$ and $SiO_4^{4-}//T^{31}$ (Fig. 13a), whereas the structures of 'uranium micas' contain sheets of the XXII type that have $CN_U = 6$ and $PO_4^{3-}//K^4$ (Fig. 13b). Taking into account, that, in uranyl compounds the coordination mode of phosphate ions is either T^{31} or K^4, this question can be re-formulated as 'Why is only the K^4 phosphate coordination mode realized in the $[UO_2PO_4]^{-}$ complexes?"

2. "Why does the structure of $[UO_2SO_4]$ (**XXIII**) not contain sheets identical to those found in the structures of 'uranium micas', despite the fact that the coordination mode of tetrahedral anions is K^4 in both $[UO_2PO_4]^{-}$ and XXIII complexes?" Taking into account, that, in contrast to $[UO_2PO_4]^{-}$, in the structure of XXIII, one of the uranyl O atoms is coordinated by the adjacent U(VI) atom (for this reason, $CN_U = 7$), this question can be re-formulated as 'Why is this very rare mutual coordination of uranyl ions realized for $[UO_2XO_4]^{z-}$ complexes (X = Si, P, S) only when X = S?'

3. 'Why are the $[UO_2XO_4]^{z-}$ complexes with X = Si or P stable in relation to water and constitute parts of many hydrate minerals, whereas similar complexes with X = S can be easily hydrated and transformed into $[UO_2SO_4(H_2O)_2]$ complexes with $SO_4^{2-}//T^3$?'

To answer the first question, let us calculate the N_e values for all complexes under consideration. Taking into account the E_L values for $SiO_4^{4-}//T^{31}$ and $PO_4^{3-}//K^4$ (Table 3), we obtain $N_e = 7.8 + 10.5 = 18.3\ e^-$ for $[UO_2SiO_4]^{2-}$, and $N_e = 7.8 + 10.3 = 18.1\ e^-$ for $[UO_2PO_4]^-$. For a hypothetical $[UO_2PO_4]^-$ complex with the uranophane-type structure (**XXIV**) (i.e. for $PO_4^{3-}//T^{31}$ with $E_L = 9.2\ e^-$, Table 3), we obtain $N_e = 7.8 + 9.2 = 17\ e^-$. Thus, for the complex XXIV, the N_e value is not within the range of 18±0.3 e^-, which is typical for stable uranyl complexes. Since $N_e < 18$, the complex XXIV is electron-deficient, that is, unstable and highly reactive. Therefore, for the composition $[UO_2PO_4]^-$, only the K^4 coordination mode is realized (Fig. 13), since $\Delta N_e = 0.1\ e^-$ for XXII is less than $\Delta N_e = 1\ e^-$ for XXIV.

We note that, under assumption that $E_L(XO_4^{z-}//K^4) - E_L(XO_4^{z-}//T^{31}) \cong$ const and using data given in Table 3, we obtain $E_L = 11.6\ e^-$ for $SiO_4^{4-}//K^4$. Using this value, we can establish the N_e value for the hypothetical complex $[UO_2SiO_4]^{2-}$ (**XXV**) with the 'uranium-mica' topology (Fig. 13b). Namely, this complex has $N_e = 7.8 + 11.6 = 19.4 > 18\ e^-$, i.e. XXV is an electron-excessive complex. Therefore, the XXI complex is realized in nature for $[UO_2SiO_4]^{2-}$, which has $\Delta N_e = 0.3\ e^-$, whereas the complex of the XXV type has $\Delta N_e = 1.4\ e^-$.

In order to answer the second question, we note that, for a hypothetical $[UO_2SO_4]$ complex with 'uranium-mica' structure (**XXVI**), $N_e = 7.8 + 8.2 = 16\ e^-$ and $\Delta N_U = 2\ e^-$. That is, it is again the electron-excessive complex. Since, in the structure of XXVI, sulfate ions have the K^4 coordination mode of maximal dentate number and maximal value of $E_L = 8.2\ e^-$ (Table 3), then it is impossible to increase the N_e value to 18 by changing the sulfate coordination mode. Therefore, in order to achieve the 18-electron configuration, each U atom is forced to form additional coordination bond of the $\rightarrow UO_2 \rightarrow UO_2 \rightarrow UO_2 \rightarrow$ type to the O atom of the adjacent uranyl ion. As a result, each uranyl ion acts as a monodentate ligand of the M^1 type relative to the adjacent U atom. Because for $UO_2^{2+}//M^1$, $E_L = 1.7\ e^-$ (Table 3), formation of these uranyl-uranyl bonds results in the appearance of zigzag UO_2 chains (Fig. 14). As a consequence, $\Delta N_e = 0.3\ e^-$, since $N_e = 7.8 + 1.7 + 8.2 = 17.7\ e^-$. Thus, the cation-cation interactions in the structures of isotypic $[UO_2XO_4]$ (X = S, Se, Cr, Mo or W) are explained by the fact that U atoms are forced to accept electrons from adjacent uranyl ions in order to form stable 18-electronic shells.

Now let us come to the last question, which is related to the different reactivity of the complexes to water according to the reaction:

$$[UO_2XO_4]^{z-} + nH_2O \leftrightarrow [UO_2XO_4(H_2O)_n]^{z-}, \quad (29)$$

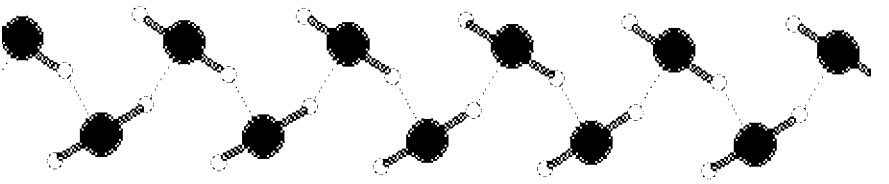

Figure 14. Schematic representation of the uranium-oxygen chains $UO_{1/1}O_{2/2} = UO_2$ formed by uranyl ions in the structures of isotypic UO_2TO_4 (T = S, Se, Cr, Mo, W). Black and white circles denote U and O atoms, respectively.

Formally, this reaction can be considered as a reaction of attachment of water molecules. Since for the initial complexes (XXI)-(XXIII) it holds that $N_e \approx 18\ e^-$ the reaction (29) should be accompanied by the change of the ligand coordination mode. This is necessary in order to compensate the increase of the N_e value due to the inclusion of water molecules (each H_2O molecule increases N_e by 1.9 e^-, see Table 3). In general, this process can be considered as a replacement of coordination bonds of the $XO_4^{z-} \rightarrow UO_2^{2+}$ type by bonds of the $H_2O \rightarrow UO_2^{2+}$ type. The deliberate occurrence of such a replacement, on the one hand, should not lead to the increase of ΔN_e in comparison to the initial complex, and, on the other hand, should be easily possible only under condition that the E_i value of the replacing ligand is higher than the E_i value of the ligand replaced. Since the E_i value for SiO_4^{4-} and $PO_4^{3-} >> E_i(H_2O)$ (Table 3), the H_2O molecules are unable to replace the ligands and the reaction (29) should proceed from right to the left. In the case of anhydrous sulfates, there are $\rightarrow UO_2 \rightarrow UO_2 \rightarrow$ bonds with $E_i = E_L \approx 1.7\ e^-$ and therefore $E_i(SO_4^{2-}) \geq E_i(H_2O) > E_i(UO_2^{2+})$. As a consequence, the reaction (29) should be easily realizable. Moreover, from the structural point of view, this reaction should proceed by the following stages:

$$[UO_2SO_4] + 5H_2O \leftrightarrow [UO_2SO_4(H_2O)] + 4H_2O \leftrightarrow [UO_2SO_4(H_2O)_2] + 3H_2O \leftrightarrow$$
$$\leftrightarrow [UO_2SO_4(H_2O)_3] + 2H_2O \leftrightarrow [UO_2SO_4(H_2O)_4] + H_2O \leftrightarrow [UO_2(H_2O)_5]SO_4 \ . \quad (30)$$

At the first stage of this reaction, the weakest electron donor in the U coordination sphere (uranyl O atom with $E_i = 1.7\ e^-$) is replaced by the water molecule which is stronger as an electron donor ($E_i = 1.9\ e^-$). Since the sulfate coordination mode at this stage is conserved (K^4), the resulting monohydrate has $N_e = 7.8 + 8.2 + 1.9 = 17.9\ e^-$. The second stage of the reaction (30) involves change in the sulfate coordination mode from K^4 to T^3. For the resulting diaquacomplex, $N_e = 7.8 + 6.3 + 2 \cdot 1.9 = 17.9\ e^-$, i.e. is the same as for the monohydrate. From the two complexes $[UO_2SO_4(H_2O)]$ (**XXVII**) and $[UO_2SO_4(H_2O)_2]$ (**XXVIII**) that have the same $\Delta N_e = 0.1\ e^-$, the latter is more

stable, most likely due to the formation of energetically favorable system of hydrogen bonds as a result of the optimized H:O ratio (XXVII: 3.5; XXVIII: 2). The third stage of the reaction (30) would lead to the formation of the $[UO_2SO_4(H_2O)_3]$ complex (**XXIX**) with $SO_4^{2-}//B^2$. This complex has $E_L = 4.25$ e^- (Table 3) and $N_e = 7.8 + 4.25 + 3 \cdot 1.9 = 17.75$ e^-. Since the ΔN_e value increases from 0.1 to 0.25 e^-, the formation of the complex XXIX is difficult. However, from the viewpoint of the 18-electron rule, this complex is also stable (though not favorable in comparison to XXVIII). It seems that, under specific conditions, it can be realized in crystals, as, e.g. in the structure of $[UO_2SO_4.3H_2O]\cdot 0.5$(18-crown-6) {SODGIB}, where it is most likely stabilized by the hydrogen bonding system (O:H = 1.5). The fourth and fifth stages of the reaction (30) do not take place in sulfate-containing systems, because the resulting complexes are unstable ($\Delta N_e = 0.4$ and 0.7 e^-, respectively).

9. Conclusions

As it can be seen from the discussion presented above, the proposed method of quantitative estimation of electron-donor ability of ligands is based upon principally new geometric model of crystal structures. Within this model, the atoms are considered as 'soft' (deformable) spheres of the fixed volume, and the whole structure as a closest three-dimensional packing of these atoms. This packing is equivalent to the Voronoi-Dirichlet partition. The model is in agreement with the existing experimental data and classical concepts of the complex formation in uranyl-based systems (in particular, with the Chernyaev-Shchelokov row). In addition, it provides a unique framework for the interpretation of the experimental facts that have been unexplained previously. The power of the proposed model (and, in particular, its predictive ability) is most likely due to the fact that the 3-dimensional image of chemical bonds in crystals does in fact have many advantages over the classic 1-dimensional description.

The fact that the same model can be applied equally well to crystals as well as to solutions is not something superficial. In our opinion, this provides additional evidence that the short-range order in atomic arrangements conforms to the same laws in both crystals and complexes existing in solutions. The successful application of crystal-structure-based values of electron-donor characteristics of ligands to the problems of complex formation (choice of coordination number, sequence and direction of replacement reactions, etc.) is most probably owing to the adequate character of the model and its description of the chemical interactions.

The principal feature of the stereoatomic model is that it does not use either ionic or atomic radii or any data concerning character of the chemical bonds. In

this work, we demonstrated its power using uranyl complexes as an example. However, this model works well for inorganic and coordination compounds of other metals as well. In particular, the Voronoi-Dirichlet polyhedra and the 18-electron rule help to understand why cation-cation interactions (which are quite rare for uranyl compounds) are common for the neptunyl-based oxocompounds [29].

Since the stereoatomic model allows one to use the abundant crystal-structure data accumulated to the present time for the solution of modern problems of coordination and supramolecular chemistry, one can hope that it will increase its efficiency in the future and will support further progress towards solution of the main problem of chemistry – understanding relations between composition, structure and properties of chemical compounds.

References

1. V.M. Goldschmidt and L. Thomassen, Z. Anorg. Allg. Chem. 163 (1927) 257.
2. Inorganic crystal structure database. Gmelin-institut fur Anorganische Chemie & FIC Karlsruhe. 2004.
3. Cambridge structural database system. November 2004 Release. Cambridge Crystallographic Data Centre. 2004.
4. P.F. Walsh and D.E. Ellis, J. Chem. Phys. 65 (1976) 2387.
5. P. Pyykko, L.J. Laakkonen and K. Tatsumi // Inorg. Chem. 1989. V.28. N 10. P. 1801.
6. D.N. Suglobov and L.G. Mashirov, Radiokhimiya 17 (1975) 699.
7. P. Pyykko, J. Li and N. Runeberg, J. Phys. Chem. 98 (1994) 4809.
8. V.A. Blatov and V.N. Serezhkin, Radiokhimiya 33 (1991) 14.
9. I.I. Chernyaev, ed. Complex Compounds of Uranium. Nauka, Moscow, 1964. 502 p.
10. R.N. Shchelokov, Chemistry of Platinum and Heavy Metals. Nauka, Moscow, 1975. p. 110.
11. V.M. Vdovenko, L.G. Mashirov and D.N. Suglobov, Dokl. AN SSSR 167 (1966) 1299.
12. D.N. Suglobov and L.G. Mashirov, Radiokhimiya, 17 (1975) 699.
13. L.B. Serezhkina and V.N. Serezhkin, Zh. Neorg. Khim. 41 (1996) 427.
14. L.B. Serezhkina and V.N. Serezhkin, Zh. Neorg. Khim. 41 (1996) 438.
15. V.N. Serezhkin, Yu.N. Mikhailov and Yu.A. Buslaev, Zh. Neorg. Khim. 42 (1997) 2036.
16. V.A. Blatov, A.P. Shevchenko and V.N. Serezhkin, Koord. Khim. 25 (1999) 483.
17. V.A. Blatov and V.N. Serezhkin, Russian J. Inorg. Chem. 45 (2000) Suppl. 2, S105.
18. V.N. Serezhkin, L.B. Serezhkina and D.V. Pushkin, Dokl. RAN 379 (2001) 497.
19. V.N. Serezhkin, L.B. Serezhkina, A.P. Shevchenko and D.V. Pushkin, Zh. Fiz. Khim. 79 (2005) 1058.
20. D.V. Korolkov and G.A. Skorobogatov, Theoretical Chemistry. St.Petersburg University Press, 2005. pp. 503-582.
21. V.N. Serezhkin,V.A. Blatov and A.P. Shevchenko, Koord. Khim. 21 (1995) 163.
22. V.A. Blatov, A.P. Shevchenko and V.N. Serezhkin, Dokl. RAN 343 (1995) 771.
23. V.A. Blatov, A.P. Shevchenko and V.N. Serezhkin, Acta Crystallogr. A51 (1995) 909.
24. V.N. Serezhkin and Yu.A. Buslaev, Zh. Neorg. Khim. 42 (1997) 1180.
25. V.I. Minkin, B.Ya. Simkin and R.M. Minyaev, Theory of Molecular Structure. Rostov-na-Donu, Phoenix, 1997. 560 p.
26. M.A. Porai-Koshits and V.N. Serezhkin, Zh. Neorg. Khim. 39 (1994) 1109.
27. S. Tsushima and A. Suziki, J. Molecular Struct. (Theochem) 529 (2000) 21.

28. L.V. Kobets, N.N. Kostyuk and E.A. Filippov, Chemistry of Uranium. Moscow, Nauka, p. 143.
29. V.N. Serezhkin, M.A. Krivopalova and L.B. Serezhkina, Koord. Khim. 24 (1998) 64.

This page intentionally left blank

Structural Chemistry of Inorganic Actinide Compounds
S.V. Krivovichev, P.C. Burns & I.G. Tananaev (Editors)

Chapter 3

Hydrated oxides, hydroxides and peroxides of transuranium elements

Ivan G. Tananaev

A.N. Frumkin Institute of Physical Chemistry and Electrochemistry, Russian Academy of Sciences, Leninsky pr. 31, Moscow, 119991, Russia

1. Introduction

Hydroxides of transuranium elements (TUE) can be obtained as amorphous precipitates from aqueous solutions with certain pH values. This process is preceded by hydrolysis that can be considered as a stepwise removal of H^+ from H_2O molecules from the first coordination sphere of the TUE ions. In order to characterize hydrolytic behavior of the TUE ions, one can use hydrolysis constants according to the following reactions:

$$An^{n+} + H_2O = AnOH^{(n-1)} + H^+ \ (n = 3 \text{ or } 4) \quad (1)$$

$$AnO_2{}^{m+} + H_2O = AnO_2OH^{(m-1)} + H^+ \ (m = 1 \text{ or } 2) \quad (2)$$

Products of these reactions that contain more than one hydroxyl group in the coordination sphere of the metal ions have a strong tendency to polymerize. Owing to this tendency, the reactions (1) and (2) are accompanied by slow and non-equilibrium polymerization of hydroxo-species and their consequent precipitation. The hydrolitic reactivity of TUE ions can be expressed by the following row:

$$An^{4+} > AnO_2{}^{2+} > An^{3+} \sim AnO_2{}^{+} \quad (3)$$

Solubility data for Np, Pu, and Am hydroxo compounds in the III to VI oxidation states in alkaline media were first published in 1949 by the researchers of the Manhattan Project. Later, these data were confirmed and refined by other researchers from different countries. In the following, we consider some data on hydroxides and peroxides of transuranium elements.

2. Transuranium element(III) hydroxides

Transuranium(III) hydroxides form from aqueous solutions at relatively high pH. Their stabilities are remarkably different. For example, Np(III) in the form of $Np(OH)_3$ slowly oxidizes even under anaerobic conditions [1]. Therefore, the Np(III) hydroxide has not yet been synthesized. The Pu(III) hydroxide $Pu(OH)_3$ has a blue color. It can be prepared as an amorphous precipitate using NH_4OH or NaOH. In contrast, $Am(OH)_3$ (pink) and $Cm(OH)_3$ (colorless) can be isolated from solution in the form of a jelly-like precipitate that, under heating, can be transformed into a fine-crystallized state. The crystallization time increases with temperature, and at 130°C (in the autoclave) may take more than one hour [2].

The hydroxides of berklium(III), $Bk(OH)_3$, and californium(III), $Cf(OH)_3$, behave in a similar fashion [3]. In their crystalline forms, $Am(OH)_3$ and $Cm(OH)_3$ are anhydrous (as are hydroxides of light rare-earth elements), and are hexagonal, $C^2_{6h} - P6_3/m$ space group, a = 6.420 and 6.391 Å, c = 3.745 and 3.712 Å, for Am and Cm compounds, respectively. Due to self-irradiation, the unit-cell parameters increase with time, as does the sample amorphization. In the case of $^{244}Cm(OH)_3$, the structure decomposes within 1 day, but the same process for $^{241}Am(OH)_3$ takes up to 4-6 months [4]. The Mössbauer spectrum of $Am(OH)_3$ [5] is characterized by δ = 4.6 cm/c (relative to AmO_2). The nuclear magnetic resonance (NMR) studies indicate that, among the TUE(III) hydroxides, the Am compound has the most covalent chemical bonds. The TUE(III) hydroxides are readily soluble in different mineral acids; under these conditions, the solutions of hydrated An^{3+} ions are produced.

In contrast to plutonium(III) hydroxide, $Am(OH)_3$ does not react with oxygen. However, this compound is still highly reactive, and easily participates in different heterogeneous redox-reactions. Oxidation of $Am(OH)_3$ by hypocloride, and peroxydisulphate in dilute base is the primarily route for $Am(OH)_4$ or $AmO_2 \cdot xH_2O$ preparation [6]. The same product results also during the room-temperature interaction of 2 mM Am(III) hydroxide with $K_3Fe(CN)_6$ in greater than 0.07 M NaOH solution. In 2M NaOH solution 0.04M $K_3Fe(CN)_6$ oxidizes $Am(OH)_3$ to Am(V) [7]. In the solid state, or in an aqueous pulp, $Am(OH)_3$ actively reacts with ozone. This reaction in dilute alkaline solutions results in the formation of americium(VI) solutions. The americium(III) oxidation rate does not depend on the composition of the solution (0.1M $NaHCO_3$, 0.1M Na_2CO_3 + 1-2M NaOH, 0.1-1M NaOH) at room temperature, and Am(VI) is finally formed. In fact, the 0.1-1M LiOH solutions are preferred media for obtaining the Am(VI) solutions by means of the described technique [8]. The values of the observed rates of the Am(III) → Am(VI) reaction increases from $2.2 \cdot 10^{-5}$ to $9.25 \cdot 10^{-5}$ $M \cdot min^{-1}$ with the increase of the initial Am

amount from $6.5 \cdot 10^{-4}$ to $2.6 \cdot 10^{-3}$ M, and decreases from $2.73 \cdot 10^{-5}$ to $2.22 \cdot 10^{-5}$ $M \cdot min^{-1}$ with an increase of $[OH^-]$ from 0.1 to 1.0 M.

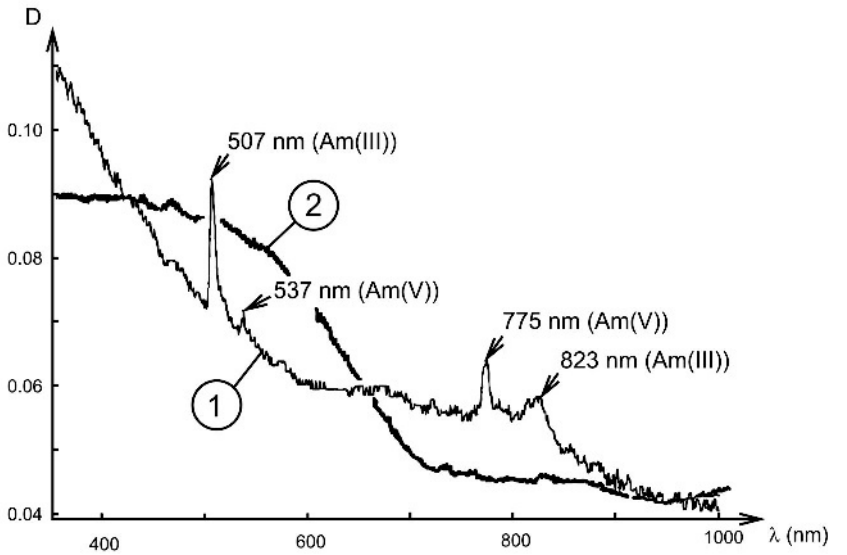

Fig. 1. The absorption spectra of: (1) Am(III) and Am(V) hydroxides in 1M NaOH solution at 20°C; (2) The product of interaction of Am(III) and Am(V) hydroxides in 1M NaOH at 70°C or >6M NaOH at 20°C.

During ozonation, the $Am(OH)_3$ pulp dissolves in several minutes and the solution color turns red, and, under these conditions, Am(III) is stepwise oxidizes to Am(IV), Am(V) and Am(VI). The completion time of the oxidation reaction does not exceed 15 – 20 min. Spontaneous [Am(V)]↔[Am(VI)] oscillations have been observed in the 0.1M $NaHCO_3$ media (Fig. 1). Using the ^{241}Am and ^{243}Am species, it was shown that the oscillations can not be explained by the Am self α-radiolysis generation of reducers in initial solutions. The oscillations take place only during bubbling of ozone through the reaction system. It was concluded that the oscillation phenomena may occur due to: (1) oxidation of Am(V) to Am(VI) by ozone; (2) the consequent reduction of the latter by the products of ozone decay; (3) their interactions, resulting in the appearance of HO_2^- and H_2O_2, which react rapidly with Am(VI) and ozone. The period of the [Am(VI)]↔[Am(V)] oscillations was estimated to be not more than 2 min [9].

An important observation has been made recently: the mixing of equivalent amounts of ^{243}Am(III) and ^{243}Am(V) hydroxides in 1M NaOH at 50-70°C, or in 7M NaOH at 25°C during over the course of few minutes, results in formation of pure Am(IV) species via the reproportionation reaction Am(III) + Am(V) =

2Am(IV) (Fig. 2). The reaction between Am(VI) and Am(III) hydroxides in equivalent amounts provides the same result [10].

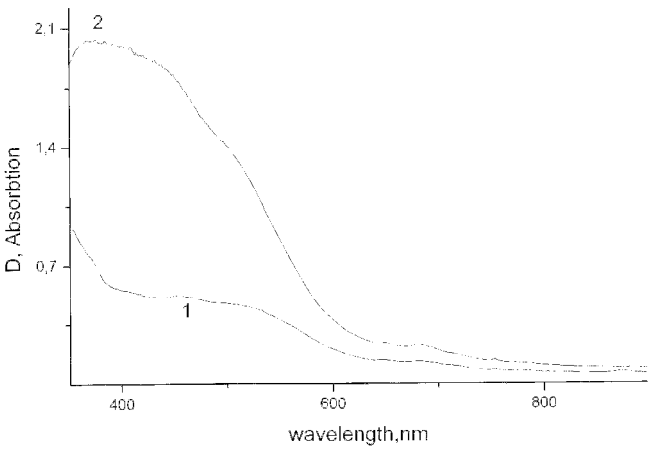

Fig. 2. The changes of absorption spectra of the Am species in 0.12M $NaHCO_3$ solution during the interaction of $Am(OH)_3$ aqueous suspension with ozone at 20°C. l = 1 cm. The oscillations of [^{243}Am(VI)] are limited by curves (1) and (2). Total [Am] in the solution was 7.7 10^{-4}M.

$Cm(OH)_3$ in alkaline solutions does not interact with O_3, ClO^-, or $S_2O_8^-$ [11].

The data for TUE hydroxide solubility in different media have recently receive a great deal of attention due to their importance for development of clean-up technologies, etc. It is known that the $Pu(OH)_3$ solubility in water and 5M ammonium solution is equal to $7.5 \cdot 10^{-3}$ M and $3.8 \cdot 10^{-4}$ M, respectively [12]. The solubility product of the Pu(III) hydroxide is about $2 \cdot 10^{-20}$ [13,14]. According to the data of different authors, the solubility products of $Pu(OH)_3$ and $Am(OH)_3$ hydroxides are equal to about 10^{-25} [15]. The solubility of Pu(III) hydroxide in 5M NH_4OH is $3.8 \cdot 10^{-4}$ M [16], and the solubility of Am(III) in 0.01-5M NH_4OH is $1.6 \cdot 10^{-6}$ M [17]. The suggested chemical form of these alkali-dissolved hydroxides is a neutral $Am(OH)_3$-type molecule, which does not tend to have an amphoteric nature or to form complexes with OH^- ions. Despite the low solubility of TUE(III) hydroxides, in the crystalline form they can be easily dissolved. Thus, the concentration of the $Am(OH)_3$ and $Cm(OH)_3$ colloid solutions may exceed more than 100 g/L [4].

3. Transuranium element (IV) hydroxides

TUE(IV) hydroxides with the general composition $AnO_2 \cdot xH_2O$ ($x < 2$) are known for Np, Pu, and Am. Moreover, the compound $NH_4Np(OH)_5$ has been synthesized by hydrothermal methods at 550 K and a pressure of ~ $1{,}5 \cdot 10^8$

Pa. This compound is monoclinic, $P2_1$, a = 8.704, b = 8.704, c = 7.067 Å, γ = 127.16°, $\rho_{calculated}$ = 5.29 g/cm^3, Z = 4. There are two Np sites that are 9-coordinated by O atoms. The structure is based upon $[Np_2(OH)_{10}]^{2-}$ layers with NH_4^+ ions in the interlayer space [18].

The tendency of Pu(IV) to hydrolyze and to form real solutions, colloid solutions, or insoluble precipitates has been known since the Manhattan Project. The main results of the earlier work in this field were summarized by Seaborg and Katz [19]. Since then, studies have been performed to examine in detail the equilibrium of Pu(IV) hydrolytic reactions in different media [20,21]. Great attention has also focused on the preparation, structure and properties of Pu(IV) polymers or colloids [22-27]. These compounds have found an important application in sol-gel technology for the preparation of nuclear fuel materials [28]. However, studies of the properties and behavior of solid Pu(IV) hydroxide in complex heterogeneous systems are rather rare. A most important result of these studies was the conclusion that Pu(IV) hydroxide, after some aging, consists of very small PuO_2 crystallites and, therefore, should be considered as a Pu(IV) hydrous oxide [23,24].

Tetravalent Np and Pu hydroxides were isolated from solutions with pH >3. These appear as amorphous precipitates with colors from light-yellow to dark-brown. These compounds can be easily dissolved in different mineral acids.

The properties of $PuO_2{\cdot}xH_2O$ are of interest from the viewpoint of treatment of alkaline waste tanks at Hanford (USA). The studies of $PuO_2{\cdot}xH_2O$ were focused on determination of composition and structural properties of this compound aged in complicated salt systems. At the present time, there is very limited information concerning the ability of Pu(IV) hydrous oxide to include in its composition minor quantities of nitrate ions [29]. To obtain more definite data, a number of $PuO_2{\cdot}xH_2O$ samples were analyzed for NO_3^- content. It was found that the nitrate content in $PuO_2{\cdot}xH_2O$ prepared under different conditions does not exceed 0.03 mol%. Such a small concentration cannot remarkably affect the $PuO_2{\cdot}xH_2O$ properties and was neglected in subsequent experiments [30].

Long-term aging of the compounds that were modeled by their coagulation at elevated temperatures including hydrothermal conditions, does not result in the formation of well crystallized phases. The “x” value depends strongly on the conditions of the drying of $PuO_2{\cdot}xH_2O$, but it is not sensitive to the precipitation method (direct or reverse) and coagulation time. For the $PuO_2{\cdot}xH_2O$ samples prepared at 10 to 60°C and dried in desiccators over KOH pellets and then over 25% H_2SO_4, the mean values of “x” are equal to 1.6 and 2.8, respectively. The rather large difference of these values confirms the strong hygroscopic properties of $PuO_2{\cdot}xH_2O$. As the temperature increases the x values tend to go down. The composition of $PuO_2{\cdot}xH_2O$ obtained at 180 to 200°C and dried over KOH is characterized by an average x = 0.60.

Thermogravimetric scans of various $PuO_2 \cdot xH_2O$ samples are similar and do not depend upon the preparation conditions. In all cases, the mass loss is monotonous in the range from 50 to 250°C. All differential thermal analysis curves show gentle endothermic picks at about 110°C. This confirms that water in $PuO_2 \cdot xH_2O$ does not have discrete states, but is characterized by a continuous range of bonding energy.

Anhydrous PuO_2, produced from $PuO_2 \cdot xH_2O$ by heating, possesses clearly expressed hygroscopic properties. They remain even after prolonged heating of the compound at 500°C and disappear only at 800°C. The small influence of temperature on the $PuO_2 \cdot xH_2O$ hygroscopicity can be explained by the rather high thermal stability of primary crystallites. This supposition was confirmed by direct estimations of crystallite size in the $PuO_2 \cdot xH_2O$ samples, after they were heated to different temperatures. The estimates of crystallite size were derived by X-ray powder diffraction methods. It was found that $PuO_2 \cdot xH_2O$ crystallite size increases only from ~2.5 to 7 nm in the range of temperatures from 20 to 800°C (Fig. 3). Infrared (IR) spectra of different $PuO_2 \cdot xH_2O$ samples closely resemble each other and show an intense band with a maximum at 3400 cm^{-1}, 3 weak bands in the interval 1700-1250 cm^{-1} and an additional strong, and usually split band between 600 and 350 cm^{-1}. The band at 3400 cm^{-1} arises from vibrations of water in the $PuO_2 \cdot xH_2O$ structure, is relatively wide and smooth, and has no shoulder. This fact confirms the above mentioned assumption that there are no discrete states of water molecules in the compound structure. The bands with a maximum at 1640 cm^{-1} and in the low frequency region can be attributed to deformation vibrations of H_2O and vibrations of Pu-O bonds in PuO_2 crystallites, respectively (Fig. 4).

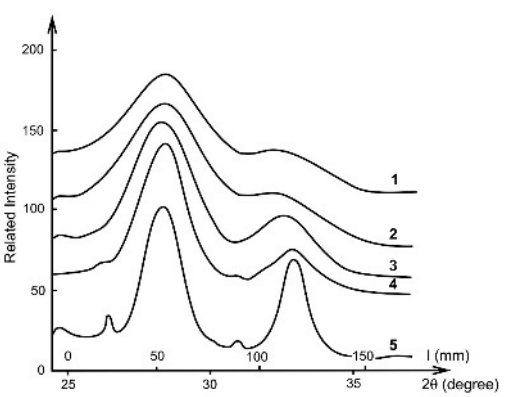

Fig. 3. X-ray diffraction patterns of PuO_2*xH_2O (the shape of the 111 line) as a function of heating temperature (in °C): 1 - 75; 2 - 200; 3 - 300; 4 - 400; 5 - 800.

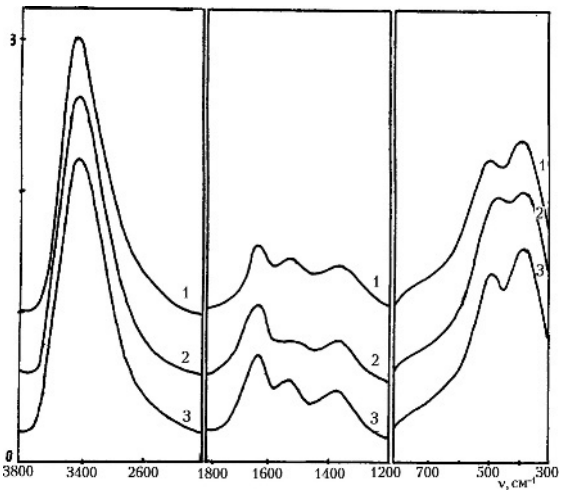

Fig. 4. IR spectra of $PuO_2 \cdot xH_2O$ samples (the vertical axis gives absorption in relative units). The conditions of coagulation: 1) 1 h in 0.2M NaOH at 12°C; 2) 5 h in 0.2M NaOH at 200°C; 3) 9 h in 8M NaOH at 100°C.

Sedimentation of $PuO_2 \cdot xH_2O$ is usually complete in 2 to 3 hours. The rate of the process decreases with an increase of the liquid phase density in the sequence H_2O > 1M NaOH > 3M NaOH > 3M NaOH + 3M $NaNO_3$. The influence of the aging conditions on the precipitation rate of $PuO_2 \cdot xH_2O$ is irregular and is not very strong. Only for compounds prepared under hydrothermal conditions at 160-200°C, the precipitation rate in water and 1M NaOH is considerably higher than those found for precipitates prepared at lower temperatures.

In contrast to precipitation rate, the specific volumes of the $PuO_2 \cdot xH_2O$ precipitates are practically independent on the liquid phase composition and density. However, the specific volumes significantly decrease with $PuO_2 \cdot xH_2O$ aging. Samples coagulated under hydrothermal conditions at 180 to 200°C generally have specific volumes 3 times lower than those of precipitates aged at room temperature. Precipitate volumes after centrifugation are less sensitive to the aging conditions. Their average value is equal to ~5 ml/g Pu. The plutonium concentration in mother solutions over $PuO_2 \cdot xH_2O$, centrifuged 2 minutes after the beginning of precipitation, was found to be about 2 to 3 orders of magnitude higher than observed for the solubility of the compound under the same conditions. The plutonium concentration decreases as a function of time. However, it remains high even after a day of coagulation. The precipitation of $PuO_2 \cdot xH_2O$ likely proceeds through the formation of colloids and very fine particles that remain as a suspension during centrifugation. The use of ultrafiltration instead of centrifugation provides about a factor of 100 decrease in the plutonium concentration in the mother solutions.

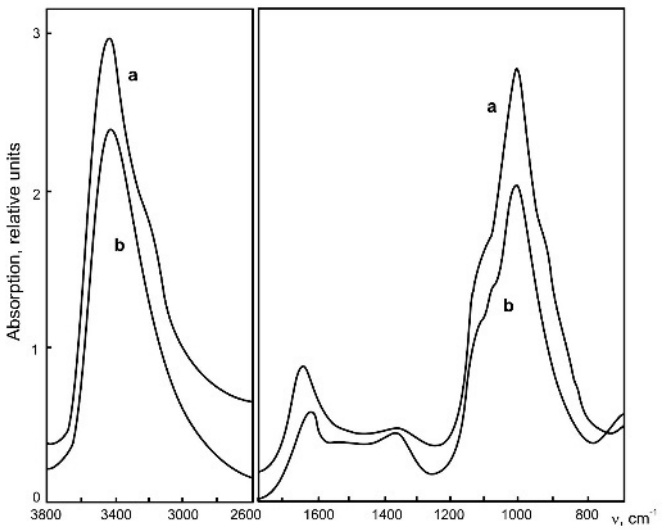

Fig. 5. IR spectra of $PuO_2 \cdot 0.88SiO_2 \cdot xH_2O$ (a) and $PuO_2 \cdot 0.15P_2O_5 \cdot xH_2O$ (b) samples.

Special experiments showed that the compounds precipitated from 0.2M NaOH at room temperature or from 1M NaOH at 60°C in the presence 2M NO_2^-, 0.1M $C_2O_4^{2-}$, $HOCH_2COO^-$, EDTA, HEDTA, citrate, 0.5M CO_3^{2-} and SO_4^{2-} had, after careful water washing, the same composition and hygroscopic properties as $PuO_2 \cdot xH_2O$ obtained by Pu(IV) precipitation from pure NaOH solutions. The mentioned anions do not significantly alter the rate or completeness of $PuO_2 \cdot xH_2O$ precipitation. Pu(IV) precipitation characteristics, however, are altered for alkaline solutions containing silicate or phosphate anions. In both cases, changes in the color and volume of precipitates have been observed (Fig. 5). Water washing of the precipitates gave considerable peptization. The results of direct analyses showed that the Pu(IV) compounds precipitated from alkaline solution in the presence of 0.05M SiO_3^{2-} at low NaOH concentrations were more likely silicates than $PuO_2 \cdot xH_2O$. Significant amounts of silicate were detected even in products obtained in 7 M NaOH. In addition, silicate was found to interact with $PuO_2 \cdot xH_2O$ prepared separately under hydrothermal conditions. The alkali precipitation behavior of Pu(IV) is similar in the presence of phosphate and silicate. However, the degree of anion capture and the stability of compounds at high NaOH concentration for phosphate are significantly lower than that for silicate.

Based on these results, it is reasonable to conclude that $PuO_2 \cdot xH_2O$ cannot be present in alkaline tank wastes containing significant silicate concentrations. Under such conditions, Pu(IV) should exist as various basic silicates depending on the waste composition. However, this conclusion may be complicated by the behavior of mixed hydroxides of Pu(IV) and Fe(III) or other

elements in alkaline silicate media. This problem requires special investigation [31-33].

During the experimental determination of Pu(IV) hydroxide solubility, the slow increase of the Pu concentration in solution, and simultaneous decrease of pH was detected [34]. It is suggested that this effect is related to the accumulation of nitric acid in the solution due to the self α-irradiation of the suspension. Actually, during storage of 0.5 g of $^{238}PuO_2 \cdot xH_2O$ in 30 ml three times distillated water in an isolated system within 1266 aging days of the pulp, the concentration of NO_3^- was stabilized at the level of about 0.04M, and the pH values were changed from 7 to 1.52.

The primary investigations concerning aging of crystalline $^{239}PuO_2$ and amorphous $^{239}PuO_2 \cdot xH_2O$ in aqueous suspensions were carried out by Rai and Ryan [35]. These authors provided monitoring of the samples in solutions over 1300 days. The hypothesis that the amorphization of crystalline PuO_2 is closely related to permanent oxidation of Pu(IV) to Pu(V) or Pu(VI) was proposed. The solubilities of the Pu(V) and Pu(VI) compounds are much higher.

This hypothesis is in agreement with other experimental data [36,37]. For example, Fig. 6 shows that, in the presence of $^{239}PuO_2 \cdot xH_2O$, accumulation of Pu(V) is observed even in alkaline solutions. On the basis of the literature data [49,54] that states $\varepsilon_{810}^{Pu(V)} = 12$ L/M·cm, the [Pu(V)] concentration is calculated to be $3 \cdot 10^{-5}$ M.

Additional information exists concerning the ease of Pu(IV) to Pu(V) oxidation in neutral and subacid solutions [38-42]. Under these conditions, increasing the alkaline concentration results in the strong stabilization of Pu(V). It was found that, on the surface of the Pu(IV) hydroxides, plutonium is oxidized to Pu(V) by atmospheric oxygen and O^- and OH^-_2 radicals – products of water decomposition, and possible nitrate- and nitrite-ions. The yield of back reduction of Pu(V) has been calculated as following [43]:

$$G[-Pu(V)] = k\,(100/0.693A), \qquad (4)$$

where $k = -2.3 d\log[Pu(V)]/dt$ (in days), and $A = \Sigma g_i E_\alpha/(100 T_{1/2})$; g_i - % degree of Pu in the sample, E_α - energy of α-particles, in eV, and $T_{1/2}$ – half-life period of the nuclide (in days). The value A for ^{239}Pu is calculated as 0.765. This number is very important for predicting the Pu behavior in the alkaline waste.

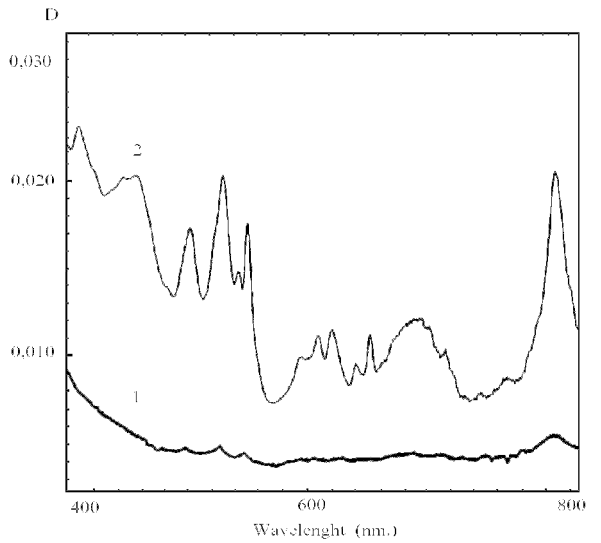

Fig. 6. Absorption spectra of Plutonium (IV) and (V) [36]. 4M NaOH under the $^{239}PuO_2 \cdot xH_2O$ sediment at 26°C. Contact time 14 days; l = 5 cm. 1 mM Pu(V) in 8M NaOH at 12°C; l = 1 cm.

For preparation of the Am(IV) hydroxide, a suspension of 1-10 mg of ^{241}Am(III) or ^{243}Am(III) hydroxide should be treated by an ozone-oxygen gas mixture of $[O_3]$ = 2-5% (vol.) within 40 min at room temperature. The obtained Am(VI) solution is then subjected to irradiation by ultrasonic waves of 22-44 kHz frequency with an intensity of about ~1 W/cm^2 until the appearance of brown precipitate representing the Am(III) hydroxoperoxide. The latter can be readily transformed into an Am(IV) hydrous oxide by treatment by 7-10 M NaOH [10]. $AmO_2 \cdot xH_2O$ is stable, and heating to 90°C does not result in the disproportionation of Am(IV). Slow reduction of Am(IV) to Am(III) occurs due to the americium alpha radiation. At 25°C, the solubility of $AmO_2 \cdot xH_2O$ in 13M NH_4F is 0.02M and the solid phase in equilibrium is $(NH_4)_4AmF_8$. Concentrated solutions of KF, RbF, and CsF also react with $Am(OH)_4$ yielding sparingly soluble Am(IV)-fluoride complexes. In 13M NH_4F, 0.02M Am(IV) has a pink color and a characteristic absorption spectrum that is different from those of Am(III), Am(V), and Am(VI). The narrow Am(IV) peak at 456 nm (ε = 30 L/mol·cm) is separated from peaks of other americium valence states and can be used to determine Am(IV) quantitatively [44].

According to different data, the logarithms of the solubility products of $Np(OH)_4$ and $Pu(OH)_4$ are ~(53-56) and (52-57), respectively. The solubility of $NpO_2 \cdot xH_2O$ in a neutral media without complex-forming agents is of the order of 10^{-8} M. The solubility of $NpO_2 \cdot xH_2O$ in 0.8M NaOH and 0.8M Na_2SO_4 solutions is equal to $8.4.10^{-6}$ M [1]. Rai and Ryan [35] demonstrated that, under conditions excluding Np(IV) oxidation, the solubility of its carbonate (0.01M)

in solutions within the pH range of 6 - 14.2 is less than $5 \cdot 10^{-9}$ M, and that it does not increase upon the addition of 0.01 M Na_2CO_3. In the solutions studied ([NaOH] < 1.2 M), these authors did not find signs of the amphoteric nature of the Np(IV) hydroxide and the formation of $Np(OH)_5^-$ complexes [45].
The solubility of the $PuO_2 \cdot xH_2O$ hydroxide and PuO_2 oxide in water at pH = 6-8 under conditions excluding oxidation was found to be 10^{-6} - 10^{-7} M [46] and 10^{-7} - 10^{-9} M [47], respectively. Our attempts to find literature data on the solubility of $PuO_2 \cdot xH_2O$ in NaOH solutions under conditions excluding oxidation were unsuccessful. The rate of oxidation of $PuO_2 \cdot xH_2O$ with oxygen from air for 2-4 h in 0.2-2M NaOH is too slow to be reliably measured under the conditions specified [48]. The solubility of $PuO_2 \cdot xH_2O$ in 1-15 M NaOH solutions during long-term storage in the presence of air was studied by Delegard [49]. Under these conditions, the solubility of this compound was shown to increase with an increase in the alkali concentration (from 10^{-7} to 10^{-8} M in 1M NaOH to 10^{-3} M in 15 M NaOH). According to spectrophotometric data for these solutions, alkali-dissolved plutonium is mainly in the pentavalent state, which is explained by the oxidation of $Pu(OH)_4$ with oxygen and radiolysis products. The addition of carbonates and aluminates increases the solubility of $PuO_2 \cdot xH_2O$ in 1–15M NaOH.

TRE(IV) hydroxides are insoluble in both water and basic solutions. The mature samples of $PuO_2 \cdot xH_2O$ dissolve in mineral acids very slowly and incompletely. The dissolution of hydroxides is rapidly accelerated in the presence of F^- ions. The decomposition of polymeric forms of $PuO_2 \cdot xH_2O$ usually proceeds in solutions of nitric acid with $[H^+] > 2M$ containing 3-10 g/L H_2O_2 during heating. Dissolution of $NpO_2 \cdot xH_2O$ in $[HNO_3] > 0.3M$ is accompanied by Np(IV) oxidation [50].

4. Transuranium elements(V) hydroxides

TUE(IV) hydroxides possess weak amphoteric properties, and are known for neptunium and americium. Preparation of fine Pu(V) hydroxide is complicated by the increasing tendency towards PuO_2^+ disproportionation. The preparation of Pu(V) hydroxide by alkalization of Pu(V) solution has been reported [51]. This compound (gray–white in color) with the composition $PuO_2OH \cdot H_2O$ has a solubility constant (K_s) that changes from $\sim 5 \cdot 10^{-10}$ [51] to $2.5 \cdot 10^9$ M^2 [52]. In our opinion, the Pu(V) hydroxide $PuO_2OH \cdot H_2O$ is impossible to obtain, because, under these conditions, Pu(V) is highly unstable and, following disproportionation, only mixtures of Pu(IV) and Pu(VI) are produced with their subsequent transformation (for example, due to the interaction with CO_2). Pu(V) could be stable only in solutions with $[OH^-] \sim$ 6-8M [53-55]. Moreover, under these conditions, the $AnO_2OH \bullet H_2O$ hydroxides

(An = Np, Pu, Am) transform into crystalline hydroxo-compounds with the composition $M_2AnO_2(OH)_3 \cdot xH_2O$ (M = alkaline metal cation) [56-59].

The compound $NpO_2OH \cdot xH_2O$ (n ~ 0.8) is often used as a starting compound for preparation of stock Np(V) solutions. This compound has been isolated from a solution of pentavalent neptunium during alkalization by a small excess of NH_4OH or NaOH as green amorphous sediment that, under frequent washing by water, can easily be peptized. If the washing of the sediment done using a 50% water – ethanol mixture (Vodka), the peptization is not observed. Heating of $NpO_2OH \cdot xH_2O$ in the interval from 180 to 200°C leads to the formation of Np_2O_5, and, under temperatures more than 420°C, NpO_2 is produced. Mössbauer spectra of $NpO_2OH \cdot xH_2O$ registered at 4.2 K are characterized by the following parameters (in cm/sec): δ = -1.8 (related to NpO_2), 1/4eqQ = 2.25 and $g_o\mu_nH_{ef}$ = 9.84 [60]. In a dried sample at 100°C, in the presence of ozone, Np is stabilized in the hexa-, and partly (till 40%) heptavalent states [61]. Interaction of $NpO_2OH \cdot xH_2O$ in aqueous suspension with ozone leads to the formation of $NpO_3 \cdot 2H_2O$ with the Np(VII) admixtures. Addition of a great excess of alkalies to solutions containing Np(V) and the long-term storage of the sediments results in colored crystalline compounds $MNpO_2(OH)_2 \cdot xH_2O$ (M = Li, Na, K, Rb, Cs), and $M_2NpO_2(OH)_3 \cdot xH_2O$ (M = Na, K, Rb, Cs) [56-59]. Interactions of $MNpO_2(OH)_2 \cdot xH_2O$ and $M_2NpO_2(OH)_3 \cdot xH_2O$ with carbonate compounds results in the formation of $MNpO_2CO_3 \cdot xH_2O$ compounds, and their calcination at 300°C for $MNpO_2(OH)_2 \cdot xH_2O$ (M = Na and K) leads to the formation of MNp_2O_7 [59].

It has long been known that pentavalent neptunium forms $NpO_2(OH)_2^-$ and $NpO_2(OH)_3^{2-}$ hydroxocomplexes in aqueous alkaline solutions [62], but there is almost no information available concerning the crystal structures and properties of these compounds. Unfortunately, all of these complexes crystallize very poorly, so direct X-ray diffraction studies are difficult. Therefore, valuable information concerning their structure and other properties need to be obtained by indirect methods. In this regard, ^{237}Np Mössbauer, ESR, IR, and electronic absorption spectra of $MNpO_2(OH)_2 \cdot xH_2O$ (I), $M_2NpO_2(OH)_3 \cdot xH_2O$ (II) hydroxo complexes with M = Li, Na, K, Rb, and Cs, and $NpO_2(OH) \cdot xH_2O$ (III) have been studied.

Electronic absorption spectra (EAS) of $MNpO_2(OH)_2 \cdot xH_2O$ (M= Li, Na, K, Rb, and Cs) and $M_2NpO_2(OH)_3 \cdot xH_2O$ (M = Na, K, Rb, and Cs), as well as of $NpO_2OH \cdot xH_2O$ are shown in Fig. 7a-f. It is clear that the intensities of the main absorption band near 1000 nm are low (the molar extinction coefficient is within the range of $\varepsilon \approx$ 10-30 dm/mol·cm), whereas high intensities ($\varepsilon \approx$ 180-200 dm/mol·cm) were observed for this band in the absorption spectra of the $M_2NpO_2(OH)_3 \cdot xH_2O$ series. Band positions and molar extinction coefficients are listed in Table 1**.** It should be noted that the absorption band maxima (λ_{max})

are shifted towards the long-range region of the spectra relative to the absorption maximum of $\lambda_{max} \approx 980$ nm of the $NpO_2OH \cdot xH_2O$ cation in aqueous solution. Additionally, the bands in the spectra of $Rb_2NpO_2(OH)_3 \cdot xH_2O$ and $Cs_2NpO_2(OH)_3 \cdot xH_2O$ are split in two, unlike absorption spectra of $Na_2NpO_2(OH)_3 \cdot xH_2O$ and $K_2NpO_2(OH)_3 \cdot xH_2O$ (see Fig. 7), where only single absorption bands have been observed.

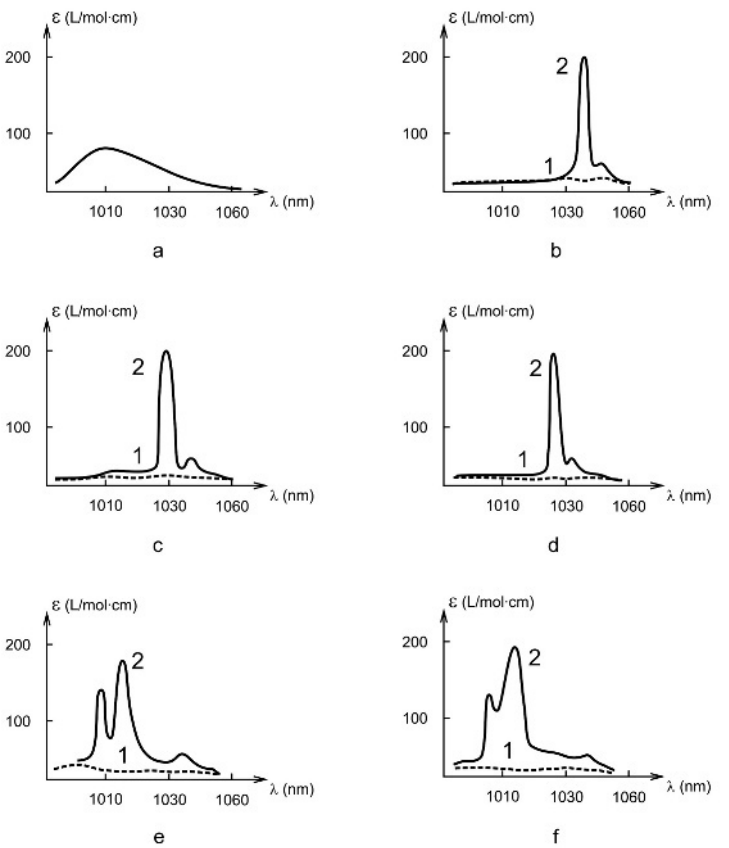

Fig. 7. Portions of absorption spectra of Np(V) hydroxo-compounds in a matrix of solid NaCl: a.$NpO_2OH \cdot xH_2O$; b. $LiNpO_2(OH)_2 \cdot xH_2O$ (1) and $Li_2NpO_2(OH)_3 \cdot xH_2O$ (2); c. $NaNpO_2(OH)_2 \cdot xH_2O$ (1) and $Na_2NpO_2(OH)_3 \cdot xH_2O$ (2); d. $KNpO_2(OH)_2 \cdot xH_2O$ (1) and $K_2NpO_2(OH)_3 \cdot xH_2O$ (2); e. $RbNpO_2(OH)_2 \cdot xH_2O$ (1) and $Rb_2NpO_2(OH)_3 \cdot xH_2O$ (2); f. $CsNpO_2(OH)_2 \cdot xH_2O$ (1) and $Cs_2NpO_2(OH)_3 \cdot xH_2O$ (2)

Table 1. Maximum absorption wavelenghts and intensities of the main band in electronic absorption spectra of $MNpO_2(OH)_2 \cdot xH_2O$, $M_2NpO_2(OH)_3 \cdot xH_2O$, and $NpO_2(OH) \cdot xH_2O$

Compound	Absorption band, λ (nm)	Molar extiction coefficients, ε (L/mol·cm)
$NpO_2(OH) \cdot xH_2O$	1010-1015	60-70
$M_2NpO_2(OH)_3 \cdot xH_2O$	1000-1040	10-30
$Na_2NpO_2(OH)_3 \cdot xH_2O$	1030	180-200
$K_2NpO_2(OH)_3 \cdot xH_2O$	1028	180-200
$Rb_2NpO_2(OH)_3 \cdot xH_2O$	1025	130
	1010	123
$Cs_2NpO_2(OH)_3 \cdot xH_2O$	1021	137
	1006	122

IR spectra were recorded for the $MNpO_2(OH)_2 \cdot xH_2O$ complexes with M = Na, K, Rb, and Cs. The absorption bands in the 740-780 cm^{-1} frequency range were detected in the IR spectra for all compounds investigated. These bands are assigned to the asymmetric stretching vibration mode ν_{as} of the NpO_2^+ group. Band frequencies are listed in Table 2 together with the data on the λ_{max} absorption maximum wavelengths of the main band near 1000 nm in optical spectra of $M_2NpO_2(OH)_3 \cdot xH_2O$. It is interesting to note that there is an apparent correlation between the ν_{as} frequency in IR spectra and ionic radius of the outer-sphere cation M, i.e. ν_{as} frequency rises with increase of the size of the cation. On the other hand, the ν_{as} frequency correlates well with λ_{max} in optical spectra: the higher the ν_{as}, the smaller λ_{max}. In addition, as in optical spectra, the ν_{as} band splits into two components in the IR spectra for the Rb and Cs compounds.

Table 2. Frequences of the ν vibration mode in IR spectra of $M_2NpO_2(OH)_3 \cdot xH_2O$ hydroxo-complexes and their comparison with the data on optical absorption spectra

Element	Ionic radius (Å)	ν (cm^{-1})	Position of the main band in EAS (λ, nm)
Na	0.98	740	1030
K	1.33	750	1028
Rb	1.48	764	1025
		772	1010
Cs	1.67	772	1021
		776	1006

Table 3. Observed signals in ESR spectra of $MNpO_2(OH)_2 \cdot xH_2O$, $M_2NpO_2(OH)_3 \cdot xH_2O$, and $NpO_2(OH) \cdot xH_2O$ hydroxides and their comparison with molar extinction coefficients of the main band at ~1000 nm in electronic absorption spectra

Compound	ESP signal with $g_{\parallel} \sim 6$; $g_{\perp} \sim 0$ (at 77 and 300 K)	Other ESP signal (300 K)	Molar extiction coefficients ε (L/mol·cm) at ~1000 nm
$NpO_2(OH) \cdot xH_2O$	Off	Broad signal at g ~ 3	~60
$MNpO_2(OH)_2 \cdot xH_2O$	Off	Off	10-20
$Na_2NpO_2(OH)_3 \cdot xH_2O$	Moderate	Broad signal at g ~ 3	~200
$K_2NpO_2(OH)_3 \cdot xH_2O$	Moderate	$g_1 = 2.60$; $g_2 = 2.34$ Weak signal at g = 2.21	~200
$Rb_2NpO_2(OH)_3 \cdot xH_2O$	Weak signal	$g_1 = 2.92$; $g_2 = 2.34$ $g_3 = 2.21$	~200
$Cs_2NpO_2(OH)_3 \cdot xH_2O$	Weak signal	Broad signal at g = 2.21 – 2.26	~200

Parameters of ESR spectra of the compounds I, II, and $NpO_2(OH) \cdot xH_2O$ are listed in Table 3**.** Specific attention was paid to the anisotropic signal with $g_{||} \sim 6$ and $g_{\perp} \sim 0$ components which is characteristic of the ground $|^3H, +4\rangle$ electronic state of the $5f^2$-configuration of the NpO_2^+ cation [63]. This signal was not observed in the ESR spectra of the compounds I and $NpO_2(OH) \cdot xH_2O$ complex, while for the compounds II with M = Na, K, Rb, and Cs, the signal was detected. Others ESR signals with g < 3 were assigned to impurities of transition metal ions or to paramagnetic radiation defects.

Mössbauer ^{237}Np spectra were recorded for three compounds, $NaNpO_2(OH)_2xH_2O$, $Na_2NpO_2(OH)_3 \cdot xH_2O$, and $Rb_2NpO_2(OH)_3 \cdot xH_2O$, at liquid helium temperature. Mössbauer spectra of all these compounds exhibit nearly the same isomer shifts, and quadrupole and magnetic splitting parameters, which are listed in Table 4. These parameters are quite similar to those Mössbauer parameters that are typical for other Np(V) compounds containing the NpO_2^+ group. A typical Mössbauer spectrum is shown in Fig. 8 for the $Rb_2NpO_2(OH)_3 \cdot xH_2O$ complex. The paramagnetic moment m estimated from

the hyperfine magnetic field on ^{237}Np nuclei is about 2.8 μ_B. This value is quite consistent with the magnetic moment of the ground $|^3H_4,\pm4>$ electronic state of the linear NpO_2^+ group ($\mu_{eff} \sim 3\ \mu_B$).

Table 4. Parameters of Mossbauer ^{237}Np spectra of some $^{237}Np(V)$ hydroxocomplexes

Parametrs	$NaNpO_2(OH)_2 \cdot xH_2O$	$Na_2NpO_2(OH)_3 \cdot xH_2O$	$Rb_2NpO_2(OH)_3 \cdot xH_2O$
Isomer shift related to NpO_2; δ, mm/s	-10(2)	-8(2)	-8(1)
Quadropole splitting constant; $e^2qQ/4$, mm/s	25(2)	24(2)	27(1)
Parameter magnetic splitting; $g_o\mu_{nucl}B_{eff}$, mm/s	96(2)	95(2)	96(1)
B_{eff}	606(10)	600(10)	606(6)

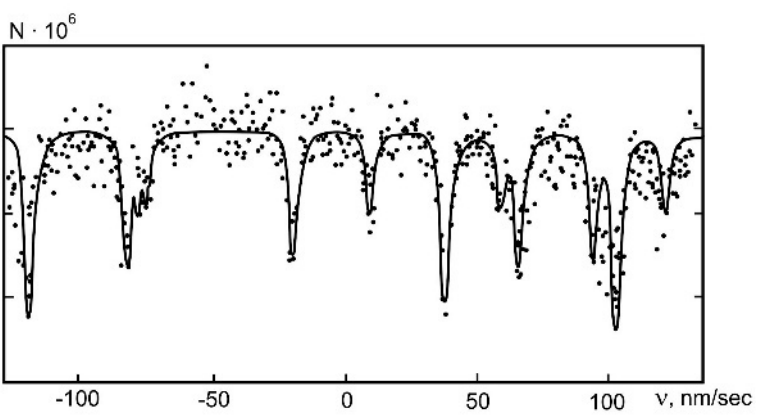

Fig. 8. Mössbauer spectra of Na_6NpO_6 (1) and $Rb_2NpO_2(OH)_3 \cdot xH_2O$ (2) at 4.2K; δ are given relative to NpO_2.

The above mentioned data on Mössbauer, ESR, IR, and electronic absorption spectra unambiguously indicate the presence of the NpO_2^+ dioxo cation in all of the complexes investigated. In this regard, it is reasonable to begin discussion of the above spectroscopic data with qualitative consideration of the electronic structure of the $5f^2$-electronic configuration of pentavalent neptunium in a model neptunyl complex, NpO_2L_n. It is known, that the NpO_2^+ dioxo cation is a linear group with short Np-O distances (1.8–1.9 Å), while distances between neptunium and ligands L in the equatorial plane are much longer. For this reason, splitting of the $5f^2$-configuration is determined mainly

by the strong crystal field (CF) of axial symmetry arising from two oxygen atoms of the neptunyl group. The influence of equatorial ligands on the splitting is certainly much weaker. In particular, under the influence of axial CF, the ground $^3H_4$ manifold is split into five levels, $^3H_4$,+M>, where M = O, +1, +2, +3, and +4, as shown in Fig. 9**.** The ground state of the NpO_2^+ dioxocation is known to be the $^3H_4$,+4> doublet [63]. The theoretical g-tensor of the ground $^3H_4$,+4> doublet is expected to have g|| ~6 and g⊥~0 components. However, if the non-axial component of the CF potential is taken into account, then splitting of the ground $^3H_4$,+4> doublet (and other $^3H_4$,+M> doublets with M ≠ 0) into two singlets can occur (Fig. 9). Degeneracy of the $^3H_4$,+4> doublet holds in D_{3h}, D_{5h}, and D_{6h} symmetries of the NpO_2L_n complex, so the ESR signal with g|| ~6 and g⊥~0 components is expected to appear for these symmetries. In other symmetries, such as D_{2h} or D_{4h}, the ground $^3H_4$,+4> doublet is split into two doublet states. If the splitting energy, D, is large enough (D > 1 cm^{-1}), the ESR signal disappears. In addition, the splitting leads to freezing of the magnetic moment on the neptunium atom at low temperatures. This effect is most prominent in the case of D_{4h} symmetry, since the $^3H_4$,+4> and $^3H_4$,-4> electronic states are effectively mixed only by the tetragonal CF component, but not the trigonal, pentagonal or hexagonal CF components. For example, in the $Cs_3NpO_2Cl_4$ compound containing $NpO_2Cl_4^{3-}$ anions of nearly perfect D_{4h} symmetry [64], the magnetic susceptibility at low temperatures becomes temperature-independent and, additionally, magnetic splitting was not observed in Mössbauer spectra of $Cs_3NpO_2Cl_4$ because of the large splitting energy of the ground $^3H_4$,+4> doublet which was estimated to be about of 20 cm^{-1} [65].

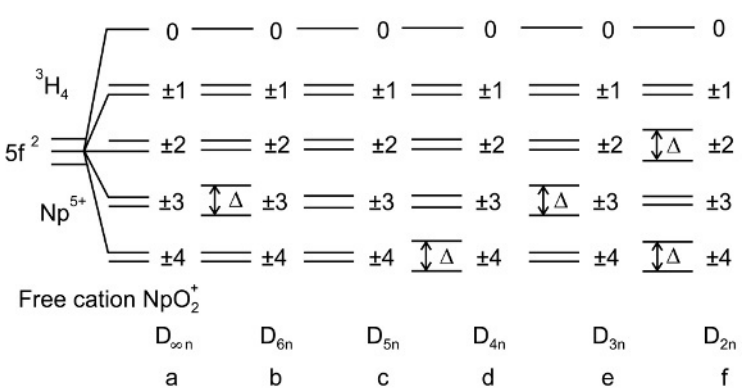

Fig. 9. The scheme of splitting of levels main multiplet $^3H_4$ $5f^2$-configuration Np(V) in the crystal field with different symmetry

On the other hand, the intensities of *5f* - *5f* transitions in neptunyl complexes are strongly affected by both the number of ligands in the equatorial

plane and the symmetry of the NpO_2L_n polyhedron. In particular, intensities of transitions within the $5f^2$-configuration depend on whether the inversion center in the NpO_2L_n complex is present or not, since these transitions are forbidden as electric-dipole ones. Thus, in the D_{2h}, D_{4h}, and D_{6h} symmetries, 5*f*-5*f* absorption band intensities are expected to be low because of the Laporte rule. For the D_{3h} and D_{5h} symmetries, intensities increase owing to admixtures of electronic states of opposite parity to the $5f^2$-configuration caused by odd terms of the CF potential. This effect is the most prominent for the main absorption band at ~1000 nm in the case of D_{5h} symmetry of the NpO_2L_n complex. It is well known that the NpO_2^+ cation in aqueous solutions (where it is assumed to exist as the $NpO_2^+(H_2O)_5$ D_{5h} -aquacomplex) is characterized by the high intensity of the band at 980 nm (with the molar extinction coefficient ε~400 dm/mol· cm) in absorption spectra. This band is at least ten times as intensive as the other 5*f*-5*f* bands. A quite different situation occurs for D_{4h} and D_{6h} complexes, such as $NpO_2Cl_4^{3-}$ or $NpO_2(CH_3COO)_3^{2-}$, where the above band is not distinguished in intensity from other bands [66,67]. Similar effects are also observed for the main absorption band at 830 nm of PuO_2^{2+} dioxocation which is isoelectronic with the NpO_2^+ cation. D_{3h} symmetry never occurs in neptunyl complexes in their pure form because the coordination number n=3 in the equatorial plane is too low for the NpO_2L_n species.

The above mentioned results can naturally be interpreted in the framework of theoretical considerations. Indeed, by combining the observation of the presence or absence of the ESR signal with g|| ~6 and g⊥~0 and the magnitude of intensity of the absorption band at 1000 nm one can identify, with some degree of accuracy, the number of ligands n in the equatorial plane and symmetry of NpO_2L_n coordination polyhedron in the series of compounds I and II. Corresponding comparisons for different symmetries are listed in Table 5.

Comparison the data listed in Tables 3 and 5 supports the conclusion that the symmetry of the coordination polyhedron of Np(V) in all compounds II corresponds to the D_{5h} point group since these compounds reveal both the high intensity of the band at 1000 nm in absorption spectra and the presence of the ESR signal with the g||~6 and g⊥~0 g-tensor components. As for the compounds I, it is apparent from Table 5 that there are several structure models which are possible corresponding to the D_{4h}, D_{3h}, D_{2h} symmetry groups, respectively, or to lower symmetries. To select the correct model, one should consider additional information concerning structure properties and Mössbauer spectra. First of all, it should be noted that the coordination numbers 5 and 4 are not compatible with the low intensity of the absorption band in the optical spectra and the presence of magnetic splitting in Mossbauer spectra of I, respectively.

Table 5. Comparison between presence/absence of the ESR signal ($g_{\parallel}$ ~6 and $g_{\perp}$~0) and intensity of the band near 1000 nm in absorption spectra in Np(V) compounds at different symmetries of NpO L coordination polyhedra

Symmetry group of NpO_2L_n polyhedron	Presence of the ESR signal, on/off	Intensity of the 5f-5f absorption band at 1000 nm
D_{6h}	On	low
D_{5h}	On	high
D_{4h}	Off	low
D_{3h}	On	moderate or low
D_{2h}	Off	low
C_{2v}	Off	moderate or low

Since the NpO_2^+ cation is coordinated by six ligands in the equatorial plane, D_{4h} symmetry should be excluded from consideration. We can, therefore, assume that the geometry of the NpO_2L_6 polyhedron in I corresponds to a slightly distorted perfect hexagonal bipyramid, whose formal symmetry may be represented by any of the D_{2h}, D_{3h} or lower symmetry groups. Slight deviations from the perfect D_{6h}-symmetry causes splitting of the ground $^3H_4$,+4> doublet because of the appearance of small tetragonal CF components. This splitting is large enough to suppress the ESR signal, but it is not large enough to freeze the magnetic moment of $5f^2$-configuration that manifests itself in the magnetic splitting in Mössbauer spectra of I. The above regularities in changes in optical and ESR spectra of Np(V) hydroxocomplexes I and II can be explained in the framework of the structure model proposed below. Compounds I are assumed to have a layered structure similar to that earlier suggested for $UO_2(OH)_2$ hydroxide [68]. Each layer in I is a two-dimensional hexagonal lattice whose sites are occupied by hydroxide groups and NpO_2^+ cations. The axes of neptunyl cations are perpendicular to the planes of the layers and outer-sphere alkali cations M (as well as hydrate water molecules) located in the interlayer space. Each neptunyl cation is surrounded by six hydroxyl groups in the plane forming slightly distorted $NpO_2(OH)_6$ hexagonal bipyramid of D_{6h}-symmetry. Two neighboring neptunium atoms are connected via two bridging hydroxyl groups.

Dramatic changes in electronic absorption and ESR spectra are explained by perfect transformation of the crystal structure when going from the Np(V) hydxocompexes I to those from the from series II. We suggest that the layered structure of I transforms to a chain-like structure in II followed by reduction of the number of the ligand L in the equatorial plane of the NpO_2L_6 polyhedron from 6 to 5. Each chain in II is composed of NpO_2L_5 patterns connected via two bridging ligands L (where L is either a hydroxyl group or

oxygen atom). The geometry of the NpO_2L_5 pattern corresponds to a slightly distorted pentagonal bipyramid with D_{5h}-symmetry. Such a structural type has been observed for many other Np(V) compounds containing the NpO_2^+ group, such as $(NpO_2)_2SO_4{\cdot}2H_2O$ [69]. In contrast to D_{6h}-symmetry, small distortions of the NpO_2L_5 species do not lead to the appearance of a significant tetragonal CF component that is responsible for the splitting of the ground $^3H_4$,+4> doublet. For this reason, the ESR signal with the g|| ~6 and g⊥~0 components is observed in the compounds II. Alkali metal cations are assumed to be locate between neptunium chains. It seems that the structure of the chains depends on the size of outer-sphere cations. This assumption is in accordance with the difference in structure of the main absorption band near 1000 nm in optical spectra and the ν band in IR spectra of complexes II with light and heavy alkali metals, as mentioned above. The splitting of the band at ~1000 nm in optical spectra of $Rb_2NpO_2(OH)_3{\cdot}xH_2O$ and $Cs_2NpO_2(OH)_3{\cdot}xH_2O$ can be associated with differences in the neptunium chain structure in these complexes with that in the $Na_2NpO_2(OH)_3{\cdot}xH_2O$ and $K_2NpO_2(OH)_3{\cdot}xH_2O$ complexes: it is likely that there are at least two different NpO_2L_5 species in neptunium chains in the Rb and Cs compounds. Increase of the ν frequency in the IR spectra and blue shifts of the main absorption band in optical spectra of the $M_2NpO_2(OH)_3{\cdot}xH_2O$ series when going from Na to Cs seems to be associated with shortening of the Np-O distances in the NpO_2^+ group due to a decrease of the polarization capability of heavy alkali metal cations. As for the $NpO_2(OH){\cdot}xH_2O$ hydroxocomplex, its crystal structure cannot be unambiguously designated from the above spectroscopic data. However, it is probable that rather the moderate absorption intensity of the main absorption band and lack of an ESR signal are compatible with a strongly distorted D_6-type structure similar to the $MNpO_2(OH)_2{\cdot}xH_2O$ structure rather than with the D_{5h}-type structure.

Precipitation of $AmO_2OH{\cdot}xH_2O$ was achieved by addition of excessive KOH or NH_4OH to diluted aqueous solutions of Am(V). When using KOH, a reddish-yellow precipitate forms first that, after 20-30 minutes of mixing, becomes light and loose. The Am content in the mother solution with a KOH concentration of KOH 0.46M was 0.028 g/l. The Am concentration in 0.86 and 7.0M NH_4OH solution was 0.22 and 1.41 g/l, respectively (measured as concentration in solution under precipitate). Dried Am(V) hydroxide is a light-pink powder that, under 100°C, becomes darker and transforms into AmO_2 under heating [70].

In strong alkaline solutions, hydroxocompounds of Am(V) have been obtained. There are two methods of their preparation: (1) storage of $AmO_2OH{\cdot}xH_2O$ sediment under the MOH (M = alkaline metals) for 1-2 days, and (2) preparation of an Am(VI) alkaline solution and its storage in plastic test tubes. Under these conditions, ^{243}Am(VI) (~20% per hour) is reduced to Am(V).

The values of the apparent rate constant (k_a) of the first-order reaction in 3M and 1M NaOH are the same ~$(5,3\pm0,3)\cdot10^{-4}$ s^{-1} and in 0.1M NaOH k_a is increased to $1,7\cdot10^{-3}$ s^{-1}. During reduction of An(VI) in LiOH, NaOH, KOH, and CsOH solutions the hydroxo complexes of Am(V) with the general composition $MAmO_2(OH)_2\cdot xH_2O$ and $M_2AmO_2(OH)_3\cdot xH_2O$ (M = Li, Na, K, and Cs) have been obtained [7].

Np(V) hydroxide has a very low soluble in water. Its solubility product is $1.85\cdot10^{-10}$ M^2 (23°C, I = 0.02) [61]. The data available from the literature on the solubility of Np(V) hydroxide in 1M NaOH are remarkably different: 6.10^{-4} [71], $1.2.10^{-4}$ [72], and $1.3.10^{-5}$ M [73]. These differences are likely due to the metastability of this system and a slow formation of the solid phase. The solubilities of Pu(V) hydroxo compounds were shown to increase with an increase in the alkali concentration: (up to $3\cdot10^{-3}$ M in 4 M NaOH). This value remains constant for 2-3 h and slowly decreases during storage [74,75]. The solubilities of Am(V) hydroxo compounds were determined to be $1.2.10^{-4}$ M in 0.46 M KOH and lower than $0.8.10^{-4}$ M in 5.3 M NaOH [76]. In LiOH solutions, the solubilities of pentavalent Np, Pu, and Am hydroxo compounds are higher than those in analogous NaOH solutions by a factor of 2–3 [77].

5. Transuranium elements(VI) hydroxides

Transuranium elements(VI) hydroxides have the general composition $AnO_3\cdot xH_2O$, where An = Np or Pu, and x = 0.8-2.0. The $AnO_3\cdot H_2O$ compounds can easily be obtained by addition of NH_4OH, alkali ((pH~10), or pyridine (pH~8,5) to weakly acidic AnO_2^{2+} solutions [78]. In the past, it was erroneously suggested [79] that, under these conditions, double $M_2An_2O_7$ precipitates form (M = alkali metal cation or NH_4^+). $NpO_3\cdot2H_2O$ has been prepared by ozonation of the $NpO_2OH\cdot xH_2O$ suspension in water at room temperature [80], or by Np(V) solutions in the $LiNO_3$ - KNO_3 liquid eutectic at about 150°C [81]. It should be noted that dihydrate prepared by reactions of O_3 with $NpO_2OH\cdot xH_2O$ may contain observable quantities of Np(VII) [82]. If oxidation of Np(V) hydroxide by ozone happens at 90°C, formation of $NpO_3\bullet H_2O$ has been observed [81]. This compound can also be obtained by drying the dihydrate compound in vacuum at 90-100°C [83]. Oxidation of fresh precipitates of the Pu(IV) hydroxide by ozone at 90°C results in other precipitates that, after heating in vacuum at 130°C, has been proven to be $PuO_3\cdot0.8H_2O$ [80]. In air, this compound reversibly transforms into $PuO_3\cdot H_2O$.

$NpO_3\cdot H_2O$ is isostructural with $UO_3\cdot H_2O$ and is orthorhombic, *Pbca*, *a* = 5.607, *b* = 6.270, *c* = 9.956 Å, ρ_{calc} = 5.74 g/cm^3 [80]. According to the IR spectra, this compound contains OH^- groups and can be formulated as $NpO_2(OH)_2$. $PuO_3\cdot0.8H_2O$ is not isostructural with any known UO_3 hydrates. This compound has its specific IR spectrum, which is different from that of

$PuO_3 \cdot 2H_2O$. Attempts to obtain NpO_3 by dehydration of $NpO_3 \cdot H_2O$ were unsuccessful. In vacuum, at 330°C, $NpO_3 \cdot H_2O$ decomposes to Np_2O_5. $PuO_3 \cdot 0.8H_2O$ transforms into PuO_2 at temperatures higher than 200°C [80].

Np(VI) and Pu(VI) hydroxides are weakly soluble in water, but are highly-soluble in mineral acids with formation of the hydrated NpO_2^{2+} and PuO_2^{2+} ions or their complexes. The solubility product of $PuO_2(OH)_2$ has been estimated as $3 \cdot 10^{-25}$ [79]. The solubility heats of $NpO_2(OH)_2$ in 1M HCl and 1M $HClO_4$ are -53.17 and -53.80 kJ/mol, respectively [84]. This allowed calculation of $\Delta H_{formation}$ = -1370 kJ/mol.

The TUE(VI) hydroxides have amphoteric properties. They are significantly soluble in concentrated alkaline solutions [80,83,85,86]. The highest Np(VI) and Pu(VI) concentrations are obtained in LiOH solutions [87]. The solubilities of Pu(VI) hydroxo compounds increase with an increase in the alkali concentration (from $3.2 \cdot 10^{-5}$ M in 1M NaOH to $1 \cdot 10^{-4}$ M in 10 M NaOH) [86]. The An(VI)-alkaline solution systems are metastable and are characterized by the slow formation of a solid phase. In addition, these systems may contain high Np(VI) and Am(VI) concentrations (up to 10^{-3} M), and still higher Pu(VI) concentrations.

Heptavalent Np and Pu solid-phase compounds of several types have been obtained: $MAnO_4 \cdot xH_2O$, $M_3AnO_5 \cdot xH_2O$, M_5AnO_6, which are stable only in alkaline solutions. Np(VII) compounds and its alkaline solutions exhibit a high stability and can be stored for months [88]. In alkaline solutions, Pu(VII) is reduced in water. These solutions remain stable for several hours up to the point of a noticeable accumulation of plutonium(VI).

The Am(VII) solid compound had been synthesized by interaction of a Am(VI) perxenate complex with ozone in the solid phase at room temperature. The spectrum contains maxima at 712 and 750 nm is the same as the spectrum of the ~50% mixture of Am(VII) and Am(VI) species, prepared a the 3.5M NaOH solution [89]. The generalities of the spectrum of the solid Am precipitate obtained in our work are very much like the spectra of Np(VII) in alkaline solutions, but are shifted to the long wave range. The Am(VII) compound is unstable even in the solid state under an oxygen atmosphere and decomposes during 30 min at room temperature. In alkaline solutions, Am(VII) is reduced faster than Pu(VII).

The solubilities of heptavalent Np and Pu in alkaline solutions are significantly higher than those of these hydroxides in the (III)-(VI) oxidation states. Thus, real 1M NaOH solutions containing $5 \cdot 10^{-2}$ M of Np(VII) or Pu(VII), and 2M LiOH solutions containing 0.2M of Np(VII) were obtained [88].

6. Peroxides

The TUE peroxides have been obtained for Am(III), Np(IV) and Pu(IV). They are poorly studied, though precipitation of Np and Pu from acidic media by hydrogen peroxide has long been recognized [90,91] and has several practical applications [92,93]. The composition of so-called Am(III) hydroxo-peroxide is still unknown. It was obtained by addition of an excess of ammonium to 0.1M Am(III) solution that contained 0.2M H_2O_2 [94]. At pH ~ 5, the solution turns yellow-brown, and then a precipitate of the same color forms. The latter was not soluble in concentrated NH_4F. Treatment of the precipitate with a concentrated solution of NH_4OH or KOH results in the formation of $Am(OH)_4$ that was found to be soluble in 15M NH_4F with formation of complex Am(IV) fluorides. After washing with water, the Am(III) hydroxo-peroxide was soluble in 1M H_2SO_4 that provided the Am(III) solution.

Np(IV) peroxide can be obtained from weakly acidic solutions as a colorless or light-grey jelly-like precipitate [90]. In order to obtain a denser product, precipitation should be carried out from solutions with 3-4M HNO_3 at 8 - 10°C by slow addition of equal volumes of 30%-solution of H_2O_2 [92]. It is recommended that the precipitate be washed with 1.5M HNO_3, containing 15 wt. % of H_2O_2. The minimal remaining concentration of Np in the mother solution (20 - 25 mg/L (23°C)) was observed for $[HNO_3]$ = 1.5 - 2M and $[H_2O_2]$ = 4.6M. A method of Np separation was proposed that is based upon its reduction by H_2O_2 in concentrated HNO_3 and precipitation at $[H^+]$ = 3M [95]. From solutions with $[HNO_3] < 3$M, Np(IV) precipitates as very small cubic crystals ($a \sim 17$ Å) that have the ratio of peroxide oxygen (O_{per}) to Np ratio equal to O_{per} : Np = 2.9. In more acidic solutions, hexagonal crystals form with O_{per} : Np = 3.3 [96]. Cubic crystals immersed into concentrated HNO_3 transform into hexagonal crystals. This process is irreversible.

Solubility of the Np(IV) peroxide at 23°C versus $[HNO_3]$ has its minimum at $[H^+]$ = 1–2.5M [96]. In 2.5M HNO_3, the solubility is inversely proportional to $[H_2O_2]$ (in the range of 1.5–6.5M). For the range of $[HNO_3]$ from 3 to 5M, the solubility can be described by the equation:

$$S = 9.93([H^+]^4/[H_2O_2]^2) \text{ mg/L} \quad (5)$$

On the basis of its precipitation and properties, Pu(IV) peroxide is similar to the Np(IV) compound. It forms from acidic solutions as a dark-green fine-crystalline powder, which is preceded by the formation of soluble reddish-brown peroxide Pu(IV) complexes [91]. Optimal precipitation conditions correspond to $[HNO_3]$ = 1-2M and $[H_2O_2]$ = 2.5M. As in the case of Np, two crystalline modifications have been identified: cubic ($a \sim 16.5$ Å) and hexagonal [97]. The first one forms in weakly acidic media and has O_{per} : Pu = 3.0. The hexagonal form precipitates at $[HNO_3] > 2$M and, in the humid state, has O_{per} : Pu = 3.4 [93]. In the structure of Pu(IV) peroxide, there are considerable

amounts of anions that exist in the mother solution [91,93]. It is of interest that sulfate ions can be incorporated into the precipitate especially easy, whereas admixtures of nitrate and chloride ions are remarkably lower. The cubic structure is less capable to incorporate anions than the hexagonal one. At >130°C Pu(IV) peroxide transforms into PuO_2 [91].

The $(NpO_2)_2O_2$ peroxide has a green color and has been prepared by addition of H_2O_2 to a concentration of 0.02–0.7M to neutral (pH ~6) $1.2 \cdot 10^{-2}$ M solution of Np(V) cooled to ~ 1°C [98]. With the addition of NaOH, $(NpO_2)_2O_2$ transforms into double peroxide salts of Np(V) and Na.

Recently, Burns et al. [99] reported some exceptional actinide peroxide structures that are considered in other chapter of this book.

The author would like to express his sincere thanks to his first teacher Prof. N.N. Krot who introduced him to this field of research more than 20 years ago. Thanks are also due to A.I. Lyubeznova for the invaluable help in preparation of figures and materials.

References

1. (a) T.J. La Chappel, L.B. Magnusson, J.C. Hindman, Chemistry of Np. First Preparation and Solubilities of Some Np Compounds. In: Transuranium Elements, NNES, Eds. G.I. Seaborg, J.J. Katz, and Manning W.M., New York: Mc Graw Hill, vol. 14B, part II, pp. 1097 – 1110. (b) K.A. Krans, J.R. Dam, Hydrolytic Behaviour of Pu(III). Acid Base Titration of Pu(III), Ibid., vol. 14B, part I, pp. 466 - 477
2. W.O. Milligan, M.R. Beasley, M.N. Lloyd, Acta Crystallogr. B24 (1968) 979.
3. E.A. Erin, V.V. Kopytov, V.Ya. Vasilyev, Radiokhimiya 19 (1977) 464.
4. R.G. Haire, M.N. Lloyd, W.O. Milligan et al., J. Inorg. Nucl. Chem. 39 (1977) 843.
5. V.P. Perminov, M.S. Grigoriev, M.P. Glazunov, N.N. Krot, Abstracts on XXXII Meeting on Nuclear Spectroscopy and Structure of Nuclear Cell. Leningrad. Nauka, 1982. P. 510.
6. R.A. Penneman, J.S. Coleman, T.K. Keenan, J. Inorg. Nucl. Chem. 17 (1961) 138.
7. M.V. Nikonov, A.V. Gogolev, I.G. Tananaev, B.F. Myasoedov, D.L. Clark, C.R. Chimie 7 (2004) 1205.
8. M.V. Nikonov, I.G. Tananaev, B.F. Myasoedov, D.L. Clark, Int. Conf. “Actinides-2005”. Manchester. UK. Abstr.
9. M.V. Nikonov, A.V. Gogolev, I.G. Tananaev, B.F. Myasoedov, Radiokhimiya 46 (2004) 226.
10. M.V. Nikonov, A.V. Gogolev, I.G. Tananaev, B.F. Myasoedov, D.L. Clark, Radiokhimiya 47 (2005) 234.
11. M.P. Mefod`eva, N.N. Krot, Soedineniya transuranovykch elementov (Compounds of Transuranium Elements). 1987. Nauka, Moscow. 320 p.
12. V.M. Vdovenko, Sovremennaya radiokhimiya (Modern Radiochemistry). Moscow, Atomizdat, 1969.
13. J.J. Katz, G.T. Seaborg, Khimiya actinidnykh elementov (Chemistry of Actinide Elements). Moscow, Atomizdat, 1958, p. 542.
14. J.J. Katz, G.T. Seaborg, Khimiya actinidnykh elementov (Chemistry of Actinide Elements). Moscow, Atomizdat, 1960, p. 328

15. V.F. Peretrukhin, V.P. Shilov, A.K. Pikaev, Alkaline Chemistry of Transuranium Elements and Technetium and Treatment of Alkaline Radioactive Wastes, Report WHC-EP-0817 of Westinghouse Hanford Company, Ed. C.H.Delegard, Richland, WA USA, 1995. p. 2-18
16. B.B. Cunningham, Preparation and Properties of Pu Compounds. In: The Actinide Elements, Eds. Seaborg J.J.and Katz, New York, 1954, Chapter 10, p. 308.
17. E.M. Pazukhin, S.M. Kochergin, Radiokhimiya 31 (1989) 72.
18. A. Cousson, H. Abazli, F. Nectoux, Abstracts. Actinides-1985. Provance. CEA, 1985. p. 97.
19. G.T. Seaborg, J.J. Katz, Ed. The Actinide Elements. 1954.
20. S.W. Rabideau, J. Am. Chem. Soc. 79 (1957) 3675.
21. S.W. Rabideau, R.J. Kline, J. Phys. Chem. 64 (1960) 680.
22. D.W. Ockenden, G.A. Welch, J. Chem. Soc. 9 (1956) 3358.
23. R.G. Haire, M.H. Lloyd, M.L. Beasley, W.O. Milligan, J. Electron Microsc. 20 (1971) 8.
24. D.A. Costanzo, R.E. Biggers, J.T. Bell, J. Inorg. Nucl. Chem. 35 (1973) 609.
25. J.T. Bell, D.A. Costanzo, R.E. Biggers, J. Inorg. Nucl. Chem. 35 (1973) 623.
26. J.T. Bell, C.F. Coleman, D.A. Costanzo, R.E. Biggers, J. Inorg. Nucl. Chem. 35 (1973) 629.
27. M.P. Neu, R.K. Schulze, S.D. Conradson, J.D. Farr, R.G. Haire, Polymeric Plutonium(IV) Hydroxide: Formation, Prevalence, and Structural Characteristics. 1998.
28. K.P. Louwrier, C. Ronchi, T. Steemers, E. Zamorani, Sol-Gel Process on Plutonium Oxide at the European Institute for Transuranium elements. In: Sol-Gel Processes for Uranium Nuclear Fuel, 1968. pp. 97-106
29. J. M. Cleveland, The Chemistry of Plutonium. Gordon and Breach, New York, 1970.
30. A.M. Fedoseev, N.N. Krot, N.A. Budantseva, A.A. Bessonov, A.B. Yusov, Report PNNL-11900, 1998.
31. N.N. Krot, V.P. Shilov, A.B. Yusov, I.G. Tananaev, M.S. Grigoriev, A.Yu. Garnov, V.P. Perminov, L.N. Astafurova. Plutonium (VI) Precipitates formed in Alkaline Media in the presence of Various Anions. 1998. September. Report PNNL–11901.
32. A.B. Yusov, A.Yu. Garnov, V.P. Shilov, I.G. Tananaev, M.S. Grigoriev, N.N. Krot, Radiokhimiya 42 (2000) 140.
33. A.B. Yusov, A.Yu. Garnov, V.P. Shilov, I.G. Tananaev, M.S. Grigoriev, N.N. Krot, Radiokhimiya 42 (2000) 146.
34. D. Rai, R.G. Strickert, J.L. Ryan, Inorg. Nucl. Chem. Letters 16 (1980) 551.
35. D. Rai, J.L. Ryan, Radiochim. Acta 30 (1982) 213.
36. I.G. Tananaev, PhD. Thesis, 1998. IPC RAS Moscow. 357 p.
37. J.I. Kim, B. Kanellakopulos, Radiochim. Acta 48 (1989) 145.
38. B. Allard, J. Rydberg, In.: Plutonium Chemistry, ACS Symposium Series 216, American Chemical Society, Washington, DC., 1983. pp. 275-295.
39. H. Capdevila, P. Vitorge, E. Giffaut, Radiochim. Acta. 58/59 (1992) 45.
40. H. Capdevila, P. Vitorge, Radiochim. Acta 82 (1998) 11.
41. D. Rai, Radiochim. Acta 82 (1998) 11.
42. N.A. Budantseva, I.G. Tananaev, A.M. Fedosseev, A.A. Bessonov, C.H. Delegard, Investigation of the Behavior of Plutonium (V) in Alkaline Media. Report PNNL-11624, 1998.
43. N.A. Budantseva, I.G. Tananaev, A.M. Fedosseev, C.H. Delegard, J. Alloys Compds. 272-273 (1998) 813.
44. L.B. Asprey, R.A. Penneman, Inorg. Chem. 1 (1962) 134.
45. D. Rai, J.L. Ryan, Inorg. Chem. 24 (1985) 247.
46. H. Nitsche, Radiochim. Acta 52/53 (1991) 3.
47. Peretroukhin, V.F., Kryutchkov S.V., Silin V.I., Tananaev I.G., Belyaeva L.I., Trushina V.E., Ushakov S.I, Grigor'ev M.S., 1996, "Determination of the Solubility of Np(IV)-(VI),

Pu(III)-(VI), Am(III)-(VI) and Tc(IV),(V) Hydroxo Compounds in 0.5-14 M NaOH Solutions", WHC-EP-0897, Westinghouse Hanford Company, Richland, Washington, USA..
48. R.E. Connick, W.H. McVey, G.E. Sheline, Note on the Stability of Pu(IV) in Alkaline Solution. In: The Transuranium Elements, Eds. Seaborg G.T., Katz, J.J., and Manning W.M., vol. 14B, part I. p. 335.
49. C. Delegard, Radiochim. Acta 41 (1987) 11.
50. L.P. Sokhina, L.M. Ramazanov, L.V. Goncharuk, Radiokhimiya 15 (1973) 794.
51. A.D. Gelman, V.P. Zaitseva // Dokl. AN SSSR 157 (1964) 1403.
52. M. Kraus, In: Mirnoye Ispolzovaniye Atomnoy Energii (Peaceful Use of the Atomic Energy), ed. A.P. Vinogradov, Moscow, 1958. Vol. 7, pp. 304-318.
53. J.Y. Bourges, Radiochem. Radioanal. Letters 12 (1972) 111.
54. N.A. Boudantseva, I.G. Tananaev, A.M. Fedosseev, C.H. Delegard, J. Alloys Compds. 271-273 (1998) 231.
55. N.A. Boudantseva, I.G. Tananaev, A.M. Fedosseev, C.H. Delegard, Investigation of the behaving of plutonium (V) in Alkaline Media. Report PNNL-11624. Pacific Northwest National Lab-oratory Richland. USA. Sept 1997.
56. I.G. Tananaev, Radiokhimiya 33 (1991) 24.
57. I.G. Tananaev, Radiokhimiya 33 (1991) 72.
58. I.G. Tananaev, Radiokhimiya 34 (1992) 3.
59. G.I. Visyascheva, Yu.F. Volkov, G.A. Simakin, I.I. Kapshukov, Radiokhimiya 26 (1984) 171.
60. J.A. Stone, W.L. Pillinger, Symp. Faradey Soc. 1 (1967) 77.
61. E.P. Sevost`yanova, G.V. Khalturin, Radiokhimiya 18 (1976) 870.
62. I.G. Tananaev, Radiokhimiya 32 (1990) 53.
63. V.A. Glebov, Radiokhimia 21 (1979) 793.
64. A.A. Lychev, L.G. Mashirov, Yu.I. Smolin, Yu.F. Shepelev, Abstracts on Third All-Union Conf. on Chemistry of Neptunium and Plutonium, Nov.24-26 1987, Leningrad, USSR, p.98.
65. J.H. Karraker, J.A. Stone, J. Inorg. Nucl. Chem. 41 (1979) 1153.
66. N.G. Gorshkov, I.N. Ladygin, L.G. Mashirov, D.N. Suglobov, Radiokhimia 20 (1978) 570.
67. N.G. Gorshkov, L.G. Mashirov, D.N. Suglobov, Radiokhimia 22 (1980) 419.
68. J.C. Taylor, Acta Crystallogr. 27 (1971) 1088.
69. M.S. Grigoriev, A.I. Yanovskii, A.M. Fedoseev, N.A. Budantseva, Yu.T. Struchkov, N.N. Krot, Dokl. AN SSSR 300 (1988) 618.
70. V.G. Zubarev, N.N. Krot, Radiokhimiya 24 (1982) 319.
71. G.A. Simakin, N.V. Matyashchuk, M.V. Vladimirova, Radiokhimiya 15 (1973) 98.
72. Ch. Lierse, W. Treiber, J.I. Kim, Radiochim. Acta 38 (1985) 27.
73. V. Neck, J.I. Kim, B. Kannellakopulos, Radiochim. Acta 56 (1992) 25.
74. J. Bourges, Radiochem. Radioanal. Lett. 12 (1972) 111.
75. V.F. Peretrukhin, D.P. Alekseeva, Radiokhimya 16 (1974) 843.
76. B.N. Ivanov-Emin, L.A. Nisel`son, Zh. Neorg. Khim. 5 (1960) 1921.
77. I.G. Tananaev, Radiokhimiya 34 (1992) 63.
78. J.M. Cleveland, Inorg. And Nucl. Chem. Lett. 6 (1970) 535.
79. A.D. Gelman, A.I. Moskvin, L.M. Zaitseva, M.P. Mefod`eva, Kompleksnye Soedineniya Transuranovykh elementov (Complex Compounds of Transuranium Elements), USSR Academy of Sciences Publ., 1961, p. 223.
80. K.W. Bagnall, J.B. Laidler, J. Chem. Soc. 8 (1964) 2693.
81. D. Cohen, Inorg. Chem. 2 (1969) 866.
82. A.A. Chaikchorky, M.Yu. Matuzenko, Yu.I. Belyaev, Radiokhimiya 16 (1974) 850.
83. Yu.I. Belyaev, T.A. Ilyinskaya, A.N. Kudryavtsev, Radiokhimiya 17 (1975) 968.

84. Yu.I. Belyaev, N.L. Smirnov, A.P. Taranov, Radiokhimiya 21 (1979) 682.
85. A.A. Chaikchorky, M.Yu. Matuzenko, E.V. Leikina, Radiokhimiya 17 (1975) 919.
86. J.A. Perez-Bustamante, Radiochim. Acta. 4 (1965) 67.
87. D. Cohen, S. Frid, Inorg. Nucl. Chem. Lett. 5 (1969) 653.
88. N.N. Krot, A.D. Gelman, M.P. Mefod'eva, V.F. Peretroukhin, V.P. Shilov, V.I. Spitsin, Heptavalent State of Np, Pu, and Am. Nauka: Moscow, 1977. Available in English as Heptavalent State of Np, Pu and Am, UCRL-Trans-11798, Lawrence Livermore National Laboratory. Livermore, CA
89. M.V. Nikonov, A.V. Gogolev, I.G. Tananaev, B.F. Myasoedov, Radiokhimiya 47 (2005) 441.
90. J.J. Katz, D.M. Gruen, J. Amer. Chem. Soc. 71 (1949) 2106.
91. J.W. Hamaker, C.W. Koch, In: The Transuranium Elements, ed. G.T. Seaborg, J.J. Katz, W.M. Manning. N.Y.: Mc Grow-Hill, 1949. Vol. 14B, pt I. pp. 666-681.
92. J.A. Porter, Ind. Eng. Chem. Process Des. Develop. 3 (1964) 289.
93. J.A. Learly, A.N. Morgan, W.J. Maroman, Ind. Eng. Chem. 51 (1959) 27.
94. K. Buijs, K.P. Louwrier, Inorg. Nucl. Chem. 28 (1966) 2463.
95. A.A. Chaikchorky, L.P. Muravieva, Yu.A. Barbanel, Radiokhimiya 12 (1970) 528.
96. E.K. Dukes, G.A. Burney, J. Inorg. Nucl. Chem. 24 (1962) 899.
97. R.C.L. Mooney, W.H. Zachariasen, In: The Transuranium Elements, ed. G.T. Seaborg, J.J. Katz, W.M. Manning. N.Y.: Mc Grow-Hill, 1949. Vol. 14B, pt II. pp. 1442–1447.
98. C. Musicas, J. Chem. Phys. 71 (1974) 197.
99. P.C. Burns, K.-A. Hughes Kubatko, G. Sigmon, B.J. Fryer, J.E. Gagnon, M.R. Antonio, L. Soderholm, Angew. Chem. Int. Ed. 44 (2005) 2135.

This page intentionally left blank

Structural Chemistry of Inorganic Actinide Compounds
S.V. Krivovichev, P.C. Burns & I.G. Tananaev (Editors)

Chapter 4

Actinide compounds containing hexavalent cations of the VI group elements (S, Se, Mo, Cr, W)

Sergey V. Krivovichev[a], Peter C. Burns[b]

[a]*Department of Crystallography, Faculty of Geology, St.Petersburg State University, University Emb. 7/9, 199034 St.Petersburg Russia*
[b]*Department of Civil Engineering and Geological Sciences, University of Notre Dame Notre Dame, IN 46556-0767 U.S.A.*

1. Introduction

Actinide and, especially, uranium oxysalts with hexavalent cations of the elements of the VIth group of the Periodic Table are important phases from mineralogical, environmental and technological points of view. These compounds are common constituents of the oxidized zones of uranium mineral deposits [1], form as a result of the alteration of spent nuclear fuel (SNF) [2], form during burnup of nuclear fuels in reactors [3], represent insoluble reisudes undesirable for the recovery of plutonium from the SNF solutions [4], impact upon the transport of actinides in contaminated soils [5, 6], and the mobility of radionuclides in a geological repository for nuclear waste [7-13], etc. Knowledge of the structures of these compounds is essential for understanding their behaviour in a wide range of environmental and technological processes.
This chapter is devoted to description and classification of actinide inorganic compounds containing hexavalent cations of S, Cr, Se, and Mo. The purpose of the chapter is to provide comprehensive information on crystallographic parameters and structural topology of these phases. First, we describe structures of compounds with actinides in their tri- and tetravalent states. For the sake of convenience, these compounds are separated into complex (U-Mo-O, U-Mo-W-O, and U-W-O) oxides, actinide tungstates and molybdates, and actinide sulfates. The rest of the chapter is devoted to actinyl phases, i.e. phases with actinides in high oxidations states (5+ and 6+). These compounds are subdivided on the basis of the principles of their structural architecture into: (i)

structures described on the basis of the concept of anion-topology; (ii) structures containing structural units with corner-sharing actinyl polyhedra and TO_4 tetrahedra (T = S, Cr, Se, and Mo); (iii) structures containing structural units with edge-sharing actinyl polyhedra and TO_4 tetrahedra (T = S, Cr, Se, and Mo); (iv) structures with corner sharing between actinyl polyhedra. The group (ii) is analysed in more detail in order to provide estimates of the flexibility of structural units on the basis of statistical analysis of bond lengths and angles. The basic conclusions are presented at the end of the chapter. Description of each group of compounds is accompanied by a listing of their basic crystallographic data and structure illustrations corresponding to the phases considered.

2. Tri- and tetravalent actinide compounds

2.1. U-Mo, U-W, and U-Mo-W complex oxides

The U-Mo-O binary oxide system was first studied by Kovba and Trunov [14,15]. These authors reported existence of several U-Mo oxocompounds with different stoichiometries: U_2MoO_8, $UMoO_5$, UMo_2O_8, UMo_7O_{22}, and $UMo_{11}O_{35}$. Later structural studies demonstrated that, in their structures, either U or Mo coordination polyhedra polymerize to form extended structural units and these compounds should be considered as complex oxides rather than uranium molybdate salts. Similar structural features have also been observed for complex oxides in the U-W-O and U-Mo-W-O systems [16-21].

The structures of some of the U-M-O complex oxides (M = Mo, W) can be considered as homologous series containing ReO_3-type slabs of MO_6 octahedra [19-21]. The ReO_3 structure is a three-dimensional framework of corner-sharing ReO_6 octahedra (Fig. 1a,b). The framework can be cut into slabs several octahedra wide (Fig. 1b). The general formula of the U-M complex oxides is UOM_nO_{3n+1}, where n is the number of octahedra across the ReO_3-type slab. U atoms are coordinated by seven O atoms to form UO_7 pentagonal bipyramids (PBs). The U-O_{ap} bonds (ap: apical) to the apical O_{ap} atoms of the PB are relatively short (2.00-2.10 Å), whereas the U-O_{eq} bonds (eq: equatorial) to the equatorial anions (O_{eq}) are longer (2.20-2.40 Å). The UO_7 bipyramids share equatorial edges to form chains extending along the b axis. The most straightforward way to describe the structures of the UOM_nO_{3n+1} phases is to represent them as based upon layers parallel to (001) and consisting of chains of UO_7 polyhedra and octahedral chains. The whole structure is built by stacking the layers one onto another and by linking them via the O_{ap} atoms and the apical corners of the MO_6 octahedra. The alternative view on the structures of the

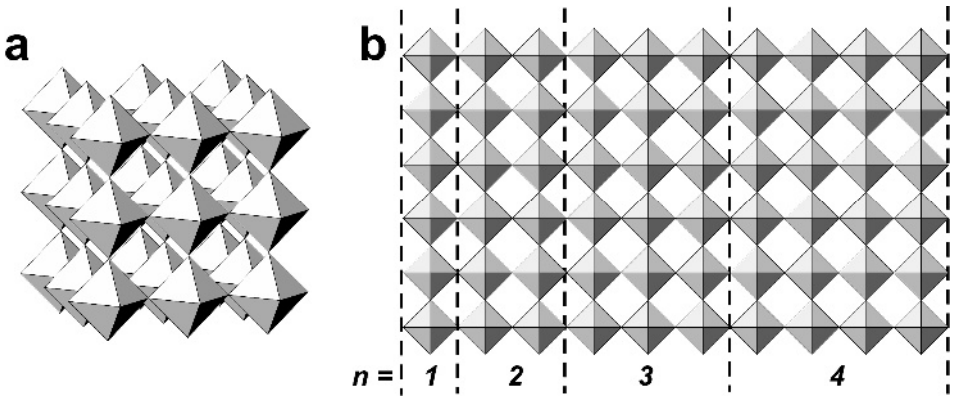

Fig. 1. ReO_3 octahedral framework (a) can be cut into slabs with *n* octahedra across (b).

UOM_nO_{3n+1} compounds is their representation as an array of the ReO_3-type slabs separated by the ...–U–O_{ap}–U–O_{ap}–U–O_{ap}–... chains.

Since in these structures, U has a coordination of pentagonal bipyramid, they are usually denoted as (*n*)-PB structures. Schematic representations of heteropolyhedral layers observed in these structures are shown in Fig. 2a-d. Table 1 provides chemical formulae of corresponding compounds. As can be seen, in the structures with $n = 2k+1$, all uranium chains are translationally equivalent, whereas, in the structures with $n = 2k$, adjacent chains are not translationally equivalent which results in doubling of the unit-cell parameter perpendicular to the extension of the chains. Intergrowths structures with different *n* can be observed by transmission electron microscopy (TEM). Fig. 3 shows the TEM image obtained by Sundberg and Marinder [21] for the ordered $U_4W_{13}O_{47}$ intergrowth of (3)-PB and (4)-PB structures (Fig. 4e). The alternation of the (3)- and (4)-octahedral slabs is periodic and can be defined as $(4,3,3,3,4)_2$-PB.

In some of the U-M-O compex oxides (M = Mo, W), U can be replaced by Mo or W. In this case, the ReO_3-type slabs are connected by MoO_6 octahedra such that six-sided tunnels are formed, in which strings of U atoms occur in hexagonal bipyramidal (HB) coordination [19]. Fig. 4 shows the structure which can be derived from that of β-$UOMo_2O_7$ [22-24] by replacing every second UO_7 bipyramid in the uranium chain by a MoO_6 octahedron (**O**). This structure is characteristic for $UOMo_5O_{15}$ [25]. Phases with similar architectures are usually denoted as (*n*)-HB, where *n* is a number of octahedra across the ReO_3-type slab. Phases with $n = 2$, 3, 4 and 5 have been described in the UO_2-MoO_2-MoO_3-WO_3 system. The U-M substitution may have either ordered or disordered character which results in a series of the U-M complex oxides with different stoichiometries (Table 1). It should be noted that the (*n*)-HB series can

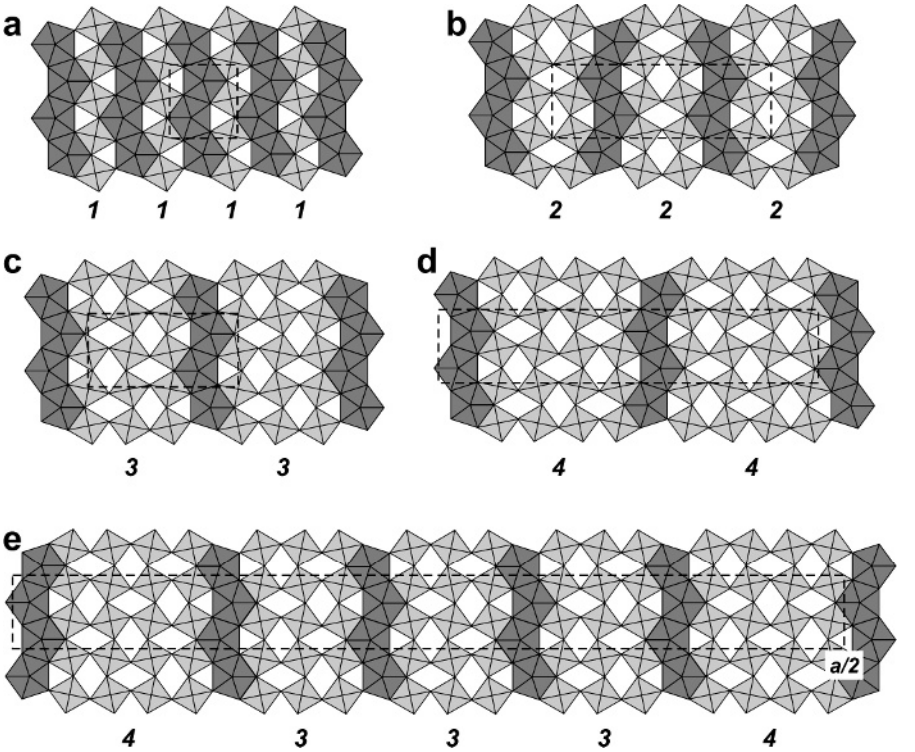

Fig. 2. Idealized structure models of (*n*)-PB structures with *n* = 1 (a), 2 (b), 3 (c), 4 (d) and 4,3,3,3,4 (e).

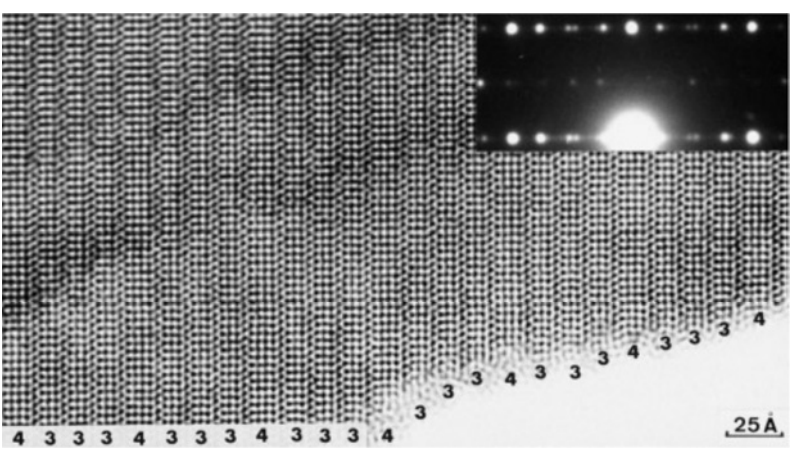

Fig. 3. High-resolution TEM image of a UW_3O_{11} fragment showing an ordered intergrowth structure $(4,3,3,3)_2$-PB. Reproduced from [21] with permission.

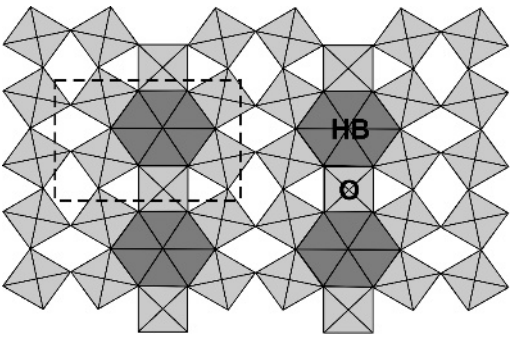

Fig. 4. Idealized structure model of the (2)-HB phase with hexagonal bipyramidal (HB) coordination of uranium atoms. **O** denotes MO_6 octahedron that links adjacent ReO_3-type slabs.

Table 1. Crystallographic data for the U-Mo-W complex oxides

type	formula	sp. gr.	*a* [Å]	*b* [Å]	*c* [Å]	ref
(1)-PB	$UMoO_5$	*Pcca*	7.349	4.125	12.746	31
(2)-PB	β-UMo_2O_8	*Pban*	20.076	7.323	4.116	24
(3)-PB	UW_3O_{11}	$P22_12$	13.802	7.400	4.071	21
(4)-PB	UW_4O_{14}	-	35.048	7.396	4.0514	21
(5)-PB	UW_5O_{17}	-	21.3	7.4	4.05	21
$(4,3,3,3)_2$-PB	$U_4W_{13}O_{47}$	-	118	7.4	4.1	21
(2)-HB	UMo_5O_{16}-I	*P*112	9.903	7.182	4.134*	25
	UMo_5O_{16}-II	*P*222	9.885	7.167	4.133	25
	β-$U_3Mo_{20}O_{64}$	*P*222	9.900	7.189	4.107	25
	α-$U_3Mo_{20}O_{64}$	*Cccm*	8.246	28.760	19.780	29
	γ-$U_3Mo_{20}O_{64}$	*Pbmm*	4.134	14.330	9.873	30
	$UMo_{10}O_{32}$	*Cccm*	16.180	14.480	19.720	28
(3)-HB	$UMoW_{10}O_{35}$	*Pmma*	7.386	4.076	13.79	19
(4)-HB	$UMo_3W_9O_{38}$	*Pcca*	7.276	3.946	34.58	19
(5)-HB	$UMoW_{13}O_{44}$	*Pccm*	4.038	7.388	42.52	19
	$UMo_3W_{11}O_{44}$	*Pccm*	3.928	7.288	41.98	19
(7)-HB	$UMo_3W_{11}O_{44}$	*Cmmm*	56.98	7.288	3.929	19
	U_2MoO_8	*Pbam*	6.734	23.240	4.115	27

* $\gamma = 90.20^o$

also be considered as derivatives of the hexagonal tungsten bronze (HTB) structures [20].

Taking into account the structural diversity of the (*n*)-PB and (*n*)-HB structures as well as the existence of their intergrowths, the number of phases that can be obtained in the U-Mo-W-O system can be extremely high. Kovba [19] pointed out that one of the reasons for such rich diversity is the variable valences of U, Mo and W. Indeed, even in the simplest (2)-PB phase β-$UOMo_2O_7$ [22-24], the formal valence of U is questionable. Assuming the hexavalent oxidation state for Mo, the formal valence of U should be 4+. However, Burns et al. [26] calculated bond-valence sum incident upon the U site as 5.17 *vu*. Special spectroscopic investigations would be desirable in order to clarify the situation.

As a rule, the octahedral coordination about Mo and W in U-Mo-W complex oxides is strongly distorted. In the most typical MO_6 configuration, the M atom is shifted towards one of the apices with the formation of the [1+4+1] coordination [short M-O bond (1.6-1.7 Å) in trans-position to the long bond (2.2-2.5 Å) and four intermediate bonds (~ 2.0 Å)].

The structure of U_2MoO_8 [27] consists of layers of UO_7 bipyramids and MoO_6 octahedra (Fig. 5). The UO_7 polyhedra are distorted with U-O_{ap} bonds of 2.06-2.08 Å and U-O_{eq} bonds in the range from 2.11-2.73 Å. According to Serezhkin et al. [27], the oxidation states of U and Mo in this compound are 5+ and 6+, respectively. The UO_7 pentagonal bipyramids share edges to form complex chains extending along the *a* axis. The chains are linked into layers by pairs of edge-sharing MoO_6 octahedra. The layers are parallel to (001) and share the O_{ap} atoms and apical corners of the MO_6 octahedra to produce a three-dimensional framework. The structure of U_2MoO_8 can be considered as a parent structure to several uranyl compounds (see below).

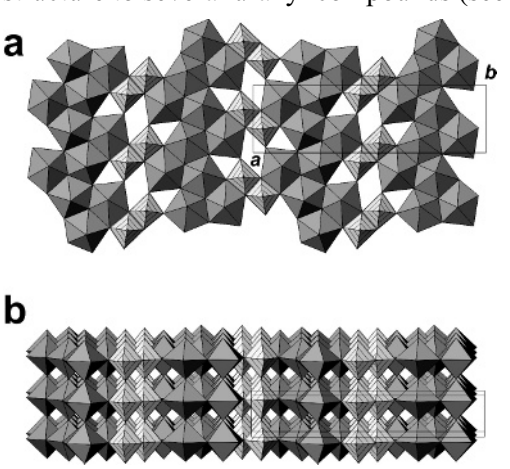

Fig. 5. Layer of UO_7 bipyramids and MoO_6 octahedra in the structure of U_2MoO_8 (a) and linkage of the layers into 3D framework (b).

2.2. Trivalent and tetravalent actinide molybdates and tungstates

Phases with tetrahedrally coordinated M^{6+} cations can be considered as molybdates and tungstates of tri- and tetravalent actinides, i.e. phases containing tetrahedral $M^{6+}O_4$ oxoanions (Table 2). There are two modifications of actinide phases with the $An(MO_4)_2$ stoichiometry. The structures of the high-temperature phases α-UMo_2O_8 [32] and β-$Th(MoO_4)_2$ [35,40] contain An^{4+} ions in two coordination environments. One is a regular octahedral coordination with the An^{4+}-O distances of about 2.30 Å (Fig. 6a), another is nine-coordinate (tricapped trigonal prism) with the An^{4+}-O distances ranging from 2.4 to 2.5 Å (Fig. 6b). The structure is composed of corner-sharing An and Mo coordination polyhedra (Fig. 6c). The phases α-$Th(MoO_4)_2$ [35,36,39] and γ-UMo_2O_8 [33] are isostructural and contain actinide ions in square antiprismatic coordination (Fig. 7a). The structure is based upon framework formed by corner-sharing of AnO_8 and MoO_4 polyhedra (Fig. 7b).

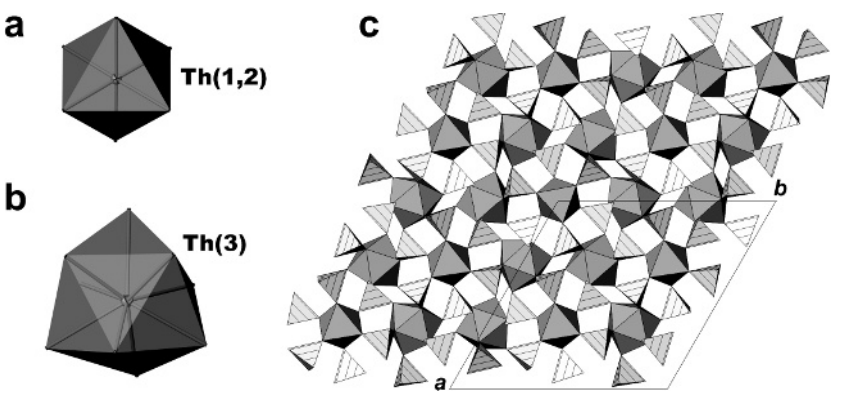

Fig. 6. Octahedral and ninefold coordinations of Th in the structure of β-$Th(MoO_4)_2$ (a and b, respectively) and the structure projected along the *c* axis (c) (MoO_4 tetrahedra are lined).

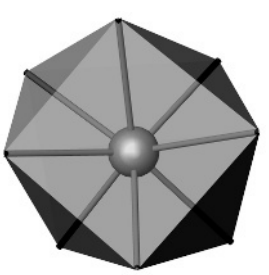

Fig. 7. Square antiprismatic coordination of U in the structure of γ-UMo_2O_8 projected along the *a* axis (MoO_4 tetrahedra are lined).

Table 2. Crystallographic data for tri- and tetravalent actinide molybdates and tungstates

Chemical formula	sp.gr.	*a* [Å] / α [°]	*b* [Å] / β [°]	*c* [Å] / γ [°]	ref
$An(MO_4)_2$ and related compounds					
α-UMo_2O_8	*P*3	17.300 / 90	17.300 / 90	6.145 / 120	32
β-$Th(MoO_4)_2$	$P\bar{3}$	17.593 / 90	17.593 / 90	6.238 / 120	35,40
$CdTh(MoO_4)_3$	$P6_3/m$	9.803 / 90	9.803 / 90	6.350 / 120	37
$(Cu,Mn)U(MoO_4)_3$	$P6_3/m$	9.790 / 90	9.790 / 90	6.202 / 120	53
γ-UMo_2O_8 [$U(MoO_4)_2$]	*Pbca*	10.191 / 90	9.586 / 90	14.274 / 90	33
$U(WO_4)_2$	*Pbca*	10.240 / 90	9.545 / 90	14.260 / 90	34
α-$Th(MoO_4)_2$	*Pbca*	10.318 / 90	9.737 / 90	14.475 / 90	35,36,39
α-$Np(MoO_4)_2$*	*Pbca*	10.120 / 90	9.440 / 90	14.100 / 90	45
$Pu(MoO_4)_2$*	*Pmna*	9.422 / 90	13.993 / 90	10.039 / 90	50
Compounds with scheelite-related structure					
$Am_2(MoO_4)_3$	$I4_1/a$	5.247 / 90	5.247 / 90	11.542 / 90	51
$K_2Th(MoO_4)_3$	$C2/c$	17.630 / 90	12.130 / 105.80	5.363 / 90	38,41
$K_2Np(MoO_4)_3$*	$C2/c$	17.643 / 90	12.037 / 104.82	5.266 / 90	49
$K_2Pu(MoO_4)_3$*	$C2/c$	17.538 / 90	11.992 / 104.80	5.243 / 90	49
$Rb_2Np(MoO_4)_3$*	$C2/c$	18.080 / 90	12.110 / 104.10	5.210 / 90	49
$Rb_2Pu(MoO_4)_3$*	$C2/c$	17.769 / 90	12.068 / 104.78	5.282 / 90	49
$Cs_2Pu(MoO_4)_3$*	*I*---	26.516 / 90	9.702 / 90	5.178 / 90	49
$K_4Th(MoO_4)_4$	$I4_1/a$	11.586 / 90	11.586 / 90	13.069 / 90	49
$Li_4Np(MoO_4)_4$*	-	11.105 / 90	11.105 / 90	10.648 / 90	46
$Li_4Pu(MoO_4)_4$*	-	11.085 / 90	11.085 / 90	10.600 / 90	50
$Na_4Np(MoO_4)_4$*	-	11.240 / 90	11.240 / 90	11.800 / 90	47
$Na_4Pu(MoO_4)_4$*	-	11.200 / 90	11.200 / 90	11.690 / 90	50
$KAm(MoO_4)_2$*	-	17.100 / 90	22.430 / 91.26	5.413 / 90	49
$Li_2Np(WO_4)_3$*	-	9.777 / 90	5.651 / 93.77	5.053 / 90	52
α-$Li_4Np(WO_4)_4$*	-	19.75 / 90	17.403 / 93.09	10.021 / 90	52
β-$Li_4Np(WO_4)_4$*	-	9.873 / 90	17.440 / 92.96	5.009 / 90	52
Compounds with palmierite-related structure					
$K_8Th(MoO_4)_6$	$P\bar{1}$	10.255 / 75.87	10.260 / 96.81	14.466 / 118.43	43
$K_8Np(MoO_4)_6$*	*C*-/-	10.488 / 90	17.608 / 116.73	7.822 / 90	48

Table 2. Crystallographic data for tri- and tetravalent actinide molybdates and tungstates (continued)

Chemical formula	sp.gr.	*a* [Å] / α [°]	*b* [Å] / β [°]	*c* [Å] / γ [°]	ref
$Rb_8Pu(MoO_4)_6$*	*C-/-*	10.670 / 90	17.710 / 116.30	7.990 / 90	49
$K_8Pu(MoO_4)_6$*	*C-/-*	10.416 / 90	17.535 / 116.59	7.748 / 90	49
$K_5Am(MoO_4)_4$*	*C-/-*	10.335 / 90	5.965 / 116.57	7.708 / 90	49
Other compounds					
$Cu_2Th_4(MoO_4)_9$	$I\bar{4}3d$	14.477 / 90	14.477 / 90	14.477 / 90	44

* structure has not been refined

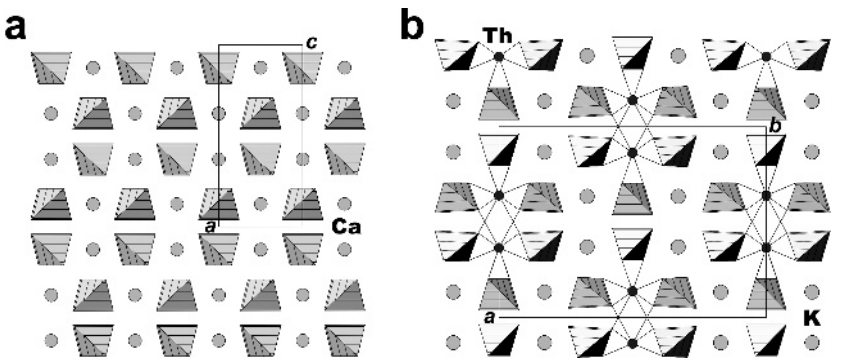

Fig. 8. The structure of scheelite, $CaWO_4$ (a) and its derivative structure, $K_2Th(MoO_4)_3$ with one third of Ca atoms replaced by Th and two thirds replaced by K (b).

Crystal chemistry of Th, Np, Pu and Am molybdates with alkali metal cations (A = K, Rb, Cs) was investigated by Tabuteau and Pages [49]. These authors demonstrated that, in the A_2MoO_4-$An(MoO_4)_2$ (An = Np, Pu, Th) and K_2MoO_4-$Am_2(MoO_4)_3$ systems, compounds with the 1:1 stoichiometry adopt a distorted scheelite-type structure (or superstructure), whereas compounds with the 4:1 and 5:1 stoichiometries crystallize in palmierite-related structure types. Fig. 8a shows the tetragonal structure of scheelite, $CaWO_4$, projected along the b axis. The structure of $K_2Th(MoO_4)_3$ [38,41] (Fig. 8b) can be obtained from that of scheelite by replacing one third of Ca atoms by Th and two thirds by K. This transition is accompanied by a monoclinic distortion of the scheelite structure type. It is noteworthy that $Am^{3+}{}_2(MoO_4)_3$ is isostructural with scheelite and the Am position is 2/3-occupied, thus the formula of this phase can be written as $Am_{2/3}\square_{1/3}(MoO_4)$ (□ = vacancy). Tabuteau et al. [52] reported synthesis and crystallographic data for $Li_2Np(WO_4)_3$ and two modifications of

$Li_4Np(WO_4)_4$ and pointed out their similarity to the wolframite ($FeWO_4$) structure type which in turn can be considered as a distorted scheelite structure.

The structure of palmierite(glaserite)-related $K_8Th(MoO_4)_6$ [43] is shown in Fig. 9. Its characteristic feature is the presence of a pseudohexagonal array of K and Th atoms sandwiched between the layers of MoO_4 tetrahedra.

There are three tetravalent actinide phases that contain divalent transition metal elements. The structures of $CdTh(MoO_4)_3$ [37] and $(Cu,Mn)U(MoO_4)_3$ [53] are isotypic and are derivatives of the α-UMo_2O_8 structure with six-coordinate U replaced by Cd or Cu. The structure of $Cu_2Th_4(MoO_4)_9$ [44] is based upon a complex framework of edge- and corner-linked ThO_9 and MoO_4 coordination polyhedra.

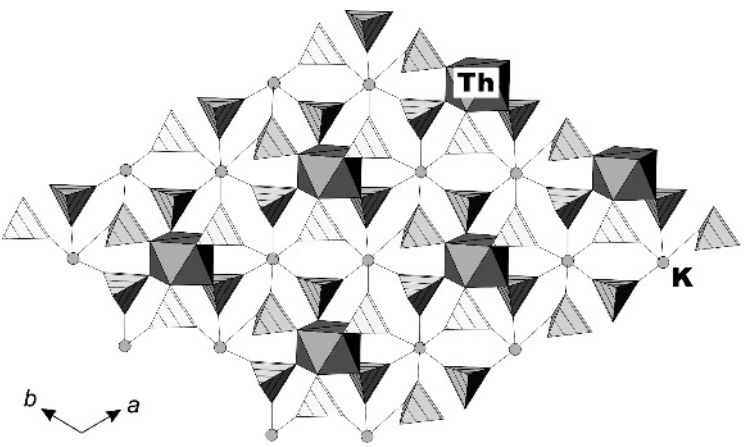

Fig. 9. Pseudohexagonal layer of K and Th atoms and MoO_4 tetrahedra in the palmierite-related structure of $K_8Th(MoO_4)_6$ (MoO_4 tetrahedra are lined).

2.3. Sulfates of tri- and tetravalent actinides

There are two crystal structures reported for sulfates of trivalent actinides: $Am^{3+}_2(SO_4)_3(H_2O)_8$ [54] and $(NH_4)U^{3+}(SO_4)_2(H_2O)_4$ [68] (Table 3). In the Am compound, the Am^{3+} ion is in eightfold square antiprismatic coordination, with four O atoms and four H_2O molecules [Am^{3+}-φ = 2.38-2.55 Å (φ = O, H_2O)]. The $Am^{3+}O_4(H_2O)_4$ polyhedra share corners with sulfate tetrahedra to produce sheets parallel to the ($\bar{1}01$) plane (Fig. 10a, b). The SO_4^{2-} tetrahedral anions are of two topological types: the $S(1)O_4$ tetrahedra are tridentate, whereas the $S(2)O_4$ tetrahedra are bidentate. $Am^{3+}_2(SO_4)_3(H_2O)_8$ is isostructural with the $M^{3+}_2(SO_4)_3(H_2O)_8$ phases, where M is a rare earth metal [71-78]. In the structure of $(NH_4)U^{3+}(SO_4)_2(H_2O)_4$ [68], U^{3+} ions are ninefold coordinated by O atoms and H_2O molecules (U^{3+}-φ = 2.37-2.60 Å).

Table 3. Crystallographic data for tri- and tetravalent actinide sulfates

Chemical formula	sp. gr.	*a* [Å] / α [°]	*b* [Å] / β [°]	*c* [Å] / γ [°]	ref
$Am^{3+}_2(SO_4)_3(H_2O)_8$	*C*2/*c*	13.619 / 90	6.837 / 102.67	18.405 / 90	54
$Th(OH)_2SO_4$	*Pnma*	11.733 / 90	6.040 / 90	7.059 / 90	55
$U(OH)_2SO_4$	*Pnma*	11.572 / 90	5.926 / 90	6.969 / 90	66
$K_4(Th(SO_4)_4(H_2O)_2)$	$C\ \bar{1}$	10.096 / 95.15	16.752 / 95.22	9.762 / 91.00	56
$Th(SO_4)_2(H_2O)_8$	$P2_1/n$	8.510 / 90	11.860 / 92.65	13.460 / 90	57
$Pu(SO_4)_2(H_2O)_4$	*Pnma*	14.544 / 90	10.980 / 90	5.667 / 90	58
$Np(SO_4)_2(H_2O)_4$	*Pnma*	14.597 / 90	11.036 / 90	5.663 / 90	63
$U(SO_4)_2(H_2O)_4$	*Pnma*	14.674 / 90	11.093 / 90	5.688 / 90	65
$Cs_2Th(SO_4)_3(H_2O)_2$	$P2_1/c$	6.415 / 90	15.950 / 90.88	13.078 / 90	59
$K_{5.5}(H_5O_2)_{0.5}Np(SO_4)_5(H_2O)$	$P2_1/c$	14.053 / 90	8.304 / 107.70	18.910 / 90	60
$K_4Pu(SO_4)_4(H_2O)_2$	$P2_1/c$	12.418 / 90	11.158 / 111.82	13.553 / 90	61
$Na_{10}Np_2(SO_4)_9(H_2O)_4$	*Pbcn*	27.259 / 90	6.897 / 90	17.721 / 90	62
$Cs_2Np(SO_4)_3(H_2O)_2$	$P2_1$	6.433 / 90	9.522 / 92.56	11.111 / 90	64
$U_6(SO_4)_6(OH)_4O_4$	*I*4/*m*	10.741 / 90	10.741 / 90	10.377 / 90	67
$(NH_4)U^{3+}(SO_4)_2(H_2O)_4$	$P2_1/c$	6.707 / 90	19.033 / 97.34	8.831 / 90	68
$TlPu^{3+}(SO_4)_2(H_2O)_4$*	$P2_1/c$	6.546 / 90	18.990 / 95.72	8.735 / 90	70
$Pu_2(OH)_2(SO_4)_3(H_2O)_4$*	*C*2/*c*	13.510 / 90	6.710 / 95.70	15.520 / 90	69

* structure has not been refined

The U polyhedra share edges with two SO_4 tetrahedra and corners only with two other SO_4 tetrahedra to form heteropolyhedral sheets parallel to (010) (Fig. 10c, d). The adjacent sheets are linked through a complex system of hydrogen bonds. All sulfate tetrahedra are bidentate. Again, the $(NH_4)U^{3+}(SO_4)_2(H_2O)_4$ phase is isostructural with trivalent rare earth sulfates with the composition $AM^{3+}(SO_4)_2(H_2O)_4$ (A = NH_4, Rb, Cs, Tl; M = rare earth metal) [70, 77, 79-82].

Structures of some sulfates of tetravalent actinides are isotypic with their tetravalent rare earth analogues (presumably, Ce(IV)). For example, phases with the composition $M^{4+}(SO_4)_2(H_2O)_4$ (M = U, Np, Pu) [58, 63, 65] are isostructural with $Ce(SO_4)_2(H_2O)_4$ [83]. In their structures, the $MO_4(H_2O)_4$ square antiprisms share corners with SO_4 tetrahedra to produce sheets parallel to (100) (Fig. 11).

The structures of the $Cs_2M^{4+}(SO_4)_3(H_2O)_2$ compounds (M = Th, Np) are closely related to the structure of $(NH_4)U^{3+}(SO_4)_2(H_2O)_4$. The transition from one to another can be achieved by replacement of $2H_2O$ groups by an additional

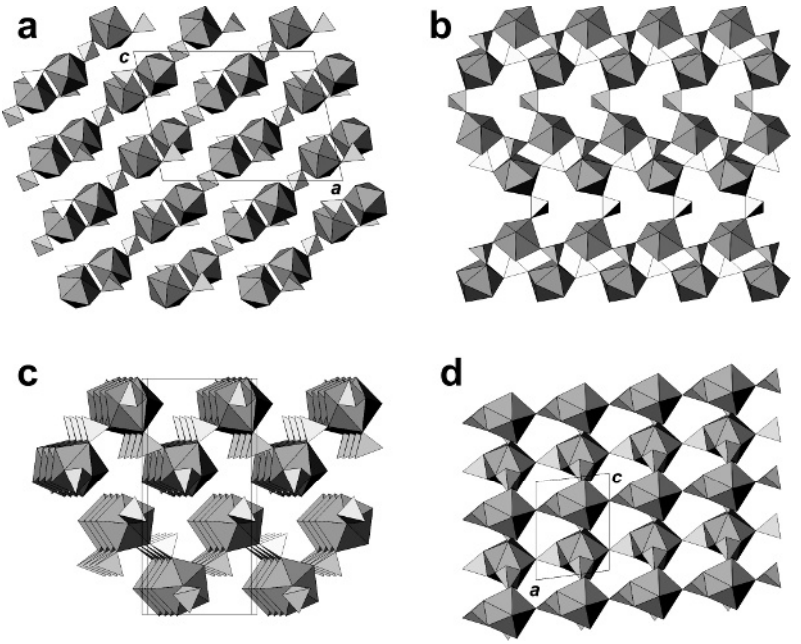

Fig. 10. Crystal structure of $Am^{3+}{}_2(SO_4)_3(H_2O)_8$ projected along the *b* axis (a) and sheet of Am polyhedra and SO_4 tetrahedra (b); structure of $(NH_4)U^{3+}(SO_4)_2(H_2O)_4$ shown approximately along the *c* axis (c) and sheet of U polyhedra and SO_4 tetrahedra. Legend: M polyhedra = dark-grey; SO_4 tetrahedra = light-grey.

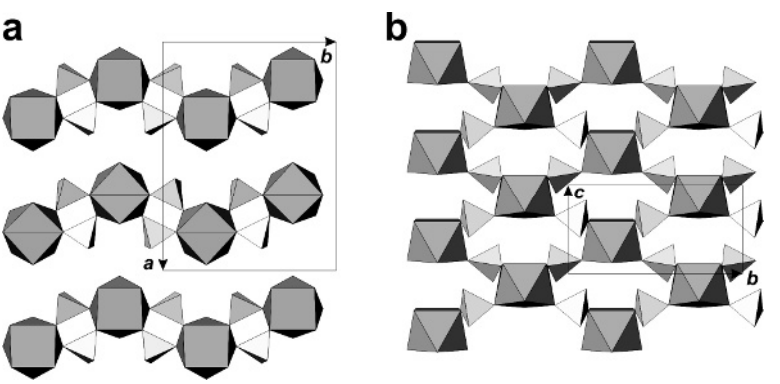

Fig. 11. The structure of $M^{4+}(SO_4)_2(H_2O)_4$ (M = U, Np, Pu) projected along the *c* (a) and *a* (b) axes. Legend: M polyhedra = dark-grey; SO_4 tetrahedra = light-grey.

SO_4 tetrahedron and Cs^+ cation. Indeed, the structures of the Th and Np compounds are based on the same type of sheet as observed in the U compound, but with two H_2O groups in the $M\varphi_9$ polyhedra replaced by two O atoms of monodentate sulfate tetrahedron (Fig. 12).

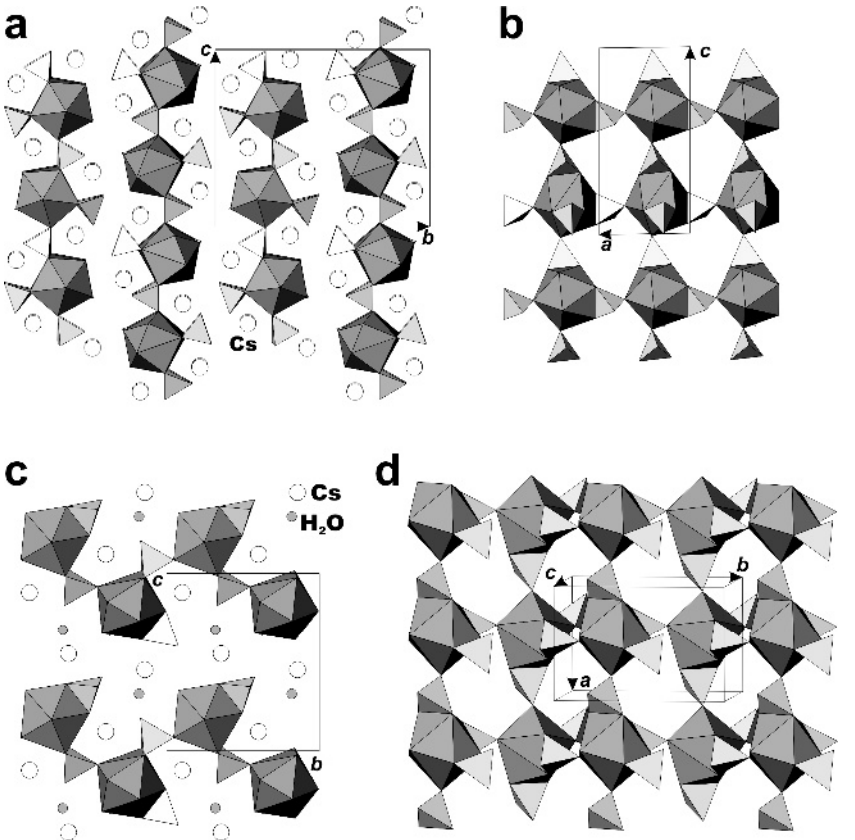

Fig. 12. The structures of $Cs_2M^{4+}(SO_4)_3(H_2O)_2$ (M = Th, Np) shown parallel (a, c, respectively) and perpendicular (b, d, respectively) to the sheets of M polyhedra (dark-grey) and SO_4 tetrahedra (light-grey).

Polymerization of coordination polyhedra of actinides and sulfate anions does not always result in 2D topologies. Fig. 13a shows the Np^{4+} coordination in the structure of $Na_{10}Np_2(SO_4)_9(H_2O)_4$ [62]. The coordination sphere of the Np^{4+} ion includes eight O atoms of SO_4 groups and one H_2O molecule. The Np polyhedra and SO_4 tetrahedra share common O atoms to produce the complex chains shown in Fig. 13b.

The structures of $K_{5.5}(H_5O_2)_{0.5}Np(SO_4)_5(H_2O)$ [60] and $K_4Pu(SO_4)_4(H_2O)_2$ [61] are remarkable in that, despite the presence of H_2O molecules, the M^{4+} actinide ions are coordinated exclusively by the O atoms of the sulfate groups (Fig. 14). In the first compound, the Np^{4+} ion is tenfold coordinated by O atoms from the five SO_4 tetrahedra such that $[Np^{4+}(SO_4)_5]^{6-}$ clusters are formed (Fig. 14a). In the structure of the Pu compound, two Pu^{4+}

ions link through bidentate SO_4 groups to form $[Pu^{4+}{}_2(SO_4)_8]^{8-}$ clusters (Fig. 14b).

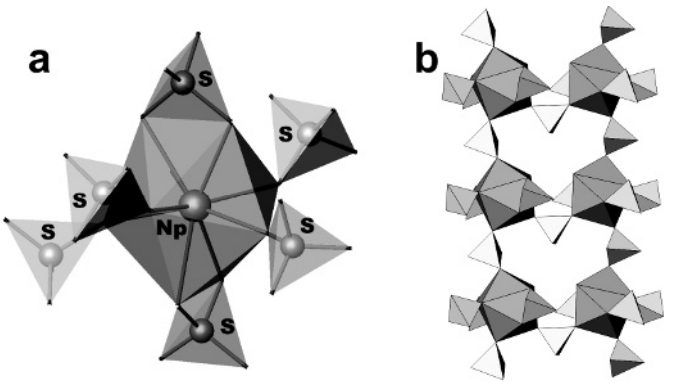

Fig. 13. Coordination of Np^{4+} ions (a) and Np polyhedra (dark-grey) and SO_4 tetrahedra (light-grey) (b) in the structure of $Na_{10}Np_2(SO_4)_9(H_2O)_4$.

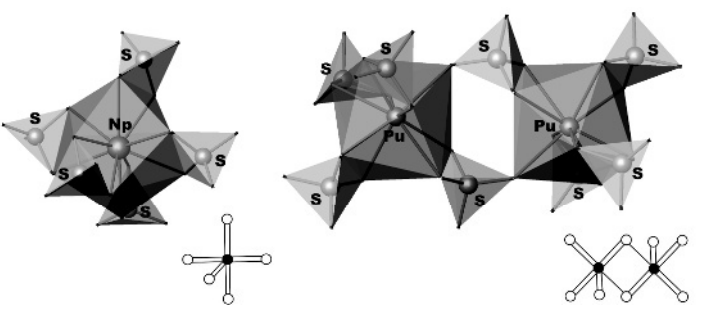

Fig. 14. The $[Np^{4+}(SO_4)_5]^{6-}$ cluster from the structure of $K_{5.5}(H_5O_2)_{0.5}Np(SO_4)_5(H_2O)$ (a) and the $[Pu^{4+}{}_2(SO_4)_8]^{8-}$ cluster from the structure of $K_4Pu(SO_4)_4(H_2O)_2$. Insets provide the 0D black-and-white graphs symbolizing topologies of linkage of the M and S polyhedra.

The topologies of polyhedral linkage in the structures considered above can be investigated using a graphical approach [86]. The M^{n+} coordination centers and S^{6+} cations are symbolized by black and white vertices, respectively. Two vertices are linked by an edge if corresponding cations have at least one common O atom in their coordination sphere, and the number of edges between the two vertices corresponds to the number of common O atoms. As a result, a black-and-white graph is obtained that reflects the topology of linkage of coordination polyhedra. The 0D graphs shown as insets in Fig. 14 symbolize topologies of linkage of M and S polyhedra in the respective structures. Fig. 15 shows 2D black-and-white graphs that correspond to the structural topologies observed in $Cs_2M^{4+}(SO_4)_3(H_2O)_2$ (M = Th, Np) (Fig. 15a), $M^{4+}(SO_4)_2(H_2O)_4$ (M

= U, Np, Pu) (Fig. 15b), $(NH_4)U^{3+}(SO_4)_2(H_2O)_4$ (Fig. 15c), and $Am^{3+}{}_2(SO_4)_3(H_2O)_8$ (Fig. 15d).

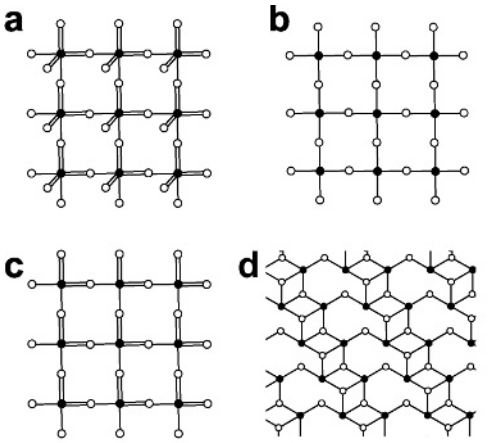

Fig. 15. The black-and-white 2D graphs that correspond to the structural topologies of 2D structural units observed in $Cs_2M^{4+}(SO_4)_3(H_2O)_2$ (M = Th, Np) (a), $M^{4+}(SO_4)_2(H_2O)_4$ (M = U, Np, Pu) (b), $(NH_4)U^{3+}(SO_4)_2(H_2O)_4$ (c), and $Am^{3+}{}_2(SO_4)_3(H_2O)_8$ (d). Black and white vertices symbolize M and SO_4 polyhedra, respectively, number of edges between the vertices correspond to the number of O atoms shared between the respective polyhedra.

In the structures of hydroxosulfates of tetravalent actinides, actinide coordination polyhedra polymerize through hydroxo bridges to form extended oligomeric units. For example, in the structures of the $M(OH)_2SO_4$ compounds (M = Th, U), the M polyhedra share edges to form chains extending along the b axis (Fig. 16). The structure of $Pu_2(OH)_2(SO_4)_3(H_2O)_4$ [69] can be considered as based upon 2D sheets with the topology observed for $Am^{3+}{}_2(SO_4)_3(H_2O)_8$ (Figs. 10b, 15d). However, in contrast to the Am compound, the Pu polyhedra in the adjacent sheets are not isolated by H_2O molecules but are linked through hydroxo groups into pairs, thus providing linkage of the sheets into a 3D framework. It is interesting that tetravalent actinide hydroxosulfates are isostructural with their Zr and Hf analogues [84, 85, 87, 88].

The crystal structure of $U_6(SO_4)_6(OH)_4O_4$ (Fig. 17) contains both additional O^{2-} and OH^- anions that are not bonded to S^{6+}. The U atoms and additional anions form the $[U_6O_4(OH)_4]^{12+}$ polynuclear cations shown in Fig. 15b. The U atom coordination is a regular octahedron, whereas the O^{2-} and OH^- anions are under each triangular face of the octahedron. The $[U_6O_4(OH)_4]^{12+}$ complexes are linked into frameworks through sulfate tetrahedra. The U^{4+} ions are in square antiprismatic coordination. It is noteworthy that the compound is isostructural with its Ce analogue [89].

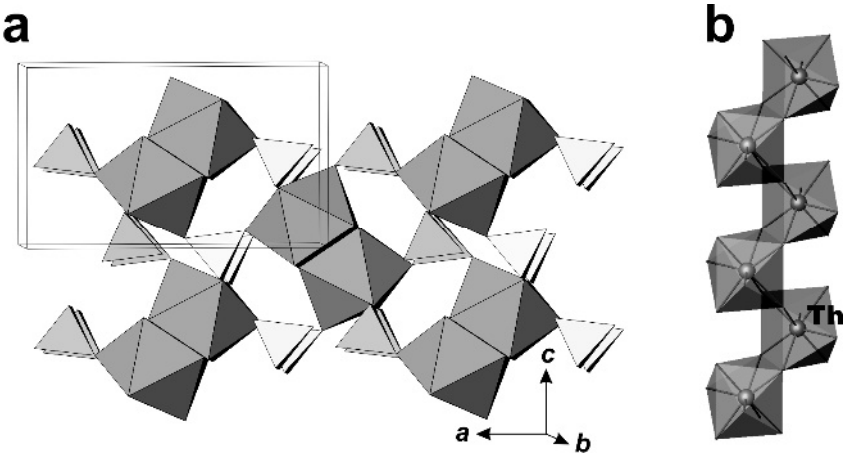

Fig. 16. The structure of the $M(OH)_2SO_4$ compounds (M = Th, U) (a) contains extended chains of edge-sharing M polyhedra (b).

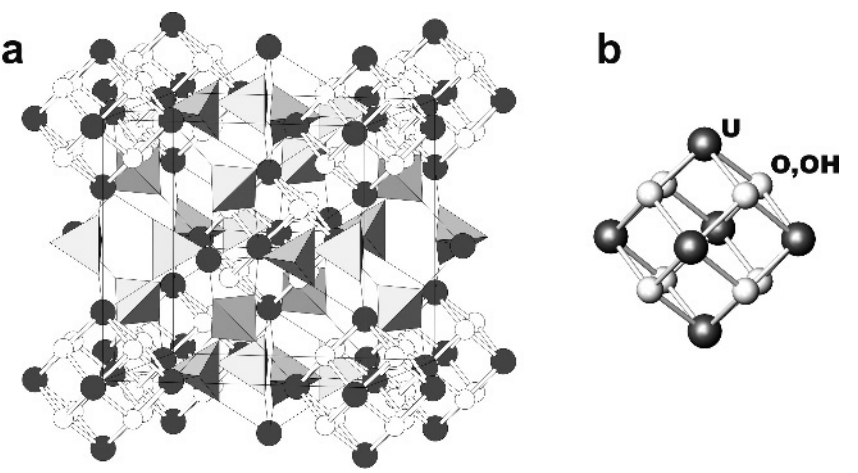

Fig. 17. The structure of $U_6(SO_4)_6(OH)_4O_4$ (a) and the $[U_6O_4(OH)_4]^{12+}$ hexanuclear cation (b).

3. Actinyl compounds

3.1. Structures based upon sheets of edge-sharing actinyl polyhedra

3.1.1. The concept of sheet anion topology

The structures of layered actinyl compounds with edge-sharing actinide polyhedra can be described using anion topologies suggested for the description

of complex U^{6+} architectures by Burns et al. [90-92] (see Chapter 1). The anion topology is a tiling of the 2D plane into convex polygons. In order to distinguish between different anion topologies, we use their cyclic symbol defined as $n_1^{m1}n_2^{m2}n_3^{m3}$..., where n is the number of corners in a given polygon (3 for a triangle, 4 for a square, 5 for a pentagon, etc.), and m is the proportional number of these polygons in the anion topology. For example, the topology shown in Fig. 18b consists of pentagons, squares and triangles in the proportion 2:1:2, respectively. Thus, the cyclic symbol for this anion topology is $5^24^13^2$. Table 4 provides a list of actinyl compounds classified according to the cyclic symbols of their anion topologies.

The compounds which will be analyzed in this section can be subdivided into five groups: (a) structures that are derivatives of the complex U-Mo-W oxides; (b) structures with W and Mo in square pyramidal coordination; (c) structures with trimeric and dimeric units of actinyl polyhedra; (d) structures with chains of edge-sharing actinyl polyhedra; (e) structures with sheets of actinyl polyhedra linked by sulfate tetrahedra.

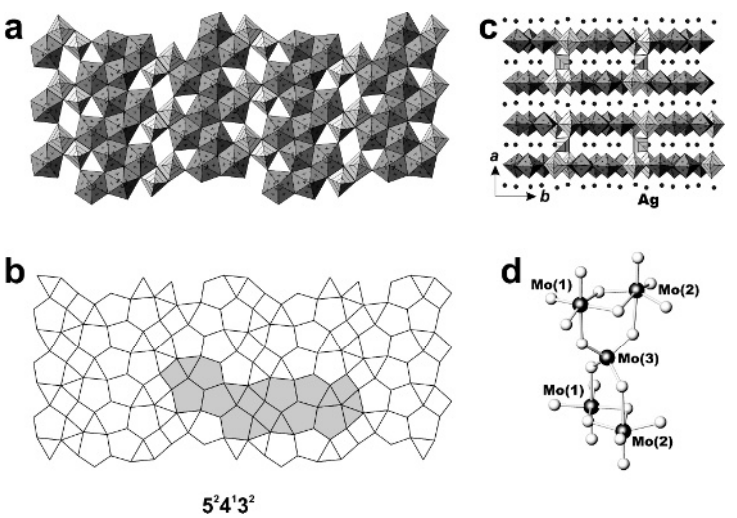

Fig. 18. The sheet of the UO_7 pentagonal bipyramids (cross-hatched) and the distorted $Mo^{6+}O_6$ octahedra (lined) in the structure of $Ag_{10}[(UO_2)_8(Mo_5O_{20})O_8]$ (a) and its anion topology (b). Projection of the structure along the *c* axis (c) and ball-and-stick view of the $[Mo_5O_{20}]^{10+}$ moiety (d).

3.1.2. Structures related to the complex U-Mo-W oxides

Fig. 18a shows the sheet of UO_7 pentagonal bipyramids and distorted $Mo^{6+}O_6$ octahedra observed in the structure of $Ag_{10}[(UO_2)_8(Mo_5O_{20})O_8]$ [95]. This sheet is identical to that found in the structure of U_2MoO_8 (Fig. 5).

Table 4. Crystallographic data for actinyl compounds based on sheets described using theory of anion topologies

Anion topology	Chemical formula	sp. gr.	*a* [Å] / α [°]	*b* [Å] / β [°]	*c* [Å] / γ [°]	ref
$5^14^13^1$-II	$Cs[NpO_2MoO_4]$	$P2_1/c$	7.302 / 90	8.837 / 104.68	10.868 / 90	93
$5^14^13^3$	$Ag_6[(UO_2)_3O(MoO_4)_5]$	$C2/c$	16.451 / 90	11.324 /100.01	12.742 / 90	96
$5^34^13^9$	$Cs_4[(UO_2)_3O(MoO_4)_2(MoO_5)]$	$P1$	7.510 / 79.28	7.897 / 81.27	9.774 / 87.25	97
5^33^4	$K_2[(UO_2)_2(MoO_4)O_2]$	$P2_1/c$	8.250 / 90	15.337 /104.75	8.351 / 90	98
$5^84^33^6$	$K_8[(UO_2)_8(MoO_5)_3O_6]$	$P4/n$	23.488 / 90	23.488 / 90	6.786 / 90	98
$5^84^53^6$	$Rb_2[(UO_2)_2(WO_5)O]$	$P2_1/n$	8.234 / 90	28.740 /104.59	9.378 / 90	99
	$K_2[(UO_2)_2(WO_5)O]$	$P2_1/n$	8.083 / 90	28.724 /102.14	9.012 / 90	99
	$Tl_2[(UO_2)(MoO_5)O]$	$P2_1/n$	8.253 / 90	28.508 /104.12	9.156 / 90	103
$8^15^44^63^8$	$Cs_6[(UO_2)_4(W_5O_{21})(OH)_2(H_2O)_2]$	$I4cm$	15.959 / 90	15.959 / 90	14.215 / 90	101
$6^15^13^1$	$K_2[(UO_2)(W_2O_8)]$	$Pmcn$	7.588 / 90	8.616 / 90	13.946 / 90	99
	$Na_2[(UO_2)W_2O_8]$	$P\bar{1}$	6.648 / 89.95	7.531 / 86.19	8.487 / 73.30	100
	α-$Ag_2[(UO_2)W_2O_8]$	$P2_1/c$	8.426 / 90	7.490 / 95.44	12.927 / 90	100
	β-$Ag_2[(UO_2)W_2O_8]$	$Pnma$	8.642 / 90	7.561 / 90	12.451 / 90	100
$5^24^13^2$	$Na_{10}[(UO_2)_8(W_5O_{20})O_8]$	$C2/c$	24.359 / 90	23.506 / 94.85	6.807 / 90	99

Table 4. Crystallographic data for actinyl compounds based on sheets described using theory of anion topologies (continued)

Anion topology	Chemical formula	sp. gr.	*a* [Å] / α [°]	*b* [Å] / β [°]	*c* [Å] / γ [°]	ref
$5^2 4^1 3^2$	$Ag_{10}[(UO_2)_8(Mo_5O_{20})O_8]$	*C*2/*c*	24.672 / 90	23.401 / 94.99	6.793 / 90	102
$5^1 4^1 3^1$-I	$[(UO_2)MoO_4(H_2O)](H_2O)$ umohoite	*P* $\bar{1}$	6.375 / 82.64	7.529 / 85.95	14.628 / 89.91	104 105
	$Li_2[(UO_2)W_2O_8]$	*Pbcn*	7.937 / 90	12.786 / 90	7.425 / 90	116
	$Li_2[(UO_2)_4W_4O_{16}]$	*C*2/*c*	14.019 / 90	6.312 / 98.86	22.296 / 90	116
	$Cs[NpO_2(CrO_4)](H_2O)$	$P2_1$	6.887 / 90	7.378 / 101.32	7.566 / 90	118
	$(NH_4)_4[(NpO_2)_2(CrO_4)_3]$	*P* $\bar{1}$	9.816 / 98.81	10.163 / 91.41	10.289 115.51	118
$5^1 4^3 3^1$	$[(UO_2)Mo_2O_7(H_2O)_2](H_2O)$ iriginite	*Pbcm*	6.705 / 90	12.731 / 90	11.524 / 90	116
	$[(UO_2)Mo_2O_7(H_2O)_2]$	*C*2/*c*	35.071 / 90	6.717 / 90.07	11.513 / 90	117 118
	$Ca[UO_2Mo_4O_{14}]$	*P*2/*n*	11.447 / 90	6.651 / 90.44	8.236 / 90	94, 95
$6^1 5^2 4^2 3^2$	$Cu[(UO_2)_2(OH)_2(SO_4)_2](H_2O)_8$ johannite	*P* $\bar{1}$	8.903 / 109.87	9.499 / 112.01	6.812 / 100.40	109
	$[C(NH_2)_3][(UO_2)(OH)(MoO_4)]$	$P2_1/c$	15.411 / 90	7.086 / 113.13	18.108 / 90	110
	$(UO_2)_3(MoO_4)_2(OH)_2(H_2O)_{10}$	*Pbca*	18.816 / 90	19.523 / 90	13.946 / 90	111
	$(UO_2)_4(MoO_4)_3(OH)_2(H_2O)_4$	$P2_1/m$	9.764 / 90	8.705 / 103.08	14.077 / 90	111
	$[N_2C_6H_{16}][UO_2F(SO_4)]_2$ USFO-3	*Pmmn*	6.950 / 90	17.215 / 90	7.087 / 90	119
	$Sr[UO_2(OH)(CrO_4)](H_2O)_8$	*P* $\bar{1}$	8.923 / 106.63	9.965 / 99.09	11.602 / 97.26	120
$5^4 4^1 3^2$-I	$K[(UO_2)(OH)(CrO_4)](H_2O)_{1.5}$	$P2_1/c$	13.292 / 90	9.477 / 104.12	13.137 / 90	121

Table 4. Crystallographic data for actinyl compounds based on sheets described using theory of anion topologies (continued)

Anion topology	Chemical formula	sp. gr.	*a* [Å] / α [°]	*b* [Å] / β [°]	*c* [Å] / γ [°]	ref
$5^2 4^3 3^2$	$Zn(UO_2)_2(SO_4)O_2](H_2O)_{3.5}$	*C*2/*m*	8.644 / 90	14.166 104.04	17.701 / 90	112 113
	$Co[(UO_2)_2(SO_4)O_2](H_2O)_{3.5}$	*C*2/*m*	8.650 / 90	14.252 104.09	17.742 / 90	113
	$K_{2.71}[(UO_2)_4(SO_4)_2O_3(OH)](H_2O)_3$	*C*2	8.752 / 90	13.920 104.18	17.697 / 90	113 114
	$Na_5(H_2O)_{12}[(UO_2)_8(SO_4)_4O_5(OH)_3]$	$P2_1/n$	17.643 / 90	14.627 104.46	17.692 / 90	113
	$(NH_4)_4[(UO_2)_2(SO_4)O_2]_2(H_2O)$	*C*2/*m*	8.699 / 90	14.166 104.12	17.847 / 90	113
	$(NH_4)_2[(UO_2)_2(SO_4)O_2]$	*Cmca*	14.252 / 90	8.775 / 90	17.186 / 90	113
	$Mg[(UO_2)_2(SO_4)O_2](H_2O)_{3.5}$	*C*2/*m*	8.651 / 90	14.194 104.13	17.721 / 90	113
	$Mg_2[(UO_2)_2(SO_4)O_2]_2(H_2O)_{11}$	$P2_1/c$	8.646 / 90	17.200 102.12	18.464 / 90	113
	$Mg_3(H_2O)_{18}[(UO_2)_4O_3(OH)(SO_4)_2]_2(H_2O)_{10}$ marecottite	$P\bar{1}$	10.815 / 66.22	11.249 / 72.41	13.851 / 69.95	115
$5^4 4^1 3^2$-II	$(K,Na)Na_3[(UO_2)_5O_6(SO_4)]$	*Pbca*	13.286 / 90	13.726 / 90	19.712 / 90	117
$5^3 3^1$	$(H_3O)_3[(UO_2)_3O(OH)_3(SeO_4)_2]$	*R*32	9.567 / 90	9.567 / 90	22.703 / 120	122

However, in the structure of U_2MoO_8, adjacent sheets are linked together by sharing apical anions of the U and Mo polyhedra. In the structure of the Ag compound, two adjacent sheets are linked by additional $Mo^{6+}O_4$ tetrahedra which results in the formation of the complex $[Mo_5O_{20}]^{10+}$ moiety shown in Fig. 18d. The Ag^+ cations occupy the interior of the double uranyl molybdate sheets and are between the double sheets (Fig. 18d).

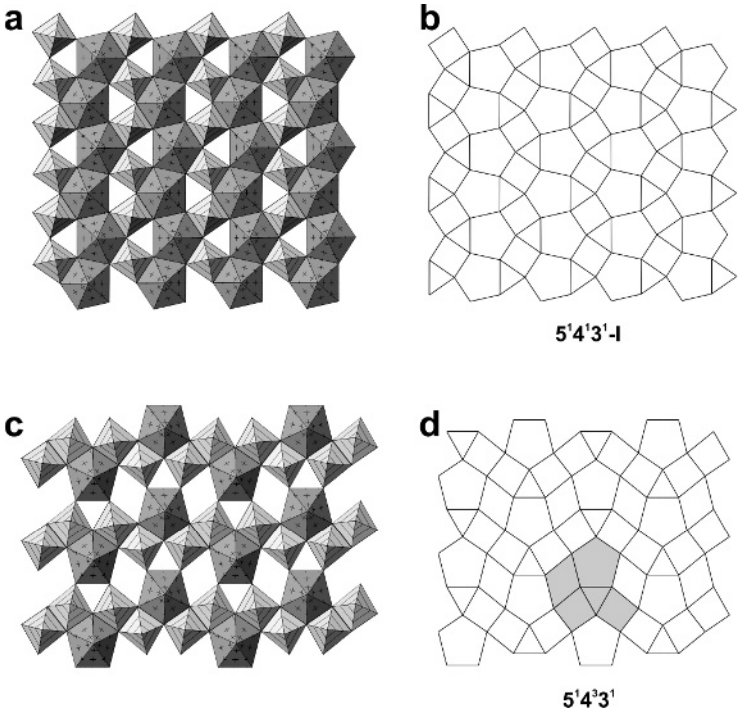

Fig. 19. The sheets of U and Mo polyhedra in the structures of umohoite (a) and iriginite (c) and their anion topologies (b and d, respectively). Legend: U polyhedra = cross-hatched; Mo polyhedra = lined.

The structure of umohoite $[(UO_2)MoO_4(H_2O)](H_2O)$ has been extensively investigated over four decades. The first structural model for umohoite was provided by Makarov and Anikina 1963 [123]. However, recent investigations [104, 105] demonstrated that their model was incorrect. The new model is based upon sheets of UO_7 pentagonal bipyramids and $MoO_5(H_2O)$ octahedra as is shown in Fig. 19a. The topology of polyhedral linkage within the sheet is the same as observed for the layers of U(IV) and Mo(VI) coordination polyhedra in the structure of $UMoO_5$ which is a member of the (1)-PB series of complex U-Mo oxides (see above). However, in contrast to the structure of $UMoO_5$, the uranyl molybdate sheets in umohoite are not linked by strong covalent bonds, rather linkages are through weak hydrogen bonds only. The anion topology of the sheets in umohoite corresponds to the uranophane anion topology consisting of pentagons, squares and triangles. In umohoite, pentagons and squares are occupied by U and Mo, respectively, whereas the triangles are vacant.

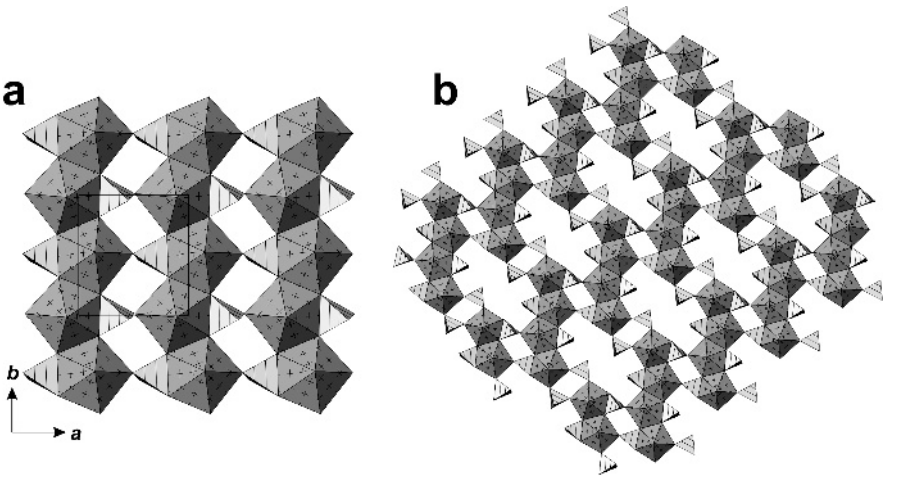

Fig. 20. The neptunyl chromate sheets in the structures of $Cs[NpO_2(CrO_4)](H_2O)$ (a) and $(NH_4)_4[(NpO_2)_2(CrO_4)_3]$ (b). Legend: Np polyhedra = cross-hatched; Cr polyhedra = lined.

Another scheme of cation distribution within the $5^14^13^1$-I (uranophane) anion topology is observed in $Cs[NpO_2(CrO_4)](H_2O)$ [118]. Here, pentagons are occupied by the $[NpO_2]^+$ cations, triangles by chromate tetrahedra, and squares are vacant (Fig. 20a). A remarkable version of the uranophane-type sheet is the $[(NpO_2)_2(CrO_4)_3]^{4-}$ sheet in $(NH_4)_4[(NpO_2)_2(CrO_4)_3]$ [118] (Fig. 20b). Only two thirds of the triangles are occupied by Np, which results in the formation of tetramers of NpO_7 pentagonal bipyramids that are linked by the $[CrO_4]^{2-}$ tetrahedra. Obbade et al. [116] reported structures of two Li uranyl tungstates that can also be considered as based upon uranophane anion topology. The structure of $Li_2(UO_2)(WO_4)_2$ contains a 3D framework consisting of the ReO_3-type slabs of WO_6 octahedra linked by chains of edge-sharing uranyl pentagonal bipyramids (Fig. 21a). The framework can be derived from the (1)-PB structure of $UMoO_5$ by eliminating half of the chains of the U polyhedra. A much more complex situation was found for $Li_2(UO_2)_4(WO_4)_4O$ [116]. In this, 1-(PB)-type sheets are cut into strips consisting of trimers of UO_7 pentagonal bipyramids and tetramers of tungstate octahedra (Fig. 22e). The strips are linked into complex layers by sharing apical vertices of the U and W polyhedra (Fig. 22d). The layers are further connected into a framework by additional UO_6 square bipyramids (Fig. 22a).

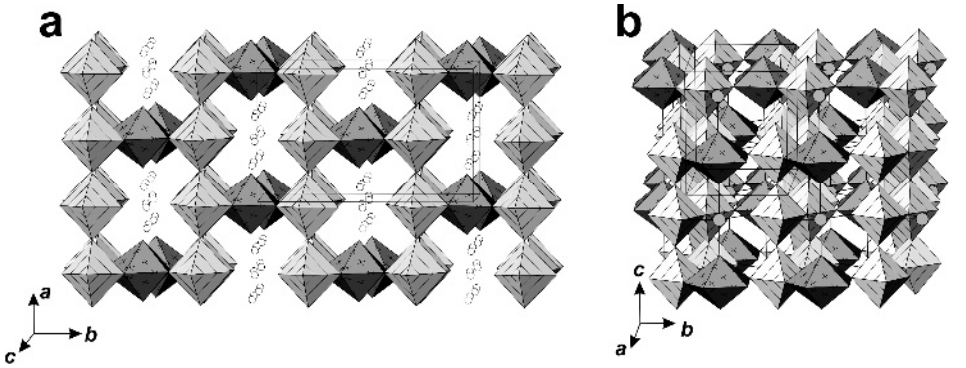

Fig. 21. Framework of the U and W polyhedra in the structure of $Li_2(UO_2)(WO_4)_2$ (Li^+ ions shown as spheres) (a), and framework of the U and Mo polyhedra in the structure of $Ca[UO_2Mo_4O_{14}]$ (Ca^{2+} cations shown as dark spheres) (b).

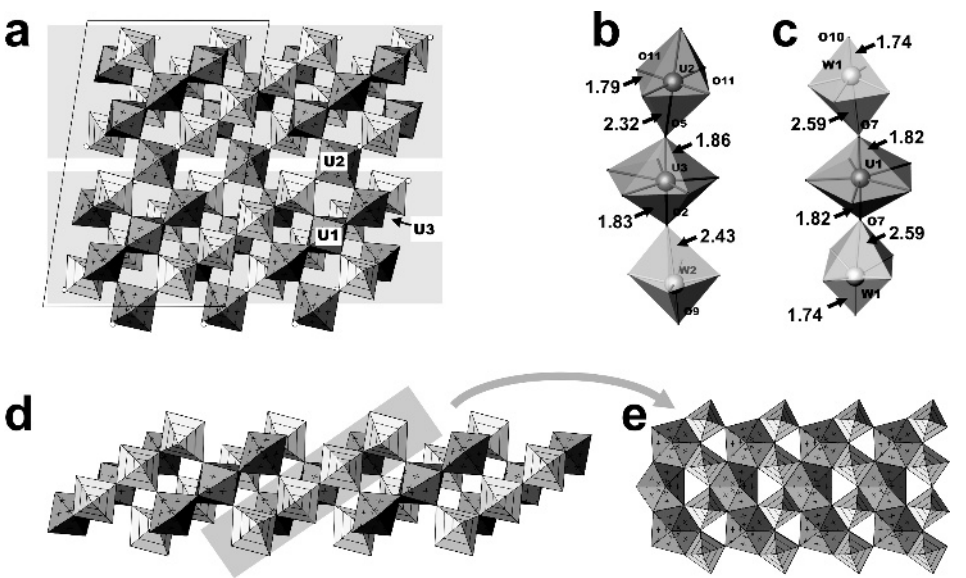

Fig. 22. Projection of the structure of $Li_2(UO_2)_4(WO_4)_4O$ along the *b* axis (a). Shading is used to separate adjacent layers cross-linked by $U(2)O_6$ square bipyramids. Interactions of uranyl cations with adjacent polyhedra (b, c). Layer of the UO_7 pentagonal bipyramids and WO_6 octahedra (d) as consisting of tapes with uranophane-type topology (e).

The structure of $Li_2(UO_2)_4(WO_4)_4O$ is a rare example of a uranyl compound where O atoms of the uranyl cation are involved with polymerization of coordination polyhedra of high-valence cations. Figs. 22b and 22c show two fragments of the structure where uranyl cations interact with adjacent uranyl and tungsten polyhedra. Thus, the O atom of the $[U(3)O_2]^{2+}$ cation (Fig. 22b) is

an equatorial anion of the $[U(2)O_6]$ square bipyramid and an apical anion for the $[W(2)O_6]$ octahedron. The O atoms of the $[U(1)O_2]^{2+}$ cation (Fig. 22c) are the apical anions of the $[W(1)O_6]$ octahedra.

In natural environments, umohoite frequently occurs in close association with another uranyl molybdate hydrate mineral, iriginite $[(UO_2)Mo_2O_7(H_2O)_2](H_2O)$ [116]. The structure of iriginite is based upon sheets consisting of chains of the $MoO_5(H_2O)$ octahedra connected by single uranyl pentagonal bipyramids (Fig. 19c). The electroneutral $[(UO_2)Mo_2O_7(H_2O)_2]$ sheets are linked through hydrogen bonds that involve interlayer H_2O molecules. In the structure of the lower hydrate of iriginite, $[(UO_2)Mo_2O_7(H_2O)_2]$ [117], there are no interlayer H_2O molecules. Linkage of the iriginite-type sheets by sharing apical anions of the Mo octahedra results in the 3D framework observed in the structure of $Ca[UO_2Mo_4O_{14}]$. In this structure, half of the U atoms are replaced by Ca^{2+} cations relative to iriginite (Fig. 21b).

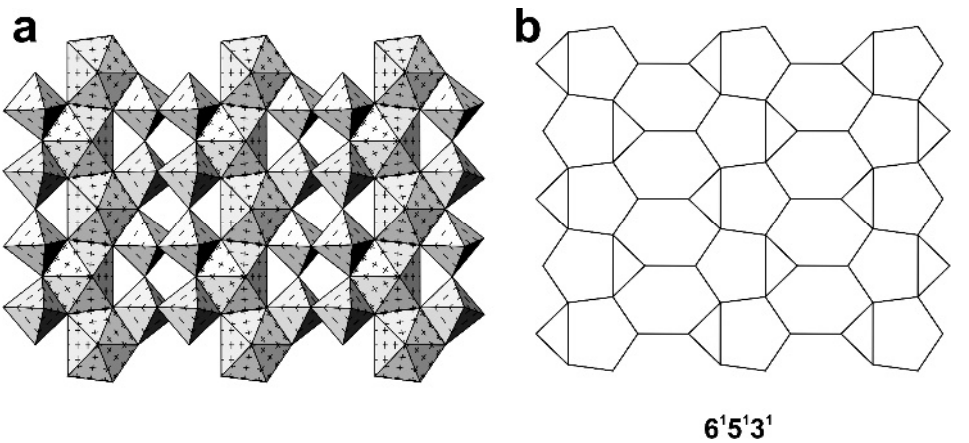

Fig. 23. Sheet of the UO_7 bipyramids (cross-hatched) and WO_6 octahedra (lined) in the structure of $Na_2[(UO_2)W_2O_8]$ (a) and its anion topology (b).

The structures of the phases with the general formula $A_2[(UO_2)(W_2O_8)]$ (A = Na, K, Ag) are based upon the sheet shown in Fig. 23. The sheet contains chains of edge-sharing UO_7 pentagonal bipyramids interlinked by the double $[W_2O_8]$ chains of distorted WO_6 octahedra. The double $[W_2O_8]$ chains consist of two single chains of corner-sharing octahedra. Two octahedra from the adjacent chains share a common edge, resulting in the formation of the $[W_2O_8]$ unit. The $A_2[(UO_2)(W_2O_8)]$ phases can thus be considered as derivatives of the (2)-PB complex U-W oxides but with edge-sharing between the single tungstate chains.

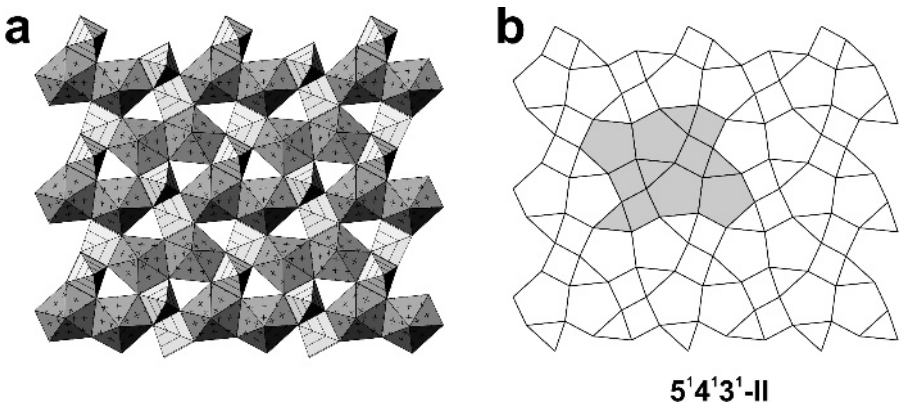

Fig. 24. Sheet of NpO_7 bipyramids (cross-hatched) and MoO_5 square pyramids (lined) in the structure of $Cs[NpO_2MoO_4]$ (a) and its anion topology (b).

3.1.3. Structures with W and Mo in square pyramidal coordination

In the structures considered above, hexavalent cations (Mo^{6+} and W^{6+}) occur in [1+4+1]-distorted octahedral coordination. Elimination of an apical ligand gives a distorted square pyramidal polyhedron coordination that occurs in several actinyl molybdate and tungstate phases.

In the structure of $Cs[NpO_2MoO_4]$ [93], Np occurs in edge-sharing dimers of NpO_7 pentagonal bipyramids, and Mo is in edge-sharing dimers of MoO_5 square pyramids. The two sets of dimers share edges, forming sheets of composition $[(NpO_2)_2Mo_2O_8]^{2-}$ (Fig. 24) that are topologically identical to uranyl divanadate sheets, $[(UO_2)_2V_2O_8]^{2-}$, that occur in compounds of the carnotite group [91, 92].

In the structures of $A_2[(UO_2)_2(WO_5)O]$ (A = K, Rb) and $Tl_2[(UO_2)_2(MoO_5)O]$, eight uranyl bipyramids share edges to form octamers that further share edges with single MO_5 square bipyramids (M = Mo, W) (Fig. 25a, b). In the structure of $K_8[(UO_2)_8(MoO_5)_3O_6]$, MoO_5 pyramids are again isolated from each other and share edges with hexamers of six edge-sharing UO_7 polyhedra (Fig. 25c, d). The structure of $Cs_6[(UO_2)_4(W_5O_{21})(OH)_2(H_2O)_2]$ is based upon a complex uranyl tungstate sheet consisting of UO_7 bipyramids, single WO_5 square pyramids and edge-sharing dimers of WO_5 square pyramids (Fig. 25e, f).

3.1.4. Structures with trimeric and dimeric units of actinyl polyhedra

Fig. 26a shows the complex uranyl molybdate sheet from the structure of $Cs_4[(UO_2)_3O(MoO_4)_2(MoO_5)]$. Within the sheet, three uranyl pentagonal bipyramids are linked into trimeric units interconnected by Mo polyhedra. In the structure, Mo occurs in three different coordinations (Fig. 26c). The Mo(3) atom

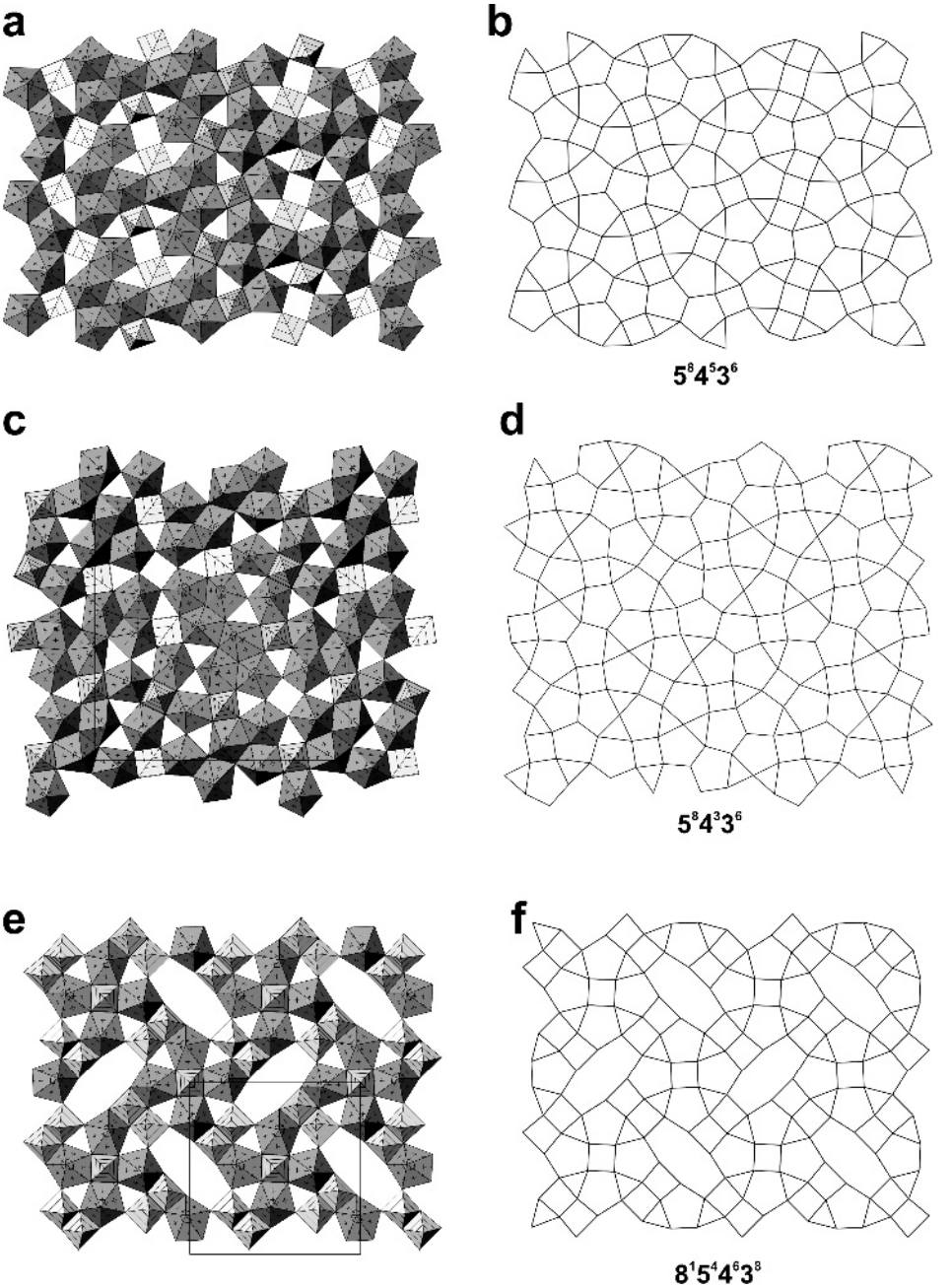

Fig. 25. Sheets of MO_5 square pyramids (lined; M = Mo, W) and UO_7 pentagonal bipyramids (cross-hatched) in the structures of $Tl_2[(UO_2)_2(MoO_5)O]$ (a), $K_8[(UO_2)_8(MoO_5)_3O_6]$ (c), and $Cs_6[(UO_2)_4(W_5O_{21})(OH)_2(H_2O)_2]$ (e) and their anion topologies (b, d, and f, respectively).

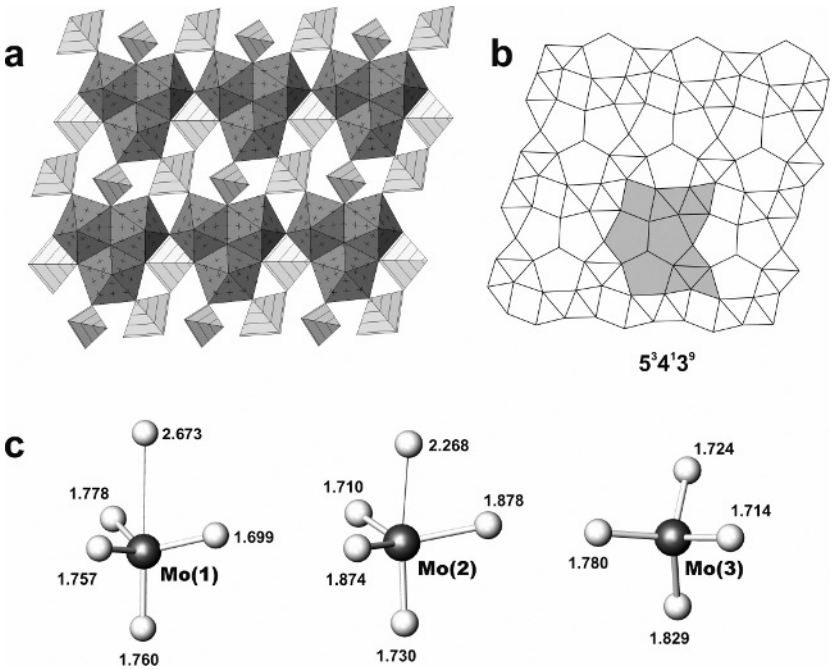

Fig. 26. Sheet of trimers of uranyl bipyramids and MoO_n polyhedra (n = 4, 5) in the structure of $Cs_4[(UO_2)_3O(MoO_4)_2(MoO_5)]$ (a), its anion topology (b) and coordination of the Mo^{6+} cations.

is in a slightly distorted tetrahedral coordination with Mo^{6+}-O bond lengths in the range of 1.714-1.829 Å. The $Mo(2)O_5$ configuration is a distorted trigonal bipyramid with one of the apical Mo^{6+}-O bonds being elongated (2.268 Å), thus this coordination is a [4+1]-distorted configuration. The coordination of the Mo(1) atom can be considered as transitional between tetrahedral and distorted trigonal bipyramidal since the apical anion is at 2.673 Å from the Mo cations. The structure of $Ag_6[(UO_2)_3O(MoO_4)_5]$ is based upon a sheet consisting of uranyl trimeric units interlinked by MoO_4 tetrahedra (Fig. 27a, b). In the structure of $(H_3O)_3[(UO_2)_3O(OH)_3(SeO_4)_2]$, trimeric uranyl units are cross-linked by tridentate SeO_4 tetrahedra (Fig. 27c, d).

In the structure of johannite, $Cu[(UO_2)_2(OH)_2(SO_4)_2](H_2O)_8$, and related uranyl sulfates, molybdates, and chromates (Table 4), two uranyl pentagonal bipyramids share two OH^- anions to form edge-sharing dimers. The dimers share corners with TO_4 tetrahedra (T = S, Cr, Mo) to form continious sheets with the phosphuranylite-type anion topology (Fig. 28a, b) [91, 92]. The uranyl chromate sheet in the structure of $K[(UO_2)(OH)(CrO_4)](H_2O)_{1.5}$ also contains dimers of edge-sharing uranyl pentagonal bipyramids but the topology of

linkage by chromate tetrahedra is different which results in a different anion topology (Fig. 28c, d).

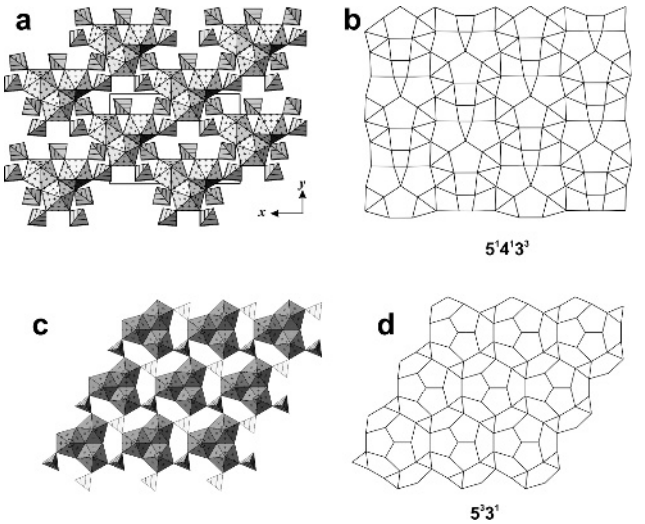

Fig. 27. Sheet of trimers of uranyl bipyramids (cross-hathed) and tetrahedral oxoanions (lined) in the structures of $Ag_6[(UO_2)_3O(MoO_4)_5]$ (a) and $(H_3O)_3[(UO_2)_3O(OH)_3(SeO_4)_2]$ (c) and their anion topologies (b and d, respectively).

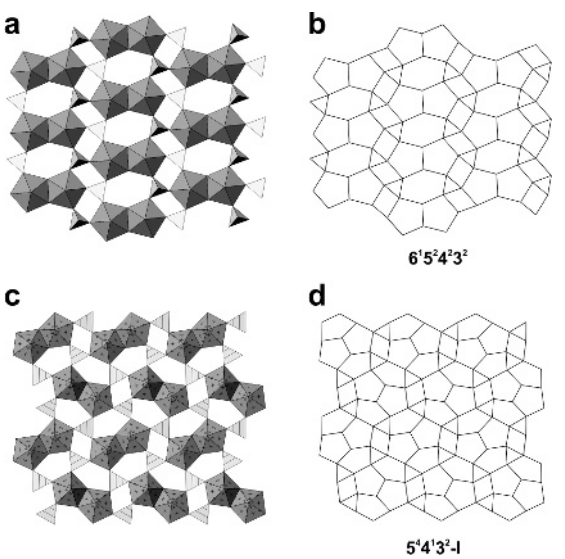

Fig. 28. Sheets of uranyl bipyramids and tetrahedral oxoanions tetrahedra in the structures of johannite (a) and $K[(UO_2)(OH)(CrO_4)](H_2O)_{1.5}$ (c) and their anion topologies (b and d, respectively).

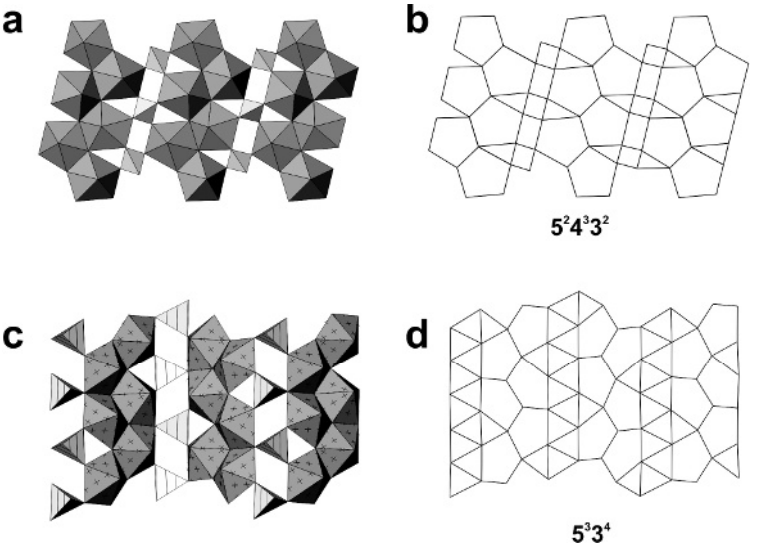

Fig. 29. Sheets of uranyl bipyramids and tetrahedral oxoanions in the structures of zippeite-type compounds (a), and $K_2[(UO_2)_2(MoO_4)O_2]$ (c), and their anion topologies (b and d, respectively).

3.1.5. Structures with sheets containing chains of edge-sharing actinyl polyhedra

Minerals of the zippeite group are amongst the most important compounds that form in oxidation zones of uranium mineral deposits [113]. Their structures are all based upon the uranyl sulfate sheet shown in Fig. 29a. Within the sheet, each uranyl pentagonal bipyramid is linked to two others by sharing equatorial edges, and to two additional pentagonal bipyramids by sharing equatorial vertices only, resulting in a chain of uranyl pentagonal bipyramids that is two polyhedra wide. Each uranyl pentagonal bipyramid shares three of its equatorial ligands within the chain; the remaining two are linked to SO_4 tetrahedra that cross-link the chains [113]. All sulfate tetrahedra are tetradentate, bridging between four U centers. The uranyl sulfate sheets in the structures of zippeite-group phases have a variety of compositions due to different patterns of $O^{2-} \leftrightarrow OH^-$ substitutions at the anion sites that are shared between three uranyl pentagonal bipyramids (Table 4).

The uranyl molybdate sheets in the structure of $K_2[(UO_2)_2(MoO_4)O_2]$ (Fig. 29c, d) are structurally related to the uranyl sulfate sheets in the compounds of the zippeite group. However, the chain of uranyl pentagonal bipyramids has a different topology. Whereas in the zippeite-type sheet each uranyl bipyramid shares two equatorial edges with other bipyramids, in $K_2[(UO_2)_2(MoO_4)O_2]$ one bipyramid shares two edges, whereas two others

share three. All sulfate tetrahedra are tridentate instead of tetradentate (as in zippeites).

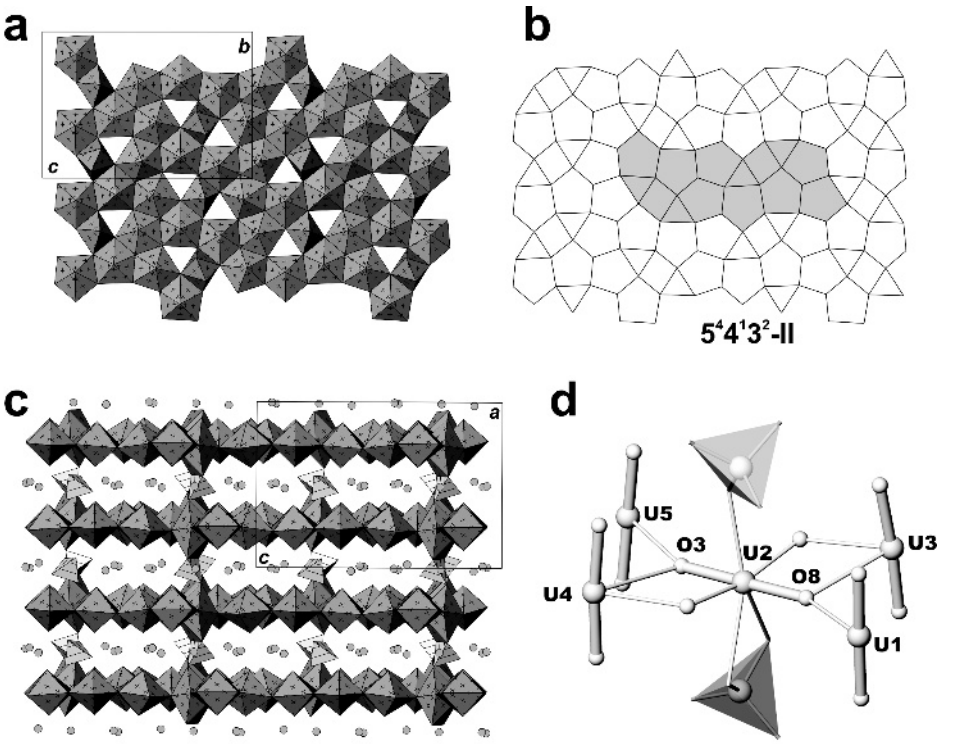

Fig. 30. Sheet of uranyl coordination polyhedra (cross-hatched) in the structure of $(K,Na)Na_3[(UO_2)_5O_6(SO_4)]$ (a) and its anion topology (b). Projection of the structure along the *b* axis (c; sulfate tetrahedra are lined) and local coordination of the $[U(2)O_2]^{2+}$ uranyl cation.

3.1.6. Structures with sheets of actinyl polyhedra linked by sulfate tetrahedra

The structure of $(K,Na)Na_3[(UO_2)_5O_6(SO_4)]$ contains sheets of edge-sharing UO_7 pentagonal bipyramids (Fig. 30a). Four out of five uranyl pentagonal bipyramids have their uranyl cations oriented approximately perpendicular to the plane of the sheet, whereas one has its uranyl cation lying within the sheet. This uranyl cation interacts with four others in the manner shown in Fig. 30d. In addition, this uranyl cation shares two equatorial anions with a sulfate tetrahedron. Each sulfate group shares an edge with the UO_7 bipyramid from one sheet and a corner with the UO_7 bipyramid from another sheet, thus providing their linkage into a 3D framework (Fig. 30c).

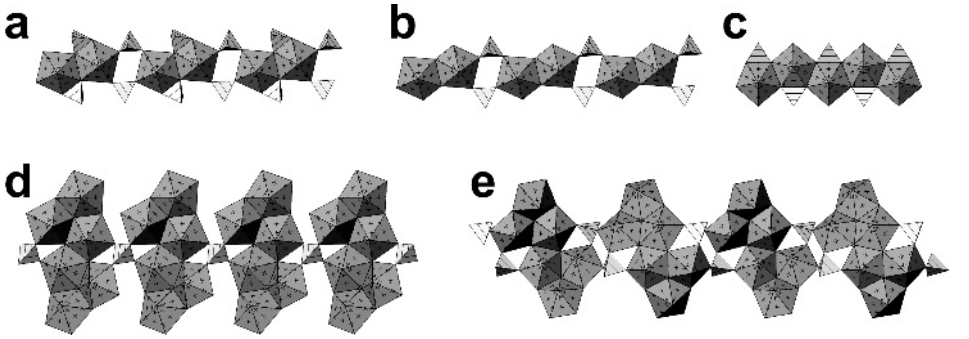

Fig. 31. Chains with edge-sharing actinyl polyhedra: (a) chain from the structure of $Cs_3[NpO_2(SO_4)_2](H_2O)_2$; (b) chain observed in $K_2[(UO_2)F_2(SO_4)](H_2O)$ and $[N_2C_6H_{16}][UO_2F_2(SO_4)]$; (c) chain in $Cs[NpO_2(CrO_4)](H_2O)_2$; (d) uranopilite chain; (e) chain found in $Ca[(UO_2)_6(SO_4)_2O_2(OH)_6(H_2O)_4](H_2O)_8$.

3.2. Structures based upon chains with edge-sharing actinyl polyhedra (anion-topology derivatives)

Crystallographic data for compounds based upon chains with edge-sharing actinyl polyhedra are given in Table 5. The structural diagrams of the chains are given in Fig. 31. In the structure of $Cs_3[NpO_2(SO_4)_2](H_2O)_2$, NpO_7 pentagonal bipyramids share edges to form dimers. The dimers are interlinked by sulfate tetrahedra into infinite chains (Fig. 31a). In addition, each Np bipyramid shares an edge with another SO_4 tetrahedron. Fig. 31b shows a chain that is similar to that given in Fig. 31a but that has no additional edge-sharing sulfate tetrahedra. This chain has been observed in the structures of $K_2[(UO_2)F_2(SO_4)](H_2O)$ and $[N_2C_6H_{16}][UO_2F_2(SO_4)]$. In the structure of $Cs[NpO_2(CrO_4)](H_2O)_2$, NpO_7 pentagonal bipyramids share edges to form infinite chains. The chains are incrustated by chromate tetrahedra that share edges with the Np bipyramids (Fig. 31c). The structures of uranopilite, $[(UO_2)_6(SO_4)O_2(OH)_6(H_2O)_6](H_2O)_8$, and the new natural compound $Ca[(UO_2)_6(SO_4)_2O_2(OH)_6(H_2O)_4](H_2O)_8$ are based upon hexamers of uranyl polyhedra cross-linked by sulfate tetrahedra. The chains of these two compounds differ in the mode of linkage of the adjacent hexamers. In the uranopilite chain (Fig. 31d), sulfate tetrahedra are tetradentate, whereas, in the Ca compound, they are tridentate (Fig. 31e). The U:S ratio is 6:1 for uranopilite and 3:1 for the Ca compound.

Table 5. Crystallographic data for actinyl compounds based upon chains with edge-sharing actinyl polyhedra

Chemical formula	sp. gr.	*a* [Å] / α [°]	*b* [Å] / β [°]	*c* [Å] / γ [°]	ref
$Cs_3[NpO_2(SO_4)_2](H_2O)_2$	$P\bar{1}$	7.522 / 87.31	9.954 / 82.24	10.710 / 70.40	124
$[N_2C_6H_{16}][UO_2F_2(SO_4)]$ USFO-2	$P\bar{1}$	6.911 / 72.66	9.661 / 87.07	10.103 / 77.96	119
$K_2[(UO_2)F_2(SO_4)](H_2O)$	$P2_1/c$	9.263 / 90	8.672 / 101.60	11.020 / 90	125
$Cs[NpO_2(CrO_4)](H_2O)_2$	*Pnma*	7.359 / 90	7.523 / 90	15.457 / 90	126
$[(UO_2)_6(SO_4)O_2(OH)_6(H_2O)_6](H_2O)_8$ uranopilite	$P\bar{1}$	8.896 / 96.61	14.029 / 98.47	14.339 / 99.80	127
$Ca[(UO_2)_6(SO_4)_2O_2(OH)_6(H_2O)_4](H_2O)_8$	$P2_1/c$	11.931 / 90	14.246 / 102.77	20.873 / 90	128

3.3. Structural units with corner-sharing between uranyl polyhedra and TO_4 tetrahedra (T = S, Cr, Se, Mo)

3.3.1. Graphical approach to complex topologies

The sheet anion topology approach works well for most sheets that are dominated by the sharing of edges between polyhedra containing cations of higher bond-valence. However, for a number of sheets connected only by sharing corners between polyhedra, this approach has only restricted application because of the high degree of flexibility observed for this sheets. To analyse topological structures and relationships within sheets dominated by corner sharing, Krivovichev and Burns [170] developed a graphical approach that was further expanded by Krivovichev [86]. Within this approach, the structure (or a part of it) is represented as a graph with nodes symbolizing coordination polyhedra. Nodes of different colors correspond to geometrically and/or chemically different polyhedra. Two nodes of the graph are linked only if the corresponding polyhedra share at least one common ligand. Fig. 32a and b show a $[(UO_2)(MoO_4)_4]^{6-}$ finite cluster from the structure of $Rb_6[(UO_2)(MoO_4)_4]$ [129]. This unit consists of a UO_6 square bipyramid that shares four equatorial O atoms with four adjacent MoO_4 tetrahedra. Graphically, the topological structure of this unit (connectivity of its polyhedra) may be described by the black-and-white representation shown in Fig. 32c. Here the black vertex symbolizes the U coordination polyhedron, and four white nodes correspond to

four Mo tetrahedra. The central black vertex is linked to white nodes by four single lines: this indicates that the corresponding U polyhedron shares four of its corners with four adjacent Mo tetrahedra, one corner per MoO_4 tetrahedron. Thus, every structural unit based upon different coordination polyhedra is associated with a graph of corresponding complexity. If only two types of polyhedra are present (e.g. octahedra and tetrahedra), one needs two colors (black and white) to distinguish between the two polyhedra types. In the following, we shall use black and white colors to denote AnO_n polyhedra and TO_4 tetrahedra (T = S, Cr, Se, Mo), respectively. To distinguish between graphs with different topologies, we shall use designations introduced in [86]: to each of the graphs described here, we assign a tentative symbol **x**An/Ty, where x is either **i** (island = finite cluster = 0D unit), **c** (chain) or **l** (layer); y is an alphabetic designator used for the graphs with the same An/T ratio.

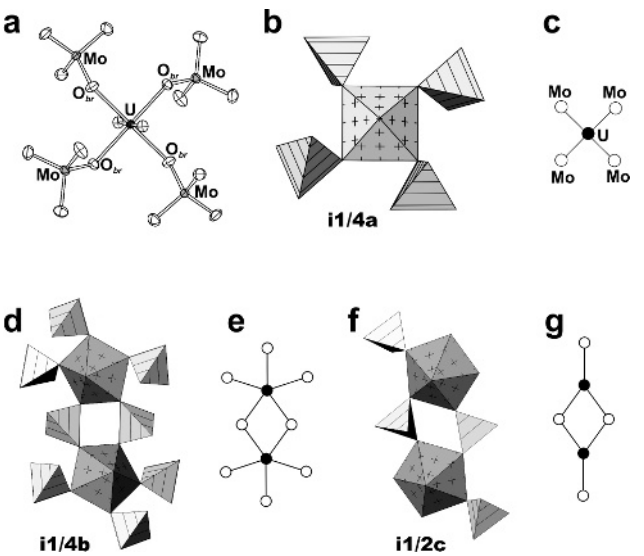

Fig. 32. Finite clusters consisting of AnO_7 pentagonal bipyramids and TO_4 tetrahedra (a, b, d, f) and their graphs (c, e, g).

3.3.2. 0D units (finite clusters)

0D structural units observed in uranyl oxysalts with TO_4 tetrahedra and their black-and-white graphs are given in Fig. 32, and the compounds are listed in Table 6. At present, we are aware of three types of finite clusters with corner sharing between AnO_n and TO_4 polyhedra. Note that the unit $[(UO_2)_2(TO_4)_4(H_2O)_4]^{4-}$ shown in Fig. 32f contains two uranyl pentagonal bipyramids with uranyl cations coordinated by two H_2O molecules in a cis-configuration.

Table 6. Crystallographic data for actinyl compounds based on 0D and 1D structural units with corner-sharing coordination polyhedra

Unit	Chemical formula	sp. gr.	*a* [Å] / α [°]	*b* [Å] / β [°]	*c* [Å] / γ [°]	ref
0D units						
i1/4a	$Rb_6[(UO_2)(MoO_4)_4]$	C*2*/c	17.312 / 90	11.529 127.63	13.916 / 90	129
	$Cs_6[(UO_2)(MoO_4)_4]$	$P\bar{1}$	11.613 102.71	12.545 / 95.28	14.466 106.18	97
	$K_8[(UO_2)(CrO_4)_4](NO_3)_2$	$P\bar{1}$	7.040 / 105.85	9.734 / 97.99	9.757 / 93.27	132
i1/4b	$Na_3Tl_3[(UO_2)(MoO_4)_4]$	*Pbcn*	20.582 / 90	7.439 / 90	26.251 / 90	131
	$Na_6[(UO_2)(MoO_4)_4]$	$P\bar{1}$	7.096 / 73.69	9.566 / 86.62	13.415 / 82.94	130
i1/2c	$[C_3H_{12}N_2][(UO_2)(SeO_4)_2(H_2O)]$	$P\bar{1}$	7.561 / 94.61	7.765 / 94.41	12.925 / 96.47	133
	$[C_3H_{12}N_2]_2[(UO_2)_2(SO_4)_4(H_2O)_4]\,(H_2O)_2$	$P\bar{1}$	7.398 / 95.18	7.633 / 94.64	12.595 / 96.58	134
1D units						
c1/1a	$[(UO_2)(SO_4)(H_2O)_3](18\text{-crown-}6)_{0.5}$	$P2_1/n$	9.314 / 90	9.339 / 103.62	16.734 / 90	135
	$UO_2(SO_4)[CH_3CON(C_2H_5)_2]_2\,(H_2O)$	$P2_1/c$	9.459 / 90	17.844 / 95.32	12.397 / 90	145
	$UO_2(OC(NH_2)_2)_3(SO_4)$	$P2_1/n$	7.619 / 90	24.706 / 91.06	6.928 / 90	146
c1/1b	$(UO_2)(CrO_4)(H_2O)_2$	*C*2/*m*	16.786 / 90	22.731 / 90.05	6.997 / 90	136
	$[(UO_2)(CrO_4)(H_2O)_2](H_2O)$	$P2_1$	9.721 / 90	7.162 / 92.39	11.091 / 90	136
	$[(UO_2)(CrO_4)(H_2O)_2]_4(H_2O)_9$	$P2_1/c$	31.397 / 90	7.170 / 97.52	16.248 / 90	136
	$[(UO_2)(CrO_4)(H_2O)_2](H_2O)_{3.5}$	$P2_1/c$	11.179 / 90	7.119 / 94.19	26.490 / 90	137
	α-$(UO_2SO_4)_2(H_2O)_7$	$P2_1ca$	11.227 / 90	6.790 / 90	21.186 / 90	138

Table 6. Crystallographic data for actinyl compounds based on 0D and 1D structural units with corner-sharing coordination polyhedra (continued)

Unit	Chemical formula	sp. gr.	*a* [Å] / α [°]	*b* [Å] / β [°]	*c* [Å] / γ [°]	ref
	$[UO_2SO_4(H_2O)_2](H_2O)$	$P2_1/a$	16.887 / 90	12.492 / 90.88	6.735 / 90	139
	β-$(UO_2SO_4)_2(H_2O)_7$	$C2/c$	13.700 / 90	10.790 /110.80	11.910 / 90	140
	$UO_2SeO_4(H_2O)_4$	$C2/c$	14.653 / 90	10.799 /119.95	12.664 / 90	141
	$[CH_2ClCONH_2][UO_2(SO_4)(H_2O)]$	$P\bar{1}$	6.892 / 104.40	8.786 / 109.71	9.494 / 90.33	142
	$[UO_2(SO_4)(H_2O)]$ (12-crown-4)$_{0.5}(H_2O)$	$P\bar{1}$	7.007 / 91.31	8.041 / 93.60	10.776 /100.18	135
	$[(CH_3)_4N][UO_2(SO_4)(H_2O)]$ Cl	$P2_1$	8.989 / 90	6.877 / 109.77	10.981 / 90	143
	$[N_2C_6H_{18}][(UO_2)_2(H_2O)_3(SO_4)_3]$	$P\bar{1}$	6.823 / 101.37	8.738 / 98.13	19.238 / 90.06	144
	α-$UO_2(SO_4)(CO(NH_2)_2)_2$	$P2_1/c$	6.875 / 90	12.758 / 91.76	11.572 / 90	147 148
	β-$UO_2(SO_4)(CO(NH_2)_2)_2$	$P2_1/c$	6.747 / 90	14.110 /106.53	11.348 / 90	148
	$NpO_2(CrO_4)(OC(NH_2)_2)_2$	$P2_1/n$	7.192 / 90	12.902 / 92.19	11.226 / 90	149
	$UO_2(CrO_4)[CH_3NH CONHCOCH_3](H_2O)$	$P2_1/n$	9.270 / 90	6.953 / 103.52	18.531 / 90	150
	$UO_2(CrO_4)[CH_3CONH_2]_2$	$P2_1/c$	7.172 / 90	13.425 /133.33	15.625 / 90	151
c1/2a-1	$[N_2C_3H_{12}][UO_2(H_2O)(SO_4)_2]$	$P2/c$	7.258 / 90	7.370 / 99.41	11.851 / 90	154
	$[N_2C_4H_{12}][UO_2(H_2O)(SO_4)_2]$	$C2/c$	14.768 / 90	7.659 / 104.84	11.681 / 90	155
	$[N_2C_3H_{12}][UO_2(H_2O)(SO_4)_2]$	$P\bar{1}$	7.330 / 92.03	7.370 / 106.04	11.682 / 93.68	156
	$[N_2C_5H_{14}][UO_2(H_2O)(SO_4)_2]$	$P22_12_1$	7.696 / 90	11.772 / 90	14.704 / 90	153

Table 6. Crystallographic data for actinyl compounds based on 0D and 1D structural units with corner-sharing coordination polyhedra (continued)

Unit	Chemical formula	sp. gr.	*a* [Å] / α [°]	*b* [Å] / β [°]	*c* [Å] / γ [°]	ref
	$[C_5H_{14}N_2][UO_2(H_2O)(SO_4)_2]$	$P\bar{1}$	8.003 / 72.70	8.187 / 81.78	10.891 / 78.79	157
	$[N_2C_4H_{14}][UO_2(H_2O)(SO_4)_2]$	$P\bar{1}$	7.420 / 79.12	7.838 / 79.90	12.032 / 83.11	152
	$[N_2C_2H_{10}][UO_2(H_2O)(SO_4)_2]$	*C*2/*c*	15.616 / 90	7.302 / 118.73	11.711 / 90	158 159
	$Mn[UO_2(SO_4)_2(H_2O)](H_2O)_4$	$P2_1$	6.506 / 90	11.368 / 90.79	8.338 / 90	160
	$[C_5H_{14}N_2][(UO_2)(SeO_4)_2(H_2O)]$	*Cc*	14.957 / 90	8.428 / 104.52	11.908 / 90	161
	$[C_5H_{16}N_2]_2[(UO_2)(SeO_4)_2(H_2O)](NO_3)_2$	*C*2/*c*	28.916 / 90	8.084 / 110.91	11.986 / 90	133
	$[C_4H_{12}N_2][(UO_2)(SeO_4)_2(H_2O)]$	*C*2/*c*	15.845 / 90	7.441 / 101.42	12.000 / 90	161
	$[C_4H_{14}N_2][(UO_2)(SeO_4)_2(H_2O)]$	*P*2/*c*	7.941 / 90	8.286 / 106.20	11.303 / 90	161
	$[C_5H_{14}N_2][(UO_2)(SeO_4)_2(H_2O)]$	*Cc*	16.606 / 90	7.413 / 101.30	12.232 / 90	161
	$[C_{10}H_{26}N_2][(UO_2)(SeO_4)_2(H_2O)](H_2SeO_4)_{0.85}(H_2O)_2$	$P\bar{1}$	7.546 / 77.68	14.991 / 85.46	22.379 / 82.72	161
	$[C_3H_{12}N_2][(UO_2)(SeO_4)_2(H_2O)]$	$P\bar{1}$	7.548 / 89.53	7.574 / 79.89	12.174 / 88.02	161
	$Mg[(UO_2)(SeO_4)_2(H_2O)](H_2O)_4$	$P2_1/c$	8.467 / 90	11.631 / 90.96	13.167 / 90	41
	$Zn[(UO_2)(SeO_4)_2(H_2O)](H_2O)_4$	$P2_1/c$	8.449 / 90	11.586 / 92.38	13.240 / 90	41
c1/2a-2	$Li_2[(UO_2)(MoO_4)_2]$	$P\bar{1}$	5.346 / 108.27	5.830 / 100.57	8.265 / 104.12	162
	$Cu_4(UO_2)(MoO_4)_2(OH)_6$ deloryite	*C*2/*m*	19.940 / 90	6.116 / 104.18	5.520 / 90	163 164
c1/2c	$[N_2C_5H_{14}][UO_2(H_2O)(SO_4)_2]$	$P\bar{1}$	10.754 / 88.00	11.430 / 79.66	11.580 / 80.63	155

Table 6. Crystallographic data for actinyl compounds based on 0D and 1D structural units with corner-sharing coordination polyhedra (continued)

Unit	Chemical formula	sp. gr.	*a* [Å] / α [°]	*b* [Å] / β [°]	*c* [Å] / γ [°]	ref
c1/2f	$Rb[UO_2(CrO_4)(IO_3)(H_2O)]$	$P\bar{1}$	7.313 / 88.74	8.056 / 87.07	8.487 / 71.67	165
c1/2g	$[N_4C_6H_{22}][UO_2(H_2O)(SO_4)_2]_2(H_2O)_2$	$P\bar{1}$	6.732 / 72.34	9.298 / 89.14	13.146 / 70.03	169
	$[N_2C_6H_{18}][(UO_2)_2(H_2O)_3(SO_4)_3]$	$P\bar{1}$	6.823 / 101.37	8.738 / 98.13	19.238 / 90.06	144
	$[C_4H_{14}N_2][(UO_2)(SeO_4)_2(H_2O)]$	$P\bar{1}$	6.853 / 99.62	10.537 / 94.45	10.574 /100.52	133
	$[C_6H_{16}N_2][(UO_2)(SeO_4)_2(H_2O)]$	$P\bar{1}$	6.989 / 81.07	10.851 / 77.46	11.298 / 87.41	161
c1/3b	$Na_{13-x}Tl_{3+x}[(UO_2)(MoO_4)_3]_4(H_2O)_{6+x}$	$P2/c$	19.794 / 90	7.191 / 97.83	22.884 / 90	131
	$Na_3Tl_5[(UO_2)(MoO_4)_3]_2(H_2O)_3$	$P2_12_12_1$	10.766 / 90	11.962	12.900 / 90	131
	$Na_4[(UO_2)(CrO_4)_3]$	$P\bar{1}$	7.155 / 80.20	8.442 / 79.31	11.510 / 70.42	166
	$K_5[(UO_2)(CrO_4)_3](NO_3)(H_2O)_3$	$P2_12_12_1$	6.111 / 90	12.136 / 90	27.464 / 90	132
	$[C_2H_8N]_3[(UO_2)(SeO_4)_2(HSeO_4)]$	$P2_1/c$	12.746 / 90	12.426 /113.43	14.993 / 90	161
c1/3c	$Cs_2[(UO_2)(CrO_4)(IO_3)_2]$	$P2_1/n$	7.393 / 90	8.135 / 90.65	22.126 / 90	167
	$K_2[(UO_2)(CrO_4)(IO_3)_2]$	$P2_1/c$	11.133 / 90	7.288 / 107.98	15.566 / 90	165
	$Rb_2[(UO_2)(CrO_4)(IO_3)_2]$	$P2_1/c$	11.346 / 90	7.326 / 108.17	15.933 / 90	165

3.3.3. 1D units (chains)

1D structural units observed in uranyl oxysalts with TO_4 tetrahedra and their black-and-white graphs are given in Fig. 33, and the compounds are listed in Table 6. The $[AnO_2(TO_4)(H_2O)_2]$ chain that corresponds to the **c1/1b** graph is of special interest. Within the chain (Fig. 34a), the $AnO_5(H_2O)_2$ pentagonal bipyramids share three equatorial O atoms with TO_4 tetrahedra, whereas TO_4

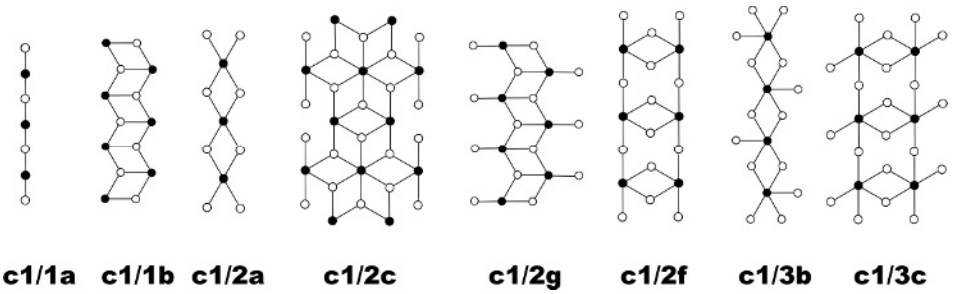

Fig. 33. Black-and-white graphs describing topological structure of 1D chains in structures with corner sharing between actinyl polyhedra and TO_4 tetrahedra.

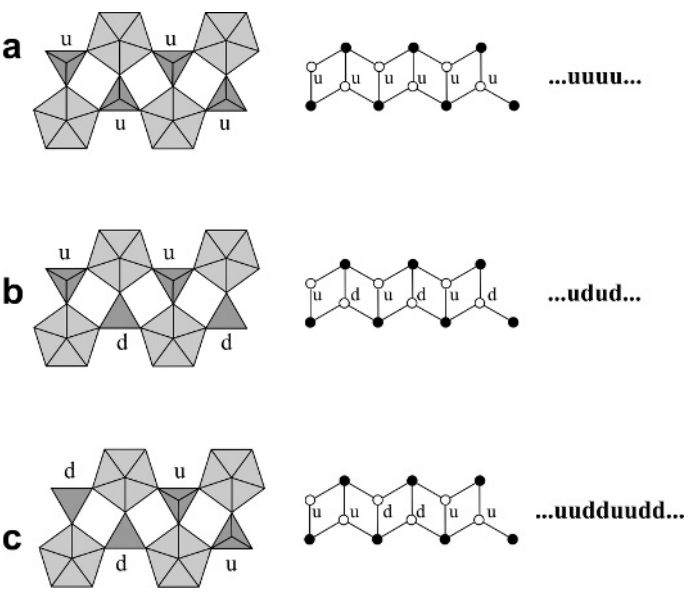

Fig. 34. To the description of geometrical isomerism of $[AnO_2(TO_4)(H_2O)_2]$ chains that correspond to the **c1/1b** graph. See text for details.

tetrahedra have three vertices each that are shared with actinyl pentagonal bipyramids and one apical ligand that points either up (**u**) or down (**d**) relative to the plane of the chain. In different structures, the orientations of apical ligands along the chain extension may be different. For example, in the structures of $[UO_2(CrO_4)(H_2O)_2]$ and $[UO_2(CrO_4)(H_2O)_2](H_2O)$, the orientations alternate in the order "...up-down-up-down..." or ...**udud**... [or $(\mathbf{ud})_\infty$] (Fig. 34b). In contrast, the structure of $[UO_2(CrO_4)(H_2O)_2]_4(H_2O)_9$ contains two types of chains: one with the sequence ...**ududud**... [=$(\mathbf{ud})_\infty$] and one with the sequence ...**uuuu**... = $(\mathbf{u})_\infty$ with the non-shared corners of chromate tetrahedra on one side

of the chain only (Fig. 34a). The structure of β-$[UO_2(SO_4)(H_2O)_2](H_2O)_3$ contains chains with the sequence ...**uudduudd**... or $(\mathbf{uudd})_\infty$. We note that, despite different orientations of tetrahedra, the three chains shown in Fig. 34 correspond to the **c1/1b** graph. The three chains are geometrical isomers accounting to the terminology introduced by Moore [171] (see also [172]). In general, geometrical isomers are polyhedral units that have the same graph but are topologically different due to some specific properties of polyhedral linkage (e.g. cis-trans-isomerism). It is likely that the occurence of a certain type of isomer is impacted by the specificity of interactions of polyhedral units with each other and with other structural elements. Fig. 35 shows structures of four uranyl chromate hydrates with the general composition $[UO_2(CrO_4)(H_2O)_2](H_2O)_n$ projected along the chain extension [n = 0 (a), 1 (c), 2.25 (b), and 3.5 (d)]. In all four structures, the $(\mathbf{ud})_\infty$ isomers are present, but, in the structure with n = 2.25, the $(\mathbf{u})_\infty$ are present as well. Apparently, the occurence of isomers is somehow related to the number of water molecules present in the structure, i.e. to features of the hydrogen bond system.

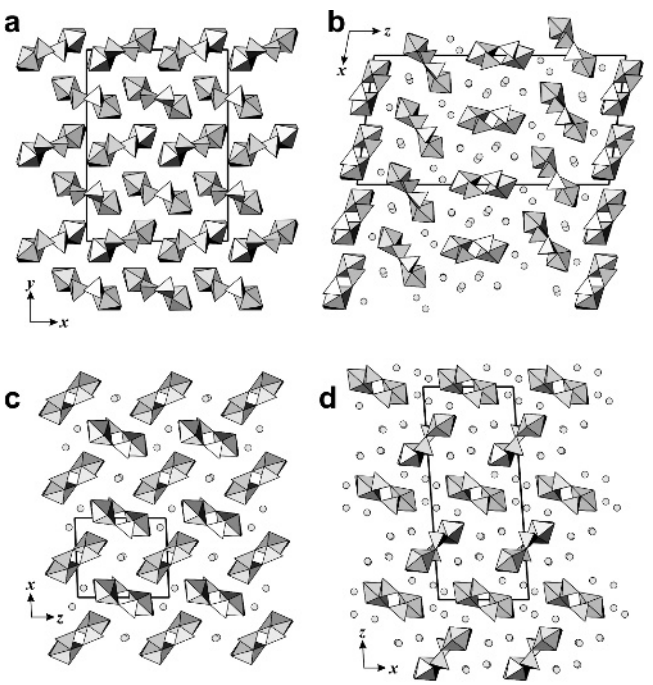

Fig. 35. Structures of four uranyl chromate hydrates with the general composition $[UO_2(CrO_4)(H_2O)_2](H_2O)_n$ projected along the chain extension [n = 0 (a), 1 (c), 2.25 (b), and 3.5 (d)].

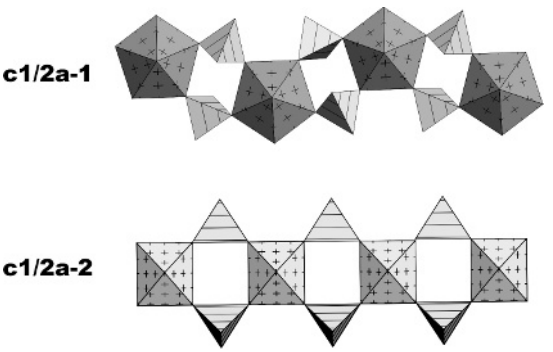

Fig. 36. Two types of the **c1/2a** chains.

The **c1/2a** graph (Fig. 33) corresponds to two chemically different chains shown in Fig. 36. One chain (Fig. 36a) consists of $AnO_6(H_2O)$ pentagonal bipyramids and TO_4 tetrahedra, whereas another one (Fig. 36b) is built by corner sharing between AnO_6 square bipyramids and TO_4 tetrahedra.

The remarkable class of 1D structural units with corner-sharing actinyl polyhedra and TO_4 tetrahedra are uranyl selenate nanotubules that have recently been described by Krivovichev et al. [173, 174]. They will be considered in detail in Chapter 11.

3.3.4. 2D units (sheets)

The concept of a basic graph. We define the connectedness, **s**, of a polyhedron as the number of adjacent polyhedra with which it shares common corners. Fig. 37a shows a $[(UO_2)_3(CrO_4)_5]^{4-}$ sheet observed in the structure of $Mg_2[(UO_2)_3(CrO_4)_5](H_2O)_{17}$ [210]. Its black-and-white graph (Fig. 37b) is (5;3)-connected (black and white nodes are linked to five and three adjacent nodes each, respectively). The idealized version of this graph is shown in Fig. 37d. This graph can be obtained from the more complete graph shown in Fig. 37c by deleting some of its white nodes and all edges associated with them. The graph shown in Fig. 37c is very regular: it consists of six-connected black and three-connected white nodes [and therefore it is (6;3)-connected]. The elementary unit of this graph is a rhomb that contains two black and two white nodes. The **s** values of the nodes of the rhomb written in the cyclic order are 3-6-3-6. Consequently, this graph is denoted {3.6.3.6}. As shown by Krivovichev [86], the {3.6.3.6} graph is a basic graph, which means that it is parent to a number of other graphs corresponding to the sheets of coordination polyhedra observed in the salts of inorganic oxoacids. The black-and-white graphs of these sheets can be obtained from the {3.6.3.6} graph by simply deleting an edge or a vertex together with all of its associated edges. There are several other basic graphs in the salts of inorganic oxoacids that are discussed in more details in [86].

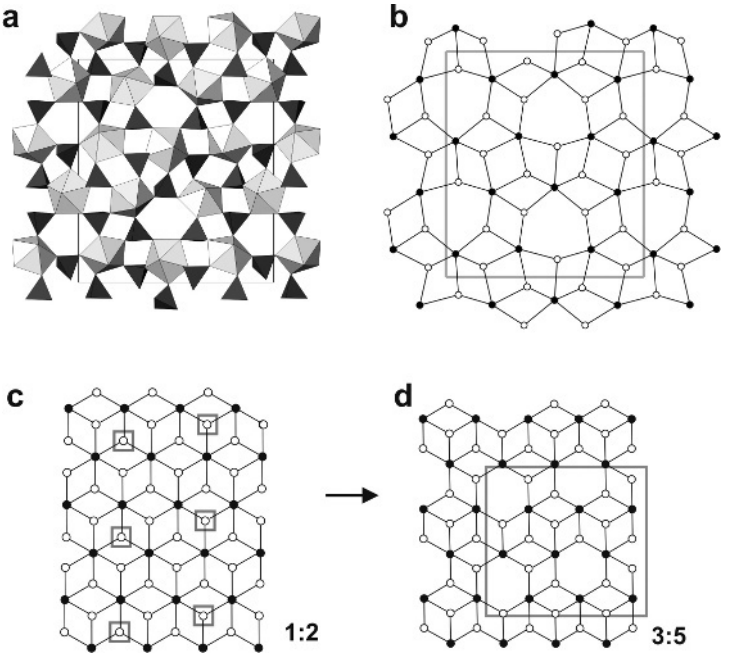

Fig. 37. (a) $[(UO_2)_3(CrO_4)_5]^{4-}$ sheet observed in the structure of $Mg_2[(UO_2)_3(CrO_4)_5](H_2O)_{17}$; (b) its black-and-white graph (legend as in Fig. 1c); (c) the {**3.6.3.6**} graph; (d) an idealized version of the graph shown in (b). The graph in (d) can be obtained from the graph in (c) by eliminating marked white nodes and all links incident upon them.

The {3.6.3.6} derivatives with An:T = 1:2. There are 7 {3.6.3.6}-derivative graphs that are underlying topologies of heteropolyhedral units in actinyl oxosalts with $T^{6+}O_4$ tetrahedra. A catalogue of these graphs is shown in Fig. 38, and the list of corresponding compounds is given in Table 7. Note that the {3.6.3.6} graph itself (denoted as **l1/2a**) has not been observed for actinyl compounds, probably because it requires 6-connectedness of the black corners, i.e. hexagonal bipyramidal coordination for actinide cations. This type of coordination is not favored in inorganic oxosalts (except carbonates and nitrates) because the pentagonal coordination of actinyl cations has more advantages in terms of anion packing and bond-valence distributions. The simplest {3.6.3.6} derivative is the **l1/2b** graph that consists of 4-connected black and 2-connected white vertices (Fig. 38). This graph corresponds to a large number of sheet topologies with the composition $[AnO_2(SO_4)_2(H_2O)]$. It is noteworthy that, in this group of layered structures, an interesting type of geometrical isomerism is observed [185]. Figs. 39a and b show polyhedral diagrams of the $[UO_2(SeO_4)_2(H_2O)]^{2-}$ sheets observed in the structures of $[C_2H_{10}N_2][(UO_2)(SeO_4)_2(H_2O)](H_2O)$ and $[CH_6N_3]_2[(UO_2)(SeO_4)_2(H_2O)](H_2O)_{1.5}$, respectively. The black-and-white graphs of these sheets are shown in

Table 7. Crystallographic data for actinyl compounds based on 2D structural units with corner-sharing coordination polyhedra and U:T = 1:2

Unit	Chemical formula	sp. gr.	*a* [Å] / α [°]	*b* [Å] / β [°]	*c* [Å] / γ [°]	ref
l1/2b	$K_2[UO_2(SO_4)_2(H_2O)](H_2O)$	*Pnma*	13.806 / 90	11.577 / 90	7.292 / 90	175
	$Mg[UO_2(SO_4)_2(H_2O)](H_2O)_{10}$	*C*2/*c*	11.334 / 90	7.715 / 102.22	21.709 / 90	176
	$[UO_2(SO_4)(H_2SO_4)(H_2O)](H_2O)_4$	*C*2/*c*	11.008 / 90	8.242 / 113.71	15.619 / 90	177
	$[N_5C_8H_{28}]_2[(UO_2)_5(H_2O)_5(SO_4)_{10}](H_2O)$	*Pbnm*	7.764 / 90	14.169 / 90	56.469 / 90	169
	$[C(NH_2)_3]_2[UO_2(SO_4)_2(H_2O)](H_2O)_2$	*C*2/*c*	11.220 / 90	8.027 / 101.00	18.681 / 90	178
	$[CN_4H_7]_2[UO_2(SO_4)_2(H_2O)]$	*C*2/*c*	11.297 / 90	7.834 / 100.18	17.984 / 90	179
	$Cs_2[UO_2(SeO_4)_2(H_2O)](H_2O)$	$Pna2_1$	14.367 / 90	11.682 / 90	7.826 / 90	181
	$Rb_2[(UO_2)(SeO_4)_2(H_2O)](H_2O)$	$Pna2_1$	13.677 / 90	11.870 / 90	7.640 / 90	182
	$(NH_4)_2[(UO_2)(SeO_4)_2(H_2O)](H_2O)$	$P2_12_12_1$	8.204 / 90	11.631 / 90	14.028 / 90	183
	$[Co(NH_3)_6][NpO_2(SeO_4)_2(H_2O)](H_2O)_2$	*C*2/*c*	11.739 / 90	8.607 / 104.67	16.871 / 90	180
	$[C_2N_2H_{10}][UO_2(SeO_4)_2(H_2O)](H_2O)$	*C*2/*c*	11.787 / 90	7.701 / 102.02	16.600 / 90	184
	$[C_8H_{20}N]_2[(UO_2)(SeO_4)_2(H_2O)](H_2O)$	$P\ \bar{1}$	7.498 / 89.69	11.897 / 90.05	32.056 / 88.80	184
	$[C_6H_{16}N_3]_2[(UO_2)(SeO_4)_2(H_2O)]$	*Cc*	11.733 / 90	8.117 / 92.54	16.152 / 90	184
	$[C_4H_{14}N_2][(UO_2)(SeO_4)_2(H_2O)]$	$P112_1/n$	7.590 / 90	11.929 / 90	16.852 / 90	184
	$[C_4H_{12}N_2][(UO_2)(SeO_4)_2(H_2O)]$	*C*2/*c*	15.845 / 90	7.441 / 101.42	12.000 / 90	184
	$[C_8H_{26}N_4][(UO_2)(SeO_4)_2(H_2O)](H_2O)$	$P2_1/n$	7.820 / 90	16.516 / 90.66	11.683 / 90	184

Table 7. Crystallographic data for actinyl compounds based on 2D structural units with corner-sharing coordination polyhedra and U:T = 1:2 (continued)

Unit	Chemical formula	sp. gr.	*a* [Å] / α [°]	*b* [Å] / β [°]	*c* [Å] / γ [°]	ref
	$(H_3O)[C_3H_5N_2][(UO_2)(SeO_4)_2(H_2O)]$	*Imm*2	11.787 3 / 90	16.2520 / 90	7.938 / 90	184
	$[CH_6N_3]_2[(UO_2)(SeO_4)_2(H_2O)](H_2O)_{1.5}$	*C*2/*c*	37.314 / 90	7.177 / 109.27	13.205 / 90	185
l1/2c	$(NH_4)_2UO_2(SO_4)_2(H_2O)_2$	$P2_1/c$	7.783 / 90	7.403 / 102.25	20.918 / 90	186
	$[N_2C_6H_{14}][UO_2(H_2O)(SO_4)_2]$	$P2_1/n$	8.648 / 90	7.714 / 90.73	21.255 / 90	155
	$[C_5H_{14}N_2]_2[(UO_2)(SeO_4)_2(H_2O)]_2(H_2O)$	$P2_12_12_1$	7.547 / 90	17.303 / 90	23.907 / 90	184
	$[C_4H_{12}N]_2[(UO_2)(SeO_4)_2(H_2O)]$	$P\bar{1}$	7.372 / 79.89	14.066 / 79.93	20.974 / 75.30	184
l1/2d	$K_2[(UO_2)(MoO_4)_2]$	$P2_1/c$	12.269 / 90	13.468 / 95.10	12.857 / 90	189
	$Rb_2[(UO_2)(MoO_4)_2]$	$P2_1/c$	12.302 / 90	13.638 / 94.98	13.509 / 90	129
	$Cs_2[(UO_2)(MoO_4)_2]$	*Pbca*	11.763 / 90	14.081 / 90	14.323 / 90	190
	$Tl_2(UO_2)(MoO_4)_2$	$Pca2_1$	10.977 / 90	14.004 / 90	14.041 / 90	194
	$Tl_2(UO_2)(CrO_4)_2$	$Pca2_1$	10.703 / 90	13.425 / 90	13.936 / 90	194
	$Cs_2[(UO_2)(MoO_4)_2](H_2O)$	$P2_1/c$	8.272 / 90	11.067 / 95.63	14.031 / 90	190 191
	$(NH_4)_2[(UO_2)(MoO_4)_2](H_2O)$	$P2_1/c$	7.916 / 90	10.885 / 98.40	13.476 / 90	192
	$Rb_2[(UO_2)(MoO_4)_2](H_2O)$	$P2_1/c$	7.967 / 90	10.956 / 96.69	13.679 / 90	193
	$K_2[(UO_2)(MoO_4)_2](H_2O)$	$P2_1/c$	7.893 / 90	10.907 / 98.70	13.558 / 90	188
	$Na_2[(UO_2)(MoO_4)_2](H_2O)_4$	$P2_1/n$	8.902 / 90	11.515 / 107.74	13.815 / 90	131

Table 7. Crystallographic data for actinyl compounds based on 2D structural units with corner-sharing coordination polyhedra and U:T = 1:2 (continued)

Unit	Chemical formula	sp. gr.	*a* [Å] / α [°]	*b* [Å] / β [°]	*c* [Å] / γ [°]	ref
	$(C_5H_{14}N_2)[(UO_2)(MoO_4)_2](H_2O)$	*Pbca*	12.697 / 90	13.247 / 90	17.793 / 90	110
	$(C_2H_{10}N_2)[(UO_2)(MoO_4)_2]$	$P\bar{1}$	8.400 / 86.11	11.260 / 86.43	13.124 / 76.54	170
	$(H_5O_2)_2[(UO_2)(SeO_4)_2]$	$P2_1/n$	8.311 / 90	11.080 / 103.88	13.227 / 90	184
	$[C_{12}N_2H_{30}][(UO_2)(SeO_4)_2](H_2O)_x$	$C2/c$	33.805 / 90	13.242 / 92.53	11.256 / 90	184
	$[C_{10}H_{26}N_2][(UO_2)(SeO_4)_2](H_2SeO_4)_{0.50}(H_2O)$	$C2/c$	29.280 / 90	13.301 / 93.30	11.451 / 90	184
	$[CH_6N_3]_3[(UO_2)_2(SeO_4)_3(HSeO_4)](H_2O)_2$	$P2_12_12_1$	10.726 / 90	13.918 / 90	18.321 / 90	185
	$[C_5H_{14}N][(UO_2)(SeO_4)(SeO_2OH)]$	$P2_1/n$	11.553 / 90	10.644 / 108.04	12.138 / 90	196
	$[C_4H_{10}NO][(UO_2)(SeO_4)(HSeO_4)]$	$P2_1/n$	9.635 / 90	13.508 / 111.43	10.945 / 90	197
	$Na_2[UO_2(SeO_4)_2](H_2O)_4$	$P2_1/c$	8.650 / 90	11.003 / 108.08	13.879 / 90	198
l1/2e	$K_3[(NpO_2)(MoO_4)_2]$	$P\bar{1}$	7.363 / 91.40	7.885 / 94.30	10.287 /109.24	195
	$Na_2[(UO_2)(MoO_4)_2]$	$P2_12_12_1$	7.230 / 90	11.324 / 90	12.013 / 90	188
	$K_4(H_5O_2)(NpO_2)[(NpO_2)_2(MoO_4)_4](H_2O)_4$	$P\bar{1}$	7.305 / 68.77	8.676 / 73.15	12.345 / 85.02	199
	$(C_4H_{12}N_2)[(UO_2)(MoO_4)_2]$	$P\bar{1}$	7.096 / 97.01	8.388 / 96.45	11.634 /110.46	110
l1/2g	$Mg(UO_2)_3(MoO_4)_4(H_2O)_8$	$Cmc2_1$	17.105 / 90	13.786 / 90	10.908 / 90	200
	$Zn(UO_2)_3(MoO_4)_4(H_2O)_8$	$Cmc2_1$	17.056 / 90	13.786 / 90	10.919 / 90	200
	$(NH_4)_2[(UO_2)_6(MoO_4)_7(H_2O)_2]$	Pbcm	13.970 / 90	10.747 / 90	25.607 / 90	201

Table 7. Crystallographic data for actinyl compounds based on 2D structural units with corner-sharing coordination polyhedra and U:T = 1:2 (continued)

Unit	Chemical formula	sp. gr.	*a* [Å] / α [°]	*b* [Å] / β [°]	*c* [Å] / γ [°]	ref
	$Cs_2[(UO_2)_6(MoO_4)_7(H_2O)_2]$	*Pbcm*	13.990 / 90	10.808 / 90	25.671 / 90	201
	$Rb_2[(UO_2)_6(MoO_4)_7(H_2O)_2]$	*Pbcm*	13.961 / 90	10.7515 / 90	25.579 / 90	129
l1/2l	$[N_3C_6H_{18}][(UO_2)_2(H_2O)(SO_4)_3(HSO_4)](H_2O)_{4.5}$	$P2_1/a$	15.767 / 90	10.581 / 99.92	16.771 / 90	187
l1/2m	$(H_3O)_2[C_{12}H_{30}N_2]_3[(UO_2)_4(SeO_4)_8](H_2O)_5$	$P2_1/n$	11.344 / 90	24.804 / 96.70	29.250 / 90	202

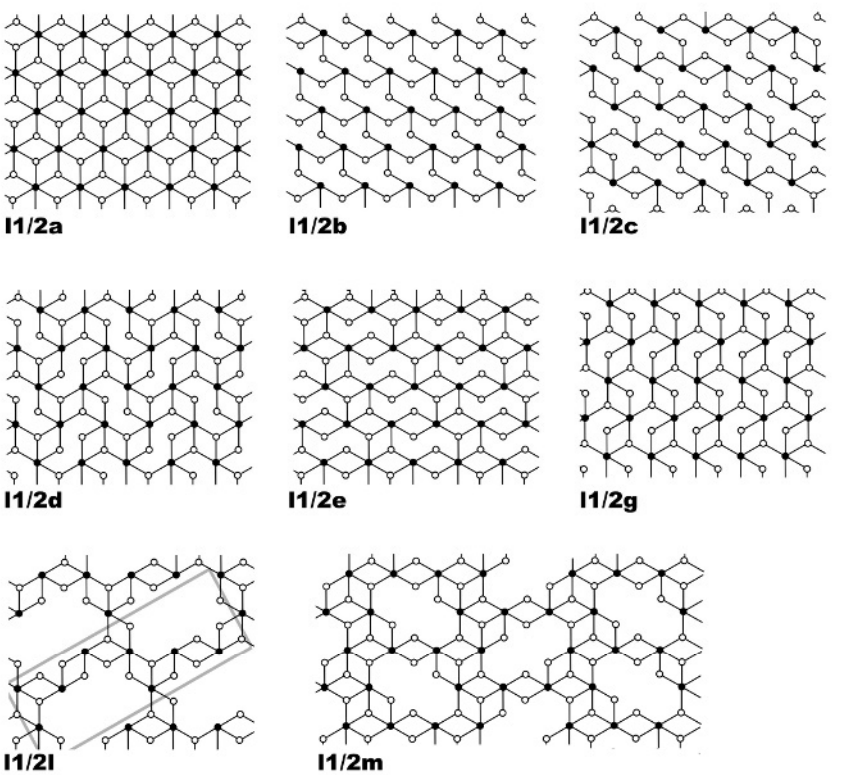

Fig. 38. Black-and-white 2D graphs derivative from the {**3.6.3.6**} graph. Graphs with black:white ratio of 1:2.

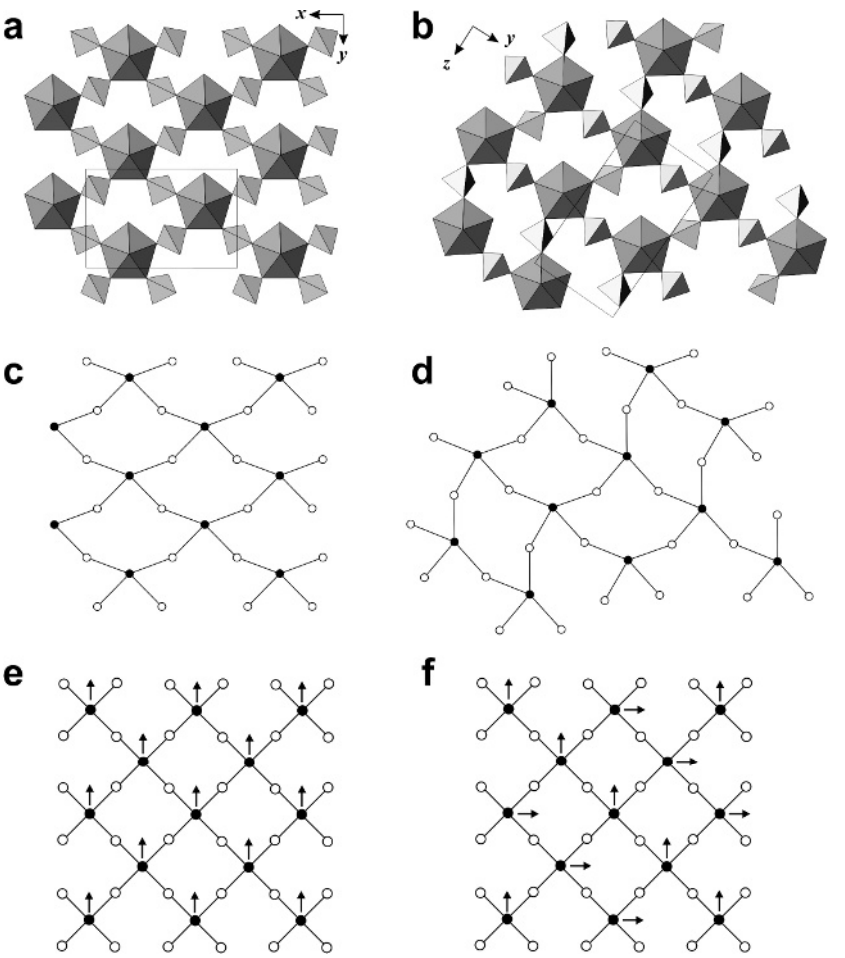

Fig. 39. The $[(UO_2)(SeO_4)_2(H_2O)]^{2-}$ sheets from the structures of $[C_2H_{10}N_2][(UO_2)(SeO_4)_2(H_2O)](H_2O)$ (a) and $[CH_6N_3]_2[(UO_2)(SeO_4)_2(H_2O)](H_2O)_{1.5}$ (b). Black-and-white graph showing the topological connectivity of the U and Se polyhedra (symbolized by black and white vertices, respectively) (c and d, respectively) and idealized graphs with the arrows symbolizing the $U \rightarrow H_2O$ vectors (e and f, respectively).

Fig. 39c and d, respectively. The graphs are topologically the same and can be transformed one into the other by continuous topological transformation without breaking the edges. However, detailed topological analysis reveals that the $[(UO_2)(SeO_4)_2(H_2O)]^{2-}$ sheets are different because of the different positions of the H_2O molecules of the $[UO_6(H_2O)]^{6-}$ bipyramids. The difference can be visualized by adding the $U \rightarrow H_2O$ vectors to the black-and-white graphs. The idealized versions of the graphs with the $U \rightarrow H_2O$ vectors are shown in Fig. 39e and f, respectively. It is clear that the $U \rightarrow H_2O$ vectors in the structure of

$[C_2H_{10}N_2][(UO_2)(SeO_4)_2(H_2O)](H_2O)$ are all pointing in the same direction, whereas, in the structure of $[CH_6N_3]_2[(UO_2)(SeO_4)_2(H_2O)](H_2O)_{1.5}$, two systems of U→$H_2O$ vectors can be distingushed. The $[(UO_2)(SeO_4)_2(H_2O)]^{2-}$ sheets shown in Fig. 39 can be described as different geometrical isomers. However, in this case, geometrical isomerism is induced not by different orientation of tetrahedra but by the selective hydration of the uranyl coordination polyhedra.

The **l1/2g** graph deserves special attention as well. It corresponds to the $[(UO_2)(MoO_4)_2]^{2-}$ sheet observed in the structures of $M(UO_2)_3(MoO_4)_4(H_2O)_8$ (M = Mg, Zn) [200] and $M_2[(UO_2)_6(MoO_4)_7(H_2O)_2]$ (M = NH_4, Rb, Cs) [201]. In the structures of $M(UO_2)_3(MoO_4)_4(H_2O)_8$, these sheets are linked by additional $UO_6(H_2O)$ bipyramids, resulting in a framework. In $M_2[(UO_2)_6(MoO_4)_7(H_2O)_2]$, two such sheets are linked together to form double sheets, which are further linked by additional $UO_6(H_2O)$ bipyramids, resulting in a framework (Fig. 40).

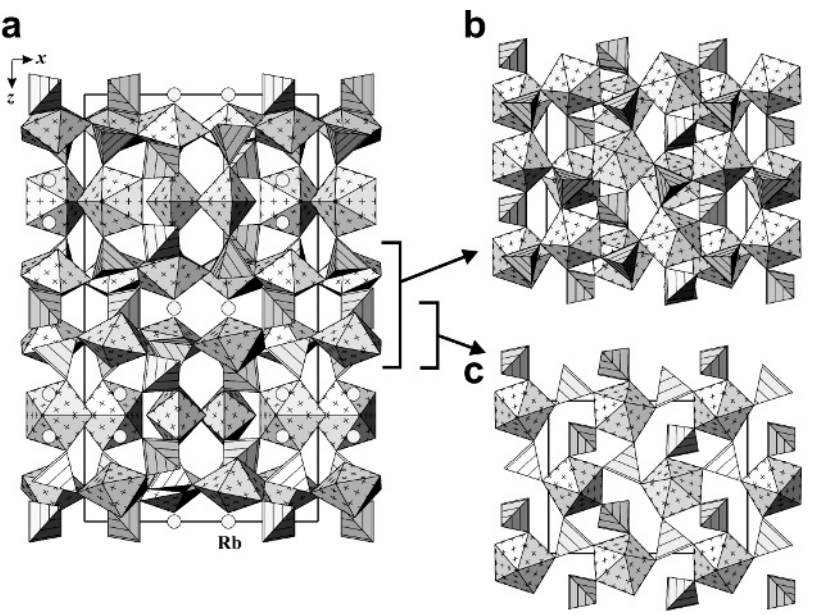

Fig. 40. The structure of $M_2[(UO_2)_6(MoO_4)_7(H_2O)_2]$ (M = NH_4, Rb, Cs) (a) as consisting from double uranyl molybdate sheets (b), and projection of the single sheet (c).

It is noteworthy that the **l1/2b**, **l1/2c**, **l1/2d**, **l1/2e**, and **l1/2g** graphs can be derived from the basic **l1/2a** graph by deleting edges only. In contrast, transition from **l1/2a** to the **l1/2l** and **l1/2m** graphs requires elimination of black and white vertices in the ratio 1:2 in order to mantain the 1:2 ratio of the basic graph.

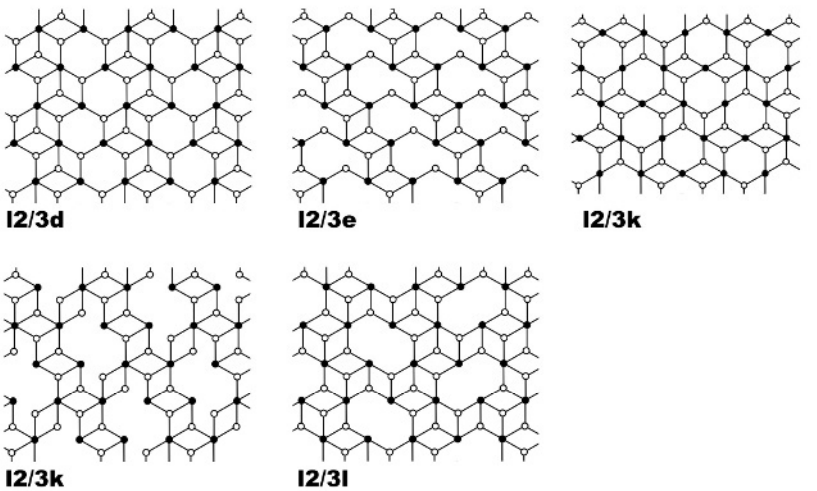

Fig. 41. Black-and-white 2D graphs derivative from the {**3.6.3.6**} graph. Graphs with black:white ratio of 2:3.

The {3.6.3.6} derivatives with An:T = 2:3 (Fig. 41; Table 8). The 2:3 graphs can be obtained from the basic graph by deleting one-fourth of its white corners. This results in the formation of empty hexagonal rings as in the **l2/3d** and **l2/3k** graphs, or more elaborated 8- and 12-membered rings as in the **l2/3e**, **l2/3k**, and **l2/3l** graphs.

Figs. 42a and c show polyhedral diagrams of two sheets of the composition $[(UO_2)_2(SeO_4)_3(H_2O)_2]^{2-}$ observed in the structures of $(H_3O)_2[(UO_2)_2(SeO_4)_3(H_2O)_2](H_2O)_{3.5}$ [205] and $Rb_2[(UO_2)_2(SeO_4)_3(H_2O)_2](H_2O)_4$ [182], respectively. Both sheets correspond to the same **l2/3k** graph. This graph consists of **c1/1b** chains cross-linked by 4-membered rhomb-shaped rings. The sheets shown in Fig. 42a and c differ in the sequence of the orientation of tetrahedra along the **c1/1b** chains. The sequences are $(\mathbf{uudd})_\infty$ for the Rb compound (Fig. 42b) and $(\mathbf{ud})_\infty$ for the oxonium compound. Thus, according to the discussion of geometrical isomerism given above, the uranyl selenate sheets in these compounds should be considered as geometrical isomers.

The {3.6.3.6} derivatives with An:T = 3:5, 5:8, and 4:7. Black-and-white graphs with these characteristic values of the black:white ratio are shown in Fig. 43. Except **l5/8d**, all of these graphs are derived from the {3.6.3.6} graph by simply deleting white vertices and some edges. The **l3/5a** and **l3/5b** graphs differ only in the arrangement of the 6-membered rings. For both of these

Table 8. Crystallographic data for actinyl compounds based on 2D structural units with corner-sharing coordination polyhedra and U:T = 2:3

Unit	Chemical formula	sp. gr.	*a* [Å] / α [°]	*b* [Å] / β [°]	*c* [Å] / γ [°]	ref
l2/3d	$[N_2C_3H_{12}][(UO_2)_2(H_2O)(SO_4)_3]$	$P2_1/n$	10.739 / 90	10.379 / 106.94	18.027 / 90	154
	$[N_2C_4H_{14}][(UO_2)_2(H_2O)(SO_4)_3](H_2O)$	$P2_1/c$	11.246 / 90	10.539 / 92.99	17.043 / 90	153
l2/3e	$K_2[(UO_2)_2(CrO_4)_3(H_2O)_2](H_2O)_4$	$P2_1$/c	10.742 / 90	14.529 / 108.14	14.139 / 90	132
	$(NH_4)_2[(UO_2)_2(CrO_4)_3(H_2O)_2](H_2O)_4$	$P2_1$/c	10.776 / 90	14.765 / 107.97	14.138 / 90	203
l2/3k	$[N_2C_3H_{12}][(NpO_2)_2(CrO_4)_3(H_2O)](H_2O)_3$	$P2_12_12_1$	10.805 / 90	11.238 / 90	17.615 / 90	204
	$K_2[(NpO_2)_2(CrO_4)_3(H_2O)](H_2O)_3$	$P2_1$/c	10.429 / 90	10.797 / 90.61	16.121 / 90	219
	$[C_4H_{10}NO]_2[(UO_2)_2(SeO_4)_3(H_2O)]$	$P2_12_12_1$	12.383 / 90	10.980 / 90	18.066 / 90	197
	$(H_3O)[C_6H_{16}N][(UO_2)_2(SeO_4)_3(H_2O)](H_2O)$	$P2_1$	8.816 / 90	12.446 / 103.70	10.821 / 90	161
	$(H_5O_2)[C_6H_{16}N][(UO_2)_2(SeO_4)_3(H_2O)]$	$P2_1$/c	10.753 / 90	12.322 / 91.05	18.142 / 90	161
	$[C_4H_{12}N](H_3O)[(UO_2)_2(SeO_4)_3(H_2O)]$	$P2_1$/c	10.769 / 90	12.502 / 98.17	15.462 / 90	161
	$[C_6H_{18}N_2][(UO_2)_2(SeO_4)_3(H_2O)]$	$P2_1$	8.402 / 90	12.411 / 102.95	10.923 / 90	161
	$[C_4H_{12}N]_2[(UO_2)_2(SeO_4)_3(H_2O)]$	$P2_1$/c	11.348 / 90	11.385 / 91.87	18.959 / 90	161
	$[C_4H_{14}N_2][(UO_2)_2(SeO_4)_3(H_2O)](H_2O)_2$	$P2_1$/c	11.068 / 90	10.455 / 114.56	20.266 / 90	161
	$[C_3H_{10}N]_2[(UO_2)_2(SeO_4)_3(H_2O)](H_2O)$	$P2_1$/c	11.472 / 90	11.218 / 99.63	18.733 / 90	161
	$[C_7H_{20}N_2][(UO_2)_2(SeO_4)_3(H_2O)]$	$P2_1$	8.710 / 90	12.417 / 101.35	10.884 / 90	161
	$[C_5H_{16}N_2][(UO_2)_2(SeO_4)_3(H_2O)]$	$P2_1$	8.049 / 90	12.263 / 99.92	10.724 / 90	161

Table 8. Crystallographic data for actinyl compounds based on 2D structural units with corner-sharing coordination polyhedra and U:T = 2:3 (continued)

Unit	Chemical formula	sp. gr.	*a* [Å] / α [°]	*b* [Å] / β [°]	*c* [Å] / γ [°]	ref
	$[C_8H_{22}N_2][(UO_2)_2(SeO_4)_3(H_2O)]$	$P2_1$	8.779 / 90	12.487 100.61	10.933 / 90	161
	$[C_5N_2H_{16}][(UO_2)_2(SeO_4)_3(H_2O)](H_2O)$	$P2_1/c$	12.030 / 90	10.785 / 91.87	17.490 / 90	161
l2/3k	$(H_3O)_2[(UO_2)_2(SeO_4)_3(H_2O)_2](H_2O)_{3.5}$	$P2_1/m$	11.940 / 90	13.645 / 109.43	13.727 / 90	205
	$Rb_2[(UO_2)_2(SeO_4)_3(H_2O)_2](H_2O)_4$	$P\bar{1}$	8.426 / 102.61	11.864 / 107.25	13.328 / 102.51	182
l2/3l	$[C_8H_{26}N_4]_{0.5}[(UO_2)_2(SO_4)_3(H_2O)]$	$P2_1/n$	11.840 / 90	10.319 / 107.77	16.592 / 90	206
l2/3m	β-$Cs_2[(UO_2)_2(MoO_4)_3]$	$P4_2/n$	10.137 / 90	10.137 / 90	16.283 / 90	216
	$Cs_2[(UO_2)_2(SO_4)_3]$	$P\bar{4}2_1m$	9.620 / 90	9.620 / 90	8.130 / 90	217
	$[(NpO_2)_2(SO_4)_2(H_2SO_4)](H_2O)_4$	$P2_12_12$	9.474 / 90	10.065 / 90	8.409 / 90	177
	$[N_2C_3H_5]_2[(UO_2)_2(SO_4)_3]$	$P2_12_12_1$	9.768 / 90	10.025 / 90	19.914 / 90	156
	$(H_3O)[C_3H_5N_2][(UO_2)_2(SeO_4)_3]$	$P\bar{4}2_1m$	10.177 / 90	10.177 / 90	9.969 / 90	161
l3/5a	$[C_3N_2H_{12}](H_3O)_2[(UO_2)_3(MoO_4)_5]$	Pbnm	10.465 / 90	16.395 / 90	20.241 / 90	110
	$Na_6[(Np^{5+}O_2)_2(Np^{6+}O_2)(MoO_4)_5](H_2O)_{13}$	*Pnma*	16.893 / 90	19.832 / 90	11.049 / 90	207
	α-$Mg_2[(UO_2)_3(SeO_4)_5](H_2O)_{16}$	$C2/c$	19.544 / 90	10.478 / 91.35	18.020 / 90	208
	$Co_2[(UO_2)_3(SeO_4)_5](H_2O)_{16}$	$P\bar{1}$	10.458 / 89.45	11.032 / 90.28	17.893 / 61.76	209
	$Zn_2[(UO_2)_3(SeO_4)_5](H_2O)_{16}$	$P\bar{1}$	10.438 / 89.19	11.063 / 89.85	17.895 / 61.72	209
l3/5b	$K_4[(UO_2)_3(CrO_4)_5](H_2O)_8$	$P2_1/c$	8.234 / 90	18.804 / 89.98	21.241 / 90	132

Table 8. Crystallographic data for actinyl compounds based on 2D structural units with corner-sharing coordination polyhedra and U:T = 2:3 (continued)

Unit	Chemical formula	sp. gr.	*a* [Å] / α [°]	*b* [Å] / β [°]	*c* [Å] / γ [°]	ref
	$Mg_2[(UO_2)_3(CrO_4)_5](H_2O)_{17}$	*Pbca*	19.921 / 90	21.053 / 90	18.497 / 90	210
	$Ca_2[(UO_2)_3(CrO_4)_5](H_2O)_{19}$	*P*2$_1$/*m*	11.036 / 90	17.536 /118.18	11.506 / 90	210
	β-$Mg_2[(UO_2)_3(SeO_4)_5](H_2O)_{16}$	*Pbcm*	10.381 / 90	22.234 / 90	33.739 / 90	208
	$Zn_2[(UO_2)_3(SeO_4)_5](H_2O)_{17}$	*Pbca*	18.429 / 90	19.979 / 90	20.690 / 90	211
	$Cu_2[(UO_2)_3((S,Cr)O_4)_5](H_2O)_{17}$	*Pbca*	18.059 / 90	19.990 / 90	20.555 / 90	212
l3/5c	$Rb_4[(UO_2)_3(SeO_4)_5(H_2O)]$	*Pbnm*	11.376 / 90	15.069 / 90	19.209 / 90	182
	$[C_5H_{14}N]_4(UO_2)_3(SeO_4)_4(HSeO_3)(H_2O)(H_2SeO_3)(HSeO_4)$	*P* $\bar{1}$	11.707 / 73.90	14.817 / 76.22	16.977 / 89.36	213
	$(H_3O)[C_5H_{14}N]_2[(UO_2)_3(SeO_4)_4(HSeO_4)(H_2O)]$	*C*2/*c*	16.757 / 90	11.724 / 98.88	19.049 / 90	214
	$(H_3O)[C_5H_{14}N]_2[(UO_2)_3(SeO_4)_4(HSeO_4)(H_2O)](H_2O)$	*P*2$_1$/*n*	10.825 / 90	19.001 /100.32	18.646 / 90	214
l3/5d	$[C_9H_{24}N_2]_2[(UO_2)_3(SeO_4)_5(H_2O)_2](H_2O)_{12}$	*P*6$_3$/*mmc*	19.557 / 90	19.557 / 90	47.878 / 120	161
l5/8a	$(C_6H_{14}N_2)_3[(UO_2)_5(MoO_4)_8](H_2O)_4$	*P* $\bar{1}$	11.856 / 96.73	11.870 / 91.11	12.675 / 110.19	170
l5/8b	$[N_3C_6H_{18}]_2[(UO_2)_5(H_2O)(SO_4)_8](H_2O)_5$	*P*2$_1$/*n*	21.560 / 90	10.290 / 96.74	22.840 / 90	187
l5/8c	$[C_3H_{12}N_2][(UO_2)_5(SeO_4)_8(H_2O)](H_2SeO_3)_{0.74}(H_2O)_4$	*P*2$_1$/*n*	10.384 / 90	21.362 / 94.69	24.766 / 90	161
l5/8d	$(H_3O)_6[(UO_2)_5(SeO_4)_8(H_2O)_5](H_2O)_5$	*P*2$_1$/*m*	13.835 / 90	13.437 /108.00	14.310 / 90	215
l5/8e	$[Co(H_2O)_6]_3[(UO_2)_5(SO_4)_8(H_2O)](H_2O)_5$	*P*2$_1$/*c*	27.160 / 90	9.986 / 106.52	22.780 / 90	218
l4/7a	$[C_3H_{10}N]_8[(UO_2)_4(SeO_4)_7](HSeO_4)(NO_3)(H_2O)_4$	*P* $\bar{1}$	13.012 / 93.83	13.614 / 94.83	22.069 / 103.72	161
l4/7b	$K_6[(UO_2)_4(CrO_4)_7](H_2O)_6$	*P*2$_1$2$_1$2	10.958	22.582	7.955	220

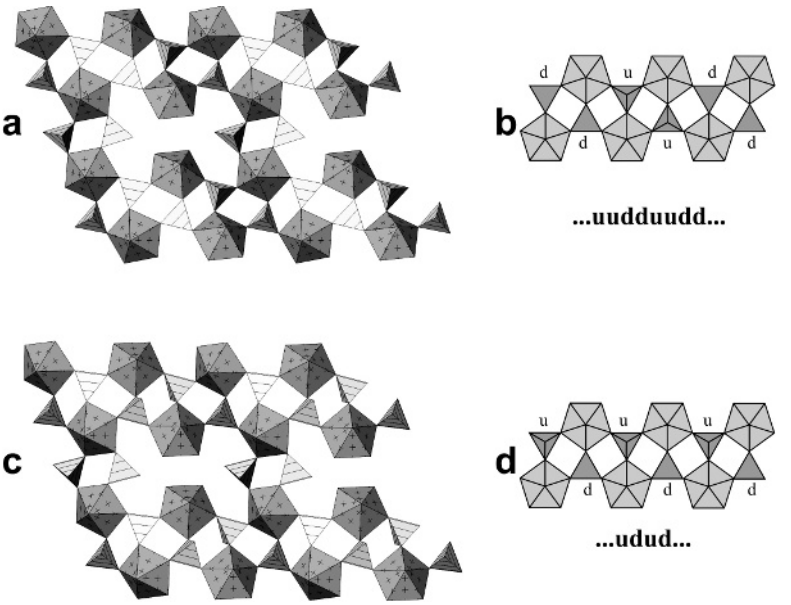

Fig. 42. To the description of geometrical isomerism of the $[(UO_2)_2(SeO_4)_3(H_2O)_2]^{2-}$ sheets with the **l2/3k** topology. See text for details.

graphs, orientational geometrical isomerism of corresponding structural units has been observed.

Fig. 44 a and b show the $[(UO_2)_3(CrO_4)_5]^{4-}$ sheets observed in the structures of $Mg_2[(UO_2)_3(CrO_4)_5](H_2O)_{17}$ and $Ca_2[(UO_2)_3(CrO_4)_5](H_2O)_{19}$, respectively [210]. These sheets contain UO_7 pentagonal bipyramids that share corners with CrO_4 tetrahedra. The topology of these sheets corresponds to the graph **l3/5b**. However, a detailed analysis of the polyhedral diagrams shown in Fig. 44 shows that these two sheets are geometrical isomers and cannot be transformed, one into the other, without the breaking of chemical bonds. Fig. 45b shows a black-and-white graph corresponding to the $[(UO_2)_3(CrO_4)_5]^{4-}$ sheet in $Ca_2[(UO_2)_3(CrO_4)_5](H_2O)_{19}$, with the letters **u** (up) and **d** (down) written near the white nodes. With the graph oriented as in Fig. 45b, the sequences of tetrahedral orientations along the horizontal line may be written in rows. Thus, the first row of the **u** and **d** symbols near the white nodes may be written as ...**ududud**.... The second row contains vacant sites for white nodes. Adopting the symbol □ for a vacancy, the sequence of the **u**, **d**, and □ symbols for the second row is written as ...**du□ud□du□ud**.... The third and fourth rows repeat the first and second rows, respectively. Thus, one may write **u**, **d**, and □ symbols for a given row in a tabular form, as shown in Fig. 45e for the graph given in Fig. 45b (it is important to maintain the vertical order of the rows: the symbol of the next row should be exactly below the corresponding symbol of

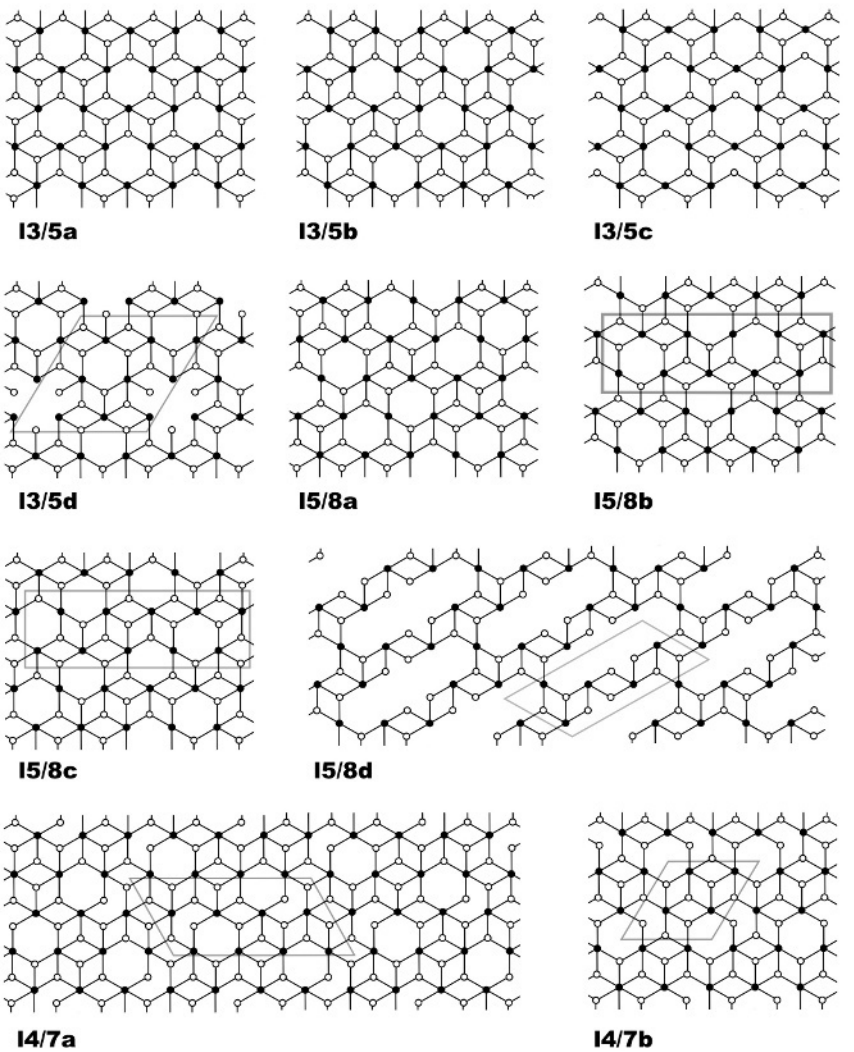

Fig. 43. Black-and-white 2D graphs derivative from the {**3.6.3.6**} graph. Graphs with black:white ratio of 3:5, 5:8, and 4:7.

the preceding row). As the graph shown in Fig. 45b is thought to be infinite in the horizontal and vertical directions, the corresponding table of the **u**, **d**, and □ symbols is also infinite within the plane of the figure. In this symbolic table, one can choose an orthogonal part (elementary unit) that may be used to reproduce the entire table by independent translations along the horizontal and

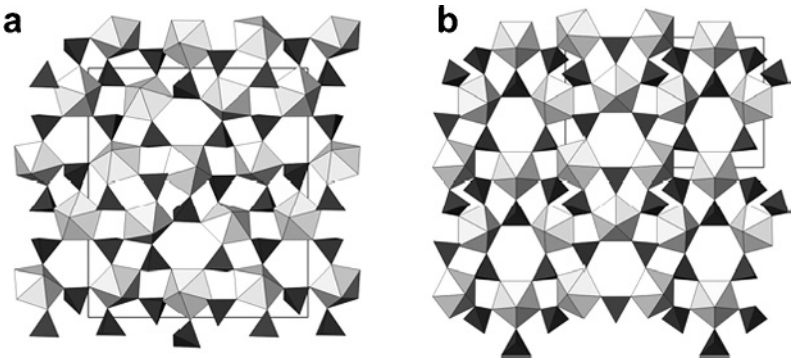

Fig. 44. The $[(UO_2)_3(CrO_4)_5]$ sheets observed in the structures of $Mg_2[(UO_2)_3(CrO_4)_5](H_2O)_{17}$ and $Ca_2[(UO_2)_3(CrO_4)_5](H_2O)_{19}$ (a and b, respectively).

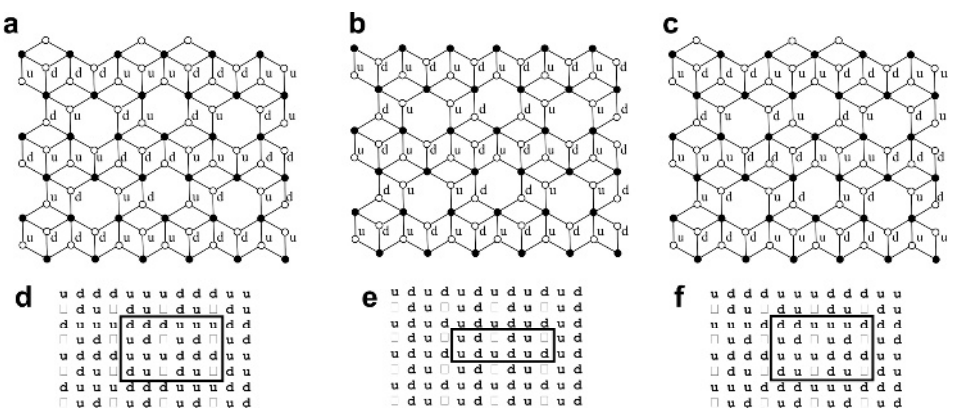

Fig. 45. Black-and-white graphs with the **u**, **d** and □ symbols of the $[(UO_2)_3(CrO_4)_5]$ sheets in the structures of $Mg_2[(UO_2)_3(CrO_4)_5](H_2O)_{17}$ (a), $Ca_2[(UO_2)_3(CrO_4)_5](H_2O)_{19}$ (b) and $K_4[(UO_2)_3(CrO_4)_5](H_2O)_8$ (c); their corresponding **u**, **d** and □ symbolic tables (d, e and f, respectively). The orientation matrices of tetrahedra are indicated in (d), (e) and (f) by bold lines.

vertical directions. The corresponding elementary unit for the table of symbols shown in Fig. 45b is indicated by the bold line. This elementary unit consists of six columns and two rows and may be used to construct the entire table by vertical and horizontal translations. We call this unit an orientation matrix of tetrahedra. Obviously, this matrix can also be written in a row as (**ud□du□**)(**ududud**) implying that the first six symbols in brackets correspond to the first row and the second six symbols in brackets correspond to the second row of the matrix. Fig. 45a shows black-and-white graphs with **u** and **d** symbols written near the white nodes for the $[(UO_2)_3(CrO_4)_5]^{4-}$ sheet in $Mg_2[(UO_2)_3(CrO_4)_5](H_2O)_{17}$. The corresponding 2D table of the **u**, **d**, and □ symbols is shown in Fig. 45d. The orientation matrix of tetrahedra for the sheet

is different from that observed for the Ca compound and may be written as (**dddduuu**)(**ud□ud□**)(**uuuddd**)(**du□du□**). In contrast to the 2×6 matrix of the sheet in the Ca chromate, this matrix has dimensions 4×6, which indicates that the structure of the sheet in the Mg compound is more complicated. Fig. 45c shows the graph that corresponds to the structure of the $[(UO_2)_3(CrO_4)_5]^{4-}$ sheet in $K_4[(UO_2)_3(CrO_4)_5](H_2O)_8$ [132]. Its structure is related but distinct from that of the uranyl chromate sheet in the Ca chromate. The corresponding orientation matrix of tetrahedra is (**dduuud**)(**ud□ud□**)(**uuuddd**)(**du□du□**). It differs from the matrix of the sheet in the Ca compound by the first row only.

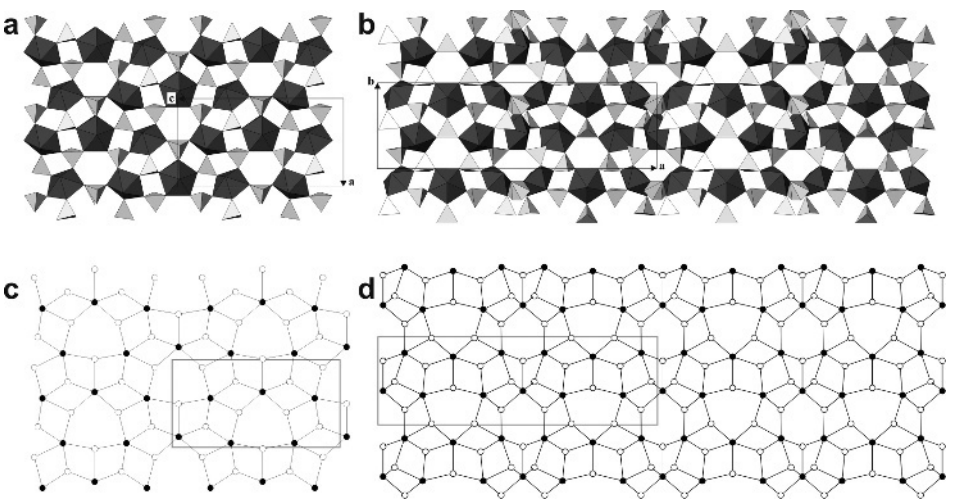

Fig. 46. The $[(UO_2)_3(SeO_4)_5]^{4-}$ sheets in the crystal structures of α- (a) and β-$Mg_2[(UO_2)_3(SeO_4)_5](H_2O)_{16}$ (b) and their nodal representations (c and d, respectively). Legend: $[UO_7]^{8-}$ bipyramids = black circles; $[SeO_4]^{2-}$ tetrahedra = white circles.

An interesting isomeric variation of the **l3/5b** topology has recently been observed in β-$Mg_2[(UO_2)_3(SeO_4)_5](H_2O)_{16}$ [208]. A polyhedral diagram of the $[(UO_2)_3(SeO_4)_5]^{4-}$ sheet from this structure is shown in Fig. 46b. Analysis of its black-and-white graph (Fig. 46d) indicates that it does really correspond to the **l3/5b** topology. However, the system of tetrahedral orientations is fundamentally different from those observed in uranyl chromates discussed above. The point is that one of the tetrahedra within the sheet has a disordered "up-and-down" orientation for which we adopt the symbol **m**. Figs. 47c and f provide descriptions of tetrahedral orientations in graphical and tabular forms, respectively. The orientation matrix is rather complicated as it has dimensions of 12×2 and can be written as (**dd□dd□uu□uu□/uuduumdduddm**). This high degree of complexity is most probably the result of the strongly modulated

geometrical shape of the uranyl selenate sheet (Fig. 48b). It is noteworthy that β-$Mg_2[(UO_2)_3(SeO_4)_5](H_2O)_{16}$ is unstable under atmospheric conditions.

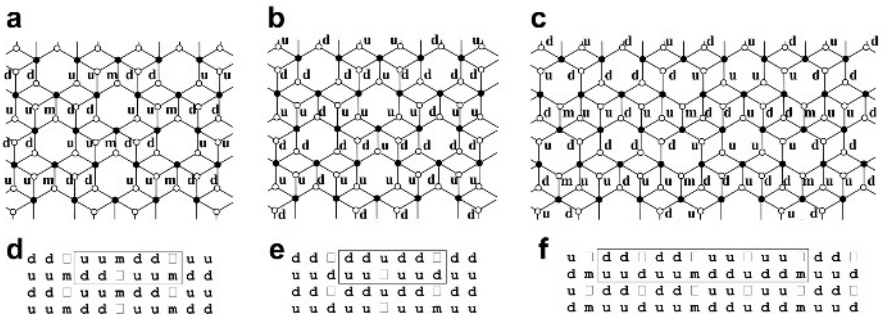

Fig. 47. Idealized versions of the graphs shown in Fig. 3a and b (a and c, respectively) can be produced from the (3.6.3.6) graph by elimination of one sixth of its white vertices and all edges incident upon them. Idealized black-and-white graph of the $[(UO_2)_3(SeO_4)_5]^{4-}$ sheets observed in α- (d) and β-$Mg_2[(UO_2)_3(SeO_4)_5](H_2O)_{16}$ (f), and $[(UO_2)_3(MoO_4)_5]^{4-}$ sheet observed in $(NH_3(CH_2)_3NH_3)(H_3O)_2[(UO_2)_3(MoO_4)_5]$ (e) together with the tetrahedral orientation symbols written next to the white vertices; tabular forms of orientation symbols for these sheets (g, h and i, respectively). See text for details.

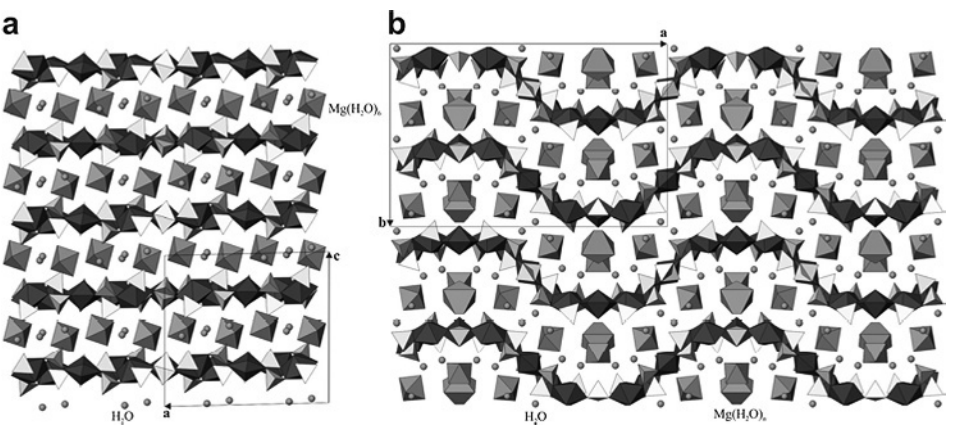

Fig. 48. Projections of the structures of α- (a) and β-$Mg_2[(UO_2)_3(SeO_4)_5](H_2O)_{16}$ (b) along the *b* or *c* axis, respectively.

In contrast to the β-form, α-$Mg_2[(UO_2)_3(SeO_4)_5](H_2O)_{16}$ is stable in air. Its structure contains flat $[(UO_2)_3(SeO_4)_5]^{4-}$ sheets with the **l3/5a** topology (Figs. 47a, c; Fig. 48a). The same topology is also characteristic for the actinyl molybdate sheets in $[C_3N_2H_{12}](H_3O)_2[(UO_2)_3(MoO_4)_5]$ and $Na_6[(Np^{5+}O_2)_2(Np^{6+}O_2)(MoO_4)_5](H_2O)_{13}$. However, the sheets in selenate and molybdate compounds correspond to different geometrical isomers (Fig. 47). The uranyl selenate sheet has the (**uumdd□/dd□uum**) orientation matrix (in

compact form), whereas, in the molybdates, the orientation matrix is (**ddudd□/uu□uud**).

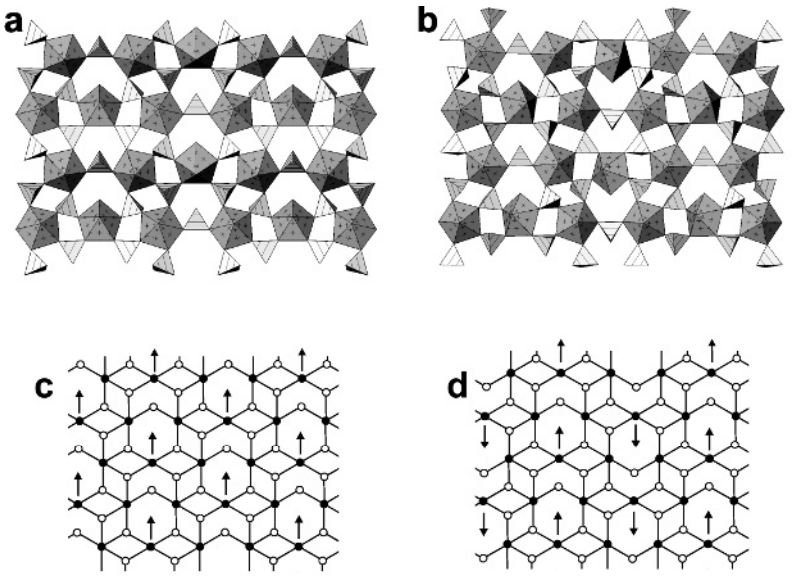

Fig. 49. $[(UO_2)_3(SeO_4)_5(H_2O)]^{4-}$ sheets observed in the structures of $Rb_4[(UO_2)_3(SeO_4)_5(H_2O)]$ (a) and $(H_3O)[C_5H_{14}N]_2[(UO_2)_3(SeO_4)_4(HSeO_4)(H_2O)](H_2O)$ (b), respectively. The sheets are different by the orientations of their U→H_2O vector systems (c and d).

Figs. 49a and b depict two $[(UO_2)_3(SeO_4)_5(H_2O)]^{4-}$ sheets observed in the structures of $Rb_4[(UO_2)_3(SeO_4)_5(H_2O)]$ [182] and $(H_3O)[C_5H_{14}N]_2[(UO_2)_3(SeO_4)_4(HSeO_4)(H_2O)](H_2O)$ [214], respectively. The sheets are topologically characterized by the **l3/5c** graph shown in Fig. 43. Both sheets consist of two types of uranyl cations. One is coordinated by five O atoms of the SeO_4 tetrahedra, thus forming UO_7 pentagonal bipyramids, whereas the other is coordinated by four O atoms and one H_2O molecule which results in a $UO_6(H_2O)$ bipyramid. It is apparent in Figs. 49a and b that the sheets differ in the orientation of the $UO_6(H_2O)$ bipyramids. This difference can be visualized by adding the U→H_2O vectors to the black-and-white graphs of the sheets. The idealized versions of the graphs with the U→H_2O vectors are shown in Fig. 49c and d, respectively. In $Rb_4[(UO_2)_3(SeO_4)_5(H_2O)]$, all U→$H_2O$ vectors within the sheet pointing in the same direction, whereas, in $(H_3O)[C_5H_{14}N]_2[(UO_2)_3(SeO_4)_4(HSeO_4)(H_2O)](H_2O)$, the U→$H_2O$ vectors with different orientations alternate. As was the case with the **l1/2b**-type sheets (see above), the sheets shown in Figs. 49a and b can be designated as different geometrical isomers induced by selective hydration of the U polyhedra.

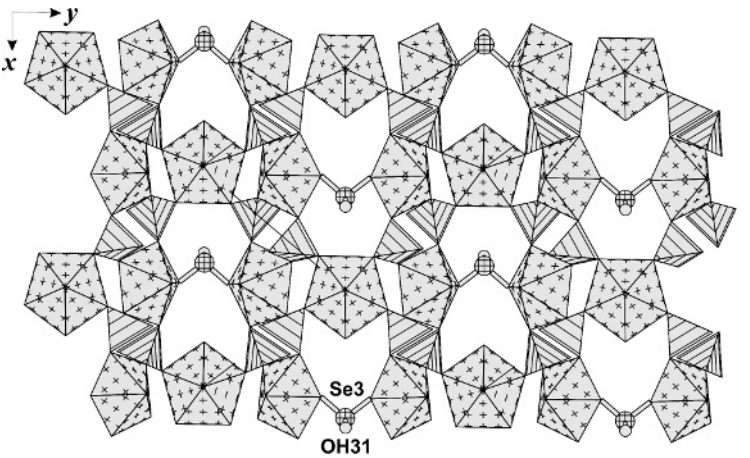

Fig. 50. Uranyl selenate-selenite sheet in the structure of $[C_5H_{14}N]_4[(UO_2)_3(SeO_4)_4(HSeO_3)(H_2O)](H_2SeO_3)(HSeO_4)$.

Further analysis of the **l3/5c** graph indicates that its white vertices are either 2- or 3-connected. Fig. 50 shows the uranyl selenate-selenite sheet from the structure of $[C_5H_{14}N]_4[(UO_2)_3(SeO_4)_4(HSeO_3)(H_2O)](H_2SeO_3)(HSeO_4)$ [213]. The topology of this sheet can also be described by the **l3/5c** graph, however, with 2-connected white vertices corresponding to $Se^{4+}O_3^{2-}$ selenite groups. The selenite group is a triangular pyramid with its apical vertex occupied by the Se^{4+} cation that has a stereochemically active lone-electron pair. The 3-connected white vertices of the **l3/5c** graph correspond to tetrahedral SeO_4^{2-} oxoanions. Once again, the presence of tridentate tetrahedra gives rise to the occurence of orientational geometrical isomerism. Fig. 51a shows the **l3/5c** graph with u and d symbols written near the white vertices. This diagram corresponds to the system of orientation of tetrahedra in the uranyl selenate-selenite sheet shown in Fig. 50. In principle, if 2-connected white vertices correspond to tetrahedral oxoanions, their orientation relative to the plane of the sheet does not really matter since bidentate tetrahedra possess enough freedom to change their orientation without affecting the topological structure of the sheet. However, in the case when 2-connected vertices correspond to $Se^{4+}O_3^{2-}$ groups, one has to distinguish between the non-shared O apical corner and another corner which is occupied by the lone electron pair. For this reason, the diagram in Fig. 51a provides orientation symbols for the 2-connected vertices as well. The system of tetrahedral orientations in tabular form is given in Fig. 51d; it corresponds to the matrix (**ududud**)(**ud□du□**). Figs. 51b and c describe topological structures of the uranyl selenate sheets in the structures of $(H_3O)[C_5H_{14}N]_2[(UO_2)_3(SeO_4)_4(HSeO_4)(H_2O)]$ and $(H_3O)[C_5H_{14}N]_2[(UO_2)_3(SeO_4)_4(HSeO_4)(H_2O)](H_2O)$, respectively. It is of interest that these compounds

are uranyl selenates templated by protonated N-methylbutylamine molecules and their compositions differ by one H_2O molecule only. However, their uranyl sheets are topologically different and correspond to two different geometrical isomers. Since in this case, 2-connected white vertices symbolize bidentate SeO_4 tetrahedra, their orientation relative to the plane of the sheet is not important which is symbolized by the **m** symbol. Tables of the orientations of tetrahedra are given in Figs. 51e and f. The uranyl selenate sheet observed in the low hydrate has a 3×2 orientation matrix (**dum**)(**du**□). The matrix of the sheet in higher hydrate has the 6×4 dimensions and can be written as (**dumdum**)(**du**□**ud**□)(**udmudm**)(**du**□**ud**□).

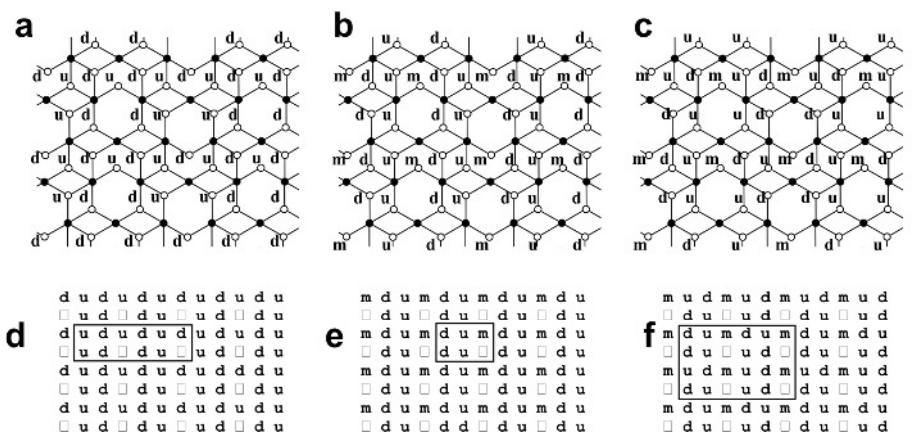

Fig. 51. The **l3/5c** graph with **u**, **d, m** and □ symbols symbols written near the white vertices for the sheets in the structures of $[C_5H_{14}N]_4[(UO_2)_3(SeO_4)_4(HSeO_3)(H_2O)](H_2SeO_3)(HSeO_4)$ (a), $(H_3O)[C_5H_{14}N]_2[(UO_2)_3(SeO_4)_4(HSeO_4)(H_2O)]$ (b) and $(H_3O)[C_5H_{14}N]_2[(UO_2)_3(SeO_4)_4(HSeO_4)(H_2O)](H_2O)$ (c), and their corresponding **u**, **d** and □ symbolic tables (d, e and f, respectively). The orientation matrices of tetrahedra are indicated in (d), (e) and (f) by bold lines.

From all graphs shown in Fig. 43, the **l5/8d** graph is remarkable in the presence of 16-membered rings. The uranyl selenate sheet having this topology is shown in Fig. 52a. It has been observed in the structure of $(H_3O)_6[(UO_2)_5(SeO_4)_8(H_2O)_5](H_2O)_5$ [215]. This uranyl selenate sheet can be simply obtained by connection of the **c1/2a** chains by additional 4-connected black vertex.

The {5.3.5.3}{5.3.5.4} graph. Fig. 53a shows a black-and-white graph of a relatively complex topological structure. It consists of two elementary rhombs and can be described by the symbol {5.3.5.3}{5.3.5.4}. Actinyl-based 2D structural units with this topology have been observed, e.g. in the structure of β-$Cs_2[(UO_2)_2(MoO_4)_3]$ [216]. Its fundamental difference from the structural

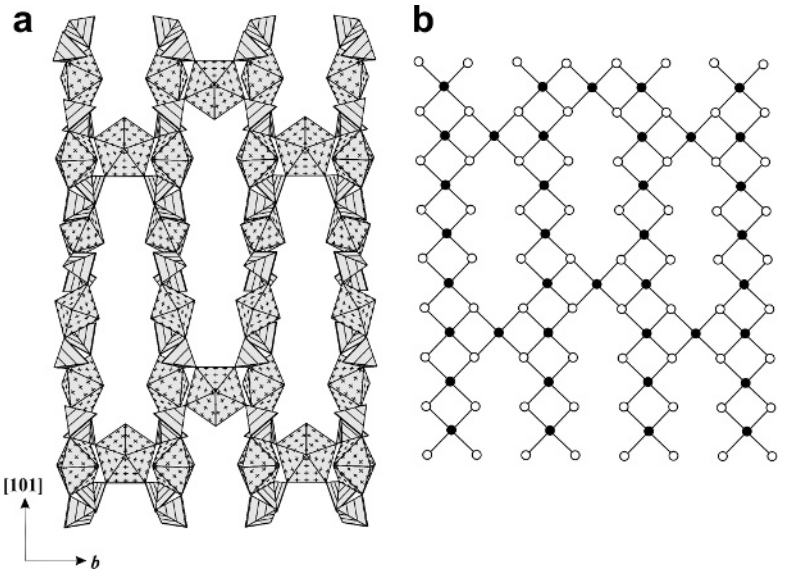

Fig. 52. Uranyl selenate sheet in the structure of $(H_3O)_6[(UO_2)_5(SeO_4)_8(H_2O)_5](H_2O)_5$ (a) and its 2D graph (b).

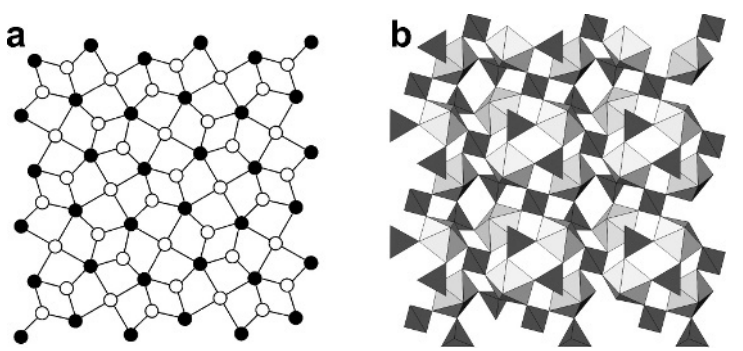

Fig. 53. The {**5.3.5.3**}{**5.3.5.4**} graph (a) and corresponding heteropolyhedral unit from the structure of β-$Cs_2[(UO_2)_2(MoO_4)_3]$ (b).

units based upon the {3.6.3.6} graph is that it contains tetradentate tetrahedral oxoanions which are absent in the {3.6.3.6}-derivatives by definition. It should be noted that the {5.3.5.3}{5.3.5.4} graph should be considered as a basic graph.

Modular structure of the uranyl sulfate sheet in ***$[Co(H_2O)_6]_3[(UO_2)_5(SO_4)_8(H_2O)](H_2O)_5$.*** An example of 2D topology that can be derived from two different basic graphs is given in Fig. 54. It was found in $[Co(H_2O)_6]_3[(UO_2)_5(SO_4)_8(H_2O)](H_2O)_5$ [218]. The structure of this compound

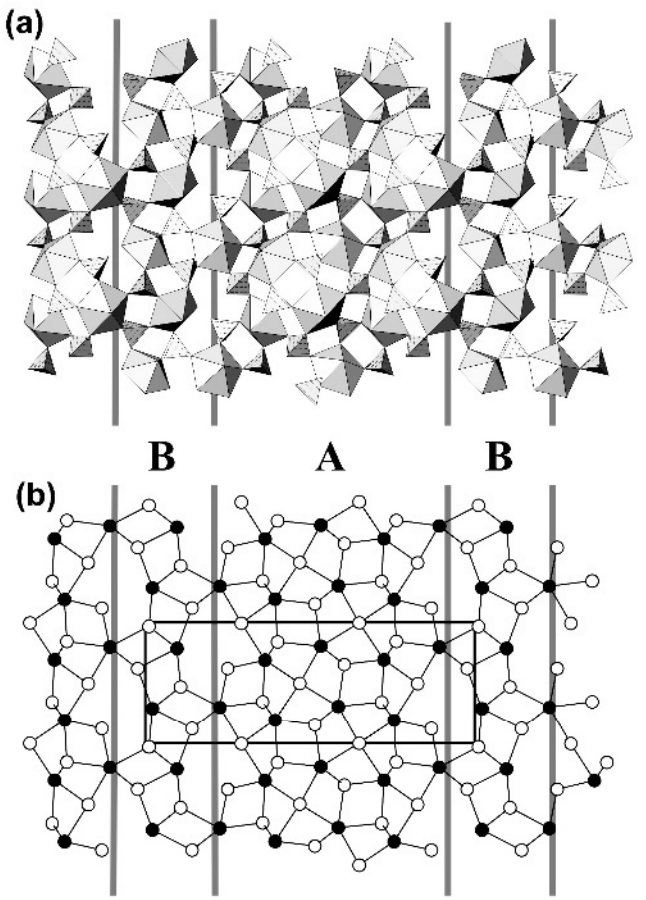

Fig. 54. The $[(UO_2)_5(SO_4)_8(H_2O)]$ sheet in the structure of $[Co(H_2O)_6]_3[(UO_2)_5(SO_4)_8(H_2O)](H_2O)_5$ (a), and its graphical representation (b). The **A** and **B** chains are delineated by grey lines. See text for more details.

is based upon the $[(UO_2)_5(SO_4)_8(H_2O)]^{6-}$ sheets consisting of corner-sharing UO_7 pentagonal bipyramids and SO_4 tetrahedra (Fig. 54a). The black-and-white graph corresponding to the topological structure of the uranyl sulfate sheet is shown in Fig. 54b. This graph can be constructed using two parent {3.6.3.6} and {5.3.5.3}{5.3.5.4} graphs given in Fig. 55. Cutting the {4.5.3.5} graph along the grey lines in Fig. 55a gives a complex **A** chain shown in Fig. 55c. Another **B** chain can be obtained from the {3.6.3.6} graph as shown in Fig. 55b. In order to obtain the resulting graph, the **A** and **B** chains should be joined

together in the ...**ABABAB**.. sequence (Fig. 55e). Since the topology of the uranyl sulfate sheet can be derived using two basic graphs, one can say that this 2D unit has a modular structure related to the {3.6.3.6} and {5.3.5.3}{5.3.5.4} graphs.

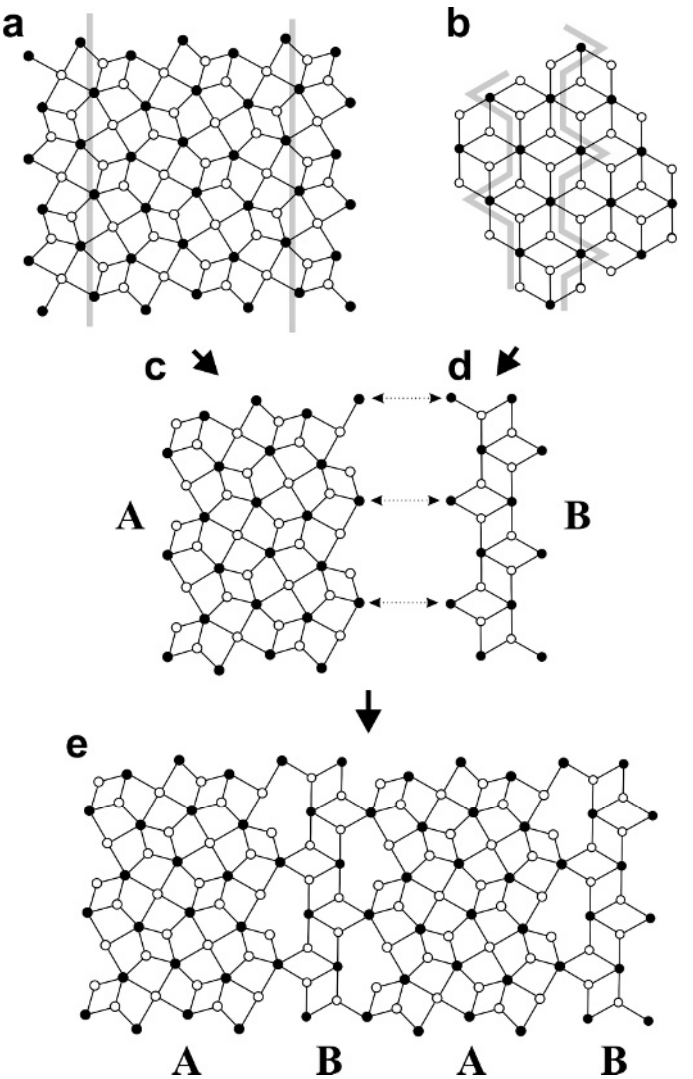

Fig. 55. (a) The {**5.3.5.3**}{**5.3.5.4**} graph; (b) the {**3.6.3.6**} graph; (c) the **A** chain from the graph shown in (a) as delineated by grey lines; (d) the **B** chain from the graph shown in (b) as delineated by grey lines; (e) the composite graph obtained by merging the **A** and **B** chains shown in (c) and (d), respectively.

3.3.5. 3D units (frameworks)

Actinyl compounds with tetrahedral oxoanions TO_4 (T = S, Cr, Se, Mo) that are based upon 3D networks of corner-sharing coorination polyhedra are listed in Table 9. To proceed with their structural description, we shall use graph theory analysis of heteropolyhedral frameworks as developed in [221]. It turns out that the most actinyl-based 3D units with corner-sharing between chemically different polyhedra can be described as based upon 1D structural elements for which we adopt the term "fundamental chain" suggested by Liebau [222] for tetrahedral frameworks in silicates and related materials. However, some actinyl oxosalt structures are better described as consisting of polymerized 2D sheets. For convenience, the frameworks will be classified into three major groups: (1) frameworks based upon fundamental chains; (2) microporous chiral uranyl molybdate frameworks; (3) frameworks based upon 2D sheets.

Frameworks based upon fundamental chains. Fig. 56a shows the 3D uranyl molybdate framework from the structure of α-$Cs_2[(UO_2)_2(MoO_4)_3]$. It consists of corner-sharing UO_7 pentagonal bipyramids and MoO_4 tetrahedra. The framework has 1D channels running parallel to the a axis that are occupied by Cs^+ cations. The framework can be derived from the uranyl molybdate sheet observed in β-$Cs_2[(UO_2)_2(MoO_4)_3]$ (Fig. 53) by cutting it into 1D chains (Fig. 56b, c) and re-assembling them so that the 3D structure is formed. In fact, the α → β high-temperature reconstructive phase transition in $Cs_2[(UO_2)_2(MoO_4)_3]$ has recently been observed by Nazarchuk et al. [223]. This phase transition involves a 3D → 2D transformation of the uranyl molybdate network.

The only known example of uranyl selenate framework structure, $(H_3O)_2[(UO_2)(SeO_4)_3(H_2O)](H_2O)_4$, based upon 3D framework of U and Se polyhedra is shown in Fig. 57a.A description based upon polyhedra fails to capture the details of the framework. By application of the black-and-white graph theory technique, the architectural principles become transparent (Fig. 57b). The uranyl selenate framework is built up by linkage of the U:Se = 2:3 chains of uranyl bipyramids and selenate tetrahedra whose graph is depicted in Fig. 57c. The graph consists solely of 4-membered rings of black and white vertices.

The uranyl molybdate framework in the structure of $Ba(UO_2)_3(MoO_4)_4(H_2O)_4$ (Fig. 58a) can easily be described as based upon two types of fundamental chains, **l1/2a** and **l1/1b** (Figs. 58b and c, respectively). Both chains are parallel to the b axis and cross-linked into the framework by sharing their corners.

Microporous uranyl molybdate chiral frameworks. The general chemical formula of these compounds can be written as $A_r[(UO_2)_n(MoO_4)_m(H_2O)_p](H_2O)_q$, where A is either an inorganic or organic

Table 9. Crystallographic data for actinyl compounds based on 3D structural units with corner-sharing coordination polyhedra

Chemical formula	sp. gr.	*a* [Å]	*b* [Å] / β [°]	*c* [Å]	ref
α-$Cs_2[(UO_2)_2(MoO_4)_3]$	$Pna2_1$	20.430	8.555 / 90	9.855	216
$Rb_2[(UO_2)_2(MoO_4)_3]$	$Pna2_1$	20.214	8.374 / 90	9.746	129
$Tl_2[(UO_2)_2(MoO_4)_3]$	$Pna2_1$	20.130	8.281 / 90	9.705	229
$Ba(UO_2)_3(MoO_4)_4(H_2O)_4$	*Pbca*	17.797	11.975 / 90	23.330	232
$(H_3O)_2[(UO_2)_2(SeO_4)_3(H_2O)](H_2O)_4$	$P2_1/c$	10.726	14.727 / 96.98	13.727	234
$(NH_4)_4[(UO_2)_5(MoO_4)_7](H_2O)$	$P6_1$	11.407	11.407 / 90	70.659	225
$[(C_2H_5)_2NH_2]_2$ $[(UO_2)_4(MoO_4)_5(H_2O)](H_2O)$	$P6_522$	11.361	11.361 / 90	52.698	226
$(UO_2)_{0.82}[C_8H_{20}N]_{0.36}$ $[(UO_2)_6(MoO_4)_7(H_2O)_2](H_2O)_n$	$C222_1$	12.230	18.966 / 90	22.392	227
$[C_6H_{14}N_2]$ $[(UO_2)_6(MoO_4)_7(H_2O)_2](H_2O)_m$	$C222_1$	11.326	19.860 / 90	23.731	227
α-$[C_6H_{16}N]_2$ $[(UO_2)_6(MoO_4)_7(H_2O)_2](H_2O)_2$	$C222_1$	11.305	19.962 / 90	24.416	228
β-$[C_6H_{16}N]_2$ $[(UO_2)_6(MoO_4)_7(H_2O)_2](H_2O)_2$	$P2_12_12_1$	11.211	19.880 / 90	24.421	228
$[NC_4H_{12}]_2[(UO_2)_6(H_2O)_2(SO_4)_7]$	$C222_1$	10.345	18.542 / 90	22.700	233
$Mg(UO_2)_6(MoO_4)_7(H_2O)_{14}$	$C222_1$	11.313	20.163 / 90	23.877	231
$Sr(UO_2)_6(MoO_4)_7(H_2O)_{14}$	$C222_1$	11.166	20.281 / 90	24.061	231
$Na_2[(UO_2)_3(MoO_4)_4]$	*I2/m*	14.479	13.956 /108.22	22.972	224
$K_2[(UO_2)_3(MoO_4)_4]$	*I2/m*	14.461	13.923 /108.22	23.009	224
$UO_2MoO_4(H_2O)_2$	$P2_1/c$	13.612	11.005 /113.05	10.854	230

(e.g. protonated amine) cation. There are three topological types of chiral open-framework uranyl molybdates that are characterized by different U:Mo = n:m ratios of 6:7, 5:7, and 4:5. The structure of the only known 5:7 compound, $(NH_4)_4[(UO_2)_5(MoO_4)_7](H_2O)$, consists of a three-dimensional framework of composition $[(UO_2)_5(MoO_4)_7]^{4-}$ (Fig. 59a). The framework contains a three-dimensional system of channels. The largest channel is parallel to [001] and has the dimensions 7.5 × 7.5 Å, which results in a crystallographic free diameter (effective pore width) of 4.8 × 4.8 Å (based on an oxygen radius of 1.35 Å).

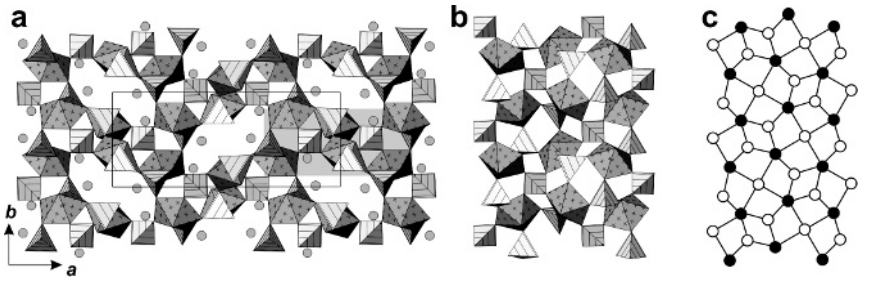

Fig. 56. 3D uranyl molybdate framework from the structure of α-$Cs_2[(UO_2)_2(MoO_4)_3]$ (a). The framework can be can be derived from the uranyl molybdate sheet observed in β-$Cs_2[(UO_2)_2(MoO_4)_3]$ (Fig. 53) by cutting it into 1D chains (Fig. 56b, c) and re-assembling them into a 3D structure.

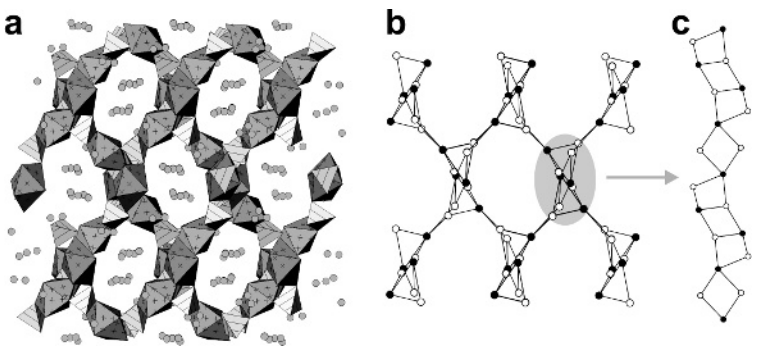

Fig. 57. 3D framework of U and Se polyhedra in the structure of $(H_3O)_2[(UO_2)(SeO_4)_3(H_2O)](H_2O)_4$ (a). Its black-and-white graph (b) can be described as built by polymerization of 1D chains shown in (c).

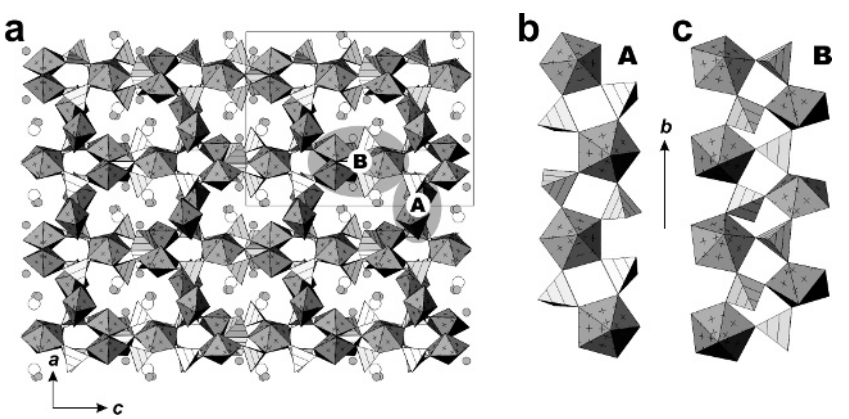

Fig. 58. Uranyl molybdate framework in the structure of $Ba(UO_2)_3(MoO_4)_4(H_2O)_4$ (a) can be described as based upon two types of fundamental chains, **l1/2a** and **l1/1b** (b and c, respectively).

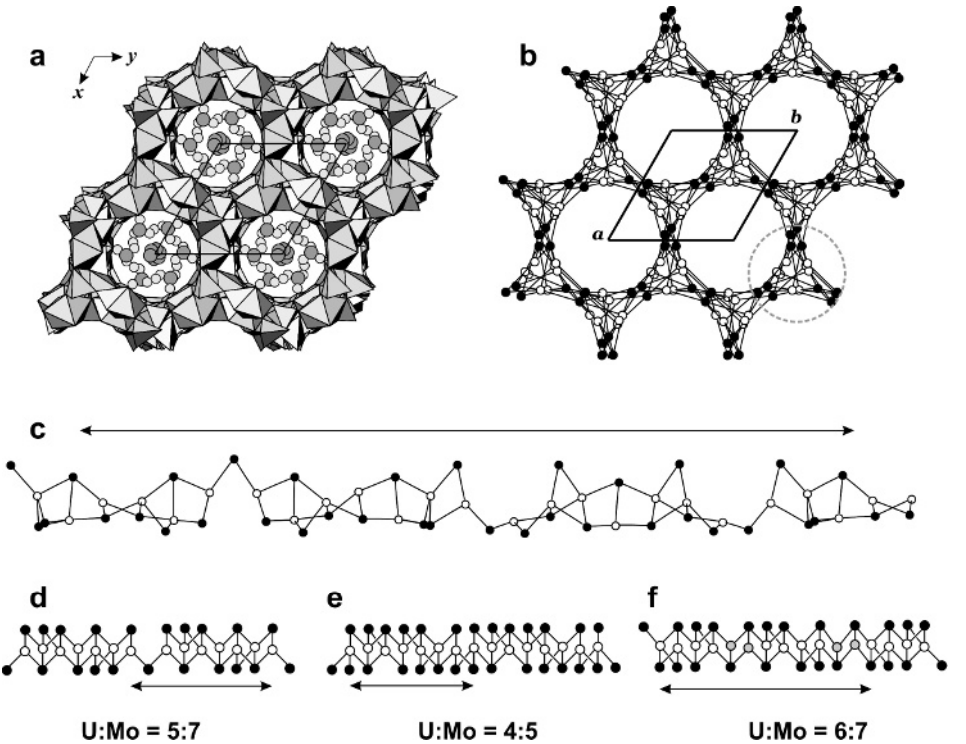

Fig. 59. The structure of $(NH_4)_4[(UO_2)_5(MoO_4)_7](H_2O)$ projected along the c axis (a), nodal representation of its $[(UO_2)_5(MoO_4)_7]$ framework (b), nodal representation of its fundamental chain (c), and graphs isomorphous to nodal representations of fundamental chains of chiral uranyl molybdate frameworks with the U:Mo ratio of 5:7, 4:5 and 6:7 (d, e and f, respectively).

Smaller channels extend parallel to [100], [110], [010], [-110], [1-10] and [-1-10] and have dimensions 5.2 × 6.3 Å (giving an effective pore width of 2.5 × 3.6 Å). Four symmetrically unique NH_4^+ cations and H_2O molecules are located in the framework channels. The $[(UO_2)_5(MoO_4)_7]^{4-}$ framework is unusually complex. Its nodal representation is shown in Fig. 59b. Each node corresponds to a UO_7 bipyramid (black) or a MoO_4 tetrahedron (white). All black vertices are 5-connected and all white vertices are either 3- or 4-connected. Using the nodal representation, the uranyl molybdate framework in the structure of $(NH_4)_4[(UO_2)_5(MoO_4)_7](H_2O)$ can be described in terms of fundamental chains. The nodal representation of the fundamental chain corresponding to the uranyl molybdate framework is shown in Fig. 59c. The chain is a sequence of 3- and 4-connected MoO_4 tetrahedra (white vertices) linked through one, two or three UO_7 pentagonal bipyramids (black vertices). The graph shown in Fig. 59c can be further reduced to the simplified isomorphic graph shown in Fig. 59d. This reduction preserves all topological linkages between the nodes. Note that the

graph shown in Fig. 59d is periodic and its identity unit includes seven white vertices, whereas, in the real structure, the identity period of the fundamental chain includes 21 white vertices. Thus the topological structure of the fundamental chain is simpler than its geometrical realization.

Distinction of a fundamental chain permits the comparison of the 5:7 uranyl molybdate framework in $(NH_4)_4[(UO_2)_5(MoO_4)_7](H_2O)$ with the 6:7 and 4:5 chiral uranyl molybdate frameworks. The two latter frameworks can also be described as based upon fundamental chains of UO_7 and MoO_4 polyhedra. The reduced black-and-white graphs of these chains are shown in Figs. 59e and f for 6:7 and 4:5 frameworks, respectively. Detailed examination of these graphs demonstrated that they cannot be transformed one into another without significant topological reconstruction. Thus, the fundamental chains that form bases for the chiral uranyl molybdate frameworks with U:Mo = 5:7, 4:5 and 6:7 are topologically different, though closely related.

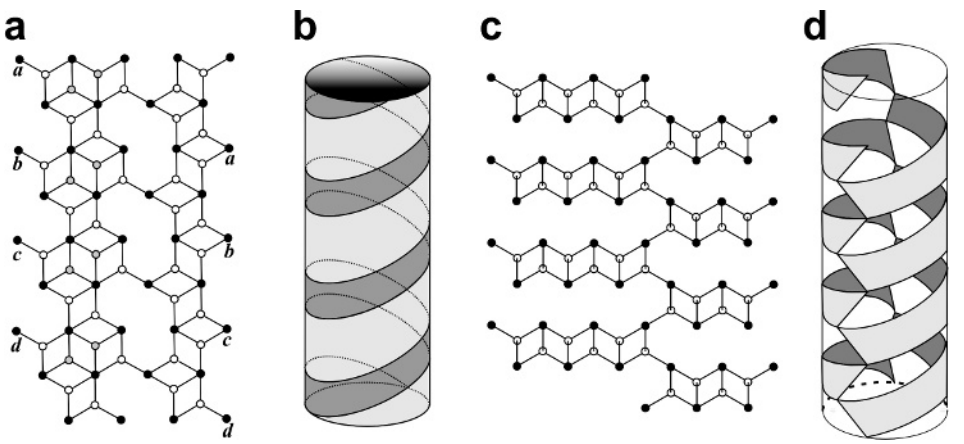

Fig. 60. Chiral tubular units in the structures of the U:Mo = 4:5 and 5:7 uranyl molybdate frameworks can be described in terms of tubular units (b and d, respectively). The tubular units can be obtained by folding and gluing tapes shown in (a) and (c), respectively.

The alternative description of the 4:5 and 5:7 uranyl molybdate frameworks can be made in terms of tubes or tubular units fused into a 3D framework. Such tubular units for the 4:5 and 5:7 structures are shown in Fig. 60. The topological structure of these tubes can be exposed by unfolding them onto a 2D plane so that the result is a 1D graph with local topology identical to that of the tube. To reform the tubular unit, one has to fold the tape and to join the points identified by the same letters. The tubular graphs shown in Figs. 60b and d symbolize channels in the uranyl molybdate frameworks. It is noteworthy that they have a chiral helical structure that is in agreement with the symmetry of the channels in the real structures (6_522 for 4:5 and 6_5 for 5:7 frameworks).

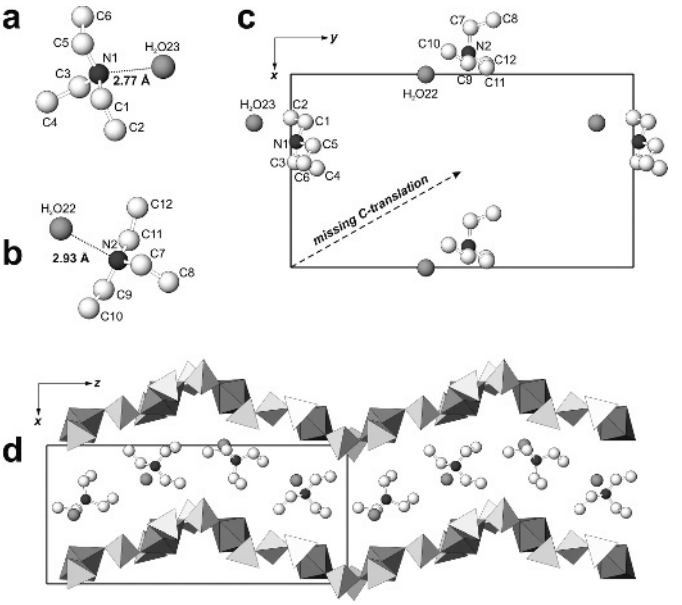

Fig. 61. To the description of displacive phase transition in $[C_6H_{16}N]_2[(UO_2)_6(MoO_4)_7(H_2O)_2](H_2O)_2$: configurations of the two non-equivalent $[C_6H_{16}N]^+$ cations and adjacent H_2O groups (a, b), arrangement of extra-framework $[C_6H_{16}N]^+$ cations and H_2O groups located at $z \sim 0$ within the *xy* plane (c) and cross-section of the wave-like channel in the uranyl molybdate framework occupied by $[C_6H_{16}N]^+$ cations and H_2O groups (d).

The microporous uranyl molybdate frameworks are highly flexible, as recently demonstrated by the discovery of a low-temperature displacive phase transition in $[C_6H_{16}N]_2[(UO_2)_6(MoO_4)_7(H_2O)_2](H_2O)_2$. This compound contains a U:Mo = 6:7 chiral framework with large channels along the c axis filled by extra-framework H_2O groups and protonated triethylamine molecules as guest molecules (Fig. 61). At 293 K (ambient conditions), guest molecules within the channels are disordered and the structure possess the $C222_1$ space group. However, at 263 K, a transition to the ordered state of the guest molecules (Fig. 61c) is observed that corresponds to the $P2_12_12_1$ space group. The low temperature phase contains two symmetrically independent $[C_6H_{16}N]^+$ molecules and two symmetrically independent non-framework H_2O groups. With decreasing temperature each $[C_6H_{16}N]^+$ molecule in the framework channels (Fig. 61a, b) takes on one of the two orientations. These orientations are non-equivalent relative to the C-translation present in the $C222_1$ space group. Due to the hydrogen bonding interactions between the framework and the guest molecules, the framework loses its C-translational symmetry. This second-order displacive phase transition is possible due to the high flexibility of the uranyl molybdate substructure.

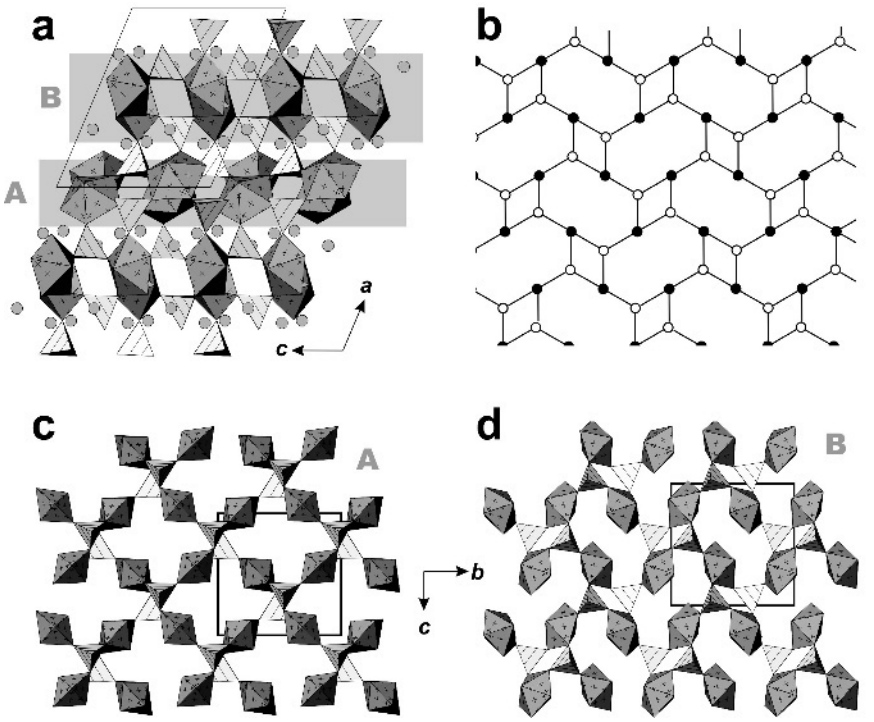

Fig. 62. The structure of $UO_2MoO_4(H_2O)_2$ projected along the *b* axis (a). The uranyl molybdate framework in this compound can be splitted into alternating **A** and **B** sheets (c and d, respectively) which are of the same topology (b).

Frameworks based upon 2D sheets. For some uranyl oxosalt frameworks, description in terms of polymerized 2D sheets seems to be more appropriate and clear. Fig. 62a shows the crystal structure of $UO_2MoO_4(H_2O)_2$ projected along the b axis. The uranyl molybdate framework in this compound can be splitted into alternating **A** and **B** sheets shown in Figs. 62c and d, respectively. The sheets possess the same topology (described by the graph shown in Fig. 62b), but different geometrical configurations. The adjacent sheets connect by corner sharing of polyhedra.

Fig. 63 shows the construction of the topologically complex uranyl molybdate framework in $A_2[(UO_2)_3(MoO_4)_4]$ (A = Na, K). It can be described as consisting of uranyl molybdate sheets having the **l2/3k** topology (Fig. 63a, b) that are cross-linked by additional UO_7 bipyramids and MoO_4 tetrahedra. The linkage involves formation of (non-chiral) channels running along the b axis (Fig. 63d).

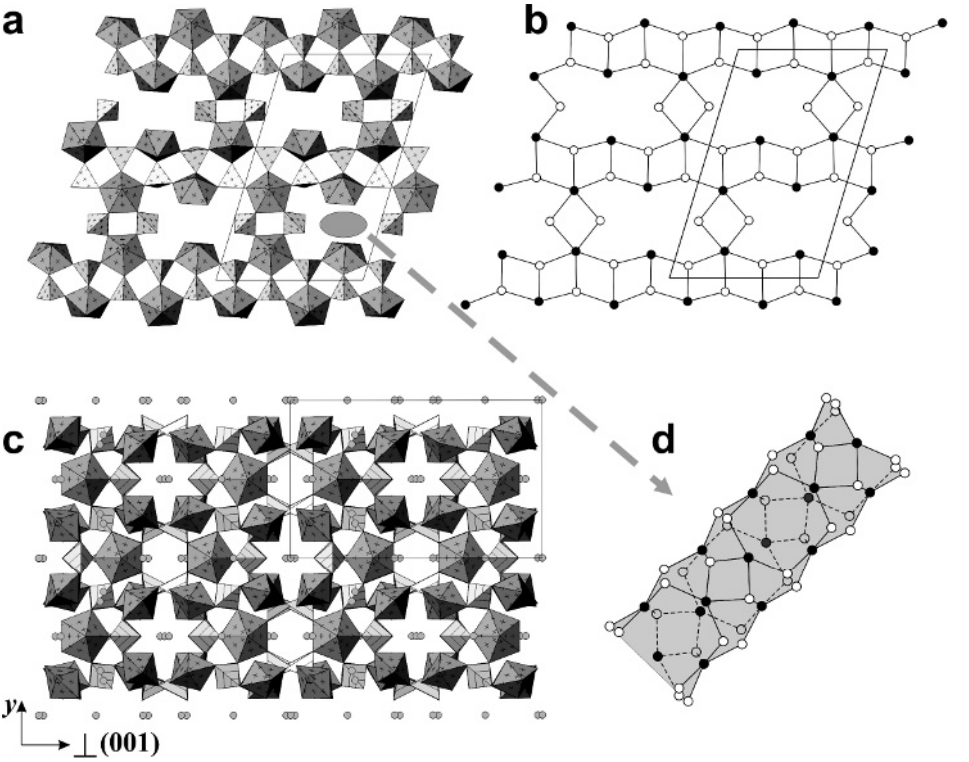

Fig. 63. Uranyl molybdate framework in $A_2[(UO_2)_3(MoO_4)_4]$ (A = Na, K) can be described as consisting of uranyl molybdate sheets having the **l2/3k** topology (a, b) cross-linked by additional UO_7 bipyramids and MoO_4 tetrahedra (c). The linkage involves formation of (non-chiral) channels running along the *b* axis (d).

3.4. Structural units with edge-sharing between actinyl polyhedra and SO_4 tetrahedra

Edge sharing between actinyl polyhedra and tetrahedral oxoanions has been frequently observed in uranyl sulfates. The 0D and 1D uranyl sulfate units consisting of edge-sharing subunits are shown in Fig. 64 (see Table 10 for the list of compounds). Their topological structures can be conveniently described using a graphical approach with double links between the vertices symbolizing edge sharing of coordination polyhedra.

The simplest unit is a UO_8 hexagonal bipyramid that shares three equatorial edges with three adjacent SO_4 tetrahedra so that a $[UO_2(SO_4)_3]^{4-}$ complex is formed (Fig. 64a). Figs. 64c and d depict two isochemical clusters with the formula $[(UO_2)_2(SO_4)_6]^{8-}$. The clusters consist of two UO_7 pentagonal bipyramids each that share one equatorial edge and three corners with the

Table 10. Crystallographic data for actinyl compounds based on structural units with edge sharing between actinyl coordination polyhedra and TO_4 tetrahedra

Fig.	Chemical formula	sp. gr.	*a* [Å] / α [°]	*b* [Å] / β [°]	*c* [Å] / γ [°]	ref
64a	$[N_2C_5H_{14}]_2[UO_2(SO_4)_3]$	*C*2/*c*	14.498 / 90	11.911 / 110.48	13.016 / 90	153
64b	$Na_{10}[UO_2(SO_4)_4](SO_4)_2(H_2O)_3$	*Cc*	9.307 / 90	28.706 / 93.40	9.615 / 90	236
	$KNa_5[UO_2(SO_4)_4](H_2O)$	*C*2/*c*	16.917 / 90	5.600 / 90.44	35.340 / 90	237
	$Na_6[UO_2(SO_4)_4](H_2O)_2$	$P\bar{1}$	5.550 / 91.48	11.246 / 92.58	14.256 / 97.59	238
64c	$K_4[UO_2(SO_4)_3]$	*Pnma*	13.053	23.200	9.379	235
64d	$[N_4C_6H_{22}]_2[(UO_2)_2(SO_4)_6](H_2O)$	$P\bar{1}$	11.232 / 88.41	13.214 / 74.59	14.352 / 66.55	156
	$[N_2C_4H_{14}]_2[UO_2(SO_4)_3](H_2O)_2$	$P\bar{1}$	8.458 / 100.82	10.283 / 96.39	15.294 / 112.52	158
	$[Co(NH_3)_6](H_8O_3)[NpO_2(SO_4)_3]$	*Pbca*	19.437	14.595	12.744	239
64e	$[N_2C_{10}H_{10}][UO_2(SO_4)_2](H_2O)$	$P\bar{1}$	6.951 / 79.20	7.710 / 80.14	15.920 / 80.97	156
	$[N_2C_6H_{18}][UO_2(SO_4)_2](H_2O)$	$P2_1/m$	10.139 / 90	6.954 / 99.29	11.723 / 90	158
	$[C_6H_{16}N_2][UO_2(SO_4)_2](H_2O)$	$P\bar{1}$	6.781 / 76.75	10.064 / 75.61	12.975 / 74.40	244
	$[Co(NH_3)_6][NpO_2(SO_4)_2](H_2O)_2$	*Pnma*	17.480	7.143	12.515	238
64f	$[C_4H_{12}N][UO_2(NO_3)(SO_4)]$	*C*2/*m*	21.106 / 90	6.935 / 97.55	8.428 / 90	240
	$[C_4H_{13}N][(UO_2)(SeO_4)(NO_3)]$	*C*2/*m*	21.244 / 90	7.109 / 97.69	8.658 / 90	133
65a	$[C_{10}H_{28}N_4][(UO_2)_2(SO_4)_4]$	*Pbca*	9.583	15.606	18.121	241
65a	$[N_4C_6H_{22}][UO_2(SO_4)_2]_2$	*Pbca*	9.377	12.952	18.907	169
65c	$[N_2C_4H_{14}][UO_2(SO_4)_2]$	$P2_12_12_1$	9.332	9.774	13.890	153
66c	$[N_2C_5H_{16}][UO_2(SO_4)_2]$	$P2_1/c$	7.983 / 90	19.846 / 111.66	9.787 / 90	158
66a	$Cs_2[NpO_2(SO_4)_2]$	$P2_1/n$	10.760 / 90	9.012 / 110.77	11.829 / 90	242

Table 10. Crystallographic data for actinyl compounds based on structural units with edge sharing between actinyl coordination polyhedra and TO_4 tetrahedra (continued)

Fig.	Chemical formula	sp. gr.	*a* [Å] / α [°]	*b* [Å] / β [°]	*c* [Å] / γ [°]	ref
	$[C_7H_{20}N_2][(UO_2)_2(SO_4)_3(H_2O)]$	$P\bar{1}$	6.786 / 88.62	8.514 / 81.64	19.044 / 84.86	243

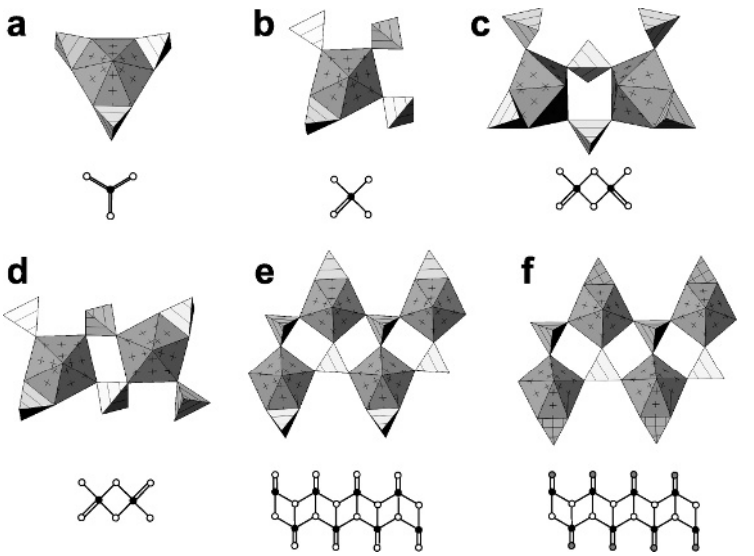

Fig. 64. The 0D and 1D uranyl sulfate units consisting of edge-sharing subunits and their graphs. See text for details.

adjacent SO_4 tetrahedra. Two of these tetrahedra are bidentate and link the UO_7 bipyramids into the cluster. The clusters shown in Figs. 64c and d differ in the mutual positions of the edge-sharing tetrahedra relative to the uranyl bipyramids and thus can be considered as structural isomers.

Fig. 64e shows a $[UO_2(SO_4)_2]^{2-}$ chain that can be considered as based upon the **c1/1b** chain topology with each black vertex having a double link to the additional white vertex. Replacement of the latter by a grey vertex results in a chain shown in Fig. 64f. Here grey vertices correspond to the NO_3^- triangular groups that share edges with the UO_7 pentagonal bipyramids.

Fig. 65 shows two examples of the 2D units with UO_7 bipyramids sharing edges with SO_4 tetrahedra. Each UO_7 bipyramid shares one edge and three corners with the sulfate tetrahedra. In turn, the sulfate tetrahedra are of two types. Tetrahedra of the first type are bidentate and share two of their corners with UO_7 bipyramids. Tetrahedra of the second type are again bidentate but they share one edge and one corner each with the uranyl polyhedra.

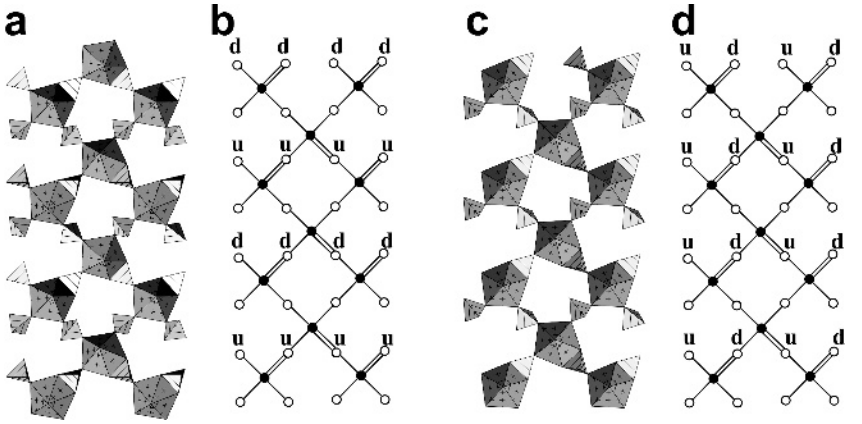

Fig. 65. To the description of geometrical isomerism of the $[(UO_2)(SO_4)_2]^{2-}$ sheets with edge-sharing between U polyhedra and S tetrahedra. See text for details.

Thus, one corner remains non-shared and can be oriented either up or down relative to the plane of the sheet. The possibility of different orientations induces the appearance of orientational geometrical isomers shown in Fig. 65. By analogy with the geometrical isomers described above, the isomers under discussion can be described using **u** and **d** symbols of tetrahedra orientation. The isomer shown in Figs. 65a and b can be described as a (**u**)(**d**) isomer (its orientation matrix has the 1×2 dimensions), whereas the isomer shown in Figs. 65c and d is a (**ud**) isomer (matrix dimensions are 2×1). The same type of isomerism is found for the actinyl sulfate sheets shown in Fig. 66.

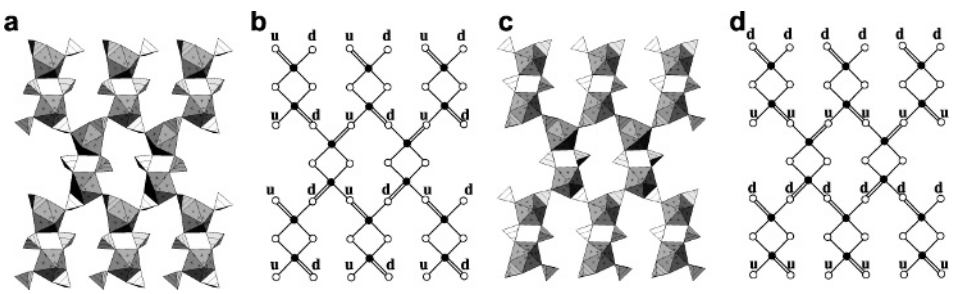

Fig. 66. To the description of geometrical isomerism of the $[(AnO_2)(SO_4)_2]^{2-}$ sheets with edge-sharing between An polyhedra and S tetrahedra. See text for details.

Fig. 67 shows a uranyl sulfate sheet constructed by the alternation of the **c1/1b** chains and the chains shown in Fig. 67d. The chains are parallel to each other and are linked by sharing corners.

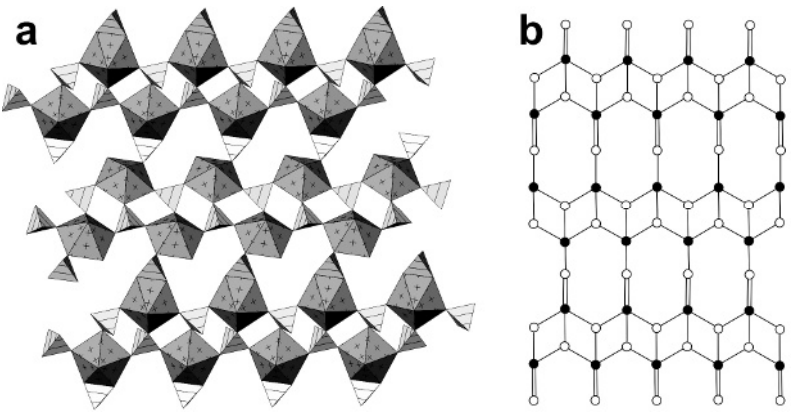

Fig. 67. The uranyl sulfate sheet in $[C_7H_{20}N_2][(UO_2)_2(SO_4)_3(H_2O)]$ (a) and its 2D graph (b).

3.5. Structural units with corner-sharing between actinyl polyhedra

This group of compounds includes those containing corner-sharing actinyl polyhedra (Table 11). It is important to remember that coordination polyhedra of actinides in high oxidation states possess two different types of anions: (i) apical anions that are part of the actinyl $[An^{m+}O_2]^{m-4+}$ ions and (ii) equatorial anions. If an apical anion of one polyhedron is shared with the other, we deal with the so-called "cation-cation" interactions.

Fig. 68a shows the $[(UO_2)_2O(MoO_4)_4]^{6-}$ chain observed in the structures of $A_6[(UO_2)_2O(MoO_4)_4]$ (A = Na, K, Rb). The chain contains a dimer of uranyl pentagonal bipyramids that share a common O atom. The bridging O_{br} atom only bonds to two U^{6+} cations; thus the U–O_{br} bond-length is, as a rule, shorter than usual (for example, in Na compound it equals 2.1142(4) Å). The dimers, with composition $[(UO_2)O_4O(UO_2)O_4]^{14-}$, are linked into chains by sharing corners with MoO_4 tetrahedra. The black-and-white graph of the uranyl molybdate chain is shown in Fig. 68b. Note that, because of the linkage between U polyhedra, the black vertices symbolizing U centers should be linked together by additional edges.

A whole range of 2D topologies with corner sharing between adjacent uranyl polyhedra is observed in F-containing uranyl sulfates. In the structure of $Rb[UO_2(SO_4)F]$, each uranyl cation is coordinated in the equatorial plane by three O atoms of the sulfate groups and two F^- anions. The F^- anions are bridging between two U^{6+} cations which results in formation of chains of corner-sharing uranyl pentagonal bipyramids. The chains are further interlinked into a 2D sheet by sharing corners with adjacent SO_4 tetrahedra (Fig. 69a). Fig. 69b shows a 2D black-and-white graph reflecting the topology of the uranyl

Table 11. Crystallographic data for actinyl compounds with corner-sharing actinyl coordination polyhedra

name	chemical formula	sp. gr.	*a* [Å] / α [°]	*b* [Å] / β [°]	*c* [Å] / γ [°]	ref
	$Na_6[(UO_2)_2O(MoO_4)_4]$	$P\bar{1}$	7.637 / 72.33	8.164 / 79.36	8.746 / 65.80	130
	$K_6[(UO_2)_2O(MoO_4)_4]$	$P\bar{1}$	7.828 / 83.89	7.830 / 73.13	10.302 / 80.34	130
	$Rb_6[(UO_2)_2O(MoO_4)_4]$	$P\bar{1}$	10.157 / 76.92	10.182 / 76.55	13.113 / 65.24	129
	$Rb[UO_2(SO_4)F]$	$Pca2_1$	25.393	6.735	11.496	245
USFO-1	$[N_2C_4H_{14}][UO_2F(SO_4)]_2$	$P2_1/c$	6.775 / 90	8.409 / 93.25	14.149 / 90	246
USFO-4	$[N_2C_3H_{12}][UO_2F(SO_4)]_2(H_2O)$	*Pnma*	13.578	14.618	8.117	119
USFO-5	$[N_2C_5H_{14}][UO_2F(H_2O)(SO_4)]_2$	$P2_1/n$	8.435 / 90	15.558 / 96.67	14.844 / 90	119
USFO-6	$[N_2C_6H_{18}]_2[UO_2F(SO_4)]_4(H_2O)$	$P\bar{1}$	10.883 / 75.66	10.939 / 73.61	16.533 / 89.77	119
USFO-7	$[N_2C_3H_{12}][UO_2F(SO_4)]_2(H_2O)$	$P2_1$	6.775 / 90	8.159 / 94.56	14.366 / 90	119
	β-UO_2SO_4	$P2_1/c$	6.760 / 90	5.711 / 102.91	12.824 / 90	247
	$(NpO_2)_2(SO_4)(H_2O)_2$	$P2_1/c$	10.527 / 90	5.792 / 98.13	13.350 / 90	248
	$(NpO_2)_2(SO_4)(H_2O)$	*Pnma*	15.790	6.932	6.714	249

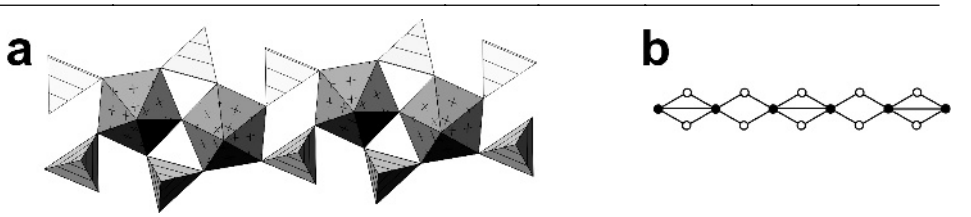

Fig. 68. The $[(UO_2)_2O(MoO_4)_4]^{6-}$ chain observed in the structures of $A_6[(UO_2)_2O(MoO_4)_4]$ (A = Na, K, Rb) (a) and its graph (b).

sulfate sheet. This graph can again be produced from the more symmetrical high-connectivity graph shown in Fig. 69c. The latter graph consists of 3-connected white and 12-connected black vertices and can be denoted as {3.12.12}. The {3.12.12} graph is a basic graph because it can be used to

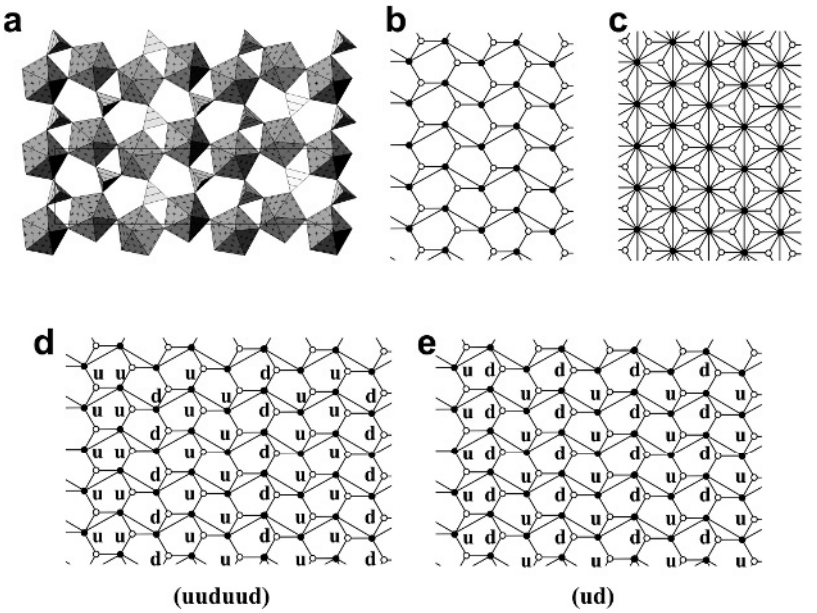

Fig. 69. The uranyl fluoride sulfate sheet in the structure of $Rb[UO_2(SO_4)F]$ (a). Its idealized graph (b) can be obtained from {3.12.12} basic graph (c) by deleting some of its corners and edges. The presence of tridentate tetrahedra results in appearance of geometrical isomers (d, e: see text for details).

produce a number of structural topologies as shown below. Note that white vertices in the graph shown in Fig. 69b correspond to tridentate sulfate tetrahedra that may be turned either up or down relative to the plane of the sheet. The presence of tridentate tetrahedra indicates that orientational geometrical isomerism is possible. This is what indeed takes place in the structures of F-bearing uranyl sulfates. Figs. 38d and e show two black-and-white graphs with **d** and **u** symbols denoting orientation of tetrahedra. In the structure of $Rb[UO_2(SO_4)F]$, the sequence of orientations can be described as (**uuduud**) [note that it cannot be reduced to (**uud**) because graph periodicity along the chain of black vertices is 2]. In the structures of USFO-1 and USFO-7 (Table 11), the up- and down-orientations alternate and the sequence can be written as (**ud**).

Fig. 70 shows 2D sheets and their topological description for other uranyl sulfates with F^- anions. In the structures of USFO-4 and USFO-5, uranyl pentagonal bipyramids again share corners to form chains that are further interlinked by sulfate tetrahedra. In USFO-4 (Fig. 70a), the sulfate tetrahedra are tridentate and the 2D graph (Fig. 70d) corresponds to structural topologies observed in some phosphate minerals [172].

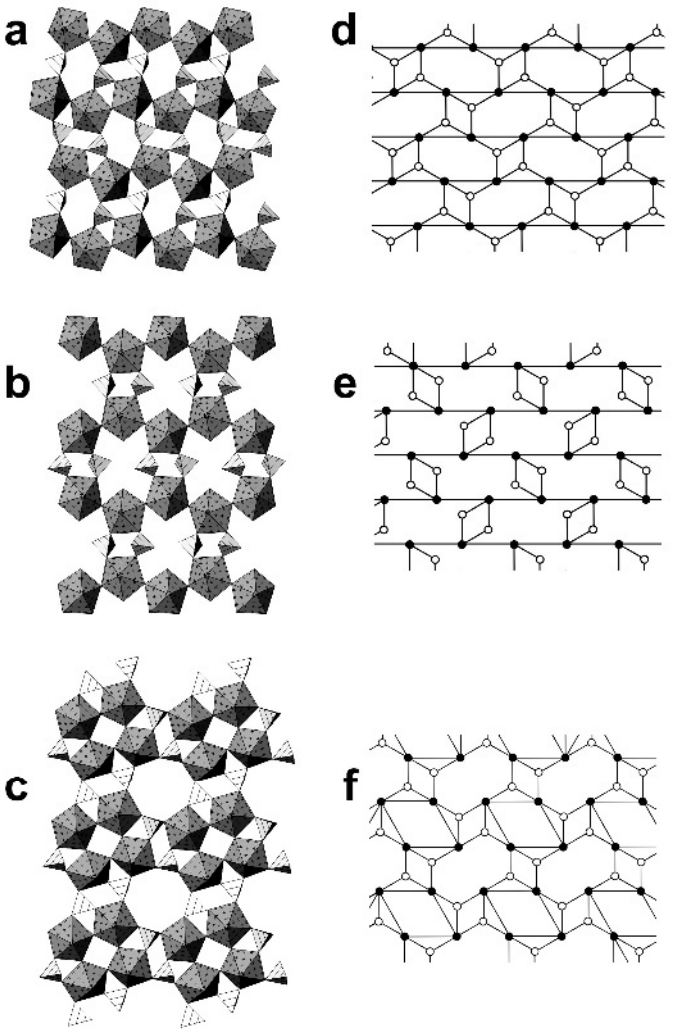

Fig. 70. 2D sheets and their graphs for some uranyl sulfates with F^- anions. See text for details.

In USFO-5 (Fig. 70b), sulfate tetrahedra are bidentate. The 2D sheet in the structure of USFO-6 (Fig. 70c) is remarkable in that it contains tetramers of corner-sharing uranyl bipyramids linked by tridentate sulfate tetrahedra. Note that the graphs shown in Figs. 70d, e and f are derivatives of the basic {3.12.12} graph (Fig. 69c).

In the structure of β-UO_2SO_4, linkage of uranyl pentagonal bipyramids involves sharing of apical O atoms, i.e. those of uranyl cations. In these cation-

cation interactions, the O atom of one uranyl ion is an equatorial ligand of another uranyl ion. The uranyl bipyramids form chains running along [010] which are interlinked into 3D framework by sulfate tetrahedra (Fig. 71).

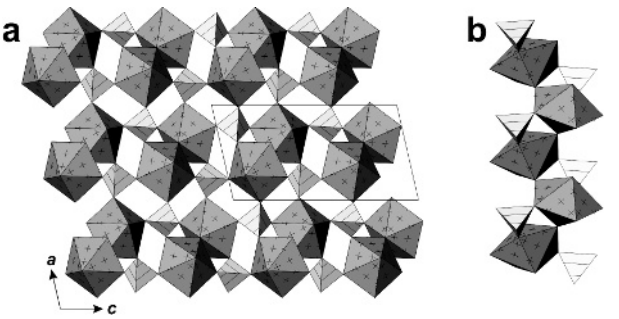

Fig. 71. Framework of UO_7 bipyramids and SO_4 tetrahedra in the structure of β-UO_2SO_4 (a) consists of chains of U polyhedra (b).

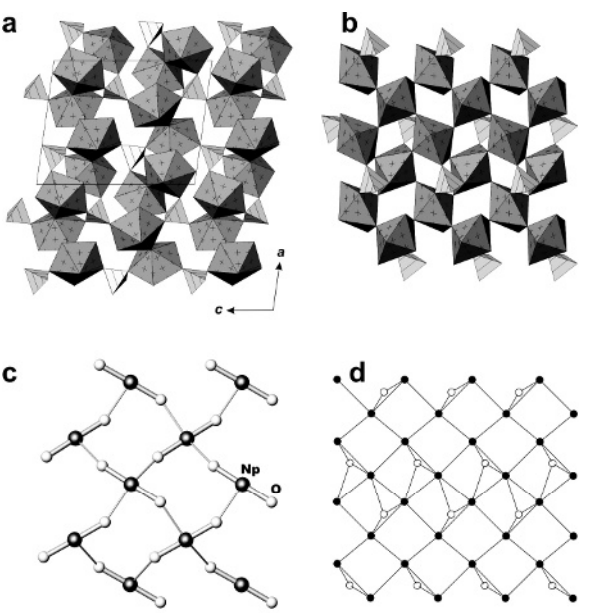

Fig. 72. The neptunyl sulfate framework in structure of $(Np^{5+}O_2)_2(SO_4)(H_2O)_2$ (a) is based upon 2D sheets shown in (b) (arrangement of neptunyl ions in the sheet is depicted in (c)), and black-and-white graph of the sheet (d).

The structure of $(Np^{5+}O_2)_2(SO_4)(H_2O)_2$ (Fig. 72) is based upon 3D framework of neptunyl and sulfate polyhedra. The $Np^{5+}O_7$ bipyramids are involved in cation-cation interactions to produce the 2D sheets shown in Fig. 72b (the arrangement of the neptunyl ions in the sheet is depicted in Fig. 72c).

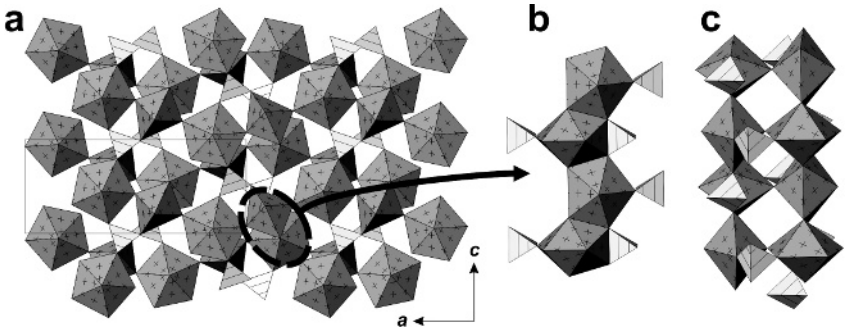

Fig. 73. The structure of $(Np^{5+}O_2)_2(SO_4)(H_2O)$ (a) is based upon chains that can be considered as elements of the uranophane anion-topology (b) linked into pairs (c).

The sheets are parallel to (001) and are linked together by sulfate tetrahedra. The black-and-white graph showing the topology of the neptunyl sheet and the relative position of sulfate tetrahedra is shown in Fig. 72d. Note that this graph can also be obtained from the basic {3.12.12} graph.

The structure of $(Np^{5+}O_2)_2(SO_4)(H_2O)$ (Fig. 73) contains two symmetrically independent Np^{5+} cations in sevenfold and eightfold coordinations to O atoms. The neptunyl polyhedra share edges to produce chains similar to those observed in the structure of $Cs[NpO_2(CrO_4)](H_2O)_2$ and which can be considered as elements of the uranophane anion-topology (see above). The chains are linked by cation-cation interactions between the neptunyl ions, and through the sharing of vertices between neptunyl polyhedra and sulfate tetrahedra to form a 3D framework.

4. Flexibility of structural units with corner-sharing UO_7 pentagonal bipyramids and TO_4 tetrahedra (T = S, Cr, Se, Mo)

The structural diversity of structural units with corner-sharing UO_7 pentagonal bipyramids and TO_4 tetrahedra (T = S, Cr, Se, Mo) permits a statistical analysis of their geometry and flexibility in terms of the T-O bond lengths and T-O_{br}-U bond angles (O_{br} is an oxygen atom bridging between the adjacent T^{6+} and U^{6+} coordination centers). Similar analysis for T = S, Cr and Mo was performed by Krivovichev [250] and the present analysis includes also uranyl selenate units that have received much attention recently. Table 12 provides average T-O bond lengths for bridging (O_{br}) and terminal (O_t) atoms of TO_4 tetrahedra. It is apparent that the T-O_{br} bonds are usually longer than the T-O_t bonds.

The distributions of the U-O_{br}-T bond angles for different T elements are shown in Fig. 74. It is of interest that the bond angle distributions for T = S, Cr and Se are much more sharp than one for T = Mo.

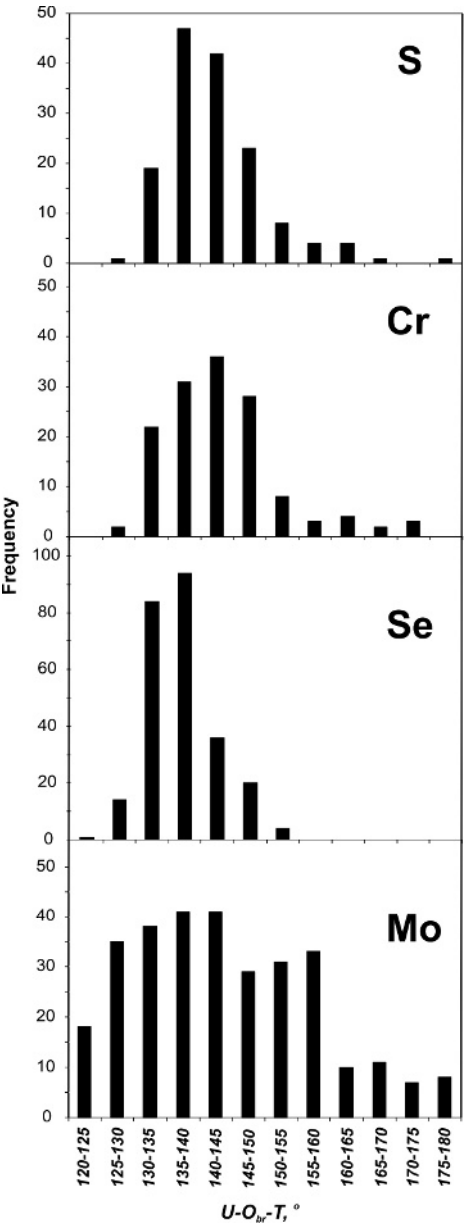

Fig. 74. The distributions of the U-O_{br}-*T* bond angles for structural units composed of UO_7 bipyramids sharing corners with TO_4 tetrahedra.

The most plausible explanation for this observation is that the Mo^{6+}-O bonds are longer than the *T*-O bond lengths for *T* = S, Cr and Se which allows more

flexibility for the uranyl molybdate units than for the uranyl sulfate, chromate or selenate units. Indeed, the great structural diversity of 3D framework topologies are typical for uranyl molybdates, whereas framework structures are quite rare for other hexavalent T^{6+} cations in uranyl compounds. This also shows that the uranyl molybdates can potentially occur in a wider range of topologies than observed previously. Since uranyl molybdates are insoluble and stable under atmospheric conditions, they could be excellent candidates for construction of materials based upon flexible nanostructures of different dimensionalities.

5. Concluding remarks

This chapter demonstrates a wide structural diversity of actinyl compounds containing hexavalent cations of S, Cr, Se, Mo, and W. In conclusion, it is worthy to mention several factors that control such diversity:

(i) coordination of cations: both actinide and hexavalent cations may have different coordinations (e.g., Mo^{6+} cations occur in tetrahedral, trigonal bipyramidal, tetragonal pyramidal, and octahedral coordinations);

(ii) mode of linkage of coordination polyhedra: all combinations of corner and edge sharing between polyhedra are allowed; of special interest is the high frequency of edge sharing between UO_7 pentagonal bipyramids and SO_4 tetrahedra (see section 3.4); actinyl polyhedra polymerize by sharing either equatorial anions or even apical anions (cation-cation interactions);

(iii) high flexibility of structural units consisting of actinyl polyhedra and TO_4 tetrahedra which can be analysed by means of statistical investigations of U-O_{br}-T bond angles; among different units, uranyl molybdates show the widest variation of the angular characteristics, in agreement with their strong tendency to formation framework structures.

SVK had been supported in this work by grants from RFBR (), FCNTP () and RNP progam of the Russian Ministry of Science and Education ().

References

1. R.J. Finch and T. Murakami, Rev. Mineral. 38 (1999) 91.
2. E.C. Buck, D.J. Wronkiewicz, P.A. Finn and J.K. Bates, J. Nucl. Mater. 249 (1997) 70.
3. N.L. Misra, K.L. Chawla, V. Venugopal, N.C. Jayadevan and D.D. Sood, J. Nucl. Mater. 226 (1995) 120.
4. R.A. Penneman, R.G. Haire and M.H. Lloyd, ACS Symp. Ser. 117, edited by J.D. Navratil and W.W. Schulz, pp. 571-581. Washington, DC: American Chemical Society.
5. E.C. Buck, N.R. Brown and N.L. Dietz, Env. Sci. Technol. 30 (1996) 81.
6. Y. Roh, S.Y. Lee, M.P. Elles and K.S. Cho, J. Env. Sci. Health A35 (2000) 1043.
7. D.J. Wronkiewicz, J.K. Bates, T.J. Gerding, E. Veleckis and B.S. Tani, J. Nucl. Mater. 190 (1992) 107.
8. D.J. Wronkiewicz, J.K. Bates, S.F. Wolf and E.C. Buck, J. Nucl. Mater. 238 (1996) 78.

9. S. Sharmasarkar and G.F. Vance, J. Env. Qual. 31 (2002) 1516.
10. L.L. Barton, K. Choudhurty, B.M. Thomason, K. Steenhoudt and A.R. Groffman, Rad. Waste Manag. Env. Restor. 20 (1996) 141.
11. E.R. Landa, J. Radioanal. Nucl. Chem. 255 (2003) 559.
12. F. Chen, P.C. Burns and R.C. Ewing, J. Nucl. Mater. 275 (1999) 81.
13. P.C. Burns, R.C. Ewing and M.L. Miller, J. Nucl. Mater. 245 (1997) 1.
14. L.M. Kovba and V.K. Trunov, Radiokhimiya 7 (1965) 316.
15. V.K. Trunov, O.N. Rozanova and L.M. Kovba, Zh. Neorg. Khim. 10 (1965) 2576.
16. L.M. Kovba, O.N. Rozanova and V.K. Trunov, Radiokhimiya 19 (1977) 260.
17. N.D. Zakharov, M.A. Gribeluk, B.K. Vainstein, O.N. Rozanova, K. Uchida and S. Horiuchi, Acta Crystallogr. B39 (1983) 575.
18. N.D. Zakharov, M.A. Gribelyuk, B.K. Vainshtein, L.M. Kovba and S. Horiuchi, Acta Crystallogr. A44 (1988) 821.
19. L.M. Kovba, In: Problemy Kristallokhimii (Problems of Crystal Chemistry), ed. by M.A. Porai-Koshitz, 1987. P. 120-147. Moscow, Nauka, 1988.
20. M. Sundberg and V. Tabachenko, Microsc. Microanal. Microstruct. 1 (1990) 373.
21. M. Sundberg and B.-O. Marinder, J. Solid State Chem. 121 (1996) 167.
22. P. Pailleret, C. R. Hebd. S. Acad. Sci. Ser. C 265 (1967) 85.
23. L.M. Kovba, Radiokhimiya 13 (1971) 909.
24. T.L. Cremers, P.G. Eller, R.A. Penneman and C.C. Herrick, Acta Crystallogr. C39 (1983) 1163.
25. V.V. Tabachenko, O.G. D'yachenko and M.R. Sundberg, Eur. J. Solid State Inorg. Chem. 32 (1995) 1137.
26. P.C. Burns, R.C. Ewing and F.C. Hawthorne, Can. Mineral. 35 (1997) 1551.
27. V.N. Serezhkin, L.M. Kovba and V.K. Trunov, Kristallogr. 18 (1973) 514.
28. V.N. Serezhkin, L.M. Kovba and V.K. Trunov, Kristallogr. 19 (1974) 379.
29. V.N. Serezhkin, L.M. Kovba and V.K. Trunov, Kristallogr. 18 (1973) 961.
30. V.N. Serezhkin, L.M. Kovba and V.K. Trunov, Zh. Strukt. Khim. 14 (1973) 742.
31. O.G. D'yachenko, V.V. Tabachenko,R. Tali, L.M. Kovba, B.O. Marinder and M.R. Sundberg, Acta Crystallogr. B52 (1996) 961.
32. V.N. Serezhkin, L.M. Kovba and V.K. Trunov, Radiokhimiya 16 (1974) 231.
33. S.V. Krivovichev and P.C. Burns, Dokl. Phys. 49 (2004) 76.
34. O.N. Rozanova, Z.Ya. Pol'shchikova and L.M. Kovba, Radiokhimiya 20 (1978) 125.
35. J. Thoret, Rev. Chim. Miner. 11 (1974) 237.
36. J. Thoret, A. Rimsky and W. Freundlich, C. R. Hebd. S. Acad. Sci. Ser. C 270 (1970) 2045.
37. S. Launay and A. Rimsky, Acta Crystallogr. B36 (1980) 910.
38. N.N. Bushuev and V.K. Trunov, Kristallogr. 21 (1976) 69.
39. T.L. Cremers, P.G. Eller and R.A. Penneman, Acta Crystallogr. C39 (1983) 1165.
40. E.M. Larson, P.G. Eller, T.L. Cremers, R.A. Penneman and C.C. Herrick, Acta Crystallogr. C45 (1989) 1669.
41. M. Huyghe, M.-R. Lee, M. Quarton and F. Robert, Acta Crystallogr. C47 (1991) 244.
42. M. Huyghe, M.-R. Lee, M. Quarton and F. Robert, Acta Crystallogr. C47 (1991) 1797.
43. M. Huyghe, M.-R. Lee, S. Jaulmes and M. Quarton, Acta Crystallogr. C49 (1993) 950.
44. S. Launay, S. Jaulmes, F. Lucas and M. Quarton, J. Solid State Chem. 136 (1998) 199.
45. W. Freundlich and M. Pages, C. R. Hebd. S. Acad. Sci. Ser. C 269 (1969) 392.
46. M. Pages and W. Freundlich, J. Inorg. Nucl. Chem. 34 (1972) 2797.
47. W. Freundlich and M. Pages, C. R. Hebd. S. Acad. Sci. Ser. C 273 (1971) 44.
48. PDF 34-0008.
49. A. Tabuteau and M. Pages, J. Inorg. Nucl. Chem. 42 (1980) 401.
50. A. Tabuteau, M. Pages and W. Freundlich, Mater. Res. Bull. 7 (1972) 691.

51. A. Tabuteau, M. Pages, J. Solid State Chem. 26 (1978) 153.
52. A. Tabuteau, T. Thevenin and M. Pages, Rev. Chim. Miner. 19 (1982) 173.
53. O. Sedello and H. Müller-Buschbaum, Z. Naturforsch. 51b (1996) 450.
54. J.H. Burns and R.D. Baybarz, Inorg. Chem. 11 (1972) 2233.
55. G. Lundgren, Arkiv foer Kemi 2 (1950) 535.
56. E.G. Arutyunyan, M.A. Porai-Koshits and A.K. Molodkin, Zh. Strukt. Khim. 7 (1966) 733.
57. J. Habash, and A.J. Smith, Acta Crystallogr. C39 (1983) 413.
58. N.C. Jayadevan, K.D. Singh Mudher and D.M. Chackraburtty, Z. Kristallogr. 161 (1982) 7.
59. J. Habash and A.J. Smith, J. Crystallogr. Spectrosc. Res. 22 (1992) 21.
60. I.A. Charushnikova, N.N. Krot and Z.A. Starikova, Radiochem. 41 (1999) 108.
61. K.D. Singh Mudher and K. Krishnan, J. Alloys Compds. 313 (2000) 65.
62. I.A. Charushnikova, N.N. Krot and Z.A. Starikova, Radiokhimiya 42 (2000) 36.
63. I.A. Charushnikova, N.N. Krot and Z.A. Starikova, Radiochem. 42 (2000) 434.
64. I.A. Charushnikova, N.N. Krot and Z.A. Starikova, Radiochem. 42 (2000) 42.
65. P. Kierkegaard, Acta Chem. Scand. 10 (1956) 599.
66. G. Lundgren, Arkiv foer Kemi 4 (1952) 421.
67. G. Lundgren, Arkiv foer Kemi 5 (1952) 349.
68. J.I. Bullock, M.F.C. Ladd, D.C. Povey and A.E. Storey, Inorg. Chim. Acta 43 (1980) 101.
69. D.W. Wester, Inorg. Chem. 21 (1982) 3382.
70. P.N. Iyer and N.K. Kulkarni, J. Alloys Compds. 217 (1995) 253.
71. N.V. Podberezskaya and S.V. Borisov, Zh. Strukt. Khim., 17 (1976) 186.
72. E. Gebert Sherry, J. Solid State Chem. 19 (1976) 271.
73. I.S. Ahmed Farag, M.A. El Kordy and N.A. Ahmed, Z. Kristallogr. 155 (1981) 165.
74. H. Bartl and E. Rodek, Z. Kristallogr. 162 (1983) 13.
75. L. Hiltunen and L. Niinisto, Cryst. Struct. Commun. 5 (1976) 561.
76. H.-U. Hummel, E. Fischer, T. Fischer, P. Joerg and G. Pezzei, Z. Anorg. Allg. Chem. 619 (1993) 805.
77. P.C. Junk, C.J. Kepert, B.W. Skelton and A.H. White, Austr. J. Chem. 52 (1999) 601.
78. M.S. Wickleder, Z. Anorg. Allg. Chem. 625 (1999) 1548.
79. B. Eriksson, L.O. Larsson, L. Niinisto and U. Skoglund, Inorg. Chem. 13 (1974) 290.
80. P. Bukovec and L. Golic, Docum. Chem. Yugosl. Vest. Slov. Kem. Dr. 22 (1975) 19.
81. S. Jasty, P.D. Robinson and V.M. Malhotra, Phys. Rev. B43 (1991) 13215.
82. L.D. Iskhakova, Z.A. Starikova and V.K. Trunov, Koord. Khim. 7 (1981) 1713.
83. O. Lindgren, Acta Chem. Scand. A31 (1977) 453.
84. D.B. McWhan and G. Lundgren, Inorg. Chem. 5 (1966) 284.
85. O. Lindgren, Acta Chem. Scand. A31 (1977) 163.
86. S.V. Krivovichev, Crystallogr. Rev. 10 (2004) 185.
87. M. Hansson, Acta Chem. Scand. 27 (1973) 2455.
88. M.E. Brahimi, J, Durand and L. Cot, Eur. J. Solid State Inorg. Chem. 25 (1988) 185.
89. G. Lundgren, Arkiv foer Kemi 10 (1956) 183.
90. M.L. Miller, R.J. Finch, P.C. Burns and R.C. Ewing, J. Mater. Res. 11 (1996) 3048.
91. P.C. Burns, M.L. Miller and R.C. Ewing, Can. Mineral. 34 (1996) 845.
92. P.C. Burns, Rev. Mineral. 38 (1999) 23.
93. M.S. Grigor'ev, N.A. Baturin, T.E. Plotnikova, A.M. Fedoseev and N.A. Budantseva, Radiokhimiya 37 (1995) 19.
94. M.-R. Lee and S. Jaulmes, J. Solid State Chem. 67 (1987) 364.
95. R.E. Marsh, J. Solid State Chem. 73 (1988) 577.
96. S.V. Krivovichev and P.C. Burns, Inorg. Chem. 41 (2002) 4108.
97. S.V. Krivovichev and P.C. Burns, Can. Mineral. 40 (2002) 201.

98. S. Obbade, S. Yagoubi, C. Dion, M. Saadi and F. Abraham, J. Solid State Chem. 174 (2003) 19.
99. S. Obbade, C. Dion, E. Bekaert, S. Yagoubi, M. Saadi and F. Abraham, J. Solid State Chem. 172 (2003) 305.
100. S.V. Krivovichev and P.C. Burns, Solid State Sci. 5 (2003) 373.
101. R.E. Sykora and T.E. Albrecht-Schmitt, J. Solid State Chem. 177 (2004) 3729.
102. S.V. Krivovichev and P.C. Burns, Can. Mineral. 41 (2003) 1455.
103. S.V. Krivovichev and P.C. Burns, Can. Mineral. 41 (2003) 1225.
104. S.V. Krivovichev and P.C. Burns, Can. Mineral. 38 (2000) 717.
105. R.K. Rastsvetaeva, A.V. Barinova, G.A. Sidorenko and D.Yu. Pushcharovskii, Dokl. Akad. Nauk 373 (2000) 202.
106. S.V. Krivovichev and P.C. Burns, Can. Mineral. 38 (2000) 847.
107. S.V. Krivovichev and P.C. Burns, Can. Mineral. 40 (2002) 1571.
108. V.N. Serezhkin, V.F. Chuvaev, L.M. Kovba and V.K. Trunov, Dokl. Akad. Nauk 210 (2000) 873.
109. K. Mereiter, Tscherm. Mineral. Petrogr. Mitt. 30 (1982) 47.
110. P.S. Halasyamani, R.J. Francis, S.M. Walker and D. O'Hare, Inorg. Chem. 38 (1999) 271.
111. R. Tali, V.V. Tabachenko, L.M. Kovba and L.N. Dem'yanets, Zh. Neorg. Khim. 39 (1994) 1752.
112. V.I. Spitsyn, L.M. Kovba, V.V. Tabachenko, N.V. Tabachenko and Yu.N. Mikhailov, Izv. AN SSSR, Ser. Khim. 1982 (1982) 807.
113. P.C. Burns, K.M. Deely and L.A. Hayden, Can. Mineral. 41 (2003) 687.
114. R. Vochten, L. van Haverbeke, K. van Springel, N. Blaton and O.M. Peeters, Can. Mineral. 33 (1995) 1091.
115. J. Brugger, P.C. Burns and N. Meisser, Amer. Mineral. 88 (2003) 676.
116. S. Obbade, S. Yagoubi, C. Dion, M. Saadi and F. Abraham, J. Solid State Chem. 177 (2004) 1681.
117. S.V. Krivovichev, unpublished.
118. M.S. Grigor'ev, N.A. Baturin, A.M. Fedoseev and N.A. Budantseva, Radiokhimiya 33 (1991) 53.
119. M.B. Doran, B.E. Cockbain and D. O'Hare, Dalton Trans., 2005 (2005) 1774.
120. V.N. Serezhkin, N.V. Boiko and V.K. Trunov, Zh. Strukt. Khim. 23 (1982) 121.
121. L.B. Serezhkina, V.K. Trunov, L.N. Kholodkovskaya and N.V. Kuchumova, Koord. Khim. 16 (1990) 1288.
122. E.V. Mit'kovskaya, Yu.N. Mikhailov, Yu.E. Gorbunova, L.B. Serezhkina and V.N. Serezhkin, Zh. Neorg. Khim. 48 (2003) 755.
123. E.S. Makarov and L.I. Anikina, Geokhimiya 1 (1963) 14.
124. M.S. Grigor'ev, A.I. Yanovskii, A.M. Fedoseev, N.A. Budantseva, Yu.T. Struchkov and N.N. Krot, Radiokhimiya 33 (1991) 17.
125. N.W. Alcock, M.M. Roberts and M.C. Chakravorti, Acta Crystallogr. B36 (1980) 687.
126. M.S. Grigor'ev, T.E. Plotnikova, N.A. Baturin, N.A. Budantseva and A.M. Fedoseev, Radiokhimiya 37 (1995) 102.
127. P.C. Burns, Can. Mineral. 39 (2001) 1139.
128. S.V. Krivovichev and J. Brugger, unpublished.
129. S.V. Krivovichev and P.C. Burns, J. Solid State Chem. 168 (2002) 245.
130. S.V. Krivovichev and P.C. Burns, Can. Mineral. 39 (2001) 197.
131. S.V. Krivovichev and P.C. Burns, Can. Mineral. 41 (2003) 707.
132. S.V. Krivovichev and P.C. Burns, Z. Kristallogr. 218 (2003) 725.
133. S.V. Krivovichev and V. Kahlenberg, Z. Anorg. Allg. Chem., in press.
134. M.B. Doran, A.J. Norquist, and D. O'Hare, Acta Crystallogr., E61 (2005) m881.

135. R.D. Rogers, A.H. Bond, W.G. Hipple, A.N. Rollins and R.F. Henry, Inorg. Chem. 30 (1991) 2671.
136. S.V. Krivovichev and P.C. Burns, Z. Kristallogr. 218 (2003) 568.
137. V.N. Serezhkin and V.K. Trunov, Kristallogr. 26 (1981) 301.
138. A. Zalkin, H. Ruben and D.H. Templeton, Inorg. Chem. 17 (1978) 3701.
139. N. van der Putten and B.O. Loopstra, Cryst. Struct. Commun. 3 (1974) 377.
140. N.P. Brandenburg and B.O. Loopstra, Cryst. Struct. Commun. 2 (1973) 243.
141. V.N. Serezhkin, M.A. Soldatkina and V.A. Efremov, Zh. Strukt. Khim. 22 (1981) 171.
142. Yu.N. Mikhailov, V.E. Mistryukov, L.B. Serezhkina, E.A. Demchenko, Yu.E. Gorbunova and V.N. Serezhkin, Russ. J. Inorg. Chem. 40 (1995) 1238.
143. L.B. Serezhkina, V.K. Trunov, Russ. J. Inorg. Chem. 34 (1989) 543.
144. A.J. Norquist, M.B. Doran, P.M. Thomas and D. O'Hare, Dalton Trans., 2003 (2003) 1168.
145. Yu.N. Mikhailov, Yu.E. Gorbunova, E.A. Demchenko, L.B. Serezhkina and V.N. Serezhkin, Russ. J. Inorg. Chem. 42 (1997) 1177.
146. H. Ruben, B. Spencer, D.H. Templeton, Inorg. Chem. 19 (1980) 776.
147. M.A. Soldatkina, V.N. Serezhkin and V.K. Trunov, Zh. Strukt. Khim. 22 (1981) 146.
148. J. Toivonen and L. Niinisto, Inorg. Chem. 22 (1983) 1557.
149. G.B. Andreev, M.Yu. Antipin, A.M. Fedoseev and N.A. Budantseva, Kristallogr. 46 (2001) 433.
150. Yu.N. Mikhailov, Yu.E. Gorbunova, E.A. Demchenko, L.B. Serezhkina and V.N. Serezhkin, Zh. Neorg. Khim. 43 (1998) 971.
151. V.N. Serezhkin, M.A. Soldatkina, V.A. Efremov and V.K. Trunov, Koord. Khim. 7 (1981) 629.
152. M.B. Doran, B.E. Cockbain, A.J. Norquist and D. O'Hare, Dalton Trans., 2004 (2004) 3810.
153. M.B. Doran, A.J. Norquist, and D. O'Hare, Inorg. Chem., 42 (2003) 6989.
154. P.M. Thomas, A.J. Norquist, M.B. Doran and D. O'Hare, J. Mater. Chem., 13 (2003) 88.
155. A.J. Norquist, P.M. Thomas, M.B. Doran and D. O'Hare, Chem. Mater., 14 (2002) 5179.
156. A.J. Norquist, M.B. Doran, P.M. Thomas and D. O'Hare, Dalton Trans., 2003 (2003) 1168.
157. C.L. Stuart, M.B. Doran, A.J. Norquist and D. O'Hare, Acta Crystallogr., E59 (2003) m446.
158. A.J. Norquist, M.B. Doran and D. O'Hare, Solid State Sci., 5 (2003) 1149.
159. Yu.N. Mikhailov, Yu.E. Gorbunova, E.A. Demchenko, L.B. Serezhkina and V.N. Serezhkin, Russ. J. Inorg. Chem. 45 (2000) 1571.
160. V.V. Tabachenko, V.N. Serezhkin, L.B. Serezhkina and L.M. Kovba, Koord. Khim. 5 (1979) 1563.
161. S.V. Krivovichev, I.G. Tananaev and B.F. Myasoedov, in preparation.
162. S.V. Krivovichev and P.V. Burns, Solid State Sci. 5 (2003) 481.
163. R. Tali, V.V. Tabachenko and L.M. Kovba, Zh. Neorg. Khim. 38 (1993) 1450.
164. D.Yu. Pushcharovskii, R.K. Rastsvetaeva and H. Sarp, J. Alloys Compds. 239 (1996) 23.
165. R.E. Sykora, S.M. McDaniel, D.M. Wells and T.E. Albrecht-Schmitt, Inorg. Chem. 41 (2002) 5126.
166. S.V. Krivovichev and P.C. Burns, Z. Anorg. Allg. Chem. 629 (2003) 1965.
167. R.E. Sykora, D.M. Wells and T.E. Albrecht-Schmitt, Inorg. Chem. 41 (2002) 2304.
168. S.V. Krivovichev and V. Kahlenberg, Z. Naturforsch. 62b (2005) 538.
169. A.J. Norquist, M.B. Doran and D. O'Hare, Inorg. Chem., 44 (2005) 3837.
170. S.V. Krivovichev and P.C. Burns, J. Solid State Chem. 168 (2002) 245.
171. P.B. Moore, N. Jb. Miner. Mh. 1970 (1970) 163.
172. S.V. Krivovichev, N. Jb. Miner. Mh. 2004 (2004) 209.

173. S.V. Krivovichev, V. Kahlenberg, R. Kaindl, E. Mersdorf, I.G. Tananaev and B.F. Myasoedov, Angew. Chem. Intern. Ed. 44 (2005) 1134.
174. S.V. Krivovichev, V. Kahlenberg, R. Kaindl, E. Mersdorf, I.G. Tananaev and B.F. Myasoedov, J. Amer. Chem. Soc. 127 (2005) 1072.
175. L. Niinisto, J. Toivonen and J. Valkonen, Acta Chem. Scand. A33 (1979) 621.
176. V.N. Serezhkin, M.A. Soldatkina and V.A. Efremov, Zh. Strukt. Khim. 22 (1981) 174.
177. N.W. Alcock, M.M. Roberts and D. Brown, Dalton Trans. 1982 (1982) 869.
178. R.F. Baggio, M.A.R. de Benyacar, B.O. Perazzo and P.K. de Perazzo, Acta Crystallogr. B33 (1977) 3495.
179. I.V. Medrish, A.V. Vologzhanina, Z.A. Starikova, M.Yu. Antipin, L.B. Serezhkina, and V.N. Serezhkin, Russ. J. Inorg. Chem. 50 (2005) 360.
180. M.S. Grigor'ev, T.E. Plotnikova, N.A. Budantseva, A.M. Fedoseev, A.I. Yanovskii and Yu.T. Struchkov, Radiokhimiya 34 (1992) 1.
181. Yu.N. Mikhailov, Yu.E. Gorbunova, O.V. Shishkina, L.B. Serezhkina and V.N. Serezhkin, Zh. Neorg. Khim. 46 (2001) 1828.
182. S.V. Krivovichev and V. Kahlenberg, Z. Anorg. Allg. Chem. 631 (2005) 739.
183. Yu.N. Mikhailov, Yu.E. Gorbunova, L.B. Serezhkina, E.A. Demchenko and V.N. Serezhkin, Russ. J. Inorg. Chem. 42 (1997) 1283.
184. S.V. Krivovichev, I.G. Tananaev and B.F. Myasoedov, in preparation.
185. S.V. Krivovichev, V. Kahlenberg, I.G. Tananaev and B.F. Myasoedov, Z. Anorg. Allg. Chem., in press.
186. L. Niinisto, J. Toivonen and J. Valkonen, J., Acta Chem. Scand. A32 (1978) 647.
187. A.J. Norquist, M.B. Doran, P.M. Thomas and D. O'Hare, Inorg. Chem., 42 (2003) 5949.
188. S.V. Krivovichev, R.J. Finch and P.C. Burns, Can. Mineral. 40 (2002) 193.
189. G.G. Sadikov, T.I. Krasovskaya, Yu.A. Polyakov and V.P. Nikolaev, Izv. Akad. Nauk SSSR, Neorg. Mater. 24 (1988) 109.
190. S.V. Krivovichev and P.C. Burns, Can. Mineral. 43 (2005) 713.
191. R.K. Rastsvetaeva, A.V. Barinova, A.M. Fedoseev, N.A. Budantseva and Yu.V. Nekrasov, Dokl. Akad. Nauk 365 (1999) 68.
192. G.B. Andreev, M.Yu. Antipin, A.M. Fedoseev and N.A. Budantseva, Koord. Khim. 27 (2001) 227.
193. V.N. Khrustalev, G.B. Andreev, M.Yu. Antipin, A.M. Fedoseev, N.A. Budantseva and I.B. Shirokova, Zh. Neorg. Khim. 45 (2000) 1996.
194. S.V. Krivovichev, A.J. Locock and P.C. Burns, Z. Kristallogr. 220 (2005) 10.
195. M.S. Grigor'ev, I.A. Charushnikova, A.M. Fedoseev, N.A. Budantseva, A.I. Yanovskii and Yu.T. Struchkov, Radiokhimiya 34 (1992) 7.
196. S.V. Krivovichev, I.G. Tananaev, V. Kahlenberg and B.F. Myasoedov, Dokl. Phys. Chem. 403 (2005) 124.
197. S.V. Krivovichev, V. Kahlenberg, I.G. Tananaev and B.F. Myasoedov, J. Alloys Compds., accepted.
198. Yu.N. Mikhailov, Yu.E. Gorbunova, E.E. Baeva, L.B. Serezhkina and V.N. Serezhkin, Zh. Neorg. Khim. 46 (2001) 2017.
199. M.S. Grigor'ev, I.A. Charushnikova, A.M. Fedoseev, N.A. Budantseva, N.A. Baturin and L.L. Regel', Radiokhimiya 33 (1991) 19.
200. V.V. Tabachenko, L.M. Kovba, V.N. Serezhkin, Koord. Khim. 9 (1983) 1568.
201. S.V. Krivovichev and P.C. Burns, Can. Mineral. 39 (2001) 207.
202. S.V. Krivovichev, V. Kahlenberg, R. Kaindl and E. Mersdorf, Eur. J. Inorg. Chem. 2005 (2005) 1653.
203. Yu.N. Mikhailov, Yu.E. Gorbunova, L.B. Serezhkina and V.N. Serezhkin, Russ. J. Inorg. Chem. 42 (1997) 652.

204. N.A. Budantseva, G.B. Andreev, A.M. Fedoseev and M.Yu. Antipin, Russ. J. Coord. Chem. 29 (2003) 653.
205. S.V. Krivovichev and V. Kahlenberg, Radiochem. accepted.
206. M.B. Doran, A.J. Norquist, C.L. Stuart and D. O'Hare, Acta Crystallogr., E60 (2004) m996.
207. M.S. Grigor'ev, A.M. Fedoseev and N.A. Budantseva, Russ. J. Coord. Chem. 29 (2003) 877.
208. S.V. Krivovichev and V. Kahlenberg, Z. Anorg. Allg. Chem. 630 (2004) 2736.
209. S.V. Krivovichev and V. Kahlenberg, J. Alloys Compds. 395 (2005) 41.
210. S.V. Krivovichev and P.C. Burns, Z. Kristallogr. 218 (2003) 683.
211. S.V. Krivovichev and V. Kahlenberg, J. Alloys Compds 389 (2005) 55.
212. S.V. Krivovichev and P.C. Burns, Radiochem. 46 (2004) 441.
213. S.V. Krivovichev, I.G. Tananaev, V. Kahlenberg and B.F. Myasoedov, Radiochem., submitted.
214. S.V. Krivovichev, I.G. Tananaev, V. Kahlenberg and B.F. Myasoedov, Radiochem., submitted.
215. S.V. Krivovichev and V. Kahlenberg, Radiochem. accepted.
216. S.V. Krivovichev, C.L. Cahill and Burns P.C., Inorg. Chem. 41 (2002) 34.
217. M. Ross and H.T. Evans, Jr., J. Inorg. Nucl. Chem. 15 (1960) 338.
218. S.V. Krivovichev and P.C. Burns, unpublished.
219. M.S. Grigor'ev, A.M. Fedoseev, N.A. Budantseva, A.A. Bessonov and J.-C. Krupa, Crystallogr. Rep. 49 (2004) 676.
220. R.E. Sykora, S.M. McDaniel and T.E. Albrecht-Schmitt, J. Solid State Chem. 177 (2004) 1431.
221. S.V. Krivovichev, Rev. Miner. Geochem. 57 (2005) 17.
222. F. Liebau, Structural Chemistry of Silicates. Structure, Bonding, and Classification. Springer 1985.
223. E.V. Nazarchuk, S.V. Krivovichev and S.K. Filatov, Radiochem. 46 (2004) 405.
224. S.V. Krivovichev, E.V. Nazarchuk and P.C. Burns, in preparation.
225. S.V. Krivovichev, C.L. Cahill and P.C. Burns, Inorg. Chem. 42 (2003) 2459.
226. S.V. Krivovichev, C.L. Cahill, E.V. Nazarchuk, P.C. Burns, T. Armbruster and W. Depmeier, Micropor. Mesopor. Mater. 78 (2005) 209.
227. S.V. Krivovichev, P.C. Burns, T. Armbruster, E.V. Nazarchuk and W. Depmeier, Micropor. Mesopor. Mater. 78 (2005) 217.
228. S.V. Krivovichev, T. Armbruster, D.Yu. Chernyshov, P.C. Burns, E.V. Nazarchuk and W. Depmeier, Micropor. Mesopor. Mater. 78 (2005) 225.
229. E.V. Nazarchuk, S.V. Krivovichev and P.C. Burns, Radiochem., submitted.
230. V.N. Serezhkin, V.A. Efremov, V.K. Trunov, Kristallogr. 25 (1980) 861.
231. V.V. Tabachenko, L.M. Kovba and V.N. Serezhkin, Koord. Khim. 10 (1984) 558.
232. V.V. Tabachenko, V.L. Balashov, L.M. Kovba and V.N. Serezhkin, Koord. Khim. 10 (1984) 854.
233. M. Doran, A.J. Norquist and D. O'Hare, Chem. Commun., 2002 (2002) 2946.
234. V.A. Blatov, L.B. Serezhkina, V.N. Serezhkin and V.K. Trunov, Koord. Khim. 14 (1988) 1705.
235. Yu.N. Mikhailov, L.A. Kokh, V.G. Kuznetsov, T.G. Grevtseva, S.K. Sokol and G.V. Ellert, Koord. Khim. 3 (1977) 508.
236. P.C. Burns and L.A. Hayden, Acta Crystallogr. C58 (2002) 121.
237. L.A. Hayden and P.C. Burns, Can. Mineral. 40 (2002) 211.
238. L.A. Hayden and P.C. Burns, J. Solid State Chem. 163 (2002) 313.
239. M.S. Grigor'ev, A.M. Fedoseev, N.A. Budantseva, A.I. Yanovskii, Yu.T. Struchkov, and N.N. Krot, Radiokhimiya 33 (1991) 54.

240. A.J. Norquist, M.B. Doran and D. O'Hare, Acta Crystallogr., E59 (2003) m373.
241. M.B. Doran, A.J. Norquist, and D. O'Hare, Acta Crystallogr., E59 (2003) m762.
242. A.M. Fedoseev, N.A. Budantseva, M.S. Grigor'ev, A.A. Bessonov, L.N. Astafurova, T.S. Lapitskaya, and J.C. Krupa, Radiochim. Acta 86 (1999) 17.
243. A.J. Norquist, M.B. Doran and D. O'Hare, Acta Crystallogr., E61 (2005) m807.
244. M.B. Doran, A.J. Norquist, and D. O'Hare, Acta Crystallogr., E59 (2003) m765.
245. Yu.N. Mikhailov, Yu.E. Gorbunova, E.V. Mit'kovskaya, L.B. Serezhkina and V.N. Serezhkin, Radiochem. 44 (2002) 315.
246. M.B. Doran, B.E. Cockbain, A.J. Norquist and D. O'Hare, Dalton Trans., 2004 (2004) 3810.
247. N.P. Brandenburg and B.O. Loopstra, Acta Crystallogr. B34 (1978) 3734.
248. M.S. Grigor'ev, A.I. Yanovskii, A.M. Fedoseev, N.A. Budantseva, Yu.T. Struchkov, N.N. Krot and V.I. Spitsyn, Dokl. AN SSSR 300 (1988) 618-622.
249. M.S. Grigor'ev, N.A. Baturin, N.A. Budantseva, A.M. Fedoseev, Radiokhimiya 35 (1993) 29-38.
250. S.V. Krivovichev, Radiochem. 46 (2004) 401.

Structural Chemistry of Inorganic Actinide Compounds
S.V. Krivovichev, P.C. Burns & I.G. Tananaev (Editors)

Chapter 5

Actinide compounds with heavy oxoanions containing a stereochemically active lone-pair of electrons

Richard E. Sykora,[a] Tatiana Y. Shvareva,[b] and Thomas E. Albrecht-Schmitt[b]

[a]*Department of Chemistry, University of South Alabama, Mobile, Alabama 36688, USA*
[b]*Department of Chemistry and Biochemisty and E. C. Leach Nuclear Science Center, Auburn University, Auburn, Alabama 36849, USA*

1. Introduction

The purpose of this chapter is to address the role of heavy oxoanions containing a chemically inert, but stereochemically active, lone-pair of electrons on the structures of purely inorganic actinide compounds. This work is not intended to be a comprehensive survey of all compounds that fall into this class, but rather its goal is to highlight key compounds with atypical structures where the influence of the lone-pair of electrons can be ascertained, if only in part.

The solid-state chemistry of actinide compounds with heavy oxoanions of this type has a long and rich history. These oxoanions can include core ions of Sb(III), Bi(III), Se(IV), Te(IV), Br(V), and I(V). Initial reports of solids of this type date back to Rammelsburg's 1842 publication on the preparation of $3UO_2(BrO_3)_2{\cdot}UO_3$ [1]. This compound was shown to be an impure form of $UO_2(BrO_3)_2{\cdot}H_2O$ by Weigel and Engelhardt, 141 years later [2]! Early disclosers on various hydrated forms of uranyl iodate are legion. This initial work was plagued by contradictory results, inconclusive analyses, and irreproducible data. However, as early as 1913, the correct formula of hydrated uranyl iodate, $UO_2(IO_3)_2(H_2O)$, was published [3]. This compound was shown to be isostructural with $UO_2(BrO_3)_2{\cdot}H_2O$ via a comparison of the X-ray powder diffraction patterns [2]. Almost two decades past before single crystal

structures of $UO_2(IO_3)_2(H_2O)$ and $UO_2(IO_3)_2$ were published, solving a mystery that had persisted for more than 150 years [4].

It is important to note that while well-defined synthetic compounds containing this class of anions are relatively new, mother nature has provided many examples of uranyl selenites [5, 7, 8, 11, 12] and tellurites [23-25], and at least one uranyl bismuthite [31] for study. From these minerals and synthetic phases some general statements can be made concerning the role of the lone-pair of electrons in these compounds. In order to do this, we must first look at the structures that are observed for these heavy oxoanions by themselves. Figure 1 depicts the structures of oxoanions found in various actinide phases; these include EO_3 and EO_4 moieties. As can be seen from these structures the presence of the lone-pair of electrons dramatically perturbs the overall geometry of the anions, creating trigonal pyramidal and square pyramidal moieties.

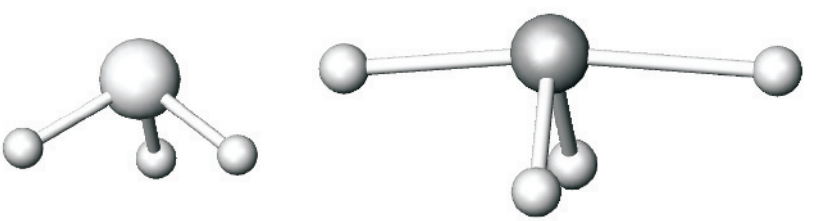

Figure 1. An illustration of the structures of various heavy oxoanions possessing a stereochemically active lone-pair of electrons.

The lone-pair of electrons cannot be directly observed, only their influence, and therefore the size of the lone-pair can only be indirectly measured. Systematic investigation of intermolecular I···I distances have yielded a value of 1.80 Å for the van der Waals radius of the lone-pair in iodate [32]. In addition to short E–O bonds, longer E···O interactions also exist between two or more different oxoanions. These interactions are generally on the order of 2.5 to 2.7 Å creating EO_{3+1}, EO_{3+2}, EO_{3+3}, EO_{3+4} groups [4, 33, 35-39]. In the case of the EO_{3+3} unit, the central atom can be thought of as residing in a distorted octahedral hole with three long and three short interactions. This type of interaction also takes place in EO_4 units.

There are substantial variations on the coordination numbers and geometries for actinide compounds containing a chemically inert, but stereochemically active, lone-pair of electrons. These oxoanions are to varying degrees oxidizing in nature and therefore it is expected that the penta- and hexavalent oxidation state will be found for the early actinides. This prediction is born out with iodate (a

strong oxidizing agent) and only U(VI) [4, 33-35, 40-45], Np(V,VI) [22, 43, 45, 46], and Pu(VI) [46-48] compounds are known. Selenite is only weakly oxidizing at best and a mixed-valent Np(IV,V) selenite is known [21]. In contrast, the transplutonium actinides Am, Cm, and Cf are all exclusively found in the +III oxidation state [50-52]. There is evidence from separation processes that Bk(IV) iodate exists, but a crystal structure is lacking [53].

There are a number of features that will be evident from the structures described herein that help illustrate the role that the inert pair of electrons plays in these structures. Some of the motifs will include the formation of polar structures where the oxoanions are aligned along one crystallographic axis, and the creation of channels to house the lone-pair electrons, which in at least one case gives rise to a chiral network.

1.1. Some Selenites of Interest

In contrast to uranyl selenites where monovalent cations are used to balance the charge of an anionic lattice, many uranyl selenites with divalent cations possess different structure types. Guilleminite, $Ba[(UO_2)_3(SeO_3)_2O_2](H_2O)_3$ [12], marthozite, $Cu[(UO_2)_3(SeO_3)_2O_2](H_2O)_8$ [5], and $Sr[(UO_2)_3(SeO_3)_2O_2]\cdot 4H_2O$ [20] all contain topologically identical $^2_\infty[(UO_2)_3(SeO_3)_2O_2]^{2-}$ sheets that are formed from chains of edge-sharing UO_7 pentagonal bipyramids and UO_8 hexagonal bipyramids that are bridged by SeO_3^{2-} anions. This sheet topology is based on that of phosphuranylite, $KCa(H_2O)_3(UO_2)[(UO_2)_3(PO_4)_2O_2]_2\cdot 8H_2O$ [54]. It is interesting to note that the carbonate anion can play the same role as that of selenite in uranyl phases, where the sheet topology of fontanite, $Ca[(UO_2)_3(CO_3)_2O_2]\cdot 6H_2O$ [55], is also based on that of phosphuranylite.

1.2 $Sr[(UO_2)_3(SeO_3)_2O_2]\cdot 4H_2O$ [20]

The structure of $Sr[(UO_2)_3(SeO_3)_2O_2]\cdot 4H_2O$ is composed of UO_7 pentagonal bipyramidal units that share an edge to form a dimer. This dimer in turn shares two edges on each side with UO_8 hexagonal bipyramids creating one-dimensional chains that extend along the *b* axis. These chains are then linked into two-dimensional $^2_\infty[(UO_2)_3(SeO_3)_2O_2]^{2-}$ sheets that extend in the [*ab*] plane by bridging/chelating SeO_3^{2-} anions. A view of part of one of these sheets is shown in Figure 2.

Table 1. A listing of actinide selenite compounds.

	formula	*Space group*	a, Å	b, Å	c, Å	Angles, º	Ref.
			Uranyl selenites				
1.	$Cu[(UO_2)_3(SeO_3)_2O_2](H_2O)_8$ marthozite	$Pbn2_1$	6.9879(4)	16.454(1)	17.223(1)		5
2.	UO_2SeO_3	$P2_1/m$	5.408(2)	9.278(1)	4.254(1)	β=93.45(10)	6
3.	$Pb_2Cu_5(SeO_3)_6(UO_2)_2(OH)_6 \cdot 2H_2O$ demesmaekerite	$P\bar{1}$	11.955(5)	10.039(4)	5.639(2)	α=89.78(4) β=100.36(4) γ=91.34(4)	7
4.	$Cu_4(UO_2)(SeO_3)_2(OH)_6$ derriksite	$Pn2_1m$	5.570(2)	19.088(8)	5.965(2)		8
5.	$UO_2Se_2O_5$	$P\bar{1}$	9.405(2)	11.574(2)	6.698(2)	α=93.01(3) β=93.66(3) γ=109.69(1)	9
6.	$UO_2Se_2O_5 \cdot 2H_2O$	$P\bar{1}$	9.40(4)	11.85(5)	6.69(5)	α=94.3(3) β=90.3(3) γ=114.5(3)	10
7.	$(UO_2)_3(OH)_2(SeO_3)_2 \cdot 5H_2O$ haynesite	*Pnc*2 *or* *Pncm*	8.025	17.43	6.935		11
8.	$Ba(UO_2)_3(SeO_3)_2O_2(H_2O)_3$ guilleminite	$P2_1nm$	7.084(1)	7.293(1)	16.881(4)		12
9.	$(NH_4)[UO_2(HSeO_3)(SeO_3)]$	$P2_1/n$	8.348 (2)	10.326 (2)	9.929 (2)	β=97.06(2)	13
10.	$UO_2(HSeO_3)_2 \cdot H_2O$ (a)	$A2/a$	6.354(1)	12.578(2)	9.972(2)	β=82.35(1)	14
11.	$UO_2(HSeO_3)_2 \cdot H_2O$ (b)	$C2/c$	9.924(5)	12.546(5)	6.324(5)	β=98.090(5)	15
10.	$(NH_4)_2UO_2(SeO_3)_2 \cdot 0.5H_2O$	$P2_1/c$	7.193(5)	10.368(5)	13.823(50	β=91.470(5)	15
11.	$Ca(UO_2)_3(SeO_3)_2(OH)_4 \cdot 4H_2O$ piretite	$Pmn2_1$ *or* $Pmnm$	7.010(3)	17.135(7)	17.606(4)		16
12.	$Ag_2(UO_2)(SeO_3)_2$	$P2_1/n$	5.8555(6)	6.5051(7)	21.164(2)	β=96.796(2)	17
13.	$K[(UO_2)(HSeO_3)(SeO_3)]$	$P2_1/n$	8.4164(4)	10.1435(5)	9.6913(5)	β=97.556(1)	17
14.	$Rb[(UO_2)(HSeO_3)(SeO_3)]$	$P2_1/n$	8.4167(5)	10.2581(6)	9.8542(5)	β=96.825(1)	17
15.	$Cs[(UO_2)(HSeO_3)(SeO_3)]$	$P2_1/c$	13.8529(7)	10.6153(6)	12.5921(7)	β=101.0940	17
16.	$Tl[(UO_2)(HSeO_3)(SeO_3)]$	$P2_1/n$	8.364(3)	10.346(4)	9.834(4)	β=97.269(8)	17
17	$Pb(UO_2)(SeO_3)_2$	$Pmc2_1$	11.9911(7)	5.7814(3)	11.2525(6)		17
18.	$Ca[(UO_2)(SeO_3)_2]$	$P\bar{1}$	5.5502(6)	6.6415(7)	11.013(1)	α=104.055(2) β=93.342(2) γ=110.589(2)	18
19.	$Ba[(UO_2)(SeO_3)_2]$	$P2_1/c$	7.3067(6)	8.1239(7)	13.651(1)	β=100.375(2)	18
20.	$Sr[(UO_2)(SeO_3)_2] \cdot 2H_2O$	$P\bar{1}$	7.0545(5)	7.4656(5)	10.0484(6)	α=106.995(1) β=108.028(1) γ=98.875(1)	18
21.	$Na(H_3O)(UO_2)_3(SeO_3)_2O_2 \cdot 4H_2O$ larisaite	$P11m$	6.9806(9)	7.646(1)	17.249(2)	γ=90.039(4)	19

Table 1. A listing of actinide selenite compounds.

22.	$Sr[(UO_2)_3(SeO_3)_2O_2]\cdot 4H_2O$	*C2/m*	17.014(2)	7.0637(7)	7.1084(7)	β=100.544(2)	20
23.	$Sr[UO_2(SeO_3)_2]$	$P\bar{1}$	5.6722(4)	6.7627(5)	11.2622(8)	α=104.698(1) β=93.708(1) γ=109.489(1)	20
			Neptunyl selenites				
1.	$Np(NpO_2)_2(SeO_3)_3$	*Pbca*	10.6216(5)	11.9695(6)	17.8084(8)		21
2.	□-$AgNpO_2(SeO_3)$	$P2_1/n$	4.3007(3)	9.5003(7)	11.5877(9)	β=95.855(1)	22
3.	β-$AgNpO_2(SeO_3)$	$P\bar{1}$	7.1066(6)	8.3503(7)	8.3554(7)	α=89.349(1) β=77.034(1) γ=76.561(1)	22

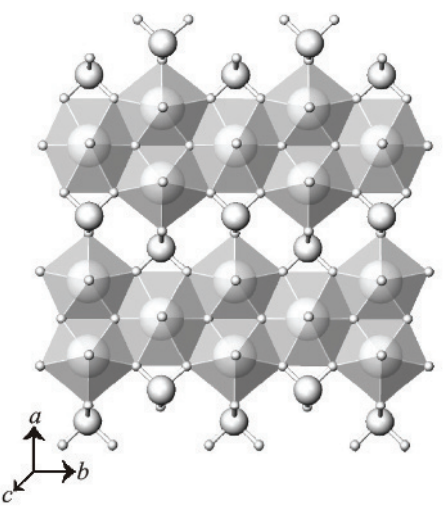

Figure 2. A view of the $^{2}_{\infty}[(UO_2)_3(SeO_3)_2O_2]^{2-}$ sheets found in Guilleminite, $Ba[(UO_2)_3(SeO_3)_2O_2]\cdot 3H_2O$, marthozite, $Cu[(UO_2)_3(SeO_3)_2O_2]\cdot 8H_2O$, and $Sr[(UO_2)_3(SeO_3)_2O_2]\cdot 4H_2O$.

1.2. $Sr[UO_2(SeO_3)_2]$ [20]

$Sr[UO_2(SeO_3)_2]$ is isostructural with $Ca[UO_2(SeO_3)_2]$, which was previously synthesized under mild hydrothermal conditions [18]. The structure of $Sr[UO_2(SeO_3)_2]$ is built from one-dimensional $^{1}_{\infty}[UO_2(SeO_3)_2]^{2-}$ ribbons that

propagate down the *b* axis. These ribbons are obtained from pentagonal bipyramidal uranium centers that are bound by two terminal oxo groups, forming the uranyl moiety, and selenite anions that occur as monodentate and chelating/bridging groups. Part of one of these one-dimensional ribbons is depicted in Figure 3.

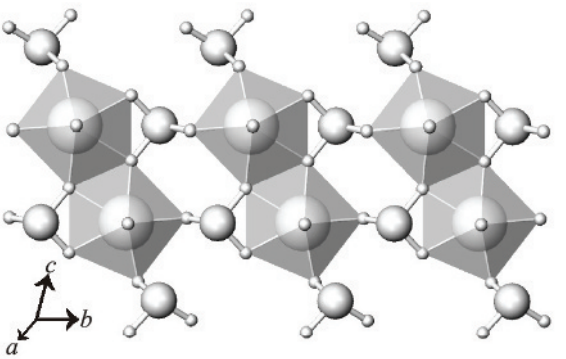

Figure 3. A view of one-dimensional $^{1}_{\infty}[UO_2(SeO_3)_2]^{2-}$ ribbons in $AE[UO_2(SeO_3)_2]$ (AE = Ca, Sr).

1.3. $PbUO_2(SeO_3)_2$ [17]

The structure of $PbUO_2(SeO_3)_2$ contains two-dimensional uranyl selenite sheets that are substantially different than those found in other uranyl selenite compounds. The selenite ligands chelate and bridge between uranyl moeities. The most unusual feature of $PbUO_2(SeO_3)_2$ is that the Pb^{2+} counter-cations cannot be neglected as they form short covalent bonds with both the terminal oxo groups from the selenite anions and the oxo group of the uranyl moieties. There are two crystallographically unique Pb^{2+} cations in this compound. Both of these cations are found in PbO_5 distorted square pyramidal coordination environments that indicate the presence of a stereochemically active lone-pair of electrons. As expected, the bonds formed with the uranyl moieties are significantly longer than those with the selenite anions. The Pb-O bonds range from 2.32(1) to 2.439(5) Å for bonds to selenite and are 2.683(5) and 2.708(6) Å for interactions between the uranyl units and Pb^{2+}. $PbUO_2(SeO_3)_2$ crystallizes in the polar orthorhombic space group $Pmc2_1$. As such, c is the polar axis. As is indicated in Figure 4, the origin of the polarity in this structure is not in the alignment of the lone-pair of electrons on the selenite anions, but rather in the alignment of the lone-pair of electrons on the Pb^{2+} centers.

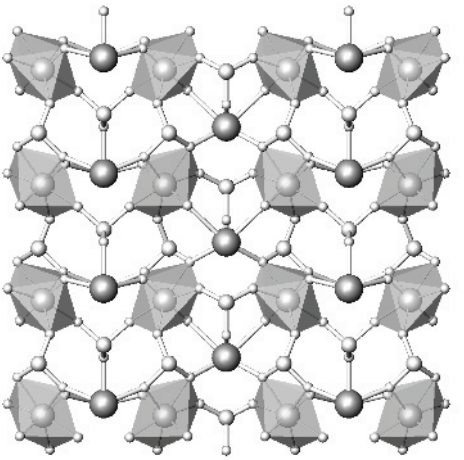

Figure 4. Alignment of the PbO_5 distorted square pyraminds along the *c*-axis in $Pb(UO_2)(SeO_3)_2$.

1.4. $Np(NpO_2)_2(SeO_3)_3$ [21]

The structure of $Np(NpO_2)_2(SeO_3)_3$ is extraordinarily complex as it contains three crystallographically unique Np centers with three different coordination environments in two different oxidation states. Two of the Np centers are +V and one is +IV. The Np(V) centers are found as both NpO_7 pentagonal bipyramids and NpO_8 hexagonal bipyramids. The Np(IV) center is found as a distorted NpO_8 dodecahedron. Cation-cation interactions (CCI's), exist between both the neptunyl units, and these units also coordinate the Np(IV) center creating a two-dimensional substructure. There are three crystallographically unique selenite anions.

The NpO_7 pentagonal bipyramids and NpO_8 hexagonal bipyramids share both corners and edges. The corner-sharing occurs via the cation-cation interaction and the edge-sharing via μ_3-oxo atoms from the selenite anions. Both of these polyhedra share corners via CCI's with the NpO_8 dodecahedra. This compound provides the first evidence for CCI's between Np(IV) and Np(V). A complete polyhedral depiction of the complex unit cell for $Np(NpO_2)_2(SeO_3)_3$ is shown in Figure 5. It can be noted from this latter figure that channels are created in the structure that run down the *b* axis. These channels house the stereochemically active lone-pair of electrons on the selenite anions.

1.5. β-AgNpO2(SeO3) [22]

The structure of β-$AgNpO_2(SeO_3)$ contains the same basic repeating units as found in $NpO_2(IO_3)$ (*vide infra*). As found in $Np(NpO_2)_2(SeO_3)_3$, neptunium oxide layers formed from NpO_2^+–NpO_2^+ bonds also occur in β-$AgNpO_2(SeO_3)$. A depiction of part of the structure of this compound viewed down the *a*-axis is shown in Figure 6. As can be seen from this figure, the structure is three-dimensional, and the neptunyl oxide layers are linked together by selenite anions. When viewed down this axis it becomes apparent that there are three types of channels running through the neptunyl selenite lattice. Two of these have oxygen atoms from the selenite anions and the oxo atoms from the neptunyl(V) cations directed into the channels that are used to bind the Ag^+ cations. The third type of channel has the stereochemically active lone-pair of the selenite anions directed into it. Given the strongly nonbonding nature of these lone-pairs, it is not surprising to find these channels vacant of Ag^+ cations.

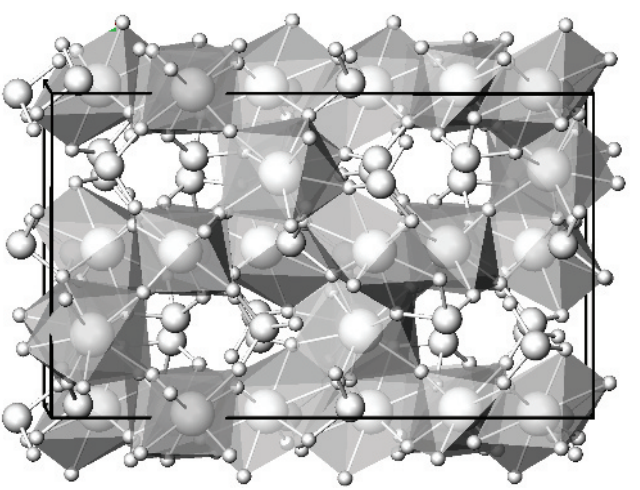

Figure 5. A complete polyhedral depiction of the complex unit cell for $Np(NpO_2)_2(SeO_3)_3$.

2. Some Tellurites of Interest

The uranyl tellurite system is remarkably rich and was first known from a few rare minerals including cliffordite, $UO_2(Te_3O_7)$ [23], moctezumite, $PbUO_2(TeO_3)_2$ [25], and schmitterite, $UO_2(TeO_3)$ [24]. The application of hydrothermal synthetic methods has resulted in a substantial explansion of this group to include $Pb_2UO_2(TeO_3)_3$ [26], $K[UO_2Te_2O_5(OH)]$ [27], $Tl_3\{(UO_2)_2[Te_2O_5(OH)](Te_2O_6)\}\cdot 2H_2O$ [27], α-$Tl_2[UO_2(TeO_3)_2]$ [28], β-$Tl_2[UO_2(TeO_3)_2]$ [27], $Sr_3[UO_2(TeO_3)_2(TeO_3)_2]$ [27], and $Na_8[(UO_2)_6(TeO_3)_{10}]$

[28]. Most recently it was shown that unlike iodates, mild hydrothermal conditions are not required from a thermodynamic standpoint to synthesize these compounds, and that relatively high-temperature molten salts can be used to facilitate the crystal growth of novel uranyl tellurites as demonstrated with the reports of $A_2[(UO_2)_3(TeO_3)_2O_2]$ (A = K, Rb, and Cs) [29] and $K_4[(UO_2)_5(TeO_3)_2O_5]$ [30].

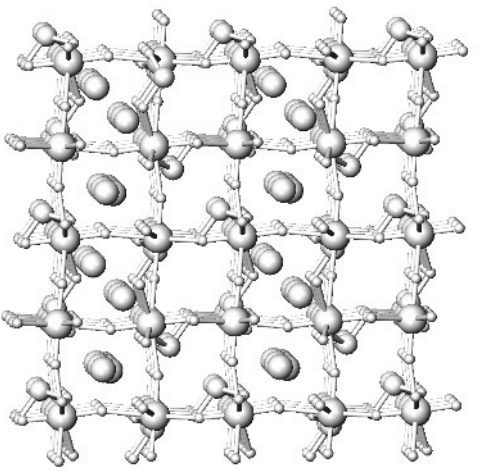

Figure 6. A view down the *a*-axis of the three-dimensional structure of β-$AgNpO_2(SeO_3)$. Note that there are three different types of channels running through this structure. Two of these house Ag^+ cations, and one appears to be empty, but is really occupied by the lone-pair of electrons from the Se(IV) centers.

Continued interest in the uranyl tellurite system stems from the fact that these compounds defy normal topological trends in uranium oxides. The expectation is that extended structures containing uranyl cations will be layered, and contain U(VI) in the form of a UO_7 pentagonal bipyramid with an approximately linear UO_2^{2+}, uranyl, core [56, 57]. However this is simply not the case for uranyl tellurites. For example, $K[UO_2Te_2O_5(OH)]$, β-$Tl_2[UO_2(TeO_3)_2]$ and $Sr_3[UO_2(TeO_3)_2(TeO_3)_2]$ contain UO_6 tetragonal bipyramids ; while $UO_2(Te_3O_7)$ incorporates UO_8 hexagonal bipyramids. $PbUO_2(TeO_3)_2$, $UO_2(TeO_3)$, $Pb_2UO_2(TeO_3)_3$, α-$Tl_2[(UO_2)(TeO_3)_2]$, $Na_8[(UO_2)_6(TeO_3)_{10}]$, and $Tl_3\{(UO_2)_2[Te_2O_5(OH)](Te_2O_6)\}\cdot 2H_2O$ all contain the more common UO_7 pentagonal bipyramid. It is also possible for multiple U(VI)-containing polyhedra to be present as was found for $A_2[(UO_2)_3(TeO_3)_2O_2]$ (A = K, Rb, and Cs), which possess both UO_6 tetragonal bipyramids and UO_7 pentagonal bipyramids.

This system is made even more intricate by examining the coordination environment around the Te(IV) centers. $PbUO_2(TeO_3)_2$, $Pb_2UO_2(TeO_3)_3$, β-$Tl_2[UO_2(TeO_3)_2]$, $Sr_3[UO_2(TeO_3)_2(TeO_3)_2]$, $Na_8[(UO_2)_6(TeO_3)_{10}]$, and $A_2[(UO_2)_3(TeO_3)_2(O)_2]$ (A = K, Rb, and Cs) all possess approximately C_{3v} tellurite, TeO_3, units. Whereas $UO_2(TeO_3)$, $K[UO_2Te_2O_5(OH)]$, and $Tl_3\{(UO_2)_2[Te_2O_5(OH)](Te_2O_6)\}\cdot 2H_2O$ contain one-dimensional chains of corner-sharing, square pyramidal TeO_4 units. Finally, TeO_5 moieties are found in $UO_2(Te_3O_7)$. The structure α-$Tl_2[(UO_2)(TeO_3)_2]$ is particularly interesting in that it contains both TeO_3 and the rarely observed Te_2O_6 group.

Table 2. A listing of actinide tellurite compounds.

	formula	*Space group*	a, Å	b, Å	c, Å	angles, º	Ref.
			Uranyl tellurites				
1.	UTe_2O_8, cliffordite	*Pa*3	11.371				23
2.	UO_2TeO_3, schmitterite	*Pmab*	7.860	10.089	5.363		24
3.	UO_2TeO_3	*Pbcm*	5.363(3)	10.161(4)	7.862(3)		6
4.	$Pb(UO_2)(TeO_3)_2$ moctezumite	$P2_1/c$	7.819(7)	7.070(3)	13.836(13)	β=93	25
5.	$Pb_2[UO_2][TeO_3]_3$	$P2_1/n$	11.605(4)	13.389(17)	6.981(1)	β=91.23(3)	26
6.	$K[UO_2Te_2O_5(OH)]$	*Cmcm*	7.9993(5)	8.7416(6)	11.4413(8)		27
7.	$Tl_3\{(UO_2)_2[Te_2O_5(OH)](Te_2O_6)\}\cdot 2H_2O$	*Pbam*	10.0623(8)	23.024(2)	7.9389(6)		27
8.	β-$Tl_2[UO_2(TeO_3)_2]$	$P2_1/n$	5.4766(4)	8.2348(6)	20.849(3)	β=92.329(1)	27
9.	$Sr_3[UO_2(TeO_3)_2](TeO_3)_2$	*C*2/*c*	20.546(1)	5.6571(3)	13.0979(8)	β=94.416(1)	27
10.	α-$Tl_2[UO_2(TeO_3)_2]$	$P\bar{1}$	7.4054(9)	7.9268(9)	8.994(1)	α=94.122(2) β=107.438(2) γ=107.180(2)	28
11.	$Na_8[(UO_2)_6(TeO_3)_{10}]$	$I2_13$	16.8969(5)				28
12.	$K_2[(UO_2)_3(TeO_3)_2O_2]$	$P\bar{1}$	6.7985(5)	7.0123(5)	7.8965(6)	α=101.852(1) β=102.974(1) γ=100.081(1)	29
13.	$Rb_2[(UO_2)_3(TeO_3)_2O_2]$	$P\bar{1}$	7.0101(6)	7.0742(6)	8.0848(7)	α=105.590(2) β=101.760(2) γ=99.456(2)	29
14.	$Cs_2[(UO_2)_3(TeO_3)_2O_2]$	$P\bar{1}$	7.0007(5)	7.5195(6)	8.4327(6)	α=109.301(1) β=100.573(1) γ=99.504(1)	29
15.	$K_4[(UO_2)_5(TeO_3)_2O_5]$	$P\bar{1}$	6.8514(5)	7.1064(5)	11.3135(8)	α=99.642(1) β=93.591(1) γ=100.506(1)	30

2.1. $Na_8[(UO_2)_6(TeO_3)_{10}]$ [28]

The structure of $Na_8[(UO_2)_6(TeO_3)_{10}]$ is built from UO_7 pentagonal bipyramids and TeO_3^{2-} anions. These anions bridge UO_7 units to create a three-dimensional network structure that is chiral. Part of the network is shown in Figure 7 with the Na^+ cations omitted. The Na^+ cations reside in small twisting interconnected cavities and channels. Three-dimensional network structures are not common with U(VI) and typically require cross-linking of uranium oxide layers by additional building units [58, 59], or the orthogonal orientation of uranyl polyhedra with respect to one another [60, 61]. The chiral nature of $Na_8[(UO_2)_6(TeO_3)_{10}]$ is likely a consequence of the presence of stereochemically active lone-pairs of electrons on the Te(IV) centers.

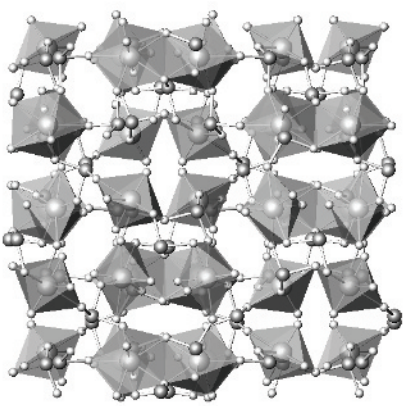

Figure 7. Part of the three-dimensional network structure of $Na_8[(UO_2)_6(TeO_3)_{10}]$. Na^+ cations have been omitted for clarity.

2.2. $K[UO_2Te_2O_5(OH)]$ [27]

The two-dimensional structure of $K[UO_2Te_2O_5(OH)]$ is most similar to UO_2TeO_3, which consists of chains of edge-sharing pentagonal bipyramidal UO_7 polyhedra that edge-share with TeO_4 square pyramids that in turn corner-share to form one-dimensional chains [24]. In $K[UO_2Te_2O_5(OH)]$ these one-dimensional chains of corner-sharing TeO_4 square pyramids occur again, however, alternating bridging oxygen atoms are actually hydroxyl groups. This creates an alternating short/long Te–O–Te—O—Te bonding pattern. The Te–O bond distance to the hydroxyl oxygen atom is 2.282(2) Å, whereas the Te–O bond distance to the unprotonated oxygen atom is 2.072(3) Å. The remaining Te–O bond distances to the oxygen atoms involved in binding the uranyl moieties are both 1.859(3) Å. The uranyl units in $K[UO_2Te_2O_5(OH)]$ are bound

by oxygen atoms from the $^{1}_{\infty}[Te_2O_5(OH)]^{3-}$ chains to create tetragonal bipyramidal environments around the U(VI) centers. The uranyl moieties therefore serve to bridge between the $^{1}_{\infty}[Te_2O_5(OH)]^{3-}$ chains to yield $^{2}_{\infty}[UO_2Te_2O_5(OH)]^{1-}$ sheets that extend in the [*ac*] plane. Part of a $^{2}_{\infty}[UO_2Te_2O_5(OH)]^{1-}$ layer viewed down the *b*-axis is depicted in Figure 8.

The joining of the tellurium oxide chains by the uranyl units also creates voids within the sheets that are remarkably reminiscent of 18-crown-6. In fact, the K^+ cations in $K[UO_2Te_2O_5(OH)]$ reside within these cavities and form six $K^+\cdots O$ contacts, with four interactions of 2.807(3) Å and two of 2.925(1) Å. In addition, the K^+ cations form rather short ionic contacts of 2.716(4) Å with oxygen atoms from uranyl groups in adjacent layers. The eight coordinate environment for the K^+ cations observed here is quite similar to that of $[K(18\text{-crown-6})(DMF)_2]^+$ [62]. In this latter cation, the $K^+\cdots O$ contact distances are as follows: 2.707(14) (× 2) Å to the oxygen atoms of the dimethylformamide molecules, and 2.830(13) (× 2), 2.775(14) (× 2), and 2.707(14) (× 2) Å to the oxygen atoms in the 18-crown-6 molecule. The average of the $K^+\cdots O$ contacts in $K[UO_2Te_2O_5(OH)]$ compares well with that of $[K(18\text{-crown-6})(DMF)_2]^+$ with distances of 2.81 and 2.77 Å, respectively. These data therefore support the role of the K^+ cations as structure-directing agents in the formation of $K[UO_2Te_2O_5(OH)]$.

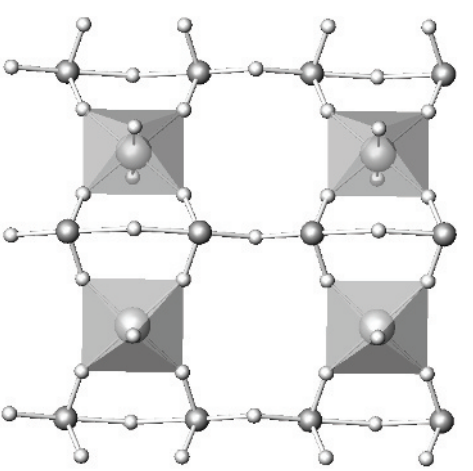

Figure 8. A view down the *b*-axis showing the two-dimensional $^{2}_{\infty}[UO_2Te_2O_5(OH)]^{1-}$ sheets present in $K[UO_2Te_2O_5(OH)]$. These sheets are comprised of one-dimensional $^{1}_{\infty}[Te_2O_5(OH)]^{3-}$ chains that are bridged by uranyl moieties. In addition, there are crown-shaped cavities within the sheets that contain the K^+ cations.

2.3. $Tl_3\{(UO_2)_2[Te_2O_5(OH)](Te_2O_6)\}\cdot 2H_2O$ [27]

The structural features of this compound have similarities with both $K[UO_2Te_2O_5(OH)]$ and UO_2TeO_3. First, there are two-dimensional $^{2}_{\infty}\{(UO_2)_2[Te_2O_5(OH)](Te_2O_6)\}^{3-}$ corrugated sheets formed from tellurium oxide chains and UO_7 pentagonal bipyramids as shown in Figure 9. The tellurium oxide chains take the form of corner-sharing TeO_4 square pyramids as found in UO_2TeO_3, and as partially protonated $^{1}_{\infty}[Te_2O_5(OH)]^{3-}$ chains similar to those found in $K[UO_2Te_2O_5(OH)]$. Furthermore, the sheets found in $Tl_3\{(UO_2)_2[Te_2O_5(OH)](Te_2O_6)\}\cdot 2H_2O$ are quite porous and again the countercations (Tl^+) are found within the layers instead of between them. The water molecules are located between the layers and are not interacting with the U(VI) centers.

There are two crystallographically unique U(VI) centers in $Tl_3\{(UO_2)_2[Te_2O_5(OH)](Te_2O_6)\}\cdot 2H_2O$, both of which occur in uranyl moieties. Both uranyl groups form U–O bonds with both types of Te(IV) chains. An important structural difference between $K[UO_2Te_2O_5(OH)]$ and $Tl_3\{(UO_2)_2[Te_2O_5(OH)](Te_2O_6)\}\cdot 2H_2O$ is that alternating bridging oxygen atoms in the unprotonated chains in $Tl_3\{(UO_2)_2[Te_2O_5(OH)](Te_2O_6)\}\cdot 2H_2O$ are μ_3-O groups because they also bind the uranium atoms. This feature is absent in $K[UO_2Te_2O_5(OH)]$, but present in $UO_2(TeO_3)$. This means that each U(VI) center forms three U–O bonds with the one-dimensional $^{1}_{\infty}[Te_2O_6]^{4-}$ anionic chains and two U–O bonds with the $^{1}_{\infty}[Te_2O_5(OH)]^{3-}$ chains.

The Te–O bonds in the $^{1}_{\infty}[Te_2O_5(OH)]^{3-}$ chains show alternating short/long distances as found in $K[UO_2Te_2O_5(OH)]$. Here these distances are 2.073(6) and 2.214(5) Å. The shorter Te–O distances are with the oxygen atoms that are involved in bonding with the U(VI) centers. These distances are 1.840(9) and 1.87(1) Å. A small Peierls distortion evidenced by minor elongation of the Te and O thermal ellipsoids along the direction of chain propagation (*c*-axis) is also observed. In contrast, the one-dimensional $^{1}_{\infty}[Te_2O_6]^{4-}$ chains show only small differences in the Te–O bonds involved in chain formation with distances of 2.043(3) and 2.065(3) Å. The remaining two Te–O bonds are 1.868(9) and 1.884(9) Å.

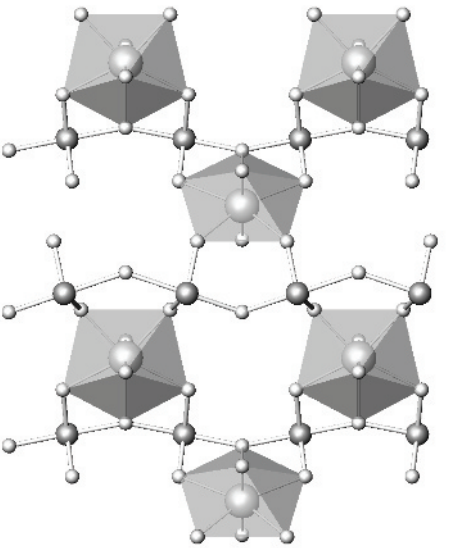

Figure 9. A depiction of part of a two-dimensional $^{2}_{\infty}\{(UO_2)_2[Te_2O_5(OH)](Te_2O_6)\}^{3-}$ sheet from $Tl_3\{(UO_2)_2[Te_2O_5(OH)](Te_2O_6)\}\cdot 2H_2O$. The tellurium oxide chains take the form of corner-sharing TeO_4 square pyramids in one-dimensional $^{1}_{\infty}[Te_2O_6]^{4-}$ chains, and as partially protonated $^{1}_{\infty}[Te_2O_5(OH)]^{3-}$ chains similar to those found in $K[UO_2Te_2O_5(OH)]$.

3. Some Iodates of Interest

The actinide iodate system is one of considerable interest that has attracted chemists for more than 150 years (*vide supra*). In fact one of the first forms that ^{239}Pu was isolated in was as the iodate salt, presumably as $Pu(IO_3)_4$ [63]. The precipitation of iodate compounds of the actinides has been used for decades as a method of separated them from lanthanides and other fission products. The precipitation of thorium iodate is perhaps best known in this regard [64-66], but several patents exist describing selective precipitation of transuranium elements [67-72]. Despite the key importance of iodate in actinide chemistry the structures of actinide iodates were not described in detail until approximately 2000.

Actinyl iodates represent some of the quintessential structures types for illustrating the role that the lone-pair of electrons can play in these solids. One-dimensional compounds in this group are legion, perhaps because the lone-pair of electrons blocks one dimension of connectivity reducing the dimensionality

from layered structures to one-dimensional chains. Most of the rare examples of polar compounds with heavy oxoanions with main group elements are found in the iodates, albeit they are still uncommon.

Table 3. A listing of actinide iodate compounds.

	formula	*Space group*	a, Å	b, Å	c, Å	angles, º	Ref.
Uranyl iodates							
1.	$UO_2(IO_3)_2$	$\boldsymbol{P2_1/n}$	4.2454(8)	16.636(5)	5.284(1)	β=107.57(2)	4
2.	$UO_2(IO_3)_2(H_2O)$	*Pbcn*	8.452(2)	7.707(2)	12.271(3)		4
3.	$K_2[(UO_2)_3(IO_3)_4O_2]$	$P\bar{1}$	7.0372(5)	7.7727(5)	8.9851(6)	α=93.386(1) β=105.668(1) γ=91.339(1)	33
4.	$Ba[(UO_2)_2(IO_3)_2O_2](H_2O)$	$P2_1/c$	8.062(4)	6.940(3)	21.67(1)	β=98.05(1)	33
5.	$Ag_4(UO_2)_4(IO_3)_2(IO_4)_2O_2$	$P2_1/n$	15.040(7)	8.051(4)	18.332(8)	β=100.738(7)	34
6.	$Rb_2[(UO_2)_3(IO_3)_4O_2]$	$P\bar{1}$	7.0834(8)	7.8935(9)	9.092(1)	α=91.741(2) β=105.110(2) γ=92.214(2)	35
7.	$Tl_2[(UO_2)_3(IO_3)_4O_2]$	$P\bar{1}$	7.0602(6)	7.9475(6)	9.0175(7)	α=91.867(1) β=105.595(1) γ=91.577(1)	35
8.	$Sr[(UO_2)_2(IO_3)_2O_2](H_2O)$	$\boldsymbol{P2_1/c}$	7.8140(5)	6.9425(4)	21.434(1)	β=99.324(1)	35
9.	$Pb[(UO_2)_2(IO_3)_2O_2](H_2O)$	$P2_1/c$	7.8441(5)	6.9328(4)	21.340(1)	β=99.062(1)	35
11.	$Rb[UO_2(CrO_4)(IO_3)(H_2O)]$	$P\bar{1}$	7.3133(5)	8.0561(6)	8.4870(6)	α=88.740(1) β=87.075(1) γ=71.672(1)	41
12.	$K_2[UO_2(CrO_4)(IO_3)_2]$	$P2_1/c$	11.1337(5)	7.2884(4)	15.5661(7)	β=107.977(1)	41
13.	$Rb_2[UO_2(CrO_4)(IO_3)_2]$	$P2_1/c$	11.3463(6)	7.3263(4)	15.9332(8)	β=108.173(1)	41
14.	$Cs_2[UO_2(CrO_4)(IO_3)_2]$	$P2_1/n$	7.3929(5)	8.1346(6)	22.126(2)	β=90.647(1)	40 41
15.	$K_2[UO_2(MoO_4)(IO_3)_2]$	$P2_1/c$	11.3717(6)	7.2903(4)	15.7122(8)	β=108.167(1)	41
16.	$Cs_2[(UO_2)_3Cl_2(IO_3)(OH)O]$ $\cdot 2H_2O$	*Pnma*	8.2762(4)	12.4809(6)	17.1297(8)		42
17.	$K_3[(UO_2)_2(IO_3)_6](IO_3)\cdot H_2O$	$P\bar{1}$	7.0609(4)	14.5686(8)	14.7047(8)	α=119.547(1) β=95.256(1) γ=93.206(1)	43
18.	$K[UO_2(IO_3)_3]$	*Pbca*	11.495(1)	7.2293(7)	25.394(2)		43
Uranyl bromates							
1.	$UO_2(BrO_3)_2\cdot H_2O$	*Pbcn*	8.533(3)	7.639(3)	12.293(4)		2
Neptunyl iodates							
1.	$NpO_2(IO_3)$	$Pna2_1$	13.816(2)	5.8949(8)	5.5852(8)		22
2.	$NpO_2(IO_3)_2(H_2O)$	*Pcan*	7.684(2)	8.450(2)	12.493(3)		45
3.	$NpO_2(IO_3)_2\cdot H_2O$	$Pna2_1$	7.314(1)	11.631(2)	9.449(2)		45

4.	$K[NpO_2(IO_3)_3]\cdot 1.5H_2O$	$P2_1/c$	7.796(4)	7.151(3)	21.79(1)	β=97.399(7)	43
5.	$NpO_2(IO_3)_2\cdot 0.5KCl\cdot 3.25H_2O$	$C2/c$	21.537(5)	11.670(3)	7.315(2)	β=93.033(4)	46
Plutonyl iodates							
1.	$PuO_2(IO_3)_2\cdot H_2O$	$Pn2_1/a$	7.3199(12)	9.4725(16)	11.636(2)		47
2.	$PuO_2(IO_3)_2\cdot 0.5KCl\cdot 2.5H_2O$	$C2/c$	21.570(4)	11.656(2)	7.348(2)	β=94.00(3)	46
3.	$(PuO_2)_2(IO_3)(OH)_3$	$P2_1/n$	7.164(2)	10.520(3)	11.561(3)	β=90.179(5)	48
Americium, Curium, Californium iodates							
1.	$K_3Am_3(IO_3)_{12}\cdot HIO_3$	$R3c$	22.096(6)		13.436(4)		49
2.	$Am(IO_3)_3$	$P2_1/c$	7.2300(5)	8.5511(6)	13.5361(10)	β=100.035(1)	50
3.	$Cm(IO_3)_3$	$P2_1/c$	7.2014(7)	8.5062(9)	13.4622(14)	β=100.142(2)	51
4.	$Cf(IO_3)_3$	$P2_1/n$	8.7994(10)	5.9388(7)	15.157(2)	β = 96.833(2)	52

3.1. $UO_2(IO_3)_2$ [4]

The structure of $UO_2(IO_3)_2$ consists of infinite one-dimensional $^1_\infty[UO_2(IO_3)_2]$ chains running down the *a*-axis that are formed from edge-sharing of hexagonal bipyramidal UO_8 units as depicted in Figure 10. This is the first observation of this coordination environment for U in a one-dimensional structure. This structure is in fact that of a bis-chelate of the uranyl dication with the chain structure forming through the μ_3-O atom of the iodate joining neighboring U centers. A view down the chain axis actually shows that this compound is pseudo-three-dimensional, as there are 2.485(6) Å contacts between iodate anions on neighboring chains. These I···O interactions result in a herringbone arrangement that runs in opposite directions on each side of the chain making the overall structure centrosymmetric.

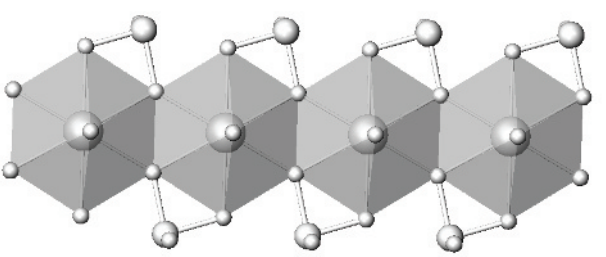

Figure 10. A view of the one-dimensional chains of edge-sharing hexagonal bipyramids in $UO_2(IO_3)_2$.

3.2. $UO_2(IO_3)_2(H_2O)$ [4]

The structure of $UO_2(IO_3)_2(H_2O)$ consists of pentagonal bipyramidal UO_7 formed from coordination of UO_2^{2+} by four oxygen atoms from four bridging iodates and the oxygen atom from a water molecule. The IO_3^- units bridge uranyl moieties to form the corrugated $^2_\infty[UO_2(IO_3)_2(H_2O)]$ layers lying parallel to the (010) plane. The binding of IO_3^- to the uranyl units occurs solely by bridging between uranium centers and no chelation occurs. This is in stark contrast to the binding mode of iodate in $UO_2(IO_3)_2$. Part of one of these layers is shown in Figure 11. As found in $UO_2(IO_3)_2$, there are additional long I···O contacts between iodate anions. In this case, these interactions, which range from 2.673(4) to 2.871(4) Å, link adjacent sheets to one another making the structure of this compound also pseudo-three-dimensional.

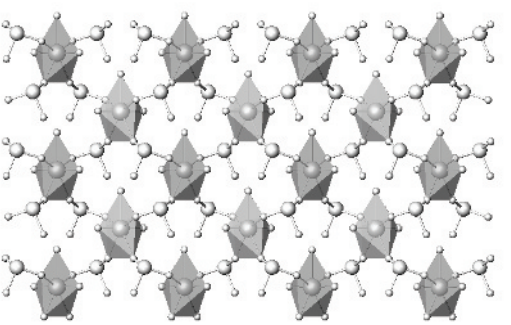

Figure 11. A depiction of the two-dimensional sheets in $UO_2(IO_3)_2(H_2O)$.

3.3. $A_2[(UO_2)_3(IO_3)_4O_2]$ (A = K, Rb, Tl) [33,35]

The isostructural series of compounds $A_2[(UO_2)_3(IO_3)_4O_2]$ display two common characteristics of actinide compounds containing oxoanions with nonbonding pairs of electrons, reduced dimensionality and intramolecular oxoanion interactions. The structures consist of infinite one-dimensional $^1_\infty[(UO_2)_3(IO_3)_4O_2]^{2-}$ chains that run down the *a*-axis. These chains are constructed from UO_7 pentagonal bipyramids and UO_6 octahedra. The UO_7 polyhedra edge-share to form dimers that are linked together by UO_6 octahedra. The edges of the uranium oxide chains are terminated by iodate anions that adopt both bridging and monodentate binding modes. The bridging iodates join the dimers of edge-sharing UO_7 pentagonal bipyramids and form two opposite corners of the distorted UO_6 octahedra. The coordination polyhedra of the uranium atoms are completed by μ_3-O^{2-} ligands that are shared by both the

dimers of edge-sharing UO_7 pentagonal bipyramids and the UO_6 octahedra. Part of one of these uranyl iodate chains is shown in Figure 12. The A^+ (A = K, Rb, Tl) cations separate the chains from one another and are coordinated by terminal oxygen atoms from iodate ligands. As found in many iodate compounds including $UO_2(IO_3)_2$ and $UO_2(IO_3)_2(H_2O)$, there are close I···O contacts of 2.397(3), 2.413(6) and 2.417(7) Å for $A_2[(UO_2)_3(IO_3)_4O_2]$ (A = K, Rb, Tl) between the terminal oxygen atoms from the monodentate iodate ligand and the neighboring iodine atom from the iodate that bridges uranium centers.

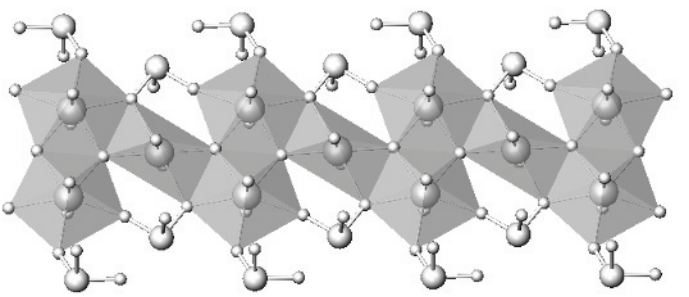

Figure 12. An illustration of the one-dimensional $^1_\infty[(UO_2)_3(IO_3)_4O_2]^{2-}$ chains in $A_2[(UO_2)_3(IO_3)_4O_2]$ (A = K, Rb, Tl).

3.4. $AE[(UO_2)_2(IO_3)_2O_2](H_2O)$ (AE = Sr, Ba, Pb) [33,35]

These isostructural compounds consist of edge-sharing distorted pentagonal bipyramidal UO_7 units that form one-dimensional uranium oxide ribbons whose edges are terminated by iodate ligands as shown in Figure 13. There are two crystallographically unique uranium centers in these compounds. These ribbons run down the *b*-axis and are separated by the AE^{2+} (AE = Sr, Ba, Pb) cations and water molecules. The pentagonal bipyramids containing U(1) share two edges with neighboring polyhedra, and these units line the edges of the ribbons, whereas the pentagonal bipyramids containing U(2) are on the interior of the ribbons and share four edges with neighboring polyhedra. As found in $A_2[(UO_2)_3(IO_3)_4O_2]$ (A = K, Rb, Tl), the iodate ligands adopt both monodentate and bridging binding modes and terminate the edges of the uranium oxide ribbons. The AE^{2+} cations are contained within distorted tricapped trigonal prisms where two rectangular faces and one triangular face are capped. Again, the longest distances of 3.289(8) Å in $Sr[(UO_2)_2(IO_3)_2O_2](H_2O)$, 3.145(11) Å in $Ba[(UO_2)_2(IO_3)_2O_2](H_2O)$, and 3.311(8) Å in $Pb[(UO_2)_2(IO_3)_2O_2](H_2O)$ are to

the oxygen atom capping the triangular face. As in $A_2[(UO_2)_3(IO_3)_4O_2]$ (A = K, Rb, Tl), there are I···O contacts, however, these are approximately 0.2 Å longer with distances of 2.605(8), 2.667(9), and 2.591(8) Å between the terminal oxygen atoms from the monodentate iodate ligand and the neighboring iodine atom from the iodate that bridges uranium centers.

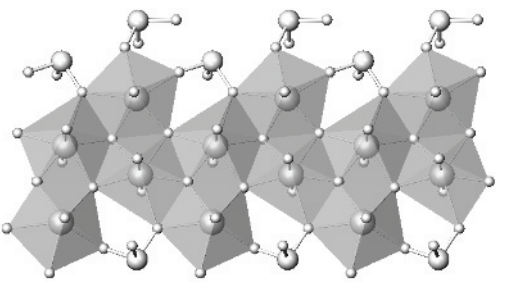

Figure 13. A view of the one-dimensional chains in $AE[(UO_2)_2(IO_3)_2O_2](H_2O)$ (AE = Sr, Ba, Pb).

3.5. $K_3[(UO_2)_2(IO_3)_6](IO_3)\cdot H_2O$ and $K[NpO_2(IO_3)_3]\cdot 1.5H_2O$ [43]

The structure of $K_3[(UO_2)_2(IO_3)_6](IO_3)\cdot H_2O$ contains one-dimensional $^1_\infty[UO_2(IO_3)_3]^{1-}$ ribbons that propagate along the *a*-axis as shown in Figure 14. These anionic chains are constructed from UO_7 pentagonal bipyramids linked together through bridging iodate groups. Monodentate iodate anions terminate the edges of the chains in $K_3[(UO_2)_2(IO_3)_6](IO_3)\cdot H_2O$ as also observed in $A_2[(UO_2)_3(IO_3)_4O_2]$ (A = K, Rb, Tl), $AE[(UO_2)_2(IO_3)_2O_2](H_2O)$ (AE = Sr, Ba, Pb), $A_2[UO_2(CrO_4)(IO_3)_2]$ (A = K, Rb, Cs) [41], and $K_2[UO_2(MoO_4)(IO_3)_2]$ [41]. Dissecting the chains into simpler structural units leads to a more thorough understanding of the structural chemistry involved. First, each uranyl, UO_2^{2+}, moiety is bound by five iodate anions, four bridging and one terminal. Three uranyl units are connected by three bridging iodate anions to form twelve-member rings. Each ring then connects with an additional ring through three bridging iodate groups. The seven-coordinate environment of each U(VI) atom is completed by the monodentate iodate that serves to terminate the edges of the ribbon. The anionic ribbons are separated by IO_3^- anions, K^+ cations, and water molecules. $K[NpO_2(IO_3)_3]\cdot 1.5H_2O$ has a very similar topology with that of $K_3[(UO_2)_2(IO_3)_6](IO_3)\cdot H_2O$. The primary difference is that the central iodate anion is disordered so that it points two both sides of the chain with 50% occupancy for each orientation.

A key feature of these anions is the possibility of the net alignment of the stereochemically active lone-pair of electrons along a single polar axis as occurs in $NpO_2(IO_3)$ [22] and $PuO_2(IO_3)_2{\cdot}H_2O$ [47]. The centrosymmetric space group of $K_3[(UO_2)_2(IO_3)_6](IO_3){\cdot}H_2O$ precludes overall polarity, however the pyramidal iodate anions do show net alignment on one side of individual $^{1}_{\infty}[UO_2(IO_3)_3]^{1-}$ ribbons.

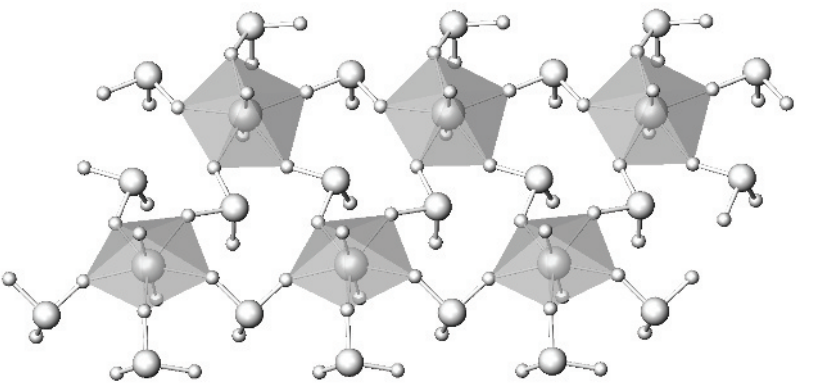

Figure 14. A view of part of a one-dimensional, anionic $^{1}_{\infty}[UO_2(IO_3)_3]^{1-}$ ribbon in $K_3[(UO_2)_2(IO_3)_6](IO_3){\cdot}H_2O$.

3.6. $Ag_4(UO_2)_4(IO_3)_2(IO_4)_2O_2$ [34]

The structure of $Ag_4(UO_2)_4(IO_3)_2(IO_4)_2O_2$ is a highly complex network consisting of three interconnected substructures. The first of these are one-dimensional uranium oxide ribbons consisting of both UO_8 hexagonal bipyramids and UO_7 pentagonal bipyramids. The UO_8 units edge-share to form one-dimensional chains that further share edges with UO_7 units to yield one-dimensional ribbons. The edges of these ribbons are partially terminated by tetraoxoiodate(V), $[IO_4]^{3-}$, anions (*vide infra*). The coordination sphere of the UO_7 units is completed, in part, through ligation by iodate anions. These iodate groups bridge between the one-dimensional uranium oxide ribbons to create undulating two-dimensional $^{2}_{\infty}[(UO_2)_4(IO_3)_2(IO_4)_2O_2]^{4-}$ sheets that run down the *b*-axis as shown in Figure 15.

Finally we come to the key feature of this structure, the tetraoxoiodate(V), $[IO_4]^{3-}$, anion. There are two crystallographically unique $[IO_4]^{3-}$ anions in $Ag_4(UO_2)_4(IO_3)_2(IO_4)_2O_2$. Both of these have approximate C_{2v} symmetry with

four oxygen atoms bent away from a tetrahedral coordination into a see-saw geometry.

I(1)-O bonds are 1.82(2), 1.88(2), 1.97(2), and 1.97(2) Å. The observed compression of the O-I-O bond angles of 154.3(7)° and 105.1(7)° indicates the presence of a lone-pair. I(2)-O bonds are 1.82(2), 1.83(2), 1.98(2), and 1.99(2) Å, and are similar to those found with I(1) as there are two short and two long I-O bonds. The $[IO_4]^{3-}$ anion containing I(2) also displays compression of O-I-O bond angles with O-I-O angles of 153.9(7)° and 99.7(7)°. The differences in the geometry of these tetraoxoiodate(V) anions are due to differences in coordination to surrounding metal centers. While both anions bridge uranium centers with three μ_3 oxygen atoms from each tetraoxoiodate(V) unit, the remaining oxygen atoms coordinate silver cations above and beneath the layers.

The central question here is how did this new ligand form? The answering of this question may lie in the structures of other uranyl iodate compounds that contain one-dimensional uranium oxide chains with their edges terminated by iodate ligands. $A_2[(UO_2)_3(IO_3)_4O_2]$ (A = K, Rb, Tl) and $AE[(UO_2)_2(IO_3)_2O_2](H_2O)$ (AE = Sr, Ba, Pb) both contain such chains where the chain edges are terminated by bridging and monodentate iodate ligands. In these compounds there are close I···O contacts ranging from 2.397(3) Å to 2.667(9) Å between the terminal oxygen atoms from the monodentate iodate ligand and the neighboring iodine atom from the iodate that bridges uranium centers. These types of interactions are very common in the structures of iodate compounds in general. If these close I···O contacts were to actually lead to a full oxygen atom transfer, then a $[IO_4]^{3-}$ anion would result. This may in fact be the mechanism by which iodate thermally disproportionates to metaperiodate, IO_4^-, and I_2, with $Ag_4(UO_2)_4(IO_3)_2(IO_4)_2O_2$ representing a trapped intermediate in this process.

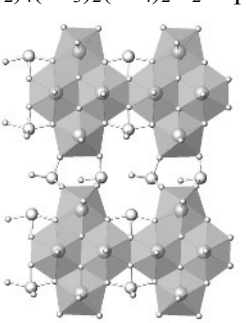

Figure 15. Two-dimensional $^2_\infty[(UO_2)_4(IO_3)_2(IO_4)_2O_2]^{4-}$ undulating sheets that run down the *b*-axis in $Ag_4(UO_2)_4(IO_3)_2(IO_4)_2O_2$. These sheets are created by iodate ligands bridging between one-dimensional uranium oxide ribbons.

3.7. $NpO_2(IO_3)$ [22]

The structure of $NpO_2(IO_3)$ consists of neptunyl(V) cations that are linked to one another by both NpO_2^+–NpO_2^+ bonds and by bridging iodate anions creating the pentagonal bipyramidal NpO_7 building unit. Oxygen atoms from the iodate anions occupy three of the equatorial sites in the NpO_7 units. The remaining two sites are filled by oxo atoms from neighboring neptunyl(V) cations. Both oxo atoms of the neptunyl(V) units are involved in coordinating adjacent Np(V) centers, leading to the creation of a two-dimensional neptunium oxide sheet similar to the one found in $[NpO_2(O_2CH)(H_2O)]$ [73-75]. The iodate anions link the neptunyl(V) sheets together into a three-dimensional network that is depicted in Figure 16. This network is polar owing to the alignment of the stereochemically active lone pair of electrons on the iodate anions along the *c*-axis, which is consistent with the polar space group, $Pna2_1$, found for $NpO_2(IO_3)$.

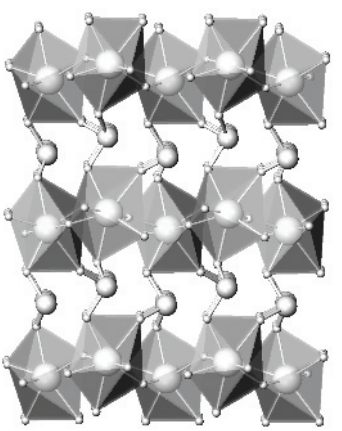

Figure 16. A depiction of part of the polar, three-dimensional network structure of $NpO_2(IO_3)$ showing the alignment of the stereochemically active lone pair of electrons on the iodate anions along the *c*-axis.

3.8. $PuO_2(IO_3)_2{\cdot}H_2O$ [47]

The structure of $PuO_2(IO_3)_2{\cdot}H_2O$ consists of infinite layers that extend in the [*ab*] plane with water molecules arranged between the layers as shown in Figure 17. The layers are built from corner-sharing $[IO_3]$ trigonal pyramidal and $[PuO_7]$ pentagonal bipyramidal units. Two crystallographically unique pyramidal IO_3^- anions bridge the plutonium centers. One of these bridges between two plutonyl units and the other between three. One of the critical

features of $PuO_2(IO_3)_2{\cdot}H_2O$ is that the structure is polar. As can be seen in Figure 17, the iodate anions are aligned so that the lone-pair of electrons are all oriented on one side of the layers. Among the iodates, only $K_3[(UO_2)_2(IO_3)_6](IO_3){\cdot}H_2O$, $NpO_2(IO_3)$, and $PuO_2(IO_3)_2{\cdot}H_2O$ achieve alignment of the iodate anions. As previously noted, while individual chains of $K_3[(UO_2)_2(IO_3)_6](IO_3){\cdot}H_2O$ are polar the chains are oriented in opposite directions in the structure canceling polarity.

A central question is then, why are acentric structures so rare in actinyl compounds, when they are relatively common in transition metal iodates? This question is answered by examining the symmetry of the actinyl unit itself. The formation of noncentrosymmetric structures owing to the alignment of the lone-pairs of electrons is not typically observed in actinyl structures, because the uranium atoms in UO_6 tetragonal bipyramids or UO_8 hexagonal bipyramids often reside on centers of inversion or higher symmetry. While UO_7 pentagonal bipyramids cannot be placed on inversion centers without disorder, they are often related to one another through such centers.

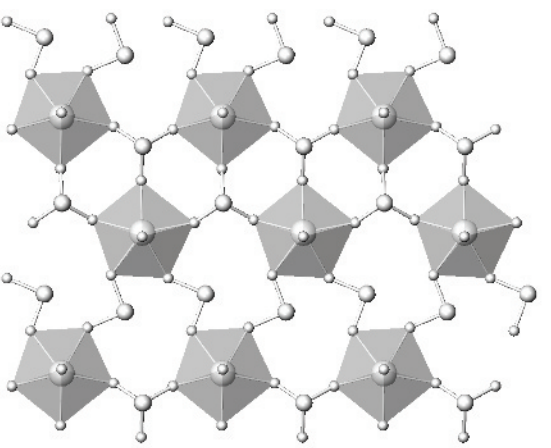

Figure 17. The structure of $PuO_2(IO_3)_2{\cdot}H_2O$ consists of infinite layers that extend in the [*ab*] plane with water molecules arranged between the layers. These layers are unusual in that they are polar.

4. Transplutonium Iodates

In contrast to the early actinide compounds already discussed, the iodates of the transplutonium actinides that have been prepared contain trivalent oxidation states for the actinide elements. For Am, several higher oxidation states are possible, but attempts to prepare Am(V) or Am(VI) analogs of these iodates

have been unsuccessful and have instead yielded compounds containing Am(III) [49,50]. The isolation and characterization of transneptunium selenites and tellurites have not been reported. As also observed in many other systems, the actinide(III) iodates are found to parallel the chemistry and structural behaviors of 4*f*-element iodates [49-52]. Lanthanide iodate chemistry has been well developed in efforts to prepare novel optoelectronic materials [76-86]. There are far fewer reports on actinide(III) iodates; the compounds that exist in the literature include: $Am(IO_3)_3$ [50], $Cm(IO_3)_3$ [51], $Cf(IO_3)_3$ [52], and $K_3Am_3(IO_3)_{12}{\cdot}HIO_3$ [49]. Structural characterization with single-crystal X-ray diffraction, Raman and emission spectroscopic data have also been reported for several of these actinide iodates.

$Am(IO_3)_3$ and $Cm(IO_3)_3$ are isostructural, crystallizing with the type I $Gd(IO_3)_3$ structure; this structure type is known with elements ranging from Ce to Lu (except for Pm) and Y, and is the series of iodate compounds with the most members [77, 79, 85]. This structure consists of An^{3+} cations bound by iodate anions to create a three-dimensional architecture. The Am or Cm centers are bound by eight bridging iodate anions to create a distorted, dodecahedral environment around the An^{3+}. Each AnO_8 polyhedron is formed by the monodentate coordination of eight iodate anions.

The Cm–O bond distances in $Cm(IO_3)_3$ range from 2.315(4) to 2.568(4) Å with an average value of 2.431(4) Å. This average value is 0.016 Å smaller than the average Am–O bond distance, 2.447(5) Å reported for $Am(IO_3)_3$, and is consistent with Am^{3+} having a larger ionic radius than Cm^{3+}. The Am−O and Cm−O distances are within the ranges expected, as calculated from published radii, and as reported previously. Due to the isostructural nature of these compounds, the iodate anions in the two compounds have similar bonding arrangements; these are described in more detail below.

For brevity, the iodate bonding arrangements in $Am(IO_3)_3$ and $Cm(IO_3)_3$ will be discussed together, crystallographic data for $Am(IO_3)_3$ is given in parentheses following that of $Cm(IO_3)_3$. There are three crystallographically unique iodate anions in the structure of $Cm(IO_3)_3$ and $Am(IO_3)_3$. The iodate anions containing I(2) and I(3) bridge three Cm^{3+} (Am^{3+}) cations, whereas the iodate containing I(1) bridges two Cm^{3+} (Am^{3+}) cations and has a terminal O(1) oxygen atom. This situation results in the formation of a three-dimensional structure. In some cases, terminal versus bridging I–O bond distances can be distinguished from one another, but in this compound this is not the case. In addition to the three short I–O distances around each iodine, there are additional I···O contacts from neighboring iodate anions. I(1) exhibits sevenfold coordination forming a

polyhedron that can best be described as a monocapped trigonal prism as a result of three short I–O bonds, two intermediate I–O, and two long I–O contacts. The iodate anions containing I(2) and I(3) have three long contacts in addition to the three oxygen atoms found in the inner shell of each iodine atom. The six-coordinate polyhedra that result for I(2) and I(3) are highly distorted.

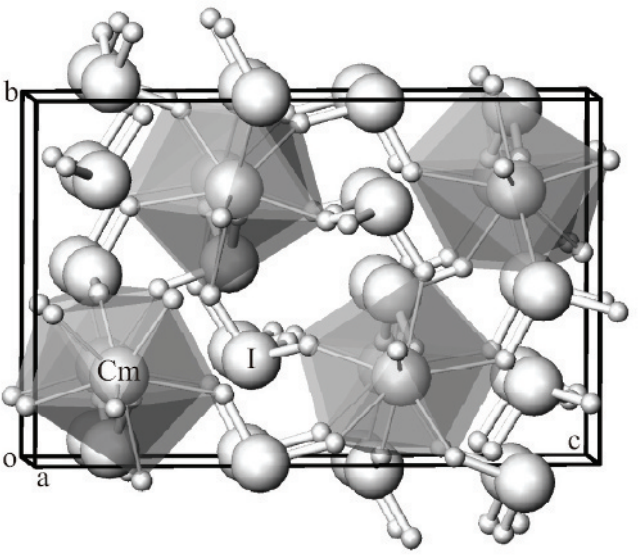

Figure 18. A view of the structure of $Am(IO_3)_3$ and $Cm(IO_3)_3$.

4.1. $Cf(IO_3)_3$ [52]

$Cf(IO_3)_3$ crystallizes with the $Bi(IO_3)_3$ structure, space group $P2_1/n$, a type that has not been reported in any other actinide iodates, although isostructural analogs containing several lanthanide cations have been reported [87]. The structure of $Cf(IO_3)_3$ is assembled from a combination of $[CfO_9]$ and $[IO_3]$ structural units. The coordination environment around the californium atom is best described as a tricapped trigonal prism; however, significant distortions away from a regular prism are present. The six oxygen atoms that form the distorted trigonal prism and one capping oxygen atom are significantly closer to the californium cation, with distances from 2.353(14) to 2.447(13) Å, than the remaining two capping oxygen atoms. These capping oxygen atoms are situated 2.709(13) and 2.921(13) Å away from Cf(1), respectively.

As is the case with $Am(IO_3)_3$ and $Cm(IO_3)_3$, the presence of three distinct iodate ions is also a feature in the $Cf(IO_3)_3$ system. The I–O bond distances and angles in the iodate anions range from 1.801(15) to 1.825(14) Å

and 88.7(6)^{o} to 99.4(6)^{o}, respectively. The iodate anion formed from I(1) is best described as an IO_{3+1} anion resulting from the coordination of three short I–O bonds and one lengthened distance of 2.425 Å. In addition to these four shorter I–O distances around I(1), there are two additional I···O contacts from neighboring iodate anions. A distorted octahedral geometry results for I(1) when these long contacts are included. I(2) exhibits a total sevenfold coordination forming a polyhedron that can best be described as a monocapped trigonal prism as a result of three short I–O bonds with distances ranging from 1.806(4) to 1.825(4) Å, two intermediate I–O distances of 2.761(14) and 2.780(14) Å, and two long I–O contacts of 2.956(14) and 3.051(14) Å. The iodate anion containing I(3) has five long contacts ranging from 2.695(14) to 3.389(14) Å in addition to the three oxygen atoms found in its inner shell.

An additional feature in the structure of $Cf(IO_3)_3$ is the presence of edge-sharing interactions between the CfO_9 polyhedra that lead to one-dimensional chains in the structure with alternating short-long Cf–Cf distances of 4.233 and 4.542 Å. This type of condensation of actinide polyhedra is not observed in the other actinide(III) iodates. In $Am(IO_3)_3$ and $Cm(IO_3)_3$, the shortest An–An distances are 5.961 and 5.926 Å, respectively. The iodate anions of I(1) and I(3) further bind the californium polyhedra together by bridging two adjacent CfO_9 polyhedra. Two-dimensional californium iodate layers, shown in Figure 19, are formed by the bridging of bidentate $I(2)O_3^-$ anions between two of the chains. The layers are connected into a pseudo-three-dimensional structure by the 2.425 Å I···O contacts of the $[I(1)O_{3+1}]^-$ anions; pseudo-dimers containing two such I···O contacts are formed between $[I(1)O_{3+1}]^-$ anions in adjacent layers. However, $Cf(IO_3)_3$ contains formally a two-dimensional, layered topology, while all of the other reported actinide(III) iodates contain three-dimensional structures.

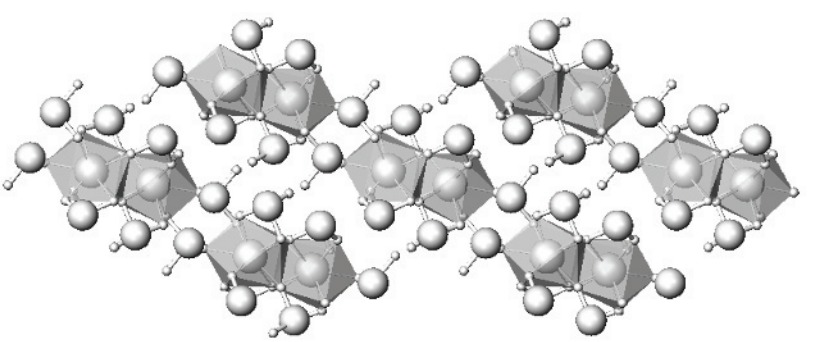

Figure 19. A view of the layered structure of $Cf(IO_3)_3$.

It is intriguing that $Cf(IO_3)_3$ contains nine-coordinate $[CfO_9]$ polyhedra, while the reported curium iodate [51] contains a $[CmO_8]$ distorted dodecahedral coordination. The smaller Cf^{3+} ion (0.949 Å) [88] would be expected to contain an equivalent or fewer inner-sphere atoms than the larger Cm^{3+} cation (0.979 Å) [88], based on ionic radii arguments alone. An additional interesting feature in the structure of $Cf(IO_3)_3$ is the presence of edge-sharing interactions between the $[CfO_9]$ polyhedra that lead to one-dimensional chains in the structure with alternating short-long Cf–Cf distances of 4.233 and 4.542 Å. Therefore, this compound offers a unique opportunity to investigate the magnetism of the Cf^{3+} cations in a low-dimensional system. It would be of fundamental interest to search for the possibility of magnetic ordering or magnetic transitions in $Cf(IO_3)_3$ and to study the role of the 5f electrons in the resultant magnetic behaviour.

4.2. $K_3Am_3(IO_3)_{12}{\cdot}HIO_3$ [49]

The only other actinide(III) iodate to be reported, $K_3Am_3(IO_3)_{12}{\cdot}HIO_3$, crystallizes in its own structure type, but it has also been shown that an isostructural compound containing cerium can be formed [89]. The structure of $K_3Am_3(IO_3)_{12}{\cdot}HIO_3$ is built around $[AmO_9]$ structural units. The coordination environment around the americium atom is best described as a tricapped trigonal prism; however, as also observed in $Cf(IO_3)_3$, there are significant distortions from a regular prism. One of the capping oxygen atoms forms a significantly longer Am–O length of 2.93(4) Å, while the remaining eight oxygen atoms are situated 2.42(3) to 2.60(3) Å away from the americium leading to an average Am–O distance of 2.52 Å. The $[AmO_9]$ polyhedra are formed from the coordination of eight monodentate $[IO_3]$ groups and one oxygen atom from the neutral HIO_3. This latter Am–O distance is found for the relatively weak interaction of the Am atom with an oxygen atom of the neutral HIO_3.

Four crystallographically unique IO_3^- anions and one HIO_3 moiety are found in the structure of $K_3Am_3(IO_3)_{12}{\cdot}HIO_3$. Each unique IO_3^- anion forms a trigonal pyramid with three I–O distances in the range 1.75(3) to 1.85(3) Å, but deviates from the ideal 3*m* point symmetry, as is observed in the majority of structures containing iodate. All of the iodate anions are bidentate, they contain one terminal oxygen atom and bridge two americium atoms with their remaining two oxygen atoms. In addition to the three oxygen atoms coordinated in the inner shell of each iodine, there are three additional long contacts for each, ranging from 2.67 to 3.01 Å. $K_3Am_3(IO_3)_{12}{\cdot}HIO_3$ represents the only acidic actinide iodate; several acidic lanthanide iodates are known, including $Pr(IO_3)_3{\cdot}HIO_3$ [90] and $3La(IO_3)_3{\cdot}HIO_3{\cdot}7H_2O$ [82]. In

$K_3Am_3(IO_3)_{12}{\cdot}HIO_3$, the HIO_3 moiety contains bond lengths of 1.9 Å, ~0.1 Å longer compared to the anionic iodates.

The structure of $K_3Am_3(IO_3)_{12}{\cdot}HIO_3$ is composed of 12-membered rings formed from the bidentate bridging of three $[AmO_9]$ polyhedra by three $[IO_3]$ groups. These rings align to form irregularly-shaped hexagonal channels found along the *c* axis. A three-dimensional network is formed by the linking of these rings with additional bidentate iodate ligands. The K cations and HIO_3 moieties are housed by the hexagonal channels. Each potassium cation forms six K···O contacts in the range of 2.40 to 2.78 Å in $K_3Am_3(IO_3)_{12}{\cdot}HIO_3$, including two interactions with the oxygen atoms from the neutral HIO_3. An interesting feature of $K_3Am_3(IO_3)_{12}{\cdot}HIO_3$ is the lack of inversion symmetry. In the structure, all of the neutral HIO_3 molecules align in the same direction, along the *c* axis, leading to a polar structure. The formation of noncentrosymmetric structures is by incorporating trigonal pyramidal anions such as iodate is an active field of research by several research groups. Although this compound will not likely find its way into a practical device due to the incorporation of the radioactive Am, lanthanide analogs could have potential applications.

5. Underdeveloped actinide oxoanions: antimonites and bismuthites

Actinide antimonites and bismuthites containing the main group element in the +3 oxidation state are currently severely restricted with only one example of each being known, $UO_2Sb_2O_4$ [91] and uranosphaerite, $Bi(UO_2)O_2OH$ [31]. From these few examples, rich chemistry has already been observed. Both compounds are layered, and both contain EO_4 square pyramidal anions.

Table 4. A listing of uranyl antimonite and bismuthite compounds.

	formula	*Space group*	a, Å	b, Å	c, Å	angles, º	Ref.
1.	$UO_2Sb_2O_4$	***C*2/m**	13.490(2)	4.0034(6)	5.1419(8)	β= 104.165(3)	90
2.	$Bi(UO_2)O_2OH$ uranosphaerite	$P2_1/n$	7.559(2)	7.811(2)	7.693(2)	β= 92.88(3)	30

5.1. Structure of $UO_2Sb_2O_4$ [91]

Only a single uranyl antimonite is known to exist. There are nominal UO_6 subunits that form the backbone of the structure of $UO_2Sb_2O_4$, although there is strong evidence that the coordination environment around uranium would be better described as a UO_8 distorted hexagonal bipyramid. In addition to the two

terminal oxo groups, the U coordination environment is completed by bridging O atoms from antimonite anions. Four of the bridging O atoms are perpendicular to the uranyl unit as expected for U(VI) compounds, however, the two of the O atoms deviate from the orthogonal plane by 12.7(2)°. These interactions are 2.815(5) Å, 0.4 to 0.6 Å longer than expected for a U–O equatorial bond length, while the other U–O bond lengths of 2.354(3) Å are well within the expected range. Bond valence sum calculations on the six closest oxygen atoms, and with all eight interacting oxygen atoms yield values of 5.66 and 5.79, respectively, which show that the longer distances are significant [56. 57, 92]. The uranium coordination is therefore a distorted hexagonal bipyramid.

The UO_8 distorted hexagonal bipyramidal units edge-share along the *b* axis to form uranium oxygen chains that are further linked into two-dimensional $^{2}_{\infty}[UO_2Sb_2O_4]$ layers by the bridging $^{1}_{\infty}[Sb_2O_4]^{2-}$ chains as shown in Figure 20. A small interlayer spacing of 4.986 Å leads to a density of 7.124 g/cm^3 and is higher than found for most other uranium/main group oxides [56, 57] that have been produced from hydrothermal syntheses. The lone pairs on the antimony atoms point toward adjacent layers and form long interactions of 3.011 Å between the antimony atoms of one layer and the O atoms of neighboring layers that help hold the structure together.

The $^{1}_{\infty}[Sb_2O_4]^{2-}$ chains found in $UO_2Sb_2O_4$ are comprised of four coordinate SbO_4 square pyramids, containing a lone pair, that edge-share along the *b* axis and are similar to Sb–O chains found in $SbNbO_4$ and $SbTaO_4$ [93, 94]. All of the oxygen atoms bound to Sb(1) are at least μ_3 and if the 2.815(5) Å U(1)···O(2) interactions are considered bonds, then three of the antimonite oxygens are μ_4. As expected, the shortest Sb–O bond length of 1.948(5) Å is to the truly μ_3 O(1).

6. Summary

The central question that needs answering as this chapter comes to a close is whether or not general statements can be made concerning the role that the inert pair of electrons on heavy oxoanions can play in determining the structures of crystalline actinide compounds? As we survey the known materials with anions of this type, it is apparent that there are many roles for these electrons, including the formation of channels and cavities, alignment to create polarity and chirality, and especially dimensional reduction. Dimensional reduction to one-

dimensional chain structures is particularly apparent in actinyl iodates, but has also been observed in selenites and tellurites. One might go as far to say that the statistics for the dimensionality of uranyl compounds have been skewed by such strong efforts to prepare compounds with anions containing nonbonding electrons. Had more time been devoted to preparing compounds with tetrahedral anions like phosphate more layered and network structures would likely be known.

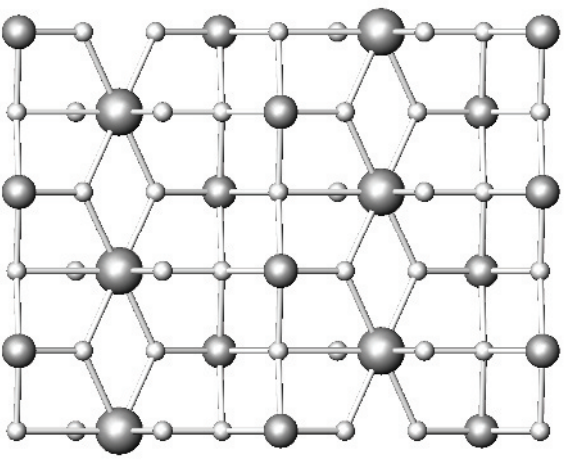

Figure 20. An illustration of the UO_8 distorted hexagonal bipyramidal units in $UO_2Sb_2O_4$ that edge-share along the *b* axis to form uranium oxygen chains that are further linked into two-dimensional $^{2}_{\infty}[UO_2Sb_2O_4]$ layers by the bridging $^{1}_{\infty}[Sb_2O_4]^{2-}$ chains.

A second question that needs to be addressed with extreme caution is do actinide compounds with these anions have any utility? For standard applications, radioactive materials are generally prohibitive, not necessarily because of actual physical damage from exposure, but because of the general publics' irrational fear of all things radioactive. Some potential applications for these compounds include ion-exchange, storage of radionuclides, catalysis, and nonlinear optical materials. The first two are perhaps the most promising. The second two will he hard to justify in the face of readily available and highly efficient transition metal-based materials.

In terms of ion-exchange, it has already been demonstrated that the K^+ cations in $K[UO_2(IO_3)_3]$ can be exchanged for Cs^+ with high selectivity and uptake values [43]. This result may indicate a potential use for these compounds in removing ^{137}Cs from radioactive waste. Much more work in this area is needed

before it will really be known if these compounds are competitive ion-exchange materials.

The use of these anions to trap and perhaps store transuranium elements has been proposed, despite the fact that these anions are generally redox active, often being strong oxidizing agents. More importantly, it is now known from X-ray diffraction studies on single crystals of $An(IO_3)_3$ (An = Am, Cm, Cf) that actinide iodates are highly susceptible to radiation damage. It appears that different mechanisms can be in operation for the destruction of the crystallinity of these compounds as both α particles and neutrons cause these materials to become amorphous. While early separation processes based on selective precipitation with iodate were well-developed and patented, far more efficient ion-exchange resins can be used to separate actinides with ease. To conclude, it is not the application of actinide compounds with a stereochemically active lone-pair of electrons that has driven this research, but rather a fundamental curiosity about the crystal chemistry of these compounds. This research has substantially expanded solid-state actinide chemistry with seventy-four crystallographically characterized compounds now been reported in the literature. There are undoubtly may more important discoveries left to be made in this field.

References

1. Rammelsberg, C. *Ann. Physik Chem.* **1843**, *59*, 25.
2. Weigel, F.; Engelhardt, L. W. H. *J. Less Common Met*. **1983**, *91,* 339.
3. Artmann, P. *Z. Anorg. Chem.* **1913**, *79*, 327.
4. Bean, A. C.; Peper, S. M.; Albrecht-Schmitt, T. E. *Chem. Mater.* **2001**, *13*, 1266.
5. Cooper, M. A.; Hawthorne, F. C. *Can. Mineral.* **2001**, *39*, 797.
6. Loopstra, B. O.; Brandenburg, N. P. *Acta Crystallogr*. **1978**, *B34*, 1335.
7. Ginderow, D.; Cesbron, F. *Acta Crystallogr.* **1983**, *C39*, 824.
8. Ginderow, D.; Cesbron, F. *Acta Crystallogr.* **1983**, *C39,* 1605.
9. Trombe, J. C.; Gleizes, A.; Galy, J. *Acta Crystallogr*. **1985**, *C41*, 1571.
10. Trombe, J. C.; Galy, J. *J. Solid State Chem.* **1986**, *61*, 308.
11. Deliens, M.; Piret, P. *Can. Mineral.* **1991**, *29*, 561.
12. Cooper, M. A.; Hawthorne, F. C. *Can. Mineral.* **1995**, *33,* 1103.
13. Mistryukov, V.E.; Michailov, Yu.N. *Koordinatsionnaya Khimiya* **1983**, *9*, 102
14. Koskenlinna, M.; Valkonen, J. *Acta Crystallogr.* **1996**, *C52*, 1857.
15. Koskenlinna, M.; Mutikainen, I.; Leskelae, T.; Leskelae, M. *Acta Chemica Scandinavica,* **1997**, *51*, 264.
16. Vochten, R.; Blaton, N.; Peeters, O.; Deliens, M. *Can. Mineral*. **1996**, *34*, 1317.
17. Almond, P. M.; Albrecht-Schmitt, T. E. *Inorg. Chem.* **2002**, *41*, 1177.
18. Almond, P. M.; Peper, S. M.; Bakker, E.; Albrecht-Schmitt, T. E. *J. Solid State Chem.* **2002**, *168*, 358.

19. Chukanov, N. V.; Pushcharovsky, D. Yu.; Pasero, M.; Merlino, S.; Barinova, A. V.; Moeckel, S.; Pekov, I. V.; Zadov, A. E.; Dubinchuk, V. T. *European Journal of Mineralogy* **2004**, *16*, 367.
20. Almond, P. M.; Albrecht-Schmitt, T. E. *Amer. Mineral.* **2004**, *89*, 976.
21. Almond, P. M.; Sykora, R. E.; Skanthakumar, S.; Soderholm, L.; Albrecht-Schmitt, T. E. *Inorg. Chem.* **2004**, *43*, 958.
22. Albrecht-Schmitt, T. E.; Almond, P. M.; Sykora, R. E. *Inorg. Chem.* **2003**, *42*, 3788.
23. Gaines, R. V. *Amer. Mineral.* **1969**, *56,* 411.
24. Gaines, R. V. *Amer. Mineral.* **1971**, *54,* 69.
25. Swihart, G. H.; Sen G.; Pardip K.; Schlemper, E. O.; Back, M. E.; Gaines, R. V. *Amer. Mineral.* **1993**, *78*, 835.
26. Brandstaetter, F. *Zeitschrift fuer Kristallographi,* **1981**, *155*, 193.
27. Almond, P. M.; Albrecht-Schmitt, T. E. *Inorg. Chem.* **2002**, *41,* 5495
28. Almond, P. M.; McKee, M. L.; Albrecht-Schmitt, T. E. *Angewandte Chemie, Int. Edition*, **2002**, *41*, 3426.
29. Woodward, J. D.; Almond, P. M.; Albrecht-Schmitt, T. E. *J. Solid State Chem.* **2004**, *177,* 3971.
30. Woodward, J. D.; Albrecht-Schmitt, T. E. *J. Solid State Chem.* **2005**, *178,* 2922.
31. Hughes, K.-A.; Burns, P. C.; Kolitsch, U. *Can. Mineral*. **2003**, *41*, 677
32. Suchanek, E.; Zhang, Z.; Lutz, H. D. *Z. Anorg. Allg. Chem*. **1996**, *622*, 1957
33. Bean, A. C.; Ruf, M.; Albrecht-Schmitt, T. E. *Inorg. Chem.* **2001**, *40*, 3959.
34. Bean, A. C.; Campana, C. F.; Kwon, O.; Albrecht-Schmitt, T. E. *J. Am. Chem. Soc.* **2001**, *123*, 8806.
35. Bean, A. C.; Albrecht-Schmitt, T. E. *J. Solid State Chem.* **2001**, *161*, 416.
36. Abrahams, S.C.; Bernstein, J.L.; Elemans, J.B.A.A.; Verschoor, G.C. *J. Chem. Phys.* **1973**, *59,* 2007.
37. Burns, P.C.; Hawthorne, F.C. *Can. Mineral.* **1993**, *31*, 313.
38. Copper, M. A.; Hawthorne, F. C.; Roberts, A. C.; Grice, J. D.; Stirling, J. A. R.; Moffatt, E. A. *Amer. Mineral.* **1998**, *83*, 390
39. Johnston, M. G.; Harrison, W. T. A. *J. Am. Chem. Soc.* **2002**, *124*, 4576.
40. Sykora, R. E.; Wells, D. M.; Albrecht-Schmitt, T. E. *Inorg. Chem.* **2002**, *41*, 2304.
41. Sykora, R. E.; McDaniel, S. M.; Wells, D. M.; Albrecht-Schmitt, T. E. *Inorg. Chem.* **2002**, *41*, 5126.
42. Bean, A. C.; Xu, Y.; Danis, J. A.; Albrecht-Schmitt, T. E.; Scott, B. L.; Runde, W. *Inorg. Chem.* **2002**, *41*, 6775.
43. Sykora, R. E.; Bean, A. C.; Scott, B. L.; Runde, W.; Albrecht-Schmitt, T. E. *J. Solid State Chem.* **2004**, *177*, 725.
44. Shvareva, T. Y.; Almond, P. M.; Albrecht-Schmitt, T. E. *J. Solid State Chem.* **2005**, *178*, 499.
45. Bean, A. C.; Scott, B. L.; Albrecht-Schmitt, T. E.; Runde, W. *Inorg. Chem.* **2003**, *42*, 5632.
46. Bean, A. C.; Scott, B. L.; Albrecht-Schmitt, T. E.; Runde, W. *J. Solid State Chem.* **2004**, *177*, 1346.
47. Runde, W.; Bean, A. C.; Albrecht-Schmitt, T. E.; Scott, B. L. *Chem. Comm. (Cambridge, United Kingdom)* **2003**, *4*, 478.
48. Bean, A. C.; Abney, K.; Scott, B. L.; Runde, W. *Inorg. Chem.* **2005**, *44*, 5209.
49. Runde, W.; Bean, A. C.; Scott, B. L. *Chem. Comm. (Cambridge, United Kingdom),* **2003**, *15*, 1848.
50. Sykora, R. E.; Assefa, Z.; Haire, R. G.; Albrecht-Schmitt, T. E. *Inorg. Chem.* **2005**, *44*, 5667.
51. Sykora, R. E.; Assefa, Z.; Haire, R. G.; Albrecht-Schmitt, T. E. *J. Solid State Chem.* **2004**, *177,* 4413.

52. Sykora, R. E.; Assefa, Z.; Albrecht-Schmitt, T. E.; Haire, R. G. *Inorg. Chem.* **2005**, *ASAP*.
53. Weaver, B. *Anal. Chem.* **1968**, 40, 1894.
54. Demartin, F.; Diella, V.; Donzelli, S.; Gramaccioli, C. M.; Pilati, T. *Acta Crystallogr.* **1991**, *B47*, 439
55. Hughes, K.-A.; Burns, P. C. *Amer. Mineral.* **2003**, 88, 962
56. Burns, P.C.; Miller, M.L.; Ewing, R.C. *Can. Mineral.* **1996***, 34,845*
57. Burns, P. C.; Ewing, R. C.; Hawthorne, F. C. *Can. Mineral. 1997*, 35, 1551
58. Wang, X.; Haung, J.; Liu, L.; Jacobson, A. J. *J. Mater. Chem*. **2002**, *12*, 406
59. Shvareva, T. Y.; Sullens, T. A.; Shehee, T. C.; Albrecht-Schmitt, T. E. *Inorg. Chem.* **2005**, *44*, 300
60. Danis, J. A.; Runde, W. H.; Scott, B.; Fettinger, J.; Eichhorn, B. *Chem.Commun.* **2001**, *22*, 2378
61. Li, Y. ; Cahill, C. L.; Burns, P. C. *Chem. Mater.* **2001**, *13*, 4026
62. Albrecht-Schmitt, T. E.; Ibers, J. A. *Inorg. Chem.* **1996**, *35*, 7273.
63. Cunningham, B. B.; Werner, L. B. *J. Amer. Chem.Soc.* **1949**, *71* 1521
64. Moeller, T.; Fritz, N. D. *Anal. Chem.* **1948**, *20*, 1055
65. Shaver, K. J.; Monsanto Chem. Co.; Miamisburg, O. *Anal. Chem.* **1956,** *28*, 2015
66. Egorov, V. N.; Korinfskaya, M. F.; Markov, V. K. *Radiokhimiya* **1969**, *11,* 560
67. Stoughton, R. W.; Duffield, R. B. **1958**, US 2856261 19581014
68. Miller, D. R.; Seaborg, G. T.; Thompson, S. G. **1959**, US 2917358 19591215
69. Fries, B. A. **1960,** US 2926067 19600223
70. Chiola, V.; Kamin, G. J. **1971,** US 3594117 19710720
71. Kudryavskii, Yu. P.; Strelkov, V. V.; Trapeznikov, Yu. F.; Kazantsev, V. P. **2003,** RU 2207393 C1 20030627
72. Tranter, T. J.; Todd, T. A.; Lewis, L. C.; Henscheid, J. P. **2004**, U.S. 2004052705, A1 200440318.
73. Grigor'ev, M. S.; Yanovskii, A. I.; Struchkov, Yu. T.; Bessonov, A. A.; Afonas'eva, T. V.; Krot, N. N. *Radiokhimiya* **1989,** *31*, 37.
74. Grigor'ev, M. S.; Yanovskii, A. I.; Struchkov, Yu. T.; Bessonov, A.A.; Afonas'eva, T. V.; Krot, N. N. *Radiochemistry* **1990**, 397.
75. Krot, N. N.; Suglobov, D. N. *Radiokhimiya* **1989**, *31*, 1.
76. Liminga, R.; Abrahams, S.C.; Bernstein, J.L. *J. Phys. Chem.* **1975**, *62,* 755.
77. Liminga, R. ; Abrahams, S.C. ; Bernstein, J.L. *J. Phys. Chem*. **1977**, *67*, 1015.
78. Nassau, K.; Shiever, J.W.; Prescott, B.E. ; Cooper, A.S. *J. Solid State Chem.* **1974**, *11,* 314.
79. Nassau, K.; Shiever, J.W.; Prescott, B.E.; Cooper, A.S. *J. Solid State Chem.* **1975**, 14, 122.
80. Abrahams, S.C.; Bernstein, J.L.; Nassau, K. *J. Solid State Chem.* **1976**, *16*, 173.
81. Abrahams, S.C.; Bernstein, J.L.; Nassau, K.; *J. Solid State Chem.* **1977**, *22*, 243.
82. Abrahams, S.C. ; Bernstein, J.L. *J. Phys. Chem.* **1978**, *69*, 2505.
83. Gupta, P.K.S.; Ammon, H.L.; Abrahams, S.C. *Acta Crystallogr.* **1989**, *C45*, 175.
84. Hector, A.L.; Henderson, S.J.; Levason, W.; Webster, M. *Z. Anorg. Allg. Chem.* **2002**, *628,* 198.
85. Douglas, P.; Hector, A.L.; Levason, W.; Light, M.E.; Matthews, M.L.; Webster, M. *Z. Anorg. Allg. Chem.* **2004**, *630*, 479.
86. Shehee, T.C.; Sykora, R.E.; Ok, K.M.; Halasyamani, P.S.; Albrecht-Schmitt, T.E. *Inorg. Chem*. **2003**, *42*, 457.
87. Bentria, B.; Benbertal, D.; Bagieu-Beucher, M.; Masse, R.; Mosset, A. *J. Chem. Crystallogr.* **2003**, *33*, 867.
88. Gschneidner, K. A. Jr., Eyring, L., Choppin G. R., Lander, G. H. (Eds.) *Handbook on the Physics and Chemistry of Rare Earths,* North-Holland, New York, 1994, V. 18, p. 483.
89. Sykora, R. E., Albrecht-Schmitt, T. E. unpublished results.

90. Abrahams, S. C.; Bernstein, J. L.; Shiever, J. W.; Nassau, K. *J. Appl. Crystallogr.* **1976,** *9*, 357.
91. Sykora, R. E.; King, J. E.; Illies, A. J.; Albrecht-Schmitt, T. E. *J. Solid State Chem.* **2004**, *177,* 1717.
92. Brese, N.E.; O' Keeffe, M. *Acta Crystallogr.* **1991**, B47, 192.
93. Ponomarev, V.I.; Filipenko, O.S.; Atomyan, L.O.; Rannev, N.V.; Ivanov, S.A.; Venevtsev, Yu.N. *Kristallografiya* **1981**, 26, 341.
94. Dihlstroem, K. *Z. Anorg. Allg. Chem.* **1938**, 239, 57.

Structural Chemistry of Inorganic Actinide Compounds
S.V. Krivovichev, P.C. Burns & I.G. Tananaev (Editors)

Chapter 6

Crystal chemistry of actinide phosphates and arsenates

Andrew J. Locock

Department of Earth and Atmospheric Sciences, University of Alberta, 1-26 Earth Sciences Building, Edmonton, Alberta, T6G 2E3, Canada

1. Introduction

Recent investigations into the crystal chemistry of actinide phosphates have primarily been driven by the requirement to remediate continuing actinide contamination in the environment and by the imperative for long-term sequestration of excess actinides generated by the nuclear fuel cycle [1-3]. In natural settings, uranium phosphate species are among the most numerous, widespread, abundant and insoluble of actinide-bearing minerals, and largely control the mobility of actinides in many groundwaters, and in actinide-contaminated soils and sediments [4, 5]. The structures and behavior of uranium-bearing and thorium-bearing phosphate minerals thus provide a basis from which to predict the long-term behavior of actinide-bearing phosphates.

This chapter presents an overview of the crystal structures of inorganic compounds in which actinide polyhedra are directly coordinated by phosphate or arsenate tetrahedra. Arsenates are considered here for comparative purposes, because of the very similar structural roles played by arsenate and phosphate ions. Structural data are taken mainly from the Inorganic Crystal Structure Database [6] and the published literature. Entries from the Powder Diffraction File of the International Centre for Diffraction Data [7] have been consulted in the case of compounds whose structures may reasonably be inferred. Mixed organic-inorganic compounds [8] and polyoxometalates are not addressed; phosphites, phosphinates and arsenites also fall outside the scope of this chapter. Data are tabulated for a given structure type, with phosphates separated

from arsenates, and organized in order of increasing atomic number of the actinide present. The chemical formulas presented here have often been re-arranged from those given by the original authors in order to emphasize structural features and to facilitate ease of comparison; in some cases, an alternative setting of a space group is also used.

1.1. Structural Hierarchy

The crystal chemistry of phosphate minerals has recently been reviewed [9, 10]. These references present a structural hierarchy based on the polymerization of polyhedra of higher bond-valence, especially tetrahedra and octahedra. In a similar fashion, an extensive structural hierarchy of uranyl minerals and inorganic compounds has been developed over the last decade [11, 12]. This chapter follows the concepts and principles of both of these structural hierarchies, but places the primary emphasis on actinide coordination. As the coordination environments of the actinides differ with valence state [13, 14], it has been found convenient to discuss the compounds of the lower valence-state actinides separately from those of the higher valence-states.

1.2. Organization

The orthophosphates and orthoarsenates (those compounds in which phosphate or arsenate tetrahedra are not polymerized with each other) of the lower valence actinides (trivalent and tetravalent states) are considered first, followed by their polyphosphates and polyarsenates (those compounds in which phosphate or arsenate tetrahedra are polymerized with each other). The orthophosphates and orthoarsenates of the hexavalent actinides are then reviewed, and the chapter concludes with the polyphosphates and polyarsenates of the hexavalent actinides.

2. Trivalent and Tetravalent Actinides

The ionic radii of the lower-valence states (An^{3+}, An^{4+}) of the early actinides are similar to those of the trivalent states of the lanthanides [15]. As might be expected on the basis of the similarities in size and charge, the early actinides in their lower valence states play similar roles to the trivalent lanthanides and Zr in the structures of phosphates and arsenates. The chemistry of both trivalent- and tetravalent-actinide phosphates has recently been re-examined in detail [16-18]. This chapter takes a structural approach to the same material, and of necessity restricts its coverage to those compounds whose crystal structures have either been determined or whose structural affiliation may reasonably be inferred. It

should be noted that careful investigation has shown that tetravalent-actinide phosphates of stoichiometry $An_3(PO_4)_4$ do not appear to exist as single crystalline phases [16]. Rather, such compositions typically consist of mixtures of two or more of the following: actinide polyphosphates, actinide orthophosphates and actinide oxides [16].

2.1. *Orthophosphates and Orthoarsenates*

In the orthophosphates and orthoarsenates, the lower-valence actinides show a range of coordination states amongst the different structures from six-coordinate to twelve-coordinate, with coordination numbers eight and nine being the most common. According to Cotton et al. [13], this range in coordination numbers results from the large size of actinide ions, their high formal charges, and the large number of valence shell orbitals potentially available for bonding. The structures are presented below in order of increasing coordination number.

2.1.1. Sixfold coordination

Only two structure-types host lower-valence actinides in sixfold coordination: eulytine, $Bi_8(SiO_4)_6$, and kosnarite, $KZr_2(PO_4)_3$. In the eulytine structure-type (Table 1), Th and U occur in the tetravalent state in $1/8^{th}$ random substitution for large divalent cations (Sr, Ba, Pb) on the single symmetrically unique octahedral position, whereas P occupies the single tetrahedral position. The structure of eulytine [26] consists of a framework of strongly distorted edge-shared octahedra that are additionally connected by corner-sharing with tetrahedra (Fig. 1).

The mineral kosnarite, $KZr_2(PO_4)_3$, is isostructural with the large class of solid ionic conductors typified by the material NASICON, $Na_{1+x}Zr_2Si_xP_{3-x}O_{12}$ [27], and by NZP, $NaZr_2(PO_4)_3$. In the kosnarite structure-type [28], tetravalent actinides occupy octahedral positions (Table 1). The structure of kosnarite has been described as a framework of corner-sharing tetrahedra and octahedra with low-valence cations in sixfold coordination occupying the interstices [10, 25] (Fig. 2). Kosnarite-type compounds have been proposed as nuclear waste forms, because of the expected advantage that as a single-phase ceramic, this structure could accommodate the wide variety of radionuclides present in high-level wastes [2]. The ease with which these compounds undergo ion exchange [27] may reduce their utility in this regard, at least with respect to the mobility of the alkali metals.

Table 1. Orthophosphates with An^{4+} in sixfold coordination

Formula	Structure	Status*	S.G.	*a* (Å)	*c* (Å)	Ref.
$(Sr_7Th)(PO_4)_6$	eulytine	inf	*I*-43*d*	10.19		19
$(Pb_7Th)(PO_4)_6$	eulytine	inf	*I*-43*d*	10.37		20
$(Ba_7Th)(PO_4)_6$	eulytine	inf	*I*-43*d*	10.58		21
$(Sr_7U)(PO_4)_6$	eulytine	inf	*I*-43*d*	10.18		22
$KU_2(PO_4)_3$	kosnarite	det	*R*-3*c*	9.11	25.00	23
$RbU_2(PO_4)_3$	kosnarite	inf	*R*-3*c*	9.07	25.65	25
$RbNp_2(PO_4)_3$	kosnarite	inf	*R*-3*c*	9.13	25.72	25
$NaPu_2(PO_4)_3$	kosnarite	inf	*R*-3*c*	9.09	23.70	24
$KPu_2(PO_4)_3$	kosnarite	inf	*R*-3*c*	9.07	24.86	25

*Structure determined (det), or structural affiliation inferred (inf)

Note: different structure types are separated by a double line

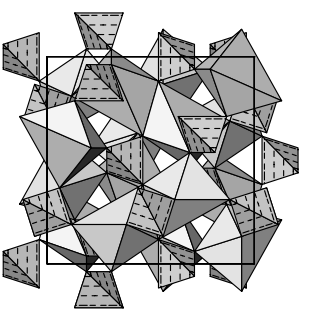

Figure 1. The structure of eulytine, $Bi_8(SiO_4)_6$, projected along [100], after [26]. Tetrahedra are stippled and octahedra are shaded.

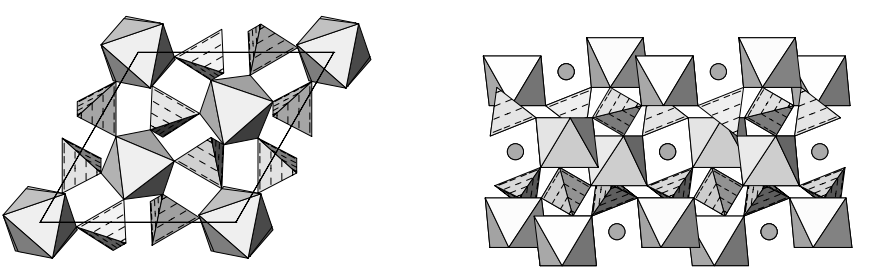

Figure 2. A portion of the structure of kosnarite, $KZr_2(PO_4)_3$, projected along [001] at left (K atoms omitted) and along [110] at right (K atoms shown as spheres), after [28].

2.1.2. Sevenfold coordination

Three structure-types host lower-valence actinides in sevenfold coordination (Table 2): $Zr_2O(PO_4)_2$ (β form), $Th_2(PO_4)_2PO_3OH(H_2O)$, and $UPO_4X(H_2O)_2$, X = Cl, Br. The structure of $U_2O(PO_4)_2$ has been refined [$Zr_2O(PO_4)_2$-type] and consists of UO_7 distorted pentagonal bipyramids that share edges to form chains that extend along the [100] direction [29, 30]. These chains share edges with phosphate tetrahedra. Adjacent uranium phosphate chains share vertices to form a framework (Fig. 3). Interestingly, this compound has negative thermal expansion up to 1000°C, mainly as a result of the libration of the PO_4 and UO_7 polyhedra in the structure [34].

Table 2. Orthophosphates with tetravalent actinides in sevenfold coordination

Formula	Structure	Status*	S.G.	*a* (Å)	*b* (Å)	*c* (Å)	β (°)	Ref.
$Th_2O(PO_4)_2$	$Zr_2O(PO_4)_2$	inf	*Cmca*	7.18	9.23	12.86		17
$U_2O(PO_4)_2$	$Zr_2O(PO_4)_2$	det	*Cmca*	7.09	9.04	12.70		29, 30
$Np_2O(PO_4)_2$	$Zr_2O(PO_4)_2$	inf	*Cmca*	7.04	9.02	12.59		17
$Th_2(PO_4)_2HPO_4(H_2O)$		det	$P2_1$	6.70	7.02	11.18	107.2	31, 32
$UPO_4Cl(H_2O)_2$	$UPO_4Cl(H_2O)_2$	det	*I*4/*m*	14.63		6.66		33
$UPO_4Br(H_2O)_2$	$UPO_4Cl(H_2O)_2$	det	*I*4/*m*	14.75		6.68		33

*Structure determined (det), or structural affiliation inferred (inf)

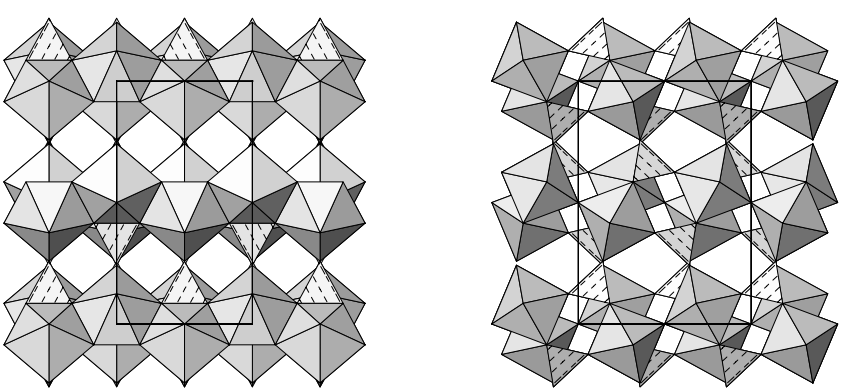

Figure 3. The structure of $U_2O(PO_4)_2$, projected along [010] at left, and along [100] at right, after [29]. Uranium-centered polyhedra are shaded, and tetrahedra are stippled.

The structure of $Th_2(PO_4)_2PO_3OH(H_2O)$ has recently been determined in space group $P2_1$ [31]. This compound has also been reported to have orthorhombic symmetry [32] and it is likely that it is actually pseudosymmetric. The matrix 102/100/010] transforms the monoclinic *P* cell reported in the structure refinement to a pseudo-orthorhombic *C* setting, *a* 21.36, *b* 6.70, *c* 7.02 Å, β 89.8°, which is extremely similar to the cell reported solely from powder data: *a* 21.37, *b* 6.70, *c* 7.02 Å, β 90° [32]. In contrast, the uranium analog $U_2(PO_4)_2PO_3OH(H_2O)$ has cell dimensions similar to its Th analog in the orthorhombic setting, but monoclinic symmetry: *a* 21.15 *b* 6.61 *c* 6.99 Å, β 91.7°; its structure has not been refined [35].

The structure of $Th_2(PO_4)_2PO_3OH(H_2O)$ consists of edge-sharing dimers of irregular ThO_7 polyhedra that are connected into a double slab by sharing edges and vertices with phosphate tetrahedra. The slabs are connected by vertex-sharing with PO_3OH tetrahedra; H_2O groups occupy the cavities of the framework (Fig. 4).

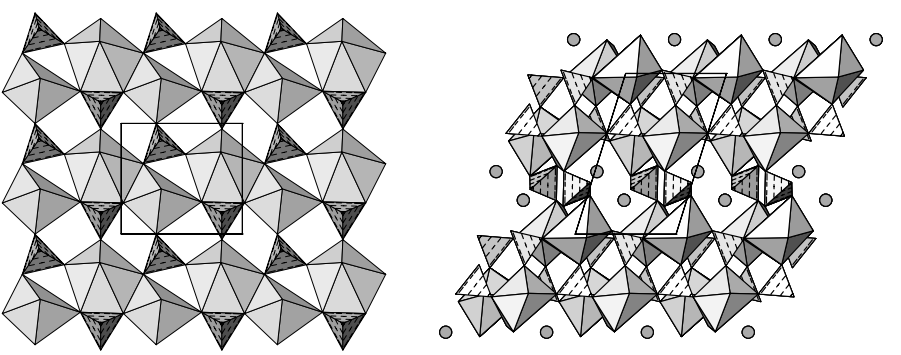

Figure 4. The structure of $Th_2(PO_4)_2PO_3OH(H_2O)$, projected along [001] at left (H_2O groups omitted), and along [010] at right (H_2O groups shown as spheres), after [31].

The structure of $UPO_4Cl(H_2O)_2$ is also adopted by its Br analog [33]. From the Wyckoff positions of the atoms, the actinide site in the structure appears to contain UO_6X_2 (X = Cl, Br) polyhedra that approximate a Johnson snub disphenoid, also known as a Siamese dodecahedron, but as the halogen site is half-occupied, the actual coordination number is seven [35]. These polyhedra share vertices with phosphate tetrahedra to form an open framework with voids that extend parallel to the [100] direction. The halogen atoms that coordinate uranium line these voids (Fig. 5).

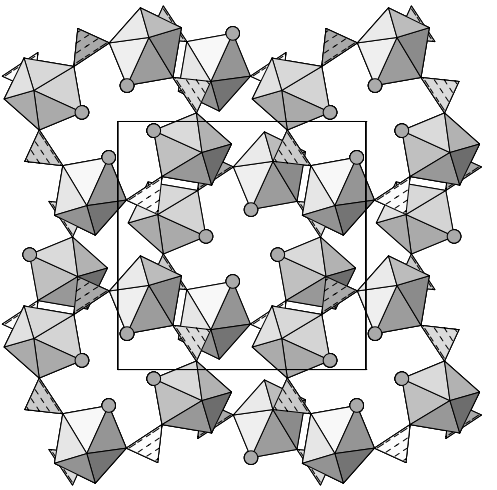

Figure 5. The structure of $UPO_4Cl(H_2O)_2$, projected along [001], after [33]. Chlorine atoms are shown as spheres.

2.1.3. Eightfold coordination

In contrast to the relative paucity of structures with the actinides in sixfold or sevenfold coordination, eightfold coordination is shown by at least six different structure-types (Table 3). The actinide-centered polyhedra in these structure generally correspond to a Johnson snub disphenoid (also known as a Siamese dodecahedron, or a twelve-faced convex deltahedron). These six structure types are presented in order of increasing polymerization and decreasing crystallographic symmetry.

The well-known scheelite ($CaWO_4$) structure-type [48] is adopted by particular actinide-bearing compositions, depending on the conditions of synthesis. In this structure type (Fig. 6), large divalent cations randomly occupy the eightfold coordinate site along with trivalent lanthanides or Bi, and with tetravalent Th (Table 3), all in equal proportion [36, 37]. This structure type consists of snub-disphenoidal polyhedra that share edges to form a framework with voids along the [100] and [010] directions. The tetrahedral positions occupy these voids and further connect the eight-coordinate polyhedra by sharing vertices (Fig. 6).

Table 3. Orthophosphates and orthoarsenates with actinides (An^{3+}, An^{4+}) in eightfold coordination

Formula	Structure	Status*	S.G.	*a* (Å)	*b* (Å)	*c* (Å)	β (°)	Ref.
$(Cd_{0.33}Bi_{0.33}Th_{0.33})AsO_4$	scheelite	inf	$I4_1/a$	5.06		11.59		36
$(Cd_{0.33}Nd_{0.33}Th_{0.33})AsO_4$	scheelite	inf	$I4_1/a$	5.04		11.51		37
$(Ca_{0.33}Sm_{0.33}Th_{0.33})AsO_4$	zircon	inf	$I4_1/amd$	7.18		6.41		38
$(Li_{0.33}Th_{0.67})(As_{0.75}V_{0.25})O_4$	zircon-related	inf	$I4_1/amd$	21.54		6.46		39
$(Li_{0.33}Np_{0.67})AsO_4$	zircon-related	inf	$I4_1/amd$	21.13		6.29		40
$(Na_{0.33}Np_{0.67})AsO_4$	zircon-related	inf	$I4_1/amd$	21.31		6.34		40
$(Li_{0.33}Pu_{0.67})AsO_4$	zircon-related	inf	$I4_1/amd$	21.11		6.30		40
$CaU(PO_4)_2$	zircon-related	det	*Pnma*	13.93	6.96	6.14		41
$(Ca_{0.5}Th_{0.5})PO_4(H_2O)$†	rhabdophane	inf	$P6_222$	6.98		6.40		42
$(Ca_{0.5}U_{0.5})PO_4(H_2O)_2$‡	rhabdophane	inf	$P6_222$	6.91		6.42		43
$Pu^{3+}PO_4(H_2O)_{0.5}$	rhabdophane	inf	$P6_222$	7.01		6.40		44
$Na_3Pu^{3+}(PO_4)_2$**	$Na_3Nd(PO_4)_2$**	inf	$Pca2_1$	7.00	15.86	18.44		45
$Na_2Th(PO_4)_2$		det	$C2/c$	7.01	21.50	9.12	111.0	46
$CuTh_2(PO_4)_3$		det	$C2/c$	22.03	6.74	7.02	108.6	47

*Structure determined (det), or structural affiliation inferred (inf)

†brockite; ‡tristramite; **related to vitusite-(Ce), $Na_3Ce(PO_4)_2$

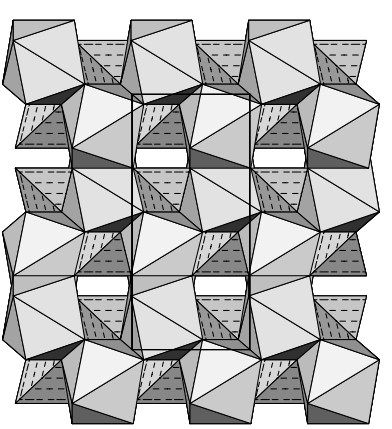

Figure 6. The structure of scheelite, $CaWO_4$, projected along [100], after [48].

The zircon structure-type ($ZrSiO_4$) [49] is also adopted occasionally by so-called "ternary" compositions (Table 3) [38]. Zircon is isostructural with the xenotime series of phosphates, typified by xenotime-(Y), YPO_4 [50, 51]. In this structure-type, the eight-coordinate polyhedra (snub disphenoids) share edges to form a framework composed of cross-linked chains that extend along the [100] and [010] directions. The framework of polyhedra exhibits prominent voids along the [111] direction; these are occupied by tetrahedra. The tetrahedra share edges with the polyhedra and thus serve to further connect the chains (Fig. 7).

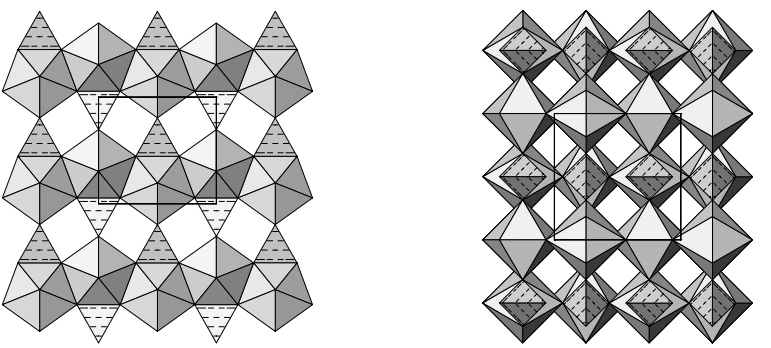

Figure 7. A portion of the structure of zircon, $ZrSiO_4$, projected along [100] at left, and along [001] at right, after [49].

Zircon-type superstructures apparently occur in actinide arsenates as a result of cation ordering when both monovalent alkali metals and tetravalent actinides occupy polyhedral sites (Table 3). Cation ordering is also a factor in the orthorhombic symmetry of the low-temperature polymorph of $CaU(PO_4)_2$ [41], shown in Figure 8, and which is closely related to the zircon structure.

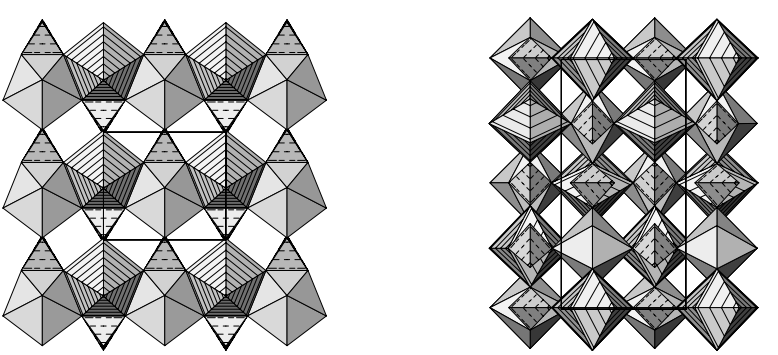

Figure 8. The structure of $CaU(PO_4)_2$, projected along [100] at left, and along [001] at right, after [41]. CaO_8 polyhedra are striped, UO_8 polyhedra are shaded, and tetrahedra are stippled.

The mineral species brockite, $(Ca_{0.5}Th_{0.5})PO_4(H_2O)$ [42], and tristramite, $(Ca_{0.5}U_{0.5})PO_4(H_2O)_2$ [43], both have the rhabdophane structure-type, as does $Pu^{3+}PO_4(H_2O)_{0.5}$ [44] (Table 3). The structure of rhabdophane-(Ce), $CePO_4(H_2O)$ [52], has been described [10] as consisting of CeO_8 polyhedra that share edges to form chains that extend along the [100] and [010] directions. The chains are linked by edge-sharing with tetrahedra to form sheets. These sheets interpenetrate to form a framework with large channels parallel to the [001] direction (Fig. 9). The large channels presumably host the H_2O groups found in variable amounts in these compounds. In the tetravalent actinide-bearing minerals, the actinides and calcium occupy the eightfold sites in equal proportion.

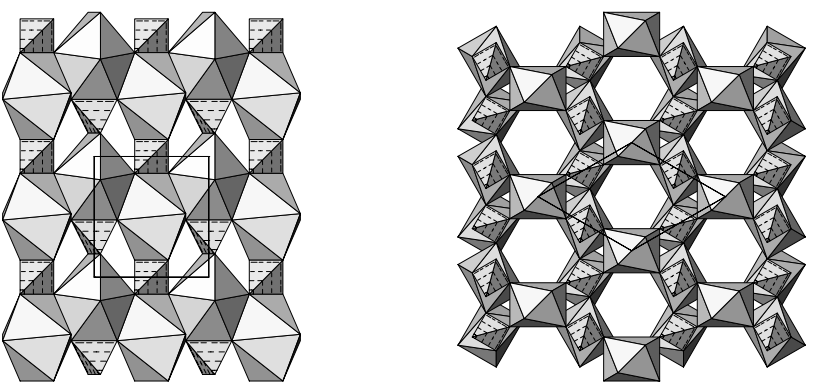

Figure 9. A portion of the structure of rhabdophane-(Ce), $CePO_4(H_2O)$, projected along [100] at left, and along [001] at right, after [52].

Although the structure of $Na_3Pu^{3+}(PO_4)_2$ has not been refined [45], it is inferred on the basis of its stoichiometry and cell dimensions (Table 3) to be similar to that of $Na_3Nd(PO_4)_2$, cell dimensions *a* 13.95, *b* 15.87, *c* 18.47 Å in space group $Pca2_1$ [53]. The Nd-bearing structure is closely related to that of the mineral species vitusite-(Ce), $Na_3Ce(PO_4)_2$, cell dimensions *a* 14.05, *b* 5.34, *c* 18.67 Å in space group $Pca2_1$ [54]. Vitusite-(Ce) has been described as a modulated structure, the substructure of which is related to the structure of the sulfate mineral aphthitalite, $K_3Na(SO_4)_2$, ("glaserite") [10]. Aphthitalite has trigonal symmetry, cell dimensions *a* 5.68, *c* 7.31 Å in space group $P\text{-}3m1$ [55]; it can be transformed to a pseudo-orthorhombic cell comparable to that of vitusite-(Ce) by the matrix [00-1/110/1-10]: *a* 7.31, *b* 5.68, *c* 9.84 Å.

The structure of vitusite-(Ce) consists of edge-shared dimers of CeO_8 that are linked into chains by edge- and vertex-sharing with phosphate tetrahedra (Fig. 10). These chains extend along the [010] direction (in space group $Pca2_1$). The

chains are stacked in the [100] direction, and connected by vertex-sharing of phosphate tetrahedra with CeO_8 polyhedra of adjacent chains, leading to an open framework with tunnels extending along the [010] direction. These tunnels are occupied by Na atoms whose coordination numbers range from six to nine [10, 54].

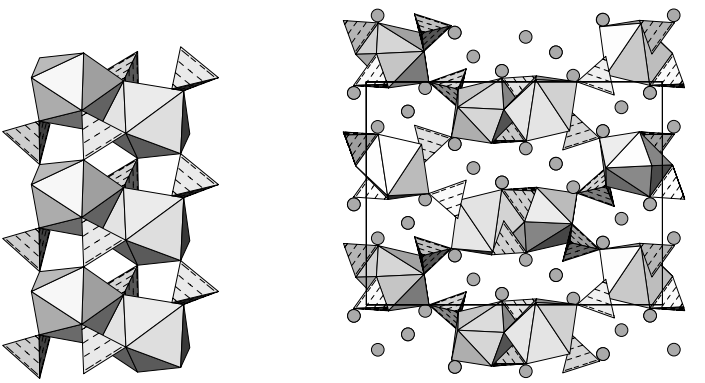

Figure 10. The chain in the structure of vitusite-(Ce), $Na_3Ce(PO_4)_2$, projected along [100] with Na atoms omitted, at left; the structure projected along [010] with Na atoms shown as spheres, at right, after [54].

The structure of $Na_2Th(PO_4)_2$ [46] also has the stacking of offset chains as a important structural motif (Fig. 11). In this compound, the two symmetrically independent ThO_8 polyhedra both share two edges and four vertices with phosphate tetrahedra. These clusters share vertices with adjacent polyhedra to form broad chains that extend along the [101] direction.

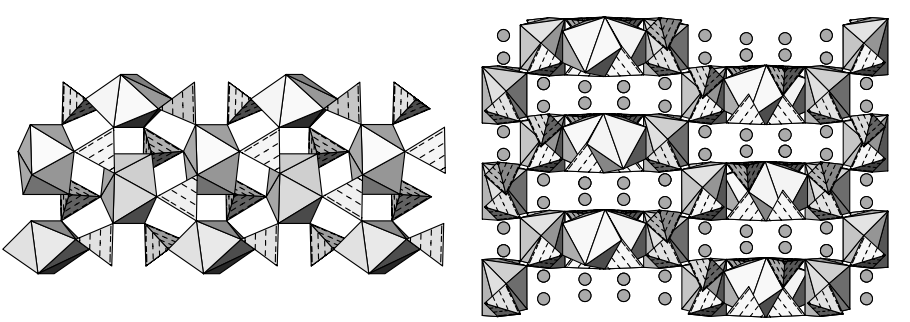

Figure 11. The chain in the structure $Na_2Th(PO_4)_2$, projected onto (10-1) with Na atoms omitted, at left; the structure projected along [101] with Na atoms shown as spheres, at right, after [46].

The chains are stacked in the [-201] direction and connected by vertex-sharing of phosphate tetrahedra with ThO_8 polyhedra of adjacent chains, leading to an open framework with large channels (approximately 2.5 x 10 Å in area) that extend along the [101] direction. These channels are occupied by Na atoms in eightfold and ninefold coordination.

One polymorph of $CuTh_2(PO_4)_3$ (Table 3) has a structure based on chains of edge-sharing ThO_8 polyhedra that extend along the [010] direction (Fig. 12). Phosphate tetrahedra share vertices with the polyhedra to form a framework structure with narrow cavities that extend along the [001] direction. These cavities are occupied by monovalent Cu atoms in twofold linear coordination by oxygen atoms at the vertices of Th-centered polyhedra [47].

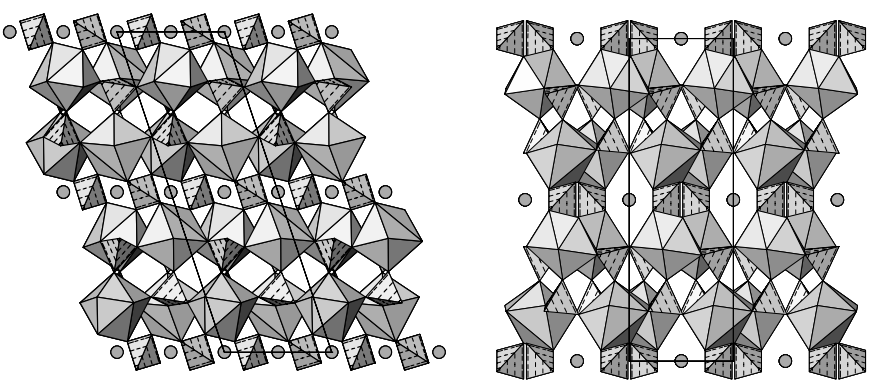

Figure 12. The structure of $CuTh_2(PO_4)_3$, projected along [010], at left; projected along [001], at right, after [47]. Monovalent copper atoms are shown as spheres.

2.1.4. Ninefold coordination

In the orthophosphates and orthoarsenates, only two structure-types host actinides in ninefold coordination: the monoclinic $KTh_2(PO_4)_3$ structure, and the monazite structure, but these two are amongst the most important as they show the widest range of chemical composition. Several compounds that possess the $KTh_2(PO_4)_3$ structure-type [56] are polymorphous (Table 4), and adopt other structure-types depending on the conditions of synthesis. For example, $KU_2(PO_4)_3$ shows the kosnarite-type structure at high temperature (Table 2), and $CuTh_2(PO_4)_3$ adopts an unrelated structure (Table 3). Note that the $KTh_2(PO_4)_3$ structure is not the same as the monoclinic “low NASICON”.

Table 4. Actinide phosphates and arsenates with the $KTh_2(PO_4)_3$ structure

Formula	Status*	*a* (Å)	*b* (Å)	*c* (Å)	β (°)	Ref.
$CuTh_2(PO_4)_3$	inf	17.27	6.94	8.02	99.6	57
$Ca_{0.5}Th_2(PO_4)_3$	inf	17.27	6.81	8.14	100.8	58
$LiTh_2(PO_4)_3$	inf	17.43	6.82	8.14	101.3	17
$NaTh_2(PO_4)_3$	det	17.37	6.81	8.13	101.1	59
$AgTh_2(PO_4)_3$	inf	17.39	6.82	8.15	101.1	17
$Sr_{0.5}Th_2(PO_4)_3$	inf	17.40	6.83	8.15	101.2	58
$Cd_{0.5}Th_2(PO_4)_3$	inf	17.42	6.79	8.16	100.4	58
$Pb_{0.9}Th_{1.8}(PO_4)_3$	det	17.42	6.87	8.13	101.3	60
$Pb_{0.5}Th_2(PO_4)_3$	inf	17.46	6.85	8.14	101.2	61
$Ba_{0.9}Th_{1.8}(PO_4)_3$	inf	17.53	6.85	8.14	101.6	62
$Ba_{0.5}Th_2(PO_4)_3$	inf	17.56	6.86	8.14	101.6	58
$Ba_{0.4}K_{0.2}Th_2(PO_4)_3$	inf	17.57	6.86	8.15	101.6	58
$Ba_{0.3}K_{0.4}Th_2(PO_4)_3$	inf	17.57	6.86	8.14	101.6	58
$KTh_2(PO_4)_3$	det	17.57	6.86	8.14	101.8	56
$K(ThU)(PO_4)_3$	inf	17.56	6.82	8.10	101.9	58
$RbTh_2(PO_4)_3$	inf	17.55	6.84	8.14	102.0	17
$TlTh_2(PO_4)_3$	inf	17.69	6.89	8.15	102.0	63
$CsTh_2(PO_4)_3$	inf	17.73	6.88	8.17	102.0	17
$LiU_2(PO_4)_3$	inf	17.39	6.73	8.04	101.5	17
$NaU_2(PO_4)_3$	inf	17.23	6.70	8.03	101.1	17
$KU_2(PO_4)_3$	det	17.48	6.76	8.02	102.0	58, 64
$NaNp_2(PO_4)_3$	inf	17.17	6.70	7.97	101.1	65
$NaPu_2(PO_4)_3$	inf	17.14	6.65	7.90	101.1	24
$LiTh_2(AsO_4)_3$	inf	17.98	6.96	8.23	99.2	40
$NaTh_2(AsO_4)_3$	inf	17.97	7.00	8.24	99.6	40
$AgTh_2(AsO_4)_3$	inf	17.98	6.99	8.36	99.6	66
$KTh_2(AsO_4)_3$	inf	18.02	7.05	8.30	99.2	67
$TlTh_2(AsO_4)_3$	inf	18.02	7.07	8.33	99.6	68

*Structure determined (det), or structural affiliation inferred (inf)

The $KTh_2(PO_4)_3$ structure (space group $C2/c$) [56] consists of ThO_9 polyhedra that share edges to form corrugated sheets parallel to the (100) face (Fig. 13). Phosphate tetrahedra share vertices and edges with the polyhedra, leading to a framework with channels that extend along the [001] direction. These channels are occupied by K atoms in eightfold coordination in the eponymous compound. However, this structure type can also accommodate large divalent cations (Ca, Sr, Cd, Pb, Ba) by substitution for monovalent cations in the channels (Table 4). The divalent cations require only partial occupancy of this site, and mixed occupancy is possible [58].

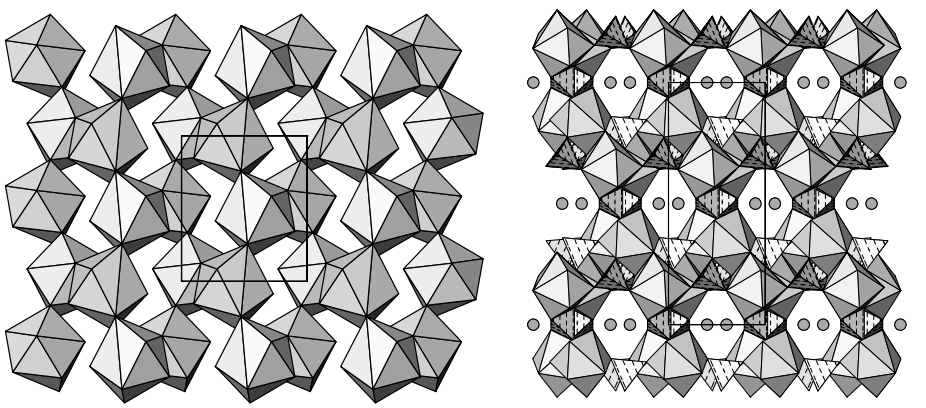

Figure 13. The ThO_9 polyhedra in the structure of $KTh_2(PO_4)_3$, projected along [100] at left; the structure projected along [001] at right, after [56]. Potassium atoms are shown as spheres.

The monazite structure is dimorphous with xenotime (zircon structure-type), and is one of the major natural hosts of Th and U in crustal rocks; the tetravalent actinides can be accommodated in conjunction with a large divalent cation in a coupled substitution for lanthanide elements, e.g., complete solid solution is found between brabantite, $(Ca_{0.5}Th_{0.5})PO_4$, and monazite-(Ce), $CePO_4$ [51]. "Ternary" compositions, and partial occupancy are also mechanisms of actinide substitution (Table 5).

Monazite has space group $P2_1/n$ (alternative setting of $P2_1/c$); the structure of monazite-(Ce) consists of CeO_9 polyhedra that share edges to form chains that extend along the [010] direction (Fig. 14). These chains are connected by edge-sharing with phosphate tetrahedra to form sheets parallel to the (100) face [10]. These layers stack in the [100] direction by further edge-sharing of the CeO_9 polyhedra to form a framework with prominent polyhedral chains that extend in the [101] direction [10].

Table 5. Actinide phosphates and arsenates with the monazite structure

Formula	Status*	*a* (Å)	*b* (Å)	*c* (Å)	β (°)	Ref.
$Pu^{3+}PO_4$	inf	6.77	6.97	6.43	103.7	69, 44
$(Mg_{0.5}Th_{0.5})PO_4$	inf	6.52	6.83	6.26	102.2	70
$(Cd_{0.5}Th_{0.5})PO_4$	inf	6.67	6.88	6.39	104.3	71
$(Ca_{0.5}Th_{0.5})PO_4$†	det	6.71	6.92	6.42	103.7	71, 72
$(Sr_{0.5}Th_{0.5})PO_4$	inf	6.79	7.01	6.52	103.5	71
$(Pb_{0.5}Th_{0.5})PO_4$	inf	6.85	7.08	6.57	103.7	71
$(Ba_{0.5}Th_{0.5})PO_4$	inf	6.95	7.16	6.68	102.9	71
$(Mg_{0.5}U_{0.5})PO_4$	inf	6.55	6.79	6.28	103.5	70
$(Ca_{0.5}U_{0.5})PO_4$	inf	6.64	6.85	6.36	103.8	70
$(Sr_{0.5}U_{0.5})PO_4$	inf	6.80	6.97	6.42	103.6	70
$(Mg_{0.17}Np_{0.67})PO_4$	inf	6.76	6.99	6.39	103.6	70
$(Ca_{0.5}Np_{0.5})PO_4$	inf	6.67	6.85	6.37	104.1	70
$(Ca_{0.17}Np_{0.67})_{\Sigma 0.84}PO_4$	inf	6.74	6.95	6.41	103.8	70
$(Sr_{0.17}Np_{0.67})_{\Sigma 0.84}PO_4$	inf	6.74	6.96	6.41	103.5	70
$(Ca_{0.5}Np_{0.35}Pu_{0.15})PO_4$	inf	6.65	6.84	6.35	104.1	73
$(Ca_{0.17}Pu_{0.67})_{\Sigma 0.84}PO_4$	inf	6.71	6.93	6.36	103.9	70
$Pu^{3+}AsO_4$	inf	6.92	7.09	6.66	105.5	74
$(Cd_{0.33}Bi_{0.33}Th_{0.33})AsO_4$	inf	6.89	7.08	6.73	105.3	36
$(Cd_{0.33}La_{0.33}Th_{0.33})AsO_4$	inf	6.85	7.02	6.66	104.8	75
$(Cd_{0.33}Pr_{0.33}Th_{0.33})AsO_4$	inf	6.84	7.02	6.65	104.7	75
$(Cd_{0.33}Nd_{0.33}Th_{0.33})AsO_4$	inf	6.82	6.98	6.63	104.6	75
$(Ca_{0.33}La_{0.33}Th_{0.33})AsO_4$	inf	6.88	7.07	6.67	104.7	76
$(Sr_{0.33}La_{0.33}Th_{0.33})AsO_4$	inf	6.95	7.15	6.95	104.6	75
$(Sr_{0.33}Pr_{0.33}Th_{0.33})AsO_4$	inf	6.92	7.10	6.71	104.7	75
$(Sr_{0.33}Nd_{0.33}Th_{0.33})AsO_4$	inf	6.89	7.09	6.68	104.5	75
$(Pb_{0.33}La_{0.33}Th_{0.33})AsO_4$	inf	6.98	7.18	6.77	104.6	75
$(Pb_{0.33}Pr_{0.33}Th_{0.33})AsO_4$	inf	6.94	7.16	6.76	104.8	75
$(Pb_{0.33}Nd_{0.33}Th_{0.33})AsO_4$	inf	6.94	7.14	6.75	104.8	75
$(Pb_{0.33}Sm_{0.33}Th_{0.33})AsO_4$	inf	6.91	7.13	6.74	104.9	75
$(Ba_{0.33}La_{0.33}Th_{0.33})AsO_4$	inf	7.03	7.23	6.84	104.8	75
$(Ba_{0.33}Pr_{0.33}Th_{0.33})AsO_4$	inf	7.01	7.22	6.82	104.8	75
$(Ba_{0.33}Nd_{0.33}Th_{0.33})AsO_4$	inf	7.00	7.21	6.82	104.7	75

*Structure determined (det), or structural affiliation inferred (inf); †brabantite

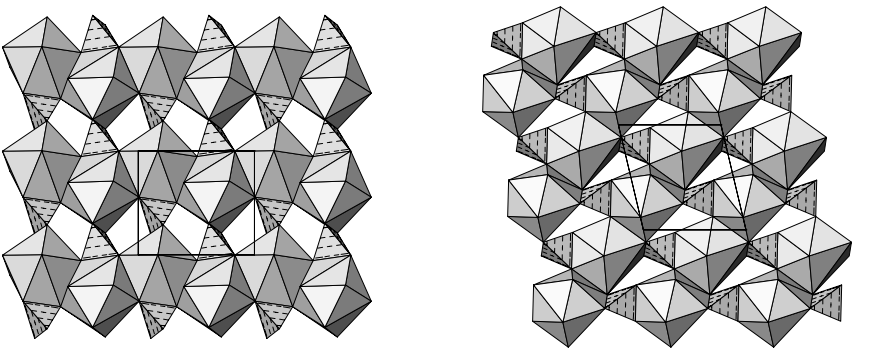

Figure 14. A portion of the structure of monazite-(Ce), $CePO_4$, projected along [100] at left, and along [010] at right, after [50].

The dimorphism of monazite and xenotime has been discussed in detail with respect to the sizes of the trivalent lanthanide elements [50]. The monazite-type structure is adopted by orthophosphates of the larger early lanthanides (La-Gd), and the xenotime-type structure is shown by the orthophosphates of the smaller lanthanides (Tb-Lu) [50]. In the case of the trivalent actinides, the orthophosphates of the transneptunium elements (Pu, Am, Cm, Bk, Cf, Es) have also been reported to adopt the monazite structure [44, 69, 76], although their unit cell dimensions and powder X-ray diffraction patterns have not been deposited [76], with the exception of Pu [44, 69].

2.1.5. Twelvefold coordination

Twelvefold coordination of lower valence actinides is inferred only for the orthophosphate mineral eylettersite, $(Th,Pb)_{1-x}Al_3(PO_4,SiO_4)_2(OH)_6$ [77], which is a member of the alunite-jarosite supergroup that includes the isotypic florencite group of phosphates and arsenates. Charge balance in eylettersite is maintained through partial occupancy of the Th site, and by substitution of Si for P.

The structure of florencite-(Ce), $CeAl_3(PO_4)_2(OH)_6$, space group *R*-3*m*, *a* 6.97, *c* 16.26 Å [78], can be described as containing an infinite sheet based on phosphate tetrahedra and Al-centered octahedra [10]. The sheets stack in the [001] direction. The octahedra share vertices to form an open sheet of chains that extend along the [100] and [010] directions (Fig. 15), resulting in large hexagonal voids and smaller triangular voids. Phosphate tetrahedra are centered above triangular voids by sharing three vertices with the octahedra of a given sheet, and project into the hexagonal voids of the adjacent octahedral sheet. In

florencite-(Ce), Ce is in twelvefold coordination and takes the form of a Platonic icosahedron. The icosahedron is centered above a triangular void in any given octahedral sheet, shares vertices with adjacent phosphate tetrahedra, and faces with the octahedra in the sheets above and below (Fig. 15).

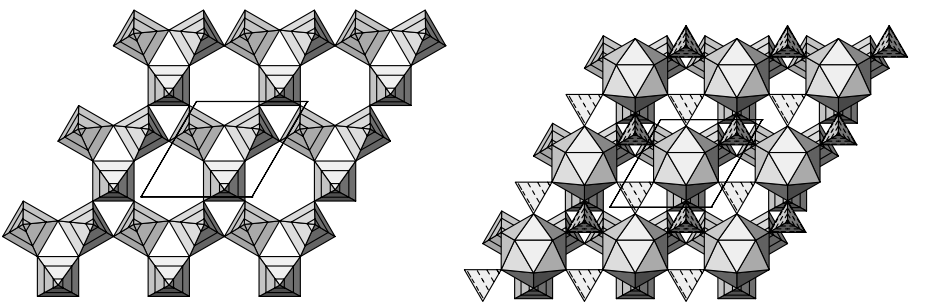

Figure 15. The sheet of AlO_6 octahedra in the structure of florencite-(Ce), $CeAl_3(PO_4)_2(OH)_6$, projected along [001] at left; the structure projected along [001] at right, after [78].

2.2. Polyphosphates and Polyarsenates

In the polyphosphates and polyarsenates, the lower-valence actinides show a range of coordination states amongst the different structures from six-coordinate to nine-coordinate, with eightfold coordination being the most common. In these compounds tetrahedra are polymerized with each other by vertex-sharing to form finite chain-segments (P_xO_{3x+1}), infinite chains (P_xO_{3x}), or ring motifs (also P_xO_{3x}). The structures are presented below in order of increasing polymerization of tetrahedra.

2.2.1. Finite chain-segments

The pyrophosphates (also known as diphosphates) and pyroarsenates of the tetravalent actinides adopt the cubic ZrP_2O_7 structure (Table 6). The structure of UP_2O_7 has been refined [79] and consists on average of U-centered octahedra that share vertices with phosphate tetrahedra. Each phosphate tetrahedron shares one vertex with another tetrahedron to form a pyrophosphate (P_2O_7) group, and three vertices with octahedron (Fig. 16). The pyrophosphate group can be considered to be a finite segment of a chain, two tetrahedra in length.

Table 6. Polyphosphates and polyarsenates of trivalent or tetravalent actinides

Formula	Structure	Status*	S.G.	*a* (Å)	*b* (Å)	*c* (Å)	β (°)	Ref.
ThP_2O_7	ZrP_2O_7	det	*Pa*-3	8.72				80
UP_2O_7	ZrP_2O_7	det	*Pa*-3	8.63				79
NpP_2O_7	ZrP_2O_7	inf	*Pa*-3	8.58				65
PuP_2O_7	ZrP_2O_7	inf	*Pa*-3	8.56				44
$ThAs_2O_7$	ZrP_2O_7	inf	*Pa*-3	9.02				81
$NpAs_2O_7$	ZrP_2O_7	inf	*Pa*-3	8.82				82
$Th_4(PO_4)_4P_2O_7$	$Th_4(PO_4)_4P_2O_7$	det	*Pbcm*	10.44	12.86	7.07		83
$ThU_3(PO_4)_4P_2O_7$	$Th_4(PO_4)_4P_2O_7$	inf	*Pbcm*	10.33	12.71	7.00		84
$Th_{2.4}Np_{1.6}(PO_4)_4P_2O_7$	$Th_4(PO_4)_4P_2O_7$	inf	*Pbcm*	10.36	12.75	7.01		85
$Th_3Pu(PO_4)_4P_2O_7$	$Th_4(PO_4)_4P_2O_7$	inf	*Pbcm*	10.37	12.78	7.02		84
$Na_6ThPO_4(P_2O_7)_2$†		det	*P*-1	6.47	8.73	8.93	93.3	86
$Th_2PO_4(P_3O_{10})$	$U_2PO_4(P_3O_{10})$	inf	$Pna2_1$	11.62	12.80	7.12		87
$U_2PO_4(P_3O_{10})$	$U_2PO_4(P_3O_{10})$	det	$Pna2_1$	11.53	12.81	7.05		88
$Th_2AsO_4(As_3O_{10})$	$U_2PO_4(P_3O_{10})$	inf	$Pna2_1$	11.95	13.24	7.38		81
$KThP_3O_{10}$		det	$P2_12_12_1$	10.02	10.19	8.23		89
$Pu^{3+}(PO_3)_3$	$Nd(PO_3)_3$	inf	$C222_1$	11.23	8.57	7.30		69
$Th(PO_3)_4$‡	$Zr(PO_3)_4$	inf	*Pbcn*‡	6.95	15.12	9.07		90
$Pa(PO_3)_4$‡	$Zr(PO_3)_4$	inf	*Pbcn*‡	6.96	15.01	8.96		91
$U(PO_3)_4$‡	$Zr(PO_3)_4$	det	*Pbcn*‡	6.91	14.95	8.99		92
$Np(PO_3)_4$‡	$Zr(PO_3)_4$	inf	*Pbcn*‡	6.95	14.97	8.99		65
$Pu(PO_3)_4$‡	$Zr(PO_3)_4$	inf	*Pbcn*‡	6.86	14.84	8.90		93
$U(PO_3)_4$**		det	*Cm***	11.51	13.01	8.15	134.0	94

*Structure determined (det), or structural affiliation inferred (inf); †α 110.1, γ 108.3°

‡Cells presented here are likely subcells, see text

**Transformed from the original setting in space group *P*1, see text

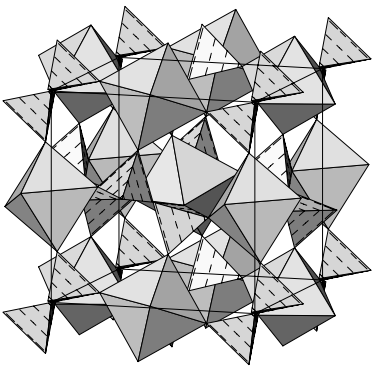

Figure 16. Clinographic projection of the structure of UP_2O_7 after [79].

The structure of $Th_4(PO_4)_4P_2O_7$ contains ThO_8 polyhedra that share edges to form chains that extend along the [001] direction in space group *Pbcm* [83]. The polyhedra of these chains share edges and vertices with phosphate tetrahedra to form a framework structure (Fig. 17), with the chains stacked along the [100] direction. One of the phosphate tetrahedra shares a vertex with its symmetry equivalent. The oxygen atom corresponding to this shared vertex is half-occupied, giving rise on the local scale to a pyrophosphate group rather than an infinite chain parallel to the[001] direction. The remaining phosphate tetrahedra are not polymerized with each other; they share edges and vertices only with the ThO_8 polyhedra (Fig. 17). This structure type has been shown experimentally to have the capacity to accommodate significant proportions of other tetravalent actinides including U, Np and Pu (Table 6).

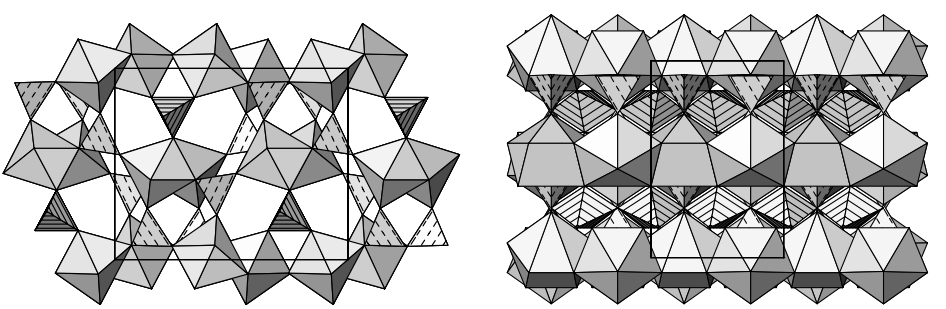

Figure 17. The structure of $Th_4(PO_4)_4P_2O_7$, projected along [001], at left; projected along [010], at right, after [83]. The disordered tetrahedra of the pyrophosphate group are striped.

A pyrophosphate group is also found in the structure of $Na_6ThPO_4(P_2O_7)_2$. Both the Th position and Na atoms occur in ninefold coordination in this structure. Dimers of edge-shared ThO_9 polyhedra are connected by sharing edges with phosphate tetrahedra into double chains that extend along the [100] direction (Fig. 18). These thorium phosphate chains are connected by pyrophosphate groups to form a framework structure with Na atoms occupying the interstices of the structure [86].

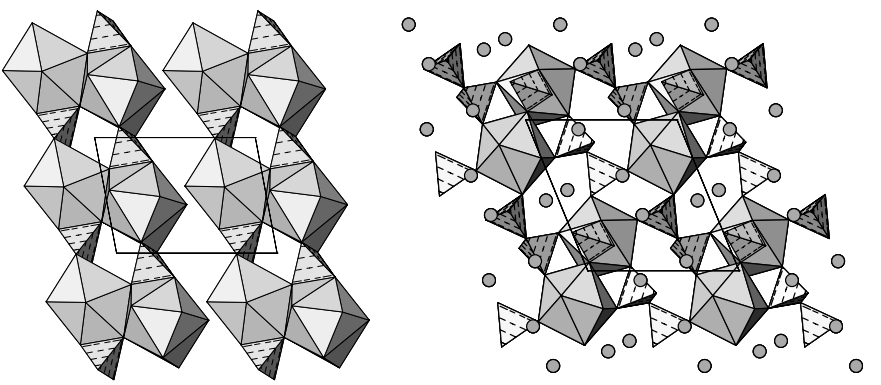

Figure 18. The thorium phosphate double chain in $Na_6ThPO_4(P_2O_7)_2$, projected along [010], at left; the structure projected along [100] with Na atoms shown as spheres, at right, after [86].

Actinide pyrophosphates and pyroarsenates, AnX_2O_7, adopt an orthorhombic polymorph in addition to the cubic structure (Table 6). This β-polymorph was also assumed to be a pyrophosphate. However, the structure of the orthorhombic U-bearing material has been determined [88] and contains a finite chain-segment three tetrahedra in length (P_3O_{10}), along with an isolated tetrahedron (PO_4), rather than pyrophosphate groups (P_2O_7). Its formula is therefore better expressed as $U_2PO_4(P_3O_{10})$. In this compound, uranium is in eightfold coordination as snub disphenoids that share edges to form chains that extend along [001] in space group $Pna2_1$ (Fig. 19). The isolated phosphate tetrahedron shares one edge with an UO_8 polyhedron and its opposite vertices with two other UO_8 polyhedra to connect three chains together. The chains are further connected into a framework structure by sharing of edges and vertices between the UO_8 polyhedra and the three tetrahedra of the L-shaped P_3O_{10} group (Fig. 19).

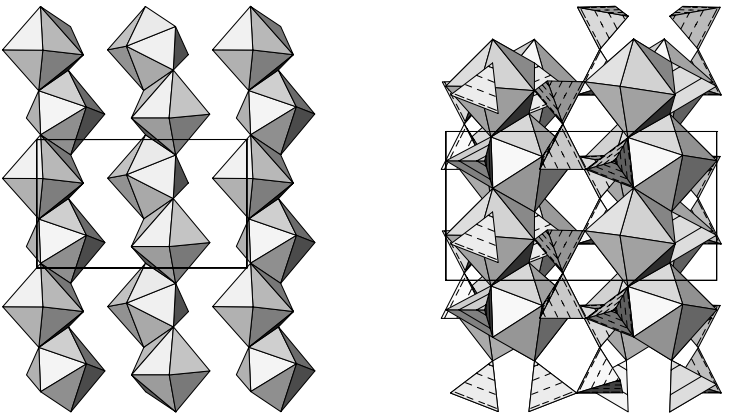

Figure 19. The chain of UO_8 polyhedra in $U_2PO_4(P_3O_{10})$, projected along [010], at left; the structure projected along [100], at right, after [88].

The pseudo-tetragonal structure of $KThP_3O_{10}$ (Table 6) also contains a finite chain-segment, three phosphate tetrahedra in length [89]. In this compound, isolated ThO_8 polyhedra are stacked in levels along the [010] direction. These polyhedra share vertices (but not edges) with the tetrahedra of the P_3O_{10} group to form a framework structure, with K atoms in ninefold coordination located in the interstices (Fig. 20).

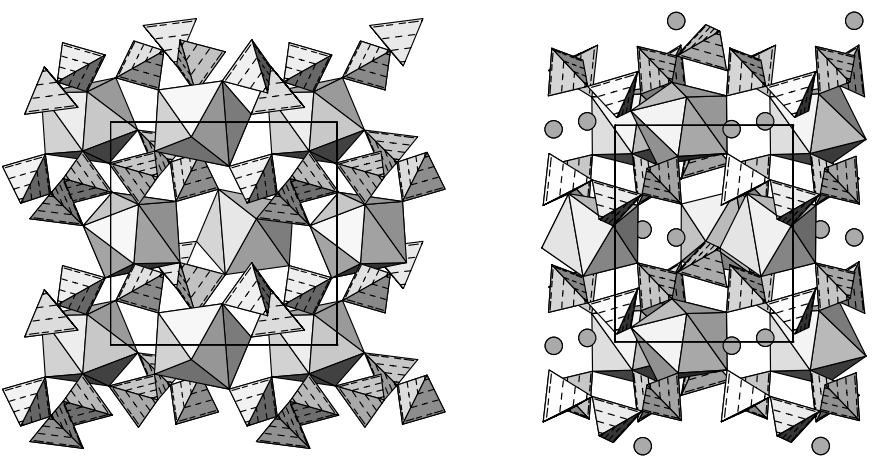

Figure 20. The structure of $KThP_3O_{10}$ with K atoms omitted, projected along [100], at left; the structure projected along [001] with K atoms shown as spheres, at right, after [89].

2.2.2. Infinite chains

Infinite chains of vertex-sharing tetrahedra are characteristic of the actinide metaphosphates (polytrioxophosphates [16]). On the basis of its stoichiometry and cell dimensions, $Pu^{3+}(PO_3)_3$ is likely isostructural with $Nd(PO_3)_3$ (Table 6). The structure of $Nd(PO_3)_3$ – *a* 11.17, *b* 8.53, *c* 7.28 Å [95] – contains highly-corrugated spiral chains of vertex-sharing phosphate tetrahedra that corkscrew along the [001] direction (Fig. 21). Chains of edge-sharing NdO_8 polyhedra also extend along the [001] direction and connect with the polyphosphate chains by corner-sharing.

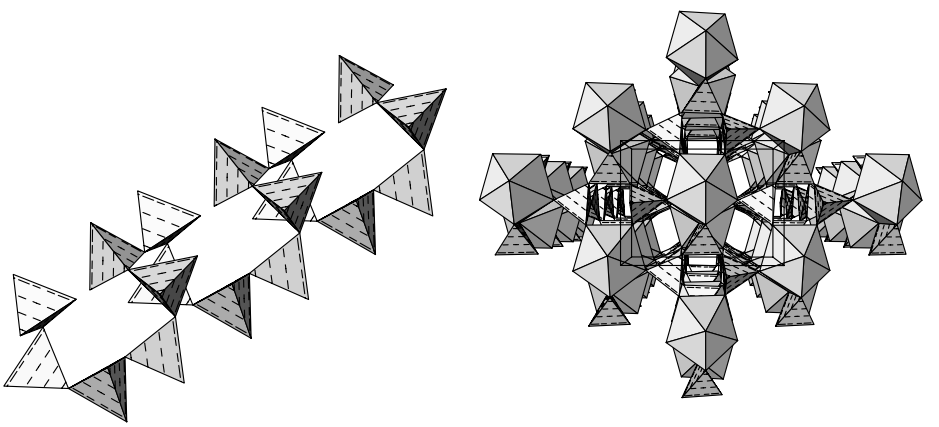

Figure 21. The phosphate chain in $Nd(PO_3)_3$ that spirals along [001], at left; a perspective view of the structure projected along [001], at right, after [95].

Several metaphosphates of the tetravalent actinides have been described (Table 6), and the structure of $U(PO_3)_4$ has been refined in the orthorhombic space group *Pbcn* [92]. However, in this model, five of the nine symmetrically independent oxygen positions are disordered and partially occupied. It is likely that the actinide metaphosphates with stoichiometry $An(PO_3)_4$ actually adopt the ordered monoclinic $Zr(PO_3)_4$ structure [96]. The unit cell of $Zr(PO_3)_4$ is pseudo-orthorhombic and nearly four times the volume of the actinide metaphosphates: *a* 13.50, *b* 28.80, *c* 8.66 Å, β 90.04(2)°. The matrix [200/0-20/00-1] transforms the primitive orthorhombic cell of $U(PO_3)_4$ to a larger *C*-centered cell comparable to that of $Zr(PO_3)_4$. It is probable that the unit cell data reported for the actinide metaphosphates with stoichiometry $An(PO_3)_4$ in Table 6 correspond to subcells, and that their true cells are four times larger and have *C*-centered monoclinic symmetry.

The structure of $Zr(PO_3)_4$ was originally reported in space group *Cc*. However, analysis of this acentric model with the ADDSYM algorithm in the program PLATON [97, 98] indicates that the correct space group is almost certainly *C*2/*c*, and this latter space group is assumed here (Table 7).

The arrangement of Zr and P atoms in $Zr(PO_3)_4$ [96] corresponds to that of the U and P atoms in the disordered structure model of $U(PO_3)_4$ [92]. It appears that the positions of the oxygen atoms alone are responsible for the larger unit cell, and the slight deviation from apparent orthorhombic symmetry in the ordered monoclinic structure of $Zr(PO_3)_4$.

Table 7. Revised atomic coordinates of $Zr(PO_3)_4$

	x	*y*	*z*		*x*	*y*	*z*
Zr1	0.5000	-0.4309	0.7500	O8	-0.2314	-0.3528	0.4833
Zr2	-0.2686	-0.3180	0.2498	O9	-0.1160	-0.3880	0.6888
Zr3	0.0000	-0.4322	0.7500	O10	-0.2407	-0.3285	-0.2353
P1	-0.1402	-0.4881	0.0261	O11	-0.1025	-0.3036	0.6190
P2	-0.1099	-0.2429	0.0267	O12	-0.3966	-0.3002	-0.1421
P3	-0.4252	-0.4071	0.3692	O13	-0.2980	-0.3558	0.0240
P4	-0.1743	-0.3474	0.6285	O14	-0.3845	-0.3820	-0.2248
P5	-0.3568	-0.4934	0.4902	O15	-0.1279	-0.2161	0.5822
P6	-0.3306	-0.3461	-0.1364	O16	0.5000	-0.4294	0.2500
P7	-0.1067	-0.2606	0.5027	O17	-0.1736	-0.2723	0.3706
P8	-0.0829	-0.3986	0.1345	O18	-0.3776	-0.2757	0.1334
O1	-0.3755	-0.3677	0.2903	O19	0.5034	-0.2368	-0.0575
O2	-0.4746	-0.3989	0.5188	O20	-0.3182	-0.2210	-0.0789
O3	-0.3494	-0.4493	0.3818	O21	-0.2471	0.4924	0.0541
O4	-0.1429	-0.3614	0.2083	O22	-0.4231	-0.4822	0.6226
O5	-0.0420	-0.3926	-0.0219	O23	-0.3778	-0.4636	-0.0935
O6	0.0000	-0.4157	0.2500	O24	-0.1244	-0.4714	-0.1331
O7	-0.1462	-0.4456	0.1402	O25	-0.0697	-0.4758	0.5841

Note: revised space group *C*2/*c*; *a* 13.50, *b* 28.80, *c* 8.66 Å, β 90.04°

Origin shifted to: 0.4992, 0.5000, 0.2445 after transformation

The structure of $Zr(PO_3)_4$ set in space group *C*2/*c* contains highly-corrugated chains of vertex-sharing phosphate tetrahedra that extend along the [101] direction (Fig. 22). Isolated ZrO_8 polyhedra (square antiprisms) share all of their vertices with phosphate tetrahedra to connect the chains into a framework.

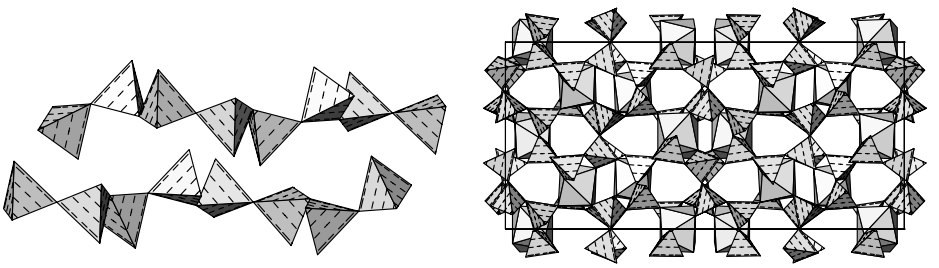

Figure 22. The phosphate chain in $Zr(PO_3)_4$ that extends along [101], projected along [010] at left; the structure projected along [001], at right, after [96].

2.2.3. Ring motifs

The cyclophosphate $U(PO_3)_4$ is polymorphous with the metaphosphate (Table 6). The cyclophosphate structure was originally reported in space group *P*1 [94]. However, analysis with the ADDSYM algorithm in the program PLATON [97, 98] indicates that the correct space group is likely *Cm*, and this latter space group is assumed here (Table 8). The unit cell was transformed with the matrix [110/-1-1-2/-100], and the origin shifted to 0, -0.3290, 0 after transformation.

Table 8. Revised atomic coordinates of cyclophosphate $U(PO_3)_4$

	x	*y*	*z*		*x*	*y*	*z*
U1	0.0473	0.2792	-0.0009	O6	-0.0635	0.0000	-0.4080
P1	0.4045	0.1135	0.2400	O7	0.7440	0.1150	0.3125
P2	0.1648	0.1118	-0.5335	O8	0.1435	0.0000	0.3690
P3	-0.0688	0.1133	-0.4775	O9	0.3060	0.1302	-0.2920
P4	0.6895	0.1140	0.7455	O10	0.0015	0.1090	-0.6015
O1	-0.1360	0.1552	-0.1280	O11	0.6435	0.1177	0.8830
O2	-0.0135	0.1957	-0.3360	O12	0.4240	0.1282	0.0820
O3	0.8065	0.2987	0.1900	O13	0.5880	0.1430	0.4970
O4	0.1485	0.1877	0.3050	O14	0.3860	0.0000	0.2780
O5	-0.2535	0.0000	-0.2430				

Revised space group *Cm*; unit cell: *a* 11.51, *b* 13.01, *c* 8.15 Å, β 134.0°

In the structure of the cyclophosphate, four tetrahedra share vertices to form a closed ring motif. The four-membered phosphate rings are arranged in layers parallel to the (010) face (Fig. 23). Uranium is in eightfold coordination as isolated square antiprisms that are also arranged in layers parallel to (010). The UO_8 polyhedra share vertices with the phosphate tetrahedra to form a framework structure.

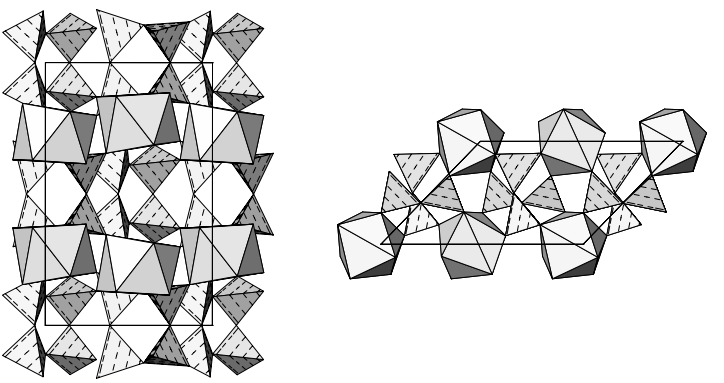

Figure 23. The structure of uranium cyclophosphate, $U(PO_3)_4$, set in space group *Cm*, projected along [001], at left; projected along [010], at right, after [94].

3. Hexavalent Actinides

In contrast to the relatively uniform coordination environments exhibited by trivalent and tetravalent actinides, hexavalent actinides usually adopt a dioxo configuration, forming an approximately linear $(AnO_2)^{2+}$ actinyl ion [11-14]. These strong actinide-oxygen interactions may be considered formally as triple bonds [99]. In crystal structures, the actinyl ion is typically coordinated at somewhat longer interatomic distances by four, five or six ligands, arranged at the equatorial vertices of square, pentagonal and hexagonal bipyramids, respectively [11-14]. As a result of the highly polarized distribution of bond strengths within the actinyl bipyramids, polymerization of these polyhedra generally occurs only through the equatorial ligands, usually yielding infinite chains or sheets, with three-dimensional framework structures occasionally being facilitated by linkages through non-actinyl polyhedra.

Pentavalent actinides can also exhibit a dioxo ion, $(AnO_2)^{+}$, but no structures of inorganic phosphate or arsenate compounds with this moiety have yet been reported, although this is an area of ongoing research [100].

3.1. Orthophosphates and Orthoarsenates

Following the structural hierarchy developed for uranyl compounds [11, 12], the orthophosphates and orthoarsenates of the hexavalent actinides may be divided into three general classes based on the polymerization of polyhedra of higher bond-valence: chain, sheet, and framework structures. Among the sheet and framework structures, there is some overlap as the phosphuranylite-type sheet is exhibited mainly by sheet structures but also by frameworks, and is discussed in the section on sheet structures. Similarly, the uranophane sheet-anion topology is adopted by some sheets but mainly by frameworks and is discussed in the latter section.

3.1.1. Chain structures

Table 9 lists the eight actinyl orthophosphates and orthoarsenates that exhibit chain structures; only three topologically separate chains of polyhedra of higher bond-valence have been described.

In walpurgite, $Bi_4O_4[(UO_2)(AsO_4)_2](H_2O)_2$, and its orthorhombic polymorph, orthowalpurgite, uranyl square bipyramids share equatorial vertices with arsenate tetrahedra to form uranyl arsenate chains [102, 103]. Bismuth in these structures is in highly distorted octahedral coordination. The bismuth octahedra share edges to form infinite sheets. These sheets are connected by sharing vertices octahedral vertices with the tetrahedra of the uranyl arsenate chains (Fig. 24).

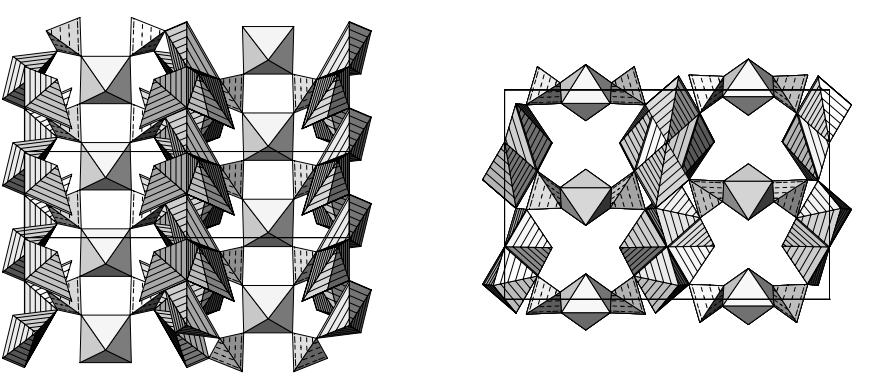

Figure 24. The structure of orthowalpurgite, $Bi_4O_4[(UO_2)(AsO_4)_2](H_2O)_2$, projected along [010], at left; projected along [100], at right, after [103]. Bismuth-centered distorted octahedra are striped. The triclinic polymorph walpurgite exhibits a very similar structure [103].

Table 9. Actinyl orthophosphate and orthoarsenate chain structures

Formula	Mineral	Status*	S. G.	*a* (Å)	*b* (Å)	*c* (Å)	α (°)	β (°)	γ (°)	Ref.
$Bi_4O_4[(UO_2)(PO_4)_2](H_2O)_2$	phosphowalpurgite	inf	*P*-1	7.06	10.24	5.46	101.2	109.9	87.9	101
$Bi_4O_4[(UO_2)(AsO_4)_2](H_2O)_2$	walpurgite	det	*P*-1	7.14	10.43	5.49	101.5	110.8	88.2	102
$Bi_4O_4[(UO_2)(AsO_4)_2](H_2O)_2$	orthowalpurgite	det	*Pbcm*	5.49	13.32	20.69				103
$Cu_2[(UO_2)(PO_4)_2]$		det	*C*2/*m*	14.04	5.76	5.03		107.2		104
$[(UO_2)(H_2PO_4)_2(H_2O)](H_2O)_2$		det	$P2_1/c$	10.82	13.90	7.48		105.7		105, 106
$[(UO_2)(H_2AsO_4)_2(H_2O)]$		det	*C*2/*c*	13.16	8.86	9.05		124.4		107
$Pb_2[(UO_2)(PO_4)_2](H_2O)_n$	parsonsite	det	*P*-1	6.84	10.41	6.67	101.4	98.3	86.3	108, 109
$Pb_2[(UO_2)(AsO_4)_2](H_2O)_n$	hallimondite	det	*P*-1	7.12	10.48	6.86	101.2	95.7	86.7	109

*Structure determined (det), or structural affiliation inferred (inf)

The uranyl phosphate chain in the structure of $Cu_2[(UO_2)(PO_4)_2]$ is topologically identical to the uranyl arsenate chain found in walpurgite [104]. Copper occurs in sixfold (4+2) coordination as elongated tetragonal bipyramids to form face-sharing chains that extend along the [010] direction. The chains of Cu polyhedra share vertices with adjacent phosphate tetrahedra of the parallel uranyl phosphate chains (Fig. 25).

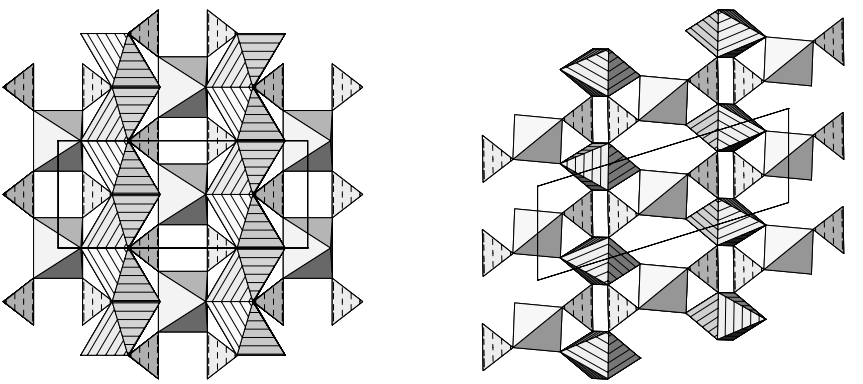

Figure 25. The structure of $Cu_2[(UO_2)(PO_4)_2]$, projected along [001], at left; projected along [010], at right, after [104]. Copper-centered tetragonal bipyramids are striped.

The chain found in the structures of both $[(UO_2)(H_2PO_4)_2(H_2O)](H_2O)_2$ and $[(UO_2)(H_2AsO_4)_2(H_2O)]$ consists of uranyl pentagonal bipyramids that share equatorial vertices with four tetrahedra [105-107]. Two of the vertices of each tetrahedron correspond to (OH) groups, and one equatorial vertex of the uranyl pentagonal bipyramid is an H_2O group. In $[(UO_2)(H_2PO_4)_2(H_2O)](H_2O)_2$, the chains extend along the [101] direction, and are connected through hydrogen bonding to the H_2O groups in the interchain regions (Fig. 26). The topologically identical uranyl arsenate chains in $[(UO_2)(H_2AsO_4)_2(H_2O)]$ also extend along the [101] direction. In this case, the chains are connected directly by hydrogen bonding, as the interchain region is devoid of H_2O groups.

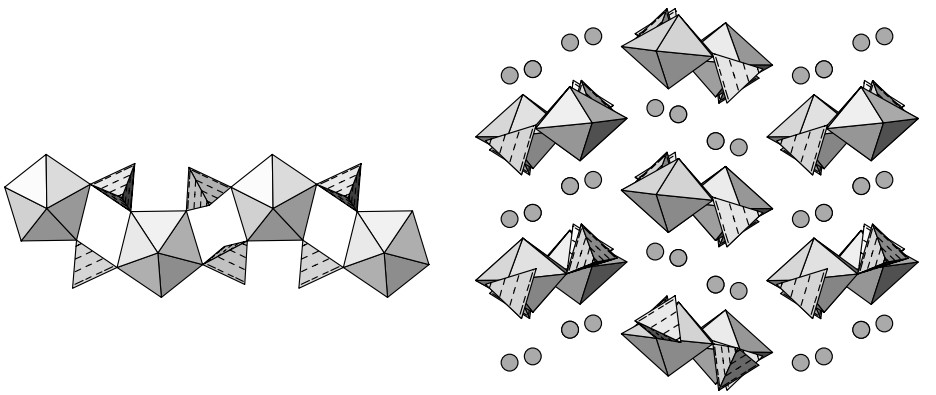

Figure 26. The chain in the structure of $[(UO_2)(H_2PO_4)_2(H_2O)](H_2O)_2$, projected onto (10-1), at left; the structure projected along [101], at right with H_2O groups in the interchain region shown as spheres, after [105, 106].

In the structures of parsonsite, $Pb_2[(UO_2)(PO_4)_2](H_2O)_n$, and hallimondite, $Pb_2[(UO_2)(AsO_4)_2](H_2O)_n$, $n \leq 0.5$, uranyl pentagonal bipyramids share an edge, forming dimers that are linked by edge- and vertex-sharing with tetrahedra to form chains along the [001] direction (Fig. 27). Two symmetrically distinct Pb positions connect the chains. The cavity between the chains and Pb positions, can be occupied by H_2O [108, 109].

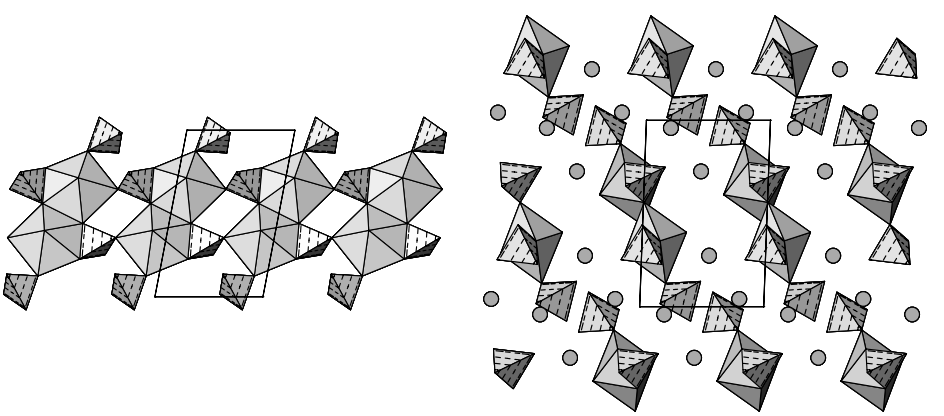

Figure 27. The chain found in parsonsite, $Pb_2[(UO_2)(PO_4)_2](H_2O)_n$, projected along [100] at left; the structure projected along [001], at right with Pb atoms in the interchain region shown as spheres, after [108].

3.1.2. Sheet structures

The layered structures of the actinyl orthophosphates and orthoarsenates are dominated by the autunite-type sheet, which has been described from (or can be inferred as occurring in) over 100 inorganic compounds with general stoichiometry: $A^{n+}[(AnO_2)(XO_4)]_n(H_2O)_m$, where A = monovalent, divalent or trivalent cations, and X = P or As. The corrugated autunite-type sheet consists of actinyl square bipyramids that share their equatorial vertices with tetrahedra to form a checkerboard-like pattern (Fig. 28). The interlayer region contains H_2O groups and either monovalent-, divalent- or trivalent-cations. The sheets are linked by hydrogen bonding, and to a lesser extent, through bonds from the interlayer cations to oxygen atoms of the sheets.

As the autunite-type sheet is made up of vertex-sharing polyhedra, it has a significant degree of structural flexibility and can vary its geometry to accommodate different interlayer contents (Fig. 28). In addition, more than one state of hydration may occur for a given divalent or trivalent cation. The interlayer spacing and relative orientations of the autunite-type sheets vary with the nature of the interlayer cation and with the state of hydration, giving rise to separate, but related, compounds. Changes in relative humidity can lead to changes in the hydration state (by dehydration or rehydration), and thus to changes in the structure and identity of the material in question. Changes in hydration state are sharply defined, although the transition conditions depend on water vapor pressure and temperature. Note that the H_2O content in these compounds does not vary continuously as in zeolites, but rather is required to maintain the integrity of the hydrogen-bonding network.

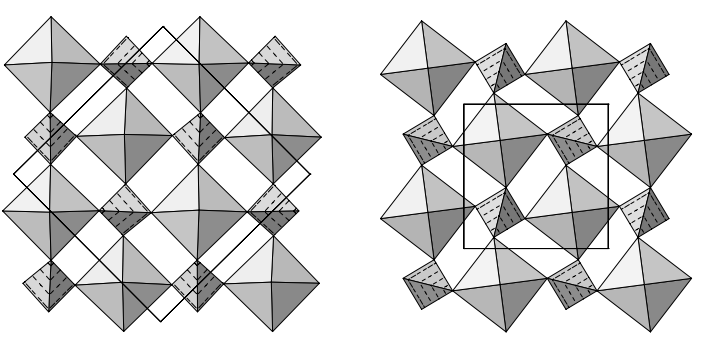

Figure 28. Variation in the autunite-type sheet. The sheet found in $Cs_2[(UO_2)(PO_4)]_2(H_2O)_5$, projected along [001] at left; the sheet found in $Li[(UO_2)(PO_4)](H_2O)_4$ projected along [001], at right, after [110].

Most compounds with the autunite-type sheet are either pseudotetragonal or tetragonal; the crystal systems observed in structure refinements range from tetragonal to triclinic, and depend on the nature of the interlayer cation and the state of hydration. It is likely that investigation of compounds with the autunite-type sheet has been complicated by their pseudosymmetry and dehydration relationships. In the following tables, for compounds whose structures have not been determined, space groups have not been assigned; crystal systems are listed instead: *C* cubic, *Q* tetragonal, *H* hexagonal, *R* rhombohedral, *T* trigonal, *O* orthorhombic, *M* monoclinic, and *A* triclinic. Both the cell dimensions and chemical formulas of such compounds should be treated as provisional.

Compounds with the autunite-type sheet and monovalent interlayer cations are presented first, followed by those compounds with divalent interlayer cations, and finally trivalent cations. Only selected examples of the structural variation amongst the compounds are illustrated here.

The compounds with the autunite-type sheet and monovalent interlayer cations are listed in Table 10 (phosphates) and in Table 11 (arsenates). In the two isostructural Li-bearing uranyl compounds [110, 119], Li is in fourfold coordination by H_2O groups in the interlayer region. Hydrogen bonds link the H_2O groups into square-planar sets, which are connected via the Li-O bonds (Fig. 29). Hydrogen bonds extend from these sets to the anions at the equatorial vertices of uranyl square bipyramids, which are also shared with tetrahedra.

In contrast to the ordered arrangement of Li atoms in the interlayer of $Li[(UO_2)(PO_4)](H_2O)_4$ and $Li[(UO_2)(AsO_4)](H_2O)_4$, compounds with Na, K, Rb, Ag, Tl, H_3O or NH_4 in the interlayer adopt a disordered structural arrangement at room temperature with stoichiometry $A[(AnO_2)(XO_4)](H_2O)_3$, where A = monovalent cation, An = hexavalent actinide, X = P or As. With the exception of $Rb[(UO_2)(AsO_4)](H_2O)_3$, these compounds crystallize in space group *P*4/*ncc* at room temperature [110]. The single symmetrically independent interlayer position in these compounds is occupied by the monovalent cation and by the O atom of an H_2O group in the ratio 1:3 (Fig. 29). The compound $Rb[(UO_2)(AsO_4)](H_2O)_3$ also exhibits site occupancy disorder of its interlayer contents. However, this material adopts space group *P*4/*n*, and of the two symmetrically unique positions in the interlayer, one is occupied by both Rb and the O atom of an H_2O group in the ratio 1:1, whereas the other position is occupied solely by the O atom of an H_2O group (Fig. 29).

Some of these compounds undergo phase transitions to ordered lower-symmetry structures with decreasing temperature (Tables 10 and 11) [118, 122].

Table 10. Autunite-type phosphates with monovalent cations

Formula	Mineral	Status*	S. G.	*a* (Å)	*c* (Å)	Ref.
$Li[(UO_2)(PO_4)](H_2O)_4$		det	*P*4/*n*	6.96	9.14	110
$Na[(UO_2)(PO_4)](H_2O)_3$	metanatroautunite	det	*P*4/*ncc*	6.96	17.27	110
$K[(UO_2)(PO_4)](H_2O)_3$†	meta-ankoleite	det	*P*4/*ncc*	6.99	17.78	111
$Rb[(UO_2)(PO_4)](H_2O)_3$		det	*P*4/*ncc*	7.01	17.98	110
$Cs_2[(UO_2)(PO_4)]_2(H_2O)_5$‡		det	$P2_1/n$	9.87	17.65	110
$H_3O[(UO_2)(PO_4)](H_2O)_3$	chernikovite	det	*P*4/*ncc*	7.00	17.49	112
$NH_4[(UO_2)(PO_4)](H_2O)_3$	uramphite	det	*P*4/*ncc*	7.03	18.09	113
$Ag[(UO_2)(PO_4)](H_2O)_3$		det	*P*4/*ncc*	6.93	16.93	110
$Tl[(UO_2)(PO_4)](H_2O)_3$		det	*P*4/*ncc*	7.02	17.98	110
$Na[(NpO_2)(PO_4)](H_2O)_3$		inf	*Q*	6.93	8.77	114
$K[(NpO_2)(PO_4)](H_2O)_3$		inf	*Q*	6.95	8.92	114
$NH_4[(NpO_2)(PO_4)](H_2O)_3$		inf	*Q*	6.95	9.00	114
$K[(PuO_2)(PO_4)](H_2O)_x$		inf	*Q*	6.96	8.94	115
$H_3O[(PuO_2)(PO_4)](H_2O)_x$		inf	*Q*	7.02	8.85	115
$NH_4[(PuO_2)(PO_4)](H_2O)_x$		inf	*Q*	7.00	9.07	115
$K[(AmO_2)(PO_4)](H_2O)_x$		inf	*Q*	6.91	9.00	116
$Rb[(AmO_2)(PO_4)](H_2O)_x$		inf	*Q*	6.94	9.02	116
$Cs[(AmO_2)(PO_4)](H_2O)_x$		inf	*Q*	6.94	8.82	116
$NH_4[(AmO_2)(PO_4)](H_2O)_3$		inf	*Q*	6.95	9.00	117

*Structure determined (det), or structural affiliation inferred (inf)

†At 10 K: space group $P2_1cn$, *a* 6.99 Å, *b* 6.97 Å, *c* 17.61 Å [118]

‡*b* 9.96 Å, β 90.4 °

It is likely that the small *c*-cell dimensions reported for some of the Np, Pu and Am-analogues of the uranyl compounds (on the order of 8.7–9.1 Å, Tables 10 and 11) are in fact subcells, as the larger *c*-dimension may be difficult to detect by conventional powder X-ray diffraction methods.

The autunite-type compounds with Cs in the interlayer region adopt lower symmetry ordered structures with a slightly different state of hydration (Tables 10 and 11) [110]. In the pseudotetragonal ($a/\sqrt{2} \approx b/\sqrt{2} \approx 7.0$ Å, $\beta = 90.4°$) structure of $Cs_2[(UO_2)(PO_4)]_2(H_2O)_5$, two independent Cs atoms occupy the interlayer in conjunction with five H_2O groups (Fig. 30).

Table 11. Autunite-type arsenates with monovalent cations

Formula	Mineral	Status*	S. G.	*a* (Å)	*c* (Å)	Ref.
$Li[(UO_2)(AsO_4)](H_2O)_4$		det	*P*4/*n*	7.10	9.19	119
$Na[(UO_2)(AsO_4)](H_2O)_3$	sodium uranospinite	det	*P*4/*ncc*	7.15	17.33	110
$K[(UO_2)(AsO_4)](H_2O)_3$	abernathyite	det	*P*4/*ncc*	7.17	17.87	110
$K(H_3O)[(UO_2)(AsO_4)]_2(H_2O)_6$		det	*P*4/*ncc*	7.17	18.05	120
$Rb[(UO_2)(AsO_4)](H_2O)_3$		det	*P*4/*n*	7.19	17.64	110
$Cs(H_3O)[(UO_2)(AsO_4)]_2(H_2O)_5$†		det	$P2_1/n$	14.26	17.22	110
$H_3O[(UO_2)(AsO_4)](H_2O)_3$‡	trögerite	det	*P*4/*ncc*	7.16	17.64	121
$NH_4[(UO_2)(AsO_4)](H_2O)_3$		det	*P*4/*ncc*	7.19	18.19	120
$Ag[(UO_2)(AsO_4)](H_2O)_3$		det	*P*4/*ncc*	7.09	17.05	110
$Tl[(UO_2)(AsO_4)](H_2O)_3$		det	*P*4/*ncc*	7.19	17.97	110
$Na[(NpO_2)(AsO_4)](H_2O)_{3.5(?)}$		inf	*Q*	7.11	8.71	114
$K[(NpO_2)(AsO_4)](H_2O)_3$		inf	*Q*	7.12	8.96	114
$H_3O[(NpO_2)(AsO_4)](H_2O)_3$		inf	*Q*	7.15	8.87	114
$NH_4[(NpO_2)(AsO_4)](H_2O)_3$		inf	*Q*	7.18	9.00	114
$K[(PuO_2)(AsO_4)](H_2O)_x$		inf	*Q*	7.12	8.92	115
$(H_3O)_{0.6}Rb_{0.4}[(PuO_2)(AsO_4)](H_2O)_x$		inf	*Q*	7.14	17.83	115
$H_3O[(PuO_2)(AsO_4)](H_2O)_x$		inf	*Q*	7.12	9.06	115
$NH_4[(PuO_2)(AsO_4)](H_2O)_x$		inf	*Q*	7.10	8.77	115
$K[(AmO_2)(AsO_4)](H_2O)_x$		inf	*Q*	7.10	9.09	116
$Rb[(AmO_2)(AsO_4)](H_2O)_x$		inf	*Q*	7.15	17.73	116
$Cs[(AmO_2)(AsO_4)](H_2O)_x$		inf	*Q*	7.09	17.72	116
$NH_4[(AmO_2)(AsO_4)](H_2O)_x$		inf	*Q*	7.11	8.93	116

*Structure determined (det), or structural affiliation inferred (inf); †*b* 7.14 Å, β 91.1°

‡At 4 K: space group *P*-1, *a* 7.16, *b* 7.11, *c* 17.55 Å, α 90.2, β 90.0, γ 90.0° [122]

The structure of $Cs(H_3O)[(UO_2)(AsO_4)]_2(H_2O)_5$ may also be considered pseudotetragonal ($\frac{1}{2}a \approx b$, $\beta = 91.1°$), but in this case, oxonium and Cs are both in ordered positions in the interlayer, along with five H_2O groups (Fig. 30).

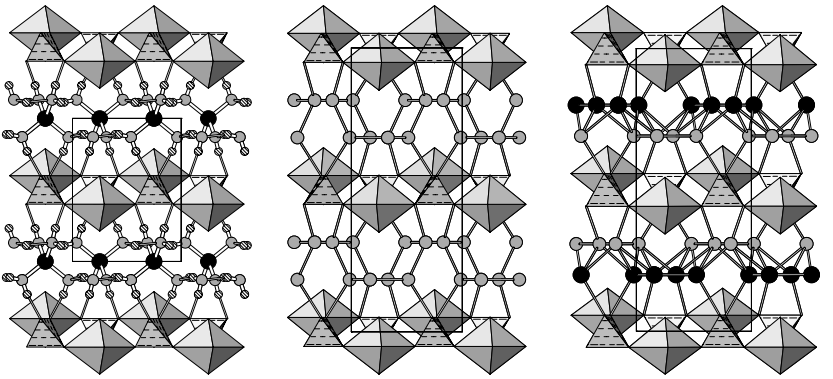

Figure 29. Variation in accommodation of monovalent ions in tetragonal structures with the autunite-type sheet, after [110]. At left, the structure of $Li[(UO_2)(PO_4)](H_2O)_4$ projected along [100], with Li atoms shown as black spheres, O atoms as larger gray spheres, and H atoms as small striped spheres. At center, the structure of $Rb[(UO_2)(PO_4)](H_2O)_3$ projected along [100]; the Rb atoms and O atoms of H_2O groups occupy the same interlayer position (in the ratio 1:3); H atoms are not shown, but a possible hydrogen-bonding scheme is shown. At right, the structure of $Rb[(UO_2)(AsO_4)](H_2O)_3$ projected along [100]; the smaller gray spheres correspond to the O atoms of H_2O groups, and the black spheres correspond to positions that are occupied by both Rb atoms and O atoms of H_2O groups in the ratio 1:1; interlayer cation-anion bonds and possible hydrogen bonding is illustrated, but H atoms are not shown.

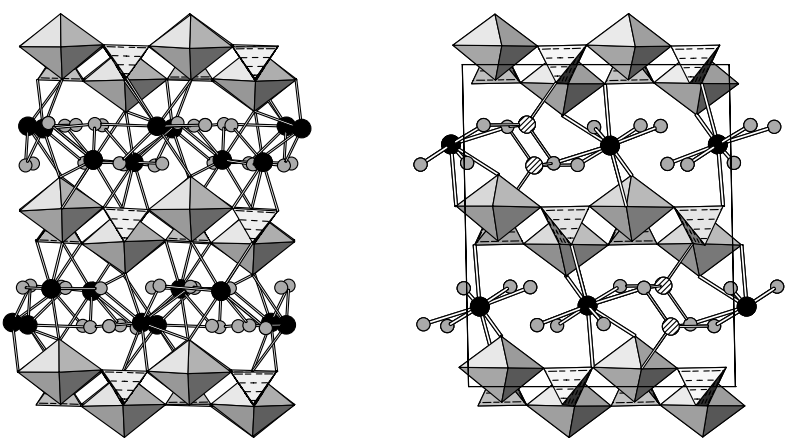

Figure 30. At left, the structure of $Cs_2[(UO_2)(PO_4)]_2(H_2O)_5$ projected along [110]; Cs atoms are shown as black spheres, and O atoms as gray spheres, after [110]. At right, the structure of $Cs(H_3O)[(UO_2)(AsO_4)]_2(H_2O)_5$ projected along [010]; Cs atoms are shown as black spheres, O atoms of H_2O groups as gray spheres, and the O atom of the oxonium group is striped. For clarity, possible networks of hydrogen bonds have been omitted, except for the oxonium group.

The autunite-type compounds with large divalent cations (Ca, Sr, Pb, Ba) in their interlayers are listed in Table 12 (phosphates) and Table 13 (arsenates). Although many of these compounds have been reported (and generally assumed to have tetragonal symmetry), only a few of their structures have been determined, all of which have either orthorhombic or monoclinic symmetry. In these structures, the large divalent interlayer cations are coordinated by H_2O groups, and by O atoms of the sheet to a lesser extent. Coordination-numbers of the divalent cations range from seven to ten. This range in possible coordination number, coupled with the flexibility of the autunite-type sheet, gives rise to more than one structure for the same interlayer cation, albeit with different hydration states and different interlayer spacings, e.g., $Sr[(UO_2)(AsO_4)]_2(H_2O)_8$ and $Sr[(UO_2)(AsO_4)]_2(H_2O)_{11}$ [128, 133].

In the structure of autunite, $Ca[(UO_2)(PO_4)]_2(H_2O)_{11}$, (Fig. 31), Ca is in sevenfold coordination by H_2O groups and is further coordinated by two O atoms of the uranyl phosphate sheet at somewhat longer distances. There are two additional H_2O groups located in the interlayer where they are held in position only by hydrogen bonding [125].

Autunite is well-known to dehydrate rapidly to form meta-autunite, for which no satisfactory structure model has yet been presented. A method of direct synthesis of meta-autunite has not been reported, and its formation by dehydration of autunite likely induces so much mosaic spread that single crystal structure determinations have not been successful. Autunite may be considered to exhibit pseudosymmetry, as the transformation matrix [-½00/001/010] yields a metrically tetragonal cell.

The structure of $Sr[(UO_2)(AsO_4)]_2(H_2O)_8$, is closely related to that of autunite (Fig. 32). In this compound, Sr is in sixfold coordination by H_2O groups and is further coordinated by two O atoms of the uranyl arsenate sheet at slightly longer distances [128, 133]. The stacking of the sheets in the octahydrate $Sr[(UO_2)(AsO_4)]_2(H_2O)_8$ differs from that found in autunite and its Sr-analogues: $Sr[(UO_2)(PO_4)]_2(H_2O)_{11}$ and $Sr[(UO_2)(AsO_4)]_2(H_2O)_{11}$ (Tables 12 and 13). In autunite, the corrugated sheets are stacked in such a fashion that the interlayer H_2O groups occupy the large cavities that extend along the [001] and [100] directions, and the interlayer cation is centered between the uranyl polyhedra of adjacent sheets (Fig. 31). Whereas in the octahydrate, although the sheets line up in a similar fashion along the [010] direction, they are offset along the [100] direction (Fig. 32), and the interlayer spacing (9.44 Å) has decreased almost 1 Å relative to $Sr[(UO_2)(AsO_4)]_2(H_2O)_{11}$ (10.48 Å).

Table 12. Autunite-type phosphates with large divalent cations

Formula	Mineral	Status*	S. G.	*a* (Å)	*b* (Å)	*c* (Å)	β (°)	Ref.
$Ca[(UO_2)(PO_4)]_2(H_2O)_{2(?)}$		inf	*O*	6.55	7.06	8.16		123
$Ca[(UO_2)(PO_4)]_2(H_2O)_{6.5(?)}$	meta-autunite	inf	*Q*	6.99		8.46		124
$Ca[(UO_2)(PO_4)]_2(H_2O)_{11}$	autunite	det	*Pnma*	14.01	20.71	7.00		125
$Sr[(UO_2)(PO_4)]_2(H_2O)_6$		inf	*Q*	6.99		8.53		126
$Sr[(UO_2)(PO_4)]_2(H_2O)_8$		inf	*Q*	7.00		18.79		127
$Sr[(UO_2)(PO_4)]_2(H_2O)_{11}$		det	*Pnma*	14.04	21.01	7.00		128
$Pb[(UO_2)(PO_4)]_2(H_2O)_4$	przhevalskite	inf	*O*	7.24	7.24	18.22		129
$Pb[(UO_2)(PO_4)]_2(H_2O)_8$		inf	*Q*	6.93		17.13		130
$Ba[(UO_2)(PO_4)]_2(H_2O)_6$	meta-uranocircite II	det	$P2_1/c$	9.88	16.87	9.79	90.1	128, 131
$Ba[(UO_2)(PO_4)]_2(H_2O)_7$	meta-uranocircite I	det	$P2_1$	6.94	17.63	6.95	90.0	128
$Ba[(UO_2)(PO_4)]_2(H_2O)_{10}$	uranocircite	inf	*M*	7.01	6.99	21.20	103.9	128
$Ca[(NpO_2)(PO_4)]_2(H_2O)_6$		inf	*Q*	6.98		8.43		114
$Sr[(NpO_2)(PO_4)]_2(H_2O)_6$		inf	*Q*	6.98		8.52		114
$Ba[(NpO_2)(PO_4)]_2(H_2O)_6$		inf	*Q*	6.98		17.31		114

*Structure determined (det), or structural affiliation inferred (inf)

Table 13. Autunite-type arsenates with large divalent cations

Formula	Mineral	Status*	S. G.	*a* (Å)	*b* (Å)	*c* (Å)	β (°)	Ref.
$Ca[(UO_2)(AsO_4)]_2(H_2O)_{6.5(?)}$	meta-uranospinite	inf	*Q*	7.14		17.00		132
$Ca[(UO_2)(AsO_4)]_2(H_2O)_{11}$	uranospinite	inf	*O*	14.35	20.66	7.17		128
$Sr[(UO_2)(AsO_4)]_2(H_2O)_8$		det	*P*2/*c*	7.15	7.10	18.90	92.7	128, 133
$Sr[(UO_2)(AsO_4)]_2(H_2O)_{11}$		det	*Pnma*	14.38	20.96	7.17		128
$Pb[(UO_2)(AsO_4)]_2(H_2O)_8$		inf	*O*	9.86	9.99	36.28		134
$Ba[(UO_2)(AsO_4)]_2(H_2O)_7$	metaheinrichite	inf	*M*	7.08	17.70	7.09	90.0	128
$Ba[(UO_2)(AsO_4)]_2(H_2O)_{10}$	heinrichite	det	*P*2/*c*	7.15	7.13	21.29	104.2	128
$Ca[(NpO_2)(AsO_4)]_2(H_2O)_6$		inf	*Q*	7.14		17.03		114
$Ca[(NpO_2)(AsO_4)]_2(H_2O)_{10}$		inf	*Q*	7.13		20.42		114
$Sr[(NpO_2)(AsO_4)]_2(H_2O)_8$		inf	*Q*	7.12		19.45		114
$Ba[(NpO_2)(AsO_4)]_2(H_2O)_7$		inf	*Q*	7.08		17.78		114
$Ca_{0.5}(H_3O)[(PuO_2)(AsO_4)]_2(H_2O)_x$		inf	*Q*	7.13		17.06		115
$Sr_{0.7}(H_3O)_{0.6}[(PuO_2)(AsO_4)]_2(H_2O)_x$		inf	*Q*	7.14		19.66		115

*Structure determined (det), or structural affiliation inferred (inf)

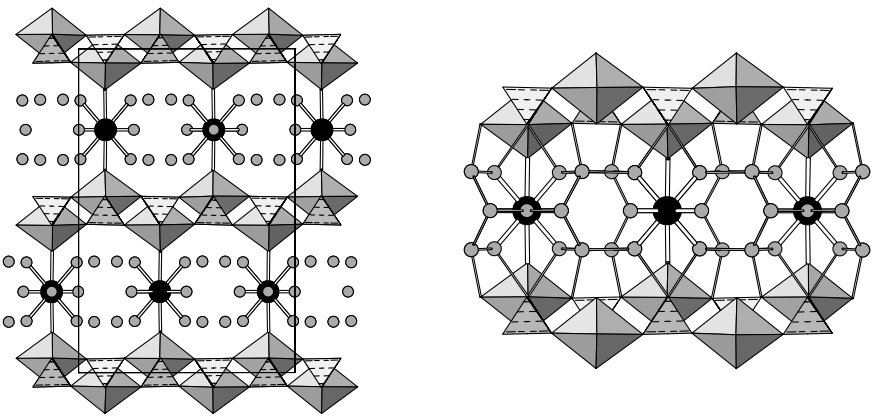

Figure 31. The structure of autunite, $Ca[(UO_2)(PO_4)]_2(H_2O)_{11}$, projected along [001] at left; Ca atoms are shown as black spheres and O atoms in the interlayer as gray spheres, after [125]. At right, a portion of the structure of autunite with H atoms omitted, but a possible hydrogen bonding scheme shown.

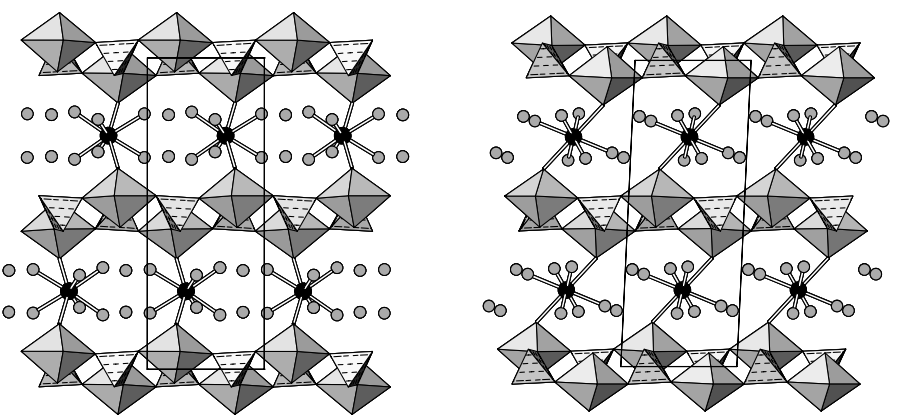

Figure 32. The structure of $Sr[(UO_2)(AsO_4)]_2(H_2O)_8$, projected along [100] at left, and along [010] at right. Sr atoms are shown as black spheres and O atoms in the interlayer as gray spheres, after [128, 133]. For clarity, possible networks of hydrogen bonds are omitted.

A wider range of structural variation is exhibited by the autunite-type compounds that contain Ba. The barium uranyl phosphate decahydrate mineral uranocircite, $Ba[(UO_2)(PO_4)]_2(H_2O)_{10}$, is likely isostructural with its arsenate analogue, heinrichite, $Ba[(UO_2)(AsO_4)]_2(H_2O)_{10}$, (Tables 12 and 13) [128, 131].

The minerals meta-uranocircite I, $Ba[(UO_2)(PO_4)]_2(H_2O)_7$, and meta-uranocircite II, $Ba[(UO_2)(PO_4)]_2(H_2O)_6$, are related to uranocircite by progressive dehydration, and by increasing connectivity of the Ba position to the sheets, rather than to interlayer H_2O groups. In heinrichite, $Ba[(UO_2)(AsO_4)]_2(H_2O)_{10}$, the Ba is in tenfold coordination by eight H_2O groups and two O atoms of the sheets (Fig. 33). In meta-uranocircite I, Ba is in ninefold coordination by six H_2O groups and three O atoms of the sheets, whereas in meta-uranocircite II, Ba is in tenfold coordination by six H_2O groups and four O atoms of the sheets. With progressive dehydration, the interlayer spacing decreases, the sheets shift in relative position, and the Ba atoms shift positions (Fig. 33).

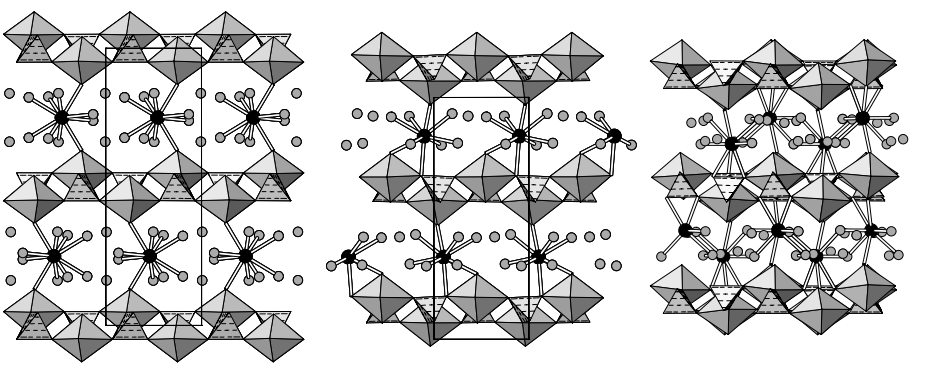

Figure 33. Variation in Ba compounds with the autunite-type sheet, after [128, 131]. At left heinrichite, $Ba[(UO_2)(AsO_4)]_2(H_2O)_{10}$, projected along [100], with Ba atoms shown as black spheres and O atoms as larger gray spheres. At center, the structure of meta-uranocircite I, $Ba[(UO_2)(PO_4)]_2(H_2O)_7$, projected along [001]. At right, the structure of meta-uranocircite II, $Ba[(UO_2)(PO_4)]_2(H_2O)_6$, projected along [101]. For clarity, hydrogen bonding is not shown.

The autunite-type compounds with Mg or divalent transition metal cations (Mn, Fe, Co, Ni, Cu, Zn, Cd) in their interlayers are listed in Table 14 (phosphates) and Table 15 (arsenates). In the known structures of these compounds, the divalent interlayer cations are all in sixfold coordination appearing as near-regular octahedra with the exception of Cu, which shows a typically Jahn-Teller distorted sixfold coordination environment appearing as tetragonal dipyramids, and whose structures will be discussed separately. Three states of hydration are observed among these (Mn, Fe, Co, Ni) structures: the triclinic dodecahydrates, the monoclinic decahydrates and the triclinic octahydrates [136, 138]. With progressive dehydration, the interlayer spacing decreases, the sheets shift in relative position, and the interlayer octahedra shift positions relative to the sheets (Fig. 34).

Table 14. Autunite-type phosphates with divalent transition metals or Mg

Formula	Mineral	Status*	S. G.	*a* (Å)	*b* (Å)	*c* (Å)	β (°)	Ref.
$Mg[(UO_2)(PO_4)]_2(H_2O)_8$	metasaléeite	inf	*Q*	7.22		17.73		135
$Mg[(UO_2)(PO_4)]_2(H_2O)_{10}$	saléeite	det	$P2_1/n$	6.95	19.95	6.98	90.6	136
$Mn[(UO_2)(PO_4)]_2(H_2O)_8$	lehnerite	inf	*M*	7.04	17.16	6.95	90.3	137
$Mn[(UO_2)(PO_4)]_2(H_2O)_{10}$		det	$I2/m$	6.97	20.38	6.98	91.0	138
$Fe^{2+}[(UO_2)(PO_4)]_2(H_2O)_8$	bassetite	inf	*M*	6.98	17.07	7.01	90.5	139
$Co[(UO_2)(PO_4)]_2(H_2O)_{10}$		det	$P2_1/n$	6.95	19.93	6.96	90.4	138
$Ni[(UO_2)(PO_4)]_2(H_2O)_{10}$		det	$P2_1/n$	6.95	19.82	6.97	90.4	138
$Ni[(UO_2)(PO_4)]_2(H_2O)_{12}$†		det	*P*-1	7.00	7.00	11.17	82.2	138
$Cu[(UO_2)(PO_4)]_2(H_2O)_8$	metatorbernite	det	*P*4/*n*	6.98		17.35		140
$Cu[(UO_2)(PO_4)]_2(H_2O)_{12}$	torbernite	det	*P*4/*nnc*	7.03		20.81		140
$Zn[(UO_2)(PO_4)]_2(H_2O)_{9.5}$		inf	*Q*	7.01		20.19		141
$Cd[(UO_2)(PO_4)]_2(H_2O)_7$		inf	*Q*	6.97		18.08		141

*Structure determined (det), or structural affiliation inferred (inf); †α 81.6, γ 88.7°

In both the dodecahydrate and decahydrate structures, the interlayer cation is coordinated by six H_2O groups, and a network of hydrogen bonding connects the interlayer octahedra to the sheets (Fig. 34). In the octahydrate structure (e.g., metakahlerite), the octahedral coordination of the interlayer cation consists of five interlayer H_2O groups, whereas the sixth vertex is a shared O atom of a dioxo group of a uranyl square bipyramid [138].

The role of Cu in autunite-type compounds differs from that of the other divalent transition metals; only the Cu-bearing compounds actually have tetragonal symmetry [140]. In these structures, Cu occurs in sixfold coordination in Jahn-Teller distorted (4+2) octahedra (tetragonal dipyramids), with four short bonds to the O atoms of interlayer H_2O groups, and two longer distances to the O atoms of uranyl ions. Only dodecahydrates (torbernite and zeunerite) and octahydrates (metatorbernite and metazeunerite) are known, and these phases are related by dehydration. The topologies of the uranyl phosphate sheets in torbernite and metatorbernite are identical, but the stacking of the sheets is different (Fig. 35). Relative to torbernite, every alternate sheet in metatorbernite is displaced by $a/\sqrt{2}$ along [110]. In torbernite, interlayer H_2O groups are accommodated in the large cavities both above and below the plane of the Cu atoms, whereas in metatorbernite, they are in the cavities either above or below the plane of the Cu atoms [140].

Table 15. Autunite-type arsenates with divalent transition metals or Mg

Formula	Mineral	Status*	S. G.	*a* (Å)	*b* (Å)	*c* (Å)	α (°)	β (°)	γ (°)	Ref.
$Mg[(UO_2)(AsO_4)]_2(H_2O)_8$	metanováčekite	inf	*Q*	7.16		8.58				142
$Mg[(UO_2)(AsO_4)]_2(H_2O)_{10}$	nováčekite II	det	$P2_1/n$	7.13	20.09	7.16		90.6		138
$Mg[(UO_2)(AsO_4)]_2(H_2O)_{12}$	nováčekite I	det	*P*-1	7.16	7.16	11.31	81.4	81.2	88.9	138
$Mn[(UO_2)(AsO_4)]_2(H_2O)_8$		det	*P*-1	7.22	9.92	13.34	75.0	84.1	82.0	138
$Mn[(UO_2)(AsO_4)]_2(H_2O)_{12}$		det	*P*-1	7.14	7.14	11.36	81.6	81.6	88.9	138
$Fe^{2+}[(UO_2)(AsO_4)]_2(H_2O)_8$	metakahlerite	det	*P*-1	7.21	9.82	13.27	75.4	84.0	81.8	138
$Fe^{2+}[(UO_2)(AsO_4)]_2(H_2O)_{12}$	kahlerite	inf	*Q*	14.30		21.97				142
$Co[(UO_2)(AsO_4)]_2(H_2O)_8$	metakirchheimerite	det	*P*-1	7.20	9.77	13.23	75.5	84.1	81.7	138
$Co[(UO_2)(AsO_4)]_2(H_2O)_{12}$	"kirchheimerite"†	det	*P*-1	7.16	7.16	11.29	81.5	81.4	88.9	138
$Ni[(UO_2)(AsO_4)]_2(H_2O)_{7\text{-}8(?)}$		inf	*Q*	7.18		17.24				143, 144
$Ni[(UO_2)(AsO_4)]_2(H_2O)_{12}$		det	*P*-1	7.15	7.16	11.26	81.5	81.4	88.9	138
$Cu[(UO_2)(AsO_4)]_2(H_2O)_8$	metazeunerite	det	*P*4/*n*	7.11		17.42				140
$Cu[(UO_2)(AsO_4)]_2(H_2O)_{12}$	zeunerite	det	*P*4/*nnc*	7.18		20.86				140
$Zn[(UO_2)(AsO_4)]_2(H_2O)_8$	metalodèvite	inf	*Q*	7.16		17.20				145
$Mg[(NpO_2)(AsO_4)]_2(H_2O)_8$		inf	*Q*	7.09		17.47				114

*Structure determined (det), or structural affiliation inferred (inf); †Not an approved mineral species

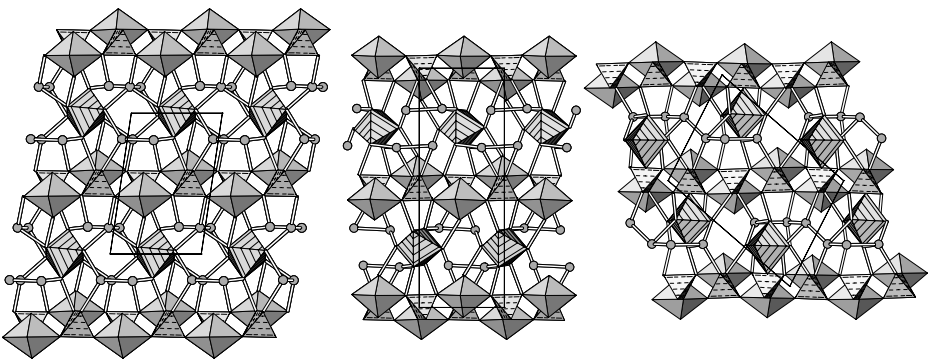

Figure 34. Variation in accommodation of Mg and divalent transition metal cations in structures with the autunite-type sheet, after [138]. At left, nováčekite I, $Mg[(UO_2)(AsO_4)]_2(H_2O)_{12}$, projected along [100], with Mg-centered octahedra striped, H atoms omitted, O atoms of H_2O groups shown as gray spheres, and a possible scheme of hydrogen bonding shown. At center, the structure of nováčekite II, $Mg[(UO_2)(AsO_4)]_2(H_2O)_{10}$, projected along [100], with the same legend. At right, the structure of metakahlerite, $Fe[(UO_2)(AsO_4)]_2(H_2O)_8$, projected along [100].

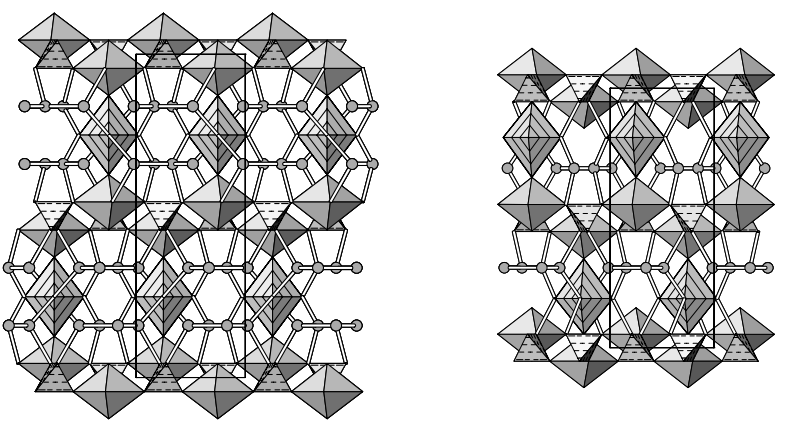

Figure 35. At left, the structure of torbernite, $Cu[(UO_2)(PO_4)]_2(H_2O)_{12}$, projected along [100], with Cu-centered polyhedra striped, H atoms omitted, O atoms of H_2O groups shown as gray spheres, and a possible scheme of hydrogen bonding shown. At right, the structure of metatorbernite, $Cu[(UO_2)(PO_4)]_2(H_2O)_8$, projected along [100] with the same legend, after [140].

Compounds with the autunite-type sheet and trivalent interlayer ions have been described with both large cations (La, Pr, Nd) and smaller cations (Al, Fe), but structures have been refined only for a few Al-bearing compounds (Table 16).

Table 16. Autunite-type compounds with trivalent interlayer cations

Formula	Mineral	Status*	S. G.	*a* (Å)	*b* (Å)	*c* (Å)	β (°)	Ref.
$Al[(UO_2)(PO_4)]_2(OH)(H_2O)_8$	threadgoldite	det	*C*2/*c*	20.17	9.85	19.72	110.7	146
$(HAl)_{0.5}[(UO_2)(PO_4)]_2(H_2O)_8$†	sabugalite	inf	*M*	20.82	9.84	9.85	111.9	147
$Al_{0.67}\square_{0.33}[(UO_2)(PO_4)]_2(H_2O)_{15.5}$‡		det	*P*-1	7.00	13.71	14.02	89.7	148
$Al_{1-x}\square_x[(UO_2)(PO_4)]_2(H_2O)_{20+3x}F_{1-3x}$	uranospathite	det	*Pnn2*	30.02	7.01	7.05		148
$Fe^{3+}[(UO_2)(PO_4)]_2(OH)(H_2O)_7$		inf	*M*	6.96	6.94	21.05	90.9	139
$Fe^{2+}Fe^{3+}[(UO_2)(PO_4)]_4(OH)(H_2O)_{13}$	vochtenite	inf	*M*	12.60	20.00	10.00	102.3	149
$La[(UO_2)(PO_4)]_3(H_2O)_{14}$		inf	*Q*	6.96		22.28		150
$Pr[(UO_2)(PO_4)]_3(H_2O)_{14}$		inf	*Q*	6.96		22.11		150
$Nd[(UO_2)(PO_4)]_3(H_2O)_{13}$		inf	*Q*	6.96		22.04		150
$Al[(UO_2)(AsO_4)]_2(F,OH)(H_2O)_{6.5}$	chistyakovaite	inf	*M*	19.99	9.79	19.62	110.7	151
$Al_{1-x}\square_x[(UO_2)(AsO_4)]_2(H_2O)_{20+3x}F_{1-3x}$	arsenuranospathite	inf	*O*	30.37	7.16	7.16		148

*Structure determined (det), or structural affiliation inferred (inf)

†Transformed from original setting by matrix [101/0-10/00-1]

‡α 78.4, γ 81.9°

As in the case of the Mg-bearing autunite-type structures, Al occurs in octahedral coordination, and a network of hydrogen bonds connects the interlayer octahedra to the actinyl-bearing sheets. The Al-bearing compounds exhibit the widest range of hydration states of any of the interlayer cations (e.g., uranospathite, $Al_{1-x}\square_x[(UO_2)(PO_4)]_2(H_2O)_{20+3x}F_{1-3x}$, the "Dagwood sandwich" of the autunite-type structures, Fig. 36). The factors that influence the coordination and hydration state of the Al-bearing compounds with the autunite-type sheet have not yet been elucidated. In threadgoldite, $Al[(UO_2)(PO_4)]_2(OH)(H_2O)_8$, Al occurs in the interlayer as a dimer of edge-sharing octahedra, $\{Al_2(OH)_2(H_2O)_8\}$, which is held in the structure by hydrogen bonding [146]. In the structures of $Al_{0.67}\square_{0.33}[(UO_2)(PO_4)]_2(H_2O)_{15.5}$ and of uranospathite, Al occurs in the interlayer coordinated by six H_2O groups to form isolated octahedra that are held in the structures by hydrogen bonding [148].

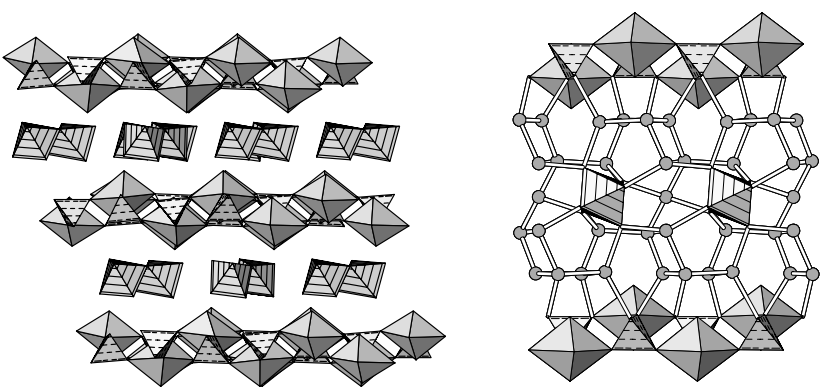

Figure 36. At left, the structure of threadgoldite, $Al[(UO_2)(PO_4)]_2(OH)(H_2O)_8$, projected along [021], with Al-centered octahedra striped, after [146]. At right, a portion of the structure of uranospathite, $Al_{1-x}\square_x[(UO_2)(PO_4)]_2(H_2O)_{20+3x}F_{1-3x}$, projected along [001], with an extensive possible network of hydrogen bonding, after [148].

All of the compounds with the autunite-type sheet *sensu stricto* are hydrates, with the sheets being held together mainly by hydrogen bonding. However, an interrupted autunite-type sheet has been reported in the anhydrous compound $K_4[(UO_2)(PO_4)_2]$ [152]. Relative to the normal autunite-type uranyl phosphate sheet (Fig. 28), half of the uranyl square bipyramids are vacant (Fig. 37). Potassium atoms in the interlayer between the interrupted uranyl phosphate sheets provide charge balance and connectivity.

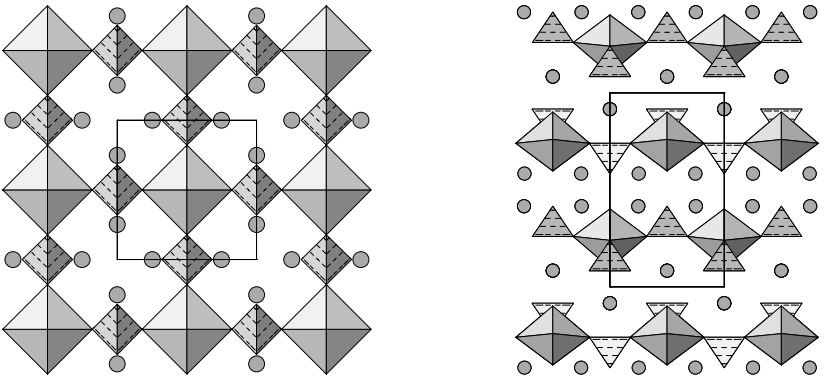

Figure 37. The structure of $K_4[(UO_2)(PO_4)_2]$, projected along [001] at left, and along [100] at right, after [152]. Potassium atoms are shown as gray spheres, and bonds omitted for clarity.

In contrast to the autunite-type sheet, which contains only actinyl square bipyramids, the structure of $Ba_3[(UO_2)(PO_4)(PO_3OH]_2(H_2O)_{0.4}$ only has uranyl pentagonal bipyramids [153]. In this compound an isolated uranyl pentagonal bipyramid shares one edge and three equatorial vertices with phosphate tetrahedra to form a highly corrugated and porous sheet (Fig. 38). The interlayer region and openings in the sheet are occupied by Ba atoms in tenfold coordination.

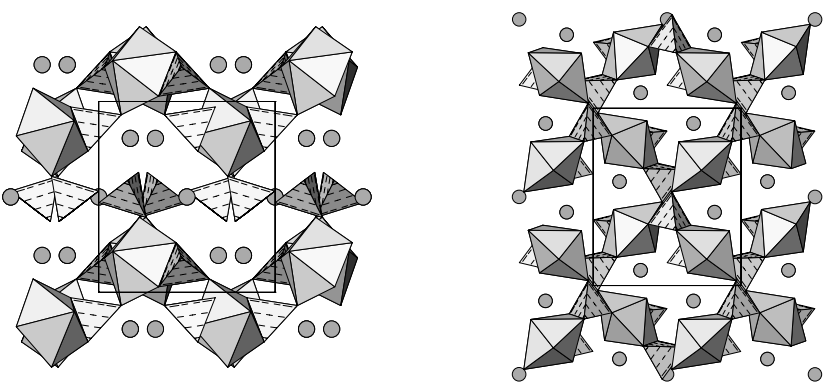

Figure 38. The structure of $Ba_3[(UO_2)(PO_4)(PO_3OH]_2(H_2O)_{0.4}$, projected along [001] at left, and along [100] at right, after [153]. Barium atoms are shown as gray spheres, and bonds omitted for clarity.

The phosphuranylite-type sheet is second most commonly observed sheet among the actinyl orthophosphates and orthoarsenates that have layered structures. The phosphuranylite-type sheet consists of dimers of edge-sharing actinyl pentagonal bipyramids that share edges with actinyl hexagonal bipyramids to form chains. Tetrahedra share edges with the hexagonal bipyamids of a given chain and vertices with an adjacent chain to form sheets of general composition $[(AnO_2)_3(XO_4)_2\varphi_2]$, where φ = O or OH (Fig. 39). The interlayer region is occupied by monovalent to tetravalent-cations or complex ions (often simultaneously), along with OH and/or H_2O groups (Table 17).

The minerals that contain the phosphuranylite-type sheet exhibit a wide and complex range of interlayer compositions, despite the limited flexibility of this sheet. The major geometrical flexibility in the phosphuranylite-type sheet is provided by the variations in the orientation of the tetrahedra, which give rise to different geometrical isomers of the sheet [168]. More importantly, the tetrahedra can also provide linkages to other polyhedra of higher bond-valence in the interlayer to form framework structures. Chemical flexibility within the sheet is achieved through the accommodation of O and OH on the vertex shared by both the hexagonal bipyramid and the dimer of pentagonal bipyramids. Selected examples of the structural variation amongst the compounds are illustrated here.

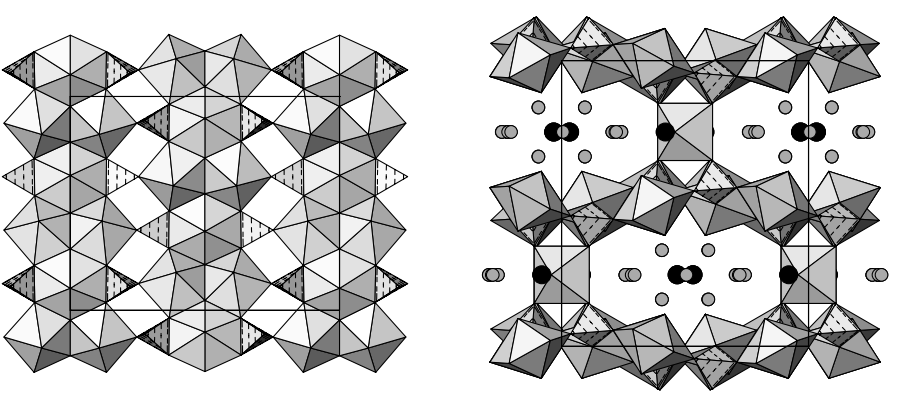

Figure 39. At left, the sheet in the structure of phosphuranylite, projected along [100]; at right, a portion of the structure of phosphuranylite, projected along [001], with K and Ca atoms both shown as black spheres, and interlayer O atoms as gray spheres, after [159].

Table 17. Compounds based on the phosphuranylite-type sheet

Formula	Mineral	Status*	S. G.	*a* (Å)	*b* (Å)	*c* (Å)	β (°)	Ref.
$Nd[(UO_2)_3(PO_4)_2O(OH)](H_2O)_6$	françoisite-(Nd)	det	$P2_1/c$	9.30	15.61	13.67	112.8	154
$Al[(UO_2)_3(PO_4)_2O(OH)](H_2O)_7$	upalite	det	$P2_1/c$	9.33	16.82	13.70	111.5	155
$Ca(UO_2)[(UO_2)_3(AsO_4)_2(OH)_2](OH)_2(H_2O)_6$	arsenuranylite	inf	*O*	15.40	13.77	17.40		156
$CaK_2(UO_2)[(UO_2)_3(PO_4)_2(OH)_2]_2(OH)_2(H_2O)_6$	yingjiangite	inf	*O*	15.71	13.69	17.42		157, 158
$CaK(H_3O)_3(UO_2)[(UO_2)_3(PO_4)_2O_2]_2(H_2O)_8$	phosphuranylite	det	*Cmcm*	15.90	13.74	17.30		159
$Pb_3[(UO_2)_3(PO_4)_2O(OH)]_2(H_2O)_{12}$	dewindtite	det	*Cmcm*	16.03	13.61	17.26		160
$Al[(UO_2)_3(PO_4)_2(OH)_2](OH)(H_2O)_{5.5}$	mundite	inf	*O*	13.76	17.08	30.98		161
$Al_2[(UO_2)_3(PO_4)_2(OH)_2](OH)_4(H_2O)_{10}$	phuralumite	det	$P2_1/c$	9.43	20.92	13.84	112.4	162
$AlTh(UO_2)[(UO_2)_3(PO_4)_2O(OH)]_2(OH)_3(H_2O)_{15}$†	althupite	det	*P*-1	10.95	18.57	13.50	68.2	163
$Ca_2[(UO_2)_3(PO_4)_2O_2](H_2O)_7$	phurcalite	det	*Pbca*	17.42	16.04	13.60		164
$Pb_2[(UO_2)_3(PO_4)_2O_2](H_2O)_5$	dumontite	det	$P2_1/m$	8.12	16.82	6.98	109.0	165
$Pb_2[(UO_2)_3(AsO_4)_2O_2](H_2O)_5$	hügelite	det	$P2_1/m$	31.07	17.30	7.04	96.5	166
$U^{6+}[(UO_2)_3(PO_4)_2(OH)_2](OH)_4(H_2O)_4$	vanmeersscheite	det	$Pmn2_1$	16.76	7.02	17.06		167
$U^{6+}[(UO_2)_3(PO_4)_2(OH)_2](OH)_4(H_2O)_2$	metavanmeersscheite	inf	*O*	34.18	33.88	14.07		167
$Ca_2Ba_4[(UO_2)_3(PO_4)_2O_2]_3(H_2O)_{16}$	bergenite	det	$P2_1/c$	10.09	17.25	17.36	113.7	168
$[(UO_2)_3(PO_4)O(OH)(H_2O)_2](H_2O)$		det	$P4_2/mbc$	14.02		13.08		169

*Structure determined (det), or structural affiliation inferred (inf); †α 110.1, γ 108.3°

The structures of phurcalite, $Ca_2[(UO_2)_3(PO_4)_2O_2](H_2O)_7$ [164], and upalite, $Al[(UO_2)_3(PO_4)_2O(OH)](H_2O)_7$ [155], are shown in Figure 40, as examples of phosphuranylite-sheet structures with a large divalent interlayer cation, and an octahedrally-coordinated trivalent cation, respectively. In phurcalite, the CaO_8 polyhedra share vertices only with the nearest sheet, whereas in upalite, the AlO_6 octahedra either share vertices with both adjacent sheets, or with neither (in which case the octahedron is held in the structure by hydrogen bonding). The other phosphuranylite-sheet structures exhibit similar themes in their interlayers.

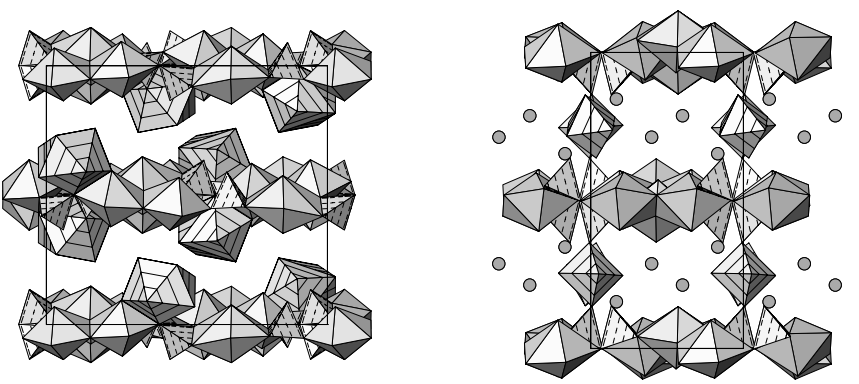

Figure 40. At left, the structure of phurcalite, $Ca_2[(UO_2)_3(PO_4)_2O_2](H_2O)_7$, projected along [001], with Ca-centered polyhedra striped and O atoms omitted, after [164]. At right, the structure of upalite, $Al[(UO_2)_3(PO_4)_2O(OH)](H_2O)_7$, projected along [100], with Al-centered octahedra striped and interlayer O atoms shown as gray spheres, after [155].

The considerable structural diversity possible in the layered structures with the phosphuranylite-type sheet is also inherent in the framework structures based on the same sheet. Althupite, $AlTh(UO_2)[(UO_2)_3(PO_4)_2O(OH)]_2(OH)_3(H_2O)_{15}$, has a complex framework structure [163] that can be described as a phosphuranylite-type sheet, $[(UO_2)_3O(OH)(PO_4)_2]^{3-}$, decorated with uranyl pentagonal bipyramids, $UO_2(H_2O)_3O_2$, and connected by a symmetrical bridge that consists of thorium polyhedra, $Th_3(OH)_3(H_2O)_3$, on either side of an aluminum octahedral dimer $Al_2(OH)_6(H_2O)_4$ (Fig. 41). The uranyl phosphate chain that makes up the phosphuranylite-type sheet has also been found in synthetic material [169] to form a framework through the edge-sharing of tetrahedra by mutually perpendicular chains (Fig. 41). This framework is unprecedented among minerals, and implies new routes for structural variation.

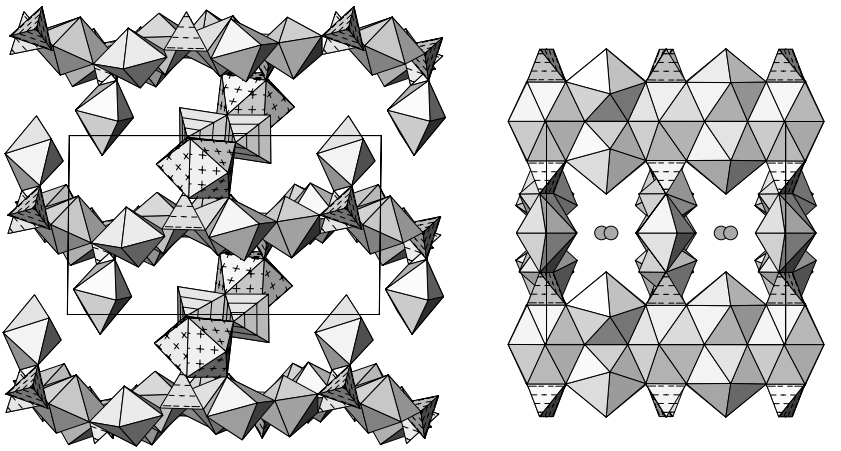

Figure 41. Comparison of frameworks based on the phosphuranylite-type sheet. At left, the structure of althupite, $AlTh(UO_2)[(UO_2)_3(PO_4)_2O(OH)]_2(OH)_3(H_2O)_{15}$, projected along [001], with Al-centered octahedra striped, and Th-centered polyhedra cross-marked, after [163]. At right, the structure of $[(UO_2)_3(PO_4)O(OH)(H_2O)_2](H_2O)$, projected along [100], after [169]. The O atoms of H_2O groups are shown as spheres in the channels of the structure.

3.1.3. Framework structures

The dominance of sheet structures among the actinyl orthophosphates and orthoarsenates is a consequence of the polarized distribution of bond strengths in actinyl polyhedra, and their resulting polymerization through only their equatorial ligands. However, framework structures can form by linkages through non-actinyl polyhedra in the third dimension, as in the structure of $[(UO_2)_3(PO_4)O(OH)(H_2O)_2](H_2O)$ (Fig. 41).

Several uranyl phosphates and uranyl arsenates form framework structures based on the uranophane sheet-anion topology. The uranyl silicate sheet found in uranophane, $Ca[(UO_2)(SiO_3OH]_2(H_2O)_5$, consists of chains of edge-sharing uranyl pentagonal bipyramids that are connected by edge- and vertex-sharing with tetrahedra. The uranyl phosphate and arsenate frameworks listed in Table 18 show topologically identical sheets, but uranyl polyhedra in the interlayer region share equatorial vertices with the tetrahedra, linking the structures in the third dimension. The degree of polymerization of the interlayer uranyl polyhedron is a function of the orientation of the tetrahedra (geometrical isomer [171]), and the composition. Thus, in $(UO_2)[(UO_2)(PO_4)]_2(H_2O)_4$, the interlayer uranyl pentagonal bipyramid shares only two vertices with the tetrahedra of adjacent sheets (Fig. 42). The structures of its arsenate analogues,

Table 18. Structures based on the uranophane sheet-anion topology

Formula	S. G.	*a* (Å)	*b* (Å)	*c* (Å)	β (°)	Ref.
$(UO_2)[(UO_2)(PO_4)]_2(H_2O)_4$	*Pnma*	7.06	17.02	13.17		170
$(UO_2)[(UO_2)(AsO_4)]_2(H_2O)_4$	$P2_1/c$	11.24	7.15	21.94	104.6	171
$(UO_2)[(UO_2)(AsO_4)]_2(H_2O)_5$	$Pca2_1$	20.13	11.70	7.15		171
$Cs(UO_2)[(UO_2)(AsO_4)]_3(H_2O)_5$	*Pbca*	16.70	13.43	21.16		172
$K_2(UO_2)[(UO_2)(PO_4)]_4(H_2O)_2$	*Cm*	13.01	15.26	9.35	132.3	173
$Rb_2(UO_2)[(UO_2)(PO_4)]_4(H_2O)_2$	*Cm*	13.05	15.72	9.48	133.1	173
$Cs_2(UO_2)[(UO_2)(PO_4)]_4(H_2O)_2$	$Cmc2_1$	14.85	13.88	12.99		173
$Tl_2(UO_2)[(UO_2)(PO_4)]_4(H_2O)_2$	*Cm*	12.98	15.16	9.34	132.3	174
$Rb_2(UO_2)[(UO_2)(AsO_4)]_4(H_2O)_{4.5}$	*C*2/*m*	13.46	15.85	14.01	92.3	175
$Cs_2(UO_2)[(UO_2)(AsO_4)]_4(H_2O)_2$	$Cmc2_1$	15.16	14.08	13.44		175
$Na_{3.5}H_{0.5}(UO_2)[Na_2(UO_2)_2(PO_4)_4]$*	*P*1	6.68	6.92	10.73	82.3	176
$Cu[Ca(H_2O)_2(UO_2)(PO_4)_2](H_2O)_2$†	$P2_1/c$	12.78	7.00	13.01	91.9	177
$[U^{4+}(UO_2)(PO_4)]$‡	*P*-1	8.82	9.22	5.48	97.7	178
$Mg[(UO_2)(AsO_4)_{1-x}(AsO_3)_x]_2(H_2O)_4$**	*C*2/*m*	18.19	7.07	6.67	99.7	179, 180

*α 84.0, γ 89.4°; †ulrichite; ‡α 102.6, γ 102.5°; **seelite

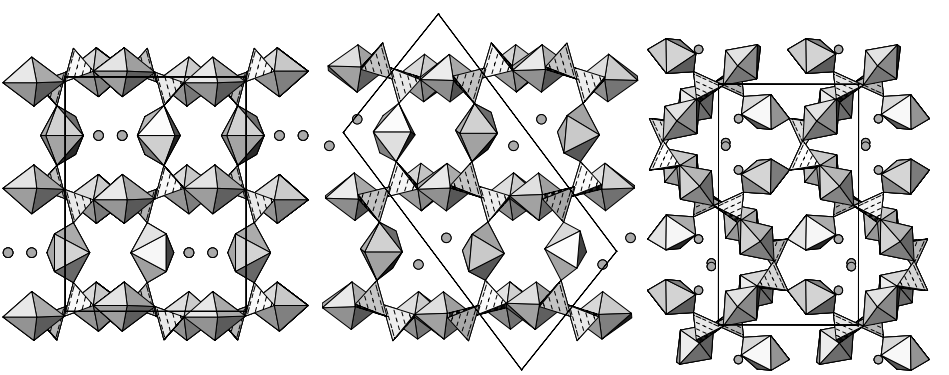

Figure 42. At left, the structure of $(UO_2)[(UO_2)(PO_4)]_2(H_2O)_4$, projected along [100], after [170]. At center, the structure of $(UO_2)[(UO_2)(AsO_4)]_2(H_2O)_4$, projected along [010], after [171]. At right, the structure of $(UO_2)[(UO_2)(AsO_4)]_2(H_2O)_5$, projected along [001], after [171]; note the heavily corrugated sheets in this structure. In all cases H_2O groups are shown as gray spheres.

$(UO_2)[(UO_2)(AsO_4)]_2(H_2O)_4$, and $(UO_2)[(UO_2)(AsO_4)]_2(H_2O)_5$ [171] form frameworks with identical connectivity (Fig. 42). Structural variation among these compounds (Table 18) is a result of both composition and synthesis conditions, and thus these frameworks are homeotypic, rather than isotypic.

The presence of low-valence interlayer cations in the frameworks leads to fewer uranyl polyhedra in the interlayer, but these polyhedra are further polymerized to the sheets. Thus, in the structure of $Cs(UO_2)[(UO_2)(AsO_4)]_3(H_2O)_5$, the uranyl pentagonal bipyramid in the interlayer shares two equatorial vertices with one adjacent sheet and one equatorial vertex with the other (Fig. 43). In the structure of $Cs_2(UO_2)[(UO_2)(AsO_4)]_4(H_2O)_2$, the interlayer uranyl polyhedron is four-connected, sharing two equatorial vertices with tetrahedra from both adjacent sheets (Fig. 43).

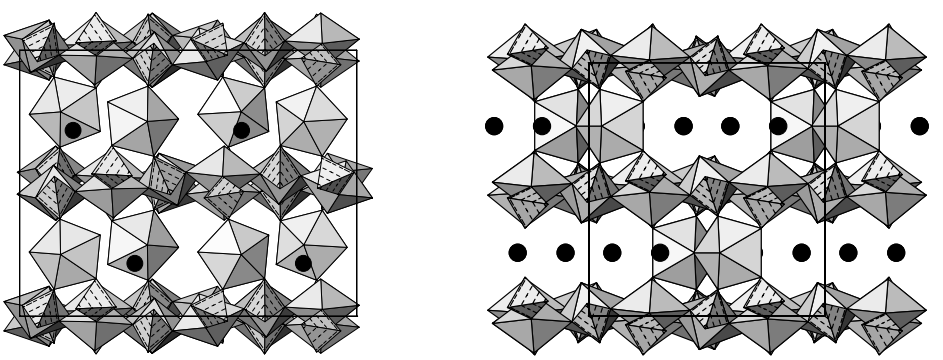

Figure 43. At left, the structure of $Cs(UO_2)[(UO_2)(AsO_4)]_3(H_2O)_5$, projected along [010], after [172]. At right, the structure of $Cs_2(UO_2)[(UO_2)(AsO_4)]_4(H_2O)_2$, projected along [001], after [175]. In both cases, Cs atoms are shown as black spheres and H_2O groups are omitted.

As in the frameworks shown in Figure 42, the compounds with general composition $A_2(UO_2)[(UO_2)(XO_4)]_4(H_2O)_n$, A = monovalent cation, X = P or As, form homeotypic frameworks, but their structures differ in detail (Figs. 43 and 44), because of the effects of composition and/or the conditions of synthesis. Thus, $K_2(UO_2)[(UO_2)(PO_4)]_4(H_2O)_2$, $Rb_2(UO_2)[(UO_2)(PO_4)]_4(H_2O)_2$, and $Tl_2(UO_2)[(UO_2)(PO_4)]_4(H_2O)_2$ crystallize in the noncentrosymmetric space group *Cm*, whereas $Cs_2(UO_2)[(UO_2)(PO_4)]_4(H_2O)_2$ and its arsenate analog are orthorhombic and adopt the noncentrosymmetric space group $Cmc2_1$, and $Rb_2(UO_2)[(UO_2)(AsO_4)]_4(H_2O)_{4.5}$ crystallizes in the centrosymmetric space group $C2/m$ (Table 18).

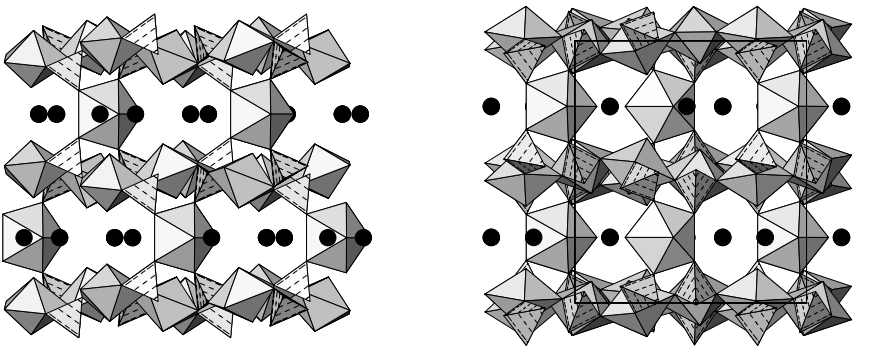

Figure 44. At left, the structure of $Tl_2(UO_2)[(UO_2)(PO_4)]_4(H_2O)_2$, projected along [101] with disordered Tl atoms shown as black spheres and H_2O groups omitted, after [174]. At right, the structure of $Rb_2(UO_2)[(UO_2)(AsO_4)]_4(H_2O)_{4.5}$, projected along [100] with Rb atoms shown as black spheres and H_2O groups omitted, after [175].

Substitution for uranyl ions can take place within the uranophane-sheet anion topology. In the framework structure of $Na_{3.5}H_{0.5}(UO_2)[Na_2(UO_2)_2(PO_4)_4]$, NaO_8 polyhedra occupy half of the pentagonal positions of the sheet (Fig. 45). Double sheets are formed by sharing of apical vertices between the uranyl pentagonal bipyramids and the NaO_8 polyhedra. Uranyl square bipyramids in the interlayer share two equatorial vertices with phosphate tetrahedra from each adjacent sheet, and their apical vertices with the NaO_8 polyhedra to form a framework. The remaining Na atoms occupy the cavities of the structure [176].

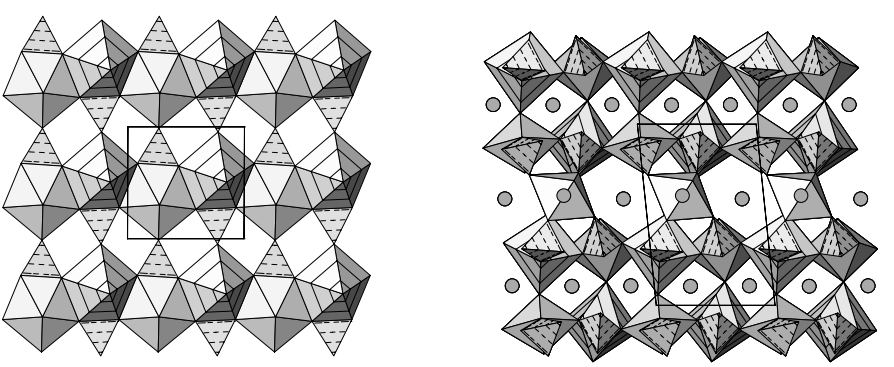

Figure 45. At left, the layer with the uranophane sheet-anion topology in the structure of $Na_{3.5}H_{0.5}(UO_2)[Na_2(UO_2)_2(PO_4)_4]$, projected along [001] with NaO_8 polyhedra striped, after [176]. At right, the structure projected along [100] with Na atoms shown as gray spheres.

The structures of ulrichite, $Cu[Ca(H_2O)_2(UO_2)(PO_4)_2](H_2O)_2$, and of the mixed-valence synthetic compound $[U^{4+}(UO_2)(PO_4)]$ also exhibit substitution for uranyl in the uranophane sheet-anion topology (Fig. 46). In ulrichite, CaO_8 polyhedra alternate with uranyl pentagonal bipyramids, and the sheets are connected by Jahn–Teller-distorted Cu-centered octahedra [177]. In the structure of $[U^{4+}(UO_2)(PO_4)]$, both U^{4+} and U^{6+} are in sevenfold coordination to form pentagonal bipyramids. Dimers of U^{4+} polyhedra alternate with dimers of uranyl pentagonal bipyramids along the uranium phosphate chains that make up the sheet (Fig. 46). The U^{4+} polyhedra also share vertices with tetrahedra of adjacent sheets to form a framework structure [178].

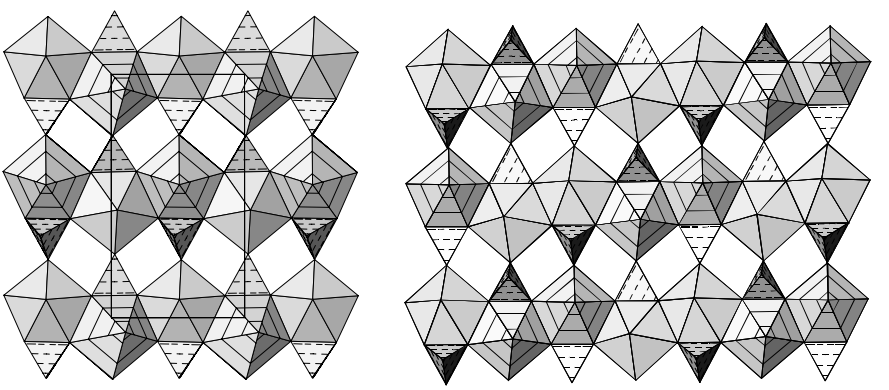

Figure 46. At left, the sheet in the structure of ulrichite, $Cu[Ca(H_2O)_2(UO_2)(PO_4)_2](H_2O)_2$, projected along [001] with CaO_8 polyhedra striped, after [177]. At right, the sheet in the structure of $[U^{4+}(UO_2)(PO_4)]$, projected along [11-2] with U^{4+} pentagonal bipyramids striped, after [178].

The structure of seelite, $Mg[(UO_2)(AsO_4)_{1-x}(AsO_3)_x]_2(H_2O)_4$, shows substitution on the tetrahedral position in the uranophane sheet-anion topology, rather than the pentagonal bipyramidal position. In seelite (not illustrated), As^{3+} is disordered with As^{5+} over the single As site in the structure. The site occupancy disorder of arsenite for arsenate is accompanied by disorder of the interlayer contents, which ideally contain Mg in octahedral coordination by H_2O groups [180].

3.2. Polyphosphates

As in the actinyl orthophosphates, hexavalent uranium occurs as the uranyl ion in square bipyramids and pentagonal bipyramids in the uranyl polyphosphates listed in Table 19. In these compounds, tetrahedra are polymerized with each

other by vertex-sharing to form pyrophosphate groups (P_2O_7), ring motifs (P_xO_{3x}), infinite chains (also P_xO_{3x}), or frameworks (P_xO_{3x-1}). The structures are presented below in order of increasing polymerization of tetrahedra.

Table 19. Polyphosphate structures of hexavalent actinides

Formula	S.G.	*a* (Å)	*b* (Å)	*c* (Å)	β (°)	Ref.
$Cs_2UO_2P_2O_7$	$P2_1/c$	6.99	10.84	13.42	106.1	181
$Na_2UO_2P_2O_7$	$Pna2_1$	13.26	8.13	6.97		182
$CsUO_2(PO_3)_3$	*Pmmn*	12.67	12.81	6.15		183
$UO_2(PO_3OH)(PO_3)_2$	$P2_1/c$	9.81	8.69	20.81	94.1	184
$(UO_2)_2P_6O_{17}$	*Cc*	8.65	11.09	17.45	106.1	185

Note: different structure types are separated by a double line

The structure of $Cs_2UO_2P_2O_7$ consists of uranyl square bipyramids that share equatorial vertices with pyrophosphate groups to form an open sheet (Fig. 47). The Cs atoms are centered below the cavities in the sheets and occupy the interlayer region [181]. The uranyl pyrophosphate sheet in $Cs_2UO_2P_2O_7$ can be compared to the uranyl phosphate sheet found in autunite-type compounds (Fig. 28); the pyrophosphate group of the $[(UO_2)(P_2O_7)]$ sheet occupies the same position as the single phosphate tetrahedron in the autunite-type sheet, $[(UO_2)(PO_4)]$.

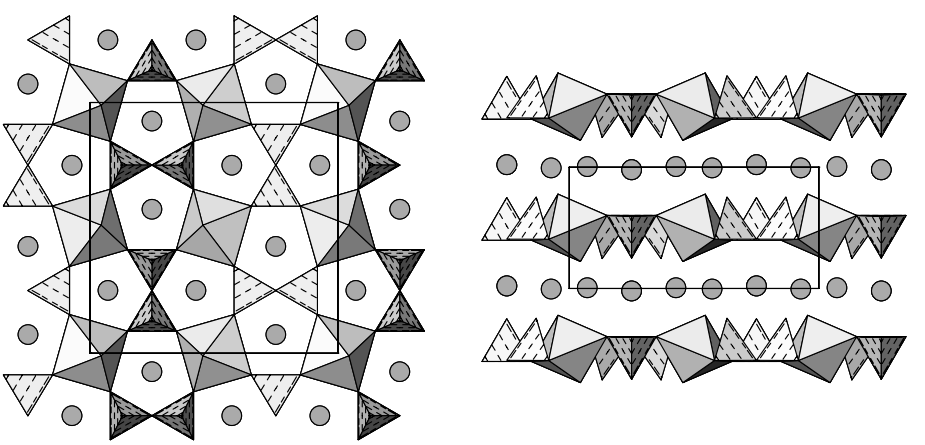

Figure 47. The structure of $Cs_2UO_2P_2O_7$, projected along [001] at left, and along [010] at right, with Cs atoms depicted as gray spheres, after [181].

Despite having a similar stoichiometry, the structure of $Na_2UO_2P_2O_7$ is not related to that of $Cs_2UO_2P_2O_7$. In $Na_2UO_2P_2O_7$, uranyl pentagonal bipyramids share edges with NaO_7 polyhedra to form chains that extend along the [001] direction (Fig. 48). The chains are connected by sharing edges and vertices with the tetrahedra of pyrophosphate groups to form sheets that correspond to the uranophane sheet-anion topology. The sheets are connected along the [010] direction by the pyrophosphate groups, and by the sharing of apical vertices between the uranyl polyhedra and the NaO_7 polyhedra of adjacent sheets [182]. The remaining Na position occupies the cavities of the framework.

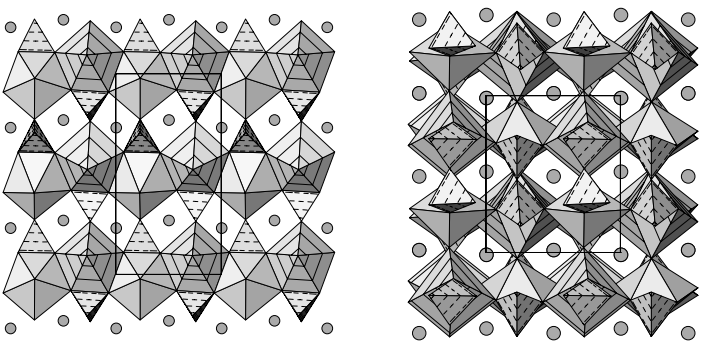

Figure 48. The structure of $Na_2UO_2P_2O_7$, projected along [010] at left, and along [100] at right, with NaO_7 polyhedra striped and Na atoms depicted as gray spheres, after [182].

A ring of six vertex-sharing phosphate tetrahedra is present in the structure of $CsUO_2(PO_3)_3$ (Fig. 49). Uranyl pentagonal bipyramids share their five equatorial vertices with four sets of rings to form a framework [183].

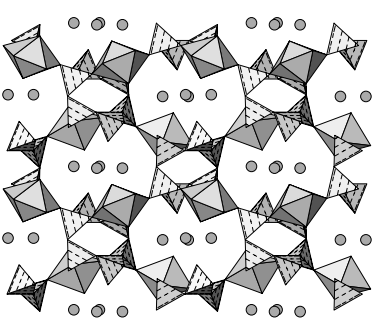

Figure 49. The $CsUO_2(PO_3)_3$ structure projected onto (100), with Cs atoms as spheres, after [183].

The structure of $UO_2(PO_3OH)(PO_3)_2$ has an infinite chain of vertex-sharing tetrahedra that spirals along the [100] direction (Fig. 50). Uranyl pentagonal bipyramids share their equatorial vertices with the tetrahedra of the chains to form a framework [184]. The H atom of the PO3OH group projects into the cavities in the structure, which extend along the [010] direction.

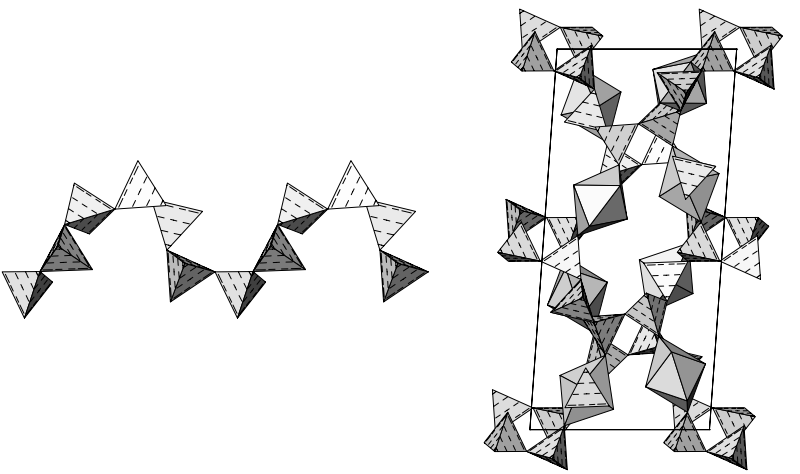

Figure 50. At left, the polyphosphate chain in the structure of $UO_2(PO_3OH)(PO_3)_2$ that spirals along [100]. At right, the structure of $UO_2(PO_3OH)(PO_3)_2$, projected along [010] with H atoms omitted, after [184].

The arrangement of tetrahedra in the structure of $(UO_2)_2P_6O_{17}$ (uranyl ultraphosphate) is perhaps the most complex observed in all actinide polyphosphates [185]. The structure is unusual in that two of the six symmetrically independent phosphate tetrahedra share three vertices each with other phosphate tetrahedra, rather than the two shared vertices found in the remaining phosphate positions (and generally in polyphosphate chain and ring structures).

In this structure, highly corrugated chains of vertex-sharing tetrahedra extend along the [110] and [1-10] directions to form the skeleton of a framework with very large cavities parallel to the chains (Fig. 51). Uranyl bipyramids occupy these cavities and share all of their equatorial vertices with the vertices of phosphate tetrahedra to reinforce the framework structure.

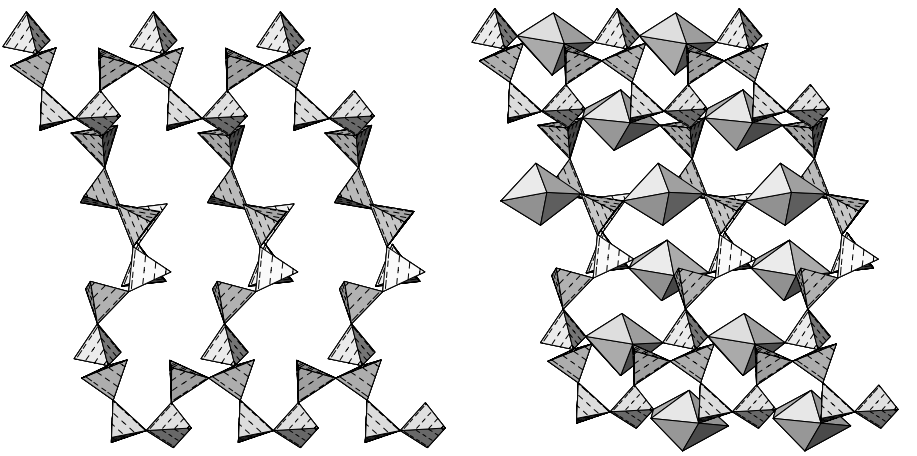

Figure 51. Details of the structure of $(UO_2)_2P_6O_{17}$, projected along [1-10]. At left, the arrangement of phosphate tetrahedra with the uranyl polyhedra omitted. At right, the arrangement of uranyl pentagonal bipyramids in the phosphate framework, after [185].

References

1. D.L. Naftz, S.J. Morrison, J.A. Davis, and C.C. Fuller (eds.), Handbook of Groundwater Remediation Using Permeable Reactive Barriers: Applications to Radionuclides, Trace Metals, and Nutrients, Academic Press, New York, 2002.
2. R.C. Ewing and L.-M. Wang, Rev. Mineral., 48 (2002) 673.
3. N. Dacheux, N. Clavier, A.-C. Robisson, O. Terra, F. Audubert, J.-E. Lartigue and C. Guy, C.R. Chimie, 7 (2004) 1141.
4. T. Murakami, T. Ohnuki, H. Isobe and T. Tsutomu, Amer. Mineral., 82 (1997) 888.
5. R. Finch and T. Murakami, Rev. Mineral., 38 (1999) 91.
6. A. Belsky, M. Hellenbrandt, V.L. Karen and P. Luksch, Acta Cryst., B58 (2002) 364.
7. J. Faber and T. Fawcett, Acta Cryst., B58 (2002) 325.
8. F.H. Allen, Acta Cryst., B58 (2002) 380.
9. F.C. Hawthorne, Mineral. Mag., 62 (1998) 141.
10. D.M.C. Huminicki and F.C. Hawthorne, Rev. Mineral., 48 (2002) 123.
11. P.C. Burns, M.L. Miller and R.C. Ewing, Can. Mineral., 34 (1996) 845.
12. P.C. Burns, Can. Mineral., 43 (2005) 1839.
13. F.A. Cotton, G. Wilkinson, C.A. Murillo, M. Bochmann, Advanced Inorganic Chemistry, John Wiley & Sons, New York, 1999, pp. 1130-1164.
14. P.C. Burns, R.C. Ewing and F.C. Hawthorne, Can. Mineral., 35 (1997) 1551.
15. R.D. Shannon, Acta Cryst., A32 (1976) 751.
16. V. Brandel and N. Dacheux, J. Solid State Chem., 177 (2004) 4743.
17. V. Brandel and N. Dacheux, J. Solid State Chem., 177 (2004) 4755.
18. A.I. Orlova and D.B. Kitaev, Radiochem., 47 (2005) 14.

19. International Centre for Diffraction Data, Powder Diffraction File #33-1354.
20. International Centre for Diffraction Data, Powder Diffraction File #33-0775.
21. International Centre for Diffraction Data, Powder Diffraction File #33-0180.
22. International Centre for Diffraction Data, Powder Diffraction File #33-1358.
23. E.R. Gobechiya, Yu. K. Kabalov, S.V. Tomilin, A.N. Lukinykh, A.A. Lizin and A.I. Orlova, Cryst. Rep., 50 (2005) 374.
24. A.A. Burnaeva, Yu. F. Volkov, A.I. Kryokuva, I.A. Korshunov and O.V. Skiba, Sov. Radiochem., 34 (1992) 528.
25. Yu.F. Volkov, S.V. Tomilin, A.I. Orlova, A.A. Lizin, Vi. Spiryakov and A.N. Lukinykh, Radiochem., 45 (2003) 319.
26. J. Barbier, J.E. Greedan, T. Asaro and G.J. McCarthy, Eur. J. Solid State Inorg. Chem., 27 (1990) 855.
27. A. Clearfield, Ann. Rev. Mater. Sci., 14 (1984) 205.
28. M. Sljukic, B. Matkovic, B. Prodic and D. Anderson, Z. Krist., 130 (1969) 148.
29. J.H. Albering and W. Jeitschko, Z. Krist., 210 (1995) 878.
30. P. Bénard, D. Louër, N. Dacheux, V. Brandel and M. Genet, Anales Quim. Int. Ed., 92 (1996) 79.
31. M.A. Salvadó, P. Pertierra, A.I. Bortun, C. Trobajo and J.R. Garcia, Inorg. Chem., 44 (2005) 3512.
32. N. Dacheux, N. Clavier, G. Wallez, V. Brandel, J. Emery, M. Quarton and M. Genet, Mater. Res. Bull.. 40 (2005) 2225.
33. P. Bénard-Rocherullé, M. Louër, D. Louër, N. Dacheux, V. Brandel and M. Genet, J. Solid State Chem., 132 (1997) 315.
34. G. Wallez, S. Launay, M. Quarton, N. Dacheux and J.-L. Soubeyroux, J. Solid State Chem., 177 (2004) 3575.
35. V. Brandel, N. Clavier and N. Dacheux, J. Solid State Chem., 178 (2005) 1054.
36. M.A. Nabar and S. Mangaonkar, J. Mater. Sci. Lett., 13 (1994) 225.
37. M.A. Nabar and R.R. Sakhardande, J. Less Common Metals, 110 (1985) 415.
38. M.A. Nabar and R.R. Sakhardande, J. Crystallogr. Spectrosc. Res., 15 (1985) 263.
39. W. Freundlich, A. Erb and M. Pagès, Rev. Chim. Miner., 11 (1974) 598.
40. M. Pagès and W. Freundlich, Plutonium 1975 and other Actinides, (1976) 205.
41. Y. Dusausoy, N.-E. Ghermani, R. Podor and M. Cuney, Eur. J. Mineral., 8 (1996) 667.
42. F.G. Fisher and R. Meyrowitz, Am. Mineral., 47 (1962) 1346.
43. D. Atkin, I.R. Basham and J.F.W. Bowles, Mineral. Mag., 47 (1983) 393.
44. C.W. Bjorklund, J. Am. Chem. Soc. 79 (1958) 6347.
45. A.A. Burnaeva, Yu.F. Volkov and A.I. Kryukova, Radiokhim., 36 (1994) 289.
46. N. Galesic, B. Matkovic, M. Topic, E. Coffou and M. Sljukic, Croat. Chem. Acta, 57 (1984) 597.
47. M. Louër, R. Brochu, D. Louër, S. Arsalane and M. Ziyad, Acta Cryst., B51 (1995) 908.
48. R.M. Hazen, L.W. Finger and J.W.E. Mariathasan, J. Phys. Chem. Solids, 46 (1985) 253.
49. K. Robinson, G.V. Gibbs and P.H. Ribbe, Amer. Mineral., 56 (1971) 782.
50. Y. Ni, J.M. Hughes, A.N. Mariano, Amer. Mineral., 80 (1995) 21.
51. L.A. Boatner, Rev. Mineral., 48 (2002) 87.
52. R.C.L. Mooney, Acta Cryst., 3 (1950) 337.
53. R. Salmon, C. Parent, M. Vlasse and G. le Flem, Mater. Res. Bull., 13 (1978) 439.
54. F. Mazzi and L. Ungaretti, Neues Jahrb. Mineral. Monatsh., (1994) 49.
55. K. Okada and J. Ossaka, Acta Cryst., B36 (1980) 919.
56. B. Matkovic, B. Prodic, and M. Sljukic, Croat. Chem. Acta, 40 (1968) 147.
57. J. Keester, Ferroelectrics, 8 (1974) 657.
58. A. Guesdon, J. Provost and B. Raveau, J. Mater. Chem., 9 (1999) 2583.

59. B. Matkovic, B. Kojic-Prodic, M. Sljukic, M. Topic, R.D. Willett and F. Pullen, Inorg. Chim. Acta, 4 (1970) 571.
60. M. Quarton, M. Zouiri, W. Freundlich, and J. Bernard, C. R. Seances Acad. Sci., Ser. 2, 299 (1984) 785.
61. A. El-Yacoubi, R. Brochu, A. Serghini, M. Louër, M. Alami Talbi, and D. Louër, Powder Diffraction, 12 (1997) 76.
62. C. Merigou, J. Le Du, M. Genet, N. Ouillon and T. Chopin, New J. Chem. (Fr.), 19 (1995) 1037.
63. M. Laügt, J. Appl. Crystallogr., 6 (1973) 299.
64. H.T. Hawkins, D.R. Spearing, D.K. Veirs, J.A. Danis, D.M. Smith, C.D. Tait and W.H. Runde, Chem. Mater., 11 (1999) 2851.
65. F. Nectoux and A. Tabuteau., Radiochem. Radioanal. Lett., 49 (1981) 43.
66. International Centre for Diffraction Data, Powder Diffraction File #36-0327.
67. International Centre for Diffraction Data, Powder Diffraction File #36-0326.
68. International Centre for Diffraction Data, Powder Diffraction File #36-0328.
69. C.E. Bamberger, R.G. Haire, H.E. Hellwedge and G.M. Begun, J. Less Common Metals, 97 (1984) 349.
70. D.B. Kitaev, Yu. F. Volkov and A.I. Orlova, Radiochem., 46 (2004) 211.
71. J.-M. Montel, J.-L. Devidal and D. Avignant, Chem. Geol., 191 (2002) 89.
72. J.J. Finney and N.N. Rao, Amer. Mineral., 52 (1967), 13.
73. A. Tabuteau, M. Pagès, J. Livet and C. Musikas, J. Mater. Sci. Lett., 7 (1988) 1315.
74. C. Keller and K.H. Walter, J. Inorg. Nucl. Chem., 27 (1965) 1253.
75. M.A. Nabar and R.R. Sakhardande, J. Alloys Cmpds., 285 (1999) 82.
76. R.G. Haire, H.E. Hellwege, D.E. Hobart and J.P. Young, J. Less Common Metals, 93 (1983) 358.
77. L. Van Wambeke, Bull. Soc. fr. Minéral., 95 (1972) 98.
78. T. Kato, Neues Jahrb. Mineral. Monatsh., (1990) 227.
79. A. Cabeza, M.A.G. Aranda, F.M. Cantero, D. Lozano, M. Martínez-Lara and S. Bruque, J. Solid State Chem. 123 (1996) 181.
80. A. Burdese and M.L. Borlera, Atti Accad. Sci. Torino, Cl. Sci. Fis., Mater. Nat., 94 (1960) 89.
81. G. Le Flem, J. Lamic and P. Hagenmuller, Bull. Soc. Chim. Fr., 6 (1966) 1880.
82. N. Meramedjian, M. Pagès and W. Freundlich, C.R. Acad. Sc. Paris, 277 (1973) 23.
83. P. Bénard, V. Brandel, N. Dacheux, S. Jaulmes, S. Launay, C. Lindecker, M. Genet, D. Louër and M. Quarton, Chem. Mater., 8 (1996) 181.
84. N. Dacheux, R. Podor, V. Brandel and M. Genet, J. Nucl. Mater., 252 (1998) 179.
85. N. Dacheux, A.C. Thomas, V. Brandel and M. Genet, J. Nucl. Mater., 257 (1998) 108.
86. B. Kojic-Prodic, M. Slukic and Z. Ruzic Toros, Acta Cryst., B38 (1982) 67.
87. A. Burdese and M.L. Borlera, Ann. Chim. (Rome), 53 (1963) 344.
88. R. Podor, M. François and N. Dacheux, J. Solid State Chem., 172 (2003) 66.
89. Z. Ruzic Toros, B. Kojic-Prodic, R. Liminga and S. Popovic, Inorg. Chim. Acta, 8 (1974) 273.
90. G. Masse, Bull. Soc. Fr. Mineral. Cristallogr., 95 (1972) 136.
91. M. Le Cloarec and A. Cazaussus. J. Inorg. Nucl. Chem., 40 (1978) 1680.
92. S.A. Linde, Yu.E. Gorbunova, V.V. Ilyukhin, A.V. Lavrov and V.G. Kuznetsov, Zh. Neorg. Khim. 24 (1979) 1786.
93. R. Douglass, Acta Cryst., 15 (1962) 505.
94. S.A. Linde, Yu.E. Gorbunova and A.V. Lavrov, Zh. Neorg. Khim. 28 (1983) 1391.
95. H.Y.-P. Hong, Acta Cryst., B30 (1974) 468.
96. Yu.E. Gorbunova, V.V. Ilyukhin, V.G. Kuznetsov, A.V. Lavrov and S.A. Linde, Dokl. Akad. Nauk SSSR, 228 (1976) 1329.

97. Y. LePage, J. Appl. Crystallogr., 20 (1987) 264.
98. A.L. Spek, J. Appl. Crystallogr., 36 (2003) 7.
99. R.B. King, Chem. Mater., 14 (2002) 3628.
100. T.Z. Forbes, P.C. Burns, L. Soderholm and S. Skanthakumar, Chem. Mater., 18 (2006), 1643.
101. J. Sejkora, J. Cejka, J. Hloušek, M. Novák and V. Šrein, Can. Mineral., 42 (2004) 963.
102. K. Mereiter, Tschermaks Mineral. Petrogr. Mitt., 30 (1982) 129.
103. W. Krause, H. Effenberger and F. Brandstätter, Eur. J. Mineral., 7 (1995) 1313.
104. A. Guesdon, J. Chardon, J. Provost and B. Raveau, J. Solid State Chem., 165 (2002) 89.
105. R. Mercier, M. Pham Thi and Ph. Colomban, Solid State Ionics, 15 (1985) 113.
106. E. Krogh Andersen, I.G. Krogh Andersen and G. Ploug-Sorensen, Solid State Protonic Conduct. Fuel Cells Sens., 3rd Eur. Workshop, (1985) 191.
107. T.M. Gesing and C.H. Ruscher, Z. Anorg. Alleg. Chem., 626 (2000) 1414.
108. P.C. Burns, Amer. Mineral., 85 (2000) 801.
109. A.J. Locock and P.C. Burns, Amer. Mineral., 90 (2005) 240.
110. A.J. Locock, P.C. Burns, M.J.M. Duke and T.M. and Flynn, Can. Mineral., 42 (2004) 973.
111. A.N. Fitch and M. Cole, Mater. Sci. Res. Bull., 26 (1991) 407.
112. B. Morosin, Acta Cryst., B34 (1978) 3732.
113. I.L. Botto, E.J. Baran and P.J. Aymonino, Z. Chem., 16 (1975) 163.
114. F. Weigel and G. Hoffmann, J. Less Common Metals, 44 (1976) 125.
115. R. Fischer, W. Gert-Dieter, T. Lehmann, G. Hoffmann and F. Weigel, J. Less Common Metals, 80 (1981) 121.
116. D. Lawaldt, R. Marquart, G.-D. Werner and F. Weigel, J. Less Common Metals, 85 (1982) 37.
117. F. Weigel and G. Hoffmann, J. Less Common Metals, 44 (1976) 133.
118. M. Cole, A.N. Fitch and E. Prince, J. Mater. Chem., 3 (1993) 519.
119. A.N. Fitch, B.E.F. Fender and A.F. Wright, Acta Cryst., B38 (1982) 1108.
120. M. Ross and H.T. Evans, Amer. Mineral., 49 (1964) 1578.
121. A.N. Fitch, L. Bernard, A.T. Howe, A.F. Wright and B.E.F. Fender, Acta Cryst. C39 (1983) 159.
122. A.N. Fitch, A.F. Wright and B.E.F. Fender, Acta Cryst., B38 (1982) 2546.
123. Y. Takano, Amer. Mineral., 46 (1961) 812.
124. International Centre for Diffraction Data, Powder Diffraction File #39-1351.
125. A.J. Locock and P.C. Burns, Amer. Min., 88 (2003) 240.
126. International Centre for Diffraction Data, Powder Diffraction File #28-1261.
127. F. Weigel and G. Hoffmann, J. Less Common Metals, 44 (1976) 99.
128. A.J. Locock, P.C. Burns and T.M. and Flynn, Can. Mineral., 43 (2005) 721.
129. M.V. Soboleva and I.A. Pudovkina, Mineraly Urana, Spravochnik (Uranium Minerals Handbook), Moscow (1957).
130. V. Ross, Amer. Mineral., 41 (1956) 915.
131. F. Khosrawan-Sazedj, Tschermaks Mineral. Petrogr. Mitt., 29 (1982) 193.
132. K. Walenta, Tschermaks Mineral. Petrogr. Mitt., 9 (1965) 252.
133. D. Yu Pushcharovskiĭ, E.V. Suleimanov, M. Pasero, S. Merlino, A.V. Barinova and E.V. Alekseev, Cryst. Rep., 48 (2003) 212.
134. International Centre for Diffraction Data, Powder Diffraction File #26-1161.
135. J.P. Cassedanne, J.O. Cassedanne and H.F. De Carvalho, Anais Acad. Brasil. Ciencias, 58, (1986) 249.
136. S.A. Miller and J.C. Taylor, Z. Krist., 177 (1986) 247.
137. R.Vochten, Amer. Mineral., 75 (1990) 221.
138. A.J. Locock, P.C. Burns and T.M. and Flynn, Can. Mineral., 42 (2004) 1699.
139. R. Vochten, E. De Grave and J. Pelsmaekers, Amer. Mineral., 69 (1984) 967.

140. A.J. Locock and P.C. Burns, Can. Mineral., 41 (2003) 489.
141. R. Pozas-Tormo, L. Moreno-Real, M. Martínez-Lara and S. Bruque-Gamez, Can. J. Chem., 64 (1986) 20.
142. K. Walenta, Tschermaks Mineral. Petrogr. Mitt., 9 (1964) 111.
143. P. Ondruš, F. Veselovský, R. Skála, I. Císařová, J. Hloušek, J. Frýda, I. Vavřín, J. Čejka, and A. Gabašová, J. Czech Geol. Soc., 42 (1997) 77.
144. M.A. Nabar and V.J. Iyer, Bull. Soc. Fr. Mineral. Cristallogr., 100 (1977) 272.
145. H. Agrinier, J. Geffroy, F. Chantret, B. Hery, B. Bachet and H. Vachey, Bull. Soc. Fr. Mineral. Cristallogr., 95 (1972) 360.
146. F. Khosrawan-Sazedj, Tschermaks Mineral. Petrogr. Mitt., 30 (1982) 111.
147. R. Vochten and J. Pelsmaekers, Phys. Chem. Mineral., 9 (1983) 23.
148. A.J. Locock, W.S. Kinman and P.C. Burns, Can. Mineral., 43 (2005) 989.
149. P.C. Zwaan, C.E.S. Arps and E. de Grave, Mineral. Mag., 53 (1989) 473.
150. R. Pozas-Tormo, L. Moreno-Real, M. Martínez-Lara and S. Bruque-Gamez, Inorg. Chem., 26 (1987) 1442.
151. N.V. Chukanov, G.A. Sidorenko, I.S. Naumova, A.E. Zadov and V. I. Kuz'min, Dokl. Earth Sci. 407 (2006) 290.
152. S.A. Linde, Yu.E. Gorbunova and A.V. Lavrov, Zh. Neorg. Khim., 25 (1980) 1992.
153. A. Guesdon and B. Raveau, Chem. Mater., 10 (1998) 3471.
154. P. Piret, M. Deliens and J. Piret-Meunier, Bull. Minéral., 111 (1988) 443.
155. P. Piret and J.-P. Declercq, Bull. Minéral., 106 (1983) 383.
156. L.I. Belova, Zap.Vses. Mineral. Obsch., 87 (1958) 598.
157. Z. Chen, Z. Huang and X. Gu, Acta Mineral. Sinica, 10 (1990) 102.
158. J. Zhang, A. Wan and W. Gong, Acta Petrol. Mineral., 11 (1992) 178.
159. F. Demartin, V. Diella, S. Donzelli, C.M. Gramaccioli and T. Pilati, Acta Cryst., B47 (1991) 439.
160. P. Piret, J. Piret-Meunier and M. Deliens, Eur. J. Mineral., 2 (1990) 399.
161. M. Deliens and P. Piret, Bull. Minéral., 104 (1981) 669.
162. P. Piret, J. Piret-Meunier and J.-P. Declercq, Acta Cryst., B35 (1979) 1880.
163. P. Piret and M. Deliens, Bull. Minéral., 110 (1987) 65.
164. D. Atencio, R. Neumann, A.J.G.C. Silva and Y.P. Mascarenhas, Can. Mineral., 29 (1991) 95.
165. P. Piret and J. Piret-Meunier, Bull. Minéral., 111 (1988) 439.
166. A.J. Locock and P.C. Burns, Mineral. Mag., 67 (2003) 1109.
167. P. Piret and M. Deliens, Bull. Minéral., 105 (1982) 125.
168. A.J. Locock and P.C. Burns, Can. Mineral., 41 (2003) 91.
169. P.C. Burns, C.M. Alexopoulos, P.J. Hotchkiss and A.J. Locock, Inorg. Chem., 43 (2004) 1816.
170. A.J. Locock and P.C. Burns, J. Solid State Chem., 163 (2002) 275.
171. A.J. Locock and P.C. Burns, J. Solid State Chem., 176 (2003) 18.
172. A.J. Locock, Ph.D. dissertation, Univ. Notre Dame, Notre Dame, Indiana, USA (2004).
173. A.J. Locock and P.C. Burns, J. Solid State Chem., 167 (2002) 226.
174. A.J. Locock and P.C. Burns, Z. Krist. 219 (2004) 259.
175. A.J. Locock and P.C. Burns, J. Solid State Chem., 175 (2003) 372.
176. Yu.E. Gorbunova, S.A. Linde, A.V. Lavrov and A.B. Pobedina, Dokl. Akad. Nauk SSSR, 251 (1980) 385.
177. U. Kolitsch and G. Giester, Mineral. Mag., 65 (2001) 717.
178. P. Bénard, D. Louër, N. Dacheux, V. Brandel and M. Genet, Chem. Mater., 6 (1994) 1049.
179. B. Bachet, C. Brassy and A. Cousson, Acta Cryst., C47 (1991) 2013.
180. P. Piret and J. and Piret-Meunier, Eur. J. Mineral., 6 (1994) 673.

181. S.A. Linde, Yu.E. Gorbunova, A.V. Lavrov and V.G. Kuznetsov, Dokl. Akad. Nauk SSSR, 242 (1978) 1083.
182. S.A. Linde, Yu.E. Gorbunova, A.V. Lavrov and A.B. Pobedina, Zh. Neorg. Khim., 29 (1984) 1533.
183. S.A. Linde, Yu.E. Gorbunova, A.V. Lavrov and A.B. Pobedina, Izvest. Akad. Nauk SSSR Neorg. Mater., 17 (1981) 1062.
184. V.A. Sarin, S.A. Linde, L.E. Fikin, V.Ya. Dudarev and Yu.E. Gorbunova, Zh. Neorg. Khim., 28 (1983) 1538.
185. Yu.E. Gorbunova, S.A. Linde and A.V. Lavrov, Zh. Neorg. Khim., 26 (1981) 713.

Structural Chemistry of Inorganic Actinide Compounds
S.V. Krivovichev, P.C. Burns & I.G. Tananaev (Editors)

Chapter 7

Structural chemistry of uranium vanadates: from 2-D to 3-D networks

Francis Abraham, Saïd Obbade

Laboratoire de Cristallochimie et Physicochimie du Solide, UMR CNRS 8012, ENSCL-USTL,B.P. 90108, 59652 Villeneuve d'Ascq Cedex, France

1. Introduction

Uranium, the heaviest natural element, is also the most widely studied actinide because: 1) depleted uranium is easy to manipulate, 2) uranium production is essential for nuclear industry, 3) it is an important constituent of nuclear waste, 4) in material science, U compounds have possible applications as ion exchangers, ionic conductors, selective oxidation catalysts or storage materials for radionuclides, 5) it occurs in several oxidation states and, finally, 6) hexavalent uranium has a propensity to display several coordination environments.

The topic of this chapter is crystal chemistry of uranium vanadates. It should be noted that the V^{5+} cation often has tetrahedral coordination and forms compounds that are isotypic to phosphate and arsenate analogs. However, in its association with the $(UO_2)^{2+}$ uranyl ion, vanadium adopts different coordination environments resulting in interesting compounds that do not have equivalents among phosphates and arsenates.

The structural units that represent building blocks for the uranyl vanadate structures are hexagonal, pentagonal and square bipyramids for U^{6+}, and tetrahedra, square pyramids and distorted octahedra for V^{5+}. Linkages of these coordination polyhedra results in numerous structural architectures depending upon the degree of polymerization of the U polyhedra and of the V polyhedra. In particular, the degree of polymerization is related to the U/V ratio. When V^{5+} occurs in square pyramids, the vanadyl V=O bonds are parallel to the uranyl ions and preclude the association of polyhedra in the direction of these linear elements, leading to 2-dimensional (2-D) arrangements. When V^{5+} is in

tetrahedral coordination, there is a tendency to form layered structures, although 3-dimensional (3-D) arrangements are sometimes observed as well. The 2-D networks and the 3-D frameworks are often anionic. The nature and dimension of these counter ions plays a major role in determining the uranyl vanadate architecture. The dimensionality of the polyhedral arrangement influences such properties of the compounds as ionic conductivity, etc.

Within the last few years, the family of uranium compounds with vanadium oxoanions is rapidly expanding. This paper reviews the structural chemistry of natural and synthetic uranium vanadium oxides known to date. For the description of layered structures, the concept of a sheet anion topology initially suggested by Burns *et al*. for uranyl-based minerals is used [1].

Throughout the chapter, we will use a simplified notation [2] to indicate the building steps of structural organization from the elementary blocks, the linkage modes and the dimensionality of the obtained entities for each step of the polyhedral condensation. The elementary units are indicated by a superscript placed in square brackets before the symbol of the chemical element: $^{[6]}U = UO_6$ square bipyramid, $^{[7]}U = UO_7$ pentagonal bipyramid, $^{[8]}U = UO_8$ hexagonal bipyramid, $^{[4]}V = VO_4$ tetrahedron, $^{[5]}V = VO_5$ square pyramid, $^{[6]}V = VO_6$ octahedron. Formation of Secondary Block Units (SBU) is indicated by the square brackets with subscripts before and after the brackets indicating the number of connected polyhedra and the type of shared element (c denotes corner sharing, e indicates edge sharing and c+e indicates both edge and corner sharing), respectively. For example, $^{0}_{2}[^{[7]}U]_e$ indicates dimeric units of edge-sharing UO_7 pentagonal bipyramids; the dimensionality of this SBU is 0. The subscript and superscript of the further square brackets describes the type of connections between the SBU and the dimensionality of the obtained arrangement. For example, $^{2}_{\infty}[^{0}_{2}[^{[7]}U]_e]_c$ means that the $^{0}_{2}[^{[7]}U]_e$ SBUs are connected through corners to form an infinite 2-dimensional network. The sign "–" between the two units, polyhedron or SBU, indicates that the second unit occupies the holes of the first one. In contrast, the sign "+" indicates that the two units are linked together.

2. 2-D polymerization of U polyhedra

In the case of 2-D polymerization, structures comprised of 2-dimensional arrangements of uranium polyhedra will be considered. The vanadium polyhedra (isolated tetrahedra or dimers of edge-sharing tetragonal bipyramids) populating holes within the uranium network do not directly participate in the structural organization.

2.1. 2-D network of dimers of [7]U pentagonal bipyramids: $^{2}_{\infty}[^{2}_{\infty}[^{0}_{2}[^{[7]}U]_{2e}]_{c}-{}^{0}_{2}[^{[5]}V]_{e}]$

The largest family of uranyl vanadium oxides has the general formula $M^{n+}_{2/n}(UO_2)_2V_2O_8.xH_2O$, where M represents mono or divalent cations. Numerous hydrated compounds of this family are minerals of the carnotite group, which are listed together with synthetic compounds in Table 1 [3-27]. Carnotite group structures consist of $[(UO_2)_2V_2O_8]^{2-}_{\infty}$ sheets of the francevillite anion topology, with M^{n+} ions and H_2O molecules in the interlayer space (Fig. 1a). All of the pentagons of the anion topology are occupied by uranyl ions, all the squares by vanadyl, and the triangles are vacant (Fig. 1b, 1c). This results in dimeric units of edge-sharing UO_7 pentagonal bipyramids, $^{0}_{2}[^{[7]}U]_e$ that are further connected by corner sharing to form a 2-D network $^{2}_{\infty}[^{0}_{2}[^{[7]}U]_e]_c$ with large cavities occupied by dimers of edge-sharing VO_5 square pyramids, $^{0}_{2}[^{[5]}V]_e$. The VO_5 pyramids in the V_2O_8 dimers are related by an inversion center at the middle of the shared edge, such that the two vanadyl bonds are on different sides of the layer. The uranyl vanadate layers are quite dense and have approximate dimensions of 8.4×10.4 $Å^2$.

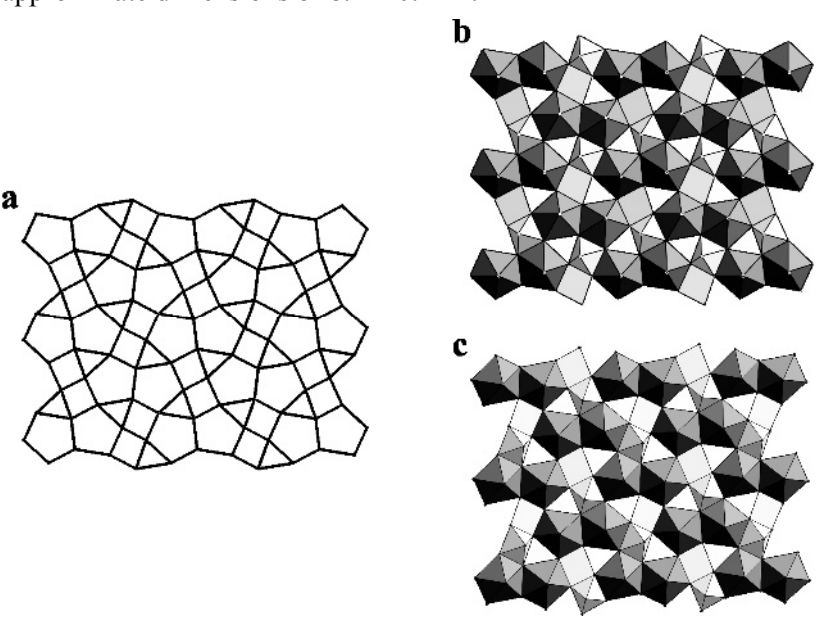

Figure 1: The francevillite anion topology **(a)** and the uranyl vanadate layers in carnotite-type compounds: **(b)** layer P in M^+-, M^{2+}- or 1, 3-diaminopropane- containing compounds; **(c)** layer P' in ethylenediamine- and 1,4-dimithylpiperazine- containing compounds.

Table 1. Minerals and synthetic uranyl vanadates containing carnotite-type layers

chemical formula / mineral name	sp. gr.	*a* [Å] / α [°]	*b* [Å] / β [°]	*c* [Å] / γ [°]	Ref
$Na_2(UO_2)V_2O_8$	$P2_1/c$	5.993 / 90	8.344 / 100.38	10.417 / 90	8,22
$K_2(UO_2)V_2O_8$ carnotite	$P2_1/c$	6.599 / 90	8.403 / 104.01	10.465 / 90	3,5,8, 10,19,22
$Rb_2(UO_2)V_2O_8$	$P2_1/c$	6.904 / 90	8.406 / 105.45	10.472 / 90	8,22
$Cs_2(UO_2)V_2O_8$ margaritasite	$P2_1/c$	7.307 / 90	8.449 / 106.04	10.525 / 90	8,10,19,21,22
$Ag_2(UO_2)V_2O_8$	$P2_1/c$	5.900 / 90	8.363 / 100.58	10.425 / 90	22,23
$Tl_2(UO_2)V_2O_8$	$P2_1/c$	6.802 / 90	8.399 / 105.47	10.473 / 90	8,22,24
$(NH_4)_2(UO_2)V_2O_8$	$P2_1/c$	6.886 / 90	8.375 / 106.07	10.468 / 90	22
$Li_2(UO_2)V_2O_8$ [c]	Ortho. *C*	13.076 / 90	7.652 / 90	10.537 / 90	22
$Li_2(UO_2)V_2O_8{\cdot}2H_2O$ [c]	Ortho. *C*	16.246 / 90	3.837 / 90	10.422 / 90	22
$(NH_4)_2(UO_2)V_2O_8{\cdot}5H_2O$	$P2_1/c$	6.599 / 90	8.403 / 104.3	10.465 / 90	22
$(NH_4)_2(UO_2)V_2O_8{\cdot}2.5H_2O$	$P2_1/c$	6.90 / 90	8.448 / 102.6	10.43 / 90	18
$K_2(UO_2)V_2O_8{\cdot}3H_2O$ carnotite	$P2_1/c$	6.91 / 90	8.41 / 103.67	10.47 / 90	3,8
$Ca(UO_2)V_2O_8{\cdot}8H_2O$ tyuyamunite	*Pncn*	20.40 / 90	8.36 / 90	10.36 / 90	4,6
$Ca(UO_2)V_2O_8{\cdot}3H_2O$ metatyuyaminite	*Pmcn*	17.34 / 90	8.49 / 90	10.54 / 90	12
$Pb_{0.96}Ba_{0.04}(UO_2)V_2O_8{\cdot}5H_2O$ francevillite	*Pnca*	16.730 / 90	8.510 / 90	10.419 / 90	20
$Pb_{0.69}Ba_{0.31}(UO_2)V_2O_8{\cdot}5H_2O$ francevillite	*Pnca*	16.645 / 90	8.450 / 90	10.479 / 90	20
$Ba(UO_2)V_2O_8{\cdot}5H_2O$ francevillite	*Pnca*	16.76 / 90	8.51 / 90	10.41 / 90	11,14
$Pb(UO_2)V_2O_8{\cdot}5H_2O$ curienite	*Pnca*	16.34 / 90	8.47 / 90	10.40 / 90	11,14, 15
$Sr(UO_2)V_2O_8{\cdot}5H_2O$	*Pnca*	16.25 / 90	8.52 / 90	10.32 / 90	11,14
$Mn(UO_2)V_2O_8{\cdot}4H_2O$	*Pmcn*	15.54 / 90	8.25 / 90	10.59 / 90	11,14
$Co(UO_2)V_2O_8{\cdot}4H_2O$	*Pmcn*	15.26 / 90	8.23 / 90	10.59 / 90	11,13,14
$Ni(UO_2)V_2O_8{\cdot}4H_2O$	*Pmcn*	15.06 / 90	8.23 / 90	10.58 / 90	6,11,14,25

Table 1 (continued)

chemical formula / mineral name	sp. gr.	*a* [Å] / α [°]	*b* [Å] / β [°]	*c* [Å] / γ [°]	Ref
$Cu_2(UO_2)V_2O_8(OH)_2 \cdot 6H_2O$ sengierite	$P2_1/c$	10.599 / 90	8.093 / 103.42	10.085 / 90	6,17
$Al(UO_2)V_2O_8(OH) \cdot 11H_2O$ vanuralite	$A2_1/c$	24.52 / 90	8.44 / 103.0	10.55 / 90	9,12
$Al(UO_2)V_2O_8(OH) \cdot 8H_2O$ metavanuralite	$P1$ or $P\bar{1}$	10.46 / 75.9	8.44 / 102.9	10.43 / 90	12
$Ba(UO_2)V_2O_8$	$P2_1/c$	6.4992 / 90	8.380 / 104.75	10.423 / 90	26
$Cu(UO_2)V_2O_8(OH)_2 \cdot 4H_2O$	$C2/c$	16.032 / 90	8.257 / 103.31	10.600 / 90	25
$Cd(UO_2)V_2O_8(OH) \cdot 4H_2O$	$Pmcn$	16.852 / 90	8.237 / 90	10.589 / 90	25
$Zn(UO_2)V_2O_8(OH) \cdot 4H_2O$	$Pmcn$	16.276 / 90	8.234 / 90	10.576 / 90	25
$(H_2dmpip)(UO_2)V_2O_8$	$P2_1/b$	13.986 / 90	8.619 / 90	10.430 / 93.12	30
$(H_2dap)(UO_2)V_2O_8$	$Pmcn$	14.738 / 90	8.640 / 90	10.432 / 90	30
$(H_2en)(UO_2)V_2O_8$	$P2_1/a$	9.315 / 90	8.617 / 114.78	10.525 / 90	30

2.1.1. Monovalent cation uranyl vanadates

The $M_2[(UO_2)_2V_2O_8] \cdot xH_2O$ compounds with M being a monovalent cation are monoclinic. The uranyl vanadate layer is parallel to (100). Adjacent P layers are related by the **a** translation, resulting in the simple PPPP sequence (Fig. 2a). For the anhydrous species that have been prepared by solid state reactions of U_3O_8, V_2O_5 and M_2CO_3 at 600°C [22]; the inter-layer distance **a**sin**β** varies linearly with the ionic radii of the 6-coordinate M^+ ions (Fig. 3) [27]. The introduction of water molecules into the interlayer space is accompanied by an increase of the interlayer distance (Table 1).

For M = Li, the hydrated compound $Li_2[(UO_2)_2V_2O_8] \cdot 4H_2O$ has been prepared, and upon heating to 175°C it dehydrates to $Li_2[(UO_2)_2V_2O_8]$ [22]. For the two Li compounds, an X-ray powder diffraction study provided an orthorhombic unit cell that does not correspond to the carnotite-type layer. The crystal structures of the two phases are unknown and further studies are necessary to describe their structural arrangements and to explain the transition at the dehydration point.

It is noteworthy that neptunyl compounds $M_2[(NpO_2)_2V_2O_8]$ with the carnotite-type structure have been synthesized for M = K, Rb, Tl [29].

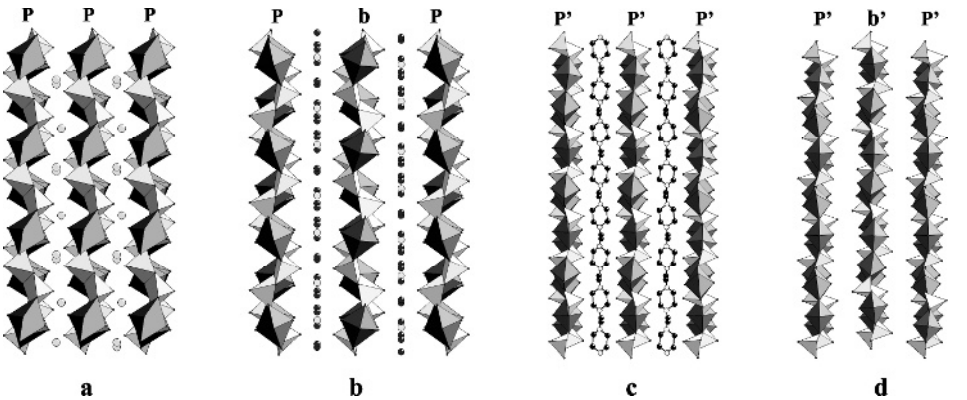

Figure 2. Stacking of the P and P' layers in carnotite type compounds containing monovalent ions (a), divalent inorganic ions (b), 1,4-dimethylpiperazine (c) and ethylenediamine (d) (not located from X-ray powder diffraction data).

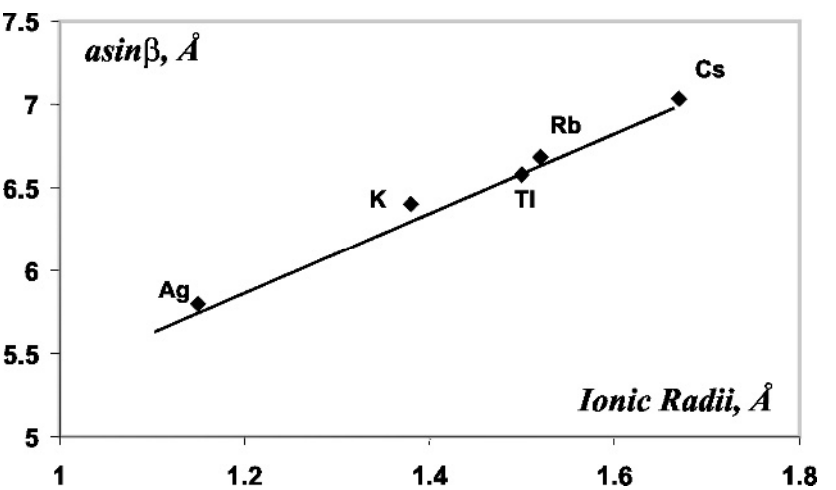

Figure 3: Variation of interlayer spacing in anhydrous monovalent cation carnotite-type compounds versus ionic radii of the 6-coordinate M^+ ion [27].

2.1.2. Divalent cation uranyl vanadates

All divalent uranyl vanadates of the carnotite group are orthorhombic, with the exception of the Cu compound. These compounds possess a second layer, labeled **b**, obtained from P by a (100) mirror plane. P and **b** layers alternate to yield a P**b**P**b** sequence (Fig. 2b).

The case of Cu corresponds to the mineral sengierite, $Cu_2[(UO_2)_2V_2O_8](OH)_2{\cdot}6H_2O$, which contains twice as many interlayer cations

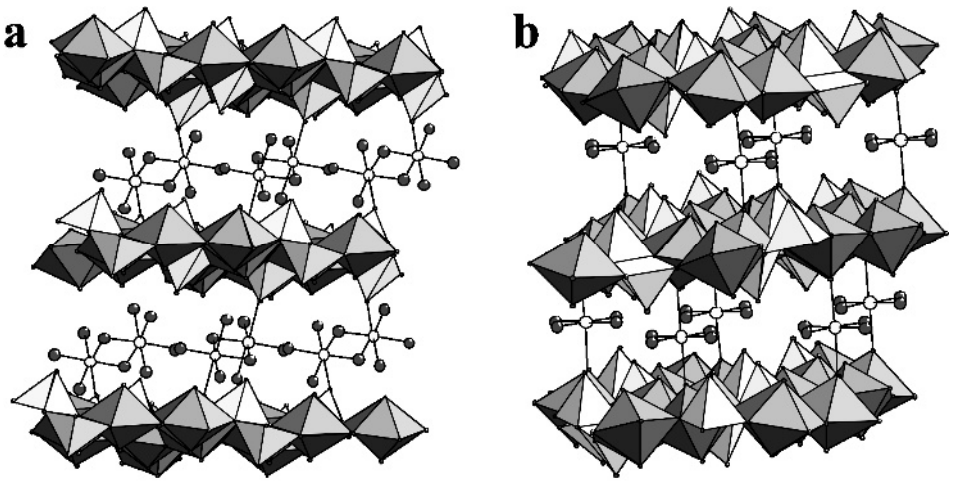

Figure 4: (a)- Crystal structure of sengierite $Cu_2(UO_2)_2(V_2O_8)(OH)_2.6H_2O$ in which the interlayer space between the carnotite-type layers is occupied by the dimeric units $Cu_2(OH)_2(H_2O)_2$ that are weakly bonded to the layers. (b)- Crystal structure of $Cu(UO_2)_2(V_2O_8).4H_2O$ in which the carnotite-type layers are connected by the $Cu(H_2O)_4O_2$ distorted octahedra.

as the other divalent cation uranyl vanadates (Table 1). The excessive positive charge is compensated by additional hydroxyl ions. The structure was determined by X-ray diffraction from synthetic single crystals [30]. The interlayer space is occupied by dimeric $[Cu_2(OH)_2(H_2O)_4]^{2+}$ units consisting of two edge-sharing CuO_4 squares. The Cu coordination is further completed by the including two oxygen atoms through long bonds, that belong to a VO_4 tetrahedra and H_2O molecule respectively, forming a distorted octahedral configuration (Fig. 4a). The hydroxyl-free Cu carnotite-type compound, $Cu[(UO_2)_2V_2O_8]\cdot 4H_2O$, has been obtained by ion exchange using $Na_2[(UO_2)_2V_2O_8]\cdot 4H_2O$ crystals or by direct hydrothermal synthesis from a mixture of $CuCl_2$, V_2O_5, and $UO_3\cdot H_2O$. In this compound, distorted $CuO_2(H_2O)_4$ octahedra are isolated from each other and share two apical oxygen atoms with uranyl ions from two adjacent uranyl vanadate layers (Fig. 4b).

2.1.3. Amine-templated uranyl vanadates

Recently, diamine-templated carnotite-type layered compounds have been synthesized under mild hydrothermal conditions [31]. In the structure with protonated 1,3-diaminopropane (dap), the sheets and the stacking sequence are identical to those observed in the divalent cation carnotite-type compounds. In the structures with 1,2-ethylenediamine (en) and 1,4-dimethylpiperazine (dmpip), half of the V_2O_8 units are reversed compared to the P sheets (Fig. 1c). These new anionic layers are labelled P' hereafter. In

$(dmpip)(UO_2)_2V_2O_8.xH_2O$, a second layer b' is deduced from P' by a twofold axis along the **c** axis so the stacking sequence is P'b'P'b' (Fig. 2d) while the stacking sequence in the structure of $(en)(UO_2)_2V_2O_8.xH_2O$ can be described as a P'P'P'P' (Fig. 2c).

Numerous uranyl phosphates and uranyl arsenates have the same general formula $M^{n+}_{1/n}(UO_2)XO_4.xH_2O$ where M can be mono-, di- and trivalent cations such as alkali metals, alkaline earths, transition metals, lanthanides or organic cations [32]. However, in these compounds, P and As are in tetrahedral coordination. These structures can exist with two different types of layers. The autunite-type sheet is observed in many minerals and synthetic compounds such as hydrogen uranyl phosphate tetrahydrate $HUO_2PO_4.4H_2O$ (HUP) which displays good selective proton conductivity at room temperature. Its layered structure and its potential applications in electrochemical systems make it a fascinating compound [33, 34]. The autunite-type sheet is built from isolated UO_6 square bipyramids that are linked by XO_4 tetrahedra (X = As, P). As far as we know, no layered uranyl vanadate containing this type of sheet has been obtained. However, it occurs as a part of 3-dimensional framework described in part 4 of this chapter. The uranophane-type sheet has been observed in some uranyl vanadates mentioned in part 4.1.

2.2. 2-D network of $^{[7]}U$ and $^{[6]}U$ polyhedra : $^{2}_{\infty}[^{2}_{\infty}[^{1}_{\infty}[^{[7]}U]_e]_c - {}^{[6]}U - {}^{[4]}V]$

The structures of uranyl oxychloro-vanadates $M_7[(UO_2)_8(VO_4)_2]O_8Cl]$ with M = Rb, Cs [35] contain sheets with the β–U_3O_8 anion-topology shown in Fig. 5a. The β–U_3O_8 [36] anion topology contains pentagons that are populated by uranyl ions to form infinite $^{1}_{\infty}[UO_5]^{4-}$ or $^{1}_{\infty}[^{[7]}U]_e$ chains of edge-sharing UO_7 pentagonal bipyramids. Adjacent chains are linked together by terminal oxygen atoms to form a 2-D network. The squares in the β–U_3O_8 anion topology are populated by U atoms in distorted octahedral environments (Fig. 5b). The adjacent layers are connected by sharing apices of square bipyramids and pentagonal bipyramids. Thus the structural arrangement of β–U_3O_8 can be described as $^{3}_{\infty}[^{2}_{\infty}[^{2}_{\infty}[^{1}_{\infty}[^{[7]}U]_e]_c\text{-}^{[6]}U]]_c$.

In $M_7(UO_2)_8(VO_4)_2O_8Cl$, infinite chains are formed by the sharing of edges between UO_7 and UO_6Cl pentagonal bipyramids with non-bridging O^{2-} and Cl^- equatorial anions alternating along the extension of the chain according to the sequence O – O – Cl (Fig. 6).

The odd number of atoms in this sequence implies that Cl atoms alternate on both sides of the chain, so the basic unit of the chain is formed by six bipyramids. The corresponding *a* parameter is close to 6×(u/2)Å (Table 2). The sheet of pentagonal bipyramids is parallel to (001) (Fig. 5c) and has pseudo-

hexagonal symmetry with the ratio a/b of the corresponding *C*-centered base close to $\sqrt{3}$ (1.82). This arrangement creates distorted hexagonal rings of

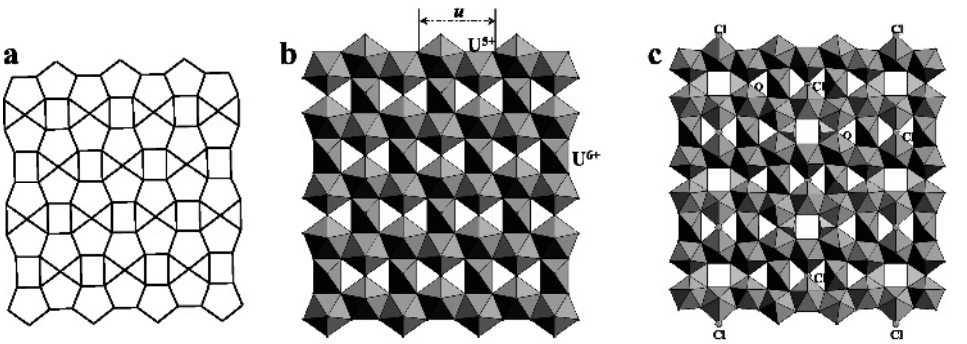

Figure 5: (a)- The β-U_3O_8 sheet anion-topology, (b)- The β-U_3O_8 layer and (c)- the layers of coordination polyhedra in the (Cs-Rb)$_7(UO_2)_8(VO_4)_2ClO_8$ compounds.

O_6 and O_5Cl, which can be described as rhombs flanked by two triangular sites. The rhombic site for the O_5Cl ring is occupied by a U atom, with the triangular sites vacant. In contrast, the rhombic site for the O_6 ring is empty, while the two triangular sites are occupied by vanadium atoms. The VO_4 tetrahedra do not play any role in the structure organization. The sheets have the formula $^{2}_{\infty}[U_8V_2O_{32}Cl]^{7-}$ (Fig. 5c). The Cs^+ ions are located within the interlayer.

Table 2. Unit cell parameters of β–U_3O_8 and $M_7[(UO_2)_8(VO_4)_2]O_8Cl]$, M = Rb, Cs

Compound	*a,* Å*	*b,* Å	*c,* Å	S. G.	Ref.
β–U_3O_8	7.069	11.445	8.303	*Cmcm*	36
$Rb_7[(UO_2)_8(VO_4)_2]O_8Cl]$	21.427	11.814	7.495	*Pmcn*	35
$Cs_7[(UO_2)_8(VO_4)_2]O_8Cl]$	21.458	11.773	14.203	*Pmmn*	35

* Direction of the chains; the *a* parameter correspond to u or 3u.

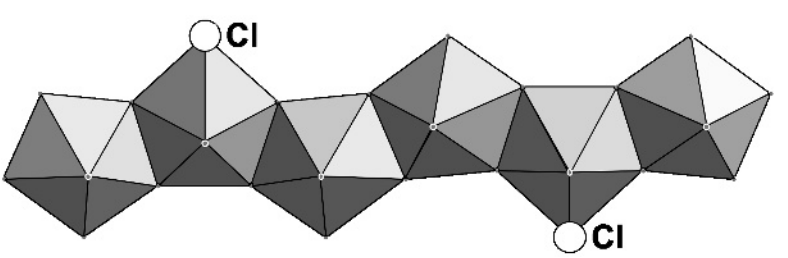

Figure 6: The $^{1}_{\infty}[U_3O_{14}Cl]^{11-}$ chains in (Cs-Rb)$_7(UO_2)_8(VO_4)_2ClO_8$ built from edge-shared UO_7 and UO_6Cl pentagonal bipyramids.

3. 1-D polymerization of U polyhedra

3.1. 2-D and 3-D structures based upon the 1-D arrangements of the UO_7 polyhedra

The uranophane anion topology is shown in Fig. 7a. In all U compounds, with the exception of ulrichite, $Cu[Ca(UO_2)(PO_4)_2]\cdot 4H_2O$ [37], all the pentagons of this anion topology are occupied by U^{6+} which results in formation of infinite $^{1}_{\infty}[UO_5]^{4-}$ chains of edge-sharing UO_7 pentagonal bipyrimids. In phosphates and arsenates, triangles in the anion topology are occupied by P or As (Fig. 7b). Owing to the tendency for V^{5+} to adopt both tetrahedral and square pyramidal coordinations, either triangles or squares in the anion topology can be occupied by V^{5+}, which gives rise to the two different sheets shown in Figs. 7b and 7g. Crystallographic parameters of the compounds in which these sheets have been observed are listed in Table 3.

3.1.1. Uranyl vanadates with 2-D uranophane-type sheets $^{2}_{\infty}[\,^{1}_{\infty}[^{[7]}U]_e + {}^{[4]}V]_{e+c}$.

Occupation of the triangles of the uranophane anion topology results in the formation of the uranophane-type sheet (Fig. 7b). Layered compounds containing uranyl vanadate anionic sheets of this type have recently been obtained with diamines, piperazine and 1,4-diazabicyclo[2,2,2]octane (*dabco*), as counter cations in the interlayer space (Fig. 7c) [31].

Table 3. Crystallographic parameters of the 2-D and 3-D uranyl vanadates built from 2-D layers with the uranophane anion topology. The unit cell parameter corresponding to the $^{1}_{\infty}[^{[7]}U]_e$ chains (u~7.09Å) is shown in bold letters, the second parameter for the layer is in italic.

chemical formula	sp. gr.	a [Å]	b [Å] / β [°]	c [Å]
$(H_2pip)[(UO_2)(VO_2)_2]\cdot 0.8H_2O$	*C*2/*m*	15.619	**7.180** / 101.50	*6.916*
$(H_2dabco)(UO_2)(VO_2)_2\cdot 0.3H_2O$	*C*2/*m*	17.439	**7.190** / 98.20	*6.899*
$(UO_2)_3(VO_2)_2\cdot 5H_2O$	*Cmcn*	17.978	*13.561*	**7.163**
$(H_2dpr)[(UO_2)_5(VO_2)_2]$	*Cmc*2_1	15.408	**14.152**	*13.652*
$(H_2dbu)[(UO_2)_5(VO_2)_2]$	*Cmc*2_1	15.654	**14.194**	*13.677*
$(UO_2)_2V_2O_7$	*P*2_1/*c*	5.6792	*13.184* / 119.75	**7.2844**
UVO_5	*Pbcm*	4.1231	*12.364*	**7.2071**

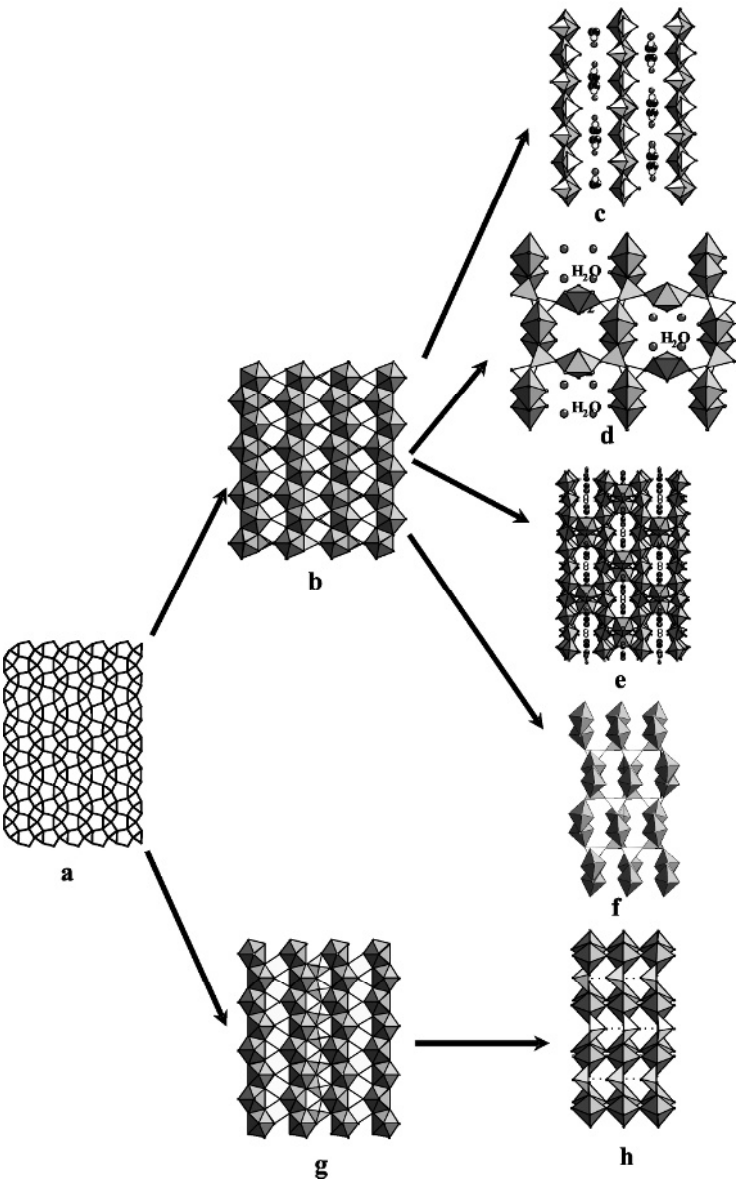

Figure 7: The uranophane sheet anion topology (a) and the uranophane-type sheet (b) found in some diamine-templated layered uranyl vanadates (c), in structure of $(UO_2)_3(VO_4)_2.5H_2O$ where layers are connected by UO_7 pentagonal bipyramids (d), in diamine-templated 3-D uranyl vanadates (e), in uranyl divanadate $U_2V_2O_{11}$ (f). The occupation of the squares of the uranophane anion topology by the VO_5 entities results in 2-D layers (g) that are linked into a 3-D framework in UVO_5.

3.1.2. Uranyl vanadates with 3-D framework based on uranophane-type sheet: $^{3}_{\infty}[^{2}_{\infty}[^{1}_{\infty}[^{[7]}U]_{e}+^{[4]}V]_{e+c}+^{[7]}U]_{c}$.

In the structure of $(UO_2)_3(VO_4)_2{\cdot}5H_2O$ [38] (Fig.7d) and recently studied diamine uranyl vanadates [39], the interlayer space between the corrugated uranophane-type sheets is occupied by linear UO_2^{2+} ions that further link the sheets into open uranyl vanadate frameworks. On the basis of the variable orientations of tetrahedra in the uranophane-type sheet, Locock and Burns have defined six different geometrical isomers [40]. In uranyl vanadate framework structures, two isomers and two types of 3-D frameworks have been observed. In $(UO_2)_3(VO_4)_2{\cdot}5H_2O$ (which can be formulated $(UO_2)[(UO_2)_2(VO_4)_2]{\cdot}5H_2O$), the *dd*/*uu* isomer has been found and the pentagonal bipyramids around the interlayer uranyl ion share two opposite equatorial oxygen atoms with two VO_4 tetrahedra of two adjacent layers. Three other equatorial ligands are H_2O molecules (Fig. 7d). The same framework can be found in the isotypic phosphate $(UO_2)_3(PO_4)_2{\cdot}4H_2O$ [41] and arsenate $(UO_2)_3(AsO_4)_2{\cdot}4H_2O$ [40].

In diamine-templated compounds such as diaminobutane- (H_2dbu) and diaminopropane-(H_2dpr) templated uranyl vanadates, the *aa/aa* isomer allows sharing of two opposite equatorial edges of the interlayer UO_7 bipyramids with four VO_4 tetrahedra of the adjacent layers, so one interlayer uranyl ion is linked to four vanadate tetrahedra (Fig. 7e). Thus, the structural notation of these compounds can be written as $^{3}_{\infty}[^{2}_{\infty}[^{1}_{\infty}[^{[7]}U]_{e}+^{[4]}V]_{e+c}+^{[7]}U]_{c}$. The interlayer space is occupied by UO_2^{2+}, $(H_2dbu)^{2+}$ or $(H_2dpr)^{2+}$ ions, and the chemical formula can be written as $(UO_2)(dbu)[(UO_2)_2(VO_4)_2]_2$ to emphasize the $[(UO_2)_2(VO_4)_2]$ sheet. Similar frameworks with various geometrical isomers of the uranophane-type sheet have been observed for numerous phosphates and arsenates [42, 43].

The 3-D framework that is present in the structure of uranyl divanadate $(UO_2)_2V_2O_7$ [44, 45] is also built from corrugated uranophane-type sheets corresponding to the geometrical isomer *dd*/*uu* according to the notation of Locock and Burns [40]. Adjacent layers are connected through terminal O atoms of the vanadate groups that form divanadate entities. As a result, a 3-D framework is formed (Fig. 7f). The structural principle for $(UO_2)_2V_2O_7$ can be described by $^{3}_{\infty}[^{2}_{\infty}[^{1}_{\infty}[^{[7]}U]_{e}+^{[4]}V]_{e+c}]_{c}$. The structure can also be considered as infinite (UO_5) chains connected through V_2O_7 divanadates units, $^{2}_{\infty}[^{1}_{\infty}[^{[7]}U]_{e}+^{0}_{2}[^{[4]}V]_{c}]_{c}$.

3.1.3. 3-D framework structure of UVO_5

In the structure of UVO_5 [22, 46, 47], all squares of the uranophane anion topology are populated by VO_5 square pyramids so that infinite $^{1}_{\infty}[VO_4]$ chains of corner-sharing VO_5 square pyramids are formed that are parallel to the

infinite $^{1}_{\infty}[UO_5]$ chains (Fig. 7g). Apical oxygen atoms of the VO_5 polyhedra of the same chain point in the same direction, i.e. either up or down relative to the plane of the sheet. The resulting $^{c}_{\infty}[UVO_6]$ layers are stacked in registry in such a way that –U–O–U–O– chains are formed (Fig. 7h). The structural principle can be formulated as $^{3}_{\infty}[\,^{2}_{\infty}[\,^{1}_{\infty}[^{[7]}U]_e+\,^{1}_{\infty}[^{[5]}V]_e]_c]_c$. The fivefold V coordination is complemented by the vanadyl O atom from the adjacent layer positioned at a long distance of 2.4 Å to form a distorted VO_6 octahedron and the =V···O=V···O=V···O= chains. In this compound, there are no uranyl ions, since the U–O bond lengths along the –U–O–U–O– chains are longer than 2.0 Å, in agreement with the oxidation state of 5+ for U. γ-$UNbO_5$ [48] is isotypic to UVO_5. In contrast, $USbO_5$ [49] is similar to UVO_5 in its layer arrangement but differs in the stacking of the layers; displacement of adjacent layers relative to each other leads to heterometallic –U–O–Sb–O–U–O–Sb– chains.

Since the $^{1}_{\infty}[UO_5]$ chains of pentagonal bipyramids are connected through the apical oxygen atoms, the structure of UVO_5 can also be described from a 2-D arrangement of UO_7 pentagonal bipyramids further connected by $^{1}_{\infty}[VO_4]$ chains: $^{3}_{\infty}[\,^{2}_{\infty}[\,^{1}_{\infty}[^{[7]}U]_e]_c+\,^{1}_{\infty}[^{[5]}V]_c]_c$.

There are no alkali metal uranyl vanadates built of this type of sheet. Chemically similar compounds, $AUVO_6$, adopt the carnotite-type structure described above which is characterized by a high stability. It is of interest that the structure of $KUNbO_6$ [50] is built from the uranophane-type sheets interleaved with K^+ ions, whereas $CsUNbO_6$ adopts the carnotite-type structure [51].

3.2. 2-D network of three U-polyhedra wide ribbons connected by VO_4 tetrahedra $^{2}_{\infty}[\,^{1}_{\infty}[\,^{1}_{\infty}[\,^{1}_{\infty}[^{[7]}U]_e]_c{-}^{[6]}U]+^{[4]}V]$

In the structures of $M_6[(UO_2)_5(VO_4)_2]O_5]$ with M = Na, K, Rb [52, 53], two parallel $^{1}_{\infty}[UO_5]^{4-}$ chains of edge-sharing UO_7 pentagonal bipyramids translated by u/2 are linked together by equatorial non-edge-shared oxygen atoms to create distorted hexagonal holes better described as a square site flanked by two triangular sites. The square sites are occupied by U atoms in distorted octahedral environments giving rise to planar ribbons three U-polyhedra wide. The ribbons are further connected by VO_4 tetrahedra to built sheets that can be considered as an intergrowth between β–U_3O_8 and uranophane-type sheets (Fig. 8a).

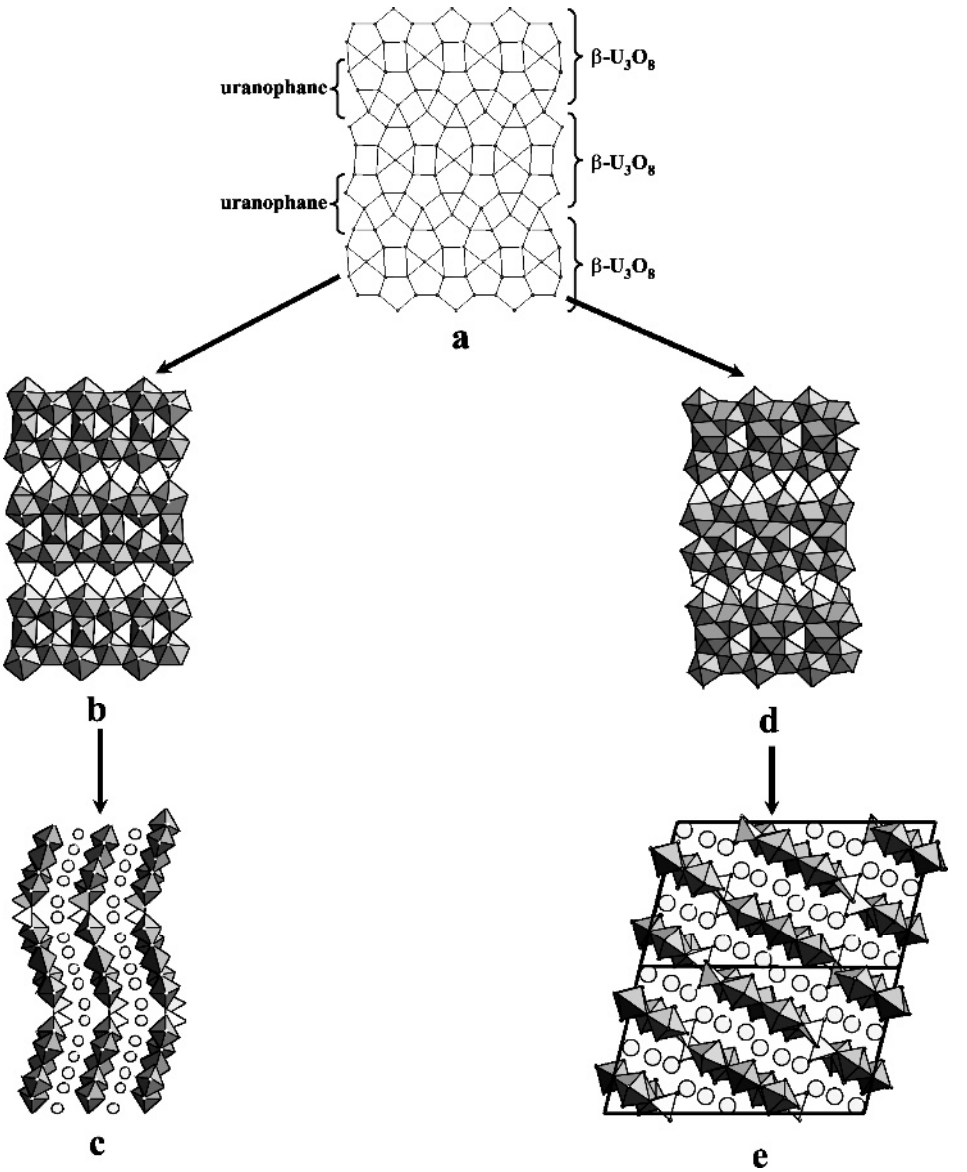

Figure 8: (a)-The sheet anion topology in the $M_6(UO_2)_5(VO_4)_2O_5$ compounds as an intergrowth between uranophane and β-U_3O_8 sheets. The orientations of the VO_4 tetrahedra populating triangular sites lead to two different isomers (b and d) and to corrugated (c) or planar (e) layers for M = Na, K, β-Rb and M = α-Rb, respectively.

Table 4. Crystallographic parameters of the $M_6[(UO_2)_5(VO_4)_2]O_5]$ (M = Na, K, Rb) compounds. The unit cell parameter corresponding to the $^1_\infty[^{[7]}U]_e$ chains (u ~ 7.09 Å) is in bold, the second parameter within the layer is in italic.

Compound	*A*, Å	*b*, Å	*c*, Å	β, °	S. G.	Ref
Na	12.584	*24.360*	**7.050**	100.61	$P2_1/c$	52
K	6.856	*24.797*	**7.135**	98.79	$P2_1/c$	52
α-Rb[a]	24.887	**7.099**	14.376	103.92	$C2/c$	53
β-Rb	**7.1635**	14.079	24.965	90.23	$P2_1/n$	53

[a] The unit cell parameter corresponding to the layer dimension perpendicular to the $^1_\infty[^{[7]}U]_e$ chains is 25.571 Å.

An important difference between the structures of $M_6U_5V_2O_{23}$ (M = Na, K, β-Rb) and α-$Rb_6U_5V_2O_{23}$ concerns the orientation of the VO_4 tetrahedra connecting successive ribbons. In the first series of the compounds, the V-O bonds to the non-shared O atoms connecting two adjacent ribbons are all oriented in the same direction (Fig. 8b), leading to an angle of about 40° between two adjacent ribbons. The rows of tetrahedra parallel to the $^1_\infty[^{[7]}U]_e$ chain direction, with "up" and "down" orientations, alternate with each other so that corrugated (modulated) layers are formed. The modulation is perpendicular to the $^1_\infty[^{[7]}U]_e$ chain direction (Fig. 8c). In contrast α-$Rb_6U_5V_2O_{23}$ contains tetrahedra with "up" and "down" orientations that alternate along the $^1_\infty[^{[7]}U]_e$ chains (Fig. 8d), which leads to almost planar layers (Fig. 8e). In this case, the $^1_\infty[UO_5]^{4-}$ chains are distorted leading to deformation of the hexagonal holes and transformation of the U polyhedron in the hole into a pentagonal bipyramid (Fig. 8d). Crystallographic information on the $M_6U_5V_2O_{23}$ (M = Na, K, Rb) compounds is given in Table 4.

3.3. 2-D arrangement of chains of $^{[6]}U$ polyhedra and V_2O_7 entities: $^2_\infty[^1[^{[6]}U]_c + ^0_2[^{[4]}V]]_c$.

The structure of $Cs_4U_2V_2O_{13}$ [54] consists of 2-dimensional $^2_\infty[(UO_2)_2(V_2O_7)O_2]^{4-}$ layers separated by Cs^+ cations (Fig. 9a). The layers are built from infinite $^1_\infty[UO_5]^{4-}$ chains of corner-sharing $(UO_2)O_4$ distorted octahedra that are further connected by symmetrical divanadate V_2O_7 units consisting of two corner-sharing VO_4 tetrahedra. Within the layer, the V_2O_7 entities are

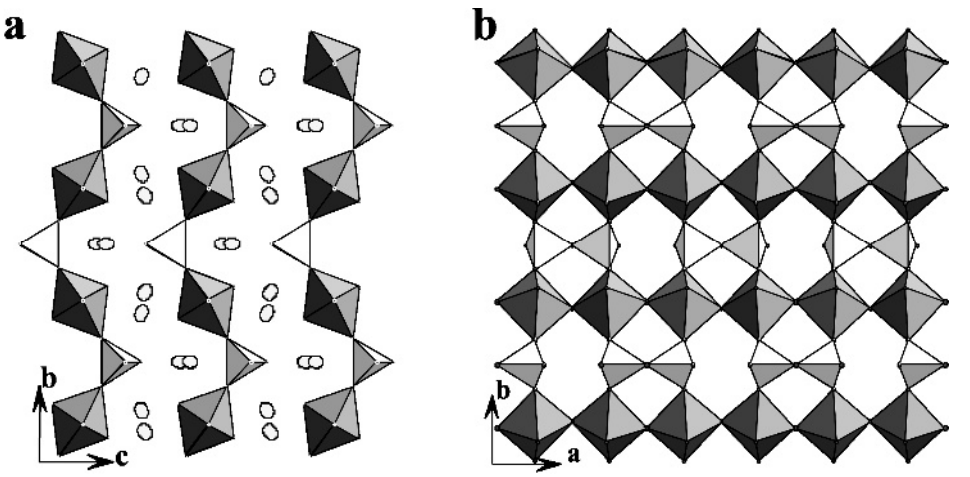

Figure 9: Diagrams showing the corrugated 2-dimensional crystal structure of $Cs_4[(UO_2)_2(V_2O_7)O_2]$ with Cs^+ cations located between the 2-dimensional $^{2}_{\infty}[(UO_2)_2(V_2O_7)O_2]^{4-}$ layers (a) and the structure of the uranyl vanadate layers consisting of the $^{1}_{\infty}[UO_5]^{4-}$ chains linked by the V_2O_7 dimers (b).

parallel to the $^{1}_{\infty}[UO_5]^{4-}$ chains. All V_2O_7 groups that connect one side of the $^{1}_{\infty}[UO_5]^{4-}$ uranyl chain are pointed down, whereas all the tetrahedra along the other side of the same uranyl chain are pointed up, leading to a structure with a stacking of corrugated layers (Fig. 9b).

Linkage of the $^{1}_{\infty}[UO_5]^{4-}$ uranyl chains by divanadate groups into layers is quite unusual. Such chains formed by corner sharing of the UO_6 tetragonal bipyramids are present in alkaline and alkaline earth uranates with the chemical formula $M^{n+}_{4/n}[(UO_2)O_3]$, where M^{+} = Li^+ [55], Na^+ [56], and M^{2+} = Sr^{2+}, Ca^{2+} [57]. In these compounds, the cohesion between the chains is provided by the alkaline or alkaline earth cations only. Such chains also occur in the structures of β- and γ- $UO_2(OH)_2$ [58, 59] and in several monouranates with the general formula $M^{n+}_{2/n}[(UO_2)O_2]$, where M = Li [60], Na [61], Sr [57], Ba [62], and Pb [63]. In these compounds, the chains are linked together to form $^{2}_{\infty}[UO_4]^{2-}$ layers. In the structure of $U_2V_2O_{11}$, the $^{1}_{\infty}[UO_5]^{4-}$ chains are linked by the V_2O_7 groups, but the chains are built from UO_7 pentagonal bipyramids sharing opposite edges (see refs. 44 and 45, and part II-1 of this chapter).

$Cs_4[(UO_2)_2(V_2O_7)O_2]$ is readily decomposed by loss of water at 60°C to form the very stable Cs-carnotite compound $Cs_2(UO_2)_2(V_2O_8)$.

3.4. 3-D arrangement of chains of UO_7 pentagonal bipyramids and chains of VO_4 tetrahedra $^{3}_{\infty}[\,^{1}_{\infty}[^{[7]}U]_c + \,^{1}_{\infty}[^{[4]}V]_c]_c$

The structure of UV_2O_8 [64, 44] consists of zigzag $^{1}_{\infty}[^{[7]}U]_c$ chains of corner-sharing UO_7 pentagonal bipyramids and metavanadate-type $(VO_3)_n$ chains of corner-sharing VO_4 tetrahedra, $^{1}_{\infty}[^{[4]}V]_c$ (Fig. 10a). The chains are linked through corners to form an open 3-D framework with rectangular cross-section tunnels (Fig. 10b). Astonishingly, the connection between the UO_7 pentagonal bipyramids is not through equatorial oxygens alone. In fact, one O atom plays a double role; it is part of a uranyl ion and is also an equatorial oxygen of another uranyl polyhedron. Two UO_7 polyhedra share this O atom creating a zigzag $(UO_2)_n$ chain, –U=O–U=O–U=O–. This compound can be considered a uranyl metavanadate with the formula $(UO_2)(VO_3)_2$. The $(UO_2)_n$ infinite chain is less common that the $(UO_5)_n$ chain of edge-sharing pentagonal bipyramids. However, it is also present in $UMoO_6$ [65], where chains are linked via discrete MoO_4 tetrahedra to form the $(UO_2)(MoO_4)$ molybdate framework.

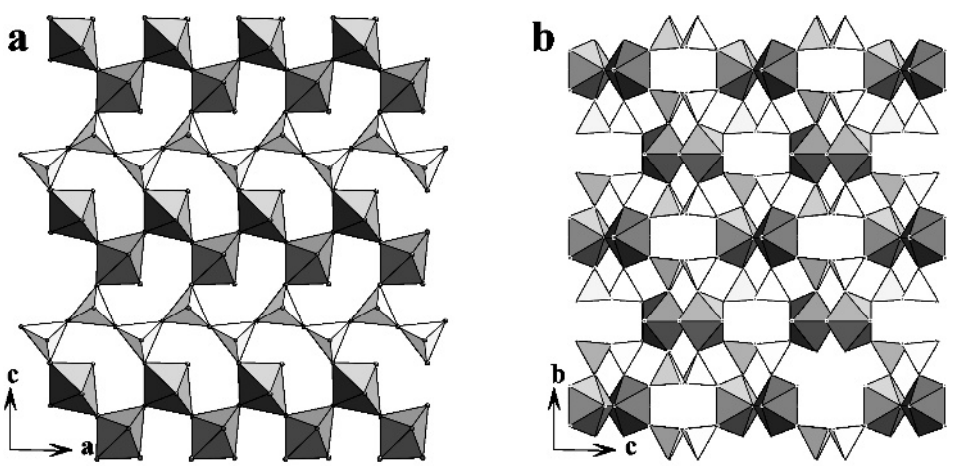

Figure 10: Crystal structure of UV_2O_8 consists of zigzag chains of UO_7 pentagonal bipyramids and $^{1}_{\infty}[VO_3]$ metavanadate-type chains (a), further linked through corners to form a 3-D framework (b).

4. 2-D and 3-D arrangements of mutually perpendicular $[^{[7]}U]_e$ chains

The $^{1}_{\infty}[UO_5]^{4-}$ chains of edge-sharing UO_7 pentagonal bipyramids are the most familiar arrangements found in uranyl compounds. As described above, in most structures, they are parallel to each other and can be connected in many ways to form planar or corrugated sheets. To our knowledge, the only example of a structure with such chains running in two perpendicular directions is that of soddyite, $(UO_2)_2SiO_4{\cdot}2H_2O$, where uranyl chains are connected through SiO_4 tetrahedra. Recently, monovalent cation uranyl vanadates provided some other interesting examples. In $Li_2(UO_2)_3(VO_4)_2O$, the chains are connected together by sharing the equatorial oxygen atoms creating a 3-D arrangement of UO_7 pentagonal bipyramids, $^{3}_{\infty}[\,^{1}_{\infty}[^{[7]}U]_e]_c$ (Fig. 11a). In the framework, the UO_6 octahedra are fixed by VO_4 tetrahedra. In fact, the UO_6 octahedra and VO_4 tetrahedra form $^{2}_{\infty}[(UO_2)(VO_4)_2]^{2-}$ or $^{2}_{\infty}[^{[4]}V{+}^{[6]}U]_c$ simple sheets (named S) with the autunite anion-topology parallel to the (001) plane of the tetragonal cell (Fig. 11b). In this topology, the population of the squares is similar to that found in $K_4[(UO_2)(PO_4)_2]$ [66], with one eighth of the squares occupied by the UO_6 octahedra and one quarter by the VO_4 tetrahedra. The unshared edges of the VO_4 tetrahedra are oriented up and down relative to the plane of the layer and are parallel to the ***a*** and ***b*** axes, respectively. This allows attachment to the edges of the $^{1}_{\infty}[UO_5]^{4-}$ chains (Fig. 11c). The structural principle of the 3-D arrangement can be written as $^{3}_{\infty}[\,^{3}_{\infty}[\,^{1}_{\infty}[^{[7]}U]_e]_c{+}\,^{2}_{\infty}[^{[4]}V{+}^{[6]}U]_c]_e$. Note that the equatorial oxygen atoms shared between two perpendicular $^{1}_{\infty}[UO_5]^{4-}$ chains on each side of the layer occupy the centers of squares that are not occupied by UO_6 octahedra.

In $M(UO_2)_4(VO_4)_3$, where M = Li, Na [67], unshared equatorial oxygen atoms of the $^{1}_{\infty}[UO_5]^{4-}$ chains are at the same time uranyl oxygens of UO_6 octahedra. This results in the formation of the $^{1}_{\infty}[U_2O_{10}]^{8-}$ chains with SBU consisting of UO_7 and an UO_6 polyhedra connected through one oxygen (Fig. 12). These chains run along the ***a*** and ***b*** directions and are connected through VO_4 tetrahedra. As in $Li_2(UO_2)_3(VO_4)_2O$, the UO_6 octahedra and VO_4 tetrahedra form autunite anion-topology sheets parallel to (001) (Fig. 13a), but with an inverted occupation of the squares by the UO_6 octahedra and the $V(2)O_4$ tetrahedra. The $V(1)O_4$ tetrahedra are attached above and below the empty squares to form the $^{2}_{\infty}[(UO_2)_2(VO_4)_3]^{5-}$ double sheets (named D) Fig. 13b.

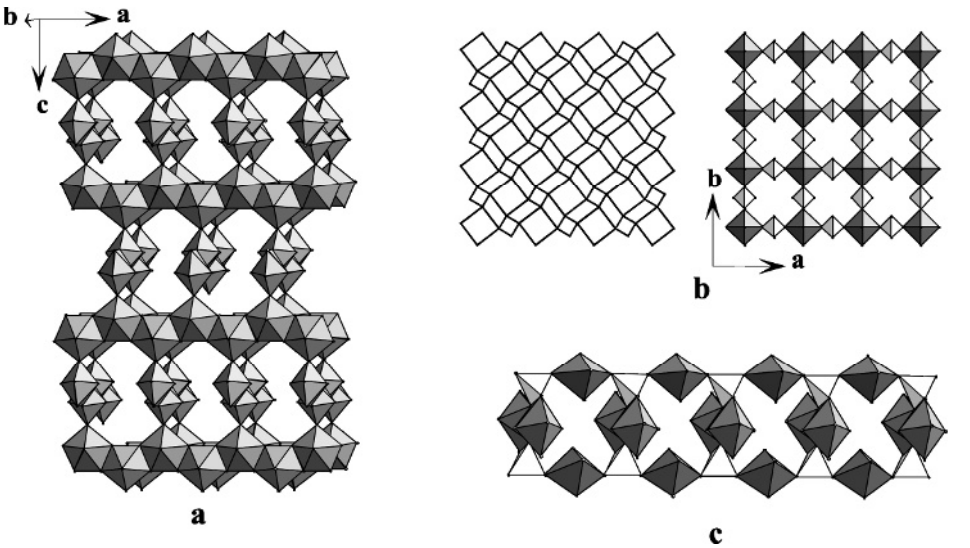

Figure 11: The 3-D framework of mutually perpendicular $^{1}_{\infty}[UO_5]^{4-}$ chains in $Li_2[(UO_2)_3(VO_4)O]$ (a), where the autunite-type sheets of corner-sharing UO_6 octahedra and VO_4 tetrahedra (b) are connected by perpendicular $^{1}_{\infty}[UO_5]^{4-}$ chains (c).

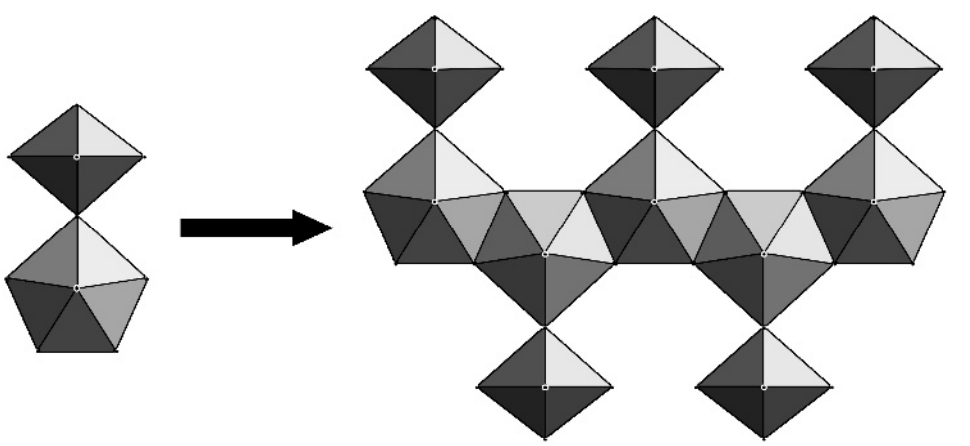

Figure 12: In $M(UO_2)_4(VO_4)_3$ (M = Li, Na), the $^{1}_{\infty}[U_2O_{10}]$ chains are formed by successive condensation of the SBU consisting of one $^{[7]}U$ and $^{[6]}U$ polyhedra connected through a common oxygen atom that is equatorial for $^{[7]}U$ and uranyl for $^{[6]}U$.

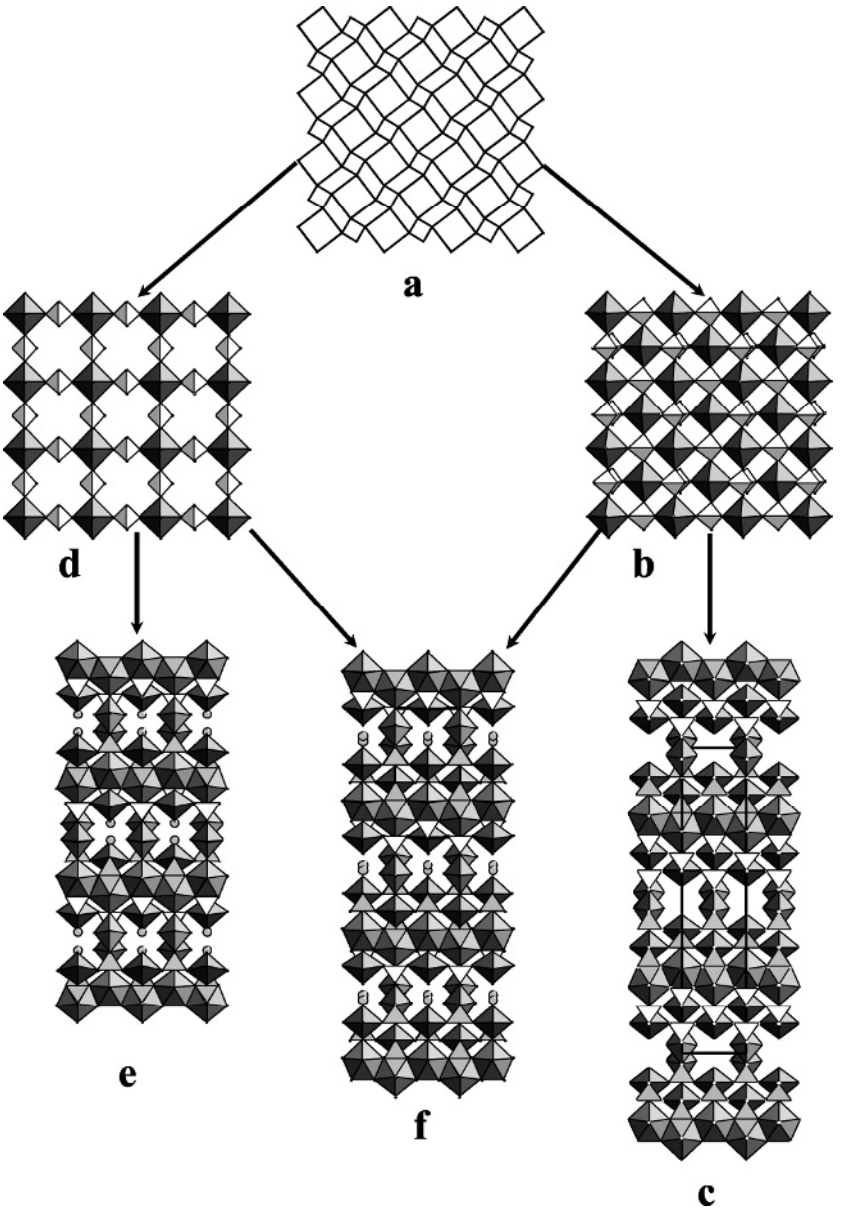

Figure 13: (a) The autinite sheet anion topology and the S (d) and D (b) layers obtained by different populations of the squares. The arrangement of the $^{1}_{\infty}[UO_5]^{4-}$ chains of edge-sharing UO_7 pentagonal bipyramids and S-type layers leads to the 3-D framework of $A_2(UO_2)_3(VO_4)_2O$ (e); with D layers the 3-D framework of $M(UO_2)_4(VO_4)_3$ is obtained (c). Successive alternation of the S and D layers has been realized in the structure of $M_3(UO_2)_7(VO_4)_5O$ (f).

Thus, above the sheet, all the non-shared O–O edges are parallel to [010], whereas all edges below the sheet are parallel to [100]. The O–O edges are shared between the $^{2}_{\infty}[(UO_2)_2(VO_4)_3]^{5-}$ sheets and the $^{1}_{\infty}[UO_5]$ chains to form a 3-D framework with nearly circular channels running alternately along [010] and [100] and limited only by uranyl oxygen ions (Fig. 13c). The channel sites contain face-sharing O_6 distorted octahedra with the Na^+ ions occupying half of each octahedral site. The structural formula of the compound can be written as $^{3}_{\infty}[\,^{1}_{\infty}[^{[7]}U]_e+\,^{2}_{\infty}[^{[4]}V+^{[6]}U]_e]_{e+c}$.

The organization of the two structures can be described as successive alternation of the $^{1}_{\infty}[(UO_2)_2]$ chains and either S layers $^{2}_{\infty}[(UO_2)(VO_4)_2O]^{2-}$ or D layers $^{2}_{\infty}[(UO_2)_2(VO_4)_3]^{5-}$, according to the scheme shown in Figs. 13c and 13e, respectively. One can imagine intergrowths between these two types structures. The simplest intergrowth presented in Fig. 13f consists of the S and D succession and gives the formula $M_3(UO_2)_7(VO_4)_5O$ which is the sum of the two formulas given above. Compounds with this structure have been successfully prepared for M = Li, Na, Ag. They are tetragonal and have very similar **a** unit-cell parameters. The **c** parameter of $Li_3(UO_2)_7(VO_4)_5O$ is equal to the quarter of the sum of the **c** parameters of the two other Li compounds. Fig. 13f shows the crystal structure of the Li compound determined from single crystal data. Crystallographic parameters of the compounds of these three families are given in Table 5.

Table 5. Crystallographic parameters of $(Li\text{-}Na)(UO_2)_4(VO_4)_3$, $Li_2(UO_2)_3(VO_4)_2O$ and $M_3(UO_2)_7(VO_4)_5O$ (M=Li, Na, Ag) compounds

Compound	*a,* Å	*c*, Å	S.G.	Ref
$Li_2(UO_2)_3(VO_4)_2O$	7.3265( )	24.6486( )	$I4_1/amd$	68
$Li(UO_2)_4(VO_4)_3$	7.2379(5)	33.677(2)	$I4_1/amd$	67
$Na(UO_2)_4(VO_4)_3$	7.2215(5)	34.067(2)	$I4_1/amd$	67
$Li_3(UO_2)_7(VO_4)_5O$	7.2794(1)	14.4961(5)	$P\,\bar{4}$	69
$Na_3(UO_2)_7(VO_4)_5O$	7.2396(3)	14.7555(3)	$P\,\bar{4}$	69
$Ag_3(UO_2)_7(VO_4)_5O$	7.2254	14.7773(3)	$P\,\bar{4}$	69

5. 2-D polymerization of VO_5 square pyramids or VO_6 octahedra

5.1. 3-D structure of UV_3O_{10}: $^{3}_{\infty}[\,^{2}_{\infty}[\,^{2}_{\infty}[^{[5]\,[5]}V]_c - {}^{[8]}U]]_c$

For the ratio U:V = 1:3, the reduced binary oxide UV_3O_{10} has been prepared by reaction between UO_3 or U_3O_8 and V_2O_5 at 650°C under vacuum or by reduction of UV_2O_8 under vacuum [70] or from mixtures of V_2O_3, V_2O_5 and α-U_3O_8 in stoichiometric proportions heated in sealed, evacuated silica tubes at 550°C [71]. The crystal structure of UV_3O_{10} has been refined using Rietveld analysis of combined powder neutron and powder X-ray data [71]. $U_2V_6O_{21}$ (or $UV_3O_{10.5}$) results from a slow oxidation of UV_3O_{10} under flowing oxygen at 550°C [70].

The 3-D structure of UV_3O_{10} can be described as based upon layers with an anion topology consisting of hexagons, squares and triangles (Fig. 14a). The squares are occupied by V, the hexagons by U and the triangles are empty (Fig. 14b). There are two independent V atoms, V(1) and V(2) with charges +4 and +5, respectively, which implies that the correct electronic formulation is $U^{6+}V^{4+}V^{5+}{}_2O_{10}$. The coordination of $V(1)^{4+}$ is completed by two oxygen atoms to form a slightly distorted $V(1)O_6$ octahedron. The coordination of $V(2)^{5+}$ is completed by a fifth oxygen atom at a shorter distance with a V=O bond resulting in a VO_5 square pyramid with the vanadyl bond approximately perpendicular to the layer. The $V(2)O_5$ square pyramids share opposite apices to form infinite $^{1}_{\infty}[V(2)O_4]^{3-}$ chains parallel to the **a** axis of the orthorhombic unit cell. Within the chain, the up and down orientations of the V = O bonds alternate. The adjacent chains are connected through the $V(1)O_6$ octahedra to form the $^{2}_{\infty}[(V(2)_2V(1)O_{10}]^{4-}$ vanadate layer parallel to (001). The shared oxygen atoms of the $V(1)O_6$ and $V(2)O_5$ polyhedra create equivalent triangles and hexagons whose centers are occupied by linear uranyl ions perpendicular to the (001) plane. The two apical oxygen atoms of one $V(1)O_6$ octahedron are shared with the apical corners of $V(2)O_5$ pyramids from two adjacent layers to built a 3D-arrangement $^{3}_{\infty}[UV_3O_{10}]$ (Fig. 14c). Note that the uranyl oxygen atom is opposite to the V=O bond at a large distance of 2.615(9) Å complementing the V(2) polyhedron to provide a very distorted $V(1)O_6$ octahedron and metal–oxygen chains in the **c** direction of the type:

$$\mathbf{U^{6+}}\overset{1.783(3)}{=\!=}\mathbf{O}\cdots\overset{2.625(9)}{\cdots}\mathbf{V(2)^{5+}}\overset{1.702(9)}{=\!=}\mathbf{O}\overset{2.1012(3)}{-\!-}\mathbf{V(1)^{4+}}\overset{2.012(3)}{-\!-}\mathbf{O}\overset{1.70293)}{=\!=}\mathbf{V(2)^{5+}}\overset{2.615(9)}{\cdots}\mathbf{O}\overset{1.783(3)}{=\!=}\mathbf{U^{6+}}$$

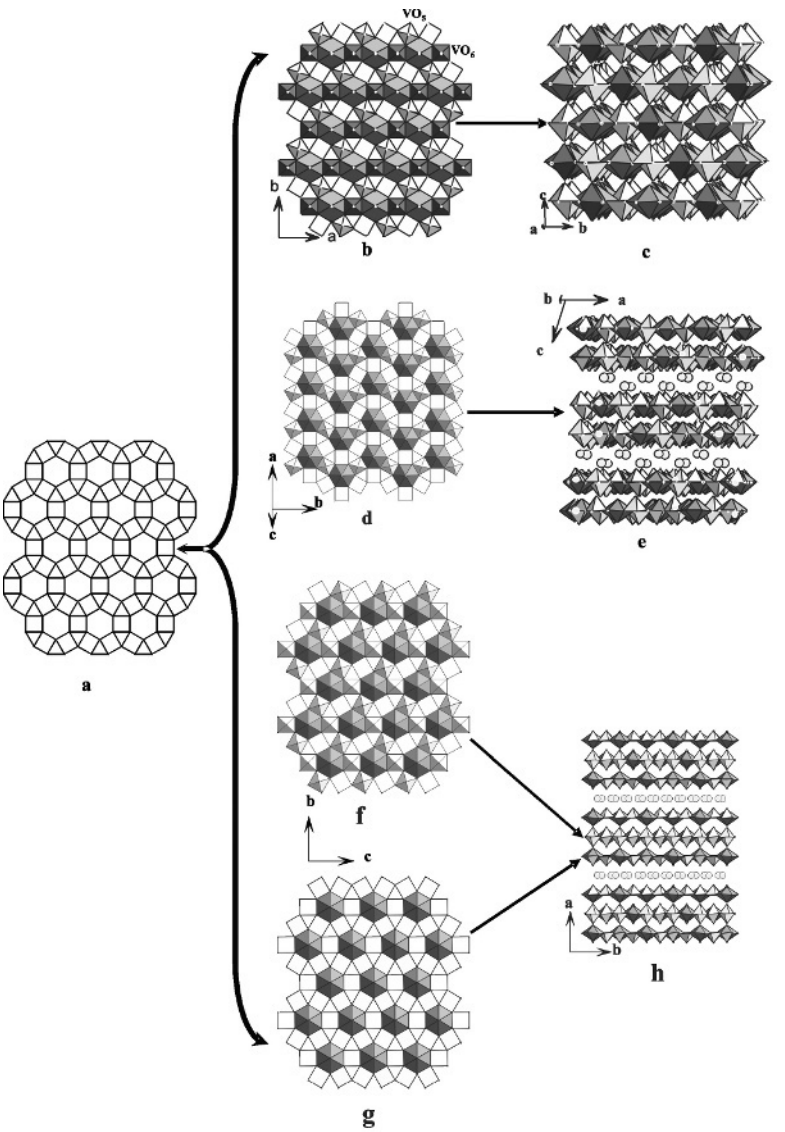

Figure 14: The sheet anion topology containing hexagons, squares and triangles (a). The squares are populated by V atoms to give various 2D arrangements, whereas the hexagonal holes are occupied by the UO_2^{2+} ions. In UV_3O_{10}, the V coordination is completed to form octahedra and square pyramids (b). Each octahedron of one layer is connected to two square pyramids of two adjacent layers to form a 3-D arrangement (c). In MUV_3O_{11} (M = K, Cs), the V atoms are in square pyramidal coordination only. Three isomers are obtained depending upon the positions of the V=O bonds perpendicular to the layer: *4down-2up* (d), *2down-4up* (f) and *6down* (g). These layers are stacked together to form double (e) or triple (h) layer blocks in $CsUV_3O_{11}$ and KUV_3O_{11}, respectively.

It is interesting to compare the structure of UV_3O_{10} [71] with that of UNb_3O_{10} [72, 73]. In the Nb compound, the $Nb(2)O_6$ octahedron is less distorted and the metal–oxygen chain has the following type:

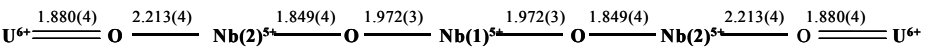

Magnetic susceptibility, XPS and ESR confirm the +5 oxidation state of U with f^1 configuration [74], and therefore the electronic formulation $U^{5+}Nb^{5+}{}_3O_{10}$.

5.2. 2-D structure of MUV_3O_{11} (M = K, Cs): $^2_\infty[\,^2_\infty[^{[5]}V]_c - ^{[8]}U]$.

Compounds with the U:V ratio of 1:3 belong to the large group of compounds with the general formula $MUO_2(XO_3)_3$ where X = P or V, and M is a monovalent cation: H_3O^+, Na^+, Cs^+, NH_4^+ [75-78]. For X = P, uranyl-polyphosphate acid $HUO_2(PO_3)_3$ [75] and Na [76] and Cs [77] salts have been isolated and their structures determined. In the structure of H or Na compounds, uranyl polyhedra are linked into a 3-D framework by polyphosphate chains. In contrast, the structure of $CsUO_2(PO_3)_3$ consists of cyclohexaphosphate rings, $[P_6O_{18}]^{6-}$, and UO_2^{2+} and Cs^+ ions. The uranyl phosphate layers are linked into a 3-D framework through –P–O–P– bridges.

For X = V, a natural compound, $U_2V_6O_{21}{\cdot}15H_2O$, exists that is recognized as uvanite, a unique mineral species. There are also many salts that have the general formula $M^{n+}{}_{1/n}UO_2(VO_3)_3.xH_2O$ with M = H_3O^+, Na^+, NH_4^+, Mg^{2+} [78]. These compounds are expected to have a layered structure on the basis of their ion exchange properties. The cations, which are probably between the $[UO_2V_3O_9]^-$ layers, can be exchanged for inorganic and organic cations. Additionally, water molecules can be replaced by other solvent molecules [78]. The crystal structures of the anhydrous compounds $M(UO_2)(VO_3)_3$ have been determined for M = K [79] and Cs [80].

KUV_3O_{11} [79] and $CsUV_3O_{11}$ [80] are layered compounds based on the same type of sheets as UV_3O_{10} (see above), but these structures contain only V^{5+} ions. The V(1) polyhedron is a square pyramid with displacement of the V(1) atom out of the plane to form a short V(1) = O vanadyl bond and an opposite longer V···O bond. In $CsUV_3O_{11}$, the $(UO_2)^{2+}$ ion is surrounded by four and two VO_5 square pyramids pointing down and up, respectively, which results in the *4down-2up* $^2_\infty[UV_3O_{10}]^-$ geometrical isomer (Fig. 14d). There are no strong chemical bonds between adjacent layers at $z = \pm 0.18$. The closest contacts are along the [104] direction and are of two types, U=O(1)···V(1)=O(3) and V(3)=O(5)···V(2)=O(4), with the "long" bonds of 2.98 and 2.66 Å, respectively. The corresponding contributions of the V···O bonds to the V bond valence sums

are only 0.08 and 0.13 valence units (v.u.), respectively. As a result, double layers are formed with Cs^+ ions in the interlayer space. As a matter of fact, $CsUV_3O_{11}$ is composed from electroneutral weakly bonded double layers $\{(UV_3O_{11})^-\text{-}(Cs)_2^{2+}\text{-}(UV_3O_{11})^-\}$ stacked along [104] (Fig. 14e). In KUV_3O_{11}, there are two types of the $^2_\infty[UV_3O_{10}]^-$ layers, *4down-2up* (Fig. 14f) and *6down* (or *6up*) (Fig. 14g). Linkage of two *6down* and one *4down-2up* layers leads to formation of triple layers (*6down* / *4down-2up* / *6up*) (Fig. 14h) with K^+ ions in the interlayer.

With the exception of the uranyl and vanadyl oxygen atoms all other oxygen atoms are shared between the VO_5 pyramids and UO_8 bipyramids so that the formula of this compound can be written as $AUO_2(VO_3)_3$. This is in general agreement with the use of the "metavanadate" name often given for this series. However, this does not really correspond to its crystal structure, which is better described as an extended covalent solid.

The extended planar array of the VO_4 squares in the *ab* plane is very similar to that of the WO_4 squares (equatorial bases of the WO_6 octahedra) in hexagonal tungsten trioxide, which has been obtained by dehydration of $WO_3{\cdot}13H_2O$ [81] or in hexagonal tungsten bronzes. The geometrical relationship between the structure of the (001) layer in UNb_3O_{10} and the corresponding layer in the hexagonal tungsten bronze was discussed in detail by Deschanvres et al. [82]. The hexagonal site of the MO_4 layer (M = Nb, V, and W) is occupied by U^{VI} in UV_3O_{10} and AUV_3O_{11} (A = K, Cs) and by U^V in UNb_3O_{10}. These sites are empty in simple hexagonal tungsten bronzes. However, they are occupied by the Bi atoms in $(BiO)TaW_2O_9$ [82].

The *ab* base of the monoclinic primitive cell of $CsUV_3O_{11}$ (Table 6) corresponds to the C-centered orthorhombic supercell of the hexagonal primitive cell as shown in Fig. 15. The unit-cell parameters are related as follows: $a_{mono} = \sqrt{3}\, a_{hex}$, $b_{mono} = b_{hex}$. The a_{mono}/b_{mono} ratio is 1.743. However, the *4down-2up* layer itself does not have hexagonal symmetry because of the different system of orientations of non-shared vertices of coordination polyhedra. It is noticeable that natural uvanite and the NH_4^+, H_3O^+, and Mg^{2+} compounds adopt a hexagonal unit cell with *a* parameters close to 6.84 Å [80]. It is noteworthy that Hilke et al. [80] determined the U and V positions for the (001) plane in $NaUV_3O_{10}$ by powder X-ray diffraction. However, hexagonal symmetry requires the presence of the *6up* or *6down* layers. The occurrence of weak bonding between the components of the double layer could account for the variable stacking in the *c* direction reported for other uvanites by Hilke et al. [80]. Further studies are needed to confirm these hypotheses.

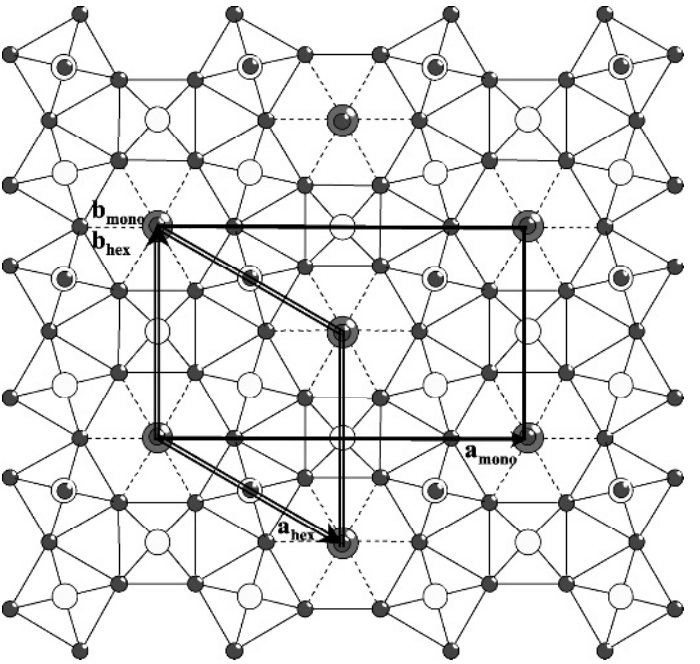

Figure 15: Relationships between the orthorhombic and hexagonal pseudo cells of the $M UV_3O_{11}$ (M = K, Cs) structures.

Table 6. Uranyl vanadates based on 2-D network of the VO_5 square pyramids and isolated UO_8 bipyramids.

Compound	*a*, Å	*b*, Å	*c*, Å	β, °	S. G.	Ref
UV_3O_{11}	12.0554	6.9426	16.2228		*Fddd*	71
$CsUV_3O_{11}$	11.904(2)	6.8321	12.095	106.989	$P2_1/a$	80
KUV_3O_{11}	11.905	6.869	34.051		*F*222	79

5.3. 3-D network of $V^{4+}O_6$ octahedra and isolated UO_6 octahedra: $^{3}_{\infty}[^{2}_{\infty}[^{[6]}V]_e{}_{-}{}^{[8]}U]_e$

The reduced compound UV_2O_6 contains U^{4+} and V^{4+} ions [46, 83]. The structure can be described as a simple *ABAB* hexagonal close packing of the O^{2-} anions, with V atoms in three octahedral sites between two adjacent layers of oxygen (Fig. 16a). The U atom occupies octahedral sites between the dioctahedral layers with the U position above the vacant site in the V-O dioctahedral layer (Fig. 16b). As a result, a 3-D octahedral framework is formed (Fig. 16c).

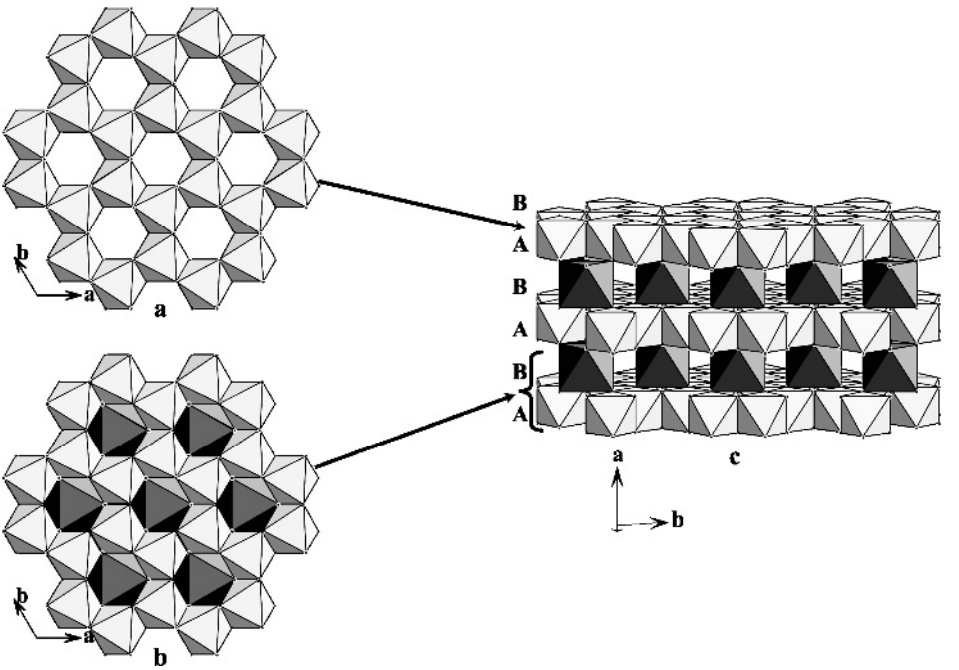

Figure 16: The crystal structure of UV_2O_6 built from 2-D dioctahedral layers of the VO_6 octahedra (a) linked by UO_6 octahedra located above the vacant sites in the dioctahedral layer (b) so that a 3-D framework is formed (c).

6. Copolymerization of the U and V polyhedra

6.1. 3-D network of UO_7 and V_2O_7 entities

The structure of $Pb(UO_2)(V_2O_7)$ consists of a 3-D framework composed of edge- and corner-sharing UO_7 pentagonal bipyramids and V_2O_7 divanadate units. The framework possesses elliptical channels that are occupied by Pb^{2+} ions (Fig. 17a). The structural formula can be written as $^{3}_{\infty}[^{[7]}U+^{0}_{2}[^{[4]}V]_c]_{e+c}$.
Although the overall structure has a 3-D connectivity, as that of $(UO_2)_2(V_2O_7)$, it may be useful to consider it as based upon the $^{2}_{\infty}[UV_2O_9]^-$ layers of UO_7 bipyramids and VO_4 tetrahedra. The layers are parallel to (001) (Fig. 17b) and are further linked by divanadate groups along the *c* axis.
If only the Pb–O distances shorter than 3 Å are considered, the Pb environment can be described as a distorted pentagonal bipyramid similar to the coordination of the U atoms. Thus, it is possible to consider the structure as containing

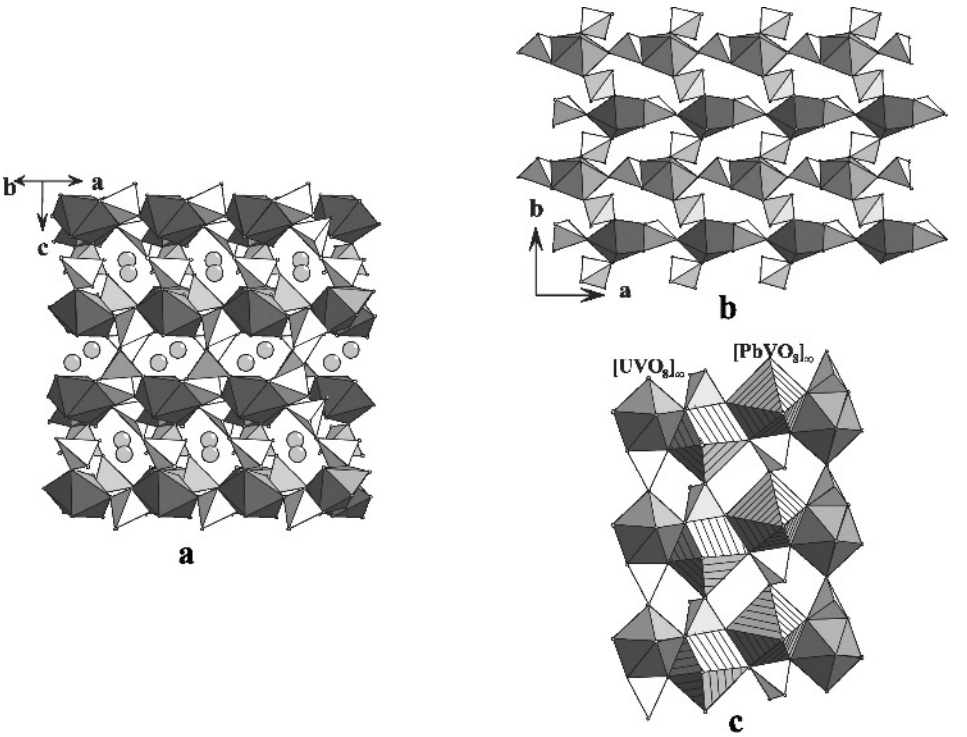

Figure 17: The 3-D framework of the structure of $PbUO_2(V_2O_7)$ projected along the [110] direction (a), which may also be described as a combination of $^{2}_{\infty}[UV_2O_9]^-$ infinite layers (b) and the infinite four polyhedra wide $^{1}_{\infty}[Pb_2(UO_2)_2(VO_4)_4O_6]$ ribbons with the uranophane anion topology (c).

infinite four-polyhedra wide $^{1}_{\infty}[Pb_2(UO_2)_2(VO_4)_4O_6]$ ribbons (Fig. 17c) that have the uranophane anion topology described in part 3 of this chapter. In $Pb(UO_2)V_2O_7$, half of the U atoms are replaced by Pb and occupy the pentagons in the sequence U-Pb-Pb-U (Fig. 17c). The infinite ribbons are connected together to form a 3-D framework.

6.2. Mixed chains of the UO_6 octahedra and VO_4 tetrahedra in $Cu_2(UO_2)(VO_4)_2$

In the first part of this chapter, we described two hydrated copper uranyl vanadates, $Cu[(UO_2)_2V_2O_8]\cdot 4H_2O$ and $Cu_2[(UO_2)_2V_2O_8](OH)_2\cdot 6H_2O$, that have structures based upon carnotite-type sheets interleaved with the $[Cu(H_2O)_4]^{2+}$ and $[Cu_2(OH)_2(H_2O)_4]^{2+}$ cations, respectively. Using solid-state synthesis methods, an anhydrous copper uranyl vanadate, $Cu_2(UO_2)(VO_4)_2$, has

been obtained. The compound is isotypic to the corresponding phosphate [85]. In the V compound,

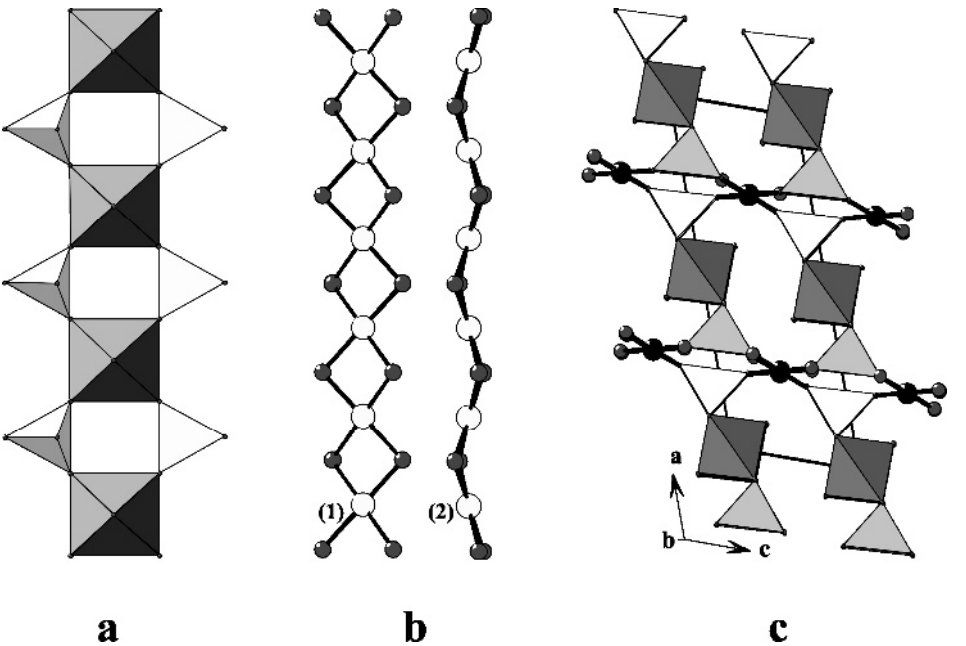

Figure 18: The 3-D framework in the structure of $Cu_2(UO_2)(VO_4)_2$ (c) consists of 1-D ribbons of the UO_6 flattened octahedra and VO_4 tetrahedra (a) linked by puckered $^1_\infty[CuO_2]$ chains of edges-sharing CuO_4 planar squares (b).

flattened UO_6 octahedra share their four equatorial corners with four VO_4 tetrahedra to form 1-D $^1_\infty[(UO_2)(VO_4)_2]$ ribbons running along the *b* axis (Fig. 18a). The structural formula can be written as $^1_\infty[^{[6]}U+^{[4]}V]_c$. Copper is coordinated by four O atoms to form CuO_4 planar groups. Puckered $^1_\infty[CuO_2]$ chains of edge-sharing CuO_4 groups (Fig. 18b) are linked to the uranyl vanadate chains so that a 3-D framework is formed (Fig. 18c).

7. Mobility of the alkaline ions in the 2-D networks and 3-D frameworks.

Figure 19 shows Arrhenius plots of conductivity vs. $10^3/T$ for several uranyl vanadates. As clearly shown, the carnotite type compounds with 2-D networks exhibit relatively low conductivity with a high activation energy. In contrast, the 3-D $M(UO_2)_4(VO_4)_3$ compounds with partial occupancies of the alkali metal *M* sites in perpendicular channels, exhibit high conductivity with a low activation

energy (0.17 and 0.27 eV for the Na and Li compounds, respectively). The case of $CsUV_3O_{11}$ is particularly interesting, since the conductivity for a large Cs^+ cation is very high and has a low activation energy. Further studies on this class of materials with 2-D structure and small ions such as Na^+ or Ag^+ would be of interest from the viewpoint of their potential applications in various electrochemical systems.

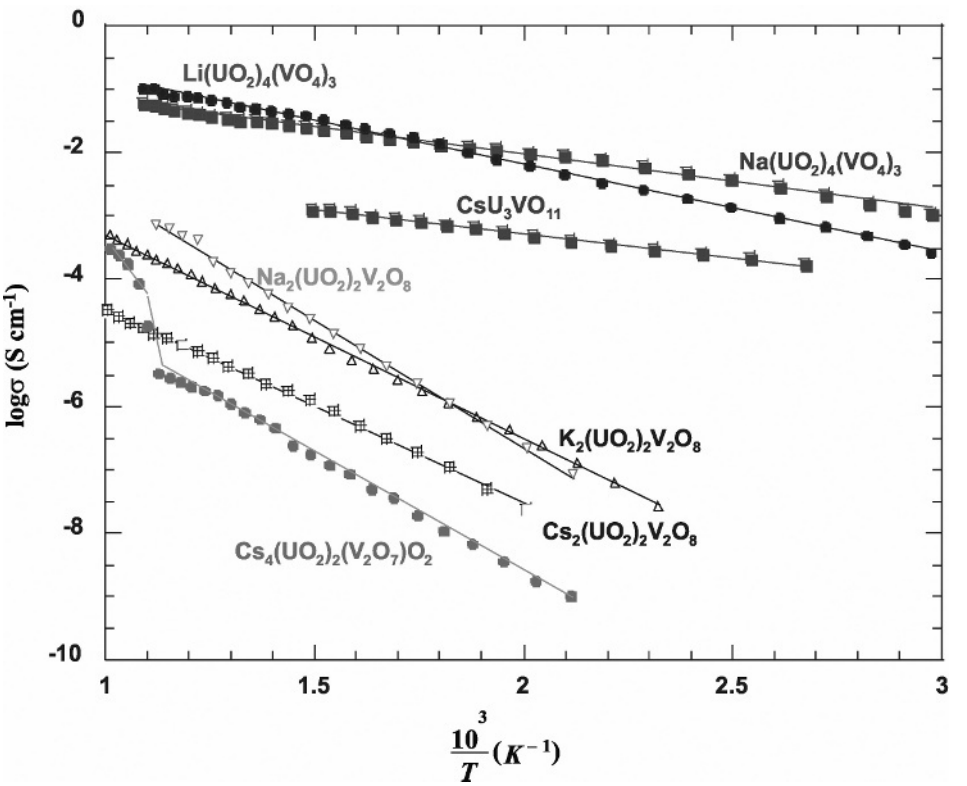

Figure 19: log σ vs. 10^3/T Arrhenius plots of some uranyl vanadates with 2-D and 3-D structural arrangements showing the high conductivity observed for the 2-D compound $CsUV_3O_{11}$ and the 3-D $M(UO_2)_4(VO_4)_3$ compounds.

8. Conclusions

The main structural characteristics of uranyl vanadates reported so far are listed in Table 7. With the exception of $Cu_2[(UO_2)_2V_2O_8](OH)_2{\cdot}6H_2O$, where the role of the $^1_\infty[(CuO_2]$ chains can not be excluded from consideration, all the arrangements of uranium and vanadium polyhedra are either 2-D layers or 3-D frameworks. It appears that, for U:V ≥ 1, structural organization is governed by

the condensation of the U polyhedra and, as a result, by the formation of 1-D, 2-D or 3-D structural units. With the exception of UVO_5, the V polyhedra are isolated VO_4 tetrahedra, V_2O_7 divanadate units or V_2O_8 dimers. These isolated

Table 7. Structural characteristics of the uranyl vanadate families.

U:V	Compound	Arrangement of U // V polyhedra	Notation
4	$M_7[(UO_2)_8(VO_4)_2]O_8Cl]$	2D of ^{7}U // Isolated ^{4}V	$^{2}_{\infty}[\,^{2}_{\infty}[\,^{1}_{\infty}[^{[7]}U]_e]_c - {}^{[6]}U - {}^{[4]}V]$
5:2	$M_6[(UO_2)_5(VO_4)_2]O_5]$	1D of ^{7}U and ^{6}U // Dimeric unit of ^{4}V	$^{2}_{\infty}[\,^{2}_{\infty}[\,^{1}_{\infty}[^{[7]}U]_e + {}^{[4]}V]_{e+c} + {}^{[7]}U]_c$
3:2	$(UO_2)_3(VO_4)_2{\cdot}5H_2O$	1D of ^{7}U and isolated ^{6}U // Isolated ^{4}V	$^{3}_{\infty}[\,^{2}_{\infty}[\,^{1}_{\infty}[^{[7]}U]_e + {}^{[4]}V]_{e+c} + {}^{[7]}U]_c$
	$Li_2(UO_2)_3(VO_4)_2O$	3D arrangement of perpendicular 1D chains of ^{7}U // Isolated ^{4}V	$^{3}_{\infty}[^{3}[\,^{1}_{\infty}[^{[7]}U]_e]_c + {}^{2}_{\infty}[^{[4]}V + {}^{[6]}U]_c]_e$
7:5	$M_3(UO_2)_7(VO_4)_5O$	2D arrangement of perpendicular 1D chains of ^{7}U // Isolated ^{4}V	$^{3}_{\infty}[\,^{1}_{\infty}[^{[7]}U]_e + {}^{2}_{\infty}[^{[4]}V + {}^{[6]}U]_c]_{e+c}$
4:3	$M(UO_2)_4(VO_4)_3$	2D arrangement of perpendicular 1D chains of ^{7}U // Isolated ^{4}V	$^{3}_{\infty}[\,^{1}_{\infty}[^{[7]}U]_e + {}^{2}_{\infty}[^{[4]}V + {}^{[6]}U]_e]_{e+c}.$
5:4	$(diamine)(UO_2)_3(VO_4)_2$	1D of ^{7}U and isolated ^{6}U // Isolated ^{4}V	$^{2}_{\infty}[^{1}[^{[7]}U]_e + {}^{[4]}V]_{e+c}$
1:1	$M^{n+}{}_{2/n}(UO_2)_2V_2O_8.$ xH_2O carnotite-type	2D of ^{7}U // Dimers of ^{5}V	$^{2}_{\infty}[\,^{2}_{\infty}[\,^{0}_{2}[^{[7]}U]_e]_c - {}^{0}_{2}[^{[5]}V]_e]$
	$U_2V_2O_{11}$	1D of ^{7}U // Dimers of ^{4}V	$^{3}_{\infty}[\,^{1}_{\infty}[^{[7]}U]_e]_c + {}^{0}_{2}[^{[4]}V]_c]$
	UVO_5	2D of ^{7}U // 1D of ^{5}V	$^{3}_{\infty}[\,^{2}_{\infty}[\,^{1}_{\infty}[^{[7]}U]_e + {}^{1}_{\infty}[^{[5]}V]_e]_c$
	$Cs_4U_2V_2O_{13}$	1D of ^{6}U // Dimers of ^{4}V	$^{2}_{\infty}[\,^{1}_{\infty}[^{[6]}U]_c + {}^{0}_{2}[^{[4]}V]]_c.$
1:2	UV_2O_8	1D of ^{7}U // 1D of ^{4}V	$^{3}_{\infty}[\,^{1}_{\infty}[^{[7]}U]_c + {}^{1}_{\infty}[^{[4]}V]_c]_c.$
	$Pb(UO_2)(V_2O_7)$	isolated ^{7}U // Dimers of ^{4}V	$^{3}_{\infty}[^{[7]}U + {}^{0}_{2}[^{[4]}V]_c]_{e+c}.$
	UV_2O_6	isolated ^{6}U // 2D of ^{6}V	$^{3}_{\infty}[^{0}[^{[7]}U] + {}^{2}_{\infty}[^{[6]}V]_e]_c$
1:3	UV_3O_{10}	isolated ^{8}U // 3D of ^{6}V and ^{5}V	$^{3}_{\infty}[\,^{2}_{\infty}[\,^{2}_{\infty}[^{[5]}V]_c - {}^{[8]}U]]_c$
	MUV_3O_{10}	isolated ^{8}U // 2D ^{5}V	$^{2}_{\infty}[\,^{2}_{\infty}[^{[5]}V]_c - {}^{[8]}U]$

units occupy holes within the arrangements of the U polyhedra or link uranium oxide substructures into arrangements of higher dimensionality. For the lowest value of U:V of 1:3, polymerization of V polyhedra is dominant and the U bipyramids are in the voids within the V substructures. For U:V = 1:2, three types of polymerization compete with each other and, as a result, three possible types are observed: 1) polymerization of the V polyhedra, 2) polymerization of both V and U polyhedra, 3) co-polymerization of the U and V polyhedra.

Thus, the U:V ratio plays a key role in the type of polymerization and on the obtained 2-D or 3-D structural architectures. However, the role of the counter ion is not obvious. It can be suggested that, as already observed for other uranyl oxoanion compounds, the counter ions have no template effects but rather act as space fillers within the uranium vanadate substructure.

There are no doubts that, using variations of the U:V ratio and chemical nature of the counter ions, many new compounds can be obtained with structures based upon six different building blocks described in the Introduction to this chapter. Other oxoanions with various geometries (tungstate and molybdate, for example) have already been used to build other frameworks. To compare these compounds with vanadates, we have initiated studies of uranyl niobates that should reveal new interesting topologies.

References

1. P.C. Burns, M.L. Miller and R.C. Ewing, Can. Mineral. 34 (1996) 845.
2. J. Lima-de-Faria, E. Hellner, F. Liebau, E. Makovicky and E. Parthé, Acta Crystallogr. A46 (1990)1.
3. M.A. Carnot, C.R. Acad. Sci. Paris 104 (1887) 1850.
4. W.F. Hillebrand, Amer. J. Sci. 5th ser. 8 (1924) 201.
5. I. Sundberg and L. G. Sillen, Arkiv foer Kemi 1 (1949) 337.
6. J.F. Vaes and P.F. Kerr, Amer. Mineral. 34 (1949) 109.
7. C. Frondel, D. Riska and J. W. Frondel, U.S. Geol. Surv. Bull. 1036-G (1956) 91.
8. P.B. Barton, Amer. Mineral. 43 (1958) 799.
9. G. Branche, P. Bariand, F. Chantret, R. Pouget and A. Rimsky, C. R. Acad. Sci. 256(25) (1963) 5374.
10. D.E. Appleman and H.T. Evans, Amer. Mineral. 50 (1965) 825.
11. F. Cesbron and N. Morin, Bull. Soc. Fr. Minéral. Cristallogr. 91 (1968) 453.
12. F. Cesbron, Bull. Soc. Fr. Minéral. Cristallogr. 93 (1970) 242.
13. J. Borene and F. Cesbron, Bull. Soc. Fr. Minéral. Cristallogr. 93 (1970) 426.
14. F. Cesbron, Bull. Soc. Fr. Minéral. Cristallogr. 93 (1970) 320.
15. J. Borene and F. Cesbron, Bull. Soc. Fr. Minéral. Cristallogr. 94 (1971) 8.
16. I.G. Smyslova, Zap. Vses. Mineral. Obsh. (URSS) 101 (1972) 87.
17. P. Piret, J.P. Declercq and D. Wauters-Stoop, Bull. Minéral. 103 (1980) 176.
18. V.I.L. Botto and E.J. Barran, Z. Anorg. Allg. Chem. 426 (1976) 321.
19. K.J. Wenrich, P.J. Modreski, R.A. Zielinski and J.L. Seeley, Amer. Mineral. 67 (1982) 1273.
20. K. Mereiter, N. Jb. Mineral. Mh. 12 (1986) 552.

21. P.G. Dickens, G.P. Stuttard, R.G.J. Ball, A.V. Powell, S. Hull and S. Patat, J. Mater. Chem. 2 (1992) 161.
22. M. Saadi, Thèse d'Université, Lille 23 novembre, 1994.
23. F. Abraham, C. Dion, N. Tancret and M. Saadi, Adv. Mater. Res. 1994 (1994) 511.
24. G.A. Sidorenko, I.S. Naumova, A.A. Valueva and K.V. Skvortsova, Mineral. Zh. 17 (1995) 67.
25. M. Saadi, Thèse d'Etat, El Jadida, 17 février, 2001.
26. E.V. Alekseev, E.V. Suleimanov, E.V . Chuprunov and G.K. Fukin, Zh. Strukt. Khim. 45 (2004) 544.
27. F. Abraham, C. Dion, and M. Saâdi, J. Mater. Chem. 3 (1993) 459.
28. R.D. Shannon, Acta Crystallogr. A32 (1976) 751.
29. A. Tabuteau, H. X. Yang, J. Jove, T. Thevenin and M. Pages, Mater. Res. Bull. 20 (1985) 595.
30. K. Mereiter, N. Jb. Mineral. Mh. 1986 (1986) 552.
31. M. Rivenet, P. Roussel and F. Abraham, J. Solid State Chem., to be submitted.
32. Y.F. Yao and J.T. Kummer, J. Inorg. Nuclear. Chem. 29 (1967) 2453.
33. J. Benavente, J. R. Ramos-Barrado, M. Martinez and S. Bruque, J. Appl. Electrochem. 25 (1995) 68.
34. F. Weigel and G. Hoffmann, J. Less-Common Met. 44 (1976) 99.
35. I. Duribreux, M. Saadi, S. Obbade, C. Dion and F. Abraham, J. Solid State Chem. 172 (2003) 351.
36. B.O. Loopstra, Acta Crystallogr. B26 (1970) 656.
37. W.D. Birch, W.G. Mumme and E.R. Segnit, Austr. Mineral. 3 (1988) 125.
38. M. Saadi, C. Dion and F. Abraham, J. Solid State Chem. 150 (2000) 72.
39. M. Rivenet, P. Roussel and F. Abraham, J. Solid State Chem., to be submitted.
40. A.J. Locock and P.C. Burns, J. Solid State Chem. 176 (2003) 18.
41. A.J. Locock and P.C. Burns, J. Solid State Chem. 163 (2002) 275.
42. A.J. Locock and P.C. Burns, J. Solid State Chem. 167 (2002) 226.
43. A.J. Locock and P.C. Burns, J. Solid State Chem. 175 (2003) 372.
44. A.M. Chippindale, P.J. Dickens, G.J. Flynn and G.P. Stuttard, J. Mater. Chem. 5 (1995) 141.
45. N. Tancret, S. Obbade and F. Abraham, Eur. J. Solid. State Inorg. Chem. 32 (1995) 195.
46. L.M. Kovba, Radiokhimiya 13 (1971) 909.
47. R. Chevalier and M. Gasperin, Bull. Soc. Fr. Minéral. Cristallogr. 93 (1970) 18.
48. M. Schleifer, J. Busch and R. Gmelin, Z. Anorg. Allg. Chem. 625 (1999) 1985.
49. P.G. Dickens and G.P. Stuttard, J. Mater. Chem. 2 (1992) 691.
50. M. Gasperin, J. Solid State Chem. 67 (1987) 219.
51. M. Gasperin, Acta Crystallogr. B43 (1987) 404.
52. C. Dion, S. Obbade, E. Rackelboom, M. Saadi and F. Abraham, J. Solid. State Chem. 155 (2000) 342.
53. S. Obbade, C. Dion, L. Duvieubourg, M. Saadi and F. Abraham, J. Solid State Chem. 173 (2003) 1.
54. S. Obbade, C. Dion, M. Saadi and F. Abraham, J. Solid State Chem. 177 (2004) 1567.
55. K.V. Reshetov and L.M. Kovba, Zh. Strukt. Khim. 7 (1966) 625.
56. R. Wolf and R. Hoppe, Rev. Chim. Minéral. 23 (1986) 828.
57. B.O. Loopstra and H.M. Rietveld, Acta Crystallogr. B25 (1969) 787.
58. J.C. Taylor and M.J. Bannister, Acta Crystallogr. B28 (1972) 2995.
59. S. Siegel and H.R. Hoekstra, Acta Crystallogr. B28 (1972) 3469.
60. E. Gebert, H.R. Hoekstra, A.H. Reis and S.W. Peterson, J. Inorg. Nucl. Chem. 40 (1978) 65.
61. L.M. Kovba, Radiokhim. 13 (1971) 309.

62. A.H. Reis, H.R. Hoekstra, E. Gebert and S.W. Peterson, J. Inorg. Nucl. Chem. 38 (1976) 1481.
63. T.L. Cremers, P.G. Eller, E.M. Larson and A. Rosenzweig, Acta Crystallogr. C42 (1986) 1684.
64. P. Pailleret, C. R. Acad. Sc. Paris, 265 (1967) 1030.
65. V.N. Serezhkin, V.K. Trunov and L.G. Makarevich, Kristallogr. 25 (1980) 858.
66. S.A. Linde, Yu.E. Gorbunova, A.V. Lavrov, Zh. Neorg. Khim. 25 (1980) 1992.
67. S. Obbade, C. Dion, M. Rivenet, M. Saadi and F. Abraham, J. Solid State Chem. 177 (2004) 2058.
68. S. Obbade, C. Dion and F. Abraham, J. Solid State Chem., to be submitted.
69. S. Obbade, C. Dion and F. Abraham, J. Solid State Chem., to be submitted.
70. J.C. Bobo, Rev. Chim. Minér. 1 (1964) 3.
71. A.M. Chippindale, S.J. Crennell and P.G. Dickens, J .Mater. Chem. 3 (1993) 33.
72. R. Chevalier and M. Gasperin, C. R. Acad. Sc. Paris 267 (1968) 481.
73. P.G. Dickens, G.J. Flynn, S. Patat and C.P. Stuttard, J. Mater. Chem. 7 (1997) 537.
74. C. Miyake, S. Ohana and S. Imoto, Inorg. Chim. Acta, 140 (1987) 133.
75. S.A. Linde, Yu.E. Gorbunova, A.V. Lavrov and V.G. Kuznetssov, Dokl. Akad. Nauk SSSR 230 (1976) 1376.
76. S.A. Linde, Yu.E. Gorbunova, A.V. Lavrov and V.G Kuznetsov, Dokl. Akad. Nauk SSSR 235 (1977) 394.
77. S.A. Linde, Yu.E. Gorbunova, A.V. Lavrov and V.G. Kuznetsov, Dokl. Akad. Nauk SSSR 241 (1978) 1083.
78. K.J. Hilke, U. Grosse-Brauckmann, G. Lagaly and A. Weiss, Z. Naturforsch. 28 (1973) 239.
79. S. Obbade, C. Dion and F. Abraham, J. Solid State Chem., to be submitted.
80. I. Duribreux, F. Abraham, C. Dion and M. Saadi, J. Solid State Chem. 146 (1999) 258.
81. B. Gérand, G. Nowogrocki, J. Guenot and M. Figlarz, J. Solid State Chem. 29 (1979) 429.
82. A. Deschanvres, L. Leparmentiers and B. Raveau, Bull. Soc. Chem. Fr. 10 (1971) 3459.
83. L.M. Kovba, Wang Shih-Hua, E.I. Sirotkina, Dokl. Akad. Nauk SSSR 148 (1963) 113.
84. S. Obbade, C. Dion, M. Saadi, S. Yagoubi and F. Abraham, J. Solid State Chem. 177 (2004) 3909.
85. A. Guesdon, J. Chardon, J. Provost and B. Raveau, J. Solid State Chem. 165 (2002) 89.

This page intentionally left blank

Structural Chemistry of Inorganic Actinide Compounds
S.V. Krivovichev, P.C. Burns & I.G. Tananaev (Editors)

Chapter 8

Chemistry and structural chemistry of anhydrous tri- and tetravalent actinide orthophosphates

Albina I. Orlova

Nizhny Novgorod State University, Gagarin av., 23, Nizhny Novgorod, 603950, Russia

1. Introduction

This chapter summarize results of structural investigations of inorganic anhydrous actinide orthophosphates containing actinides in oxidation states 3+ and 4+: thorium, uranium and transuranium elements. Crystalline actinide (III) and (IV) orthophosphates attracted attention immediately after the discovery of thorium and uranium in nature and the discovery of transuranium elements in the products of artificial processes. Phosphate minerals are natural sources of thorium, uranium, and uncommon metals and are also used in the radiochemical methods of separation of fissile materials from irradiated nuclear fuel and processes of "excess" weapon plutonium conversion into the mixed oxide fuel (MOX) for the nuclear reactors of new generation. The scientific interest in actinide phosphates is also due to use of a phosphate crystalline mineral-like matrix as a safe host-form for the long-term storage and final disposal of the most dangerous actinide-containing high level waste (HLW).
Such important technological and ecological problems can be solved successfully only using fundamental knowledge on structural chemistry of actinide compounds and, in particular, phosphates. For this purpose, use of modern instrumental methods of investigation of solids is needed.
The generalized data on the structure chemistry of anhydrous actinide(III) and (IV) orthophosphates are presented in the literature for some actinides, for example, for transuranics [1,2], or for actinide(III) and (IV) orthophosphates of selected structural modifications such as monazite, zircon or $NaZr_2(PO_4)_3$ (NZP) types [3-6]. Some of the published reviews include wider orthophosphate families, among them the phosphates of tetravalent elements [7], of tetravalent actinides [8,9], of f(III)- and f(IV)-elements [10] as well as of the anhydrous

inorganic compounds with tetrahedral oxoanions [11]. The anhydrous actinide (III) and (IV) orthophosphates discussed in this chapter have not been considered in detail, and the structure formation was not the main topic of the papers cited. The crystal chemical data on actinide phosphates were also discussed in publications on applied research focused on certain industrial needs, including radioactive waste solidification, elaboration of optical materials and so on [12,13].

Thus, much of the original work on the structural chemistry of the actinide (III) and (IV) orthophosphates is presented in the above-mentioned reviews incompletely; some of the reviews include only earlier published works. In this chapter, we shall present a general overview of structural information on the known (up to 2005-2006) anhydrous actinide (III) and (IV) orthophosphates (and some of their structural analogues with tetrahedral oxoanions XO_4 with X = Si, V, As, V).

Here we shall use the classification approach for the description of stoichiometric types of compounds with isolated tetrahedral oxoanions, including orthophosphates, proposed in [14]. This classification is convenient and useful for the systematic examination of the observed variety of known simple and complex actinide (III) and (IV) orthophosphates, for discussion of experimental results on the structural chemistry of compounds, in prediction of properties and scientifically relevant planning of experiments aimed at fabricating new substances with certain predicted structure modifications.

Possible formulas of simple, double and more complex orthophosphates of general formula $Met_m(PO_4)_n = A^I_xB^{II}_yR^{III}_zM^{IV}_pC^V_q(PO_4)_n$ (for various n values) were calculated in [14]. Here, A^I, B^{II}, R^{III}, M^{IV}, C^V (or A, B, R, M, C) = metal (Met) cations with oxidation states from 1+ to 5+ respectively, and x, y, z, p, q = stoichiometric coefficients (x + y + z + p + q = m), which may take on integer, fractional or zero values. Among them, the compounds with R^{III} and M^{IV}, can formally be those of actinide (III) or (IV) compounds.

The formula compositions of known actinide(IV) phosphates, M = Th, U, Np, Pu, and actinide(III) phosphates, R = Pu, Am, Cm, Bk, Cf, Es are represented by these formulas: $M_3(PO_4)_3$, $AM_2(PO_4)_3$, $A_3M_{1.5}(PO_4)_3$ ($A_2M(PO_4)_2$), $B_{0.5}M_2(PO_4)_3$, $B_{1.5}M_{1.5}(PO_4)_3$ ($BM(PO_4)_2$), $B_{3.5}M_{0.5}(PO_4)_3$, $M_{0.25}M'_2(PO_4)_3$, $BRM(PO_4)_3$, $B_{0.5}R_2M_{0.5}(PO_4)_3$ and RPO_4, $B_{1.5}M_{1.5}(PO_4)_3$, $A_3R(PO_4)_2$, $A_3R_2(PO_4)_3$, $R_{1/3}M'_2(PO_4)_3$ (M' = Zr). A great variety of cations A, B, R, M is typical for these stoichiometric types.

Known orthophosphates of the above-mentioned compositions are considered in the present discussion. This chapter also includes orthophosphates whose existence was questionable and in certain cases still remains a matter of dispute.

2. The tetravalent actinide orthophosphates: M – thorium, uranium, neptunium, plutonium.

2.1. M phosphates: $M_3(PO_4)_4$.

The $Th_3(PO_4)_4$ and $U_3(PO_4)_4$ phosphates were first characterized in 1957-1963 [15-18] as isostructural compounds with monoclinic unit cells, space group $P2_1$, or Pm, or $P2/m$. More recently, the data were critically revised in a number of papers [8,19-24], where the authors used new methods of studying solids, and carried out detailed experiments on the phase formation in the systems $ThO_2 – P_2O_5$ and $UO_2 – P_2O_5$. In the authors' opinion [8,19-24], attempts to synthesize single phase products such as "$M_3(PO_4)_4$" for both thorium and uranium [15-18] failed. This was also the case for the compounds of similar stoichiometry with neptunium (IV) and plutonium (IV) [19, 24].

2.2. A-M phosphates: $AM_2(PO_4)_3$, $A_2M(PO_4)_2$

$AM_2(PO_4)_3$. The orthophosphates with tetravalent actinides and monovalent elements with the general composition $AM_2(PO_4)_3$ have been investigated for more than 100 years. The first published work [25] was devoted to the thorium phosphate $NaTh_2(PO_4)_3$. The peculiarities of structure formation in the phosphate series $AM_2(PO_4)_3$ are still under study and discussion.

The structure-chemical knowledge allowed one to explain and predict the piezoelectric and ferromagnetic properties of the orthophosphates $AM_2(PO_4)_3$, their ion-exchange ability, high thermal and chemical stability, isomorphic miscibility of various cations in these phosphates, and the concentration and temperature fields where the miscibility can be realized. Advanced methods of studying structures of solids and determining their composition gave one a chance to solve some problems concerning interpretation of structure data, polymorphism of double phosphates of thorium, uranium, neptunium, plutonium and 1-valent elements and also morphotropy in the rows of the $AM_2(PO_4)_3$ compounds.

Several structural modifications of the $AM_2(PO_4)_3$ orthophosphates are known at the present time. The realization of one or another modification depends on the kind and combination of the M^{4+} and A^+ cations, on the synthesis conditions, namely temperature, nature of solvent, atmosphere and so on. For a long time, the monoclinic modification, space group $C2_1/c$ or Cc, was considered to be the most widely represented among the actinide and monovalent cation phosphates $AM_2(PO_4)_3$. Its formation had been observed for thorium phosphates and arsenates with A = Li, Na, K, Rb, Cs, Cu, Ag, Tl [26-33], for uranium compounds with A = Li, Na, K, Cs [26,29,30,34-38,39,40],

and for neptunium and plutonium compounds with A = Li, Na, K [35,37,40,41]. The *Cc* space group is typical for the Th- and U- phosphates containing relatively small monovalent cations such as lithium, sodium, and potassium [31].

The monoclinic $AM_2(PO_4)_3$ actinide phosphates were obtained by the following methods: 1) chemical interactions in boron oxide melt at 1200 ^{0}C (48 h), 2) precipitation from the A-M-chloride melts by addition of soluble A-phosphates at 700-800^{O}C (approximately 1 h), 3) interactions between the MO_2 (M = Np, Pu) oxides and aqueous solutions of alkaline element salts with H_3PO_4 followed by several stages of heating, resuspension in water, and finally the product was calcined at temperatures up to 1100 C.

The studies of the family of mixed alkaline and actinide $AM_2(PO_4)_3$ phosphates in the temperature range from 600^o to 1700 ^{o}C [35] allowed one to obtain a number of their crystalline modifications. More than 15 modifications have been found that were related through morphotropic and polymorphic phase transitions. The type of phase transitions and the number of possible structural modifications depend both on the nature of the A^+ and M^{4+} cations and the temperature conditions. The monoclinic (earlier known) form remains unchanged during heating up to 1700 ^{o}C only for the Th phases. In other cases (M = U, Np, Pu), formation of a trigonal modification of the $NaZr_2(PO_4)_3$ (NZP) type was achieved by thermal treatment of phases with monoclinic or other modifications. The detailed investigations allowed to determine the phase transition temperatures, space groups, unit cell constants and their dependence upon the nature of the A and M ions [35-37,40] The phase transitions were observed at the following temperatures: $KU_2(PO_4)_3$ 1200^{o}C, $RbU_2(PO_4)_3$ 950^{o}C, $NaNp_2(PO_4)_3$ 1300^{o}C, $KNp_2(PO_4)_3$ 1100^{o}C, $RbNp_2(PO_4)_3$ 650^{o}C, $NaPu_2(PO_4)_3$ 1100^{o}C, $KPu_2(PO_4)_3$ 1000^{o}C, $RbPu_2(PO_4)_3$ 900^{o}C. It was found that the $R\bar{3}c$ space group that is typical for $NaZr_2(PO_4)_3$ does not correspond to all the obtained compounds. For some compounds, the *c* glide plane is missing: this had been observed for $ANp_2(PO_4)_3$ with A = Na, K and $APu_2(PO_4)_3$ with A = K, Rb (possible space groups *R*3, $R\bar{3}$, *R*32, $R\bar{3}m$, *R*3*m*) [36].

Thus the existence of distinct high temperature forms of $AM_2(PO_4)_3$ (so-called β-forms) for the whole family of U, Np, Pu - phosphates became obvious, in contrast to the earlier opinion on this matter. The formation of the β-form was known only for the NaPu-phosphate [42-45], and this fact was considered as an anomaly.

Some phosphates of the $AM_2(PO_4)_3$ family form other modifications as well: neptunium phosphate $NaNp_2(PO_4)_3$ with monazite type structure, $P2_1/n$ (this type was obtained by heating the trigonal form in Ar + 5% H_2 at 1100 ^{o}C [5,35]); neptunium and plutonium phosphates $AgNp_2(PO_4)_3$ and $AgPu_2(PO_4)_3$ with scheelite type structure, $I4_1/a$ [46], thorium phosphate $NaTh_2(PO_4)_3$ with

zircon type structure, $I4_1/amd$ (the low-temperature zircon modification exists below 570 ^oC) [47].

In general, several structure modifications can be realized for the actinide (IV) phosphates $AM_2(PO_4)_3$. These include the $NaTh_2(PO_4)_3$, $NaZr_2(PO_4)_3$, monazite, scheelite and zircon structure types, with the first two types being dominant.

Structure types for the most of the $AM_2(PO_4)_3$ compounds have been determined on the basis of their powder X-ray diffraction data. Structural investigations were carried out for some representatives only: single crystal structural data for $NaTh_2(PO_4)_3$ and $KTh_2(PO_4)_3$ [29,30,48,49] and Rietveld refinement for $KU_2(PO_4)$ [38,39,50]. It is worthy of note that preparation of single crystals of phase-pure phosphate of uranium and other actinides (except thorium) was complicated partly due to the fact that oxidation states of these elements are difficult to control at high temperature during long-time processes.

As a result of single-crystal X-ray structure analysis of $NaTh_2(PO_4)_3$ and $KTh_2(PO_4)_3$, it was established that the monoclinic modification of $ATh_2(PO_4)_3$ (space group $C2/c$) is characterized by the coordination polyhedron ThO_9 (Fig. 1). The Th coordination involves nine oxygen atoms from seven PO_4 groups. The polyhedron has the form of a distorted tricapped trigonal prism. The polyhedron has three corners and edges shared with other Th polyhedra. As a result, the MO_9 and PO_4 coordination polyhedra form a three-dimensional framework. Each of the A^+ cations located in the framework cavities is surrounded by eight oxygen atoms. This modification is described by the crystal chemical formula $A^{[8]}[M^{[9]}_2(PO_4)_3]$ (superscripts $^{[8],\ [9]}$ indicate C.N. = 8 and 9).

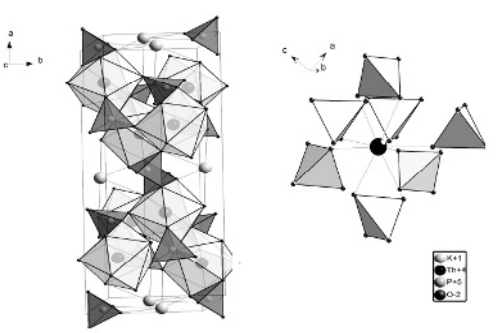

Fig. 1. $KTh_2(PO_4)_3$. Space group $C2/c$, $Z = 4$. Structure fragment and the polyhedron ThO_9 [29].

The known high-temperature rhombohedral $NaZr_2(PO_4)_3$-type modification of actinide phosphates $AM_2(PO_4)_3$ consists of a three dimensional framework built up by corner-sharing MO_6 octahedra and PO_4 tetrahedra. The A^+ cations are in sixfold coordination by the O atoms: the polyhedron AO_6 has a form of trigonal antiprism (M1 position). In addition, there are three 8-coordinate sites (M2) in

the framework cavities. The crystal chemical formula of phosphates $AM_2(PO_4)_3$ of NZP structure type is $A^{[6]}\square^{[8]}{}_3[M^{[6]}{}_2(PO_4)_3]$ (□ – vacant M2 position), so there are three types of cation positions, with two of them in cavities and one in the framework.

The NZP structure type of the high temperature modifications of actinide phosphates $AM_2(PO_4)_3$ has been confirmed by the Rietveld refinement of the uranium phosphate $KU_2(PO_4)_3$ [50]. The test sample was obtained by means of heating of the monoclinic phosphate of similar stoichiometry at 1350 ^{0}C in Ar atmosphere. As shown in Figs. 2 and 3, the UO_n polyhedra of monoclinic and rhombohedral structures of $KU_2(PO_4)_3$ are different: UO_9 and UO_6, respectively.

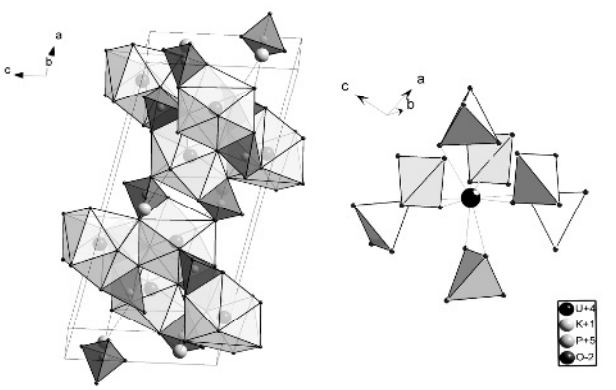

Fig. 2. $KU_2(PO_4)_3$. Space group $C2/c$, $Z = 4$. Structure fragment and polyhedron UO_9 [38].

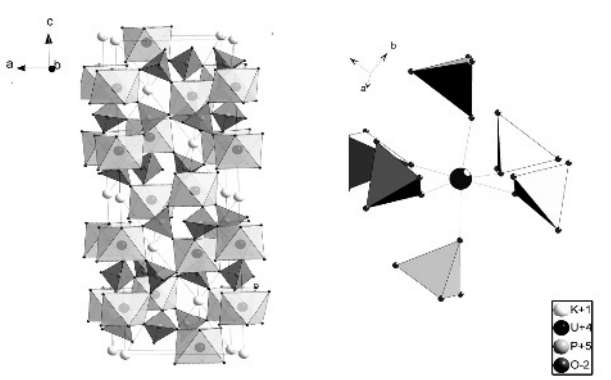

Fig. 3. $KU_2(PO_4)_3$. Space group $R\ \bar{3}c$, $Z = 6$. Structure fragment and coordination polyhedron UO_6 [50].

The results presented in [50] are in good agreement with the structural data for solid solutions of phosphates $KZr_{2-x}U_x(PO_4)_3$ with $0 \le x \le 0.2$ and $KZr_{2-x}Pu_x(PO_4)_3$ with x = 0.2 that also have a rhombohedral structure [38,39]. The solid solutions of neptunium-zirconium and plutonium-zirconium phosphates $NaZr_{2-x}Np_x(PO_4)_3$ with $0 \le x \le 0.6$ and $NaZr_{2-x}Pu_x(PO_4)_3$ with $0 \le x \le 0.2$ of rhombohedral structure (NZP type) had been described in [51]. In both cases [38,51] the incomplete solid solutions of ZrU-, ZrNp- and ZrPu-phosphates were obtained at the temperature of 1100 ^{0}C (lower than phase transition temperatures). Therefore one can guess that the x value could be increased (up to $x_{max} = 2$) if the phase formation will be carried out at temperatures higher than the phase transition temperature of the corresponding compound of the actinide and the monovalent element.

The monoclinic to rhombohedral transition, accompanied by reconstruction of the coordination sphere of the actinide atoms $MO_9 \rightarrow MO_6$ may proceed by the breaking of chemical bonds (or some of them) and the formation of new ones. The transition is accompanied by shortening of the interatomic distances M – O: for example, from the average value of 2.47 Å in UO_9 to the average value of 2.10 Å in an average polyhedron $(U/Zr)O_6$ and to the values 2.27 or 2.32 Å in the polyhedron UO_6 [38,50]. At the same time the elongation of the shortest U – U distances from 4.11-4.20 Å to 4.98 Å takes place. As a result of the transition, the polyhedral framework packing becomes more symmetric ($C2/c \rightarrow R\bar{3}c$) but less compact. The unit cell volume V/Z of the phosphate $KU_2(PO_4)_3$ (Z – number of formula units per unit cell) increases by approximately 29% (from 231.5 Å^3 to 299.7 Å^3) [38,50]. Also, it was established earlier that the value V/Z of plutonium phosphate $NaPu_2(PO_4)_3$ increases by 22% owing to similar structural transition [44]. The fact that actinide orthophosphates $AM_2(PO_4)_3$ (M = U, Np, Pu) crystallize in the NZP-type ($CN_M = 6$), makes the actinides closer to the tetravalent *d*-elements with respect to their crystal chemical features. The *a* and *c* unit-cell parameters change in the same way depending on the values of $r_{kt}A^+$ and $r_{kt}M^{4+}$ in the isostoichiometric and isostructural phosphates when they contain either tetravalent actinides or tetravalent *d*-elements [50]. A uniform monotonic dependence of a and c on $r_{kt}M^{4+}$ is observed in the series Ti, Zr, Hf, Pu, Np, U irrespective of nature of atom electronic configuration (*d* or *f*) (Fig. 4) [30,40,52], which is an additional argument for the similarity of crystal structures of the two classes of *d*- and *f*-elements compounds. In a similar manner, for the monoclinic modifications considered in [38], there is a common dependence of the *a* parameter on the value of rM^{4+} both for the actinide Th and U containing phosphates and for Ti, Zr, Hf phosphates, the parameter values being calculated by means of respective transition matrices. As predicted in [38] in accordance with the dependence $a = f(rM^{4+})$, the value of *a* for the plutonium phosphate

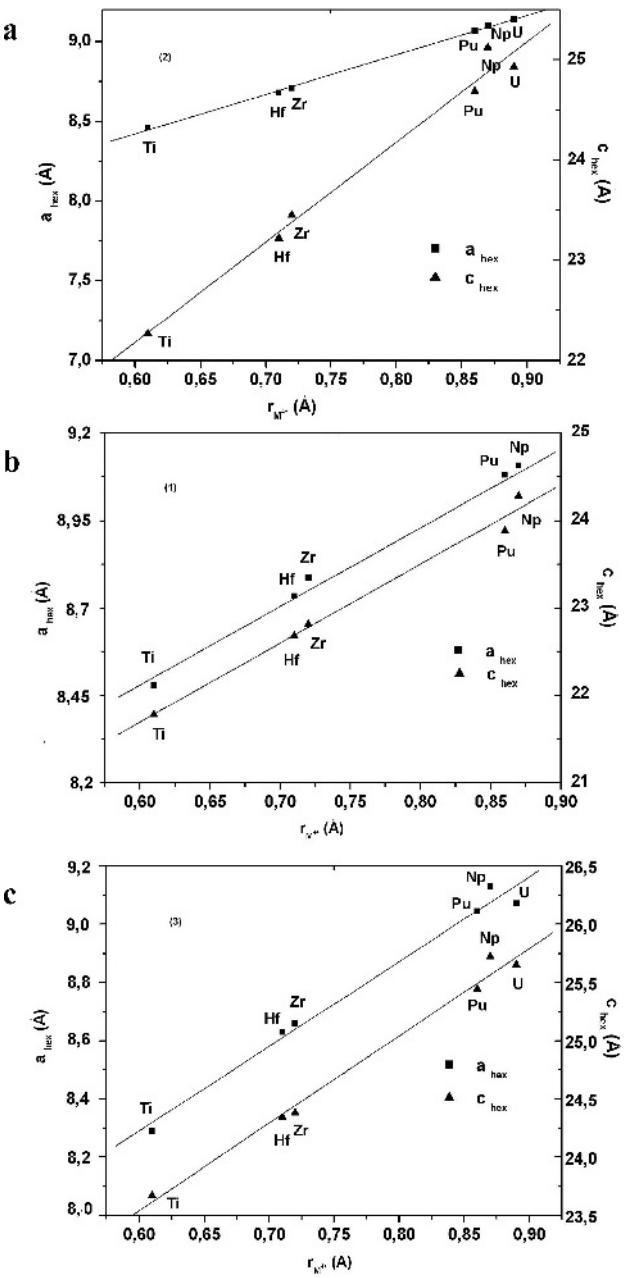

Fig. 4. Unit cell parameters of the rhombohedral $AM_2(PO_4)_3$ phosphates as a function of the M^{4+} ionic radii. M = Ti, Zr, Hf, Th, U, Np, Pu; A = Na (1), K (2), Rb (3) [40].

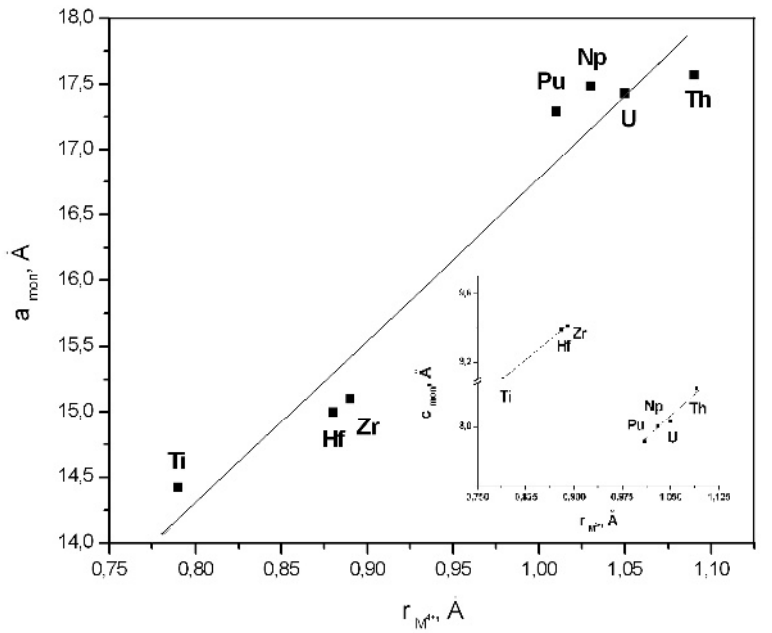

Fig. 5. Unit cell parameters for monoclinic $AM_2(PO_4)_3$ phosphates as a function of the M^{4+} ionic radii. M = Ti, Zr, Hf, Th, U, Np, Pu; A = K (rhombohedral cell data of the Ti, Zr, Hf–phosphates were recast on a monoclinic cell [38]) [40].

$KPu_2(PO_4)_3$ was in good agreement with the value established experimentally for $KPu_2(PO_4)_3$ (monoclinic modification), which was synthesized and described later in [40] (Fig. 5).

Some structures in question are monoclinic (the $NaTh_2(PO_4)_3$ type) and rhombohedral (the $NaZr_2(PO_4)_3$ type), where cations are located in differing crystallographic sites (two and three types, respectively). On the contrary, the structures of other $AM_2(PO_4)_3$ actinide phosphates have only one type of equivalent position with CN = 9 for the monazite structure (space group $P2_1/n$), CN = 8 for the zircon structure (space group $I4_1/amd$), CN = 9 for the scheelite structure (space group $I4_1/a$). These compounds can be obtained by crystallization under certain special conditions and have a general crystal chemical formula $A_{1/3}M_{2/3}PO_4$. These are: $NaNp_2(PO_4)_3$, space group $P2_1/n$ (monazite type), $T = 1100^oC$ (Ar + 5% H_2) [35, 41], $NaTh_2(PO_4)_3$, space group $I4_1/amd$ (zircon type), below 570^oC [47] and the Np, Pu vanadates and arsenates with cations Li^+, Na^+, Ag [35]; $AgNp_2(PO_4)_3$, $AgPu_2(PO_4)_3$, space group $I4_1/a$, (scheelite type) [46, 53].

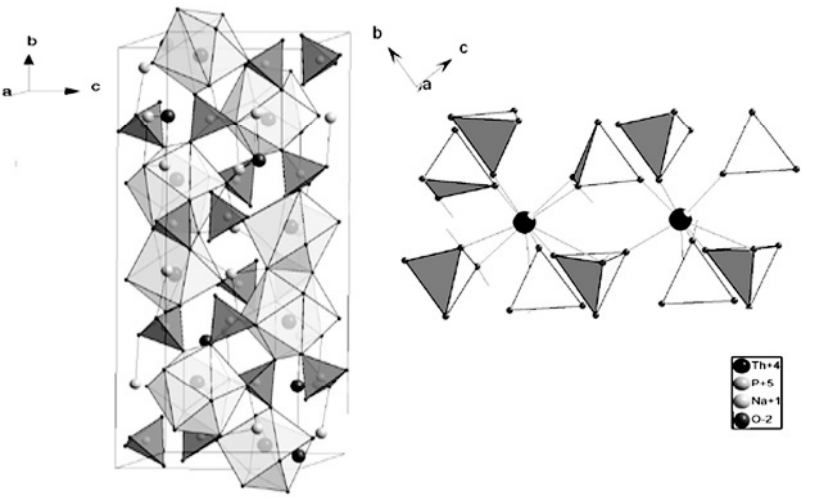

Fig. 6. $Na_2Th(PO_4)_2$. Space group $P2_1/c$, $Z = 8$. Structure fragment and coordination polyhedra ThO_8 and ThO_{10} [58].

$A_2M(PO_4)_2$. There are several known actinide (IV) phosphates $A_2M(PO_4)_2$ with A = Na, K and M = Th, Np [41, 54-58], and vanadates $A_2M(VO_4)_2$ and arsenates $A_2M(AsO_4)_2$ with A = Li, Na and M = Th, Np [59]. These are thermally stable and nearly insoluble compounds.

The structural information on this group of compounds is rather limited and is presented by the structure analysis of $Na_2Th(PO_4)_2$ [58]. Three modifications with monoclinic symmetry (space group $C2/c$, $P2_1/c$) were established, and their unit cell parameters were found to be close to each other. The Th coordination is either 8- or 10-fold. The ThO_8 and ThO_{10} polyhedra are linked by edge-sharing into dimers. Two Na sites have the CN values of 8 and 10 (Fig. 6). The polymorphic modifications are not related to any known structure types [58]. Also, the structure of the Np-compound $Na_2Np(PO_4)_2$ is still unknown [41].

2.3. B-M phospnates: $B_{0.5}M_2(PO_4)_3$, $BM(PO_4)_2$, $B_{3.5}M_{0.5}(PO_4)_3$

$B_{0.5}M_2(PO_4)_3$. The thorium, uranium, and neptunium phosphates of general formula $B_{0.5}M_2(PO_4)_3$ with B = Be, Mg, Ca, Sr, Ba are characterized by extensive polymorphism [5,53,60,61,62,63,64]. As a result of thermal treatment of Mg, Ca, and Sr neptunium phosphates with unknown structures in an Ar + 5% H_2 atmosphere, these compounds were established [5,53] as substances crystallizing with the monazite structure type. The authors of [35] have obtained a series of neptunium phosphates with an analogous composition by interaction between solutions of salts of divalent metals (Mg, or Ca, or Sr) with neptunium oxide NpO_2 and phosphoric acid followed by thermal stage-by-stage treatment

of the precipitate dried at temperatures from 80°C up to 1300°C for 2-20 hours at each stage. $Ca_{0.5}Pu_2(PO_4)_3$ belongs to the monazite structure type as well [61,62,63]. The crystalline powder (100 mg) was synthesized from phosphate precipitates obtained by coprecipitation from an aqueous solution of Ca and Pu salts. The heating process started at 80 ^{0}C, then the temperature was slowly increased up to 800 ^{0}C, and then the material was soaked for 1 hour at 800 ^{0}C and at 1000 ^{0}C. The formation of single phases took place at 1150-1250 ^{0}C for $Mg_{0.5}Np_2(PO_4)_3$, at 1250 ^{0}C for $Ca_{0.5}Np_2(PO_4)_3$ in air and at 1100-1250 ^{0}C in an argon atmosphere, at 1200 ^{0}C for the $Sr_{0.5}Np_2(PO_4)_3$, and at 1000°C for $Ca_{0.5}Pu_2(PO_4)_3$. It was observed that phase formation of unknown modifications of Ca-Np-, Mg-Np- and Ca-Pu-phosphates occured at 800, 900 and 950°C, respectively. These modifications were precursors of the monoclinic compounds (space group $P2_1/n$) formed during subsequent heating. The volume of monoclinic unit cell of Ca-phosphates reduces about 3% during the transition from Np to Pu phosphate.

The $B_{0.5}M_2(PO_4)_3$ structural formula is described as belonging to the "defect" monazite structure of $CePO_4$: heterovalent isomorphism takes place with the appearance of vacancies or interstitial cations according to the scheme $Ce(R)^{III} \leftrightarrow B^{II}_{1/6}\square_{1/6}M^{IV}_{2/3}$. Another modification has been described for Th-orthophosphates $B_{0,5}Th_2(PO_4)_3$ with B = Ca, Sr, Ba, Cd, Pb [62,64]: structure type $NaTh_2(PO_4)_3$ (monoclinic, space group $C2/c$).

$BM(PO_4)$. The existence of polymorphic modifications is typical for Th and U phosphates $BM(PO_4)_2$. Their crystallization led to formation of monoclinic phases with the monazite structure type. The minerals brabantite ($CaTh(PO_4)_2$) and huttonite ($ThSiO_4$) belong to the monazite structure type as well. Tetragonal phases have the zircon ($ZrSiO_4$) structure type [10, 53,65-70,71] ,

In the series of thorium phosphates $BTh(PO_4)_2$ with B = Be, Mg, Ca, Sr, Ba, the monazite structure type remains unchanged in a wide temperature range (900-1600 ^{0}C) only for the Ca phases. The stability of this modification is indicated by the occurence of $CaTh(PO_4)_2$ in nature as a mineral (brabantite). In [65], the huttonite-type modification had been established for $BTh(PO_4)_2$ with B = Ca, Sr, Cd, Pb and $BTh(AsO_4)_2$ with B = Sr, Ba, Pb. It also is known that, for $CaTh(AsO_4)_2$ and $CdTh(AsO_4)_2$, the tetragonal zircon structure type is also possible. $CaTh(AsO_4)_2$ has been observed as a tetragonal modification only [65].

The monoclinic monazite-type phases have been obtained for the series of uranium phosphates $BU(PO_4)_2$ with B = Mg, Ca, Sr [63].

The transition of monoclinic monazite-type $BM(PO_4)_2$ phosphates to a different structural modification occurs at 1400^{0}C (MgTh), 1300^{0}C (SrTh), 1200^{0}C (MgU), 1000^{0}C (CaU and SrU). The CaTh phosphate structure remains stable during heating up to 1600^{0}C. The monazite structure type was not established

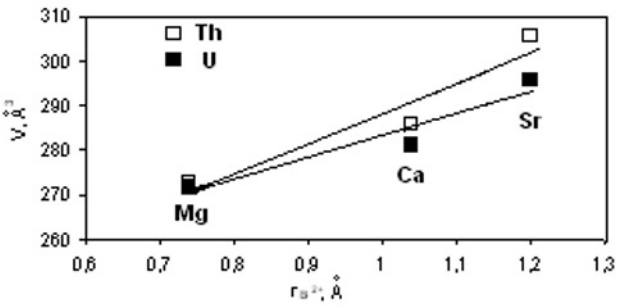

Fig. 7. Unit cell volume for phosphates $BM(PO_4)_2$, space group $P2_1/n$, as a function of the B^{2+} ionic radii. B = Mg, Ca, Sr; M = Th, U [63].

for the Be-Th and Ba-Th phosphates. In the temperature range 650-1550°C there were four modifications observed for both $BeTh(PO_4)_2$ and $BaTh(PO_4)_2$ [53]. In the $BM(PO_4)_2$ series, the unit cell volume increases linearly with increasing ionic radius of the alkaline-earth cation (Fig. 7) [63]. Known double neptunium and plutonium vanadates $BM(VO_4)_2$ (BM = (Ca, Sr, Cd) Np; (Mg, Ca, Sr, Cd) Pu) belong to the tetragonal zircon structure type [5,53].

Thus, polymorphism with the formation of monoclinic and tetragonal modifications is typical for U- and Th-compounds with general formula $BM(XO_4)_2$ (X = P, As, V). These modifications differ in the packing of the XO_4 anions, the orientation of anions around a cation, and the form of the $(B,M)O_n$ coordination polyhedra (n = 8 or 9). The crystal chemical formula of the $BM(PO_4)_2$ phosphates and their arsenate and vanadate analogues can be written as $B_{0.5}M_{0.5}XO_4$, owing to the cation disorder.

Apparently, formation of actinide (IV) compounds with more complex cationic and anionic compositions with the monazite or zircon (xenotime) structure types is possible. These compounds can be considered to be solid solutions. The possibility of forming this kind of compound is realized in the minerals mentioned above. These minerals are characterized by the complex cation compositions: monazite – (La, Ce, other lanthanides, Y, Ca, Th)(P, Si)O_4, xenotime – (Y, lanthanides, Sc, Zr, Th, U)(Si, P)O_4; zircon – (Zr, Hf, Th, U, lanthanides, Ca, Fe, Nb, Ta)(Si,P)O_4 [71]. The ionic radii and cationic proportions, anionic sizes and synthesis conditions affect the formation of each type considered.

$B_{3.5}M_{0.5}(PO_4)_3$. In the system of orthophosphates of the tetravalent M and divalent B elements $B_{0.5}M_2(PO_4)_3$ – $BM(PO_4)_3$ – $B_{3.5}M_{0.5}(PO_4)_3$, the minimum M content corresponds to the composition $B_{3.5}M_{0.5}(PO)_4$. There are Th

phosphates that contain large cations B = Sr, Ba, Pb (this is also true for the Ti, Sn, Zr, and Hf phosphates). All these compounds crystallize in the eulytine structure type with a cubic unit cell, space group $I\bar{4}3d$ [69,72]. In this structure type, the XO_4 tetrahedra form a cubic close packing array with metal cations in octahedral cavities. The cubic structure is stable for the XO_4 oxoanions with X = Si, Ge, P, As, V, S, Cr, and Mo.

M-M' phosphates: $M_{0.25}M'_2(PO_4)_3$.

$M_{0.25}M'_2(PO_4)_3$. The thorium, uranium, and plutonium phosphates $M_{0.25}M'_2(PO_4)_3$ (M = Th, U, Pu, M' = Zr) have been obtained [73-75]. Based on the X-ray data, it was established that the $M_{0.25}M'_2(PO_4)_3$ phosphates crystallize in the NZP rhombohedral structure type. These compounds extend the series of framework Zr phosphates with the general formula $T_xZr_2(PO_4)_3$ where T is a mono- to tetravalent element occurring in the framework cavities. It can be suggested that Zr, Hf, Th, U, and Pu are able to occupy the cavity positions, i.e. the tetravalent actinides can behave not only as framework-forming cations (as constituents of complex anions) but can also as charge compensators for the framework. However, this has not been observed yet. It is possible that tetravalent cations of both *d*-elements and actinides can occupy positions in both the cavities and the framework: $M_{0.25-x}Zr_x[Zr_{2-x}M_x](PO_4)_3$, although, taking into account the crystal chemical features of the elements and the peculiarity of the NZP structure, preference is to be given to the aforesaid formula $M_{0.25}Zr_2(PO_4)_3$ (x = 0).

2.4. M-B-R phosphates: $BRM(PO_4)_3$.

$BRM(PO_4)_3$. The known Th and U compounds with 2- and 3-valent cations B and R form two series of isostructural phosphates $BNdTh(PO_4)_3$, $BGdU(PO_4)_3$, where B = Mg, Ca, Sr, Ba, Cd, as well as $CaNdTh(PO_4)_3$ and $Ca_{0.5}Nd_2Th_{0.5}(PO_4)_3$. These crystallize with the monazite structure type [5,76,77] and have similar unit cell parameters.

The structure of $CaGdTh(PO_4)_3$ was refined using the monazite model [77] with a crystal chemical formula written as $Ca^{[9]}_{1/3}Gd^{[9]}_{1/3}Th^{[9]}_{1/3}(PO_4)$. Metal cation (M = Ca, Gd, Th) forms MO_9 polyhedra that have a shape of a distorted monocapped square antiprism. The PO_4 tetrahedra are connected with the MO_9 polyhedra through vertexes and edges to form a framework (Fig. 8). The distortion of the MO_9 polyhedron in the complex phosphate $CaGdTh(PO_4)_3$ is insignificant in comparison to RPO_4, whereas distortion of the tetrahedra is more significant, owing to the distortion of the O-P-O bond angles.

The $CaRTh(AsO_4)_3$ orthoarsenates may be divided into two groups: compounds with light lanthanides La, Pr, Nd with the monazite structure type and

compounds with heavy lanthanides from Sm to Tm with zircon structure type [5,46,72]. The transition from one type to the other depends upon the change in

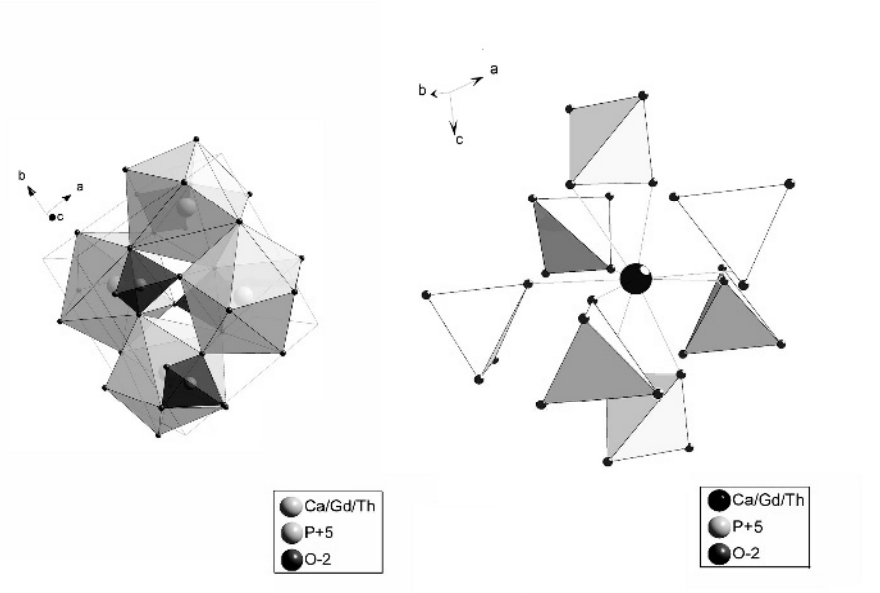

Fig. 8. $CaCdTh(PO_4)_3$. Space group $P2_1/n$, $Z = 4$. Structure fragment and coordination polyhedron $(Ca/Gd/Th)O_9$ [77].

the ionic radii due to the lanthanide contraction [5]. The influence of ionic radius of alkaline-earth elements upon the structure in the temperature range of 500-1200^{O}C was demonstrated in the series of variable composition vanadates $Ca_{1-x}Ba_xLaTh(VO_4)_3$ ($0 \le x \le 1$) [78,79,80]. In the range of higher concentration of Ca^{2+} ($0 \le x \le 0.2$), the phases have the zircon type structure, whereas higher concentration of Ba^{2+} ($0.8 \le x \le 1$) leads to the monazite structure type. In the middle compositional range, the trigonal structure of the NZP-type forms.

The crystal chemical analysis of $BRM(XO_4)_3$ compounds with M = Th and U allowed one to predict the possible existence of $CaAmPu(PO_4)_3$ and make an conjecture concerning its structure. The phosphate with this composition has recently been obtained and was found with the expected monazite structure type, space group $P2_1/n$ [81].

3. Trivalent actinide orthophosphates: plutonium, americium, curium, berkelium, californium, einsteinium

The known $M_m(PO_4)_3$ phosphates with trivalent actinides R have the following formula compositions: RPO_4, $A_3R(PO_4)_2$, $A_3R_2(PO_4)_3$, $R_{1/3}M_2(PO_4)_3$ and $BRM(PO_4)_3$.

3.1. R phosphates: RPO_4.

RPO_4. Plutonium, americium, curium, berkelium, californium and einsteinium form phosphates RPO_4 with the monoclinic monazite structure type [2, 82-86,87]. The unit cell parameters of monazite-type lanthanide phosphates depend linearly on the Ln^{3+} radii. Extrapolating of the same dependence to the experimental unit cell constant values of actinides(III), the effective ionic radii of Pu^{3+}, Am^{3+} and Cm^{3+} in the 9-fold coordination polyhedron (RO_9) were calculated. In the investigations of the phosphates of transplutonium elements (Am and further), powders used were in microgramme quantities. Indexing of the XRD data was done by the method of structural analogy using the single crystal structure data of the isostoichiometric lanthanide phosphates.

3.2. A-R phosphates:$A_3R(PO_4)_2$, $A_3R_2(PO_4)_3$.

*$A_3R(PO_4)_2$***.** The Na-Pu compound with the assumed composition $Na_3Pu(PO_4)_2$ was examined in [88, 89, 90] . The Na-Pu phosphate can be obtained by two techniques: (1) by addition of dry Na_3PO_4 powder to the $PuCl_3$-NaCl melt at 820°C and keeping it in melt for 20 minutes, or (2) by the reaction between solid PuO_2 and Na_2HPO_4 at 1020°C for 16 hours (atmosphere Ar + 4% H_2). The formation of rhombic, tetragonal modifications [88] or orthorhombic modification [89] has been observed. The thulium phosphate $Na_3Tm(PO_4)_2$ (single crystal data [90]) was chosen in [91] as a structural analogue for the $Na_3Pu(PO_4)_2$ with the orthorhombic cell. The existing uncertainly with respect to the crystallographic characteristics of $Na_3Pu(PO_4)_2$ is associated not only with the difficulties of the powder XRD pattern interpretation but also with possible formation of various crystalline modifications whose appearance might be dependent on synthesis conditions.

$A_3R_2(PO_4)_3$. There are several opinions concerning interpretation of the XRD pattern of actinide(III) phosphates with the formula $A_3R_2(PO_4)_3$ (R = Pu, Am, Cm, A = Na, K). The $Na_3Pu_2(PO_4)_3$, $Na_3Am_2(PO_4)_3$, $K_3Am_2(PO_4)_3$ and $K_3Cm_2(PO_4)_3$ compounds were obtained by addition of the Na_3PO_4 or K_3PO_4 powders at 800-820°C to the ACl-RCl_3 melts [92]. The XRD patterns were indexed as monoclinic, space group $P2_1/n$, monazite structure type [91]. The

authors [2, 89] interpreted the composition of the precipitated phosphates as RPO_4.
According to recently published data [93], the composition of lanthanide phosphates precipitated from ACl-$LnCl_3$ chloride melts depends upon molar ratio of PO_4 and R reactants in the initial system. If the ratio increases, the phosphate composition changes in the series RPO_4 - $A_3R_2(PO_4)_3$ - $A_3R(PO_4)_2$ (R = Ce, A = Na or K).

3.3. R-M' phosphates: $R_{1/3}M'_2(PO_4)_3$

$R_{1/3}M'_2(PO_4)_3$. A double americium zirconium phosphate $Am_{1/3}Zr_2(PO_4)_3$ (M' = Zr) was synthesized and characterized by X-ray diffraction methods [74,75]. This phosphate belongs to the NZP structure type. The $NH_4H_2PO_4$ solution was added to the starting solution of americium nitrate and $ZrOCl_2$; thermal treatment of the precipitates was carried out stage-by-stage up to 800°C.
In the $Ln_{1/3}Zr_2(PO_4)_3$ phosphates, a reduction of cell symmetry to $P\bar{3}c$ and $P\bar{3}$ has been observed [73, 74, 94, 95, 96] (refinement data for ErZr and LaZr-phosphates [95, 96]). At the same time, the space groups $R\bar{3}c$, $R\bar{3}$, $R3$, $R32$ are typical for the NZP-type phosphates [6]. Unit-cell symmetry of $Am_{1/3}Zr_2(PO_4)_3$ is probably also reduced to primitive trigonal as for the lanthanide analogues as might be seen from the comparison of their XRD patterns. Thus, there is a possibility that trivalent actinides may enter 6-fold positions in the cavities of the $[Zr_2(PO_4)_3]$ framework.

B-R-M phosphates: $BRM(PO_4)_3$
$BRM(PO_4)_3$. $CaAmPu(PO_4)_3$ has been synthesized recently and the monazite structure type has been attributed to it [81]. It is the only known compound among the $BRM(PO_4)_3$ phosphates where tri- and tetravalent actinides are present together. Obviously, the Am^{3+} and Pu^{4+} cations occupy cation sites with CN = 9 (monoclinic, space group $P2_1/n$). The phosphate $CaAmPu(PO_4)_3$ has an intermediate composition in the $Ca_xAm_{3-2x}Pu_x(PO_4)_3$ series with x = 1. The first member of the row is $AmPO_4$ (x = 0) and the last one is $Ca_{1.5}Pu_{1.5}(PO_4)_3$. $CaPu(PO_4)_2$ (x = 1.5) has a monazite-type structure as well.

4. Structural investigations of tetra- and trivalent actinide orthophosphates

Actinide phosphates and some actinide vanadates and arsenates crystallize in several structural modifications: $NaTh_2(PO_4)_3$, monazite, zircon, scheelite, $NaZr_2(PO_4)_3$ (NZP), and eulytine (Table 1). The monazite and NZP structure types are presented by the orthophosphates containing both trivalent and tetravalent actinides. In most cases, the above mentioned structure types are realized in natural minerals that have synthetic analogues with general formula $M_m(XO_4)_n$ where X = Si, P, W (Table 1). The most

common structure types are: $NaTh_2(PO_4)_3$ (no natural analogues), $NaZr_2(PO_4)_3$ (NZP, mineral kosnarite), and $CePO_4$ (mineral monazite). The coordination of actinides in the structures of the orthophosphates studied changes from CN = 6 (NZP, eulytine) to CN = 10 (monoclinic $A_2Th(PO_4)_2$). However, sixfold coordination is not very common for actinides in low oxidation states. Nevertheless, there are quite a number of examples mentioned above with tri- and tetravalent actinides (R and M) which possess this kind of coordination. It is noteworthy that, for some isostoichiometric phosphates, arsenates and vanadates, the structures are presented by two or more various types, depending upon the kind of cations (anions) and their properties such as charge, size, electronegativity, electronic structure, polarizability, etc. For some compounds, the polymorphic modifications are still unknown or remain the object of discussion at present.

At the same time, the structural chemistry of tri- and tetravalent actinide orthophosphates is not well-known. A small number of theoretically possible compounds have been discussed [14]. The collection of information on actinide compounds may take a long period of time, on account of the experimental difficulties of work with actinides that require special conditions and equipment. Consequently, single crystal data are available for a few compounds only; in most cases, the analysis was based on powder diffraction data and analogy to other structures.

The successful development of structural chemistry of actinide phosphates will rely in many respects on experimental results obtained from the chemical and structural research of analogous lanthanide compounds. Lanthanide phosphates have many more known structure modifications [10, 11].

Following this principle, some authors [74] have synthesized first europium phosphate $Eu_{1/3}Zr_2(PO_4)_3$ and then americium phosphate $Am_{1/3}Zr_2(PO_4)_3$ [75] and classified them as members of the NZP family. The IR spectra and structure refinement of the Eu phosphate were carried out by the Rietveld method which allowed them to ascribe to this compound the space group $P\bar{3}c$ [95] (Fig. 9). The REE phosphate with lanthanum, $La_{1/3}Zr_2(PO_4)_3$, has been prepared independently in [96]. These authors determined the structure by Rietveld analysis (X-ray and neutron powder diffraction data) and described the lattice as primitive hexagonal (space group $P\bar{3}$). Both $P\bar{3}c$ and $P\bar{3}$ groups are new for the NZP family of inorganic compounds. It is evident that structural data for the lanthanide phosphates are presented in publications wider than for the actinide phosphates. The list of known lanthanide phosphates and their modifications is much more diverse and representative than that for actinide analogues. There are the following formula types: RPO_4, $A_3R(PO_4)_2$, $B_{1.5}R_2(PO_4)_3$, $B_3R(PO_4)_7$, $B_3R(PO_4)_3$, $R_{1/2}C_{3/2}(PO_4)_3$, $ABR(PO_4)_2$, $ABR_2(PO_4)_3$, $A_2RM(PO_4)_3$, where A, B, R, M, C are 1-, 2-, 3-, 4- and 5-valent elements [10, 11].

Table 1. Structural modifications of known tri- and tetravalent actinide phosphates (and other compounds with XO_4 = SiO_4, VO_4, AsO_4)

Structural modification				Actinide (III) and (IV) phosphates	
Formula / Mineral name	Space group	CN	Number of positions	Formula type	Actinide M(IV) and R(III)
$NaTh_2(PO_4)_3$ /-	*C*2/*c*	9(M), 8(A)	3	$AM_2(PO_4)_3$ $AM_2(AsO_4)_3$* $B_{0.5}M_2(PO_4)_3$	Th, U, Np, Pu Th
$Na_2Th(PO_4)_2$ /-	*C*2/*c*	9(M), 8(A) 8,10(M,A)	3	$A_2M(PO_4)_2$ $A_2M(AsO_4)_2$	Th,U Th
$Na_2Th(PO_4)_2$ / -	$P2_1/c$		4	$A_2M(PO_4)_2$	Th
$CePO_4$ / monazite	$P2_1/n$	9	1	$AM_2(PO_4)_3$ $B_{0.5}M_2(PO_4)_3$ $BM(PO_4)_2$ $BRM(PO_4)_3$ RPO_4	Np Np, Pu Th,U Th,U,Pu,Am Pu, Am, Cm, Bk, Cf, Es
$CaTh(PO_4)_2$ / brabantite	$P2_1/n$	9	1	$BM(PO_4)_2$	Th
$ThSiO_4$ / huttonite	$P2_1/n$	9	1	$BM(PO_4)_2$ $BM(AsO_4)_2$*	Th Th
$ZrSiO_4$ / zircon	$I4_1/amd$	8	1	$AM_2(PO_4)_3$ $AM_2(VO_4)_3$* $AM_2(AsO_4)_3$*	Th Th,Np,Pu Np
YPO_4 / xenotime	$I4_1/amd$	8	1	$BM(AsO_4)_2$* $BM(VO_4)_2$*	Th Np, Pu Th
$ThSiO_4$ / thorite	$I4_1/amd$	8	1	$MSiO_4$* $BM(AsO_4)_2$*	Th U
$USiO_4$ / coffinite	$I4_1/amd$	8	1	$MSiO_4$*	
$CaWO_4$ / scheelite	$I4_1/a$	8	1	$AM_2(PO_4)_3$	Np, Pu
$NaZr_2(PO_4)_3$ / kosnarite	$R\bar{3}c$	6(M) 6(A), 8(□)[#]	3	$AM_2(PO_4)_3$ $R_{1/3}M'_2(PO_4)_3$ $M_{1/4}M'_2(PO_4)_3$	U, Np, Pu Am U, Pu
$Bi(SiO_4)_3$ / eulytite	*I*4three dimensional	6	1	$B_{3.5}M_{0.5}(PO_4)_3$	Th

[#] □ = vacancy.

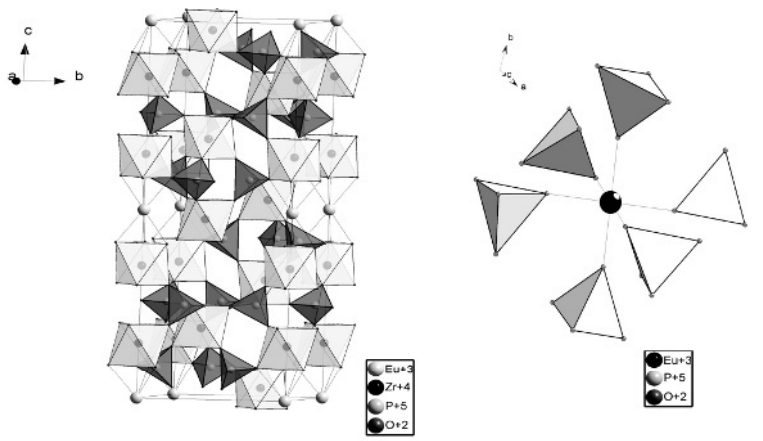

Fig. 9. $Eu_{1/3}Zr_2(PO_4)_3$. Space group $P\bar{3}c$, $Z = 6$. Structure fragment and polyhedron EuO_6 [95].

Besides such structure types as monazite, zircon, NZP, their crystal structures also adopt arcanite, glaserite, whitlockite, rhabdophane, langbeinite and some other structure types. The systematic description of structural forms of lanthanide orthophosphates and their classification according to the formula and structure types has been reported in [10]. Any of these lanthanide orthophosphate compounds can be taken as an analogue for the "structural chemical" design of new sorts of actinide phosphates with the expected structures and properties. Since the list of known tri- and tetravalent lanthanide phosphates with 1-, 2-, 3-, 4- and 5-valent elements (A, B, R, M, C) is rapidly expanding, the same can be true for new actinide-containing orthophosphates as well. The development of this field of science will be determined by the demand in promising new materials and development of advanced technologies.

For instance, the structural chemical approach was used to elaborate such crystalline materials as ceramics for immobilization of actinides and other dangerous elements and isotopes present in radioactive waste. The approach was efficient in modelling new lanthanide phosphates of framework NZP-type structure [94, 95] and of the langbeinite structure type [97-101].

The limits of concentration of lanthanides (and, apparently, of actinides too) that can participate in the $[Ln_xZr_{2-x}(PO_4)_3]^q$ framework (q^- – framework charge) of the NZP structure type, $0 \le x \le 1$, $1 \le q \le 2$, and of the langbeinite type, $x = 1$ ($q = 2$) and $0 \le x \le 2$ ($q = 3$) are different (Fig. 10) [99, 100, 102].

Fig. 11 shows the structure of $K_2PrZr(PO_4)_3$ that belongs to the langbeinite structure type [99]. The Pr atoms are sixfold coordinated. The octahedral sites of the framework are occupied by Pr and Zr in different proportions.
In the structures of $A_2[RZr(PO_4)_3]$ (A = K, Rb, Cs), the Pr atoms occupy one of the two framework positions. Replacement of Pr by Fe may be coupled with the repacement of one of the A positions by a divalent ion (Sr^{2+}, Ba^{2+}). The compound $AB[Fe_{1.25}Pr_{0.75}(PO_4)_3]$ may serve as an example of this type of substitution (B = Sr, Ba). There are several compounds with general formula

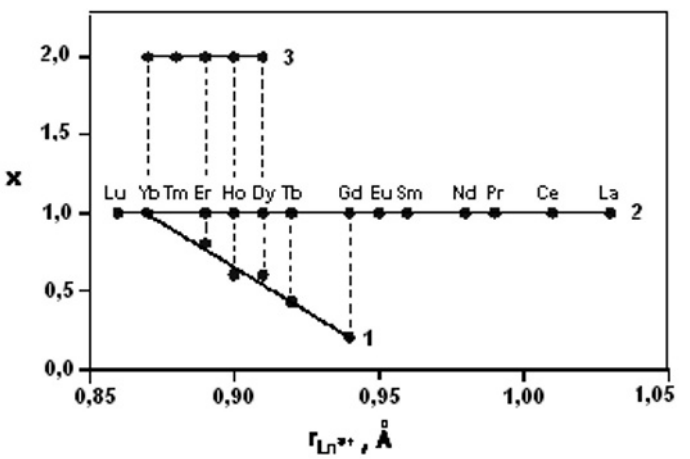

Fig. 10. Maximum value x (from two framework positions occupied by lanthanide: 1 - $0<x\leq1,0$, NZP type, $Na_{1+x}Zr_{2-x}Ln_x(PO_4)_3$ [102]; 2,3 - $0<x\leq2,0$, langbeinite type, $KBa[R_{2-x}Ln_x(PO_4)_3$ [100], 2 – x = 1,0, langbeinite type, $K_2LnZr(PO_4)_3$ [99].

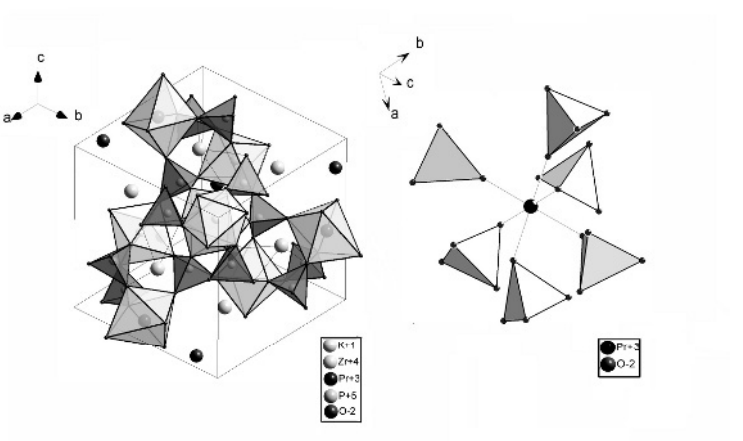

Fig. 11. The structure of $K_2PrZr(PO_4)_3$ and coordination polyhedron PrO_6 [99].

$Na_{1+x}[Zr_{2-x}R_x(PO_4)_3]$ with $x_{max} \leq 1$, where R is a rare earth cation (Fig. 10) [97-102]. One can suppose that a similar situation can be observed for actinide(III) compounds (or solid solutions). However, none of them has been reported to the present time. An overview on known structures of actinide and similar lanthanide phosphates described above demonstrates a wide variety of coordinations for tri- and tetravalent actinides. The ThO_n, UO_n, and some LnO_n polyhedra with n changing from 10 to 6 are shown in Fig. 12.

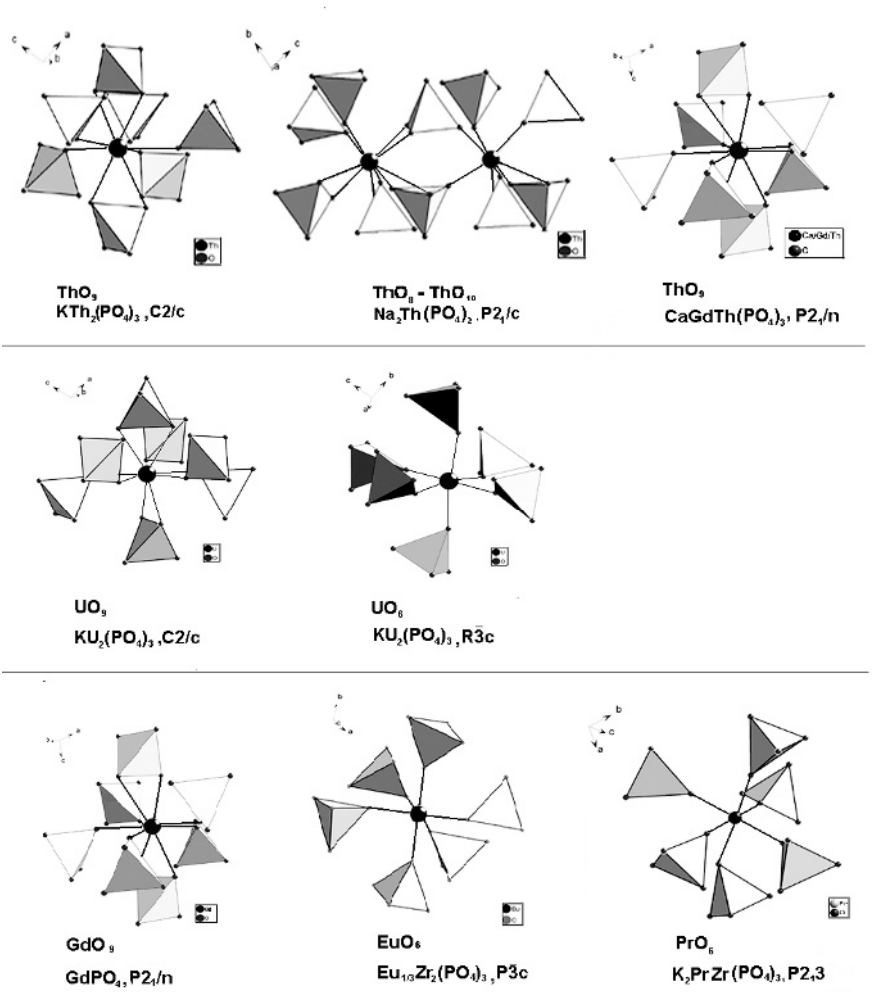

Fig. 12. Coordination polyhedra for actinide and lanthanide orthophosphates: 1 - $KTh_2(PO_4)_3$ ThO_9; 2 - $Na_2Th(PO_4)_2$ ThO_8 and ThO_{10}; 3 - $CaGdTh(PO_4)_3$ $(Ca/Gd/Th)O_9$; 4 - $KU_2(PO_4)_3$ UO_9; 5 - $KU_2(PO_4)_3$ UO_6; 6 - $GdPO_4$ CdO_9; 7 - $Eu_{1/3}Zr_2(PO_4)_3$ EuO_6; 8 - $K_2PrZr(PO_4)_3$ PrO_6.

The compositions of new phosphates with langbeinite structure type with 9-coordinated lanthanide ions have been proposed in [103, 104]. The phosphates with composition $A_{1,5}Ln_{0,5}[Fe_2(PO_4)_3]$ with A = K, Rb, Cs were synthesized, and characterized by X-ray diffraction. The predicted cubic modification, space group $P2_13$ has been confirmed. This "prediction" seems to be promising for the actinide phosphate as well.

The data presented in Table 1 allows to identify the following phenomena in actinide phosphate systems: isomorphism (isodimorphism), polymorphism and morphotropy in the isostoichiometric compounds and isostructural phases. These data indicate principal possibility of preparation of solid solutions by the iso- and heterovalent substitution mechanisms. The $M_m(PO_4)_n$ solid solutions with tri- and tetravalent actinides and lanthanides are known; the following compositions have been reported: $Na(K)Zr_{2-x}M_x(PO_4)_3$ (M = Np, Pu) and $KZr_{2-x}M_x(PO_4)_3$ (M = U, Pu) [$NaTh_2(PO_4)_3$ - $NaZr_2(PO_4)_3$ structure types]; $R_{1-x}R'_xZr_2(PO_4)_3$, (R,R' = lanthanide, actinide (Am or Cm)) [$NaZr_2(PO_4)_3$ structure]; $R_{1-x}R'_xPO_4$, $B_x(RR')_{1-2x}M_xPO_4$ (R,R' = lanthanide, lanthanide, M = Th, U) [monazite and zircon structure types]; $(M,M')SiO_4$ (M,M' = Pu, Zr) [zircon structure type] and some others, also with other XO_4 groups (V, As) [13, 38, 40, 51, 59, 76-78, 105-113].

5. Conclusions

Structural investigations of anhydrous tri- and tetravalent actinide orthophosphates were initiated by the studies of natural minerals and, at the present time, are directed towards creation of mineral-like matrices for the safe disposal of radioactive waste. Development of the field over last 120 years was controlled by a number of factors, including new scientific methods, development of new technologies, political solutions and environmental problems.

The data collected unambiguously indicate the existence of a large variety of actinide orthophosphates and their analogues (orthovanadates, orthoarsenates, orthosilicates, etc.). They are characterized by iso- and heterovalent isomorphic substitutions of cations and anions, and polymorphic and morphotropic transitions. The data analysis allows to predict many new actinide compounds of the group with different expected structures and tailored properties, including stability in different extreme physical fields and chemical media. Certain progress in this research direction has already been achieved.

The accumulated evidence of the existence of phosphate minerals containing radioactive elements stable over long geological periods of time makes it possible to search for stable ceramic materials for safe disposal of radioactive

wastes and other applications (medical sources of ionizing radiation, compact energy sources and so on).

Structural chemistry of tri- and tetravalent actinide orthophosphates (and their analogues) is an important part of scientific field dealing with the influence of f-electronic shell and electronic structure of tri- and tetravalent elements upon structure formation and properties of their solid compounds.

Accumulation of structural information on actinide compounds proceeds rather slow. The experiments are not simple and require expensive materials and equipment coupled with highly skilled investigators. Many new experiments still have to be done. However, it becomes evident that “monazites”, “zircons”, “kosnarites”, “scheelites”, “langbeinites” and many other mineral-like actinide phosphates will be widely required for solving technological and environmental problems.

References

1. C. Keller. Transurane Phosphates, in: Gmelins Handbuch der Anorganische Chemie, Verlag Chemie, Weinheim, Transurane. Part C. 1972. P. 251.
2. C.E. Bamberger, in: A.J. Freeman, C. Keller (Eds), Handbook on the Physics and Chemistry of the Actinides, Chapter 6, Solid Inorganic Phosphates of the Transuranium elements. Elsevier, Amsterdam, 1985, pp. 289-303.
3. L.A. Boatner, B.C. Sales, in: W. Lutze,. R.C. Ewing (Eds.). Radioactive Waste Forms for the Future, Chapter 8, Monazite,. Elsevier Science Publishers, Amsterdam, 1988, pp. 495–563.
4. A. Boatner, in: M.J. Kohn, J. Rakovan, J.M. Hughes (Eds.) Reviews in Mineralogy and Geochemistry V. 48. Phosphates: Geochemical, Geobiological and Materials Importance, Mineralogical Society of America, Chapter 4. Synthesis and Properties of Monazite, Pretulite and Xenotime, 2002, pp. 87-120.
5. Yu.F. Volkov, Radiokhimiya 41 (1999) 161.
6. A.I. Orlova, Radiokhimiya Radiokhimiya 44 (2002) 423.
7. I.V. Tananaev (Ed.), Tetravalent Element Phosphates, Nauka, Moscow, 1972.
8. V. Brandel, N. Dacheux, J. Solid State Chem. 177 (2004) 4743.
9. V. Brandel, N. Dacheux, J. Solid State Chem. 177 (2004) 4755.
10. A.I.Orlova, D.B. Kitaev, Radiokhimiya 47 (2005) 15..
11. Yu.F. Volkov, A.I. Orlova. Systematization and Crystal Chemical View on Inorganic Tetrahedra oxoanions Compounds, FSUE “SSC RF RIAR”, Dimitrovgrad, 2004, pp. 286.
12. R.C. Ewing, LuMin Wang, Reviews in Mineralogy and Geochemistry 48 (2002) 673.
13. D.F. Mullica, E.L. Suppenfield, L.A. Boatner, Inorg. Chim. Acta 244(1996) 247.
14. Yu.F. Volkov, A.I. Orlova, Radiokhimiya 38 (1996) 3.
15. A. Burdese, M.L. Borlera, Atti Accad. Sci. Torino, C1. Sci. Fis. Mat., 94 (1959-1960) 97.
16. A. Burdese, M.L. Borlera, Ann. Chemica 53 (1963) 333.
17. R. Jary, Ann. Chimica, [13] 2 (1957) 58.
18. A. Burdese, L.M. Barlera, Ricerca Sci. 29 (1959) 2537.
19. C.E. Bamberger, R.G. Haire, C.M. Begun, H.E. Hellwege, J. Less-Comm. Met. 97 (1984) 349.
20. P. Benard, V. Brandel, N. Dacheux, J. Chem. Mater. 8 (1996) 181.
21. V. Brandel, N. Dacheux, M. Genet, J. Radiokhimiya 43 (2001) 16.

22. V. Brandel, N. Dacheux, M. Genet, J. Solid State Chem. 121 (1996) 467.
23. N. Dacheux, R. Poder, V. Brandel, M. Genet, J. Nucl. Mat. 252 (1998) 179.
24. C.E. Bamberger, R.G. Haire, C.M. Begun, H.E. Hallwege, J. Less-Comm. Met. 102 (1984) 179.
25. A. Wallroth, J. Bull. Soc. Chim. 39 (1883) 321.
26. B. Matkovic, M. Sljukic, B. Prodic, Croat Chem. Acta 37 (1965) 115.
27. B. Matkovic, M. Sljukic, B. Prodic, Croat Chem. Acta, 38 (1966) 69.
28. B. Matkovic, B. Prodic, M. Sljukic, Acta Crystallogr. Suppl. 21 (1966) A64.
29. B. Matkovic, B. Prodic, M. Sljukic, S.W. Peterson Croat. Chem. Acta 40 (1968) 147.
30. B. Matkovic, B. Prodic, M. Sljukic, Bull. Soc. Chim. France, (1968) 1777.
31. K.L. Keester. J.T. Jacobs, Ferroelectrics 8 (1974) 657.
32. P.N. Nambodiry, V.V. Deshpande, K.S. Venkateswarlu, Thermochim. Acta, 60 (1983) 47
33. W.F. Schmidt, R.W. Mooney, J. Electrochem. Soc. 111 (1964) 668.
34. A.I. Krujkova, I.A. Korshunov, Z.V. Khripkina, G.N. Kazantzev, O.V. Skiba, Radiokhimiya 18 (1977) 314.
35. Yu.F. Volkov, R.F. Melkaja, V.I. Spirjakov, G.A. Timofeev, Radiokhimiya 36 (1994) 205.
36. Yu.F. Volkov, S.V. Tomilin, A.N. Lukinykh, V.I. Spirjakov, A.A. Lizin, A.I.Orlova, Radiokhimiya 45 (2003) 289.
37. S.V. Tomilin, A.I.Orlova, A.N. Lukinykh, A.A. Lizin, in: Book of Abstracts of the 7th International Conference "Actinides – 2005", UK, Manchester, 4-7 July, 2005, p. 117.
38. H.T. Hawkins, D.R.Spearing, D.K. Veirs, J.A. Danis, D.M. Smith, C.D. Tait, W.H. Runde, M.N. Spilde, B.E. Scheetz, Chem. Mater. 11 (1999) 2851.
39. H.T. Hawkins, Dissertation Abstracts International 61 (2001) 1030.
40. Yu. F. Volkov, S.V. Tomilin, A.I.Orlova, A.A. Lizin, V.F. Spiryakov, A.N. Lukinykh., Zh. Neorg. Khim. 50.(2005) 1776.
41. F. Nectoux, A. Tabutean, Radiochem. Radioanal. Letters 49 (1981) 43.
42. O.V. Skiba, A.I. Krujkova, A.A. Burnaeva, G.N. Kazantzev, I.A. Korschunov, E.P. Moskvichev, Radiokhimiya 23 (1981) 872.
43. A.A. Burnaeva, Yu.F. Volkov, A.I. Krujkova, V.I. Spirjakov, Radiokhimiya 29 (1987) 3
44. A.A. Burnaeva, Yu.F. Volkov, A.I. Krujkova, I.A. Korschunov, Radiokhimiya 34 (1992) 12.
45. A.I. Orlova, Yu.F. Volkov, R.F. Melkaja, L.Yu. Masterova, I.A. Kulikov, V.A. Alferov, Radiokhimiya 36 (1994) 295.
46. R. Perret, M. Damak, J. Less-Comm. Met. 108 (1985) 23.
47. V.B. Kalinin, Izv. Ross. Akad. Nauk, Neorg. Mater. 31 (1995) 604.
48. L.-O. Hagman, P. Kierkegaard, Acta Chem. Scand. 22 (1968) 1822.
49. B. Matkovic, B. Prodic, M. Sljukic, M. Topic, R.D. Willett, F. Pullen, Inorg. Chim. Acta 4 (1970) 571.
50. E.R. Gobechija, Yu.K. Kabalov, S.V. Tomilin, A.N. Lukhinyh, A.A. Lizin, A.I. Orlova, Kristallografiya 50 (2005) 374.
51. A.I. Orlova, Yu.F. Volkov, A.A. Charlamova, im: L. Jardin, G. Borisov (Eds.) Review of Excess Weapons Plutonium Disposition LLNL Contract Works in Russia, St.-Petersburg, 2002, P.407.
52. D.A. Woodcock, P. Lightfoot, J. Mater. Chem. 9 (1999) 2907.
53. [Yu.F. Volkov, A.I. Orlova, in: Sbornik Trudov, FSUE "SSC RF RIAR", Dimitrovgrad, 1996. p. 25.
54. L. Troost, L. Quvrard, C. R. Acad. Sci. Paris 102 (1886) 1422.
55. L. Troost, L. Quvrard, C. R. Acad. Sci. Paris 105 (1887) 30.
56. L. Troost, L. Quvrard, Ann. Chim. Phys. 17 (1883) 297.
57. A. Colani, Ann. Chim. Phys. 12 (1907) 59.

58. N. Galesic, B. Matkovic, M. Topic, E. Coffou, M. Sljukic, Croat. Chem. Acta 57 (1984) 597.
59. W.Freundlich, A.Erb, M.Pages, Chim. Miner. Rev., 11 (1974) 595.
60. A.I. Orlova, D.B. Kitaev, V.I. Petkov, Yu.F. Volkov, in: Book of Abstracts 3rd Russian Conference "Radiokhimiya –2000", St.-Peterburg, 2000, p.60.
61. D.B. Kitaev, A.I. Orlova, Czech. J. Phys. 53 (2003) 238.
62. A. Queston, .J. Provost, B. Raveau, J. Mater. Chem. 9 (1999) 2583.
63. D.B. Kitaev, Yu.F. Volkov, A.I. Orlova, Radiokhimiya 46 (2004) 195.
64. A. El.-Yacoubi, R. Brochu, A. Serghini, M. Louer, M. Alami Talbi, D. Louer, Powder Diffr. 12 (1997) 76.
65. H. Schwarz, Z. Anorg. Allg. Chem. 334 (1964) 175.
66. A. Ginestra, G. Variali, Gazz. Chim. Ital. 95 (1965) 1096.
67. M. Laugh, J. Appl. Cryst. 6 (1973) 299.
68. J.G. Pepin, E.R. Vance, G.J. McCarthy, Mat. Res. Bull. 16 (1981)627.
69. D. Fahmi, B. Piriou, M. Zouiri, Eur. J. Solid State Inorg. Chem. 26 (1986) 313.
70. K. Podar, M. Cuney, C.N. Trung, Amer. Mineral. 80 (1995) 1261
71. The Encyclopedia of Mineralogy,. By, Ed. K. Frye, Hutchinson Ross Publising Company. 1981. pp. 512.
72. R. Perret, S. Pinson, M. Damak, J. Less-Common. Metals 116 (1986) L5.
73. A.I. Orlova, D.M. Bykov, I.G. Trubuch, V.S. Kurashkovskaya, Yu.K. Kabalov, in Book: Abstracts of the Third International Conference of Inorganic Materials, Germany, Konstanz, 2002, p. 172.
74. V.S. Kurashkovskaya, D.M. Bykov, A.I. Orlova, Zh. Strukt. Chim. 45 (2004) 1013.
75. D.M. Bykov, A.I. Orlova, S.V. Tomilin, A.A. Lizin, A.N. Lukhinuh, Radiokhimiya 48 (2006) (in press).
76. A.I. Orlova, D.B. Kitaev, D.V. Kemenov, M.P. Orlova, G.N. Kazantzev, S.G. Samoilov, V.S. Kurashkovskaya, Radiokhimiya 45 (2003) 97.

This page intentionally left blank

Structural Chemistry of Inorganic Actinide Compounds
S.V. Krivovichev, P.C. Burns & I.G. Tananaev (Editors)

Chapter 9

Structural chemistry of actinide polyoxometalates

Michael T. Pope[a]

[a]*Department of Chemistry, Box 571227, Georgetown University, Washington DC 20057, U.S.A.*

1. Introduction

Polyoxometalates, formerly and still occasionally known as Heteropoly- and Isopolyanions (or "acids"), comprise an immense and expanding class of oxoanions of the early transition metal elements, predominantly molybdenum(VI), tungsten(VI) and vanadium(V), and to a currently much lesser extent, pentavalent niobium and tantalum. [1 – 3] There are two major characteristics of these elements that distinguish them from other polyoxoanion formers such as chromium(VI), silicon and phosphorus. The first is the ability of the metal atom to increase its coordination by oxide from 4 to (commonly) 6 or 7, and the second, a consequence of the metal's vacant and accessible d-orbitals, the ability to engage in multiple bonding with "terminal" oxygen atoms. As we shall see in this Chapter, by far the commonest environment of the metal atom in polyoxometalates (POMs) is quasi octahedral with one or two (mutually *cis*) unshared or terminal oxygens. In 1965, based upon the handful of POM structures that were known at that time, Lipscomb noted that no structures contained metal atoms with three terminal oxygens, and proposed that this would prove to be a general restriction. [4] Since that time some POM structures have been reported to violate the so-called Lipscomb criterion but in most cases which can be examined closely one of the three terminal oxygens (always in a *fac* configuration) has been found to be protonated or is a water ligand. The Lipscomb rule is of course a consequence of the strong trans influences of the M—$O_{terminal}$ multiple bonds. This leads, in the "octahedral"

fac-MO_3 case, to long and therefore weak bonds attaching M to the remainder of the polyoxometalate structure.

In a formal sense, POMs are produced via Brønsted acid-base condensation-addition processes, e.g.

$$7\ MoO_4^{2-} + 8\ H^+ \leftrightarrows Mo_7O_{24}^{6-} + 4\ H_2O \quad (1)$$

However, Eq (1) is an oversimplification since the stoichiometry of such reactions is strongly influenced by the nature of the counter-cations present and by the total ionic strength of the medium. [5]

It has been known for well over 150 years that other positive-valent elements can be incorporated into POM structures as "heteroatoms" (hence the term "heteropoly acids"). Most elements of the Periodic Table have been incorporated, some such as phosphorus yielding dozens of compositions and structures. At the present time the field of POMs appears to be limitless.

Although it is always possible, once the formula of a specific POM is known, to write an equation analogous to Eq.(1) describing its formation, this is often not the appropriate synthetic procedure. In addition to variation of counter-cation, ionic strength and pH in aqueous media, syntheses may be carried out in non-aqueous solvents, via hydro- or solventothermal methods, and by solid state reactions. The starting material may even be a pre-formed stable or metastable POM ; this is especially the case for tungstates. While in some cases the preparation of a specific POM may be rationally designed, in the majority of systems the synthesis has to be described simply as "self assembly".

From the viewpoint of a heteroatom the polyoxometalate framework that immediately surrounds it can be regarded as a multidentate "ligand". Such a ligand has some special properties: (1) it is fully oxidized and therefore can in principle accommodate heteroatoms in high oxidation states, (2) it is a "hard" sigma donor via the oxygen atoms, but can also act as a pi acceptor as a result of the availability of appropriate vacant d-orbitals of the adjacent metal atoms, [6] (3) it has high thermal stability, and the oxometalate framework has stability to ionizing radiation.

A general introduction to the chemistry of POMs [1] and more recent reviews [2,3,7] illustrate the broad range and potential scope of this field. The present article concentrates on the structural chemistry of polyoxometalates which incorporate actinide (An) elements as heteroatoms. A review of actinide

chemistry including polyoxometalate formation appeared in 1985, [8] but much has happened in the past 20 years, stimulated in part by the perceived use of POMs as agents for separation and storage ("waste forms") of radioactive elements generated by weapons development and nuclear power production. Most of the published work between 1971 and the late 1990's was carried out by Russian, Romanian and French researchers and has been reviewed in 1999.[9] A more recent brief review [10] has focused on stability constants for interaction of some lanthanide and actinide cations with POMs.

The present review focuses first on actinide complexes of polymolybdates (section 2) and polytungstates (section 3) that have been isolated and structurally characterized. There are currently no reported actinide polyvanadates, -niobates, or –tantalates. A final section (4) summarises solution studies of equilibria between actinide cations and polyoxometalate anions.

2. Molybdates

In his monumental paper on the chemistry of molybdenum Berzelius [11] is usually credited with a description of the first POMs, the Keggin anions now formulated as $[PMo_{12}O_{40}]^{3-}$ and $[AsMo_{12}O_{40}]^{3-}$. It is also likely that Berzelius made the first actinide polymolybdates in a reaction of thorium salts with molybdates. These compounds were later more thoroughly characterized in 1913 by Barbieri [12] who formulated them as e.g. $4(NH_4)_2O.ThO_2.12MoO_3.8H_2O$. Using the then-prevalent Miolati theory, the anion was considered to contain the thorium atom surrounded by six $Mo_2O_7^{2-}$ ligands. The cerium(IV) analog was described a year later.[13] The structure of the cerium anion was finally determined in 1968 [14] and this established a new structural type for POMs at that time. Two other examples of this category, with tetravalent uranium and neptunium, have since been reported. [15 -17] The structure is illustrated in Figure 1 and exhibits some interesting features. Although it is conventionally described as a central XO_{12} icosahedron surrounded by six pairs of face-shared MoO_6 octahedra, the latter reduce the overall symmetry of the cluster to D_{3d}. As is frequently observed for oxomolybdenum(VI) structures each Mo atom has two short, mutually *cis*, Mo—$O_{terminal}$ bonds (1.68 Å) each of which induces a pronounced *trans* influence (2.28Å). Indeed, if the latter weak bonds are imagined to be cut [18,19], the polyanion structure now can be described as an "octahedral" central atom surrounded by six ditetrahedral $Mo_2O_7^{2-}$ anions, in a formal sense not that far removed from the old Miolati formula.

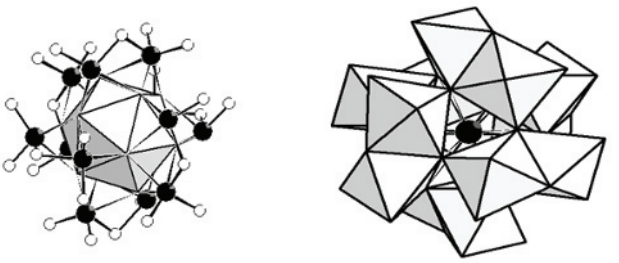

Figure 1. Two representations of the structure of $[UMo_{12}O_{42}]^{8-}$,showing the central UO_{12} icosahedron (left), and the face-sharing of MoO_6 octahedra (right)

Electrochemical investigation of $[ThMo_{12}O_{42}]^{8-}$ reveals no stepwise reduction of the anion to isostructural mixed-valence "heteropoly blues" that is observed for many other POMs, but rather an irreversible multi-electron reduction, correponding to decomposition of the anion [20]. This behavior is anticipated for polyoxometalates in which the metal has a *cis*-dioxo environment ("type II" structure [21]). However, cyclic voltammograms of $[UMo_{12}O_{42}]^{8-}$ show a reversible one-electron *oxidation* to the uranium(V) analog [20] at +0.90 *vs* sce at pH 0. The electronic absorption spectrum of the oxidized species has been reported.

Spectroscopic evidence for the interaction of $[UMo_{12}O_{42}]^{8-}$ with a variety of metal cations has led to the isolation and crystal structure determination of several adducts (see entries **1** – **9,** Table 1).

In every case (except for **4**) the two external cations lie on one of the three-fold axes of the central UO_{12} icosahedron and each is coordinated by three terminal oxygens of three different molybdenum atoms as shown for the copper derivative (**7**) in Figure 2. Only a *trans* disposition of the external cations is observed; all other possible arrangements would result in molybdenum atom(s) with no terminal oxygen atoms. The coordination spheres of the external cations, "octahedral" for Ni^{2+}, Sc^{3+}, Fe^{3+} and VO^{2+} , tricapped trigonal prismatic for Er^{3+}, Nd^{3+} and Th^{4+} , are completed by water molecules. Crystals of the thorium derivative (**1**) contain an extended one-dimensional chain structure $([Th(H_2O)_3UMo_{12}O_{42}]^{4-})_x$. The uranyl derivative (**4**) forms a layer-type structure with two types of bridging UO_2^{2+} cations (in pentagonal bipyramidal coordination) one linked via pairs of terminal oxygens, and the other via a pair of terminal oxygens and a single bridging oxygen of an Mo_2O_7 group. The unshared equatorial uranium sites are occupied by water ligands. NMR (^{17}O,

^{95}Mo) investigations of these and analogous complexes with other 3d and lanthanide cations, reveal that in solution most are labile on the NMR timescale. [31 - 33]

Table 1. Structurally characterized derivatives of $[UMo_{12}O_{42}]^{8-}$

	Compound	Reference
1	$(NH_4)_3H[ThUMo_{12}O_{42}].15H_2O$	[22]
2	$(NH_4)_2[Er_2UMo_{12}O_{42}].22H_2O.$	[23]
3	$[(C_2H_5)_4N]_4[(VO)_2(OH_2)_4UMo_{12}O_{42}].8H_2O$	[24]
4	$(NH_4)_4[(UO_2)_2(OH_2)_3UMo_{12}O_{42}].18H_2O$	[25]
5	$[Me_4N]_2H_2[Ni_2(H_2O)_6UMo_{12}O_{42}].18H_2O$	[26]
6	$H_2[Nd_2(H_2O)_{12}UMo_{12}O_{42}].12H_2O$	[27]
7	$[Me_4N]_2H_2[Cu_2(H_2O)_6UMo_{12}O_{42}].nH_2O.$	[28]
8	$(NH_4)_2[Sc_2UMo_{12}O_{42}].26H_2O$	[29]
9	$[(CH_3)_4N]_2[Fe^{III}{}_2(H_2O)_6UMo_{12}O_{42}].18H_2O.$	[30]

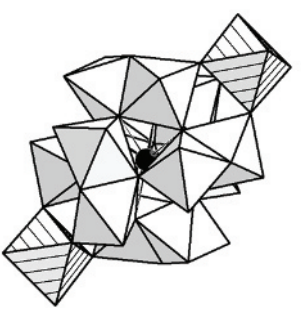

Figure 2. Polyhedral representation of $[UMo_{12}O_{42}\{Cu(H_2O)_3\}_2]^{4-}$ showing location of $CuO_3(H_2O)_3$ octahedra (hatched)

3. Tungstates

By far the largest number of actinide POMs are polytungstates, and exploration of this field has been closely linked and often inspired by the development of lanthanide polyoxometalate chemistry. Before plunging into this area it is appropriate to review the main structural features that are often observed for actinide (and lanthanide) POMs. Such features have been termed *lacunary*

anions since they are formally derived from known (plenary) anions by removal of one or more tungsten atoms and their terminal oxygen atoms. The resulting structures, in order to be at least metastable, must conform to the Lipscomb criterion mentioned above.

The commonest lacunary polytungstates are derived from three plenary tungstate structures: the ("Lindqvist") hexatungstate, $[W_6O_{19}]^{2-}$; the Keggin anion, typically α-$[PW_{12}O_{40}]^{3-}$; and the Wells-Dawson anion, typically α-$[P_2W_{18}O_{62}]^{6-}$.

The hexatungstate and its lacunary version $[W_5O_{18}]^{6-}$ are shown in ball-and-stick and polyhedral format in Figure 3. Although the lacunary pentatungstate anion has been shown to have limited kinetic stability in aqueous solution,[34] and is observed as a component of larger structures, it has not yet been isolated in the solid state.

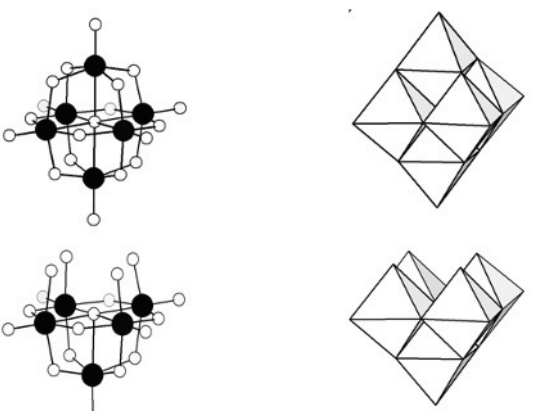

Figure 3. Upper: $[W_6O_{19}]^{2-}$ in ball-and-stick and polyhedral representation; Lower: Lacunary derivative $[W_5O_{18}]^{6-}$

The Keggin anion and three lacunary derivatives are illustrated in Figure 4. The trivacant (W_9) species are metastable in solution, but aqueous solutions of the monovacant (W_{11}) anions are indefinitely stable in the appropriate pH range.
The two known isomers of the (α)-Keggin anion with C_{3v} (β) and C_{2v} (γ) symmetry (Figure 5a) also have accessible lacunary derivatives, but the only one of relevance to present discussion is the divacant γ-$[SiW_{10}O_{36}]^{8-}$ (Figure 5b).

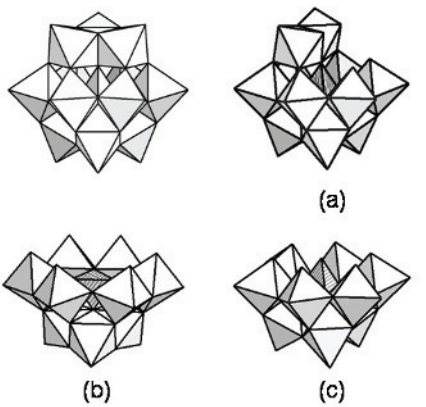

Figure 4. The Keggin anion α-$[PW_{12}O_{40}]^{3-}$ and three lacunary derivatives (a) $[PW_{11}O_{39}]^{7-}$ (b) A-$[PW_9O_{34}]^{9-}$ (c) B-$[PW_9O_{34}]^{9=}$

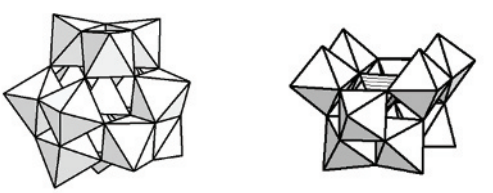

Figure 5 Left: The β isomer of the Keggin structure. Right: $[SiW_{10}O_{36}]^{8-}$ a lacunary derivative of the γ isomer of the Keggin structure.

The relevant lacunary versions of the Wells-Dawson anions are the two monovacant (α_1 and α_2) and trivacant species shown in Figure 6.

3.1. Bis(pentatungsto) Anions, $[An(W_5O_{18})_2]^{8-}$

The structure illustrated in Figure 7 was first demonstrated for the Ce(IV)-centered complex [35] but has subsequently been confirmed for the anions containing tetravalent Th,[36] U,[37] and Np [38] (and for numerous trivalent lanthanides). A Pu(IV) anion [39] almost certainly has the same structure.
The anion has nominal D_{4d} point symmetry with the actinide cation occupying a fairly regular square antiprism formed by the oxygen atoms surrounding the vacancy in the lacunary pentatungstate.

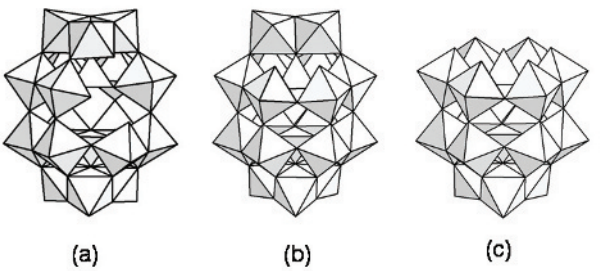

Figure 6. Three lacunary deivatives of the Wells-Dawson anion α-$[P_2W_{18}O_{62}]^{6-}$ (a) α_1-$[P_2W_{17}O_{61}]^{10-}$ (b) α_2-$[P_2W_{17}O_{61}]^{10-}$ (c) α-$[P_2W_{15}O_{56}]^{12-}$

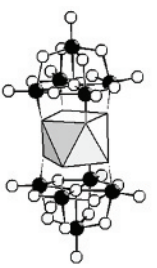

Figure 7. $[An^{IV}(W_5O_{18})_2]^{8-}$

All of these complexes, including those with the lanthanide cations, are prepared directly from WO_4^{2-} and the appropriate An^{4+} (Ln^{3+}), and have only a narrow pH-range of stability (*ca*5.5-6.5) in aqueous solution. However in the solid state the ammonium salt of $[Th(W_5O_{18})_2]^{8-}$ yields the cubic tungsten bronze Th_xWO_3 (x~0.1) when heated in an inert atmosphere to 725°C. It has been proposed that bronzes prepared in such fashion from appropriate POM salts could be used as inert waste forms for actinides and radioactive lanthanides [40].

3.2. Derivatives of monovacant lacunary anions.

The lacunary anions $[PW_{11}O_{39}]^{7-}$,$[SiW_{11}O_{39}]^{8-}$ and (α_2-) $[P_2W_{17}O_{61}]^{10-}$ were first shown to form complexes with a variety of lanthanide cations (Ln:POM =1:1 and 1:2) by Peacock and Weakley in 1971.[41] At that time only the 1:2 complexes could be isolated, and the α_1 isomer of $[P_2W_{17}O_{61}]^{10-}$ had not been discovered. The first actinide (tetravalent Th, U) analogs of the Peacock-

Weakley anions were reported within a few years.[42 – 45]. Analogous complexes containing tri- and tetravalent plutonium, americium, curium and californium have been identified in aqueous solution, although those of Cm(IV) and Cf(IV) are slowly reduced by the solvent.[46, 47] The first structural characterization of the Peacock-Weakley anions ($[Ce^{IV}(P_2W_{17}O_{61})_2]^{16-}$ [48] and $[U^{IV}(GeW_{11}O_{39})_2]^{12-}$ [43] revealed the anticpated square antiprismatic coordination environment of the heteroatom, see Figure 8. Both structures, confirmed by subsequent determinations, mostly of lanthanide(III) derivatives, have overall C_2 symmetry and have the possibility of existing in *syn*- and *anti*-conformations. With the few exceptions noted below, the complexes based upon P_2W_{17} anions adopt a *syn*- conformation (as shown in Figure 8) and those based upon α-XW_{11} anions are *anti*-, at least in the solid state. In solution, NMR evidence has been interpreted [49, 50] to indicate that a different single isomer is present or, more likely that rapid rotation (on the NMR timescale) interconverts *syn* and *anti* . Attempts to resolve the enantiomers of these complexes have been unsuccessful, presumably for the same reason.

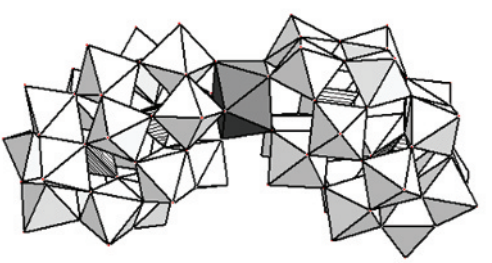

Figure 8. Polyhedral representation of the *syn* conformation of the C_2-symmetric Peacock-Weakley type anions $[M(\alpha_2\text{-}X_2W_{17}O_{61})_2]^{n-}$, showing the square-antiprismatic coordination environment of the heteroatom M.

Although the second (so-called α_1) isomer of lacunary $[P_2W_{17}O_{61}]^{10-}$ (Figure 6) was discovered in 1977 [51] most of the literature pertaining to actinide derivatives of P_2W_{17} involves the more directly accessible, and more stable, α_2 isomer. Complexes of Th and U with α_1-$[P_2W_{17}O_{61}]^{10-}$ have recently received attention.[52] Phosphorus-31 NMR of solutions of $[M(\alpha_1\text{-}P_2W_{17}O_{61})_2]^{16-}$ (M = Th, U) and of $[U(\alpha_1\text{-}P_2W_{17}O_{61})(\ \alpha_2\text{-}P_2W_{17}O_{61})]^{16-}$ clearly show the presence of isomers (Figure 9). Crystals of the ammonium and potassium salts of these anions reveal a *syn* conformation for the thorium derivative and *anti* for the uranium complexes.(Figure 10)

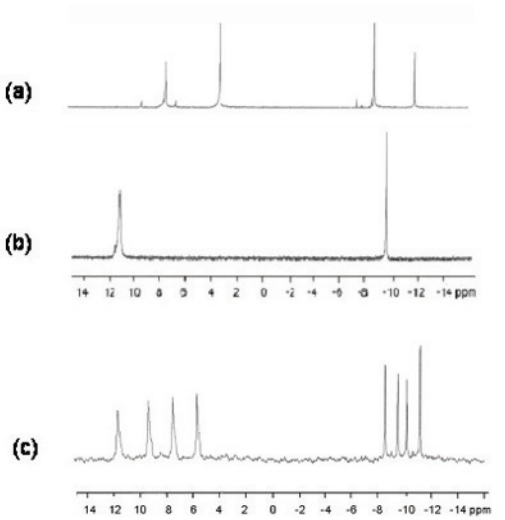

Figure 9. Phosphorus-31 NMR spectra of solutions of (a) $[U(\alpha_1\text{-}P_2W_{17}O_{61})_2]^{16-}$, (b) $[U(\alpha_2\text{-}P_2W_{17}O_{61})_2]^{16-}$ and (c) $[U(\alpha_1\text{-}P_2W_{17}O_{61})(\alpha_2\text{-}P_2W_{17}O_{61})]^{16-}$ demonstrating the non-lability (on the NMR timescale) of conformational isomers of complexes containing the $[\alpha_1\text{-}P_2W_{17}O_{61}]^{16-}$ ligand. The resonances with positive chemical shifts correspond to those phosphorus atoms close to the paramagnetic U^{IV} centers.

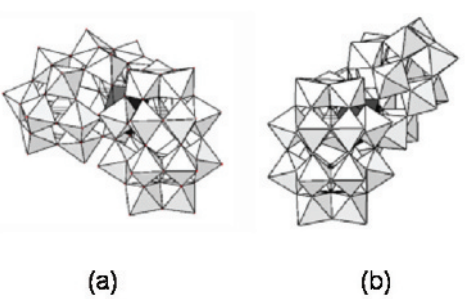

Figure 10. Polyhedral representations of the *syn* and *anti* conformational isomers of $[M(\alpha_1\text{-}P_2W_{17}O_{61})_2]^{n-}$

3.3. Derivatives of divacant lacunary anions

Reaction of the uranyl cation with the divacant lacunary anion $\gamma\text{-}[SiW_{10}O_{36}]^{8-}$ (Figure 5b) yields two species in approximately equal proportions according to ^{29}Si- and ^{183}W-NMR spectra. Crystals of one of these complexes have been structurally characterized as the tetrameric assembly $[(M(H_2O))_4(UO_2)_4(\mu\text{-}OH)_2(SiW_{10}O_{36})_4]^{22-}$ ($M = Na^+, K^+$) shown in Figure 11. [53]

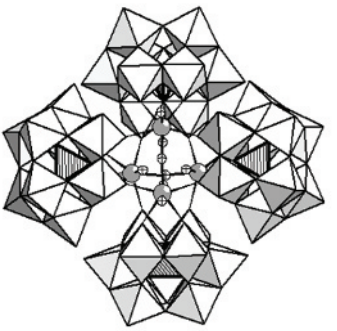

Figure 11. $[(M(H_2O))_4(UO_2)_4(\mu\text{-}OH)_2(SiW_{10}O_{36})_4]^{22-}$ ($M = Na^+, K^+$). The alkali cations and associated aqua ligands in the central cluster have been omitted for the sake of clarity.

3.4. Derivatives of trivacant lacunary anions

3.4.1. A-$[XW_9O_{34}]^{n-}$

Uranium(IV) complexes of A-type $[XW_9O_{34}]^{n-}$ (Figure 4) anions have been reported but have received no structural characterization by NMR or X-ray diffraction. Based upon elemental analysis these compounds have been formulated as $[(UO)_3(GeW_9O_{34})_2]^{14-}$ [54] and $[(UO)_3(H_2O)_6(PW_9O_{34})_2]^{12-}$ [55] It is possible that these complexes are stucturally similar to $[(Ce^{IV}O)_3(H_2O)_2(PW_9O_{34})_2]^{12-}$ (Figure 12) that was characterized by Knoth in 1986 [56] The structure of an analogous tungstoarsenate(V) anion has each of the sandwiched Ce(IV) cations bearing an aqua ligand.[57]

The uranyl cation, UO_2^{2+}, forms similar sandwich-type anions, the detailed structures of which are dependent upon the nature of the countercation. Figure 13 shows the structures of the anions present in the sodium and potassium (or ammonium) salts of the 2:2 UO_2^{2+}:W_9 complexes which were the first POMs to incorporate the uranyl group as a heteroatom [58]. In these and in all subsequent uranyl POMs the uranium adopts a pentagonal bipyramidal coordination geometry. The solid-state structures were confirmed in solution by ^{31}P and ^{183}W NMR and an equilibrium constant of 128(12) for Eq(2) at 30°C and $[Cl^-] = 33$ mM was evaluated from P-NMR measurements.

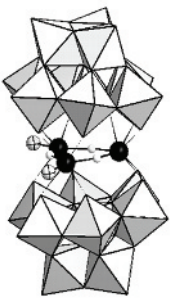

Figure 12. $[(Ce^{IV}O)_3(H_2O)_2(PW_9O_{34})_2]^{12-}$. Aqua ligands are shown as hatched white spheres.

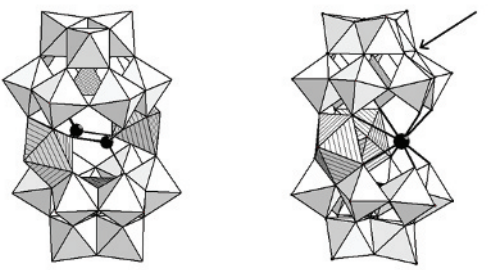

Figure 13. (a) $[Na_2(UO_2)_2(PW_9O_{34})_2]^{12-}$ (C_i), (b) $K_2(UO_2)_2(PW_9O_{34})_2]^{12-}$ (C_s). The second (labile) potassium cation is observed bound to surface bridging oxyens (arrow) of the upper polytungstate moiety (see [58])

$$[Na_2(UO_2)_2(PW_9O_{34})_2]^{12-} + 2\ K^+ \leftrightarrows [K_2(UO_2)_2(PW_9O_{34})_2]^{12-} + 2\ Na^+ \qquad (2)$$
$$\delta(P)\ -9.7 \qquad\qquad \delta(P)\ -9.9, -11.3$$

Analogous (C_i) structures to the sodium complex have been observed for $[Na_2(UO_2)_2(SiW_9O_{34})_2]^{14-}$ [53] and $[Na_2(UO_2)_2(AsW_9O_{34})_2]^{12-}$, and for the neptunyl(V) anion, $[Na_2(NpO_2)_2(PW_9O_{34})_2]^{14-}$ [59] The rapid and efficient formation of these complexes in aqueous solution and subsequent facile phase-transfer into nonaqueous solvents has been suggested as a possible route for separation of the actinyl cations.[58, 59] The possibility of incorporating a third uranyl cation to form $[(UO_2)_3(AsW_9O_{34})_2]^{12-}$ has recently been demonstrated in an ammonium salt, and a compound formulated as $Na_{10}H_2[(UO_2)_3(PW_9O_{34})_2]$ has been reported but not structually characterized.[60]

3.4.2. B-$[XW_9O_{34}]^{n-}$ and B-$[XW_9O_{33}]^{n-}$

As yet (but see section 3.4.3) no actinide derivatives of the "B" isomer of $[PW_9O_{34}]^{9-}$ illustrated in Figure 4 have been reported. However there are structural analogs, $[XW_9O_{33}]^{n-}$ with X = As^{III}, Sb^{III}, Bi^{III}, Se^{IV} and Te^{IV} in which the unshared electron pair of the heteroatom X occupies the position of the terminal phosphate oxygen atom. Several POMs incorporating U^{4+} and UO_2^{2+} with two or more XW_9O_{33} groups have been reported. The simplest are the sandwich anions $[(UO_2)_2(H_2O)_2(XW_9O_{33})_2]^n$,(X, n = Sb, 14-; Te, 12-) illustrated in Figure 14 [61] . The anions have idealized C_{2v} symmetry, and the non-parallel arrangement of the W_9 groups must result from steric crowding of the internal uranyl oxygen atoms and the stereoactive lone pairs of Sb and Te. A compound of uranium(IV) with $[SbW_9O_{33}]^{9-}$ has been described as a sandwich structure with the formula $[U_3(SbW_9O_{33})_2]^{6-}$ [62] but in the absence of any structural information the actual composition must remain in doubt.

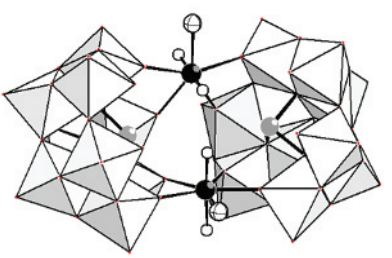

Figure 14. $[(UO_2)_2(H_2O)_2(SbW_9O_{33})_2]^{14-}$

Although no analogs of the above uranyl complexes with $[AsW_9O_{33}]^{9-}$ have yet been reported, anions containing *three* AsW_9 building blocks have been prepared by an indirect synthetic route starting from $[As_4W_{40}O_{140}]^{28-}$, the structure of which incorporates four AsW_9 units, see section 3.5. The anion, $[(UO_2)_3(H_2O)_6(W_3O_6)(AsW_9O_{33})_3]^{15-}$ shown in Figure 15 has overall C_{3v} symmetry with a group of three corner-shared $[WO_5(OH_2)]$ "octahedra" capping the cyclic assembly of uranyl-linked tungstoarsenite anions. A lacunary version of this anion, $[(UO_2)_3(H_2O)_5(W_2O_5)(AsW_9O_{33})_3]^{19-}$, isolated at a higher pH (6 *vs* 4) is lacking one of the capping tungsten atoms. In common with the behavior of other lacunary POMs, the vacancy can be occupied by other transition metal cations, and the vanadyl(IV) derivative has been characterized. [63] Thermal teatment of the ammonium salt of the plenary anion (W_{30}) yields the cubic uranium(IV) tungsten bronze, $U_{\sim 0.1}WO_3$ under relatively mild conditions (725°C under N_2). [40]

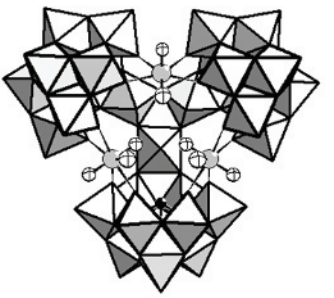

Figure 15. $[(UO_2)_3(H_2O)_6(W_3O_6)(AsW_9O_{33})_3]^{15-}$ Three aqua ligands on the uranyl groups are shown as large white spheres

Direct reaction of $[AsW_9O_{33}]^{9-}$ with a two-fold excess of UO_2^{2+} forms the curious structure illustrated in Figure 16 in good (60%) yield [53] The anion includes one $[AsW_9O_{33}]^{9-}$ and two $[AsW_8O_{30}]^{9-}$ groups linked by a single tungsten atom. The AsW_8 units can be considered as lacunary derivatives of a β-$[AsW_9O_{33}]^{9-}$anion.

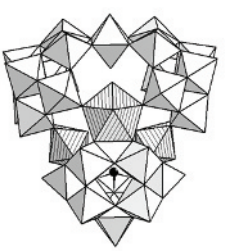

Figure 16. $[(UO_2)_3(H_2O)_3\{WO(H_2O\}(AsW_9O_{33})(AsW_8O_{30})_2]^{17-}$. The $UO_2(H_2O)\{O_4\}$ groups are shown as cross-hatched pentagonal bipyramids

3.4.3. $[P_2W_{15}O_{56}]^{12-}$

The trivacant lacunary derivative of the Wells-Dawson anion (Figure 6) presents a reactive surface identical to that of B-$[PW_9O_{34}]^{9-}$. Reaction of P_2W_{15} with uranyl salts yields the "tetrameric" anion $[(UO_2)_{12}(\mu_3\text{-}O)_4(\mu_2\text{-}H_2O)_{12}(P_2W_{15}O_{56})_4]^{32-}$ shown in Figure 17. [64] This anion has idealized tetrahedral symmetry based on four $[P_2W_{15}O_{56}]^{12-}$ ligands linked by trigonal $[(UO_2)_3O(H_2O)_3]$ groups formed by equatorial-edge-sharing of UO_7 pentagonal bipyramids. A similar arrangement has been observed in a basic uranyl nitrate, $[(UO_2)_3O(OH)_3(H_2O)_6]NO_3{\cdot}4H_2O$. [65] The POM anion has the highest atomic

ratio of U:W (1:5) yet observed in a polytungstate, and this may prove to be of significance in relation to nuclear waste storage. It is of course entirely possible that an analogous anion (with U:W = 1:3) could be prepared with B-$[PW_9O_{34}]^{9-}$ instead of $[P_2W_{15}O_{56}]^{12-}$ groups.

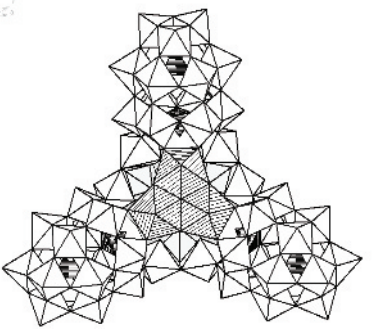

Figure 17. The tetrahedral anion $[(UO_2)_{12}(\mu_3\text{-}O)_4(\mu_2\text{-}H_2O)_{12}(P_2W_{15}O_{56})_4]^{32-}$ with one of the four equivalent U_3 linking groups shown as cross-hatched pentagonal bipyramids

A compound formulated as $Na_{18}[(U^{IV}O)_3(H_2O)_6(P_2W_{15}O_{56})_2]\cdot 27\ H_2O$ has been reported [55] but has not been structurally characterized. A sandwich-like structure does not seem plausible given the structure of the P_2W_{15} unit, and further study is certainly warranted.

3.5. Derivatives of $[As_4W_{40}O_{140}]^{28-}$

The parent tungstoarsenite, illustrated in Figure 18, was first stucturally characterized in 1980 [66] The polytungstate framework, consisting of four AsW_9O_{33} anions linked by *cis*-WO_2 groups acts as a cryptand and can accommodate guest cations in two types of site, S_1 at the center and four S_2 as indicated in the Figure. The original structure determination was of an anion with NH_4^+ in S_1 and Co^{2+} in two of the S_2 sites. Subsequent structure determinations of lanthanide derivatives have also been reported.[67] Reaction of $[As_4W_{40}O_{140}]^{28-}$ with UO_2^{2+} yields the anions already described in Section 3.4.2, but reaction with U^{4+} leads to a variety of products. The first report proposed that two octahedral U(IV) centers were incorporated in the As_4W_{40} framework, but no structural information was available.[68] Later studies showed by spectroscopic titration that four U(IV) were bound, but structural investigation of the resulting crystals had to be abandoned as a result of extensive disorder of the uranium centers. Treatment of the mother liquor with guanidinium chloride yielded, after one month, yellow crystals of a guanidinium salt of the anion, $[Na(UO_2)_3(\mu\text{-}OH)(H_2O)_6(WO)As_4W_{40}O_{140}]^{18-}$, shown in Figure 19 [53]

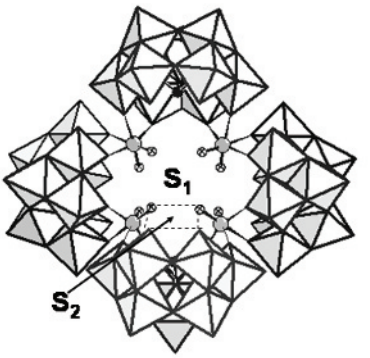

Figure 18. $[As_4W_{40}O_{140}]^{28-}$ (of D_{2d} symmetry) showing the central S_1 and one of the four equivalent S_2 cation binding sites

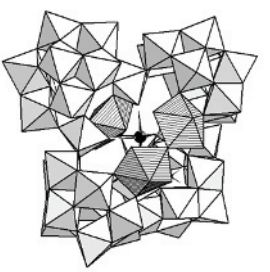

Figure 19. $[Na(UO_2)_3(\mu\text{-}OH)(H_2O)_6(WO)As_4W_{40}O_{140}]^{18-}$

3.6. Derivatives of $[P_5W_{30}O_{110}]^{15-}$

The tungstophosphate discovered by Preyssler in 1970 [69] was originally incorrectly formulated with a P_3W_{18} stoichiometry. A structure determination in 1985 [70] revealed the anion shown in Figure 20. The fivefold symmetry of the anion is based upon the fusion of five hexavacant fragments ($[PW_6O_{22}]^{3-}$) of the Keggin structure. The encapsulated sodium cation, which was shown to be nonlabile on the ^{23}Na-NMR timescale, lies upon the C_5 axis (but not in the equatorial plane) of the anion. Under hydrothermal conditions the sodium can be replaced by cations of a similar size (r ~ 1 Å) i.e. Ca^{2+} and a variety of lanthanide and actinide cations. Subsequent structure determinations of several of these derivatives, as well as a redetermination of the original sodium-encapsulated anion revealed that a water molecule was also incorporated within the central cavity.[71] The position of the central cation and water molecule was

found to vary with the with the cation identity and to some extent with the degree of protonation of the anion. It has proved possible, under more extreme conditions than used initially, to incorporate Th^{4+} , Am^{3+} and Cm^{3+} into the structure.[72] Unlike the case with the same transuranic cations in the Peacock-Weakley complexes $[An(P_2W_{17}O_{61})_2]^{n-}$ noted above, cyclic voltammetry revealed no evidence for oxidation to the tetravalent state. The same situation has been found also for the cerium complex.[73] The very slow exchange reactions involving the Preyssler anion limit the possibility that this complex would lead to practical methods for separation of actinides.

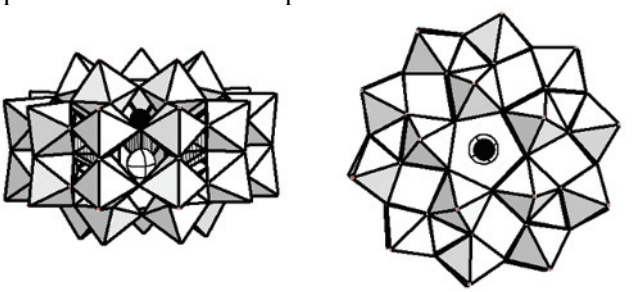

Figure 20. Two views of $[M^{n+}(H_2O)P_5W_{30}O_{110}]^{(15-n)-}$ showing the positions of the encrypted M^{n+} (black sphere) and associated aqua ligand (white cross-hatched sphere).

3.7. Organometallic Derivatives

In efforts to develop organometallic-polyoxometalate reactivity Klemperer and colleagues have reported the non-aqueous synthesis and subsequent solution- and structural characterization of tetra-n-butylammonium salts of $[(\eta^5\text{-}C_5H_5)_3An(\kappa^1\textit{O}\text{-}MW_5O_{19})_2]^{5-}$ (An = Th, U; M = Nb, Ta) [74] and $[((\eta^5\text{-}C_5H_5)_2U(\mu\text{-}\kappa^2\textit{O}\text{-}TiW_5O_{19}))_2]^{4-}$ [75]. Derived from $(\eta^5\text{-}C_5H_5)_3AnCl$ the POMs contain formally tetravalent actinide centers and Lindqvist-type (Figure 3) hexametalate ligands in which a single tungsten atom has been replaced by lower-valent Nb, Ta, or Ti, thereby enhancing the nucleophilicity of that element's terminal oxygen atom. Following the initial reports of these compounds in 1985 no further activity in this area has appeared.

4. Solution equilibria btween actinide cations and polyoxometalate anions

Stability constants for the interaction between Th^{4+} , UO_2^{2+}, NpO_2^{+}, and Am^{3+} and the "complete" polytungstates, $[Na(H_2O)P_5W_{30}O_{110}]^{14-}$ and $[P_2W_{18}O_{62}]^{6-}$ have been measured in 0.1 M NaCl, using solvent extraction. The log β values range from ~3 to ~6 and the order Th > Am >> U > Np for the P_5 anion has been interpreted in terms of steric interactions of the "yl" oxygens with the

surface oxygens of the POM. [76] Similar measurements for the complexation of Th^{4+} and UO_2^{2+} with some other polymolybdates and polyvanadates have been reported, [77–79]

5. Conclusions

In addition to their intrinsic chemical interest, for example novel structures and stabilization of unusual actinide oxidation states, the study of actinide polyoxometalates has been spurred by their potential applications in radionuclide separations and nuclear waste disposal and storage. In both of these areas POMs offer advantages, but at the present state of knowledge they also have limitations. As sequestrants and as transfer agents, the stability of POM structures towards ionizing radiation is generally greater than that of organic sequestrants, but equilibrium constants generally are less favorable. In some cases there are also kinetic limitations. In terms of storage, the thermal conversion of actinide POMs to the corresponding tungsten bronzes offers a potentially attractive route. [40] However the long-term stability of the bronzes under storage conditions has yet to be demonstrated, and there may be an economic or practical barrier; at present the highest loading of a bronze corresponds to a tungsten:actinide ratio of ~10:1.

Acknowledgment

This review was prepared during a visit to Bielefeld University. I thank the Alexander von Humboldt Foundation for generous support, and Professor Achim Müller for his hospitality and for valuable discussions.

References

[1] M. T. Pope, Isopoly and Heteropoly Oxometalates, Springer Verlag, New York 1983,
[2] M. T. Pope, Comprehensive Coordination Chemistry II, J. A. McCleverty and T. J. Meyer, Elsevier Ltd, Oxford, UK, 2004, 4, A.Wedd, ed., 635
[3] C. L. Hill, Comprehensive Coordination Chemistry II, J. A. McCleverty and T. J. Meyer, Elsevier Ltd., Oxford, UK, 2004, 4, A.Wedd, ed., 679
[4] W. N. Lipscomb, Inorg. Chem., 4 (1965) 132
[5] M. T. Pope, Prog. Inorg. Chem, 39 (1991) 181
[6] C. Rong and M. T. Pope, J. Am. Chem. Soc., 114 (1992) 2932
[7] Chem. Rev., Special Issue on Polyoxometalates, C.L. Hill, ed., 98 (1998) 1
[8] V. I. Spitsyn, Radiokhimiya, 27 (1985) 241
[9] A. B. Yusov and V. P. Shilov, Radiochemistry, 41 (1999) 1
[10] G. R. Choppin, J. Nucl. Sci. Technol., (2002) 229
[11] J. J. Berzelius, Pogg. Ann. Phys. Chem, 6 (1826) 351
[12] G. A. Barbieri, Atti Accad. Naz. Lincei, 22 (1913) 781
[13] G. A. Barbieri, Atti Accad. Naz. Lincei, 23 (1914) 805
[14] D. D. Dexter and J. V. Silverton, J. Am. Chem. Soc., 90 (1968) 3589
[15] P. Baidala, V. S. Smurova, E. A. Torchenkova and V. I. Spitsyn, Dokl.Chem. 197 (1971) 202
[16] E. A. Torchenkova, A. M. Golubev, A. S. Saprykin, N. N. Krot and V. I. Spitsyn, Dokl. Chem., 216 (1974) 430
[17] I. V. Tat'yanina, T. S. Chernaya, E. A. Torchenkova, V. I. Simonov and V. I. Spitsyn, Dokl. Chem., 247 (1979) 387
[18] V. W. Day, M. F. Fredrich, W. G. Klemperer and W. Shum, J. Am .Chem. Soc., 99 (1977) 952
[19] V. W. Day and W. G. Klemperer, Science, 228 (1985) 533
[20] S. C. Termes and M. T. Pope, Transition Met. Chem., 3 (1978) 103
[21] M. T. Pope, Inorg. Chem., 11 (1972) 1973
[22] V. N. Molchanov, I. V. Tatjanina, E. A. Torchenkova and L. P. Kazansky, J. Chem. Soc., Chem. Commun., (1981) 93
[23] I. V. Tat'yanina, E. B. Fomicheva, V. N. Molchanov, V. E. Zavodnik, V. K. Bel'skii and E. A. Torchenkova, Sov. Phys., Crystallogr. 27 (1982) 142
[24] M. K. Kotvanova, V. N. Molchanov, E. A. Torchenkova and H. I. Kim, Sov. J. Coord. Chim., 10 (1984) 552
[25] M. K. Kotvanova, V. N. Molchanov, E. A. Torchenkova and V. I. Spitsyn, Russ. J. Inorg. Chem., 29 (1984) 1027
[26] M. A. Petrukhina, V. M. Ionov, A. E. Prozorovskii, V. N. Molchanov, I. V. Tat'yanina and E. Torchenkova, Sov. J. Coord. Chem., 14 (1988) 855
[27] E. P. Samokhvalova, V. N. Molchanov, I. V. Tat'yanina and E. A. Torchenkova, Sov. J. Coord. Chem.. 16 (1990) 683
[28] M. A. Petrukhina, V. S. Sergienko, G. G. Sadikov, I. V. Tat'yanina and E. A. Torchenkova, Sov. J. Coord. Chem.. 16 (1990) 195
[29] E. P. Samokhvalova, V. N. Molchanov, I. V. Tat'yanina and E. A. Torchenkova, Koord. Khim., 16 (1990) 207
[30] M. A. Petrukhina, V. N. Molchanov, I. V. Tat'yanina and E. A. Torchenkova, Sov. Phys. Crystallogr., 35 (1990) 220
[31] E. P. Samokhvalova, M. A. Fedotov, I. V. Tat'yanina and E. A. Torchenkova, Russ. J. Inorg. Chem., 35 (1990) 1200
[32] E. P. Samokhvalova, A. P. Borisova, M. A. Fedotov, I. V. Tat'yanina and E. A. Torchenkova, Russ. J. Inorg. Chem., 34 (1989) 1451

[33] M. A. Petrukhina, M. A. Fedotov, I. V. Tat'yanina and E. A. Torchenkova, Russ. J. Inorg. Chem., 34 (1989) 1782
[34] N. Belai, M. Sadakane and M. T. Pope, J. Am. Chem. Soc., 123 (2001) 2087
[35] J. Iball, J. N. Low and T. J. R. Weakley, J. Chem. Soc., Dalton Trans., (1974) 2021
[36] W. P. Griffith, N. Morley-Smith, H. I. S. Nogueira, A. G. F. Shoair, M. Suriaatmaja, A. J. P. White and D. J. Williams, J. Organomet. Chem., 607 (2000) 146
[37] A. M. Golubev, L. P. Kazanskii, E. A. Torchenkova, V. I. Simonov and V. I. Spitsyn, Dokl. Chem. 221 (1975) 198
[38] I. A. Charushnikova, A. Y. Garnov, N. N. Krot and S. B. Katser, Radiochemistry, 39 (1997) 424
[39] A. S. Saprykin and V. I. Spitsyn, Sov. Radiochem, 18 (1976) 93
[40] K. Wassermann, M. T. Pope, M. Salmen, J. N. Dann and H.-J. Lunk, J. Solid State Chem., 149 (2000) 378
[41] R. D. Peacock and T. J. R. Weakley, J. Chem. Soc. A, (1971) 1836
[42] C. Tourné and G. Tourné, Rev. Chim. Minerale, 14 (1977) 83
[43] C. M. Tourné, G. Tourné and M. C. Brianso, Acta Crystallogr., Sect. B, 36 (1980) 2012
[44] A. V. Botar and T. J. R. Weakley, Rev. Roum. Chim., 18 (1973) 1155
[45] G. Marcu, M. Rusu and A. V. Botar, Rev. Roum. Chim., 19 (1974) 827
[46] A. S. Saprykin, V. P. Shilov, V. I. Spitsyn and N. N. Krot, Dokl. Chem., 226 (1976) 114
[47] V. N. Kosyakov, G. A. Timofeev, E. A. Erin, V. I. Andreev, V. V. Kopytov and G. A. Simakin, Sov. Radiochem. 19 (1977) 418
[48] V. N. Molchanov, L. P. Kazanskii, E. A. Torchenkova and V. I. Simonov, Sov. Phys. Crystallogr., 24 (1979) 96
[49] M. A. Fedotov, V. I. Molchanov, L. P. Kazanskii, E. A. Torchenkova and V. I. Spitsyn, Dokl. Chem. 245 (1979) 112
[50] L. P. Kazansky and M. A. Fedotov, J. Chem. Soc., Chem. Commun., (1983) 417
[51] R. Contant and J. P. Ciabrini, J. Chem. Res., Synop., (1977) 222
[52] A. Ostuni, R. E. Bachman and M. T. Pope, J. Cluster Sci., 14 (2003) 431
[53] K.-C. Kim, A. Gaunt and M. T. Pope, J. Cluster Sci., 13 (2002) 423
[54] C. Craciun and L. David, J. Alloys Compds, 323-324 (2001) 743
[55] M. Rusu, G. Marcu, D. Rusu, C. Rosu and A.-R. Tomsa, J.Radioanal. Nucl.. Chem., 242 (1999) 467
[56] W. H. Knoth, P. J. Domaille and R. L. Harlow, Inorg. Chem., 25 (1986) 1577
[57] M. H. Alizadeh, H. Eshtiagh-Hosseini and R. Khoshnavazi, J. Mol. Struct., 688 (2004) 33
[58] K.-C. Kim and M. T. Pope, J. Am. Chem. Soc., 121 (1999) 8512
[59] A. J. Gaunt, I. May, M. Helliwell and S. Richardson, J. Am. Chem. Soc., 124 (2002) 13350
[60] C. Rosu, M. Rusu and C. Ciocan, Revista de Chimie, 53 (2002) 157
[61] A. J. Gaunt, I. May, R. Copping, A. I. Bhatt, D. Collison, O. D. Fox, K. T. Holman and M. T. Pope, Dalton Trans., (2003) 3009
[62] C. Craciun, L. David, D. Rusu, M. Rusu, O. Cozar and G. Marcu, J. Radioanal. Nucl. Chem., 247 (2001) 307
[63] K.-C. Kim and M. T. Pope, J. Chem. Soc., Dalton Trans., (2001) 986
[64] A. J. Gaunt, I. May, D. Collison, K. T. Holman and M. T. Pope, J. Mol Struct., 656 (2003) 101
[65] M. Åberg, Acta Chem. Scand., A32 (1978) 101
[66] F. Robert, M. Leyrie, G. Hervé, A. Tézé and Y. Jeannin, Inorg. Chem, 19 (1980) 1746
[67] K. Wassermann and M. T. Pope, Inorg. Chem., 40 (2001) 2763
[68] M. Rusu, A. Botar and A. Curticapean, Rev. Roum. Chim., 41 (1996) 687
[69] C. Preyssler, Bull. Soc. Chim. France, (1970) 30
[70] M. H. Alizadeh, S. P. Harmalker, Y. Jeannin, J. Martin-Frère and M. T. Pope, J. Am. Chem. Soc., 107 (1985) 2662

[71] K.-C. Kim, M. T. Pope, G. J. Gama and M.H. Dickman, J. Am. Chem. Soc., 121 (1999) 11164
[72] M. R. Antonio, C. W. Williams and L. Soderholm, J. Alloys Compds, 271/3 (1998) 846
[73] M. R. Antonio and L. Soderholm, Inorg. Chem, 33 (1994) 5988
[74] V. W. Day, W. G. Klemperer and D. J. Maltbie, Organometallics, 4 (1985) 104
[75] V. W. Day, C. W. Earley, W. G. Klemperer and D. J. Maltbie, J. Am. Chem. Soc., 107 (1985) 8261
[76] G. R. Choppin and D. E. Wall, J. Radioanal. Nucl. Chem., 255 (2003) 47
[77] A. Saito and J. Shibukawa, J. Radioanal. Nucl. Chem., 126 (1988) 189
[78] A. Saito and G. R. Choppin, Radiochim. Acta, 68 (1995) 221
[79] A. Saito and G. R. Choppin, J. Alloys Compds., 271-273 (1998) 751

This page intentionally left blank

Structural Chemistry of Inorganic Actinide Compounds
S.V. Krivovichev, P.C. Burns & I.G. Tananaev (Editors)

Chapter 10

Coordination interaction of transuranium elements with N-donor ligands

Grigory B. Andreev,[a] Nina A. Budantseva,[a] Alexander M. Fedoseev[a]

[a]*Institute of Physical Chemistry and Electrochemistry of Russian Academy of Sciences, Leninsky pr., 31, Moscow, 119991, Russia*

1. Introduction

This chapter discusses the current state of the art in research on the interaction of the transuranium elements (TRUE) with N-donor ligands. Two main directions of the investigation can be distinguished. The first one relating to the problems inherent in long-term storage and disposal of nuclear wastes results from the concern about the fate of the radioactive elements in the environment [1-6]. Compounds that can coordinate to actinides through one or several nitrogen atoms are of a great variety and occur widely in the biosphere. For example, imidazole, pyridine and their derivatives are the building blocks of many biologically important molecules [7]; triazines are known to occur in some aquatic plants [8]. The presence of anthropogenic organic agents like amine-N-carboxylic acids in surface waters has the potential to remobilize metals from sediments and aquifers and to influence their bioavailability [9]. The interaction of radionuclides with such ligands needs to be studied in detail to give fundamental understanding the conditions of the incorporation of long lived α-emitters (Np and Pu primarily) into the food chain since they can present hazard to living beings [10-13]. Another aspect of the same problem is the design of new chelating ligands for selective coordination of actinde ions and their decorporation as an alternative to the traditional sequestering agents like DTPA that can exhibit toxicity [14-16]. The variety of oxidation states of the actinide cations and the simultaneous presence of more than one of these states in solution complicate their behavior. In the environmental conditions the most stable oxidation state of Np is pentavalent [1,17-19]. Under biological and physiological conditions organic agents cause disproportionation resulting in

only the Pu (IV) complexes [20-23]. For Am and Cm, only trivalent state is environmentally important [24,25].

The second problem is the separation of long-lived minor actinides (Np, Am, Cm) and their transmutation into short-lived isotopes by irradiation of neutrons. The challenge here is to separate actinides from lanthanides (both being in trivalent state under conditions of the separation porocess) which absorb neutron effectively and in so doing make difficulties for transmutation of actinides. Similarities in chemical behavior of An(III) and Ln(III) causes the difficulties in the separation of these cations and call for design of new highly selective ligands with soft donors, such as nitrogen, for solvent extraction [26]. Polydentate N-donor ligands, well known or modified, are now considered to be very promising [27-41]. However, in spite of large number of N-donor extractants studied, the structural properties of interaction between these ligands and actinides remain unexplored.

It should be noted that some data on complexation of transuranium elements with various N-donor ligands, such as azide ion, isothiocyanate ion, amine-N-polycarboxylic and heterocyclic acids, 8-hydroxyquinoline and its derivatives, were published as early as 1950-1970 [42-77]. The quantitative parameters of complexation (number and composition of complexes, stability constants, thermodynamic parameters) were determined using accessible at that time methods (spectrophotometry, potentiometry, ion exchange, solvent extraction). It was shown that transuranium elements in different oxidation states can form complexes with N-donor ligands. However, only presumptive conclusions regarding structure of complexes were drawn at that time.

A detailed study of structures of the compounds is crucial for understanding the relationship between the architecture of the ligands and their binding affinity for transuranium elements [78,79]. The X-ray single crystal diffractometry became conventional technique as applied to the investigation of transuranium elements in spite of difficulties regarding safe handling of radionuclides. This technique provides unambiguous information about modes of the ligand coordination to the metal ion and geometrical parameters of complexes. Moreover, the employment of a synchrotron radiation shows considerable promise for determination of solid state structures [80] as well as obtaining structural information on complexation in solution [81].

Despite only a little number of solid complexes with N-donor ligands have been studied, the results of crystallographic studies along with the complexation data allow conclusion on the significant affinity of several mono- and polydentate N-donor ligands for both monoatomic cations $An^{3+/4+}$ and oxocations $AnO_2^{+/2+}$ [82-105].

The Chapter is divided into several sections, each concerning specific oxidation state (from 3+ to 6+). The ligands being considered are classified into following

main groups: heterocyclic ligands containing ionogenic functional groups, neutral heterocyclic ligands, amine-N-polycarboxylic acids, and ligands with simple structure (azide, cyanide, isothiocyanate ions, acetonitrile, etc.) (Fig. 1).

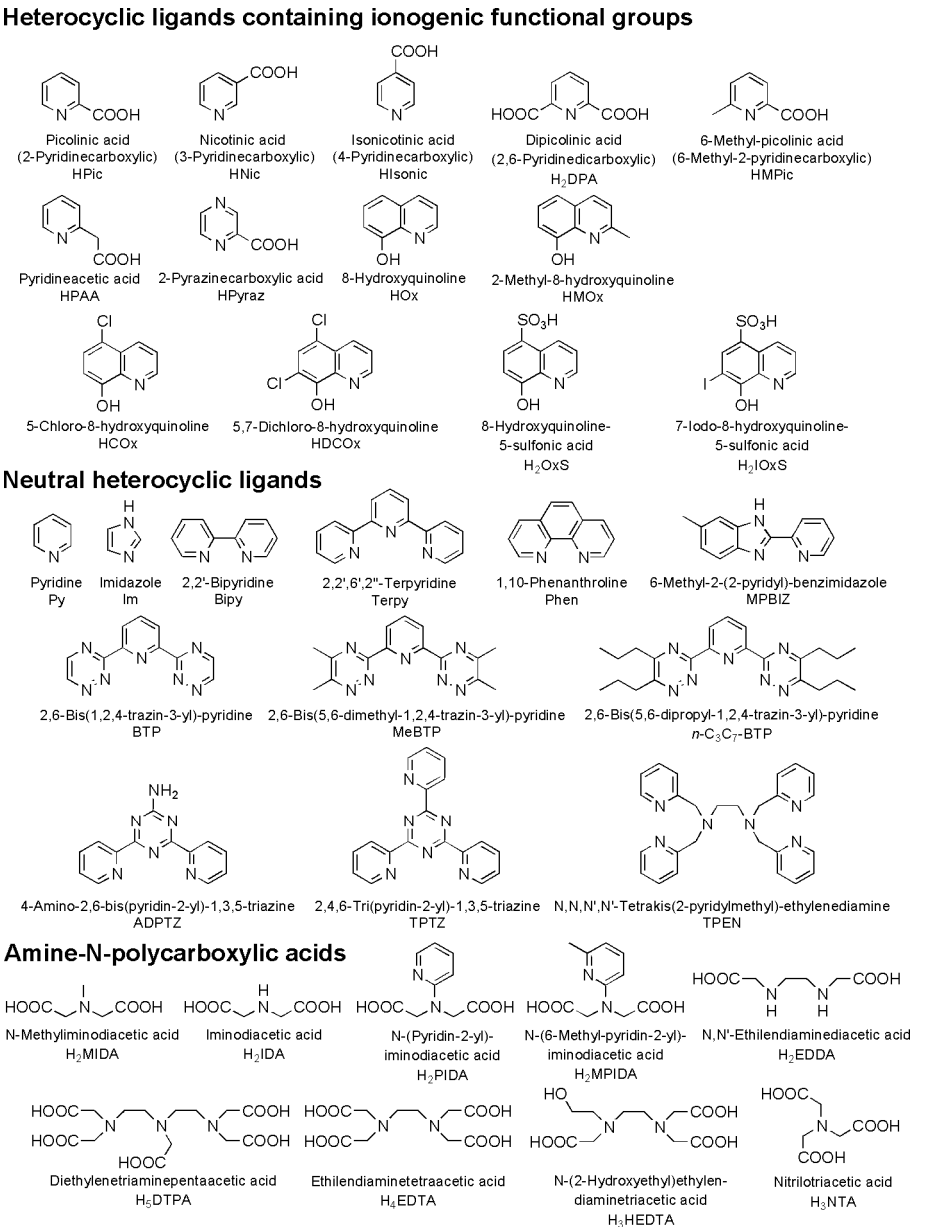

Fig. 1. Molecular structures and nomenclature of ligands.

2. Trivalent transuranium elements

2.1. Interaction with azide, acetonitrile, isothiocyanate

Plutonium complex with acetonitrile $[Pu(NCCH_3)_9](PF_6)_3 \cdot NCCH_3$ (**1**) represents the only structurally characterized solid compound of trivalent transuranium element with coordination of N-donor ligand [93]. In the crystal structure of **1**, the Pu atom is surrounded by nine acetonitrile molecules with nitrogen atoms forming tricapped trigonal prism (Fig. 2). The apical Pu-N distances are equal to 2.565(4)-2.591(4) Å, the capping distances lie in the range from 2.554(4) to 2.573(4) Å. The most significant deviation of angles from the ideal values are 131.0(1)º for N(1)Pu(1)N(7) and 102.6(1)º for N(7)Pu(1)N(3). The angle between the top (N(5)N(2)N(8)) and bottom (N(6)N(9)N(4)) planes of the prism is equal to 13º. The average Pu-N distance in the complex **1** (2.572 Å) is longer than usual Pu-O distances found, for example, in nine-coordinated aquo complex $[Pu(H_2O)_9](O_3SCF_3)_3$ (2.525 Å) [106].

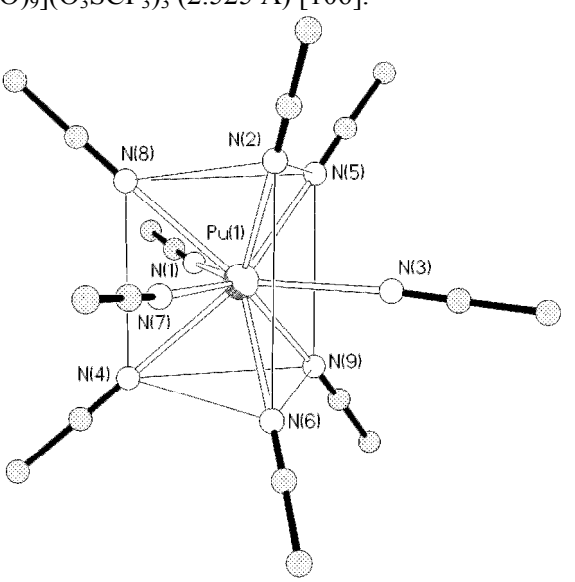

Fig. 2. Coordination polyhedron of Pu in $[Pu(NCCH_3)_9][PF_6]_3 \cdot NCCH_3$. This figure is generated from the data downloaded from the Cambridge Crystallographic Database as published originally in Ref. [93].

Interaction of An(III) with azide and isothiocyanate ions in solution was studied extensively [10,54,56,58,108]. Complexation of Am(III) with azide ion was studied by means of HTTA solvent extraction in the work [108]. Stability constant for 1:1 complex was found to be β_1=18 that is significantly lower than

for d-elements (β_1~10^5). From NMR (N^{15}) and EPR spectra it was concluded that azide ion coordinates to metal atom through one nitrogen atom in monodentate fashion, with M-N distance equal to 2.75 Å. In contrast to isothiocyanate complexes, complex with azide has nonlinear configuration.

Stability constants for complexes with NCS ion were determined by means of solvent extraction (Table 1). Thermodynamic parameters were calculated for $[Am(NCS)]^{2+}$ complex: ΔG=-0.69±0.02 kcal/mole, ΔH=-4.36±0.30 kcal/mole, ΔS=-12.3±1.0 kcal/K·mole [56]. Later, stability constants for $[Pu(NCS)]^{2+}$ and $[Pu(NCS)_2]^{+}$ complexes were measured at T=303K to be β_1=2.18±0.17 and β_2=4.10±0.21 [54]. Authors of work [58] found values β_1=0.33±0.03 and β_2=0.30±0.26 at T=298K using HDNNS solvent extraction, it was also shown that only $[Pu(NCS)]^{2+}$ complex is formed at [NCS]<0.4M. The ion exchange method was used in [10], where the values of stability constants for complexes $[Pu(NCS)]^{2+}$ and $[Pu(NCS)_2]^{+}$ were found to be lower than in other works and equal to $\log\beta_1$=0.04 and $\log\beta_2$=-0.1. Hence, different literature data indicate low complexing ability of NCS ion in relation to An(III), and no complexes other than $[An(NCS)]^{2+}$ and $[An(NCS)_2]^{+}$ can form in solution.

Table 1. Stability constants for complexes of An(III) with NCS-ion (I=1, T=298K).

	Pu	Am	Cm	Cf
K_1	2.90±0.31	3.19±0.10	2.70±0.19	3.06±0.18
K_2	1.95±0.24	2.2±0.3	2.6±0.4	

2.2. Interaction with ionogenic heterocyclic ligands

Picolinic acid forms with TRUE(III) the series of chelates with compositions [ML], $[ML_2]$ and $[ML_3]$ as is seen from the spectrophotometrical data [44]. Characteristic of nicotinic acids is the formation of protonated complex $[MHL]^{3+}$ in parallel with normal complex $[ML]^{2+}$. Ion exchange technique was used for determination of stability constans for complexes of Am and Cm with picolinic and dipicolinic acids, while stability constant for protonated complex with nicotinic acids was calculated from the spectral data (Table 2).

Formation of complexes with ratio M:L = 1:3 is observed for the 8-hydroxyquinoline and its derivatives [44]. Americium and plutonium solid compounds were obtained in the form of complexes $[Am(Ox)_3]$, $[Pu(Ox)_3]$, $[Am(DCOx)_3]$, $[Am(MCOx)_3]$. Chelates with halogenated 8-hydroxyquinoline are better extractable from the solution than complexes with 8-hydroxyquinoline. Plutonium (III) easily oxidizes in the presence of 8-

hydroxyquinoline, so the synthesis of $[Pu(Ox)_3]$ is only possible in the oxygen-free atmosphere.

Table 2. Formation constants for An(III) complexation with pyridinecarboxylic acids (I=0.1, T=298K).

M	L	log β_H	log β_1	log β_2	log β_3
Am	Pic^-		4.07	7.15 (calc. from sp. data)	
			4.28	7.99	10.51
	Nic^-	0.88 (calc. from sp. data)			
	DPA^{2-}		9.34	16.51	
Cm	Pic^-		4.38	8.01	10.83
	DPA^{2-}		9.33	16.64	

2.3. Interaction with amine-N-polycarboxylic acids

Amine-N-carboxylic acids are suitable as potential agents for separation TRU(III) and Ln(III) showing high separation factors and radiation stability. Interaction of An(III) with NTA was studied in the work [75]. Stability constants for [M(NTA)] and $M[(NTA)_2]^{3-}$ complexes were determined by ion exchange technique in 0.1 M NH_4ClO_4 in the pH range from 2.54 to 3.9. Average values are equal to $\beta_1=(4.8\pm0.2)\cdot10^{11}$, $\beta_2=(2.93\pm0.15)\cdot10^{20}$ and $\beta_1=(8.6\pm0.2)\cdot10^{11}$, $\beta_2=(8.8\pm0.3)\cdot10^{20}$ for Am and Cm, respectively. Behavior of Pu(III) in the presence of NTA was studied by potentiometry at μ=1 and T=298K. For complexes with M:NTA ratio of 1:1 and 1:2, the stability constants $\log K_1$=10.26 and $\log K_2$=9.39 were obtained. The formation of protonated complexes is also possible in this system [49].

The reaction of Pu with EDTA was investigated, and formation constants β_1=16.04, β_2=4.27 were determined. Existence of mixed complexes Pu:NTA:EDTA of composition 1:1:1 was shown, with stability constant equal to $\log K$=5.76 [49]. Thermodynamic characteristics for Am and Pu complexation with EDTA were calculated in the work [52]. The separation factor in the systems of Am or Cm, where 1:2 complexes with HEDTA are formed, is calculated to be equal to 7 [51]. Diethylentriaminepentaacetic acid (DTPA), which can serve as octadentate ligand, forms more stable complexes. Values of stability constants for complexation of transplutonic elements Am-Fm are near the same and equal to 10^{22} as was found by ion exchange technique [50]. The data on complexation of Am, Cm and Cf with different amine-N-polycarboxylic acids studied in the paper [46] are presented in Table 3.

Spectral investigation of the Am^{3+} interaction with MIDA and IDA shown that complex formation is accompanied with appearance of two new absorption bands in the spectrum of initial solution ($[Am^{3+}]=1.25\cdot10^{-3}$M, $[L]=1\cdot10^{-2}$M) [46]. The maxima of these bands are near similar and equal to 504.9, 506.8 and 504.3, 506.3 nm for systems with IDA and MIDA, respectively, although, for MIDA these bands appear at slightly higher pH values. On the analysis of spectra the conclusion was made about the existence of 1:1 and 1:2 complexes with IDA and its derivatives. The data on complexation of Am, Cm and Cf are summarized in Table 3 [46].

Table 3. Stability constants for complexes of Am, Cm and Cf with amine-N-polycarboxylic acids (I=0.1, T=298K).

Ligand	M:L	Am	Cm	Cf
$EDTA^{4-}$	1:1	15.72±0.02	15.93±0.01	16.27±0.02
	1:2	~27.4	~27.2	~28.5
$DTPA^{5-}$	1:1	14.06±0.03	14.43±0.25	
	1:2	23.07±0.08	23.48±0.05	
IDA^{2-}	1:1	7.02±0.01	7.65±0.02	
	1:2	12.39±0.04		
$MIDA^{2-}$	1:1	7.01±0.01		
	1:2	12.51±0.05		
$PIDA^{2-}$	1:1	8.96±0.15	9.21±0.08	
	1:2	17.71±0.02	17.69±0.04	

2.4. Interaction with neutral heterocyclic ligands

In recent years, a large number of polydentate heterocyclic ligands showing high resistivity to hydrolysis and radiolysis have been studied. The application of such ligands to separation problem was researched in many works [27-41,81,109,110]. As a rule, these works present data on separation factors, number and composition of complexes in solution. But indirect techniques do not give any information on structure of the complexes, and adequate structural investigations are rare.

Complex formation of Cm and Eu with 2,6-bis(5,6-dipropyl-1,2,4-triazin-3-yl)-pyridine (n-C_3H_7-BTP) was studied by means of EXAFS and TRLFS in the work [29]. The structures of complexes [Cm(n-C_3H_7-BTP)$_3$] and [Eu(n-C_3H_7-BTP)$_3$] were found to be very similar. The central atom coordinates three

molecules of the ligand, the coordination number is equal to 9, and M-N distances in the first coordination shell are almost equal in both cases, 2.568(7) and 2.559(8) Å for Cm and Eu, respectively. The number of atoms and distances in other shells were also found to be similar for Cm and Eu.

In addition to conventional shell fitting, authors have used Monte Carlo simulation. During MC calculation, the Cm atom was positioned at random position in the 10 Å diameter sphere formed by three coordinating BTP molecules, and the corresponding theoretical EXAFS spectra were calculated and compared with the experimental spectrum. From the best agreement between the theoretical and experimental EXAFS spectra, the Cm-N distances equal to 2.52 Å and 2.57, 2.59 Å for nitrogen atoms of pyridine and triazine rings, respectively, were obtained.

Authors have also conducted DFT quantum chemistry calculations with several functionals (B3LYP, BHLYP, BLYP, BP, TPSS). Depending on the functional used, the calculated Cm-N distances are equal 2.607-2.668 and 2.606-2.654 Å for pyridine and triazine rings, respectively. By this means, the calculations do not give indication which of the distances is longer one. However, in agreement with the experiments, the DFT calculations give the similar M-N distances for Eu and Cm. From the similarity of coordination spheres of Eu and Cm authors made the conclusion that the observed selectivity of *n*-C_3H_7-BTP ligand for Cm(III) over Eu(III) is not structural in origin, and is related to a higher thermodynamic stability of [Cm(*n*-C_3H_7-BTP)$_3$] complex.

Terdentate 4-amino-2,6-bis(pyridin-2-yl)-1,3,5-triazine (ADPTZ) can coordinate to Am^{3+} and Ln^{3+} with the formation of the 1:1 complexes. In the work [33] the thermodynamic characteristics for the complex formation of Am with ADPTZ were calculated: ΔG=-32.9±0.6 kJ/mole, ΔH=-28.9±3.0 kJ/mole, ΔS=14.0±10.0 J/K·mole. The stability constant equal to $\log\beta_1$=5.8±0.1 for [Am(ADPTZ)] complex was defined using spectrophotometry. The thermodynamic data show that the observed selectivity of the ligand arises from a difference in the enthalpies of complexation for Am and lanthanides. The geometry and electronic structure of the $[M(ADPTZ)(H_2O)_6]^{3+}$ complexes (for M = Am, Cm, Pu) were calculated using DFT theory with no symmetry constraint. Selected distances are presented in Table 4.

Table 4. Calculated M-N and M-O distances (Å) in $[M(ADPTZ)(H_2O)_6]^{3+}$ complexes.

M	M-N(1)	M-N(2)	M-N(3)	<M-O>
Pu	2.474	2.578	2.578	2.617
Am	2.486	2.591	2.589	2.612
Cm	2.467	2.581	2.580	2.591

Each of the rings (pyridine and triazine) is nearly coplanar with dihedral angles no more than 1.9º. The calculated Am-N is longer than Pu-N, whereas the ionic radius of Pu is larger than Am. On the basis of the fact that the mean values of M-O_w distances are longer than M-N for actinides in contrast to lanthanides, the authors make the conclusion that An-N are slightly stronger than the corresponding Ln-N bonds.

In the work [110], the quantum chemistry calculations using relativistic DFT were conducted on $[ML(H_2O)_6]^{3+}$ clusters where M=Pu, Am, or Cm and L=2,2',6',2''-terpyridine (Terpy) or 2,6-bis(5,6-dimethyl-1,2,4-triazin-3-yl)pyridine (MeBTP). The selected distances obtained from the structures optimization, which was conducted without symmetry constraint, are presented in Table 5. To investigate the effect of the coordination surrounding on the metal-ligand bonding, author performed some calculations for clusters containing chloride counterion. It is shown that M-N distances become slightly shorter, but this effect is not significant.

Table 5. Calculated M-N and M-O distances (Å). N_1 corresponds to the central pyridine ring, two N_2 atoms belong to terminal pyridine or triazine rings of Terpy or MeBTP, respectively).

Complex	M-N_1	<M-N_2>	<M-O>
$[Pu(Terpy)(H_2O)_6]^{3+}$	2.538	2.556	2.618
$[Am(Terpy)(H_2O)_6]^{3+}$	2.561	2.566	2.615
$[Cm(Terpy)(H_2O)_6]^{3+}$	2.535	2.545	2.592
$[Pu(MeBTP)(H_2O)_6]^{3+}$	2.610	2.599	2.556
$[Am(MeBTP)(H_2O)_6]^{3+}$	2.624	2.611	2.555
$[Cm(MeBTP)(H_2O)_6]^{3+}$	2.595	2.593	2.533
$[Am(Terpy)(H_2O)_5Cl]^{2+}$	2.58	2.57	
$[Cm(Terpy)(H_2O)_6Cl]^{2+}$	2.56	2.56	
$[Cm(Terpy)Cl_3]$	2.62	2.53	

The EDTA analog, N,N,N',N'-tetrakis(2-pyridylmethyl)ethylenediamine (TPEN), forms stable complexes with lanthanides Ln(TPEN) as shown in the work [111]. The stability constant for Am complex of the similar composition was calculated from potentiometry titration in the work [33]. The $[M(TPEN)]^{3+}$ complex is the major and the $[M(OH)]^{2+}$ is the minor components from the possible $[M(TPEN)]^{3+}$, $[M(OH)]^{2+}$, $[M(HTPEN)]^{4+}$, and $[M(OH)(TPEN)]^{2+}$. Spectrophotometric study of the $[M(TPEN)]^{3+}$ complex confirmed the potentiometry data. The stability constants calculated using two techniques are equal to $\log\beta=6.69\pm0.03$ and $\log\beta=6.77\pm0.01$, respectively. In spite of the fact

that the ionic radius of Am^{3+} and Sm^{3+} are very close (1.115 and 1.098 Å) [112], the value of stability constant for Am complex with TPEN is significantly larger than that for Sm ($\log\beta$=4.70±0.02), that indicates stronger binding of the softer Am compared to the Sm.

Bidentate 6-methyl-2-(2-pyridyl)benzimidazole (MPBIZ) was studied in the work [109], photoluminescence and Raman spectra were shown to be very sensitive to the change in the surrounding of An atom due to the coordination of MPBIZ molecule.

Complex $[Am(MPBIZ)_2]$ is the prevailing component in ethanol solution as shown by means of EXAFS experiment [81]. The MPBIZ molecule coordinates to Am through the nitrogen atoms in bidentate mode. The Am-N distance is equal to 2.63 Å, while the Am-O bonds are shorter. By this means, the MPBIZ ligand appears to be bonded to metal atom weaker than water molecules. The authors made the conclusion that the contribution of the covalent bond to the chemical bonds between Am and N is small.

3. Tetravalent transuranium elements

3.1. Interaction with azide, isothiocyanate

Complex formation of Np(IV) with NCS ion has been extensively studied using TTA and HDNNS solvent extraction with in different conditions [58]. Table 6 presents values of stability constants measured in 2M $NaClO_4$ at 298K.

Table 6. Stability constants for complexes of Np(IV) with NCS ion.

Equilibrium	$\log\beta$(DNNS)	$\log\beta$(TTA)
$Np^{4+}+NCS^{-}=[Np(NCS)]^{3+}$	1.48±0.06	1.49±0.01
$Np^{4+}+2NCS^{-}=[Np(NCS)_2]^{2+}$	2.26±0.05	2.06±0.08
$Np^{4+}+3NCS^{-}=[Np(NCS)_3]^{+}$	2.50±0.02	2.53±0.02

Spectrophotometrical study of the Np(IV) in the presence of NCS ion shown that absorption maxima at 722.5 and 959.5 nm are shifted to lower energy as the NCS concentration rises, that indicates the formation of inner sphere complexes. It should be noted that Pu(IV) is not stable and is reduced to Pu(III) in the presence of NCS ions.

Solid complexes of Np with NCS are described in the works [91,113]. The crystal structure of $\{N(CH_3)_4\}_4[Np(NCS)_8]$ (**2**) consists of anions $[Np(NCS)_8]^{4-}$ and tetramethylammonium cations. Coordination polyhedron of the Np atom,

distorted tetragonal antiprism, is formed by nitrogen atoms with Np-N distances from 2.39(1) to 2.42(1) Å (Fig. 3).

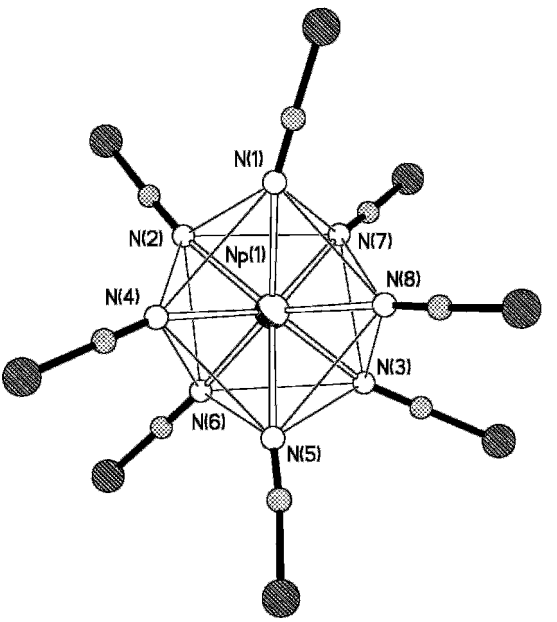

Fig. 3. Coordination polyhedron of Np in $\{N(CH_3)_4\}_4[Np(NCS)_8]$.

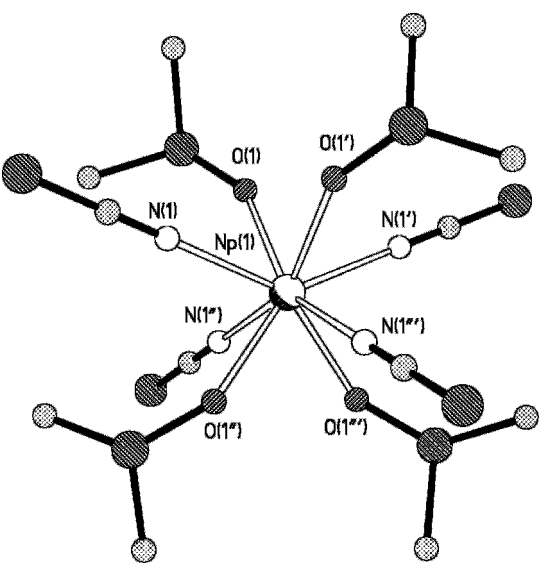

Fig. 4. Coordination surrounding of Np in $[Np(NCS)_4(DMSO)_4]$.

The change of outer sphere cation from tetramethylammonium to tetraethylammonium in the crystal structure of $\{N(C_2H_5)_4\}_4[Np(NCS)_8]$ (**3**) leads to the variation in the structure of Np atom surrounding. In this case, the coordination polyhedron is the tetragonal prism, while the Np-N distances remain near the same, 2.39(2)-2.44(2) Å.
In the crystal structure of $[Np(NCS)_4(DMSO)_4]$, (**4**) the coordination polyhedron of Np atom is formed by nitrogen atoms of NCS ions and oxygen atoms of DMSO molecules (Fig. 4). The Np-N and Np-O distances are equal to 2.44(2) and 2.29(2) Å, respectively.

3.2. Interaction with ionogenic heterocyclic ligands

Interaction of Np(IV) with dipicolinic acid in solution was not investigated. On the other hand, the formation of solid compound with ratio Np to DPA equal to 1:3 is observed [117]. Crystal structure of the complex $\{H_3NCH_2CH(NH_3)CH_3\}[Np(DPA)_3]\cdot 1.5H_2DPA\cdot H_2O$ (**5**) consists of two crystallographically unique anions $[Np(DPA)_3]$, both having the same structure, 1,2-diammoniopropane cations, water molecules and molecules of noncoordinated dipicolinic acid. Neptunium atom is surrounded by three DPA^{2-} anions acting as terdentate ligands (Fig. 5).

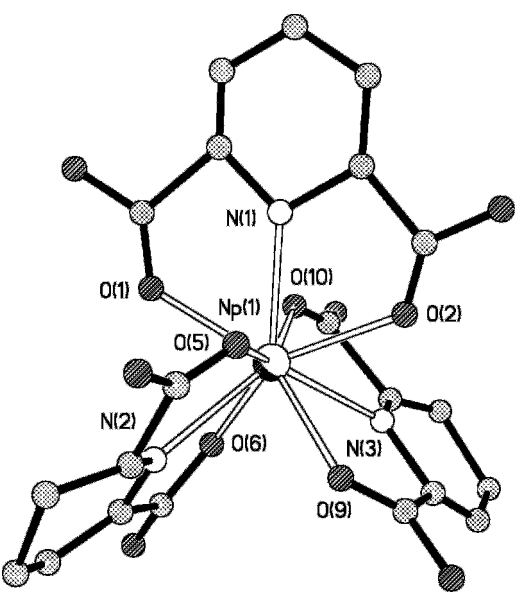

Fig. 5. Coordination surrounding of one of crystallographically unique Np atoms in the structure of $\{H_3NCH_2CH(NH_3)CH_3\}[Np(DPA)_3]\cdot 1.5H_2DPA\cdot H_2O$.

Neptunium and plutonium complexes [AnL_4] with 8-hydroxyquinoline and its derivatives were obtained in the form of solid compounds (L=Ox, MOx, COx, DCOx) [62]. In all cases the coordination number of metal atom is equal to 8, while Th(IV) and U(IV) are known to form complexes $H[M(Ox)_5]$ [114]. Stability constants were determined by solvent extraction and are equal to $\log\beta_4$=45.28 and $\log\beta_4$=46.05 for Np complexes with Ox and DCOx, respectively [62].
Tetravalent neptunium forms complexes with picolinic acid even at pH~1. In the spectrum of Np, the new low intensity absorption band at 967 nm appears in the presence of picolinic acid. From the spectrophotometrical data the formation of the chelate [Np(Pic)] with the stability constant of $\log\beta_1$=6.50±0.01 was determined [47].

3.3. Interaction with amine-N-polycarboxylic acids

In the spectrum of Np, the new absorption band at 972.9 nm appears in the presence of NTA [47,74]. Formation constants for complexes $[Np(NTA)]^+$ and $[Np(NTA)_2]^{2-}$ were calculated from the spectral data to be $\log\beta_1$=17.28±0.02 and $\log\beta_2$=32.06±0.07. The EXAFS spectrum of Np complex with NTA was investigated in the work [118]. Assuming the coordination number 8 for Np atom, the Np-N and Np-O distances were calculated for $[Np(NTA)_2]$ complex to be equal to 2.63 and 2.35 Å, respectively.
Solid Np compounds with EDTA were derived from the acidic solutions (~0.5 M HCl). Compositions of the complexes, $Np(EDTA)\cdot 3H_2O$, $(NH_4)_2H_2Np_2(EDTA)_3\cdot nH_2O$, $Ba_2Np_2(EDTA)_3\cdot nH_2O$, were determined by elemental analysis and thermogravimetry [119].
Interaction of Np(IV) and Pu(IV) with EDTA in solution has been studied extensively [68-70,74,120,121]. The data on complex formation of An with EDTA are summarized in Table 6.

Table 6. Stability constants for complexes of Np(IV) and Pu(IV) with EDTA.

Complex	log *K*	Ionic strength	Reference
[NpEDTA]	24.40	0.5	[76]
[NpEDTA]	24.55	1.0	[74]
[NpEDTA]	25.77	1.0	[119]
[PuEDTA]	25.6	0.1	[70]
[PuEDTA]	24.2	0.1	[68,69]
[PuEDTA]	26.44	1.0	[121]

Taking into account that Pu ion can accommodate up to 12 ligand donor atoms in its inner coordination sphere, authors of the work [121] undertook the study of the mixed-ligand Pu complexes with EDTA and ligands which are able to displace coordinated solvent from Pu-EDTA complex. Formation of the coordinatively saturated complexes with citrate and carbonate ions, $[Pu(EDTA)(citrate)]^{3-}$ and $[Pu(EDTA)(carbonate)]^{2-}$, was investigated using potentiometry. The stability constants values equal to $\log\beta$=33.46±0.30 and $\log\beta$=35.51±0.15, respectively, were calculated.

Octadentate anion $DTPA^{5-}$ forms stable complexes with Np in solution. In contrast to EDTA, the absorption band of $[Np(DTPA)]^-$ with maximum at 983 nm is very broad and has low intensity. Based on the spectrophotometry stability constant $\log\beta_1$=30.33±0.12 was calculated [47,74]. In the work [122], the similar value, $\log\beta_1$=29.29±0.02, was obtained using the same technique. Ion exchange measurement yields the value $\log\beta_1$=30.96 [53]. Potentiometry titration gives very similar value for Pu(IV), $\log\beta_1$=29.49±0.10 [123].

3.4. Interaction with neutral ligands

Interaction of Pu with N-donor ligands with structures similar to those of amine-N-olycarboxylic acids but containing hydroxyalkyl groups instead of carboxylic groups (Fig. 6) was investigated by potentiometry in the work [124].

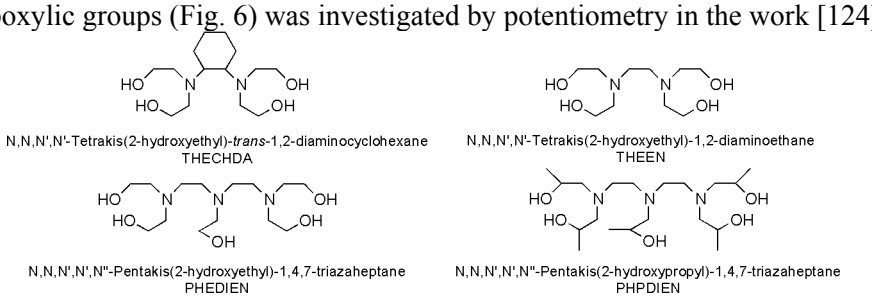

Fig. 6. Ligands discussed in the Ref. [124].

Table 7. Stability constants for Pu(IV) complexes with ligands containing hydroxyalkyl groups.

Ligand	Equilibrium	log *K*	Ligand	Equilibrium	log *K*
PHPDIEN	$M+2L+H=ML_2H$	30.42±0.06	THECHDA	$M+L=ML$	15.61±0.01
	$M+2L+OH=ML_2H_{-1}$	34.74±0.02		$ML+L=ML_2$	8.77±0.02
	$M+L+OH=MLH_{-2}$	35.55±0.01	THEEN	$M+L+3OH=MLH_{-3}$	42.15±0.01
PHEDIEN	$M+2L=ML_2$	24.20±0.01		$M+2L=ML_2$	20.76±0.02

PHPDIEN shows a greater ability to stabilize Pu against hydrolysis than PHEDIEN (Table 7). THECHDA being the preorganized ligand with donor

groups rigidly held in positions which stereochemically favor complexation shows higher logβ_2 value than THEEN.

Two Np(IV) complexes containing Bipy were derived from highly acidic solutions ([HNO_3]>8M). In both cases Bipy does not show its chelating ability and acts as outer sphere cation H_2Bipy^{2+}. Crystal structure of $H_2Bipy[Np(NO_3)_6]\cdot 2H_2O$ consists of isolated anions $[Np(NO_3)_6]^{2-}$ and cations H_2Bipy^{2+} which exhibit trans-configuration [115]. The angle between pyridine rings is 32º. In the crystal structure of $(H_2Bipy)_2[Np(NO_3)_6](NO_3)_2\cdot 2H_2O$, H_2Bipy^{2+} cation has the similar geometry with dihedral angle between pyridine rings of 22º [116].

4. Pentavalent transuranium elements

4.1. Interaction with ionogenic heterocyclic ligands

Pentavalent neptunium forms with monopyridinecarboxylic acids (picolininc, nicotinic, isonicotinic) solid complexes of different compositions. For picolinic acid, solid compounds with Np:Pic ratio from 1:1 to 1:3 were synthesized and characterized using X-ray single crystal crystallography [101]. For nicotinic and isonicotinic acids only 1:1 complexes were obtained. In all cases heterocyclic nitrogen atom participates in the formation of coordination bonds with metal atom.

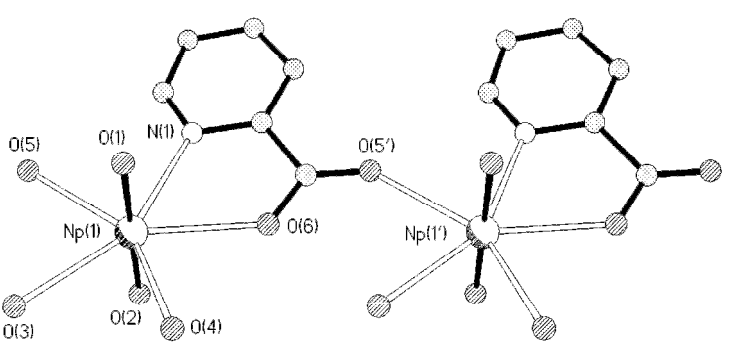

Fig. 7. Molecular structure of $[NpO_2(Pic)(H_2O)_2]$.

The crystal structure of complex $[NpO_2(Pic)(H_2O)_2]$ (**6**) consists of infinite chains situated along [100] direction (Fig. 7). Equatorial plane of each Np atom is formed by one nitrogen atom, two oxygen atoms of two different picolinate-ions and two water molecules. Neptunyl group NpO_2 is near linear and symmetrical with Np-O distances equal to 1.827(9) and 1.837(9) Å. Picolinate-

ion acts as tridentate bridging ligand connecting adjacent Np atoms through the carboxylic group. The ligand forms with Np atom five-membered metallo-ring, with the angle of 2.9º between the ring plane and least-squares equatorial plane.
There are three crystallographically independent Np atoms in the crystal structure of $\{C(NH_2)_3\}[NpO_2(Pic)_2(H_2O)]\cdot{}^{11}/_3H_2O$ (**7**) [125]. All three Np atoms have similar surrounding. The picolinate ions are bidentate chelate ligands in this structure. By this means, the equatorial planes of Np atoms are formed by nitrogen and oxygen atoms of two picolinate ions and one water molecule. This structure could not be solved with good accuracy due to poor quality of single crystal, so only model of the structure for this compound can be presented.
Compound $Cs[NpO_2(Pic)_2(HPic)]\cdot 3H_2O$ (**8**) consists of isolated $[NpO_2(Pic)_2(HPic)]$ groups (Fig. 8), Cs cations and solvate water molecules. Surrounding of Np is very similar to that in the structure **7**, but one protonated picolinate ion enters in the equatorial plane in **8** rather than water molecule in **7**. The equatorial Np-N and Np-O distances are equal to 2.598(4)-2.614(4) and 2.408(4)-2.445(3) Å, respectively. The mean deviation of atoms from the least-squares equatorial plane is equal to 0.047 Å. The picolinate anions are bidentate chelating ligands, while protonated HPic group coordinates to the metal center through oxygen atom of the carboxylic group. The axial Np-O distances are equal to 1.831(4) and 1.814(4) Å.

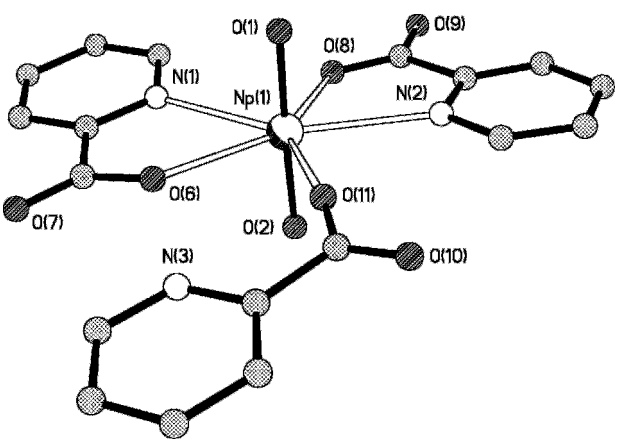

Fig. 8. Surrounding of Np atom in $Cs[NpO_2(Pic)_2(HPic)]\cdot 3H_2O$. In the structure of **7** Np atom has the similar surrounding with the only difference that HPic group is replaced with water molecule.

In compounds $[NpO_2(Nic)(H_2O)]$ (**9**) and $[NpO_2(Isonic)(H_2O)]$ (**10**), neptunyl ions act as monodentate ligands with one of O atoms entering in the equatorial plane of coordination polyhedron of the adjacent Np atom. The presence of the cation-cation bonds in the structures of **9** and **10** results in the formation of infinite cation-cation chains $[NpO_2(Nic)(H_2O)]_\infty$ and $[NpO_2(Isonic)(H_2O)]_\infty$

extending along directions [010] and [100], respectively. In addition to cation-cation bonds, adjacent neptunium atoms are linked by carboxylic groups of nicotinate and isonicotinate ions acting as tridentate bridging ligands. As a result, each Np atoms in the chain is linked to the adjacent metal atom through the oxygen of the neptunyl ion and through the carboxylic so that Np-O(neptunyl)-Np'-O-C-O cycle forms.

The equatorial planes of Np coordination polyhedra in **9** and **10** are formed by oxygen atoms of adjacent neptunyl ion, one nitrogen and two oxygen atoms of three different nicotinate or isonicotinate ions, and one water molecule (Fig. 9). The Np-O axial distances of neptunyl ion are different for bridging and terminal oxygen atoms and equal to 1.857(5) Å (for **9**), 1.837(8) Å (for **10**) and 1.813(6) Å (for **9**), 1.810(8) Å (for **10**), respectively.

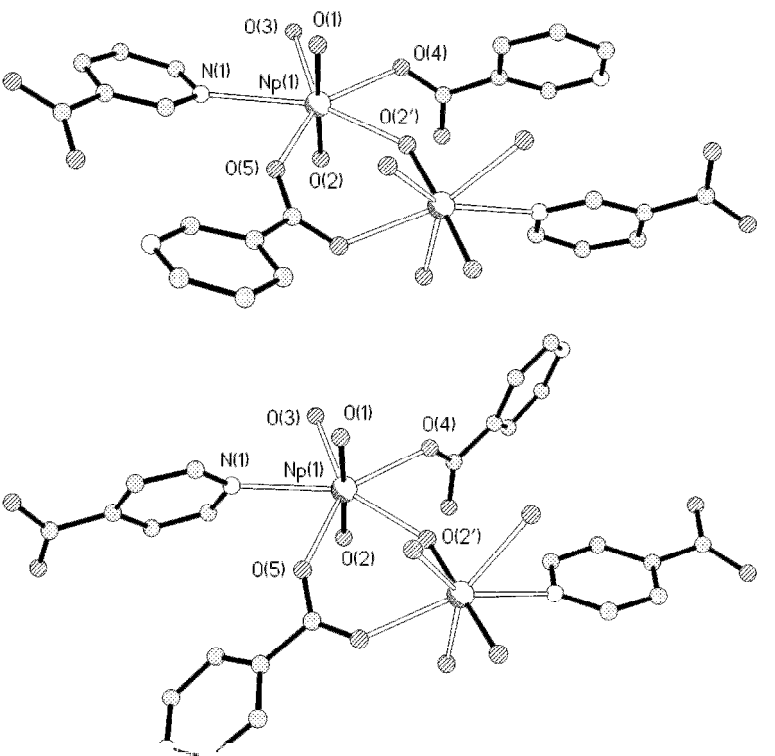

Fig. 9. Structure of cation-cation bonds in $[NpO_2(Nic)(H_2O)]$ (top) and $[NpO_2(Isonic)(H_2O)]$ (bottom).

Compounds **6-10** represent complexes of pentavalent neptunium with all isomers of pyridinemonocarboxylic acids. In all compounds, Np atom was found in seven coordinated pentagonal bipyramidal geometry where axial

position are occupied by O atoms of neptunyl group, with the donor atoms of ligands accommodated in the equatorial plane. However, distinct topologies are observed due to the different connectivity of coordination polyhedra. In the compound **6** adjacent Np atoms are connected into infinite chains by picolinate ions. Compounds **7** and **8** represent structures with isolated Np atoms.
In both structures of **9** and **10** neptunyl ion acts as monodentate bridging ligand providing one oxygen atom to the equatorial plane of the neighboring Np atom. In both cases this leads to the formation of infinite chains, where adjacent Np atoms are connected through neptunyl ion and carboxylic group of the anion. But the difference in the location of carboxylic group in anions of nicotinic and isonicotinic acids in relation to nitrogen atom of pyridine ring results in different packing of the chains in the structures of **9** and **10**. As a consequence, structure **9** has layered topology, while structure **10** has the three-dimensional one (Fig. 10).

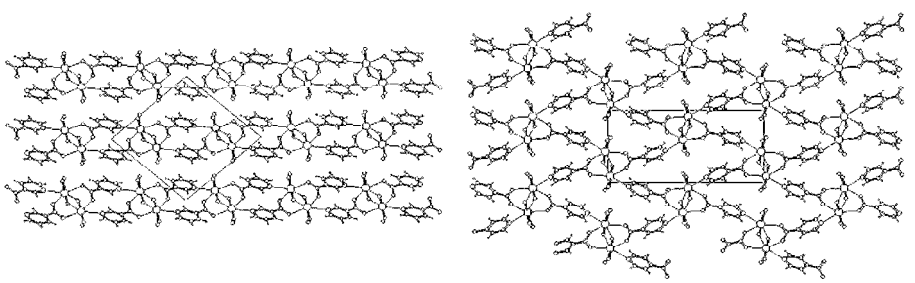

Fig. 10. The packing of infinite cation-cation chains in **9** (left) and **10** (right) viewed along the chains.

The NIR spectra of solid compounds **6-10** were measured [101]. The positions of absorption bands of solid $[NpO_2(Pic)(H_2O)_2]$ and complex particle $[NpO_2(Pic)]$ in solution were found similar. It may be concluded that the coordination spheres of Np atom are close in both cases, that is, in solution the picolinate ion coordinates to Np with the formation of chelate ring. Alternatively, significant shifts of absorption band to lower energies were observed in spectra of neptunium nicotinate and isonicotinate as the result of the formation of cation-cation structures in solid **9** and **10**.
Dipicolinic acid, being the polyfunctional ligand, can coordinate to metal in different fashion as shown for U(VI), which form with DPA complexes of various topology and ratio. For Np(V), only 2:1 and 1:2 complexes with DPA have been obtained.
Crystal structure $[(NpO_2)_2(DPA)(H_2O)_5]$ (**11**) consists of infinite chains extending along the direction [100] that are built from NpO_2^+ cations, anions of dipicolinic acids and water molecules [86]. Two crystallographically

independent Np atoms have different surrounding, while both being in the pentagonal bipyramidal coordination (Fig. 11).

Equatorial positions of Np(1) atom are occupied with two water molecules, one nitrogen and two oxygen atoms of DPA^{2-} anion. Np(1)-O_{eq} distances lie in the range from 2.40(1) to 2.46(1) Å, while Np(1)-N distance is significantly longer, 2.54(1) Å. Maximal deviation of atoms from the least-squares equatorial plane exhibits water molecule (0.090 Å). The axial Np(1)-O distances of neptunyl group are equal to 1.854(7) Å, ONp(1)O angle is equal to 179.7(5)º. The second neptunyl group has Np-O distances equal to 1.856(8) Å, with ONp(2)O angle of 178.2(4)º. Equatoraial plane of Np(2) is formed by five oxygen atoms, two of which are carboxylate atoms, other three belong to water molecules. Equatorial Np-O distances are equal to 2.43(1)-2.49(1) Å.

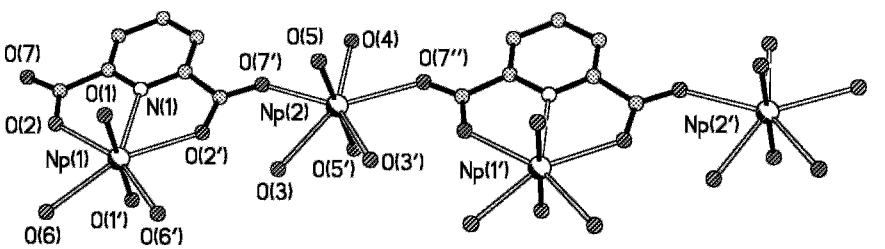

Fig. 11. Infinite chain in structure of $[(NpO_2)_2(DPA)(H_2O)_5]$.

Coordination polyhedra of Np atoms are linked into the infinite chains by carboxylic groups of DPA acting as pentadentate ligands. The distance between Np(1) and Np(2) atoms in the chain is equal to 6.197(4) Å. Minimal distance between Np atoms belonging to the different chains is equal to 5.642(4) Å. Adjacent chains are held together by means of hydrogen bonds which are formed with participation of water molecules.

Crystal structure of $\{C(NH_2)_3\}_3[NpO_2(DPA)_2]\cdot 4H_2O$ (**12**) exhibits one-dimensional topology [126]. Coordination polyhedron of Np atom is hexagonal bipyramide, whose equatorial positions are occupied by two nitrogen atoms of two DPA anions and four oxygen atoms of the same anions (Fig. 12). Np-N distances are equal to 2.668(5) Å. Distances between Np and O atoms are shorter, 2.524(5) and 2.553(5) Å. The DPA anion forms two planar condensed metallo-rings, with the angle at the metal atom of 60.0º. The axial distances Np-O in the centrosymmetrical neptunyl group are equal to 1.827(5) Å.

In the crystal structure of $Li_3[NpO_2(DPA)_2]\cdot 6H_2O$ (**13**) Np atom has the similar surrounding [97] (Fig. 13). The Np-N distances are equal to 2.669(5) and 2.652(5) Å. Distances between Np and O atoms lie in the range from 2.553(5) to 2.577(5) Å. Maximal deviation from the least-squares equatorial plane corresponds to one of the carboxylic oxygen atoms and equal to 0.22 Å. Axial

distances Np-O of the neptunyl group are equal to 1.818(5) and 1.832(5) Å, ONp(1)O angle is 179.6(2)º.

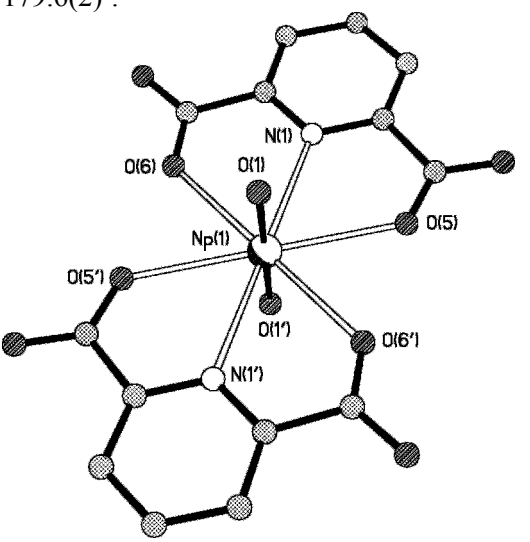

Fig. 12. Molecular structure of $\{C(NH_2)_3\}_3[NpO_2(DPA)_2]\cdot 4H_2O$.

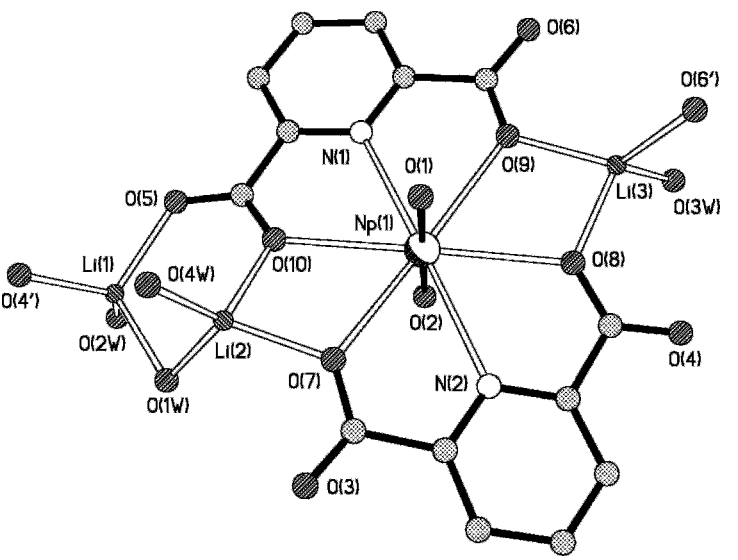

Fig. 13. Molecular structure of $Li_3[NpO_2(DPA)_2]\cdot 6H_2O$.

Coordination polyhedra of Li atoms are distortred tetrahedra. Coordination polyhedron of Li(1) is formed by two carboxylic oxygen atoms of two DPA

anions and two water molecules. Coordination polyhedron of Li(2) consists of oxygen atoms of two DPA anions and two water molecules, and shares vertex with Li(1) tetrahedron and edge with Np coordination polyhedron. This leads to the decrease of corresponding OLi(2)O angle to 84.5(5)º. Coordination polyhedron of Li(3) also shares edge with Np coordination polyhedron and consists of oxygen atoms of three carboxylic groups and one water molecule.

The complexation of pentavalent neptunium with pyridinecarboxylic acids was investigated by different methods including spectrophotometry, potentiometry and solvent extraction [18,42,101,127-130]. Depending on the technique, complexation model used in calculations and experimental conditions, different values of stability constants were obtained (Table 8).

Table 8. Data on Np(V) complexation with pyridinecarboxylic and pyridineacetic acids.

Ligand	log β_1	log β_2	I	Method	Reference
Pic^-	3.68±0.04	6.98±0.04	0.2	Spectrophotometry	[101]
	3.59±0.01	6.54±0.02	0.1	Spectrophotometry	[42]
	3.55±0.01	6.34±0.01	1.0	Spectrophotometry	[42]
	3.53±0.03	6.01±0.03	1.0	Solvent extraction	[18]
	3.45±0.02	6.03±0.02	1.0	Solvent extraction	[127]
	3.23	5.58	1.0	Solvent extraction	[128]
	3.04±0.03		0.5	Potentiometry	[130]
Nic^-	2.94±0.05		0.2	Spectrophotometry	[101]
	1.29±0.06		1.0	Spectrophotometry	[42]
	0.74±0.03		1.0	Solvent extraction	[18]
	0.57±0.03		1.0	Solvent extraction	[127]
$Isonic^-$	2.72±0.05		0.2	Spectrophotometry	[101]
	1.63±0.05		1.0	Spectrophotometry	[42]
DPA^{2-}	7.07±0.01		1.0	Solvent extraction	[127]
	7.25±0.02		1.0	Solvent extraction	[127]
	7.89±0.01		1.0	Solvent extraction	[18]
	4.82±0.04		0.5	Spectrophotometry	[130]
$MPic^-$	0.7	1.41±0.06	0.1	Spectrophotometry	[42]
PAA^-	1.58±0.04		0.1	Spectrophotometry	[42]
	1.30±0.01	1.72±0.03	1.0	Spectrophotometry	[42]

Authors of the work [131] have investigated the kinetics of complexation of Np(V) with DPA using stopped-flow spectrophotometry. At pH 1 and temperatures not exceeding 25ºC, most kinetic traces were described using a single first-order rate process. At high temperatures, the experimental traces were fit using two consecutive pseudo first-order reactions. The second process is linearly depent on DPA concentration. The rate constants calculated for the second reaction are about 50% larger than the constants determined for the first process.

There are no structural data for TRUE(V) compounds with 8-hydroxyquinoline. Nevertheless, some results presented in the work [65] indicate the significant difference in the behavior of pentavalent neptunium and plutonium in the presence of 8-hydroxyquinoline. Insoluble in water compounds of An(V) can be obtained by the precipitation from the solutions containing excess Ox. The compositions of compounds depend on experimental conditions and differ for Np and Pu. Neptunium complex $NpO_2(Ox)\cdot 2H_2O$ can be isolated at pH 5-6, while plutonium complex $PuO_2(Ox)(HOx)_2\cdot nH_2O$ is formed at pH 6-7. The rate of formation of neptunium complex depends significantly on Ox concentration and comprises several hours. At the higher pH values the $NpO_2(Ox)\cdot 2H_2O$ precipitate dissolves, and the complex $[NpO_2(Ox)_2(H_2O)]^-$ arises, which can be precipitated by the addition of tetraphenylarsonium. At the same time, plutonium complex $PuO_2(Ox)(HOx)_2\cdot nH_2O$ is formed instantly.

Synthesis of solid compounds of Np and Pu with some derivatives of 8-hydroxyquinoline, $NpO_2(MOx)(HMOx)_2\cdot nH_2O$, $PuO_2(MOx)(HMOx)_2\cdot nH_2O$, $PuO_2(DCOx)(HDCOx)_2\cdot nH_2O$, $PuO_2(COx)(HCOx)_2\cdot nH_2O$, is reported in the work [65]. Authors have also studied complex formation with 8-hydroxyquinoline, 8-hydroxyquinoline-5-sulfonic (H_2OxS) and 7-iodo-8-hydroxyquinoline-5-sulfonic acids (H_2IOxS) (Table 9).

Table 9. Stability constants for complexes of Np(V) and Pu(V) with 8-hydroxyquinoline and its derivatives (I=0.1, T=298K).

M	L	log β_1	log β_2	Method
NpO_2^+	Ox^-	6.32±0.01	11.50±0.05	Spectrophotometry
	OxS^{2-}	5.794±0.006	10.58±0.02	Spectrophotometry
		5.72±0.05	~10.42	Ion exchange
	$IOxS^{2-}$	4.94±0.01	9.54±0.02	Spectrophotometry
		4.83±0.05	9.40±0.15	Ion exchange
PuO_2^+	OxS^{2-}	5.71±0.05		Spectrophotometry
	$IOxS^{2-}$	5.08±0.04	~9.1	Ion exchange

4.2. Interaction with neutral heterocyclic ligands

Molecular structures of solid Np(V) complexes with neutral heterocyclic N-donor ligands, 2,2'-bipyridine (Bipy), 2,2',6',2''-terpyridine (Terpy), 1,10-phenanthroline (Phen), 2,4,6-tri(pyridin-2-yl)-1,3,5-triazine (TPTZ), imidazole (Im) were determined using X-ray single crystal diffractometry.

The crystal structure $[NpO_2(Bipy)(H_2O)_3](NO_3)$ (**14**) consists of complex $[NpO_2(Bipy)(H_2O)_3]^+$ cations (Fig. 14) and nitrate ions [85]. The coordination polyhedron of Np atom is pentagonal bipyramide with the equatorial positions occupied by two nitrogen atoms of Bipy molecule and three water molecules. The Np-N distances are equal to 2.62(1) and 2.66(1) Å, being significantly longer than Np-O distances which lie in the range from 2.45(1) to 2.49(1) Å. The deviations of nitrogen atoms from the least-squares equatorial plane are equal to 0.229 and -0.298 Å.

Bipyridine molecule has near planar geometry, the angle between pyridine rings is equal to 2.9º. At the same time, The least-squares plane of Bipy is inclined with respect to equatorail plane of Np coordination polyhedron by angle of 12.4º. The interesting feature of this structure is outer sphere nitrate ion that is not typical for neptunium complexes.

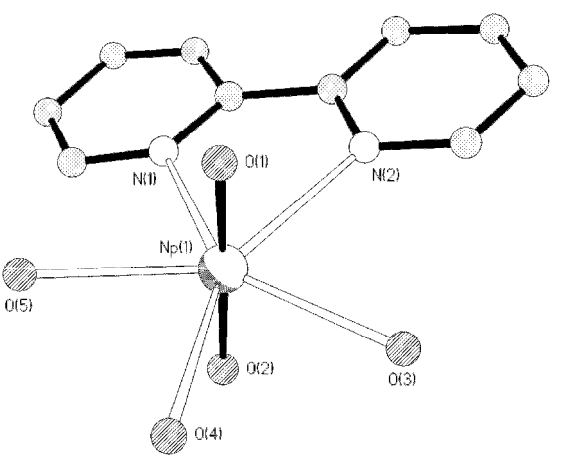

Fig. 14. Molecular structure of $[NpO_2(Bipy)(H_2O)_3](NO_3)$.

The similar values for distances between Np atom and heterocyclic N atoms, 2.617(5) and 2.649(5) Å, were found in $[NpO_2(NCS)(Bipy)(H_2O)_2]\cdot H_2O$ (**15**) (Fig. 15), [92]. The Np-NCS distance is shorter and equal to 2.500(5) Å. The deviations of atoms from the least-squares equatorial plane range from 0.047 to 0.417 Å, with maximum values corresponding to nitrogen atoms of Bipy (0.396 and 0.417 Å). Nitrogen atom of NCS ion deviates by 0.246 Å. The neptunyl group is tilted to the equatorial plane by the angle of 70.6º.

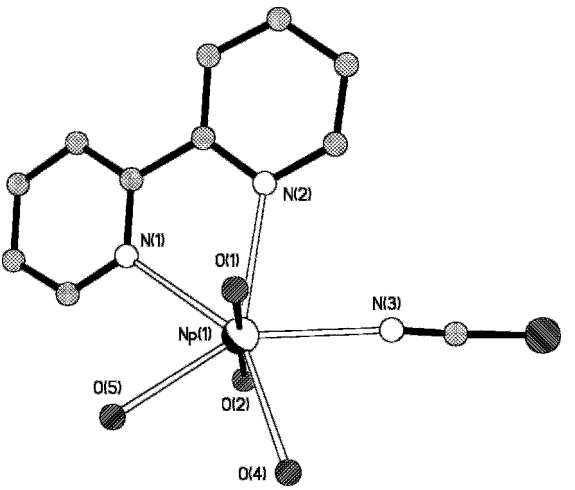

Fig. 15. Coordination surrounding of Np atom in $[NpO_2(NCS)(Bipy)(H_2O)_2]\cdot H_2O$.

In contrast to the neptunyl nitrate complex with Bipy, the structure of $[NpO_2(NO_3)(Terpy)(H_2O)]$ (**16**) represents the monodentate coordination of the nitrate which provides one oxygen as donor in the equatorial plane of Np. The remaining equatorial positions are occupied by the nitrogen atoms of Terpy molecule and a water molecule (Fig. 16) [90]. The Np-N distances have moderate values, 2.580(5)-2.602(5) Å. The largest atomic deviation from the least-squares equatorial plane is 0.360 Å.

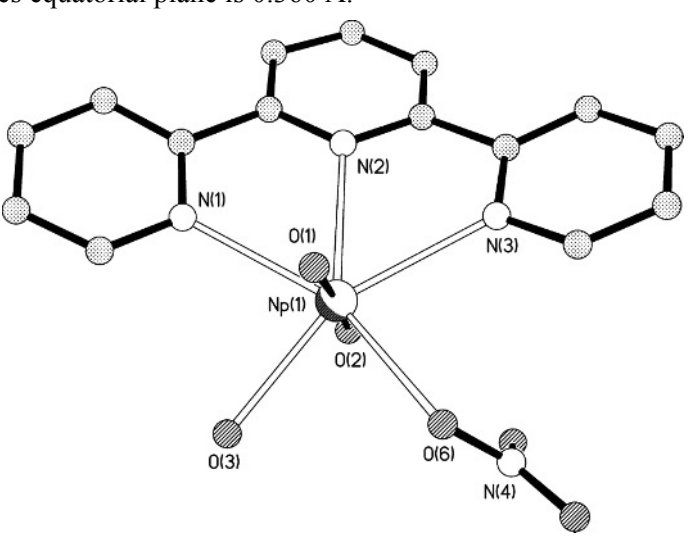

Fig. 16. Crystal structure of $[NpO_2(NO_3)(Terpy)(H_2O)]$.

The neptunium atom and the terpyridine molecule form two conjugated metallo-rings, with the angles at the metal atom of 62.6(2) and 62.5(2)º. The Py1, Py2 and Py3 pyridine rings containing N(1), N(2) and N(3) atoms, respectively, form dihedral angles of 19.0, 26.4 and 20.4º with the equatorial plane of the neptunium coordination polyhedron. The dihedral angles between rings are 14.5 (Py1-Py2), 22.6 (Py1-Py3) and 16.0º (Py2-Py3). By this means, the terpyridine molecule is subject to significant distortion.

The surrounding of each of three crystallographically unique Np atoms in $[NpO_2(Isonic)(Terpy)(H_2O)]\cdot 2H_2O$ (**17**) is close to that in **16** (Fig. 17), with the only difference that one of the equatorial positions is occupied by the oxygen atom of the monodentate isonicotinate ion [87]. In this case, too, the Terpy molecule is substantially distorted. The angles between pyridine rings lie in the range from 4.0 to 16.0º. The angles between pyridine rings and the equatorial plane of Np atom range from 3.6 to 13.9º, the angles between equatorial plane and pyridine rings of isonicotinate anions are even larger, 14.4 – 28.7º.

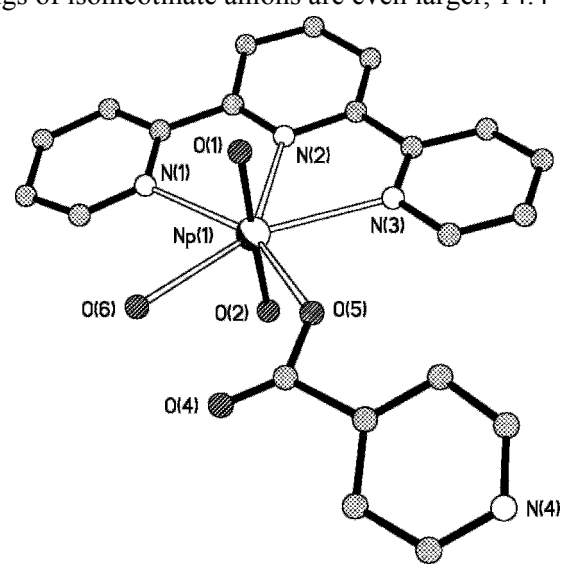

Fig. 17. Coordination surrounding of Np atom in of $[NpO_2(Isonic)(Terpy)(H_2O)]\cdot 2H_2O$.

The deviation of nitrogen atoms from the equatorial plane of Np coordination polyhedron in the crystal structure of the compound $[NpO_2(ReO_4)(Phen)(H_2O)_2]$ (**18**) (Fig. 18) is less than in two structures with Bipy and does not exceed 0.135 Å [95]. However, the planar phenanthroline molecule is inclined significantly with respect to the equatorial plane at an angle of 12.9. The equatorial interatomic bond lengths are unexceptional and equal to 2.641(9), 2.592(8) Å, and 2.445(8)-2.532(8) Å for Np-N and Np-O bonds, respectively. In contrast, the axial Np-O distances display unusually high values, 1.902(9) and 1.907(10)

Å. So high values were observed for the bridging oxygen atoms, for example, in the structures with cation-cation bonds $Na_4[(NpO_2)_2(C_{12}O_{12})]\cdot 8H_2O$ [132] and $[NpO_2(OOCH)]$ [133], but in both cases second (terminal) oxygen atom of the neptunyl group had the usual value, ~1.85 Å.

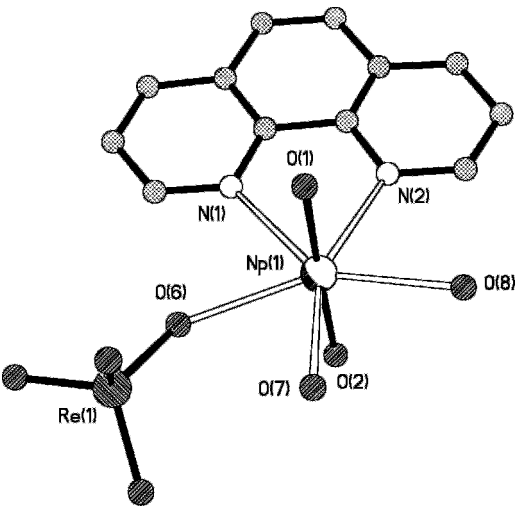

Fig. 18. Molecular structure of $[NpO_2(ReO_4)(Phen)(H_2O)_2]$.

The crystal structure of another complex with phenanthroline, $[(NpO_2)(N_3)(Phen)(H_2O)]_2\cdot 3H_2O$ (**19**), contains centrosymmetrical dinuclear molecules $[(NpO_2)(N_3)(Phen)(H_2O)]_2$ [96]. There are two crystallographycally independent dimers having similar composition in the unit cell, the structure of one of them is presented in Fig. 19.

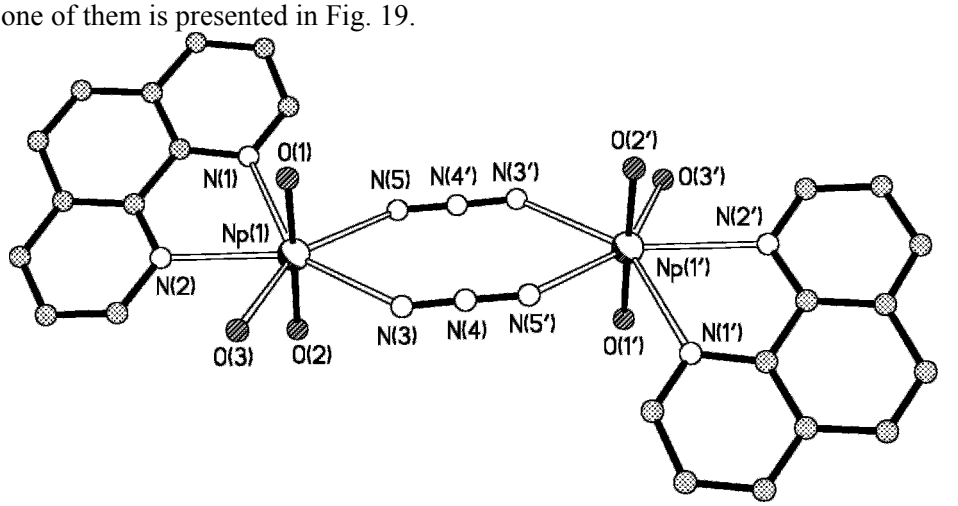

Fig. 19. Complex dimer $[(NpO_2)(N_3)(Phen)(H_2O)]_2$ in the structure of neptunyl azide $[(NpO_2)(N_3)(Phen)(H_2O)]_2\cdot 3H_2O$.

Equatorial positions of Np(1) and Np(2) coordination polyhedra are occupied by two nitrogen atoms of two azide ions, two nitrogen atoms of phenanthroline molecule, and one water molecule. Values of Np-N distances are equal to 2.492(9)-2.555(7) Å and 2.609(7)-2.661(7) Å for azide and phenanthroline nitrogen atoms, respectively. The equatorial plane of Np(1) displays more significant deviation from the planarity with maximal deviation of atoms equal to 0.410 Å. The equatorial plane of Np(2) atom is more planar, the deviation of atoms do not exceed 0.204 Å.

Azide ions act as bidentate bridging ligands connecting adjacent Np coordination polyhedra into dimers. The distances between metal centers in two crystallographically independent dimers are equal to 6.279 and 6.204 Å.

The neptunyl complexes with TPTZ were studied in the work [98]. Two solid compounds, $[NpO_2Cl(TPTZ)(H_2O)]\cdot H_2O$ and $[NpO_2Br(TPTZ)(H_2O)]\cdot 2H_2O$, were synthesized, and the crystal structure of the first complex was determined using X-ray diffractometry.

Crystal structure of $[NpO_2Cl(TPTZ)(H_2O)]\cdot H_2O$ (**20**) contains complex molecules $[NpO_2Cl(TPTZ)(H_2O)]$ (Fig. 20) and crystallization water. Molecule of TPTZ acts as the tridentate ligand coordinating the neptunium atom through nitrogen atoms of two pyridine and one triazine rings. In this case, the Np-N distances are different, with slightly higher values for nitrogen atoms of pyridine rings (2.672(2), 2.644(2) Å) in contrast to nitrogen atom of triazine ring (2.605(2) Å). The deviation of atoms from the equatorial plane does not exceed 0.178 Å.

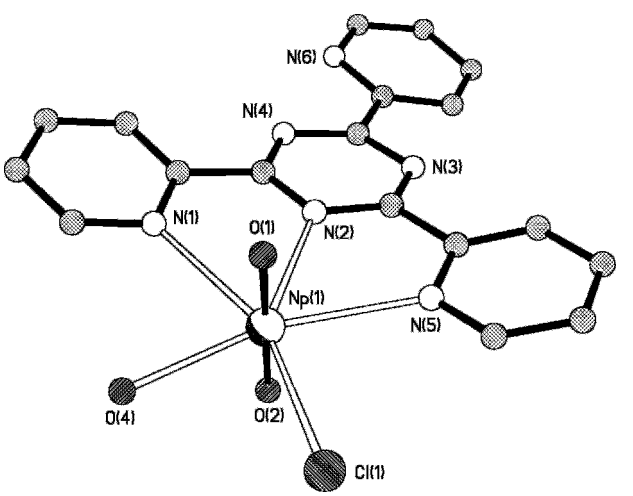

Fig. 20. Molecular structure of $[NpO_2Cl(TPTZ)(H_2O)]\cdot H_2O$.

Due to the coordination of TPTZ molecule, the significant distortion of the ligand is observed. The angles between rings comprising the ligand are equal to

4.0 – 20.8º. The maximal dihedral angle between the equatorial plane of Np atom and ligand rings corresponds to the noncoordinated pyridine ring and is equal to 17.1º. Other values lie in the range from 12.4 to 15.7º.

The NIR and IR spectra of both compounds are very similar indicating the same coordination surrounding of neptunyl group. Thermogravimetric analysis counts in the favor of the presence of two crystallization water molecules in the neptunium bromide, so the formula $[NpO_2Br(TPTZ)(H_2O)]\cdot 2H_2O$ was suggested for this compound.

Two complexes of pentavalent neptunium with imidazole were synthesized and structurally characterized [133]. In the sructure of neptunyl acetate $[(NpO_2)(CH_3COO)(Im)_2(H_2O)]$ (**21**) coordination surrounding of Np atom is formed by two imidazole molecules, bidentate acetate anion and water molecule (Fig. 21). Nitrogen atoms deviate significantly from the equatorial plane (by ± 0.430 Å). Water molecule also displays significant deviation (0.380 Å). Equatorial distances are equal to 2.551(5) Å (Np-N), 2.532(5) Å (Np-O_{Ac}) and 2.398(5) Å (Np-O_w).

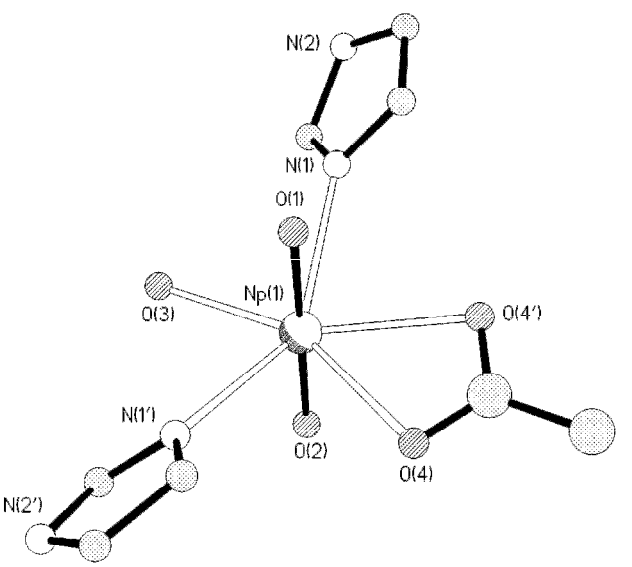

Fig. 21. Molecular structure of neptunyl acetate $[(NpO_2)(CH_3COO)(Im)_2(H_2O)]$.

In the crystal structure of $[(NpO_2)_2(C_2O_4)(Im)_6]\cdot 5Im$ (**22**), adjacent neptunyl groups are joined into $[(NpO_2)_2(C_2O_4)(Im)_6]$ dimers by tetradentate oxalate ions (Fig. 22). By this means, each of the metal centers is surrounded by two oxygen atoms of oxalate ion and three imidazole molecules. The Np-N distances lie in the range from 2.52(1) to 2.56(1) Å, Np-O bond lengths range from 2.50(1) to

2.51(1) Å. Neptunyl groups display usual values of axial Np-O distances, 1.82(1)-1.87(1) Å, but their geometry is far from linear – ONpO angles are equal to 171.8(8) and 172.8(8)º. There are also five solvate imidazole molecules in the structure, which participate in H-bonds formation.

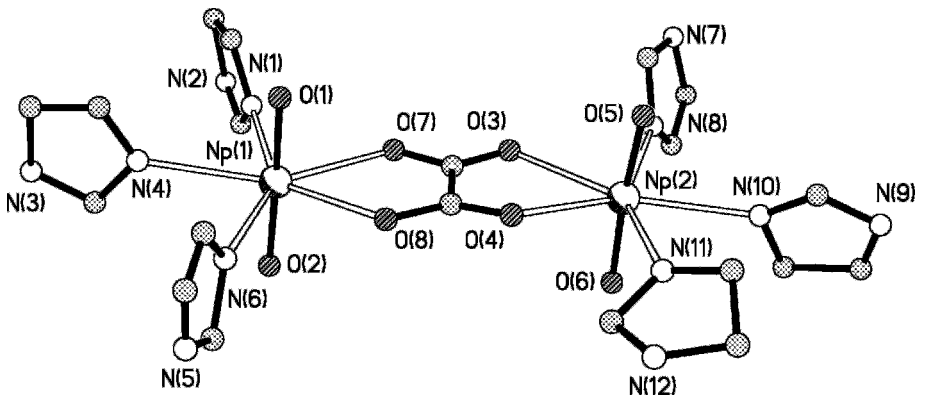

Fig. 22. Structure of $[(NpO_2)_2(C_2O_4)(Im)_6]$ molecule in neptunyl oxalate with imidazole $[(NpO_2)_2(C_2O_4)(Im)_6]\cdot 5Im$.

4.3. Interaction with expanded porphyrines

The interaction of Np and Pu with expanded porphyrines (Fig. 23) was studied in the works [94,102].

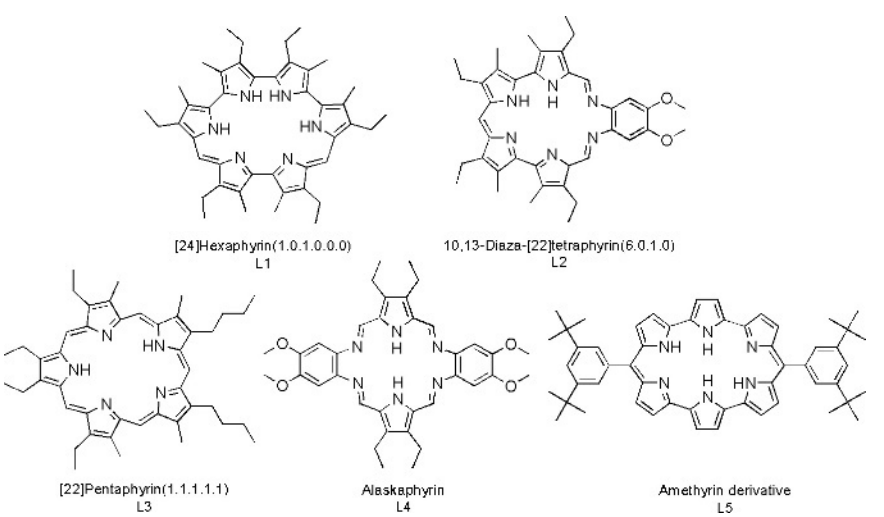

Fig. 23. Structures of expanded porphyrines.

The crystalline neptunyl complex with isoamethyrin $(HN(C_2H_5)_3)[NpO_2(L1)]$ (**23**) is presented in the work [94]. Neptunium atom is found in hexagonal equatorial surrounding formed by nitrogen atoms of the ligand (Fig. 24). The Np-N distances range from 2.649(1) to 2.880(1) Å. The nitrogen atoms in this structure are far from planar, the maximal deviation of mean plane is equal to 0.256 Å. The neptunyl group Np-O distances have different values, 1.762(1) and 1.826(1) Å, the lower value being somewhat short for Np(V) structures. However, the charge balance of the system, conducted taking into account triethylammonium cation, supports the conclusion that neptunium is pentavalent. Further, the presence of this cation can explain the difference in Np-O distances found in the structure.

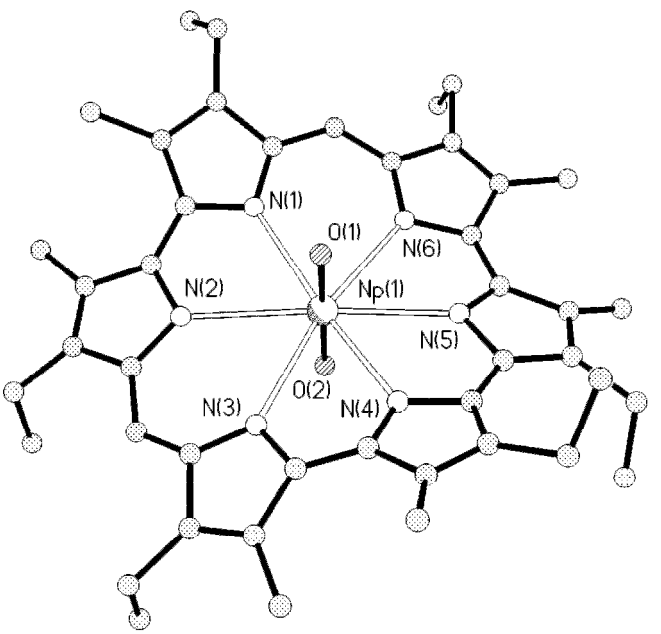

Fig. 24. Molecular structure of **23**. This figure is generated from the data downloaded from the Cambridge Crystallographic Database as published originally in Ref. [94].

The UV-VIS spectrum of $[NpO_2(L1)]^+$ complex contains absorption band at 977 nm that is considered as evidence of Np(V) presence and indication of the change in the coordination sphere of Np atom in solution. Isoamethyrin L1 also forms plutonyl complex $[PuO_2(L1)]^+$, when treated with acidic solution of plutonyl(VI) chloride. Taking into account that Pu is reduced more readily than Np, authors made the conclusion about pentavalent state of plutonium that is supported by the absence of Pu(VI) absorption peak near 830 nm. The similar changes in the spectra of L2-L5 with the addition of neptunyl or plutonyl are observed. By this means, the formation of Np(V) and Pu(V) complexes with

L1-L5 in solutions was suggested [102]. The experimental observation of the Np(VI)/Pu(VI) to Np(V)/Pu(V) reduction in the presence of expanded porphyrines is consistent with the DFT calculations conducted for complexes of Np and Pu with alaskaphyrin [104].

4.4. Interaction with amine-N-polycarboxylic acids

The crystal structure of Np complex with N-methyliminodiacetic acid $\{C(NH_2)_3\}_3[NpO_2(MIDA)_2]$ (**24**) is described in the work [88]. It consists of centrosymmetric $[NpO_2(MIDA)_2]^{3-}$ anions (Fig. 25) and outer-sphere guanidinium cations. Two MIDA anions coordinate to Np atom through nitrogen and oxygen atoms with the formation of four five-membered chelate rings in the fashion very similar to the structures of neptunyl dipicolinate **12** and **13**. But, due to the nonplanar topology of MIDA ligand, these rings also exhibit far from planar geometry, with maximal deviation of 0.338 Å. The Np-N distances are very long comparing with other complexes of Np(V) with N-donor ligands, 2.732(6) Å, and the equatorial Np-O distances are considerably shorter, 2.538(5) Å. The deviations of atoms from the least-squares equatorial plane do not exceed 0.212 Å. The Np-O distances in the symmetric neptunyl cation are equal to 1.840(6) Å.

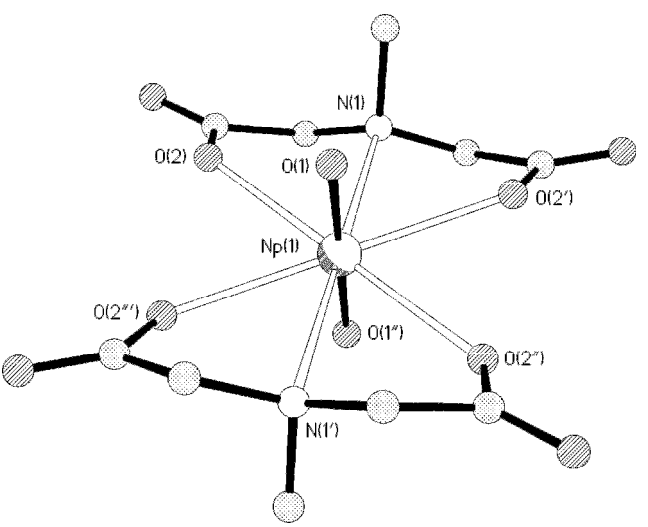

Fig. 25. Molecular structure of $[NpO_2(MIDA)_2]^{3-}$ anion in neptunyl complex with N-methyliminodiacetic acid $\{C(NH_2)_3\}_3[NpO_2(MIDA)_2]$.

Complexation of Np(V) and Pu(V) with different amine-N-polycarboxylic acids was studied extensively with use of different experimental techniques

[42,64,127,130]. The results of stability constants measurements are summarized in Table 10.

Table 10. Stability constants for normal and protonated complexes of Np(V) and Pu(V) with amine-N-polycarboxylic acids.

M	L	log β_{MHL}	log β_{ML}	I	Method	Reference
NpO_2^+	IDA^{2-}	1.35±0.52	6.27±0.11	0.1	Spectrophotometry	[64]
			5.81±0.02	1.0	Potentiometry	[130]
			5.64±0.01	1.0	Solvent extraction	[127]
			5.76±0.01	1.0	Solvent extraction	[127]
			6.27	0.1	Ion exchange	[127]
	$MIDA^{2-}$	1.28±0.48	7.37±0.05	0.1	Spectrophotometry	[64]
			6.75±0.02	1.0	Potentiometry	[130]
	$HIDA^{2-}$	1.45±0.25	6.08±0.05	0.1	Spectrophotometry	[64]
	$EDTA^{4-}$	5.30±0.08	7.30±0.06	0.1	Spectrophotometry	[64]
		4.46±0.01		1.0	Solvent extraction	[127]
		4.52±0.01		1.0	Solvent extraction	[127]
		5.30		0.1	Ion exchange	[127]
	$HEDTA^{3-}$	4.06±0.01	6.87±0.11	0.1	Spectrophotometry	[64]
	$EDDA^{2-}$		8.26±0.05	1.0	Potentiometry	[130]
	NTA^{3-}	1.77±0.37	6.80±0.10	0.1	Spectrophotometry	[64]
			7.51±0.02	1.0	Potentiometry	[130]
			6.08±0.01	1.0	Solvent extraction	[127]
			6.30±0.01	1.0	Solvent extraction	[127]
			6.81	0.1	Ion exchange	[127]
	$PIDA^{2-}$		5.86±0.06	0.1	Spectrophotometry	[42]
			5.72±0.03	1.0	Spectrophotometry	[42]
	$MPIDA^{2-}$		5.54±0.05	0.1	Spectrophotometry	[42]
			5.43±0.05	1.0	Spectrophotometry	[42]
PuO_2^+	IDA^{2-}		6.18±0.05	0.1	Spectrophotometry	[64]
	$EDTA^{4-}$		4.80±0.01	0.1	Spectrophotometry	[64]
	$HEDTA^{3-}$		4.46±0.04	0.1	Spectrophotometry	[64]
	NTA^{3-}		6.91±0.04	0.1	Spectrophotometry	[64]

4.5. Interaction with azide, cyanide and isothiocyanate

Stability constants for neptunium azide and cyanide complexes have been calculated based on the spectrophotometric data (Table 11) [55]. The formation of two solid complexes, $NpO_2CN \cdot nH_2O$ and $NaNpO_2(CN)_2 \cdot nH_2O$, have been reported [59].

Table 11. Stability constants for complexation of Np(V) with azide and cyanide measured using spectrophotometry (I=5, T=298K).

Complex	log β_1	log β_2	log β_3	log β_4	log β_5
$[NpO_2(N_3)_n]^{1-n}$	1.08	1.85	2.23	2.10	1.40
$[NpO_2(NC)_n]^{1-n}$	2.90	3.23	4.81	5.11	5.94

Complexation of Np with NCS has been extensively studied using different experimental techniques. In the work [57], stability constants were calculated from spectrophotometry and potentiometry data for ionic strength I=9 (Table 12). The stability constant $\log\beta_1$=0.32 was obtained using solvent extraction technique (I=2 M) [60]. Since the isothiocyanate ion is able to reduce Np(V), the special attention was given in this study to maintain the Np oxidation state.

Table 12. Stability constants for Np complexes with NCS determined using spectrophotometry and potentiometry (I=9, T=298K).

log β_1	log β_2	log β_3	log β_4	log β_5	Method
1.23	1.91	2.04	1.72	0.46	Spectrophotometry
1.02	1.56	1.60	1.56		Potentiometry

The solid compound $[NpO_2(NCS)\{(NH_2)_2CO\}_4] \cdot (NH_2)_2CO$ (**25**) has been studied in the work [89]. The equatorial surrounding of the Np atom is formed by nitrogen atom of NCS ion and four oxygen atoms of carbamide molecules (Fig. 25). The fifth carbamide molecule acts as solvate and is held in the crystal structure by hydrogen bonds. The Np-N distance is equal to 2.52(2) Å, while Np-O bonds are shorter, 2.45(1)-2.46(1) Å. The deviation of the nitrogen atom from the least-squares equatorial plane is equal to 0.100 Å, the deviation of the oxygen atoms range from 0.065 to 0.285 Å. The structure has unusually large parameter of the unit cell (56.843 Å) caused by the presence of the screw axis 4_3. The crystal structure of another one Np compound with coordinated isothiocyanate ion, $[NpO_2(NCS)(Bipy)(H_2O)_2] \cdot H_2O$, was described in Section 4.2. The distance between Np atom and N atom of NCS ion had similar value, 2.500(5) Å.

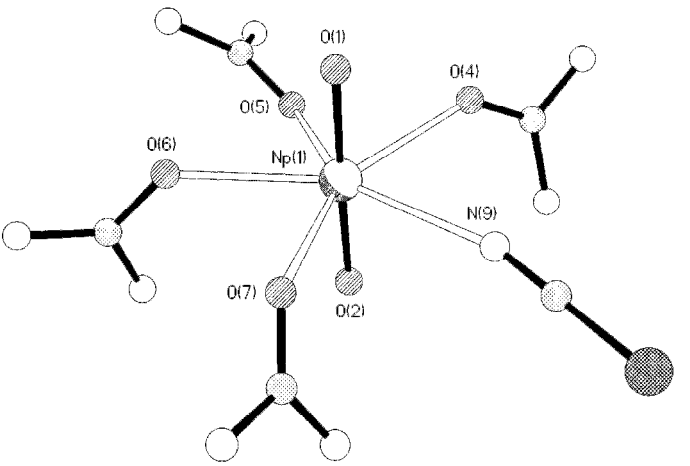

Fig. 25. Fragment of crystal structure of $[NpO_2(NCS)\{(NH_2)_2CO\}_4]\cdot(NH_2)_2CO$.

The only structurally characterized Np solid compound with azide ion is the $[(NpO_2)(N_3)(Phen)(H_2O)]_2\cdot 3H_2O$ complex (see Section 4.2). In contrast to uranyl(VI) compounds [135,136], in this structure azide ion acts as bidentate ligand connecting different metal centers.

5. Hexavalent transuranium elements

5.1. Interaction with ionogenic heterocyclic ligands

Hexavalent neptunium and plutonium complexes with 2-pyrazinecarboxylic acid $[NpO_2(Pyraz)_2(H_2O)]\cdot 2H_2O$ and $[PuO_2(Pyraz)_2(H_2O)]\cdot 2H_2O$ were reported in the work [99]. These compounds were found isostructural to previously studied uranyl complex [137]. In Table 13 the unit cell parameters calculated from the powder diffraction patterns are compared with cell parameters for the uranyl complex.

Table 13. Unit cell parameters for isostructural Np, Pu and U compounds with 2-pyrazinecarboxylic acid $[AnO_2(Pyraz)_2(H_2O)]\cdot 2H_2O$.

An	*a*, Å	*b*, Å	*c*, Å	*β*, deg
Np	6.559(4)	15.886(9)	14.637(7)	103.15(1)
Pu	6.379(7)	15.822(13)	14.464(12)	101.20(1)
U	6.591(3)	16.071(6)	14.584(7)	101.89(4)

By this means, the model structure of Np and Pu complexes was proposed. The equatorial surrounding of the actinyl cation is formed by nitrogen and oxygen atoms of two 2-pyrazinecarboxylate anions serving as bidentate chelating ligands and water molecule (Fig. 26). The proposed composition and structure of Np and Pu complexes were confirmed by thermogravimetric and spectral analysis.

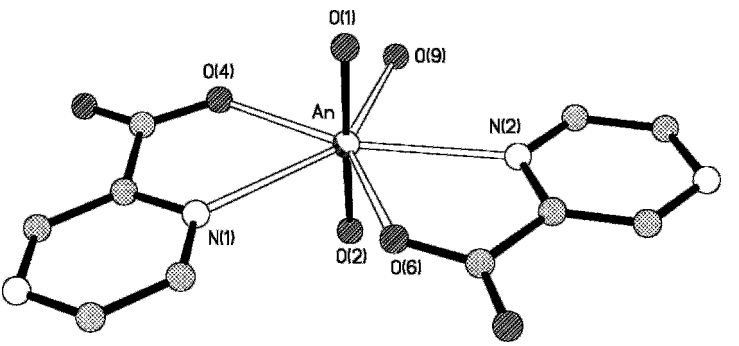

Fig. 26. Model of the molecular structure for isostructural $[NpO_2(Pyraz)_2(H_2O)]\cdot 2H_2O$ and $[PuO_2(Pyraz)_2(H_2O)]\cdot 2H_2O$.

Complex formation of Np and Pu with pyridinecarboxylic acids was studied in the works [43,63]. Stability constants for normal and protonated complexes of plutonyl(VI) were determined using spectrophotometry and potentiometric titration (Table 14).

Table 14. Stability constants for normal and protonated complexes of Pu(VI) with picolinic, methylpicolinic and nicotinic acids (I=0.01, T=298K) [43].

Ligand	log β_1	log β_H
Pic^-	4.58±0.02	0.69±0.05
$MPic^-$	2.51±0.04	0.6±0.04
Nic^-	1.73±0.03	0.98±0.07

Picolinic acid forms with TRUE(VI) normal 1:2 chelates and 1:3 complexes [43,63]. The composition of complex formed depends strongly on the conditions of synthesis. Under precipitation from hot solutions, 1:2 complexes are obtained. At the room temperature, low pH and high concentration of picolinate ion, 1:3 complexes are formed. Complexes with An to Pic ratio 1:3 can accept up to 3 water molecules when kept at air. In the 1:2 complexes, picolinate ion is coordinated by central atom through nitrogen and oxygen atoms with the formation of five-membered chelate ring as concluded from IR

spectroscopy of solid compounds. In the 1:3 complex, the third picolinate group coordinates through carboxylic oxygen only. This conclusion is also confirmed by proton NMR data [43].

Formation of the complexes $[AnO_2(Nic)_2(H_2O)_2]$ is observed for Np(VI) and Pu(VI) [43]. At high concentrations of nicotinic acid, the compounds with An to Nic ratio exceeding 2 can be obtained, but this ratio is less than 3. At the same time, the actinide atom in the 1:2 complexes with picolinic and nicotinic acids can coordinate one additional ligand, for example DMSO, with the formation of complexes like $[AnO_2(Pic)_2(DMSO)]$ and $[AnO_2(Nic)_2(DMSO)]$.

Plutonium complex $H[PuO_2(Ox)_3]$ is described in the work [138]. Another attempt to synthesize solid Pu compounds with Ox was made in the work [65], but authors found that Pu(VI) is reduced in conditions suitable for synthesis.

Work [103] describes structure of Np complex with bis(salicylidene)-ethylenediamine $[NpO_2(OH_4C_6HC{=}NCH_2CH_2N{=}CHC_6H_4O)(CH_3OH)]$ (**26**). Neptunium atom is found in pentagonal bipyramidal coordination, with equatorial positions occupied by two N and two O atoms of bis(salicylidene)-ethylendiamine anion and O atom of methanol. The Np-N distances are equal to 2.518(3) and 2.548(3) Å. There are two different types of Np-O bonds in the structure, the phenolic oxygen have shorter Np-O bond length, 2.211(3) and 2.296(3) Å, than Np-O distance for oxygen atom of methanol, 2.436(3) Å.

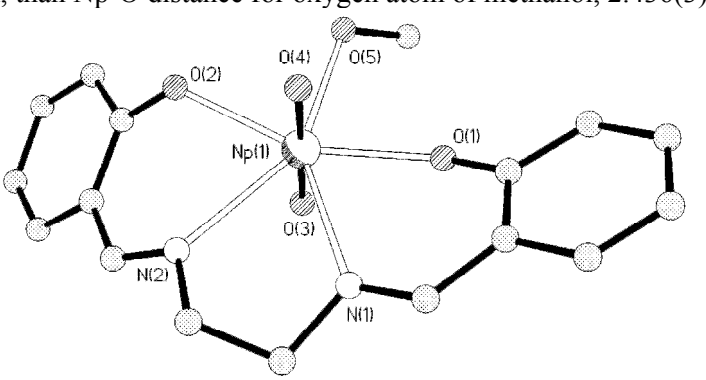

Fig. 27. Coordination surrounding of Np in **26**. This figure is generated from the data downloaded from the Cambridge Crystallographic Database as published originally in Ref. [103].

5.2. Interaction with neutral heterocyclic ligands

Neptunium complex with pyridine $[NpO_2(CH_3C(O)CHC(O)CH_3)_2(Py)]$ (**27**) is described in the work [84]. The equatorial plane of Np atom is formed by four oxygen atoms of anions and nitrogen atom of pyridine. The Np-O distances are equal to 2.333-2.372 Å, while Np-N bond is longer, 2.564 Å. The equatorial surrounding is near planar, the deviation of atoms does not exceed 0.088 Å. At

the same time, the pyridine ring is significantly inclined to the equatorial plane, with the angle equal to 49.7º.

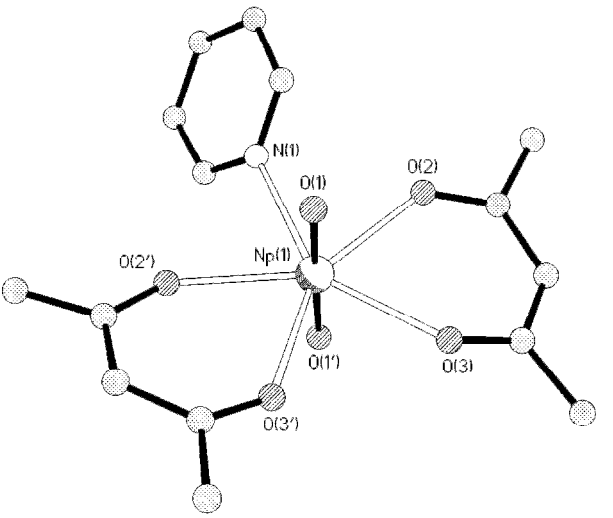

Fig. 28. Molecular structure of Np complex with pyridine. This figure is generated from the data downloaded from the Cambridge Crystallographic Database as published originally in Ref. [93].

Two complexes of hexavalent neptunium with bipyridine, $[NpO_2(CH_3COO)_2(Bipy)]$ (**28**) and $[NpO_2(NO_3)_2(Bipy)]$ (**29**), are described in the works [82,83]. In both structures neptunium atoms have similar hexagonal equatorial surroundings formed by two nitrogen atoms of Bipy and four oxygens atoms of bidentate anions, acetate or nitrate, respectively (Fig. 29).

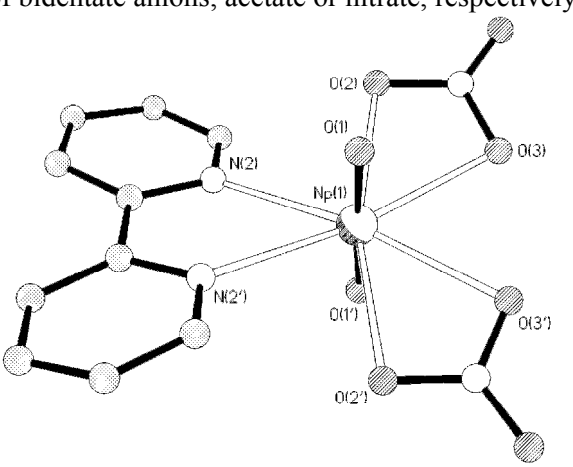

Fig. 29. Molecular structure of $[NpO_2(NO_3)_2(Bipy)]$. This figure is generated from the data downloaded from the Cambridge Crystallographic Database as published originally in Ref. [83].

The Np-N distances in the neptunium acetate are equal to 2.620 and 2.630 Å. In the neptunium nitrate, these bonds are shorter, 2.564 Å. The Np-O distances range from 2.430 to 2.477 Å and from 2.472 to 2.485 Å in the acetate and nitrate, respectively. In both cases, the equatorial planes are significantly distorted. The maximal deviations from the least-squares equatorial plane correspond to the nitrogen atoms of Bipy molecules and equal to 0.591 and 0.540 Å.
The Bipy molecule in the neptunyl nitrate **29** is noticeably twisted, with the angle between pyridine rings of 17.2º. The dihedral angles between the equatorial plane and pyridine rings are equal to 17.2º. In the neptunyl acetate the distortion of Bipy molecule is not that significant, the angle between pyridine rings is equal to 8.0º. However, the rings are substantially inclined in respect to the mean equatorial plane, with the angles being equal to 31.9 and 27.3º.

6. Conclusion

The ligands discussed above are widely diversified: certain of them can only serve as monodentate (imidazole, acetonitrile and isothiocyanate), bidentate (bipyridine, phenanthroline) or terdentate (terpyridine, TPTZ), others being the polyfunctional ligands with different donor sites may coordiate to the metal in various modes. In the latter case, the formation of chelate metallo-rings and/or the linking of the adjacent An coordination polyhedra is observed.
Ligands architecture and their preorganization are the key factors in the control of topology of complexes. By this means the formation of usual coordination polyhedra for actinide atoms is anticipated in complexes with N-donor ligands. The difference in coordination modes must reflect in geometrical parameters of the structures. The lengthening of An-N distances as compared to An-O distances is expected.
Despite the relatively large number of publications concerning N-donor ligands, the structural information is scattered. This is particularly true for trivalent TRU elements. It is the trivalent state that attracts the major attention of researchers, but the adequate structural data for TRUE(III) are especially scarce, and the most of the studies are conducted using lanthanides based on the belief that they can serve as perfect structural analogs of actinides.
Although the increase in An-N distances with respect to An-O is evident from the experimental data, the calculations on Am, Cm and Pu complexation with Terpy produce underestimated values for An-N distances. At the same time, calculations on [An(MeBTP)$(H_2O)_6$] and [Cm(*n*-C_3H_7-BTP)] complexes yield more realistic values consistent with experimental data.
The same situation holds for tetravalent TRUE. The structural experiments are very rare, and yet the lengthening of An-N is incontrovertible (Table 15).

Table 15. Lengths of M-N and M-O bonds (Å) for complexes of tri- and tetravalent TRU elements in solid state and solution as determined using X-ray crystallography (XC) and EXAFS, respectively.

Complex	An-N	An-O	Method
$[Pu(NCCH_3)_9](PF_6)_3 \cdot NCCH_3$	2.554, 2.561, 2.565, 2.566, 2.573, 2.575, 2.579, 2.582, 2.591		XC
$[Am(MPBIZ)_2(H_2O)_6]$	2.63		EXAFS
$[Cm(n\text{-}C_3H_7\text{-}BTP)_3]$	2.568		EXAFS
$[Cm(n\text{-}C_3H_7\text{-}BTP)_3]$	2.52, 2.57, 2.59		EXAFS
$\{N(CH_3)_4\}_4[Np(NCS)_8]$	2.39, 2.39, 2.39, 2.40, 2.40, 2.41, 2.41, 2.42		XC
$\{N(C_2H_5)_4\}_4[Np(NCS)_8]$	2.39, 2.44		XC
$[Np(NCS)_4(DMSO)_4]$	2.44	2.29	XC
$[Np(NTA)_2]$	2.63	2.35	EXAFS

Structurally, the most extensively studied are the complexes of pentavalent neptunium. Simple ligands, such as N_3 and NCS, coordinate to metal atom without formation of chelate ring. In this case the Np-N distances are moderate, 2.492-2.555 Å (Table 16). Heterocyclic imidazole molecule acting as a monodentate ligand exhibits near the same values of Np-N distances, 2.516-2.556 Å. The Np-N distances increase significantly with the formation of five-membered chelate ring (Np-N-C-C-N or Np-N-C-C-O). In this case, the typical values for the ligands with unsaturated N-donor lie in the range from 2.580 to 2.674 Å. For the complex with methyliminodiacetic acid containing saturated N-donor this value is considerably larger, 2.732 Å. At the same time, the largest Np-N bond length, 2.880 Å, was found in the complex with macrocyclic hexadentate hexaphyrin L1, but so high value can be attributed to the specificity of the in-cavity coordination. Somewhat short Np-N distance, 2.540 Å, was found in the complex **11** where two chelate rings are formed. At the same time, nicotinate and isonicotinate ions, albeit do not form chelate rings with Np atom, display long Np-N distances, 2.731 and 2.610 Å in **9** and **10**, respectively. This lengthening in distances may be explained by the complexity of the coordination modes when nicotinate and isonicotinate anions link adjacent cation-cation chains into 2D and 3D structures.

The number of metallo-rings formed (one or two conjugate) seems to have no effect on Np-N bond lengths for the ligands of the same type: Np-N distances in complexes **14**, **15**, **18**, **19** (with Bipy and Phen) and **17**, **20** (with Terpy and TPTZ), where one or two conjugate metallo-rings, respectively, are formed, the Np-N distances fall in the ranges from 2.59 to 2.66 Å and from 2.58 to 2.67 Å.

Table 16. Equatorial distances (Å) for Np(V) complexes determined using X-ray crystallography.

Complex	Np-N	Np-O	Np-O_{water}
$[NpO_2(Pic)(H_2O)_2]$	2.597	2.460, 2.467	2.463, 2.515
$Cs[NpO_2(Pic)_2(Hpic)]\cdot 3H_2O$	2.614, 2.598	2.445, 2.408 2.420 (Hpic)	
$[NpO_2(Nic)(H_2O)]$	2.731	2.464 (NpO_2) 2.513, 2.438	2.467
$[NpO_2(Isonic)(H_2O)]$	2.610	2.420 (NpO_2) 2.421, 2.434	2.485
$[(NpO_2)_2(DPA)(H_2O)_5]$	2.540	2.398	2.463
		2.482	2.491, 2.430
$\{C(NH_2)_3\}_3[NpO_2(DPA)_2]\cdot 4H_2O$	2.668	2.524, 2.553	
$Li_3[NpO_2(DPA)_2]\cdot 6H_2O$	2.652, 2.668	2.556, 2.553, 2.577, 2.561	
$[NpO_2(Bipy)(H_2O)_3](NO_3)$	2.62, 2.66		2.49, 2.46, 2.46
$[NpO_2(NCS)(Bipy)(H_2O)_2]\cdot H_2O$	2.617, 2.649 (Bipy) 2.500 (NCS)		2.460, 2.480
$[NpO_2(NO_3)(Terpy)(H_2O)]$	2.580, 2.602, 2.603	2.506	2.455
$[NpO_2(ReO_4)(Phen)(H_2O)_2]$	2.641, 2.593	2.457	2.532, 2.445
$[NpO_2(N_3)(Phen)(H_2O)]_2\cdot 3H_2O$	2.649, 2.613 (Phen) 2.517, 2.492 (N_3)		2.427
	2.609, 2.661 (Phen) 2.509, 2.555 (N_3)		2.423
$[NpO_2Cl(TPTZ)(H_2O)]\cdot H_2O$	2.674, 2.604, 2.645	2.820 (Cl)	2.455
$[NpO_2(CH_3COO)(Im)_2(H_2O)]$	2.551	2.532	2.398
$[(NpO_2)_2(C_2O_4)(Im)_6]\cdot 5Im$	2.556, 2.516, 2.524	2.510, 2.495	
	2.550, 2.550, 2.550	2.502, 2.495	
$\{HN(C_2H_5)_3\}[NpO_2(L1)]$	2.649, 2.649, 2.788, 2.810, 2.835, 2.880		
$\{C(NH_2)_3\}_3[NpO_2(MIDA)_2]$	2.732	2.538	
$[NpO_2(NCS)\{(NH_2)_2CO\}]\cdot(NH_2)_2CO$	2.52	2.45, 2.45, 2.45, 2.46	

For hexavalent neptunium the lengthening of An-N distances is also observed, but the correlation with coordination mode is not traced: the identical values (2.564 Å) were found in the complexes with Py **27** and Bipy **29** (Table 17).

Table 17. Equatorial distances (Å) for Np(VI) complexes determined using X-ray crystallography.

Complex	Np-N	Np-O
$[NpO_2(\text{-}CH_2N{=}CHC_6H_4O)_2(CH_3OH)]$	2.548, 2.518	2.211, 2.296 (L), 2.436
$[NpO_2\{CH_3C(O)CHC(O)CH_3\}_2(Py)]$	2.564	2.372, 2.333
$[NpO_2(CH_3COO)_2(Bipy)]$	2.620, 2.630	2.430, 2.455, 2.460, 2.477
$[NpO_2(NO_3)_2(Bipy)]$	2.564	2.472, 2.485

For Np(V) and Np(VI) the usual coordination polyhedra, pentagonal or hexagonal bipyramide, are found. However, the significant deviations (up to 0.591 Å) of nitrogen atoms from the equatorial plane are observed almost without exception. The most of the polydentate N-donor ligands forms five-membered metallo-rings with central atom. The N-An-N and N-An-O angles of the planar five-membered metallo-rings are equal 60.0-64.36º for both Np(V) and Np(VI), with the exception of **23** where lower values were found, 55.7-59.8º. In the complexes **24** and **26** the endo angles of nonplanar metallo-rings are equal to 59.67 and 66.1º, respectively. Values of the angles for six-membered metallo-rings are higher than average values for five-membered metallo-rings, as found in **23** (64.5 and 65.4º).

Although actinide cations are classified as hard acids according to the "hard and soft donor acids and basis" principle of Pearson [139-141], their coordination potential in respect to softer N-donor ligands is higher than could be expected. The challenges of working with highly radioactive materials are responsible for our relatively limited knowledge of the coordination behavior of transuranium elements. However, despite relatively few structural studies concerning the interaction of TRUE (especially for Am and Pu) with N-donor ligands, these data prove conclusively high affinity of these ligands for coordination to TRU elements in all oxidation states. In solution chemistry, this affinity is manifested in formation of stable complexes, especially in case of polydentate chelating ligands. Obviously, the unexpectedly high ability, or even the preference [142], of transuranium elements for coordination of N-donor ligands did not receive the reasonable explanation, and further investigations are called for in this area.

References

1. G. R. Choppin, J. Nucl. Radiochem. Sci., 6 (2005) 1.
2. G. R. Choppin, A. Morgenstern, J. Radioanal. Nucl. Chem., 243 (2000) 45.
3. B. Allard, U. Ollafson, B. Torstenfelt, Inorg. Chim. Acta, 94 (1984) 205.
4. G. N. Stradling, J. Alloys Compd., 271-273 (1998) 72.
5. H. Kimura, H. Takano, T. Muromura, J. Nucl. Mater., 274 (1999) 197.
6. K. L. Nash, G. R. Choppin, Sep. Sci. Technol., 32 (1997) 255.

7. T. L. Gilchrist, Heterocyclic chemistry, 2nd Edition, Longman Group UK Limited, London, 1992.
8. I.-Y. Su, X.-H. Xu, L.-M. Zong, M.-Y. Wang, N. Lu, Y. Lu, Q.-T. Zhang, Phytochemistry, 48 (1998) 583.
9. B. Nowack, J. M. VanBriesen (eds.), Biogeochemistry of chelating agents, American Chemical Society, Washington, DC, 2005.
10. R. A. Bulman, In: J. B. Goodenough (Ed.), Structure and bonding, Vol. 34, Springer-Verlag, Berlin, Heidelberg, 1981.
11. T. E. Hakonson, Health Phys., 29 (1975) 583.
12. R. A. Bulman, Coord. Chem. Rev., 31 (1980) 221.
13. D. W. Whisenhunt Jr., M. P. Neu, Z. Hou, Y. Xu, D. C. Hoffman, K. N. Raymond, Inorg. Chem., 35 (1996) 4128.
14. N. C. O'Boyle, G. P. Nicholson, T. J. Piper, D. M. Taylor, D. R. Williams, G. Williams, Appl. Radiat. Isot., 48 (1997) 183.
15. A. E. V. Gorden, J. Xu, K. N. Raymond, P. Durbin, Chem. Rev., 103 (2003) 4207.
16. R. D. Hancock, A. E. Martell, Chem. Rev., 89 (1989) 1875.
17. K. H. Lieser, U. Mühleuweg, Radiochim. Acta, 43 (1988) 27.
18. O. Tochiyama, Y. Inoue, S. Narita, Radiochim. Acta, 58/59 (1992) 129.
19. J. P. Kaszuba, W. H. Runde, Environ. Sci. Technol., 33 (1999) 4427.
20. W. J. Bair, R. C. Thomson, Science, 183 (1974) 715.
21. P. W. Durbin, Health Phys., 29 (1975) 495.
22. W. R. Harris, C. Y. Carrano, V. L. Pecoraro, K. N. Raymond, J. Am. Chem. Soc., 103 (1981) 2231.
23. D. C. Hoffman (Ed.), Advances in plutonium chemistry, American Nuclear Society, La Grange Park, Illinois, 2001.
24. N. Kaltsyannis, P. Scott, The f elements, Oxford University Press, New York, 1999.
25. K. L. Nash, In: A. H. Bond, M. L. Dietz, R. M. Rogers (Eds.), Metal-ion separation and preconcentration: progress and opportunities, Oxford University Press, Washington, DC, 1999.
26. K. L. Nash, Solvent Extr. Ion Exch., 11 (1993) 729.
27. M. G. B. Drew, P. B. Ivenson, M. J. Hudson, J. O. Liljenzin, L. Spjuth, P.-Y. Cordier, A. Enarsson, C. Hill, C. Madic, J. Chem. Soc., Dalton Trans., (2000) 821.
28. N. Boubals, M. G. B. Drew, C. Hill, M. J. Hudson, P. B. Ivenson, C. Madic, M. L. Russell, T. G. A. Youngs, J. Chem. Soc., Dalton Trans., (2002) 55.
29. M. A. Denecke, A. Rossberg, P. J. Pank, M. Weigl, B. Schimmelpfennig, A. Geist, Inorg. Chem., 44 (2005) 8418.
30. H. Takeishi, Y. Kitatsuji, T. Kimura, Y. Mequro, Z. Yoshida, S. Kihara, Anal. Chim. Acta, 431 (2001) 69.
31. M. Weigl, U. Mullich, A. Geist, K. Gompper, T. Zevaco, H. Stephan, J. Radioanal. Nucl. Chem., 256 (2003) 403.
32. L. Karmazin, M. Mazzanti, C. Gateau, C. Hill, J. Pecaut, Chem. Commun., (2002) 2892.
33. M. Miguirditchian, D. Guillaneux, D. Guillaumont, P. Moisy, C. Madic, M. P. Jensen, K. L. Nash, Inorg. Chem. 44 (2005) 1404.
34. P. Y. Cordier, C. Hill, P. Baron, C. Madic, M. J. Hudson, J. O. Liljenzin, J. Alloys Compd., 271-273 (1998) 738.
35. I. Hagström, L. Spjuth, Å. Enarsson, J. O. Liljenzin, M. Skålberg, M. J. Hudson, P. B. Ivenson, C. Madic, P. Y. Cordier, C. Hill, N. Francois, Solvent Extr. Ion Exch., 17 (1999) 221.
36. M. G. B. Drew, C. Hill, M. J. hudson, P. B. Iveson, C. Madic, L. Vaillant, T. G. A. Youngs, New J. Chem., 28 (2004) 462.
37. M. P. Jensen, L. R. Morss, J. V. Beitz, D. D. Ensor, J. Alloys Compd., 303-304 (2000) 137.

38. C. Apostolidis, A. Carvalho, A. Domingos, B. Kanellakopulos, R. Maier, N. Marques, A. Pires de Matos, J. Rebizant, Polyhedron, 18 (1998) 263.
39. Z. Kolarik, U. Müllich, F. Gassner, Solvent Extr. Ion Exch., 17 (1999) 23.
40. Z. Kolarik, U. Müllich, F. Gassner, Solvent Extr. Ion Exch., 17 (1999) 1155.
41. M. Mazzanti, R. Wietzke, J. Pécaut, J. M. Latour, P. Maldivi, M. Remy, Inorg. Chem., 41 (2002) 2389.
42. E. Brandau, Komplexbildung von fünf- und sechswertigen Actiniden mit heterocyclischen Karbonsaüren, KFK Berichte - 1068, Karlsruhe, 1970.
43. W. Robel, Komplexbildung sechswertigen Actiniden mit Pyridinkarbonsaüren, KFK Berichte - 1070, Karlsruhe, 1970.
44. S. H. Eberle, Komplexbildung der Actiniden mit organischen Liganden, KFK Berichte - 1136, Karlsruhe, 1970.
45. U. Wede, Die Chelatbildung des fünfwertigen Neptuniums und Plutoniums mit α-Aminopolykarbonsaüren, KFK Berichte - 837, Karlsruhe, 1969.
46. I. Bayat, Über Komplexe dreiwertigen Transurane mit Aminopolykarbonsaüren, KFK Berichte - 1291, Karlsruhe, 1970.
47. M. T. Paul, Die komplexbildung vierwertigen Actiniden mit Pyridin- und α-Aminopolykarbonsaüren, KFK Berichte - 1210, Karlsruhe, 1970.
48. H. Stober, Mischkomplexe und höhere Uniligandenkomplexe des fünfwertigen Neptunium – zur Koordinationfähigkeit des NpO_2^+-ions, KFK Berichte - 1657, Karlsruhe, 1972.
49. E. Merciny, J. M. Gatez, G. Duyckaerts, Anal. Chim. Acta, 100 (1978) 329.
50. R. D. Baybarz, J. Inorg. Nucl. Chem., 27 (1965) 1831.
51. N. Zaman, E. Merciny, G. Duyckaerts, Anal. Chim. Acta, 56 (1971) 271.
52. J. Fuger, B. B. Cunningham, J. Inorg. Nucl. Chem., 27 (1965) 1079.
53. C. T. Chang, M. M. Chang, C. F. Liaw, J. Inorg. Nucl. Chem., 35 (1973) 261.
54. P. K. Khopkar, J. N. Mathur, J. Inorg. Nucl. Chem., 36 (1974) 3819.
55. C. Musikas, M. Marteau, Sov. Radiochem. (Engl. Trans.), 20 (1978) 213.
56. G. R. Choppin, J. Ketels, J. Inorg. Nucl. Chem., 27 (1965) 1335.
57. C. Musikas, M. Marteau, Radiochem. Radioanal. Lett., 30 (1977) 271.
58. P. R. V. Rao, S. V. Bagawde, V. V. Ramakrishna, S. K. Patil, J. Inorg. Nucl. Chem., 40 (1978) 339.
59. C. Musikas, M. Marteau, Radiochem. Radioanal. Lett., 33 (1978) 41.
60. P. R. V. Rao, N. M. Gudi, S. V. Bagawde, S. K. Patil, J. Inorg. Nucl. Chem., 41 (1979) 235.
61. F. L. Weitl, K. N. Raymond, W. L. Smith, T. R. Howard, J. Am. Chem. Soc., 100 (1978) 1170.
62. C. Keller, S. H. Eberle, Radiochim. Acta, 4 (1965) 141.
63. S. H. Eberle, W. Robel, Inorg. Nucl. Chem. Lett., 6 (1970) 359.
64. S. H. Eberle, W. Robel, J. Inorg. Nucl. Chem., 32 (1970) 109.
65. C. Keller, S. H. Eberle, Radiochim. Acta, 8 (1967) 65.
66. K. S. Rajan, A. E. Martell, J. Inorg. Nucl. Chem., 26 (1964) 789.
67. S. H. Eberle, U. Wede, Inorg. Nucl. Chem. Lett., 5 (1969) 5.
68. J. K. Foreman, T. D. Smith, J. Chem. Soc., 1 (1957) 1752.
69. J. K. Foreman, T. D. Smith, J. Chem. Soc., 1 (1957) 1758.
70. P. Cauchetier, C. Guichard, Radiochim. Acta, 19 (1973) 137.
71. P. Cauchetier, C. Guichard, J. Inorg. Nucl. Chem., 37 (1975) 1771.
72. G. H. Carey, R. F. Bogucki, A. E. Martell, Inorg. Chem., 3 (1964) 1288.
73. R. F. Bogucki, A. E. Martell, J. Am. Chem. Soc., 80 (1958) 4170.
74. S. H. Eberle, M. T. Paul, J. Inorg. Nucl. Chem., 33 (1971) 3067.
75. S. H. Eberle, S. A. H. Ali, Radiochim. Acta, 5 (1966) 58.
76. T. Ishimori, E. Nakamura, Radiochim. Acta, 1 (1962) 6.

77. S. H. Eberle, I. Bayat, Inorg. Nucl. Chem. Lett., 5 (1969) 229.
78. B. P. Hay, R. D. Hancock, Coord. Chem. Rev., 212 (2001) 61.
79. D. H. Bush, Chem. Rev., 93 (1993) 847.
80. A. E. V. Gorden, D. K. Shuh, B. E. F. Tiedemann, R. E. Wilsdon, J. Xu, K. N. Raymond, Chem. Eur. J., 11 (2005) 2842.
81. T. Yaita, S. Tachimori, N. M. Edelstein, J. J. Bucher, L. Rao, D. K. Shuh, P. G. Allen, J. Synchrotron Rad., 8 (2001) 663.
82. N. W. Alcock, D. J. Flanders, D. Brown, Inorg. Chim. Acta, 94 (1984) 279.
83. N. W. Alcock, D. J. Flanders, D. Brown, J. Chem. Soc., Dalton Trans., (1985) 1001.
84. N. W. Alcock, D. J. Flanders, M. Pennington, D. Brown, Acta Crystallogr. C, 43 (1987) 1476.
85. G. B. Andreev, A. M. Fedoseev, N. A. Budantseva, M. Yu. Antipin, Mendeleev Commun., No. 2 (2001) 58.
86. G. B. Andreev, V. N. Khrustalev, M. Yu. Antipin, A. M. Fedoseev, N. A. Budantseva, J. C. Krupa, C. Madic, Russ. J. Coord. Chem., 26 (2000) 825.
87. A. M. Fedoseev, G. B. Andreev, N. A. Budantseva, J. C. Krupa, J. Nucl. Sci. Technol., Suppl. 3 (2002) 414.
88. N. A. Budantseva, G. B. Andreev, A. M. Fedoseev, M. Yu. Antipin, Dokl. Chem., 384 (2002) 159.
89. G. B. Andreev, A. M. Fedoseev, N. A. Budantseva, M. Yu. Antipin, Dokl. Chem., 375 (2000) 285.
90. N. A. Budantseva, G. B. Andreev, A. M. Fedoseev, M. Yu. Antipin, Crystallogr Rep., 48 (2003) 58.
91. N. A. Budantseva, G. B. Andreev, A. M. Fedoseev, M. Yu. Antipin, Radiochemistry, 45 (2003) 335.
92. G. B. Andreev, M. Yu. Antipin, A. M. Fedoseev, N. A. Budantseva, Russ. J. Coord. Chem., 27 (2001) 211.
93. A. E. Enriquez, J. H. Matonic, B. L. Scott, M. P. Neu, Chem. Commun., (2003) 1892.
94. J. L. Sessler, D. Seidel, A. E. Vivian, V. Lynch, B. L. Scott, D. W. Keogh, Angew. Chem., Int. Ed., 40 (2001) 591.
95. N. A. Budantseva, G. B. Andreev, A. M. Fedoseev, M. Yu. Antipin, Russ. J. Coord. Chem., 29 (2003) 322.
96. N. A. Budantseva, G. B. Andreev, A. M. Fedoseev, M. Yu. Antipin, Russ. J. Coord. Chem., 29 (2003) 265.
97. G. B. Andreev, M. Yu. Antipin, A. M. Fedoseev, N. A. Budantseva, Dokl. Chem., 374 (2000) 187.
98. N. A. Budantseva, G. B. Andreev, A. M. Fedoseev, A. A. Bessonov, M. Yu. Antipin, J. C. Krupa, C. R. Chimie, 8 (2005) 91.
99. G. B. Andreev, N. A. Budantseva, V. P. Perminov, A. M. Fedoseev, Radiochemistry, 47 (2005) 91.
100. G. B. Andreev, Interaction of pentavalent neptunium with N-containing ligands, Ph. D. Dissertation, Institute of Physical Chemistry RAS, Moscow, 2001.
101. N. A. Budantseva, G. B. Andreev, A. M. fedoseev, M. Yu. Antipin, J. C. Krupa, Radiochim. Acta, 94 (2006).
102. J. L. Sessler, A. E. V. Gorden, D. Seidel, S. Hannah, V. Lynch, P. L. Gordon, R. J. Donohoe, C. Drew Tait, D. Webster Keogh, Inorg. Chim. Acta, 341 (2002) 54.
103. D. G. Chuguryan, V. I. Dzyubenko, M. S. Grigoriev, A. I. Yanovsky, Yu. T. Struchkov, Sov. Radiochem. (Engl. Trans.), 30 (1988) 164.
104. M. S. Liao, T. Kar, S. Scheiner, J. Phys. Chem. A, 108 (2004) 3056.
105. J. L. Sessler, A. E. Vivian, D. Seidel, A. K. Burrell, M. Hoehner, T. D. Mody, A. Gebauer, S. J. Weghorn, V. Lynch, Coord. Chem. Rev., 216-217 (2001) 411.

106. J. H. Matonic, B. L. Scott, M. P. Neu, Inorg. Chem., 40 (2001) 2638.
107. A. Cassol, L. Magon, Ric. Sci., 36 (1966) 1194.
108. C. Musikas, C. Cuillerdier, J. Livet, A. Forchioni, C. Chachaty, Inorg. Chem., 22 (1983) 2513.
109. Z. Assefa, T. Yaita, R. G. Haire, S. Tachimori, Inorg. Chem., 42 (2003) 7375.
110. D. Guillaumont, J. Phys. Chem. A, 108 (2004) 6893.
111. M. Yashito, A. Ishikubo, T. Takarada, M. Komiyama, Chem. Lett., 8 (1995) 665.
112. R. D. Shannon, Acta Crystallogr. A, 32 (1976) 751.
113. N. A. Budantseva, G. B. Andreev, A. M. Fedoseev, M. Yu. Antipin, Proceedings of the 3rd Crystallochemical Conference, Chernogolovka, Russia, May 19-23, 2003, p. 160.
114. W. Wendlandt, G. Horton, J. Inorg. Nucl. Chem., 19 (1961) 272.
115. M. S. Grigor'ev, A. I. Yanovsky, N. N. Krot, Yu. T. Struchkov, Sov. Radiochem. (Engl. Trans.), 29 (1987) 554.
116. M. S. Grigor'ev, B. F. Gulev, N. N. Krot, Sov. Radiochem. (Engl. Trans.), 28 (1986) 625.
117. G. B. Andreev, personal communication.
118. C. Den Auwer, I. Llorens., P. Moisy, C. Vidaud, H. Funke, C. Barbot, F. Goudard, In: A. C. Scheinost, N. Schell (Eds.), Wissenschaftlich-technische berichte, FZR - 418, Rossendorf, 2005.
119. M. P. Mefodieva, A. D. Gelman, Complex formation and extraction of actinides and lanthanides, Nauka, 1974.
120. D. Rai, H. Bolton Jr., D. A. Moore, N. J. Hess, G. R. Choppin, Radiochim. Acta, 89 (2001) 67.
121. H. Boukhalfa, S. D. Reilly, W. H. Smith, M. P. Neu, Inorg. Chem., 43 (2004) 5816.
122. E. M. Piskunov, A. G. Rykov, Sov. Radiochem. (Engl. Trans.), 14 (1972) 342.
123. E. M. Piskunov, A. G. Rykov, Sov. Radiochem. (Engl. Trans.), 14 (1972) 345.
124. N. V. Jarvis, R. D. Hancock, Radiochim. Acta, 64 (1994) 15.
125. G. B. Andreev, N. A. Budantseva, A. M. Fedoseev, M. Yu. Antipin, Actinides 2005, Manchester, UK, July 4-8, 2005, Abstracts, 2P06.
126. G. B. Andreev, personal communication.
127. Y. Inoue, O. Tochiyama, Polyhedron, 2 (1983) 627.
128. Y. Inoue, O. Tochiyama, T. Takahasi, Radiochim. Acta, 31 (1982) 197.
129. G. R. Choppin, L. F. Rao, E. N. Rizkalla, J. C. Sullivan, Radiochim. Acta, 57 (1992) 173.
130. E. N. Rizkalla, F. Nectoux, S. Dabos-Seignon, M. Pages, Radiochim. Acta, 51 (1990) 151.
131. J. I. Friese, K. L. Nash, M. P. Jensen, J. C. Sullivan, Radiochim. Acta, 89 (2001) 35.
132. A. Cousson, S. Dabos, H. Abazli, F. Nectoux, M. Pages, G. Choppin, J. Less-Common. Met., 99 (1984) 233.
133. M. S. Grigor'ev, A. I. Yanovski, Yu. T. Struchkov, A. A. Bessonov, T. V. Afonasieva, N. N. Krot, Sov. Radiochem. (Engl. Trans.), 31 (1989) 37.
134. G. B. Andreev, personal communication.
135. L. Prasad, E. J. Gabe, B. Glavincevski, S. Brownstein, Acta Crystallogr. C, 39 (1983) 181.
136. P. Charpin, M. Lance, M. Nierlich, D. Vigner, J. Livet, C. Musikas, Acta Crystallogr. C, 42 (1986) 1691.
137. N. W. Alcock, S. Roe, T. Kemp, J. Leceiejwicz, Ionrg. Chim. Acta, 248 (1996) 241.
138. B. G. Harvey, H. G. Heal, A. G. Maddock, E. L. Rowley, J. Chem. Soc., (1947) 1010.
139. R. G. Pearson, J. Am. Chem. Soc., 85 (1963) 3533.
140. R. G. Pearson, Coord. Chem. Rev., 100 (1990) 403.
141. D. Datta, Inorg. Chem., 31 (1992) 2797.
142. M. J. Sarsfield, I. May, S. M. Cornet, M. Heiliwell, Inorg. Chem., 44 (2005) 7310.

This page intentionally left blank

Structural Chemistry of Inorganic Actinide Compounds
S.V. Krivovichev, P.C. Burns & I.G. Tananaev (Editors)

Chapter 11

U(VI)-containing metal-organic frameworks and coordination polymers

Christopher L. Cahill[a,b] and Lauren A. Borkowski[a]

[a]*Department of Chemistry, The George Washington University, 725 21st Street NW, Washington, DC 20052, USA*
[b]*Geophysical Laboratory, Carnegie Institution of Washington, 5251 Broad Branch Road NW, Washington, DC 20015, USA*

1. Introduction

The field of metal-organic framework materials (MOFs), or more generally, coordination polymers (CPs), has seen a tremendous amount of research activity over the past several years. Much of this interest arguably stems from a desire to expand on the utility of zeolite type (e.g. aluminosilicate etc) materials to include systems with the potential for tailored or designed structures. Applications for zeolites have generally included ion exchange, gas sorption, catalysis, water softening and the like, yet MOFs and related materials exhibit the potential for molecular recognition on a much finer scale, as well as expanded sorption capabilities. From a synthetic perspective, part of the appeal of these materials is a greater degree of control over resulting structures and topologies. This allows, to some extent, scientists to 'rationally design' compounds of interest as compared to other hydrothermal (or high-temperature) syntheses. This increased degree of control arises from both the coordination geometry preferences of the metal centers as well as the geometry of the linker molecules themselves.

A number of excellent review articles on MOFs and coordination polymers have appeared in the literature recently.[1-7] We will therefore limit our introduction to a discussion of essential structural issues necessary to appreciate this class of inorganic/organic hybrid materials. We will also point out that to the best of our knowledge, this is the first review of uranyl containing

MOFs/CPs, as the majority of these materials are based on transition metal, and more recently, lanthanide chemistry, yet a review of polymeric materials containing uranium (from more of a polymer chemistry perspective) has appeared recently.[8] We will compare and contrast some uranium specific issues to those of the transition elements as we feel that the unique coordination geometries of the actinides (in particular U(VI)) result in a number of structural features, synthetic challenges, relevance to environmental issues, and opportunities for development of functional materials.

1.1. Background: What is a MOF or Coordination Polymer?

The definitions of these two terms can vary somewhat depending on with which community one interacts, or as a matter of convenience for one's system of interest. We begin this section with a definition of each as applicable to the uranyl containing materials to be discussed herein. Generally speaking, a *coordination polymer* (CP) will be any hybrid material (that is, one that contains metal centers linked through multifunctional organic components), with an overall structural topology that is at least one dimensional. This excludes all molecular materials and many salts. The dimensionality must arise from direct connectivity between the metal centers and linkers and contain ionic and/or covalent bonds. Hydrogen bonding, although important as we will see below, will not be included as a contributor to our dimensionality designation. A *metal-organic framework* (MOF) is actually a subspecies of a CP, in that their structures must be three dimensional in overall topology through ionic and/or covalent bonding only. We emphasize the requirement of direct coordination of the metal center to an organic linker molecule as this provides a distinction from structures where the organic component serves as a 'template' or guest. Whereas these materials are in fact hybrids and indeed interesting, they do not fit our definition of a MOF or CP. These materials are addressed in separate sections throughout this volume.

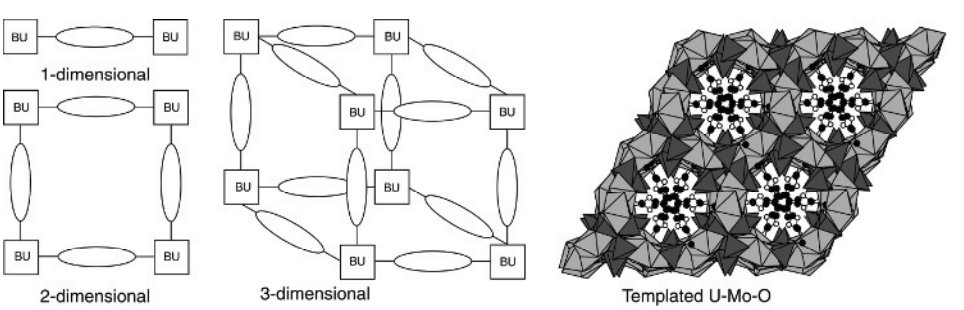

Fig. 1. Left: A skeletal representation of coordination polymers and a MOF. The inorganic building units (BU) are connected through organic linker molecules (tethered ovals) to form structures of varying dimensionality. Right: An inorganic/organic oxide hybrid material, $[(C_2H_5)_2NH_2]_2[(UO_2)_4(MoO_4)_5(H_2O)](H_2O)$[9] for comparison.

By way of Figure 1, we introduce a number of these concepts graphically. The first image is a one-dimensional CP as evidenced by connectivity in one direction. The inorganic component is labeled as 'BU' for 'building unit' as we will describe below. Examples of 2-D and 3-D structures follow, as does a hybrid, yet non-CP material for comparison. The term 'metal-organic-framework' or MOF, is reserved for the three-dimensional example only. These designations are similar to those found in a recent review by Ferey.[2] Figure 2 follows and presents an additional representation of this philosophy by way of an actual example from the U-adipate system. This structure will be discussed in more detail below, yet the concept of polymerizing uranyl centers (in this case, dimers), through multifunctional organic linker molecules into an extended three dimensional architecture is apparent.

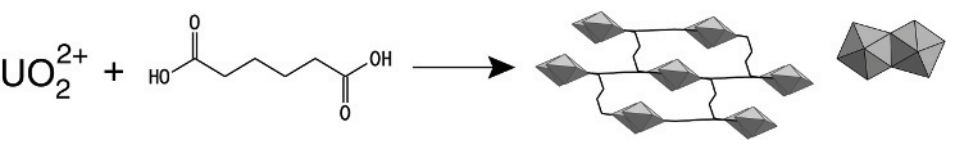

Fig. 2. A schematic of uranyl assembly with a multifunctional linker molecule (adipic acid) to form a 3-dimensional structure. A dimer secondary building unit, which consist of edge shared pentagonal bipyramids, is shown in the inset on the right. This compound is revisited in Figure 12 (below).

What is also apparent from these figures is the reasoning behind our use of the word 'linker' when referring to the organic component of these materials. One may be tempted to use the term 'ligand', yet we emphasize the role of the organic in polymerizing metal centers (or BUs) through its multifunctional nature and not simply decorating or chelating. The organic portion of these materials is an integral component of the overall structure. It should also be mentioned at this point that the chemistry of these extended materials is not entirely new, yet we will argue that the emphasis toward intentional synthesis of higher dimensional solids is a more recent phenomena. Arguably, the term 'metal-organic framework' can be traced to an emergence of interest in these materials during the early 1990's. Clearly polymeric materials have existed prior to this time, yet it is likely that many of those older contributions were synthesized as a result of other studies, and not during those focused on the potential applications of MOFs and CPs described above.

In terms of synthesis and formation mechanism for these materials, most rely on self-assembly under hydro- or solvothermal conditions. That is, metal salts are dissolved in the presence of the linker molecules and allowed to

crystallize into desired architectures. The syntheses of the materials discussed herein are relatively straightforward single-pot reactions and we will not discuss them further, yet instead encourage the reader to examine the specific references. Despite the simplicity of their syntheses, the complexity of the hydrothermal UO_2^{2+} system allows for some interesting speciation (and ultimately BU variety) that we will discuss in turn.

2. Structural Systematics for U-MOFs and U-CPs

2.1. Types of linkages possible

Prior to a systematic presentation of a number of recent examples of polymeric U-containing materials, a brief review of uranyl coordination chemistry is required. We offer this as a precursor to understanding what types of organic linker molecules can be utilized in the construction of these materials. That is, for what types of functional groups does the uranyl cation have an affinity? The coordination chemistry of the uranyl cation is extensive and has been reviewed in a number of settings.[10-12] For the purposes of our discussion, we remind readers that the chemistry of hexavalent U in aqueous solution is dominated by the formation of the uranyl cation, UO_2^{2+}. This linear triatomic species shows strong covalent bonding to its terminal oxo ligands and thus forces any further coordination to take place through the equatorial plane. The resulting coordination geometries tend to thus be square-, pentagonal-, and hexagonal bipyramidal. The variety of ligands that have been shown to coordinate in this fashion is extensive and consists primarily of O donor functional groups. These include carboxylic acids, enoates, Schiff bases and the like, with the majority of these materials being molecular in nature.

This richness in coordination geometry however allows for a range of potential organic linker molecules to be exploited. The lesson learned from coordination chemistry of molecular compounds is that by the far the most common types of functional groups coordinated to the uranyl cation are those containing oxygen donors such as carboxylates[10] and Schiff bases[11]. The challenge for scientists interested in polymerizing this species into extended architectures is to then chose *multi*functional organic linker molecules possessing these functional groups at sufficient distances from one another to promote assembly and polymerization as opposed to chelation and formation of molecular entities. Although we will examine these more closely herein, a few examples of organic linkers meeting these criteria are shown in Figure 3.

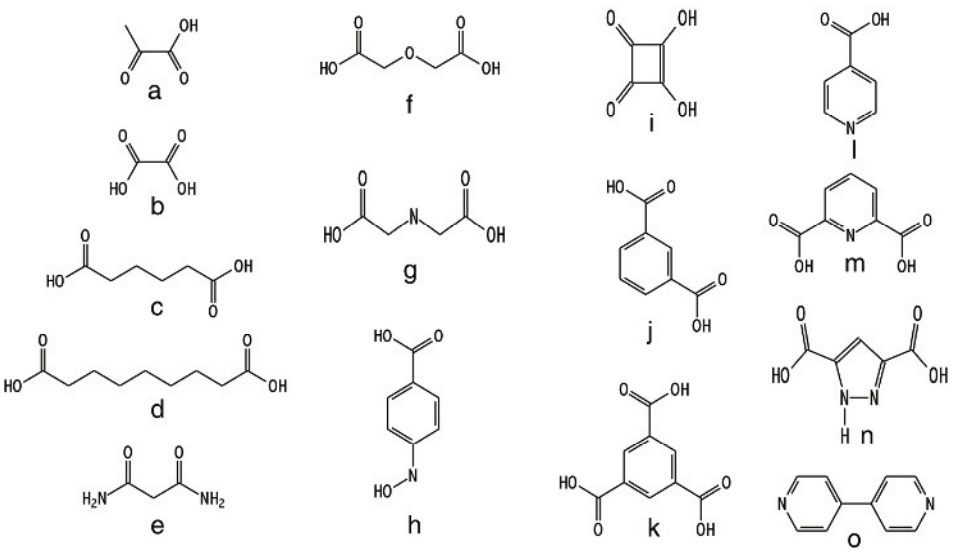

Fig. 3. Some examples of multifunctional organic linker molecules: a) lactic acid, b) oxalic acid, c) adipic acid, d) azelaic acid, e) malonamide, f) oxodiacetate, g) iminodiacetate, h) oxypyridine-4-carboxylic acid, i) squaric acid, j) 1,3-benzenedicarboxylic acid, k) 1,3,5-benzenetricarboxylic acid, l) isonicotinic acid, m) 2,6-pyridine dicarboxylic acid, n) 3,5-pyrazoledicarboxylic acid, o) 4,4'-dipyridyl

2.2. Definition and dimensionality of the building unit.

The term 'building unit' is used extensively in the literature of extended and framework hybrid solids. In general, this term, whether modified by *primary* or *secondary*, refers to the basic inorganic repeat unit that when polymerized, forms the foundation of the inorganic component of the structure. In aluminosilicate zeolites, for example, the term 'primary building unit' refers to a single TO_4 tetrahedron. Secondary building units (or SBUs) in this system then refer to theoretical topological entities that when repeated define the entire framework structure.[13] In MOFs and CPs, we refer to the primary building unit as the metal center and its first shell of coordination. As in the zeolite system, this results in metal centered polyhedra, yet by virtue of the variety of metal species encountered, is not restricted to simply tetrahedral environments. For the uranyl system, the primary building unit may be thought of as the uranyl cation and its first shell of coordination, e.g. the square-, pentagonal and hexagonal bipyramids themselves. What is perhaps of additional use however,

is the introduction of an SBU definition to describe both the coordination geometry as well as any oligomerization of primary building units into larger species such as dimers and tetramers. We present these definitions and evolution of the characterization schemes in Figure 4. Shown first (Figure 4a) is a silicate example of a primary SiO_4 BU (ball-and-stick and polyhedral representations are on the left). On the right is a nodal representation (each dot = one SiO_4 tetrahedron) of BUs polymerized to form commonly observed SBUs. Figure 4b shows a similar evolution of a ZnO_4 tetrahedron to a tetranuclear SBU as observed in MOF-5.[14] Figure 4c contains the most frequently observed BUs of the UO_2^{2+} cation followed by SBUs encountered in coordination polymer materials. It should also be mentioned that BUs and SBUs, although present in solid state structures, are not necessarily reflective of solution speciation prior to crystallization. Thus this is an area in need of further study, especially in hydrothermal systems.

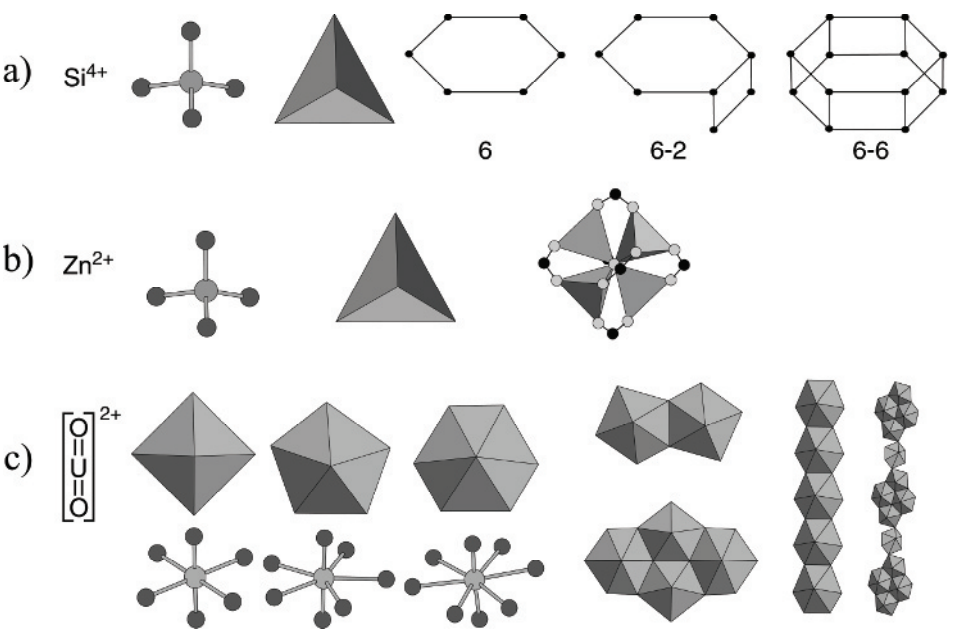

Fig. 4. a) Primary and secondary building units in the aluminosilicate zeolite system. b) Primary and secondary building units as found in transition-metal MOFs. c) Primary and secondary building units present in uranyl containing CPs and MOFs. These polyhedral representations of uranyl square-, pentagonal-, and hexagonal bipyramids will be used throughout this review.

2.3. Combining the building unit and overall topology dimensionalities: a classification scheme.

As a final component of introduction prior to examination of individual structure types, we propose a classification scheme for study and presentation of the materials described herein. Three-dimensional networks formed through linked SBUs in the transition metal systems have been examined extensively and approached from a more topological point of view.[15,16] Whereas this line of inquiry is clearly necessary and critical for understanding networks in general, it is perhaps less critical for the U-CP systems we are to describe as the overall topologies tend to be somewhat complex and often not three dimensional. Further, as introduced briefly above, the variety of SBU geometries in the uranyl systems is quite rich, with variation in both the local coordination of the uranyl cation (i.e. 4-, 5-, and 6- coordinate) as well as the extent of oligimerization into dimers, trimers, tetramers, etc. The following classification scheme thus emphasizes the *local geometry* about the uranyl cation while acknowledging the overall dimensionality of the structure. A generalized approach is given in Scheme 1, and subsequent tables within this review will include such designations.

$$D^{a,b,c}_{a',b',c'}$$

a = number of metal centers in building unit
b = coordination number of metal center
c = coordination number of additional metal center(s)

Scheme 1. A classification scheme to describe the overall dimensionality and local uranyl geometry in U(VI) containing CPs and MOFs. The superscripts describe the uranium coordination geometry whereas the subscripts refer to any second metal centers present, as in heterometallic compounds.

2.4. Resources and Software

The Cambridge Crystallographic Data Centre's (CCDC) Cambridge Structural Database (CSD)[17] has been our primary resource for the materials presented herein. The database version was V5.27 (November 2005) and all searches used the ConQuest search engine V1.8.[18] In addition, we have pursued references through literature searches and cross-checking citations contained within articles located through the CSD. In order for readers to reproduce our lists, we present our search criteria as follows: 1) A general search on the [O=U=O] entity, which resulted in 962 unique hits. This list was then shortened

considerably to 174 unique hits by removing all molecular species via the 'not polymeric' filter feature in ConQuest. This list was then examined manually using the graphics program Mercury[18] and only those materials where the organic component was structurally relevant were retained. That is, only those materials meeting our definition of coordination polymer (above) were considered. This resulted in the exclusion of a number of compounds with coordinated solvent molecules or other organic species that simply 'decorated' an otherwise inorganic material. We have also included a number of structures from our laboratory that are in preparation for publication and will thus be included in future versions of the CSD.

3. Specific Examples

This section begins a systematic treatment of specific structure types within the uranyl-CP system. Our presentation is limited (initially) to only those materials containing hexavalent uranium occurring as the UO_2^{2+} cation. The compounds are categorized based on the type of functional group found on the organic linker molecules. This will be expanded to include heterometallic systems and ultimately a few non-uranyl and non-CP examples included for perspective.

3.1. Homometallic systems (i.e. $(UO_2)^{2+}$ only) with a single linker type.

3.1.1. Carboxylates

A very rich group of CPs containing the uranyl cation is the oxalates. The oxalate species, $C_2O_4^{2-}$, is a planar, bifunctional linker molecule that may be considered as a 'hard' Lewis base in terms of Pearson's hard/soft acid-base distinction.[19] The chemistry of main-group and transition metal oxalate compounds is extensive and has been reviewed elsewhere.[1] Oxalate anions have an affinity for metals in high oxidation states and their planarity is well suited for equatorial coordination to the uranyl cation. In addition to an extensive list of molecular species, a variety of CPs have been synthesized (Table 1). Polymeric compounds containing strictly terminal (i.e. bidentate, yet chelating) oxalate ligands are not included. The uranyl cation coordinates to oxalate linkages most commonly in a bridging bidentate fashion (Figures 5-8). Chain and sheet structures are observed (with chains being more common) as the

oxalate anion is ideally suited to bridge neighboring metal centers. Most compounds have the uranyl cation in pentagonal bipyramidal coordination where equatorial positions are occupied by the oxalate O atoms, terminal H_2O or isothiocyanate groups, or bridging sulfate/selenate polyhedra. Compounds $(NH_4)_2[(UO_2)_2(C_2O_4)_2]$ (AMULUX10) (Figure 5)[20] and $(NH_4)_2[UO_2(C_2O_4)_2]$ (URNDOX) (Figure 6)[21] exemplify this connectivity. Further, $(NH_4)_2[UO_2(C_2O_4)_2]$ contains a terminal bidentate oxalate group that does not

Table 1. Uranyl coordination polymers constructed from oxalate linkages.

Formula	linker	dimensionality	CSD code	ref #
$(NH_4)_2[(UO_2)_2(C_2O_4)_2]$	oxalate	$1^{1,7}$	AMULOX10	20
$Na_2[(UO_2)_4(C_2O_4)_5(H_2O)_2]\cdot 8H_2O$	oxalate	$2^{1,7}$	AZAWAZ	22
$(NH_4)[(UO_2)(C_2O_4)(NCS)]\cdot 2H_2O$	oxalate	$1^{1,7}$	EYOLEJ	23
$(NH_4)[(UO_2)_2(OH)(C_2O_4)_2]\cdot 2H_2O$	oxalate	$2^{2,7}$	EYOLIN	24
$(UO_2(C_2O_4)(C_2H_6NO))_2\cdot 2(CH_2N_3)(H_2O)$	oxalate	$1^{1,8}$	FEFNAF	25
$K_4[(UO_2)_2(C_2O_4)_2(SO_4)_2]\cdot 6H_2O$	oxalate	$1^{1,7}$	KANXAZ	26
$K_2[(UO_2)_2(C_2O_4)_3]\cdot 4H_2O$	oxalate	$2^{1,8}$	KUROXT	27
$(NH_4)_6(UO_2)_2(C_2O_4)(SeO_4)_4\cdot 2H_2O$	oxalate	$1^{1,7}$	LOFGIW	28
$(NH_4)_2[UO_2(C_2O_4)_2]$	oxalate	$1^{1,7}$	URNDOX	21
$(UO_2(C_2O_4)_3(H_2O))_2\cdot(H_2O)$	oxalate	$1^{1,7}$	UYOXAL	29
$(UO_2)_2(C_2O_4)(OH)_2(H_2O)_2$	oxalate	$1^{2,7}$	-	30
$(UO_2)_2(C_2O_4)(OH)_2(H_2O)_2$	oxalate	$2^{\infty,7}$	-	30
$(UO_2)_2(C_2O_4)(OH)_2(H_2O)_2\cdot H_2O$	oxalate	$2^{4,7}$	-	30

contribute to polymerization. Hexagonal bipyramidal geometry is observed in $K_2[(UO_2)_2(C_2O_4)_3]\cdot 4H_2O$ (KUROXT) (Figure 7) where the uranyl cation has three bidentate oxalate linkages in the equatorial plane and thus promotes a sheet structure. This UO_2^{2+}:oxalate ratio results in anionic sheets which are in turn charge balanced with K^+ cations residing in the interlayer region. Polymerization of primary BUs to form SBUs is less common, although point shared dimers are observed in $NH_4[(UO_2)_2(OH)(C_2O_4)_2]\cdot 2H_2O$ (EYOLIN) (Figure 8)[24] and β-$(UO_2)_2(C_2O_4)(OH)_2(H_2O)_2$,[30] chains in α-

$(UO_2)_2(C_2O_4)(OH)_2(H_2O)_2$[30] and tetramers in $(UO_2)_2(C_2O_4)(OH)_2(H_2O)_2{\cdot}H_2O$.[30] U-$O_{Ur}$ bond lengths range from 1.615 to 1.840 Å with an average of 1.745 Å and U-O_{ox} bond lengths range from 2.280 to 2.589 Å with an average of 2.420 Å.

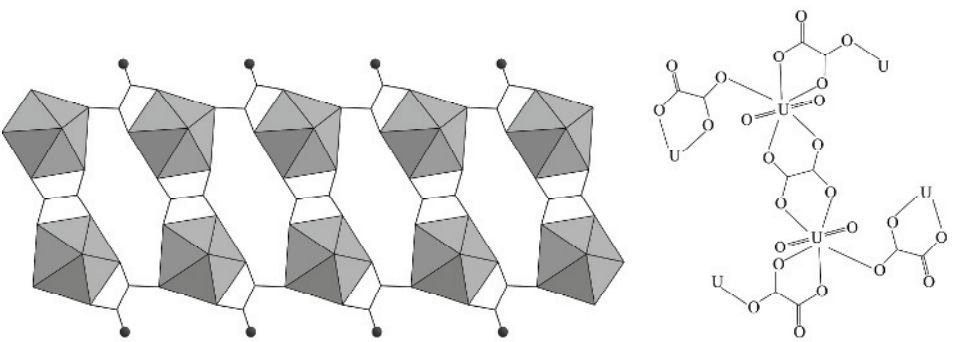

Fig. 5. The structure of $(NH_4)_2[(UO_2)_2(C_2O_4)_2]$ showing anionic chains of uranyl centered pentagonal bipyramids running along the [001] direction. At right is a diagram highlighting local coordination. Charge balancing NH_4^+ cations have been omitted for clarity.

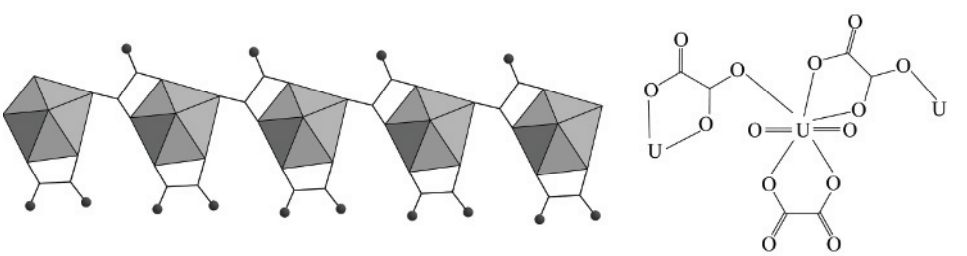

Fig. 6. The chain structure of $(NH_4)_2[UO_2(C_2O_4)_2]$. Uranyl centers are connected through a bridging bidentate oxalate linkage in addition to being coordinated to a terminal bidentate oxalate anion. Charge balancing NH_4^+ cations have been omitted for clarity.

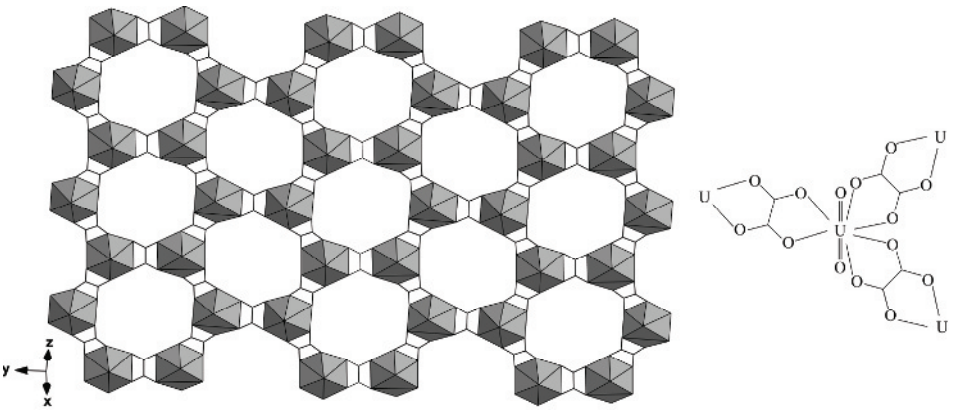

Fig. 7. The structure of $K_2[(UO_2)_2(C_2O_4)_3]\cdot 4H_2O$. Hexagonal bipyramids bridge through bidentate oxalate linkages to form anionic sheets. Charges balancing K^+ cations as well as interlayer H_2O molecules have been omitted for clarity.

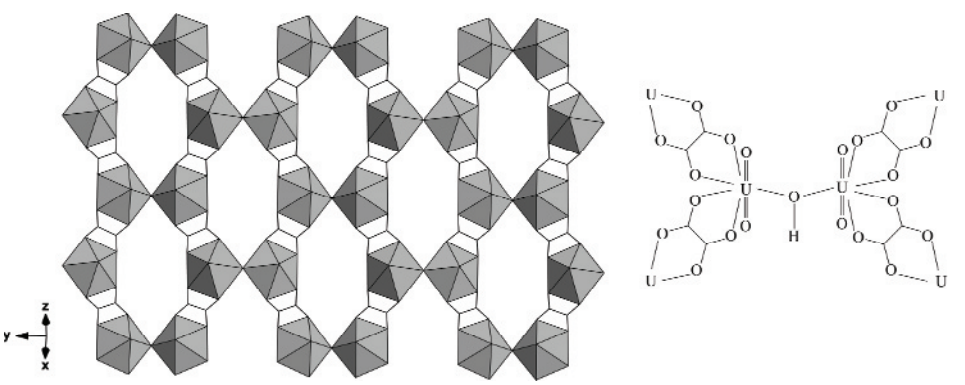

Fig. 8. The structure of $(NH_4)[(UO_2)_2(OH)(C_2O_4)_2]\cdot 2H_2O$. Bridging bidentate oxalate groups assemble uranyl centers into an anionic sheet topology. In addition, point sharing through a hydroxide group gives rise to a dimer SBU. Interlayer species have been omitted for clarity.

The oxalate anion can, in many respects, be considered to be the simplest aliphatic dicarboxylic acid. A natural extension of this description is to consider other aliphatic dicarboxylates, such as those listed in Table 2. Representative examples of these compounds are $UO_2(C_4H_2O_4)(H_2O)_2$ (KMALUB10),[31] $UO_2(C_8H_{12}O_4)$,[32] $UO_2(C_4H_4O_4)(H_2O)$ (SUCCUR),[33] and $UO_2(C_6H_8O_4)$ (BEDJEA)[34] and are shown in Figures 9-12. Isolated hexagonal bipyramidal building units are found in $UO_2(C_4H_2O_4)(H_2O)_2$ where maleic acid links uranyl cations into infinite chains. The hexagonal bipyramidal geometry is formed from coordination to two distinct bidentate acid groups as well as two *trans* water molecules per uranyl center. This chain motif wherein carboxylate

groups tether uranyl centers with *trans* substituents is also present in $UO_2(C_6H_8O_4)(H_2O)_2$ (BEDJAW)[35] and in $UO_2(C_6H_8O_4)(C_{10}H_8N_2)$ (see Table 5).

Polymerization of primary BUs is more common in this group of materials. Hexagonal bipyramids edge share to form uranyl chains in $UO_2(C_8H_{12}O_4)$ (Figure 10) resulting in a compound with an overall 2-D topology wherein the chains are linked through carboxylate groups in bridging tridentate coordination. Dimers are found in $(UO_2)_3(C_5H_6O_4)_4(H_2O)_2{\cdot}(C_6H_{16}N_2)(H_2O)_4$ (BACXUZ),[36] $(UO_2)_3(C_7H_{10}O_4)_5{\cdot}(C_{10}H_{26}N_2)_2(H_2O)_2$ (CAFWAI),[37] $UO_2(C_5H_6O_4)$,[38] $UO_2(C_6H_8O_4)$ (BEDJEA),[35] $UO_2(C_7H_{10}O_4)$ and $UO_2(C_{10}H_{16}O_4)$.[32] Interestingly, this dimer (Figure 4c) was first reported in the solid state (somewhat recently) in the structure of $UO_2(C_6H_8O_4)$. This is of note when one considers that dimers, as well as other oligomeric species, are known to exist in aqueous solution and to vary in population as a function of uranyl concentration.[48]

Table 2. Uranyl coordination polymers constructed from dicarboxylate linkages

formula	linker	dimensionality	CSD code	ref #
$Ba[UO_2(C_3H_2O_4)_2]{\cdot}H_2O$	malonate	$1^{1,7}$	URMABA10	39
$(NH_4)_2[UO_2(C_3H_2O_4)_2]{\cdot}H_2O$	malonate	$1^{1,7}$	URMALA	40
$Sr[UO_2(C_3H_2O_4)_2]{\cdot}3H_2O$	malonate	$1^{1,7}$	URMASR10	39
$(UO_2)_3(C_5H_6O_4)_4(H_2O)_2$ $\cdot(C_6H_{16}N_2)(H_2O)_4$	dimethyl malonate	$1^{1,8}_{2,8}$	BACXUZ	36
$(UO_2)_2(C_5H_6O_4)_3{\cdot}(C_{10}H_{26}N_2)$	dimethyl malonate	$1^{2,8}$	BACYEK	36
$(UO_2)_3(C_7H_{10}O_4)_5$ $\cdot(C_{10}H_{26}N_2)_2(H_2O)_2$	diethyl malonate	$1^{1,7}_{2,8}$	CAFWAI	37
$UO_2(C_3H_5O_3)_2$	lactate	$2^{1,7}$	BEDPAC	41
$UO_2(C_4H_4O_4)((CH_3)_2SO)_2$	succinate	$2^{1,7}$	DEMFAC	42
$UO_2(C_4H_4O_4)(H_2O)$	succinate	$3^{1,7}$	SUCCUR	33
$K[UO_2(C_4H_2O_4)_2]$	maleate	$1^{1,7}$	KMALUA10	43
$UO_2(C_4H_2O_4)(H_2O)_2$	maleate	$1^{1,8}$	KMALUB10	31
$Li[UO_2(C_5H_6O_4)(C_5H_7O_4)]$ $\cdot 4H_2O$	glutarate	$1^{1,8}$	GLURLI	44

$UO_2(C_5H_6O_4)$	glutarate	$2^{2,7}$	-	38
$UO_2(C_4H_7NO_4)_2$	iminodiacetate	$1^{1,8}$	BIMAOU10	45
$UO_2(C_4H_4O_5)$	oxodiacetate	$3^{1,7}$	URXDAC10	46
$UO_2(C_6H_8O_4)(H_2O)_2$	adipate	$1^{1,8}$	BEDJAW	35
$UO_2(C_6H_8O_4)$	adipate	$3^{2,7}$	BEDJEA	35
$UO_2(C_7H_{10}O_4)$	pimelate	$2^{2,7}$	-	32
$UO_2(C_8H_{12}O_4)$	suberate	$2^{\infty,8}$	-	32
$UO_2(C_9H_{14}O_4)$	azelate	$2^{\infty,8}$	-	32
$UO_2(C_{10}H_{16}O_4)$	sebacate	$2^{2,7}$	-	32
$UO_2(C_{10}H_{16}N_2O_2)(NO_3)_2$	*N,N'*-ethylenebis (2-pyrrolidone)	$1^{1,8}$	WESNUD	47

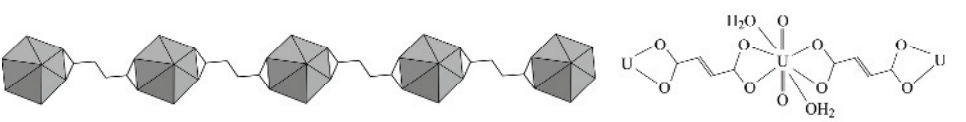

Fig. 9. The structure of $UO_2(C_4H_2O_4)(H_2O)_2$ where bidentate maleate linkers produce chains along [0-11]. Note the bound H_2O molecules *trans* to one another.

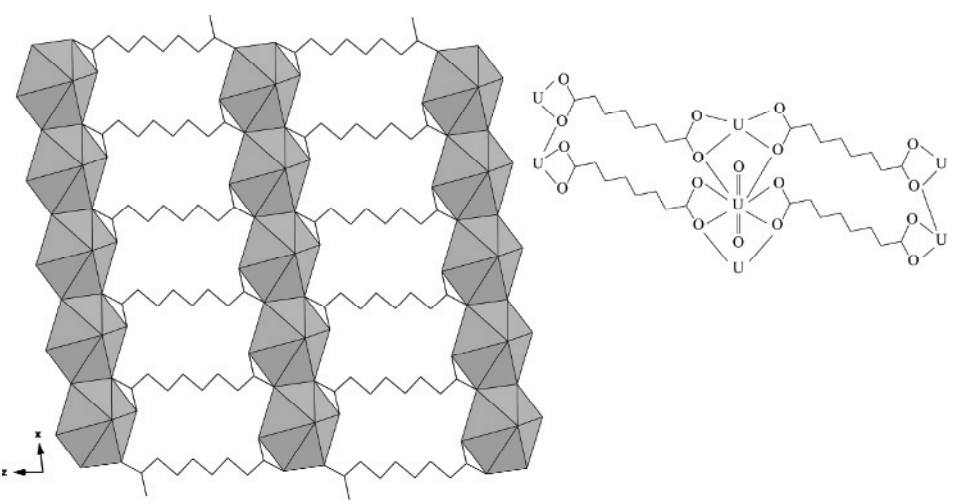

Fig. 10. The structure of $UO_2(C_8H_{12}O_4)$. Hexagonal bipyramids edge share to form chains along [100] which are then linked through suberate groups to form neutral sheets.

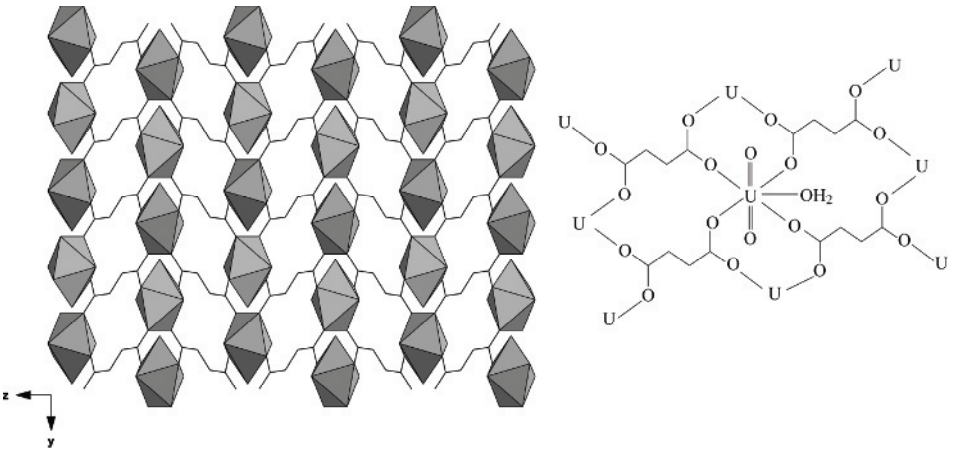

Fig. 11. The 3-dimensional structure of $UO_2(C_4H_4O_4)(H_2O)$ where a neutral framework is formed from hexagonal bipyramids linked through succinate groups.

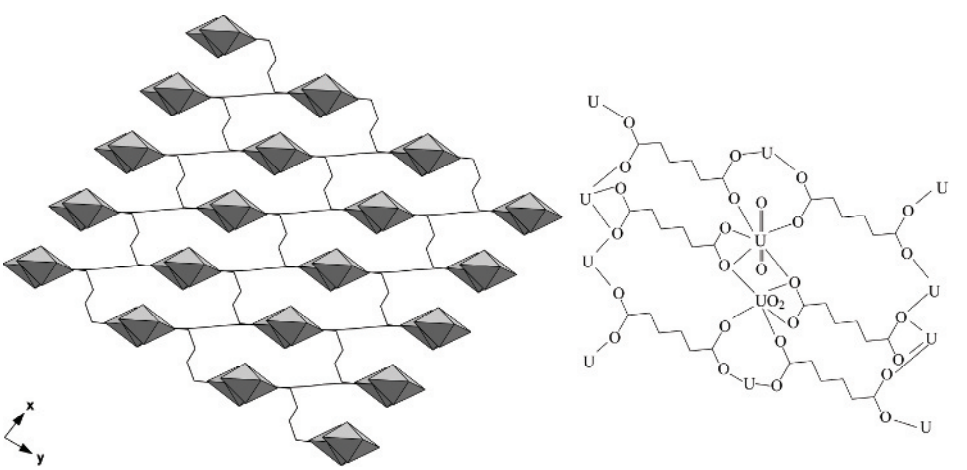

Fig. 12. The 3-dimensional structure of $UO_2(C_6H_8O_4)$. A neutral framework is formed from dimers linked through adipate groups.

Three-dimensional structures are found in $UO_2(C_4H_4O_4)(H_2O)$[33] and $UO_2(C_6H_8O_4)$[35] with succinic and adipic acids (respectively; Figures 11 and 12). The former is formed from isolated pentagonal bipyramids where the uranyl

cation is bound to four carboxylate O atoms from four distinct succinate molecules, each in bridging bidentate coordination. The fifth equatorial position is occupied by a single bound water molecule. $UO_2(C_6H_8O_4)$ contains the dimers shown in Figure 4c and the overall topology for both of these materials stems from the flexibility of the aliphatic linkers molecules.

Bond lengths for the compounds listed in Table 2 range from 1.61 to 1.80 Å for U-O_{Ur} with an average of 1.75 Å. U-Oeq lengths range from 2.22 to 2.61 Å with an average of 2.43 Å. The bond angle in the uranyl cation ranges from 174.4 to 180.0º with an average of 178.3º.

Uranyl compounds containing aromatic carboxylate linkers have been reviewed by Leciejewicz et al[10], yet we include several representative compounds in Table 3 for completeness. A range of coordination geometries including bidentate and bridging bidentate are observed in these materials. Monomeric BUs are the rule with only pentagonal or hexagonal bipyramids being reported. Figure 13 shows $UO_2(C_9H_3O_6)(H_2O)\cdot H_2O$ (ETEJOC)[49], a compound containing three unique coordination sites on the 1,3,5-benzene tricarboxylate linker group. Carboxylate groups are either terminal (i.e. unbound), bidentate

Table 3. Uranyl coordination polymers constructed from aromatic carboxylate linkages

formula	linker	dimensionality†	CSD code	ref #
$UO_2(C_6H_4NO_3)_2$	oxypyridine-4-carboxylate	$2^{1,7}$	BEDNUU	41
$UO_2(C_6H_4(COO)_2)(OC(NH_2)_2)\cdot 0.5H_2O$	1,2-benzene dicarboxylate	$1^{1,7}$	DIFZAT	50
$UO_2(C_9H_3O_6)(H_2O)\cdot H_2O$	1,3,5-benzene tricarboxylate	$1^{1,7}$	ETEJOC	38
$UO_2(C_6H_2(COO)_2(COOH)_2)(H_2O)_2$	1,2,4,5-benzene tetracarboxylate	$1^{1,8}$	FIGWUN	51
$UO_2(C_7H_6NO_4S)_2(H_2O)_2$	2-sulfamoyl benzoate	$2^{1,7}$	QIPWOB	52
$((UO_2)_{1.5}(C_8H_4O_4)_2(H_2O))_2\cdot((CH_3)_2NCOH_2)$	1,3-benzene dicarboxylate	$1^{1,8}$	UJUBIK	53
$UO_2(C_4O_4)(H_2O)$	squarate	$3^{1,7}$	BITLUL	54
$K_4[(UO_2)_2(C_5O_5)_4(H_2O)_2]$	croconate	$1^{1,7}$	YACJER	55

or bridging bidentate with the uranyl center. Pentagonal bipyramidal coordination is realized with the addition of a single bound water molecule. Bidentate coordination with 1,3-benzene dicarboxylate, as in $((UO_2)_{1.5}(C_8H_4O_4)_2(H_2O))_2\cdot((CH_3)_2NCOH_2)$ (UJUBIK)[53] gives rise to a complex 1-D chain structure as shown in Figure 14. Heaxagonal bipyramidal BUs are

observed as each uranyl center is bound to three unique BDC linkers. This topology is deceptive as the infinite chains (along [100]) are actually three uranyl centers wide, implying a pseudo-sheet structure.

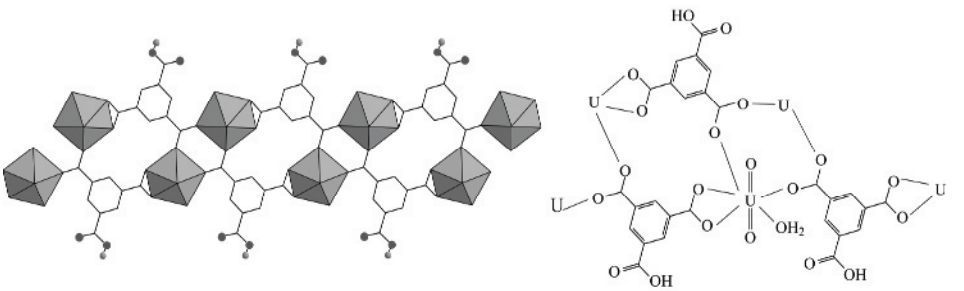

Fig. 13. A portion of the neutral chains found in $UO_2(C_9H_3O_6)(H_2O)\cdot H_2O$.

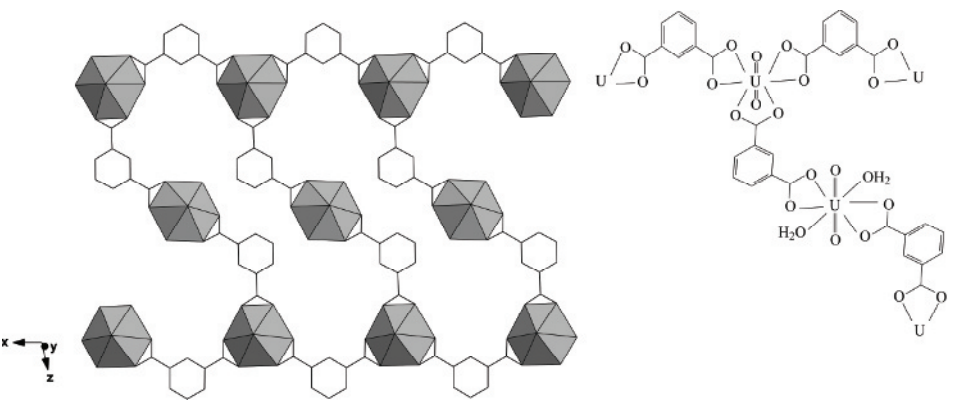

Fig. 14. A portion of the anionic chains found in $((UO_2)_{1.5}(C_8H_4O_4)_2(H_2O))_2\cdot((CH_3)_2NCOH_2)$. The protonated dimethylformamide counterions have been omitted for clarity.

The last two entries in Table 3, $UO_2(C_4O_4)(H_2O)$ (BITLUL)[54] and $K_4[(UO_2)_2(C_5O_5)_4(H_2O)_2]$ (YACJER)[55] admittedly do not contain carboxylic functional groups, yet the squarate and croconate linkers are O-donors and in some ways approximate aromatic species. $UO_2(C_4O_4)(H_2O)$ is shown in Figure 15 and is the only 3-dimensional structure of this category. The uranyl cation exhibits pentagonal bipyramidal geometry with a single water molecule and four O atoms from four distinct squarate groups, each in monodentate coordination. This local geometry is similar to that observed in $UO_2(C_4H_4O_4)(H_2O)$ (Table 2, Figure 11 above).

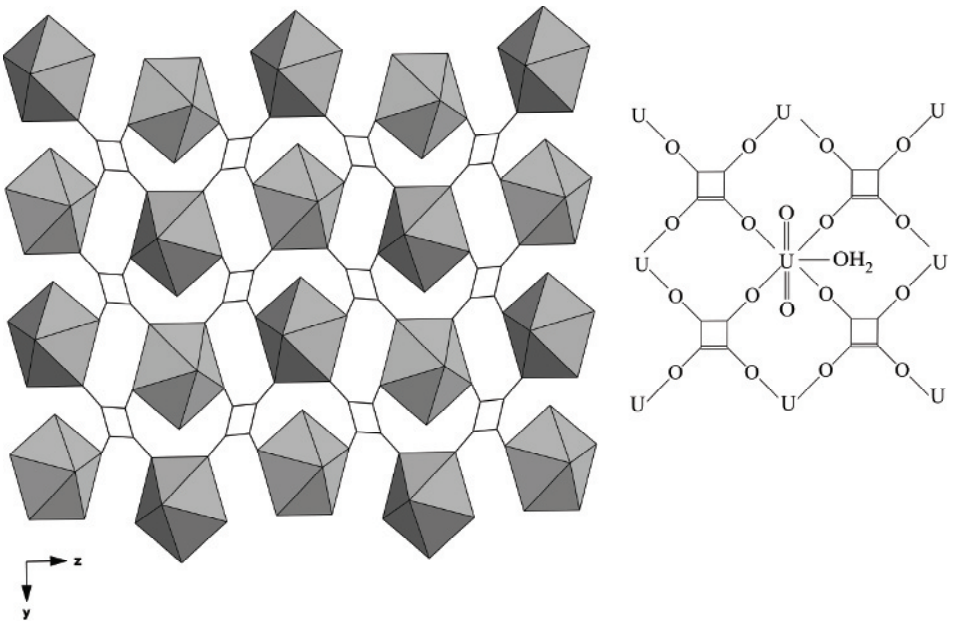

Fig. 15. The 3-dimensional structure of $UO_2(C_4O_4)(H_2O)$.

Bond lengths for the compounds listed in Table 3 range from 1.69 to 1.78 Å for U-O_{Ur} with an average of 1.75 Å. U-O_{eq} lengths range from 2.32 to 2.53 Å with an average of 2.43 Å. The bond angle in the uranyl cation ranges from 177.8 to 180.0º with an average of 178.8º.

3.1.2. N/O pairings

Compounds containing N/O donor atoms are far more common in molecular species than in polymeric ones. Table 4 lists the known polymeric materials and in turn demonstrates the more limited chemistry of these materials. We will note at this point that we are currently limited to only a few types of linkers: iminodiacetate and both pyridine and pyrazole dicarboxylates. Two-dimensional topologies are most common in this category of materials and most local geometries contain the motif shown in Figure 16.

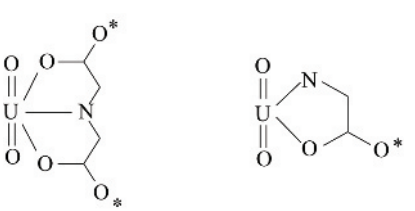

Fig. 16. A schematic of common N/O donor motifs. The * indicates oxygen sites capable of bridging to other metal centers. Left: Iminodiacetate or pyridine dicarboxylate linkages. Right: 2,3-pyrazole dicarboxylate.

$UO_2(C_4H_5NO_4)$ (IMAOXU)[56] is a representative compound where iminodiacetate effectively chelates to a single uranyl center through a nitrogen and two carboxylate oxygen atoms. The remaining carboxylate oxygens then bridge to neighboring uranyls to form an overall two-dimensional topology as

Table 4. Uranyl coordination polymers constructed from N/O donors

formula	linker	dimensionality	CSD code	ref #
$UO_2(C_4H_5NO_4)$	imino-diacetate	$2^{1,7}$	IMAOXU	56
$(UO_2)_3(C_7H_3NO_4)_4{\cdot}2(H_2O)$	2,6-pyridine dicarboxylate	$2^{1,8}$	LEWFEY	57
$UO_2(H_2O)(C_7H_3NO_4)$	2,6-pyridine dicarboxylate	$1^{1,7}$	PYDCUO	58
$(UO_2)(C_7H_3NO_4)$	2,3-pyridine dicarboxylate	$2^{1,7}$	-	59
$(UO_2)(C_7H_3NO_4)$	2,4-pyridine dicarboxylate	$3^{1,7}$	-	59
$(UO_2)(C_7H_3NO_4)$	2,6-pyridine dicarboxylate	$3^{1,7}$	-	59
$(UO_2)_2(C_7H_3NO_4)(O)(H_2O)$	2,6-pyridine dicarboxylate	$1^{\infty,7}$	-	59
$(UO_2)_3(O)(OH)_2(C_7H_4NO_4)(C_7H_3NO_4)_{0.5}$	3,4-pyridine dicarboxylate	$2^{\infty,7}$	-	60
$(UO_2)_3(O)(OH)_2(C_7H_4O_4)\ (H_2O)_2{\cdot}H_2O$	2,4-pyridine dicarboxylate	$2^{6,7}$	-	60
$UO_2(C_5H_2N_2O_4)(H_2O)$	3,5-pyrazole dicarboxylate	$2^{1,8}$	-	61

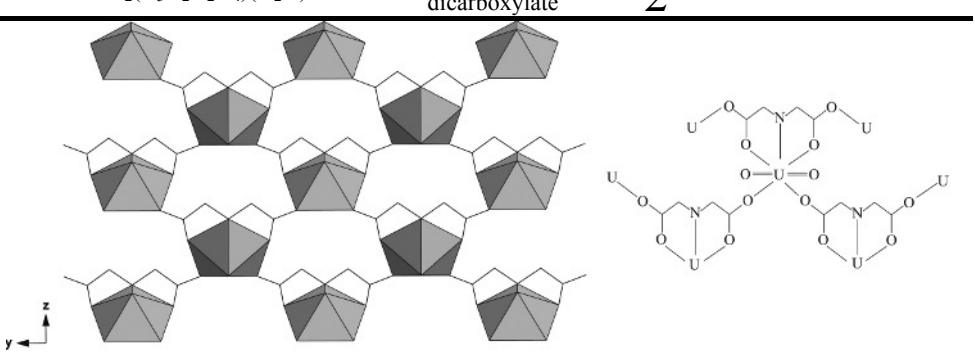

Fig. 17. The structure of $UO_2(C_4H_5NO_4)$ highlighting a common tridentate coordination seen with N/O donor containing linkers.

shown in Figure 17. An analogous geometry is seen in $(UO_2)(C_7H_3NO_4)$[59] (Figure 18) where 2,6-pyridine dicarboxylic acid (2,6-PDC) coordinates to uranyl centers in a similar fashion to the iminodiacetate in $UO_2(C_4H_5NO_4)$. Despite the similarities in local geometry (i.e. pentagonal bipramidal coordination, three linkers per uranyl) the structure of the 2,6-PDC compound is 3-dimensional. Variations on these themes are seen throughout the compounds listed in Table 4 as structural diversity is observed as related to functional group location.

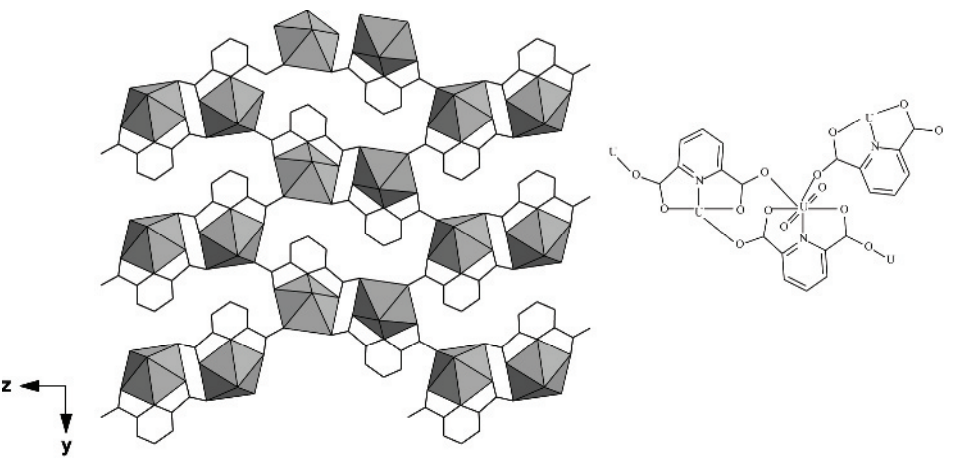

Fig. 18. A portion of the 3-dimensional structure of $(UO_2)(C_7H_3NO_4)$.

A compound where the uranyl cation is in hexagonal bipyramidal coordination is $UO_2(C_5H_2N_2O_4)(H_2O)$[61] (Figure 19) Here, 3,5-pyrazole dicarboxylate (H_3PzDC) coordinates through the now familiar N/O donor motif shown in Figure 16. Two additional H_3PzDC linkers bind through the

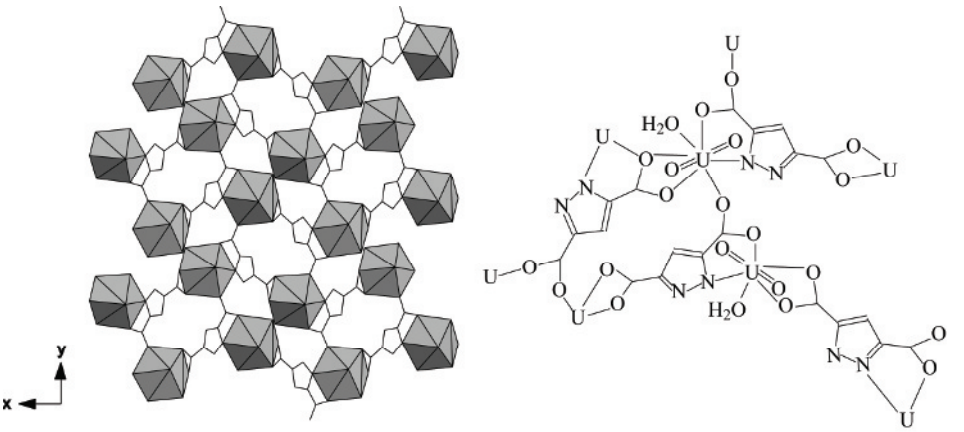

Fig. 19. The sheet structure of $UO_2(C_5H_2N_2O_4)(H_2O)$. Interlayer H_2O molecules are not shown.

carboxylate groups in bridging bidentate and bridging tridentate coordination to give an overall 2-dimensional topology. The hexagonal geometry of the uranyl is completed with a bound water molecule.

An unusual SBU is observed in $(UO_2)_3(O)(OH)_2(C_7H_4O_4)(H_2O)_2{\cdot}H_2O$[60] (Figure 20) where 2,4-pyridine dicarboxylic acid links uranyl hexamers into a 2-dimensional topology. These hexamer moieties are not observed in any other compound reported thus far. Each consists of six edge shared pentagonal bipyramids wherein the uranyl cations are coordinated to either water molecules, bridging bidentate carboxlyate oxygens or the N/O donor motif described above (Figure 16). Also of note is the terminal carboxylate oxygen atom opposite the N/O donor site. Sterics arguably prevent this site from binding to any uranyl cations and it likely serves as an H-bond acceptor from neighboring bound water molecules.

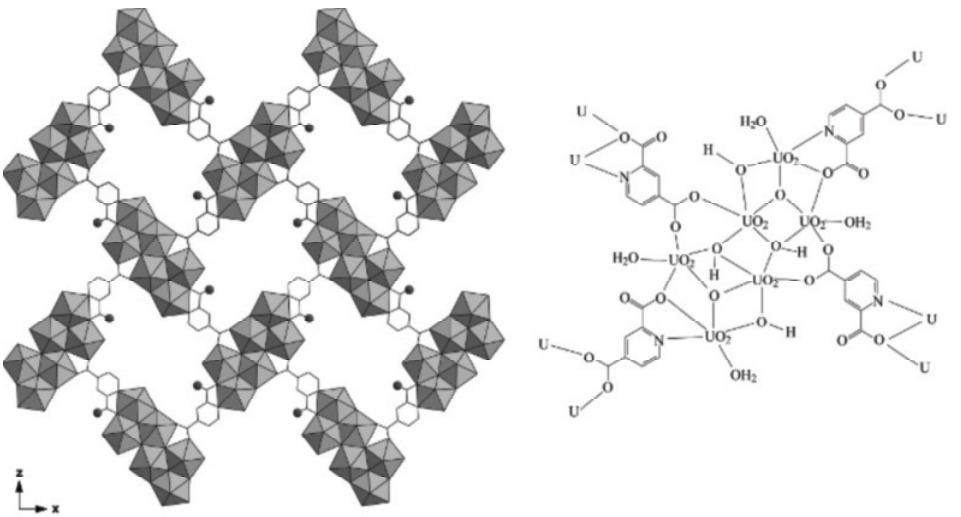

Fig. 20. The sheet structure of $(UO_2)_3(O)(OH)_2(C_7H_4O_4)$ $(H_2O)_2{\cdot}H_2O$. The hexamer SBUs have not been seen in other CP compounds to date. Interlayer water molecules are not shown.

Bond lengths for the compounds listed in Table 4 range from 1.730 to 1.795 Å for U-O_{Ur} with an average of 1.761Å. U-O_{eq} lengths range from 2.181 to 2.613 Å with an average of 2.394 Å. The bond angle in the uranyl cation ranges from 174.86 to 179.972º with an average of 176.86º. We now consider U-N distances as well and these range from 2.513 to 2.641 Å with an average of 2.592 Å.

3.1.3. Summary of O-donor geometries.

Figure 21 contains a summary of the types of coordination geometries found in the materials discussed thus far. One will note that there is not a vast range of local coordination geometries encountered and that these are not unique to polymeric structures. This observation reminds us of earlier comments (above) where we argue that polymeric structures arise from *multi*functional linker molecules. In addition, the flexibility (or lack thereof) of a given linker molecule can contribute to the overall dimensionality of the material. Thus the local geometry of polymeric structures should not be considered to be widely distinct from that observed in molecular species and instead, we must consider these other features of the organic component when discussing these structures.

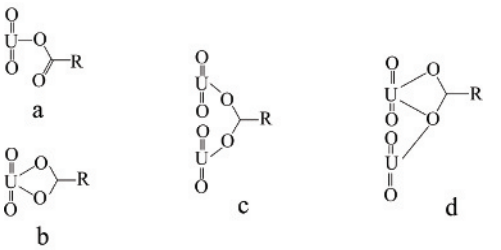

Fig. 21. A summary of carboxylic donor geometries: a) monodentate, b) bidentate, c) bridging bidentate, d) bridging tridentate.

3.2. Homometallic systems with multiple linker molecules.

The use of multiple linker molecules in the design of polymeric structures is of growing interest.[4] The general philosophy with this approach is that distinct linker molecules, each with their own characteristics in terms of functional group(s), size or flexibility, will contribute to the overall structures and thus impart their features on the overall topology. A number of examples of materials exploiting this approach is given in Table 5.

Table 5. Uranyl coordination polymers constructed from multiple linker molecules

formula	linker	dimensionality	CSD code	ref #
$UO_2(C_6H_8O_4)(C_{10}H_8N_2)$	adipate/ 4,4'-dipyridyl	$2^{1,8}$	-	32
$(UO_2)_4(O)_2(H_2O)_2(C_7H_{10}O_4)_2$ $(C_{10}H_8N_2)\cdot(H_2O)$	pimelate/ 4,4'-dipyridyl	$2^{4,7,8}$	-	32
$UO_2(C_7H_{10}O_4)(C_{10}H_8N_2)$	pimelate/ 4,4'-dipyridyl	$3^{1,8}$	-	32
$(UO_2)_2(O)(C_8H_{12}O_4)(C_{10}H_8N_2)(H_2O)$	suberate/ 4,4-dipyridyl	$2^{4,7,8}$	-	32
$(UO_2)_4(O)_2(C_8H_{12}O_4)(C_{12}H_{12}N_2)$	suberate/bpe	$2^{4,7}$	-	32
$(UO_2)_4(O)_2(C_9H_{14}O_4)_2(C_{10}H_8N_2)$ $(H_2O)_2$	azelate/ 4,4-dipyridyl	$1^{4,7}$	-	32
$(UO_2)_2(C_9H_{14}O_4)_2\,(C_{12}H_{12}N_2)$	azelate/bpe	$1^{1,7}$	-	32
$(UO_2)_2(C_{10}H_{16}O_4)_2\,(C_{10}H_8N_2)$	sebacate/ 4,4'-dipyridyl	$2^{1,7}$	-	32

A novel sheet topology is seen in $UO_2(C_6H_8O_4)(C_{10}H_8N_2)$[32] where both adipic acid and 4,4'-dipyridyl coordinate to the uranyl cation in bidentate and monodentate coordination (respectively) resulting in hexagonal bipyramidal geometry (Figure 22). This structure may be thought of as containing uranyl adipate chains running along [001] which are then 'stitched' together through *trans* 4,4'-dipyridyl groups. Using this description, this chain motif is also present in $UO_2(C_4H_2O_4)(H_2O)_2$ (KMALUB10)[31] (Figure 9) and $UO_2(C_6H_8O_4)(H_2O)_2$ (BEDJAW)[35] (Table 2), yet bound water molecules occupy the *trans* equatorial positions in these compounds. Despite this seemingly open sheet topology, this material actually has an overall dense structure as the sheets are shown to interpenetrate in the solid state and thus occupy any accessible void space. Interpenetration of lower dimensional entities that results in overall higher dimensional (and more dense) solids is a topic that has been discussed at length with respect to transition metal MOFs.[16]

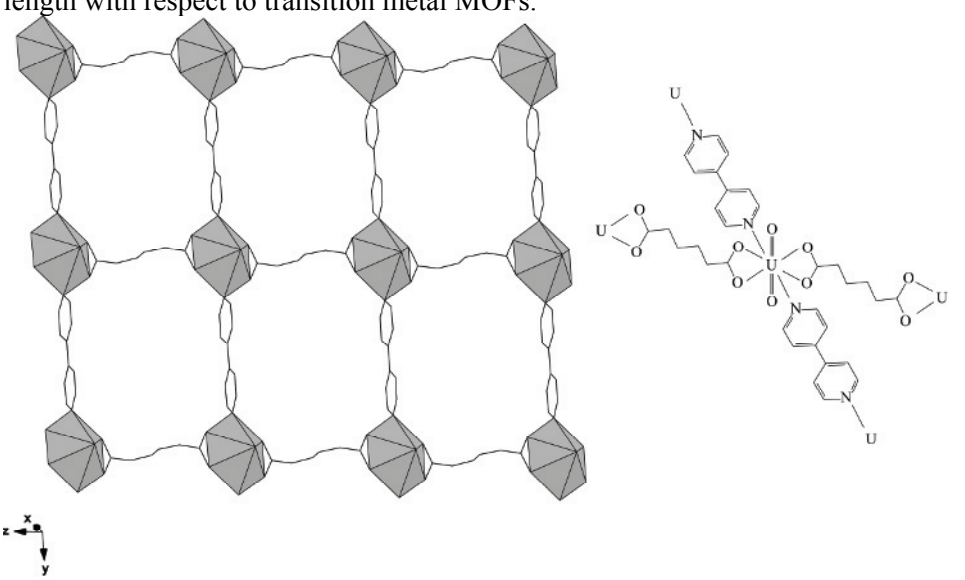

Fig. 22. A single sheet of $UO_2(C_6H_8O_4)(C_{10}H_8N_2)$. Note the positions of the pyridine groups in comparison to *trans* H_2O molecules seen in previous structures.

This mixed ligand coordination where carboxylate and pyridyl groups are bound to the same cation is not common. In fact, one could argue that this is in contrast to Pearson's hard/soft acid-base distinction[19] in that the uranyl cation is a 'hard acid' and the dipyridyl linkers are softer in nature. Indeed, UO_2^{2+}-pyridyl coordination (2,2'-bipyridine, terpyridines, etc) is quite rare, even in molecular materials, yet in these extended topologies, it is likely that sterics play a considerable role and that the 4,4'-dipyridyl is uniquely suited to displace H_2O groups and serve as a bridging moiety. This is mentioned in this context as

the 4,4'-dipyridyl molecule is an extremely common linker in transition metal MOF chemistry, yet the compounds listed in Table 5 are the first to make use of this molecule in binding to the uranyl cation.

3.3. Heterometallic systems

Heterometallic systems employ multiple building units to produce extended structures. Building units in this case will refer to two distinct metal centers such as a transition metal in addition to the uranyl cation. The net result is to combine two distinct coordination geometries: those of the UO_2^{2+} center as already described with the diversity of transition metal sites. In addition, distinctions regarding coordination preferences, such as those made by hard-soft acid-base considerations, may be harnessed to utilize not only *multi*-functional linkers, but also *hetero*-functional linkers to connect different metals through different functional groups in the same molecule. Examples of materials utilizing linker molecules with such heterofunctionality are given in Table 6. One will note that the pyridine and pyrazine dicarboxylate linkers have been described above in the N/O donor section, yet the distinct functionality of the pyridyl and carboxylate groups make these compounds candidates for heterometallic systems as well.

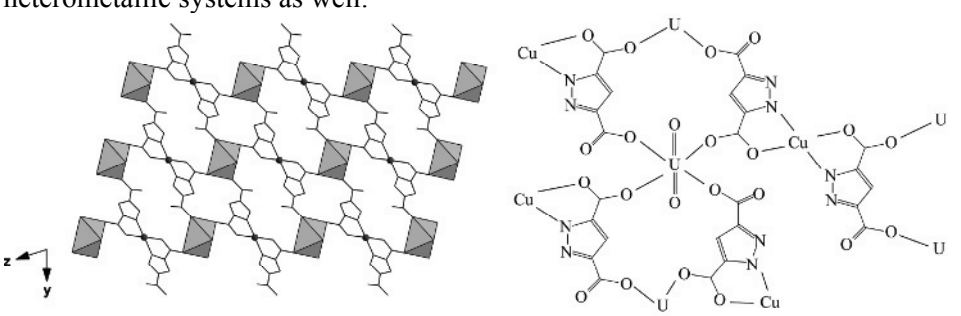

Fig. 23. The sheet structure of $UO_2Cu(C_5H_2N_2O_4)_2(H_2O)_2$. Cu(II) centers are shown as spheres and coordinated H_2O molecules have been omitted.

A representative compound that utilizes pyrazole dicarboxylate to produce a 2-dimensional, U(VI)/Cu(II) compound is $UO_2Cu(C_5H_2N_2O_4)_2(H_2O)_2$ (Figure 23).[61] Here the UO_2^{2+} center is in square bipyramidal geometry with four monodentate carboxylate oxygen atoms from four distinct linker molecules. Cu(II) is coordinated to two bidentate N/O donors and two H_2O groups to yield an overall octahedral geometry. Coordination site preferences can be seen in this compound as the uranyl cation is bound strictly to

carboxylate functional groups, whereas the Cu(II) is bound to the N/O donor groups that were described above (Figure 16).

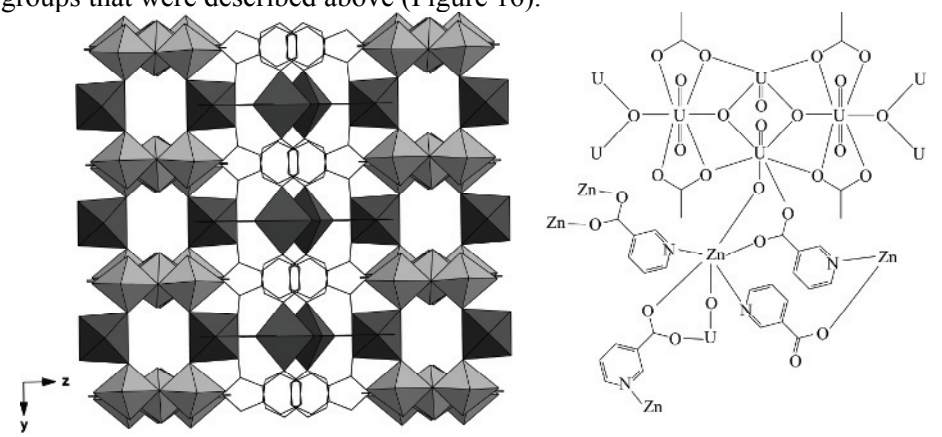

Fig. 24. The 3-dimensional structure of $(ZnO)_2(UO_2)_3(C_6H_4NO_2)_4\,(CH_3COO)_2$. Darker polyhedra are the Zn(II) centers.

Nicotinic acid, $(C_6H_5NO_2)$ has been utilized in $(ZnO)_2(UO_2)_3(C_6H_4NO_2)_4(CH_3COO)_2$ (AKECUO)[62] to produce a 3-dimensional Zn(II)/U(VI) heterometallic MOF (Figure 24). The structure of this material is quite complex and contains many of the structural motifs discussed so far. Uranyl cations are in pentagonal and hexagonal bipyramidal geometry with carboxylate oxygen atoms exclusively. These polyhedra edge share to form infinite chains that run along [100] which are then interconnected through Zn(II) centers in both octahedral and trigonal bipyramidal geometries formed from coordination to both carboxylate and pyridyl functional groups, again highlighting hard/soft distinctions. Also of note is that this compound was synthesized from a 2,3-pyridine dicarboxylic acid starting material, yet an *in situ* decarboxylation occured under the hydrothermal reaction conditions leading to the formation of the nicotinate linker. Such '*in situ* ligand synthesis' is not uncommon in hydrothermal systems, especially those containing metals.[63]

Table 6. Heterometallic coordination polymers

formula	linker	dimensionality	CSD code	ref #
$(ZnO)_2(UO_2)_3(C_6H_4NO_2)_4\,(CH_3COO)_2$	nicotinate	$3^{\infty,7,8}_{1,6}$	AKECUO	62
$(UO_2)_5(O)_4(H_2O)_2(C_2H_3O_2)_2Ni_2$ $(H_2O)_2(C_7H_3NO_4)_2(C_{10}H_8N_2)_2\cdot 2H_2O$	2,3-pyridine dicarboxylate	$3^{\infty,7,8}_{1,6}$	BICWUG	64
$UO_2(H_2O)_3V(C_4H_4NO_5)_2\cdot 2H_2O$	*N*-hydroxy iminodiacetate	$1^{1,7}_{1,8}$	NIFKOC	65

$UO_2Cu(C_5H_2N_2O_4)_2(H_2O)_2$	3,5-pyrazole dicarboxylate	$2^{1,6}_{1,6}$	-	61
$(UO_2)(C_7H_3NO_4)_2(Cu(H_2O)_4)\cdot 4H_2O$	2,6-pyridine dicarboxylate	$1^{1,8}_{1,6}$	-	59
$(UO_2)(C_7H_3NO_4)_2Ag_2$	2,6-pyridine dicarboxylate	$1^{1,8}_{2,4}$	-	59
$(UO_2)(C_7H_3NO_4)_2Pb\cdot 2H_2O$	2,6-pyridine dicarboxylate	$3^{1,8}_{1,6}$	-	59
[Ag(bipy)(UO2)(bdc)$_{1.5}$]	1,4-benzene dicarboxylate	$2^{2,7}_{1,3}$	-	66
$[Ag_2(phen)_2UO_2(betc)]$	1,2,4,5-benzene tetracarboxylate	$2^{1,8}_{1,4}$	-	66

2,6-Pyridine dicarboxylate is found to be an effective linker in heterometallic systems. Recall that this species was shown in Figure 18 and effectively chelates uranyl cations in tridentate coordination through one N and two O binding sites. The remaining O atoms from the carboxylate groups are then free to bridge to neighboring metal sites. This motif is seen in $(UO_2)(C_7H_3NO_4)_2Pb\cdot 2H_2O$[59] (Figure 25) where a 3-dimensional structure results from the 2,6-PDC bridging uranyl hexagonal bipyramids and 6-coordinate Pb(II) polyhedra into a framework. A unique combination of bridging tridentate, monodentate and terminal carboxylate oxygen atoms is observed.

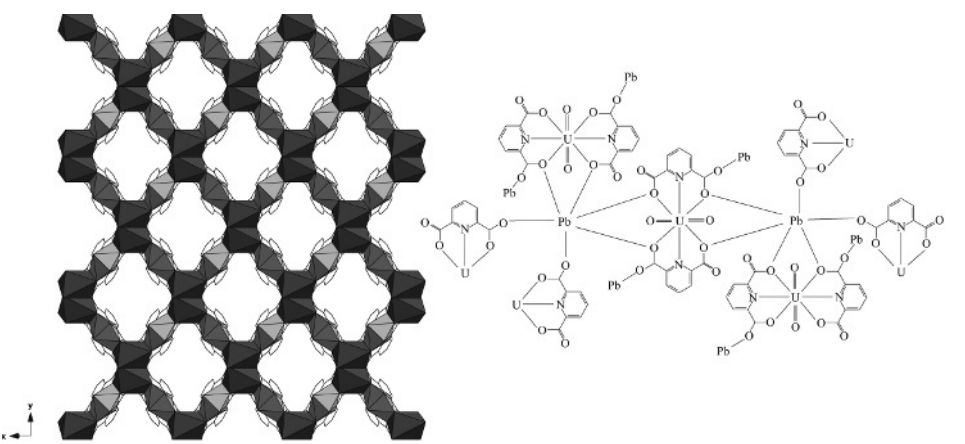

Fig. 25. The structure of $(UO_2)(C_7H_3NO_4)_2Pb\cdot 2H_2O$. Darker polyhedra are Pb(II) centers and extra-framework H_2O molecules have been omitted.

The final two compounds in Table 6 are of particular interest as they are both heterometallic and contain two distinct organic groups. The 2,2'-bipyridine and phenanthroline groups in $[Ag(bipy)(UO_2)(bdc)_{1.5}]$ and $[Ag_2(phen)_2UO_2(betc)]$ (respectively) however are coordinated in a bidentate fashion to the Ag^+ centers only and do not contribute to the overall connectivity of the CP.

4. Miscellaneous structures.

The purpose of the following section is to put the materials discussed thus far in perspective with some related compounds. We aim to 1) demonstrate the generality of the CP definition by including a few representative examples of materials containing other actinide elements and 2) give a few examples of polymeric structures containing significant organic components, yet do not meet our criteria for inclusion in the above sections.

4.1. Other Ac containing coordination polymers

Table 7 contains three representative compounds that may be considered as coordination polymers yet contain Np(V) and Th(IV) as the metal centers. Direct comparisons to U(VI) and U(IV) crystal chemistry can be made for the Np and Th centers (respectively) as Np(V) forms the linear $[O=Np=O]^+$ neptunyl cation and Th(IV) displays spherical, high coordination number environments.

Table 7. Coordination polymers constructed from other actinide elements

formula	linker	dimensionality	CSD code	ref #
$Na_6[(NpO_2)_2(C_{10}H_2O_8)_2]$ $\cdot 11H_2O$	1,2,4,5-benzene tetracarboxylate	$2^{1,7}$	CIXVOU	67
$(NpO_2)_2(C_7H_3NO_4)(H_2O)_5$	2,6-pyridine dicarboxylate	$1^{1,7}$	XEPNOV	68
$K_4[Th(C_2O_4)_4]\cdot 4H_2O$	oxalate	$1^{1,10}$	KTHTOT10	69

Figure 26 shows $Na_6[(NpO_2)_2(C_{10}H_2O_8)_2]\cdot 11H_2O$ (CIXVOU),[67] a 2-dimensional coordination polymer where the neptunyl cation is in pentagonal bipyramidal coordination with five carboxylate oxygens from four distinct 1,2,4,5-benzene tetracaboxylate groups. Three oxygens are in monodentate coordination and two are from a bidentate carboxylate group. This connectivity

gives rise to anionic sheets which are in turn charge balanced with inter-layer Na^+ cations. This tetracaboxylate linker has been seen in $UO_2(C_6H_2(COO)_2(COOH)_2)(H_2O)_2$ (FIGWUN, Table 3),[51] yet there yields a 1-dimensional chain structure.

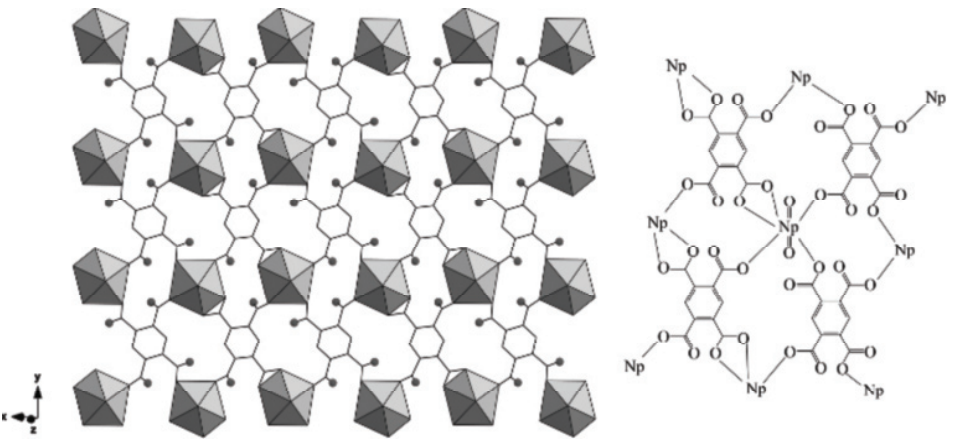

Fig. 26. The sheet structure of $Na_6[(NpO_2)_2(C_{10}H_2O_8)_2]\cdot 11H_2O$. Inter layer species have been omitted.

Another Np(V) centered compound is $(NpO_2)_2(C_7H_3NO_4)(H_2O)_5$ (XEPNOV),[68] wherein the now familiar 2,6-pyridine dicarboxylate linker is in tridentate coordination with the neptunyl cation. There are two distinct neptunyl sites in this material, both of which are pentagonal bipyramidal: one is triply coordinated to the 2,6-PDC ligand and two water molecules whereas the other is bound to three water molecules and two monodentate oxygen atoms from the PDC. This bridging bidentate coordination of the carboxylate groups was also described in $(UO_2)(C_7H_3NO_4)$ (Table 4, Figure 16, above).

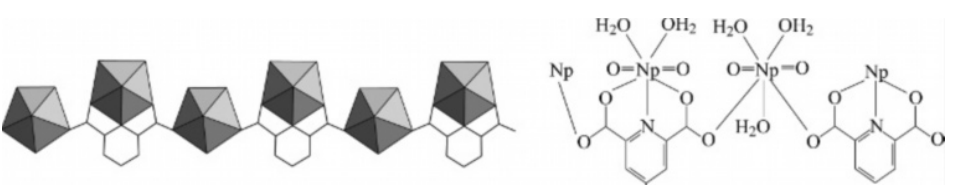

Fig. 27. The chain structure of $(NpO_2)_2(C_7H_3NO_4)(H_2O)_5$.

A thorium(IV) centered oxalate CP is shown in Figure 28. In this compound, $K_4[Th(C_2O_4)_4]\cdot 4H_2O$ (KTHTOT10),[69] there is no linear triatomic cation at the center of the Th coordination sphere. Instead, we see a 10-coordinate bicapped square antiprism wherein Th(IV) is coordinated in a

bidentate fashion to five distinct oxalate units. Three of these are terminal and two bridge to neighboring Th(IV) centers to form infinite chains.

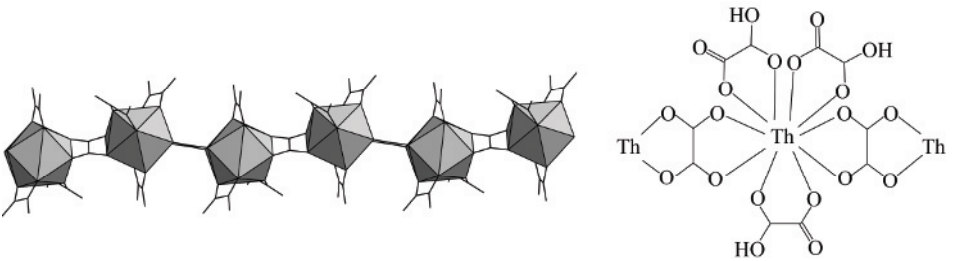

Fig. 28. The chain structure of $K_4[Th(C_2O_4)_4]\cdot 4H_2O$.

4.2. Miscellaneous polymeric materials

This final section of specific examples presents a number of compounds that do not fit our definition of a coordination polymer exactly. These are in fact polymeric materials, yet the organic molecules are monofunctional and hence should ideally be treated as ligands. Higher dimensionality is achieved either through edge sharing of uranyl polyhedra, or by bridging bidentate coordination from the ligand species. Examples of the former include $UO_2(F)_2(C_5H_5NCO_2)$ (ASEFUZ)[53] wherein chains of $[UO_3F_4]$

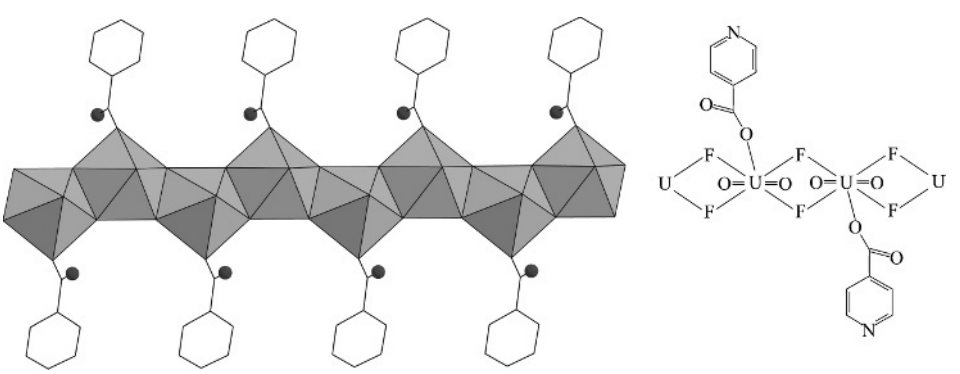

Fig. 29. The chain structure of $UO_2(F)_2(C_5H_5NCO_2)$. Note that the isonicotinate species are coordinated to the chain of uranyl polyedra, yet do not contribute to the overall dimensionality of the structure.

pentagonal bipyramids are separated by isonicotinate species in monodentate coordination that essentially 'decorate' the chains (Figure 29). This

polymerization of uranyl fluoride polyhedra is common in open structured and templated U(VI) fluoride compounds.[70-73] Such decoration is also noted in $(NH_4)_2[(UO_2)_5(O)_2(C_2H_3O_2)_8]$ (SANDER).[74] In this compound, hexagonal and pentagonal bipyramids edge share to form tetramers which are then point shared through hexagonal bipyramids to form infinite chains. Acetate groups are coordinated to this chain in both bridging bidentate and bridging tridentate coordination.

Bridging bidentate coordination of organic species often results in the formation of chain structures without direct edge sharing of uranyl polyhdera. This is seen in $UO_2(O_2PHC_6H_5)_2$ (CAJTOW)[75] (Figure 30) and $(UO_2)_2(C_2H_5SO_3)_4(H_2O)_2$ (WABGUB)[76] (Figure 31) where phosphinate and sulfonate functional groups (respectively) bridge uranyl square or pentagonal bipyramids into chain structures. Affinity for these functional groups is also evident considering the wealth of uranyl sulfate and phosphate minerals and synthetic compounds examined elsewhere in this volume.

Table 8. Non-coordination polymers constructed using the uranyl cation

formula	linker	dimensionality	CSD code	ref #
$UO_2(F)_2(C_5H_5NCO_2)$	-	$1^{\infty,7}$	ASEFUZ	77
$(NH_4)_2[(UO_2)_5(O)_2(C_2H_3O_2)_8]$	acetate	$1^{\infty,7,8}$	SANDER	74
$UO_2(O_2PHC_6H_5)_2$	phenyl phosphinate	$1^{1,6}$	CAJTOW	75
$(UO_2)_2(C_2H_5SO_3)_4(H_2O)_2$	ethane sulfonate	$1^{1,7}$	WABGUB	76

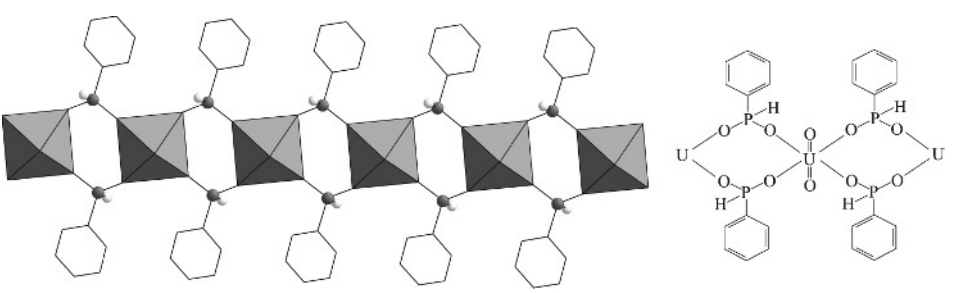

Fig. 30. The structure of $UO_2(O_2PHC_6H_5)_2$. Phenyl phosphinate ligands bridge polyhedra, yet are monofuntional.

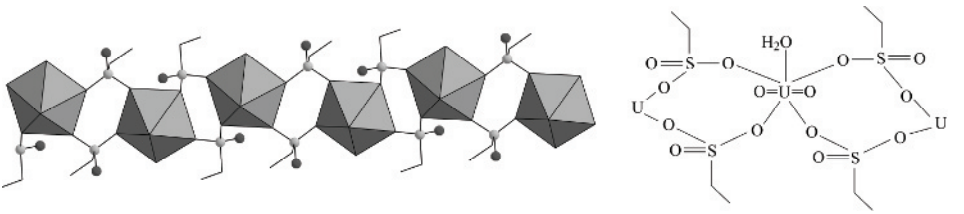

Fig. 31. The structure of $(UO_2)_2(C_2H_5SO_3)_4(H_2O)_2$.

5. Conclusions and outlook.

As can be seen from this contribution, the structural diversity of U-containing coordination polymers is rather extensive. This can be attributed to two (synergistic) factors: a rich local geometry of the uranyl cation and a diverse pool of organic linker molecules. With this in mind, it should be clear that researchers have only just begun to exploit the potential of these materials. In addition, developments within transition metal and lanthanide based MOFs are making their way into the actinide materials and we can look forward to continued progress in this regard.

We have made very little discussion of the physical and or chemical properties of uranyl containing coordination polymers. Arguably, much of the original interest in uranium structural chemistry stemmed from its role in the nuclear fuel cycle, yet promising new compounds such as those reviewed herein suggest an extension of their utility is on the horizon. New and exciting applications for these materials are currently being explored with considerable intensity. Catalytic and fluorescent behavior hold particular promise as coordination polymers offer unique opportunities for tunable fluorescence as well as heterogeneous catalysis.[60,64] The latter of these properties results from the photocatalytic ability of excited state uranyl cations.

Acknowledgements

Research efforts in the Cahill group are supported by the National Science Foundation (DMR-0348982 and DMR-0419754) and the United States Department of Energy (DE-FG02-05ER15736).

References

1. C. N. R. Rao, S. Natarajan, R. Vaidhyanathan, Angew. Chem., Int. Ed. Engl. 43 (2004) 1466.
2. G. Férey, Chem. Mater. 13 (2001) 3084.
3. G. Férey, J. Sol. State Chem. 152 (2000) 37.
4. B.-H. Ye, M.-L. Tong, X.-M. Chen, Coord. Chem. Rev. 249 (2005) 545.
5. B. Moulton, M. J. Zaworotko, Chem. Rev. 101 (2001) 1629.
6. S. L. James, Chem. Soc. Rev. 32 (2003) 276.
7. O. M. Yaghi, H. Li, C. Davis, D. Richardson, T. L. Groy, Acc. Chem. Res. 31 (1998) 474.
8. C. E. Carraher, Jr. In Macromolecules Containing Metal and Metal-Like Elements; Abd-El-Aziz, A. S., Carraher, C. E., Jr., Pittman, C. E., Jr., Zeldin, M., Eds.; John Wiley and Sons, 2005; Vol. 5, pp 343-385.
9. S.V. Krivovichev, C.L. Cahill, E. V. Nazarchuk, P. C. Burns, T. Armbruster, W. Depmeier, Micropor. Mesopor. Mater. 78 (2005) 209.
10. J. Leciejewicz, N. W. Alcock, T. J. Kemp, Struct. Bond. 82 (1995) 43.
11. M. R. Maurya, R. C. Maurya, Rev. Inorg. Chem. 15 (1995) 1.
12. F. Weigel, In: The Chemistry of the Actinide Elements; 2nd ed.; J. J. Katz, G. T. Seaborg, L.R. Morss, eds., 1986; Vol. 1, pp 169-442.
13. C. Baerlocher, W. M. Meier, D. H. Olson, Atlas of Zeolite Framework Types; 5th revised ed.; Elsevier Science B.V.: Amsterdam, 2001.
14. N. L. Rosi, J. Eckert, M. Eddaoudi, D. T. Vodak, J. Kim, M. O'Keeffe, O. M. Yaghi, Science 300 (2003) 1127.
15. M. O'Keeffe, M. Eddaoudi, H. Li, T. Reineke, O. M. Yaghi, J. Solid State Chem. 152 (2000) 3.
16. S. R. Batten, R. Robson, Angew. Chem., Int. Ed. Engl. 37 (1998) 1461.
17. F. H. Allen, Acta Crystallogr. B58 (2002) 380. Cambridge Structure Database, Version 385.324, November 2004.
18. I. J. Bruno, J. C. Cole, P. R. Edgington, M. Kessler, C. F. Macrae, P. McCabe, J. Pearson, R. Taylor, Acta Cryst. B58 (2002) 389.
19. R. G. Pearson, J. Chem. Ed. 45 (1968) 581.
20. N. W. Alcock, J. Chem. Soc., Dalton Trans. 1973 (1973) 1616.
21. N. W. Alcock, J. Chem. Soc., Dalton Trans. 1973 (1973) 1614.
22. E. E. Baeva, Y. N. Mikhailov, Y. E. Gorbunova, L. B. Serezhkina, V. N. Serezhkin, Zh. Neorg. Khim. 48 (2003) 1801.
23. M. Y. Art'emeva, Y. N. Mikhailov, Y. E. Gorbunova, L. B. Serezhkina, V. N. Serezhkin, Zh. Neorg. Khim. 48 (2003) 1470.
24. M. Y. Artem'eva, Y. N. Mikhailov, Y. E. Gorbunova, L. B. Serezhkina, V. N. Serezhkin, Zh. Neorg. Khim. 48 (2003) 1473.
25. R. N. Shchelokov, Y. N. Mikhailov, A. G. Beirakhov, I. M. Orlova, Z. R. Ashurov, Zh. Neorg. Khim. 31 (1986) 2339.
26. M. Y. Artem'eva, A. V. Vologzhanina, F. M. Dolgushin, M. Y. Antipin, L. B. Serezhkina, V. N. Serezhkin, Zh. Neorg. Khim. 49 (2004) 2068.
27. N. C. Jayadevan, K. D. S. Mudher, D. M. Chackraburtty, Acta Crystallogr. B31 (1975) 2277.
28. Y. N. Mikhailov, Y. E. Gorbunova, O. V. Shishkina, L. B. Serezhkina, V. N. Serezhkin, Zh. Neorg. Khim. 44 (1999) 1448.
29. N. D. Jayadevan, D. M. Chackraburtty, Acta Crystallogr. B28 (1972) 3178.
30. L. Duvieubourg, G. Nowogrocki, F. Abraham, S. Grandjean, J. Solid State Chem. 178 (2005) 3437.

31. G. Bombieri, F. Benetollo, R. M. Rojas, M. L. De Paz, A. Del Pra, Inorg. Chim. Acta 61 (1982) 149.
32. L. A. Borkowski, C. L. Cahill, unpublished.
33. G. Bombieri, F. Benetollo, A. Del Pra, R. Rojas, J. Inorg. Nucl. Chem. 41 (1979) 201.
34. L. A. Borkowski, C. L. Cahill, Acta Crystallogr. E59 (2003) m1127.
35. L. A. Borkowski, C. L. Cahill, Inorg. Chem. 42 (2003) 7041.
36. Y. Zhang, F. R. Livens, D. Collison, M. Helliwell, F. Heatley, A. K. Powell, S. Wocadlo, H. Eccles, Polyhedron 21 (2002) 69.
37. Y. Zhang, D. Collison, F. R. Livens, M. Helliwell, F. Heatley, A. K. Powell, S. Wocadlo, H. Eccles, Polyhedron 21 (2002) 81.
38. L. A. Borkowski, C. L. Cahill, Acta Crystallogr. E61 (2005) m816.
39. G. Bombieri, F. Benetollo, E. Forsellini, A. Del Pra, J. Inorg. Nucl. Chem. 42 (1980) 1423.
40. R. M. Rojas, A. Del Pra, G. Bombieri, F. Benetollo, J. Inorg. Nucl. Chem. 41 (1979) 541.
41. Y.-r. Xie, H. Zhao, X.-s. Wang, Z.-r. Qu, R.-g. Xiong, X. Xue, Z. Xue, X.-z. You, Eur. J. Inorg. Chem. 2003 (2003) 3712.
42. R. N. Shchelokov, Y. N. Mikhailov, I. M. Orlova, A. V. Sergeev, Z. R. Ashurov, M. T. Tashev, N. A. Parpiev, Koord. Khim. 11 (1985) 1010.
43. G. Bombieri, F. Benetollo, R. M. Rojas, M. L. De Paz, J. Inorg. Nucl. Chem. 43 (1981) 3203.
44. F. Benetollo, G. Bombieri, J.A. Herrero, R.M. Rojas, J. Inorg. Nucl. Chem. 41 (1979) 195.
45. G. Bombieri, E. Forsellini, G. Tomat, L. Magon, R. Graziani, Acta Crystallogr. B30 (1974) 2659.
46. G. Bombieri, U. Croatto, R. Graziani, E. Forsellini, L. Magnon, Acta Crystallogr. B30 (1974) 407.
47. G. A. Doyle, D. M. L. Goodgame, A. Sinden, D. J. Williams, Chem. Commun. 1993 (1993) 1170.
48. S. Ahrland, In The Chemistry of the Actinide Elements; Katz, J. J., Seaborg, G. T., Morss, L. R., Eds., 1986; Vol. 2, pp 1480-1546.
49. L. A. Borkowski, C. L. Cahill, Acta Crystallogr. E60 (2004) m198.
50. R. N. Shchelokov, Y. N. Mikhailov, I. M. Orlova, A. V. Sergeev, Z. R. Ashurov, M. T. Tashev, N. A. Parpiev, Koord. Khim. 11 (1985) 1144.
51. A. Cousson, B. Stout, F. Nectoux, M. Pages, M. Gasperin, J. Less-Comm. Met. 125 (1986) 111.
52. A. S. Batsanov, C. Bilton, R. M. K. Deng, K. B. Dillon, J. A. K. Howard, H. Okatch-Nkala, Inorg. Chim. Acta 309 (2000) 163.
53. J.-Y. Kim, A. J. Norquist, D. O'Hare, Dalton Trans. 2003 (2003) 2813.
54. A.S. Wilson, Cryst. Struct. Comm. 11 (1982) 809.
55. C. Brouca-Cabarrecq, J. C. Trombe, Inorg. Chim. Acta 191 (1992) 241.
56. G. A. Battiston, G. Sbrignadello, G. Bandoli, D. A. Clemente, G. Tomat, J. Chem. Soc., Dalton Trans. 1979 (1979) 1965.
57. A. Cousson, F. Nectoux, M. Pages, E.N. Rizkalla, Radiochim. Acta 61 (1993) 177.
58. A. Immirzi, G. Bombieri, S. Degetto, G. Marangoni, Acta Crystallogr. B31 (1975) 1023.
59. M. Frisch, C. L. Cahill, 2006, In preparation.
60. Y.-Z. Zheng, M.-L. Tong, X.-M. Chen, Eur. J. Inorg. Chem. 2005 (2005) 4109.
61. M. Frisch, C. L. Cahill, Dalton Trans. 2005 (2005) 1518.
62. W. Chen, H.-M. Yuan, J.-Y. Wang, Z.-Y. Liu, J.-J. Xu, M. Yang, J.-S. Chen, J. Am. Chem. Soc. 125 (2003) 9266.
63. X.-M. Zhang, Coord. Chem. Rev. 249 (2005) 1201.
64. Z.-T. Yu, Z.-L. Liao, Y.-S. Jiang, G.-H. Li, G.-D. Li, J.-S. Chen, Chem. Commun. 2004 (2004) 1814.

65. R. E. Berry, P. D. Smith, S. M. Harben, M. Helliwell, D. Collison, C. D. Garner, Chem. Commun. 1998 (1998) 591.
66. Z.-T. Yu, Z.-L. Liao, Y.-S. Jiang, G.-H. Li, J.-S. Chen, Chem. Eur. J. 11 (2005) 2642.
67. F. Nectoux, H. Abazli, J. Jove, A. Cousson, M. Pages, M. Gasperin, G. Choppin, J. Less-Comm. Met. 97 (1984) 1.
68. G. B. Andreev, V. N. Khrustalev, M. Y. Antipin, A. M. Fedoseev, N. A. Budantseva, Z. K. Krupa, C. Madic, Russ. J. Coord. Chem. 26 (2000) 825.
69. M. N. Akhtar, A. J. Smith, Acta Crystallogr. B31 (1975) 1361.
70. S. M. Walker, P. S. Halasyamani, S. Allen, D. O'Hare, J. Am. Chem. Soc. 121 (1999) 10513.
71. P. S. Halasyamani, R. J. Francis, J. S. Bee, D. O'Hare, Mat. Res. Soc. Symp. Proc. 547 (1999) 383.
72. C. L. Cahill, P. C. Burns, Inorg. Chem. 40 (2001) 1347.
73. C. E. Talley, A. C. Bean, T. E. Albrecht-Schmitt, Inorg. Chem. 39 (2000) 5174.
74. M. S. Grigor'ev, M. Y. Antipin, N. N. Krot, Radiochem. 46 (2004) 224.
75. D. Grohol, F. Gingl, A. Clearfield, Inorg. Chem. 38 (1999) 751.
76. N. W. Alcock, T. J. Kemp, J. Leciejewicz, Inorg. Chim. Acta 203 (1993) 81.
77. J.-Y. Kim, A. J. Norquist, D. O'Hare, Chem. Mater. 15 (2003) 1970.

Structural Chemistry of Inorganic Actinide Compounds
S.V. Krivovichev, P.C. Burns & I.G. Tananaev (Editors)

Chapter 12

Nanostructured actinide compounds: an introduction

Sergey V. Krivovichev[a,b], Peter C. Burns[c], Ivan G. Tananaev[b], Boris F. Myasoedov[b]

[a]*Department of Crystallography, Faculty of Geology, St.Petersburg State University, University Emb. 7/9, 199034 St.Petersburg Russia*
[b]*A.N. Frumkin Institute of Physical Chemistry and Electrochemistry, Russian Academy of Sciences, Leninsky pr. 31, Moscow, 119991, Russia*
[c]*Department of Civil Engineering and Geological Sciences, University of Notre Dame Notre Dame, IN 46556-0767 U.S.A.*

1. Introduction

Nanotechnology is the term generaly used to describe the creation and exploitation of materials with at least one dimension in the nanometer range (1-1000 nm). These include nanocrystals and clusters (quantum dots), nanowires, nanotubes, thin films and superlattices (3-Dimensional structures) [1,2]. Usually, nanostructures have more reactive surfaces and exhibit new functions for the same chemical composition. Investigations of organization of matter at the nano-level are under way in many chemical systems with present and potential applications in nanotechnology. Recently, nanoscale structures were reported for the first time for actinide-containing compounds as well [3-6].

It is well-known that the solid-state chemistry of inorganic oxocompounds of hexa-, penta- and heptavalent actinide ions (An) is dominated by 2-dimensional (2D) layered structures, due to the strong tendency of An^{m+} cations to form linear actinyl ions, $AnO_2^{(m-4)+}$ [7,8]. The 2D character of polyhedra polymerization makes actinide oxocompounds attractive from the viewpoint of their potential ability to form nanostructures based upon real-2D and pseudo-2D topologies. For instance, spontaneous formation of nanotubes was observed in a number of systems where exfoliation of lamellar solids into individual sheets can be achieved.

The aim of this chapter is to review current results on nanostructured inorganic actinide compounds, i.e. compounds with nanoscale clusters and structural units. At present, we discuss only those structures that are accessible via X-ray diffraction analysis, i.e. highly ordered assemblies of units with at least dimension on the level of more than 1 nm.

2. 0D structures: actinide peroxide nanospheres

Self-assembling clusters have received considerable attention because they are excellent venues for the study of structure-property relationships. Monodisperse nanoaggregates have been reported with various compositions, including C-60-buckminsterfullerene and transition-metal oxide clusters. Numerous polyoxometalates have been synthesized and described that are built from WO, MoO, and NbO framework structures [9]. Small clusters provide important insights concerning the influence of the nanoscale on electronic, magnetic, and structural properties [10,11]. Nanoparticles are also important in environmental systems [12]. Recently, Burns et al. [3] reported the synthesis and characterization of a new family of self-assembling actinide nanospheres with compositions such as $K_{16}(H_2O)_2(UO_2)(O_2)_2(H_2O)_2[(UO_2)(O_2)_{1.5}]_{28}$ and $Li_6(H_2O)_8NpO_2(H_2O)_4[(NpO_2)(O_2)(OH)]_{24}$ that are comprised of linear actinyl-peroxide building blocks, and their persistence as stable entities in alkaline solutions.

The structures of the nanoclusters were obtained by crystallizing them into molecular crystals, followed by structural analysis using single-crystal X-ray diffraction (Table 1). Once the details of the structures were obtained, their presence in alkaline solutions was verified using Small Angle X-ray Scattering at the Advanced Photon Source in Chicago. The nanospheres shown in Figure 1 contain 24 (U-24, Np-24, Fig. 1a), 28 (U-28, Fig. 1b) and 32 (U-32, Fig. 1c) actinyl polyhedra. The nanoclusters are comprised of two types of actinyl peroxide polyhedra. U-24, U-32 and Np-24 contain topologically identical $(AcO_2)(O_2^{2-})_2(OH)_2$ hexagonal bipyramids, with O atoms of the actinyl ions constituting apices of the bipyramids, and peroxide groups form two of the equatorial edges of the polyhedra. U-28 contains only $(AcO_2)(O_2^{2-})_3$ hexagonal bipyramids, in which three equatorial edges of the polyhedra are peroxide groups. In all cases, hexagonal bipyramids link by sharing three of their equatorial edges with adjacent polyhedra. In U-24, Np-24 and U-32, two of the shared edges correspond to peroxide groups, whereas the third edge consists of two hydroxyl groups. In U-28, all three shared edges are peroxide groups. Outer surfaces of the nanospheres are O atoms of the actinyl ions, which can only accept weak bonds.

Figure 2 shows the linkage of polyhedra into four-membered rings that occur in the structures of U-24, U-32 and Np-24. Each shared edge within the four-membered ring is peroxide, with lengths of ~1.45 Å, whereas the edge defined by one O atom of each of the two peroxide groups is ~2.8 Å. Linkage of four polyhedra into a ring can only be accomplished if the polyhedra are significantly tilted, such that the actinyl ions are directed towards a common point located ~ 3.5 Å below the four co-planar actinide cations (Fig. 2c). The linkage of eight identical four-membered rings of polyhedra results in the nanosphere found in U-24 and Np-24 (Fig. 2d).

The nanospheres were obtained in alkaline solutions containing both uranyl and peroxide at room temperature. Such actinyl peroxide nanospheres may form in alkaline mixtures of nuclear waste containing various salts and organic solvents, such as in high-level waste storage tanks, by incorporating peroxide created by alpha radiolysis of water. Synthesis conditions used to prepare the nanoclusters were broadly similar to those in high-level waste storage tanks, as well as soils and sediments contaminated by leakage of such waste. Formation of actinyl peroxide nanospheres in such systems is probable, and given their persistence in solution, could profoundly impact the mobility of actinides in such systems.

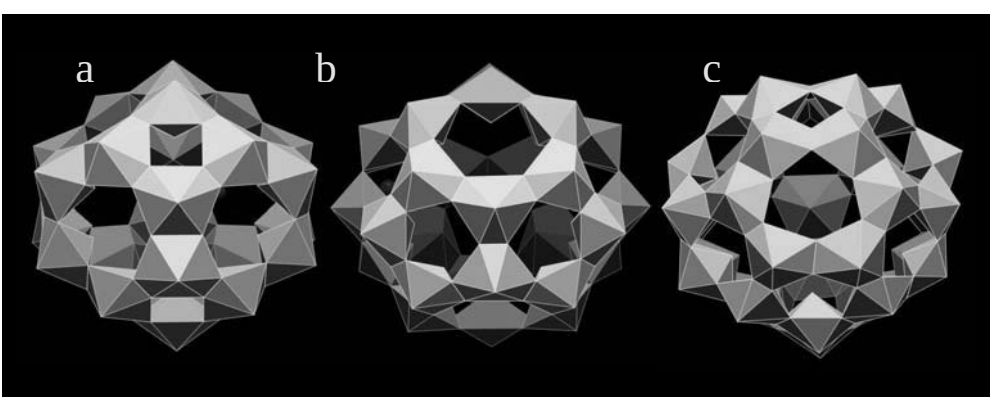

Fig. 1: Nano-scale clusters of uranyl and neptunyl peroxides. (a) cluster containing 24 uranyl or neptunyl polyhedra, (b) cluster containing 28 uranyl polyhedra, (c) cluster containing 32 uranyl polyhedra.

Table 1. Crystallographic parameters of actinyl peroxides containing peroxide nanospheres

Name	sp. gr.	a [Å] / α [°]	b [Å] / β [°]	c [Å] / γ [°]
U-24	$P\bar{1}$	19.211 / 102.40	31.003 / 99.50	32.252 / 95.36
Np-24	$I4/m$	18.155 / 90	18.155 / 90	26.693 / 90
U-28	$Pbcm$	19.261 / 90	33.813 / 90	28.163 / 90
U-32	$P2_1/c$	38.84 / 90	36.52 / 102.86	41.30 / 90

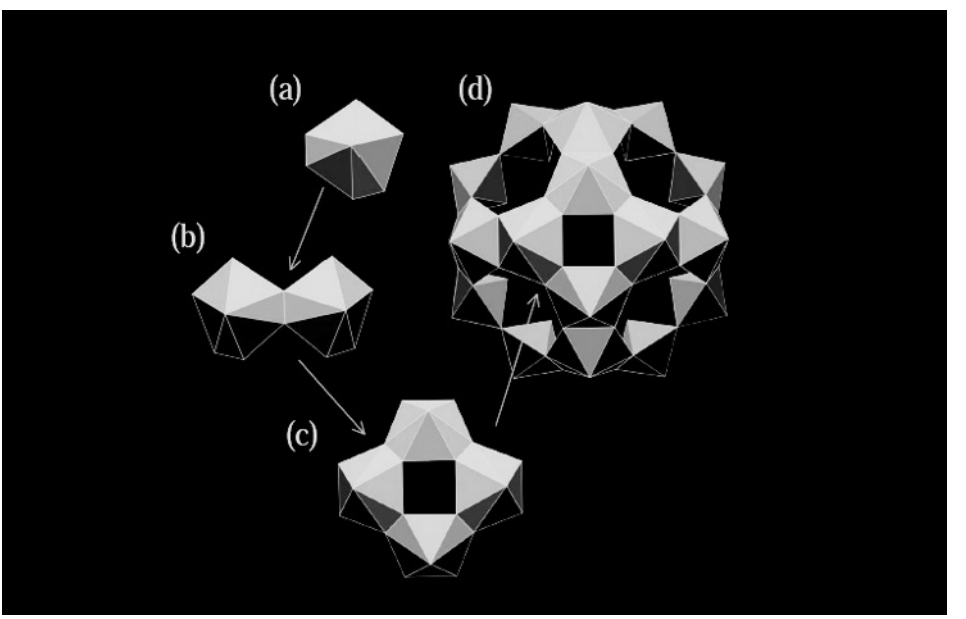

Fig. 2. Polyhedral representations of linkages in the U-24 and Np-24 nanoclusters. (a) hexagonal bipyramid with composition $(AnO_2)(O_2)_2(OH)_2$. (b) Linkages of two hexagonal bipyramids by the sharing of a peroxide edge. (c) Linkage of four hexagonal bipyramids into a four-membered ring by the sharing of four peroxide edges. (d) U-24 cluster.

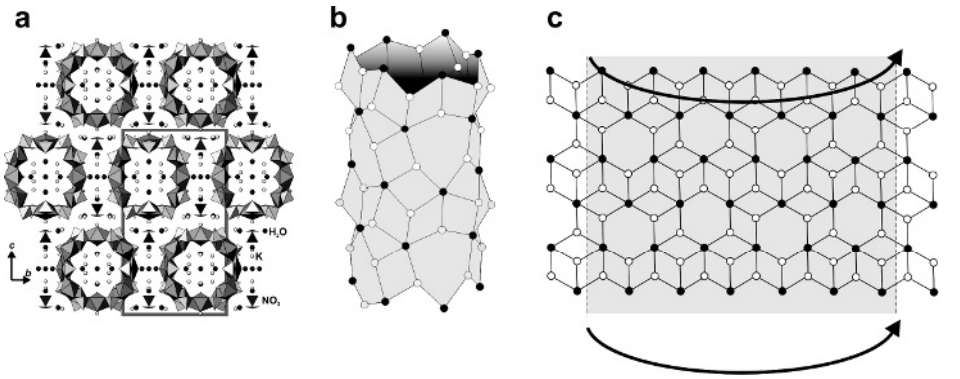

Fig. 3. The crystal structure of **1** projected along the *a* axis (a), tubular graph describing topology of the uranyl selenate nanotubule in **1** (b) and its unfolded version (c)

3. 1D structures: uranyl selenate nanotubules

Since the discovery of carbon nanotubes in 1991 [14], a great deal of attention was attracted to inorganic nanotubes as promising modules for nanotechnology applications. Oxidic nanotubes are of special interest because of their unique atomic structure and interesting physical properties [15,16]. Krivovichev et al. [4,5] have recently reported synthesis and structures of two uranium(VI) compounds, $K_5[(UO_2)_3(SeO_4)_5](NO_3)(H_2O)_{3.5}$ (**1**) and $(C_4H_{12}N)_{14}[(UO_2)_{10}(SeO_4)_{17}(H_2O)]$ (**2**), containing nanometer-sized tubules formed by corner sharing of $U^{6+}O_7$ pentagonal bipyramids and SeO_4 tetrahedra [4,5].

The most intriguing feature of the structures of compounds **1** and **2** is that they contain isolated porous nanotubules formed by corner sharing of $U^{6+}O_7$ pentagonal bipyramids and SeO_4 tetrahedra (Fig. 3a). Such nanometer-scale tubules formed by two types of coordination polyhedra are new in the realm of inorganic oxosalts; probably, the most closely related but yet distinct are elliptic porous nanorods in the structure of yuksporite, a natural material from the Kola peninsula, Russia [17]. The uranyl selenate nanotubules in the structures of **1** and **2** have circular cross-sections with outer diameters of 17 and ~ 25 Å (= 1.7 and 2.5 nm), respectively. The crystallographic free diameters of the tubules are 4.7 and 12.7 Å for **1** and **2**, respectively.

The topology of the uranyl selenate nanoscale tubules can be described by means of a graphical approach first suggested by Krivovichev and Burns [18] for analysis of structural topologies in uranyl molybdates. The $[UO_7]^{8-}$ bipyramids and $[SeO_4]^{2-}$ tetrahedra are symbolized by black and white vertices, respectively. The black-and-white graph corresponding to the topological structure of the $[(UO_2)_3(SeO_4)_5]^{4-}$ tubule in **1** is shown in Fig. 3b. Its idealized unfolded version is given in Fig. 3c. To obtain the tubular graph corresponding

to the$[(UO_2)_3(SeO_4)_5]^{4-}$ tubule, one has to cut the graph into tapes along the lines indicated in Figure 1c, to fold the tape and to glue its corresponding sides. The same procedure can be used to investigate the local topology of the tubules observed in the structure of **2**. The black-and-white graph corresponding to the topological structure of the $[(UO_2)_{10}(SeO_4)_{17}(H_2O)]^{14-}$ tubule in **2** is shown in Fig. 4a. Its idealized unfolded version is given in Fig. 4b. To obtain the tubular graph corresponding to the tubule shown in Fig. 4a, one has to cut the graph into tapes along the lines indicated in Fig. 4b, to fold the tape and to glue its sides.

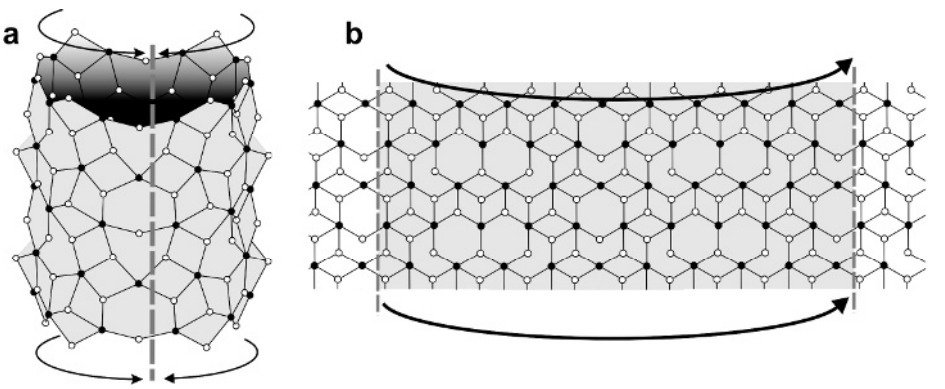

Figure 4. Tubular graph describing topology of the uranyl selenate nanotubule in **2** (a) and its unfolded version (b).

Most of the known inorganic nanotubes have a prototype lamellar material from which they can be (at least theoretically) obtained by exfoliation and folding of single-layer sheets into a tube. The same holds for the uranyl selenate tubules observed in **1**. The 3:5 graph shown in Fig. 3b is an underlying topology for $[(UO_2)_3(TO_4)_5]^{4-}$ sheets found in the structures of inorganic oxosalts with T = S, Cr, Se [19-23]. The 10:17 graph of **2** shown in Fig. 4b has not been observed previously as an underlying topology for any inorganic compound. However, some parts of it can be found as being topologically isomorphous to the U:Se = 3:5 topology recently found in the structures of $Rb_4[(UO_2)_3(SeO_4)_5(H_2O)]$ [24].

The mechanism of formation of uranyl selenate tubules in aqueous media is probably controlled for compound **2** by the presence of protonated butylamine $(C_4H_{12}N)^+$ cations. In this regard, it can be similar to the process that leads to the formation of highly undulated uranyl selenate sheets in the structure of $(H_3O)_2[C_{12}H_{30}N_2]_3[(UO_2)_4(SeO_4)_8](H_2O)_5$ (see below). The flexible uranyl selenate complexes crystallize around cylindrical micelles to produce a tubular inorganic substructure.

4. 2D structures: organic-inorganic nanocomposites

Organic-inorganic 2D nanocomposites is an emerging group of organic-inorganic materials that contain alternating organic and inorganic substructures. Here we will consider some examples of organic-inorganic nanocomposites consisting of inorganic (uranyl selenate) layers and organic 2D layers of long-chain amines and diamines (Table 2). One useful concept to analyze structures of organic-inorganic nanocomposites has been that of charge density matching [25,26] at the organic/inorganic interface. The idea is that "…two different materials will self-organize to have similar charge densities at their surfaces and, therefore, achieve local electroneutrality" [26]. This concept has been successfully applied to a large number of organic-inorganic composites, including metal phosphates [27,28], vanadates [26] and mesoporous silica [29]. The unique character of actinide chemistry, namely, tendency of high-valence actinide ions to form actinyl groups, requires special consideration for the application of charge-density matching principles to actinide compounds.

4.1. Charge-density matching principle and its application to uranyl oxocompounds

The charge density of the interface is defined as a formal charge per surface area unit. If the inorganic substructure consists of polymerized cation-oxygen coordination polyhedra (as is the case for amine-templated inorganic oxysalts), the larger the size of the polyhedra, the lower the charge density. In the case of uranyl (in general, actinyl) oxocompounds, uranyl ions are coordinated in their equatorial planes by four, five, or six anions O_{eq}, thus forming tetragonal, pentagonal, or hexagonal bipyramids, respectively. In layered structures, uranyl ions are oriented perpendicular to the plane of the sheets so that equatorial planes of bipyramids are approximately parallel to the sheets. The surface area of bipyramid ($\mathbf{S}_B$) within the plane of the sheet is controlled by the $d_{eq} = U\text{-}O_{eq}$ bond length (Fig. 5). For a pentagonal bipyramid, the surface area can be calculated as a surface area of the pentagonal bipyramid with the d_{eq} bond length being the distance from its center to its corner. The surface area $\mathbf{S}_{PB}$ can be calculated as $2.378 \times d_{eq}^2$ [Å^2]. For uranyl pentagonal bipyramids, we have d_{eq} = 2.36 Å, so $\mathbf{S}_{PB}$ = 13.24 Å^2.

For comparison, let us calculate the surface area ($\mathbf{S}_T$) of a tetrahedral unit TO_4 which is a common constituent of organically templated lamellar metal phosphates [28]. The surface area is controlled by the average <T-O> bond length which can vary from 1.5 to 1.7 Å. Since the TO_4 tetrahedron may take any position relative to the plane of the sheet, it is convenient to restrict its volume by a sphere with its center at T and its radius being the average <T-O> bond length. The surface area of the tetrahedron will be within the central

Table 2. Crystallographic data for nanostructured uranyl selenates

Name	Chemical formula	sp. gr.	*a* [Å] / α [°]	*b* [Å] / β [°]	*c* [Å] / γ [°]
2D organic-inorganic nanocomposites with tail interdigitation					
LUS-1*	$[C_8H_{20}N]_2[(UO_2)(SeO_4)_2(H_2O)](H_2O)$	$P\bar{1}$	7.498 / 89.69	11.897 / 90.05	32.056 / 88.80
2D organic-inorganic nanocomposites with acid/water interlayers					
LUS-2	$[C_{12}N_2H_{30}][(UO_2)(SeO_4)_2(H_2O)](H_2SeO_4)_{1.88}(H_2O)$	*C*2/*m*	30.116 / 90	12.160 / 91.15	7.594 / 90
LUS-3	$[C_{12}N_2H_{30}][(UO_2)(SeO_4)_2](H_2O)_x$	*C*2/*c*	33.805 / 90	13.242 / 92.53	11.256 / 90
LUS-4	$[C_{10}H_{26}N_2][(UO_2)(SeO_4)_2](H_2SeO_4)_{0.50}(H_2O)$	*C*2/*c*	29.280 / 90	13.301 / 93.30	11.451 / 90
LUS-5	$[C_{10}H_{26}N_2][(UO_2)(SeO_4)_2(H_2O)](H_2SeO_4)_{0.85}(H_2O)_2$	$P\bar{1}$	7.546 / 77.68	14.991 / 85.46	22.379 / 82.72
2D-1D organic-inorganic nanocomposites					
-	$(H_3O)_2[C_{12}H_{30}N_2]_3[(UO_2)_4(SeO_4)_8](H_2O)_5$	$P2_1/n$	11.344 / 90	24.804 / 96.70	29.250 / 90
Nanotubules					
-	$K_5[(UO_2)_3(SeO_4)_5](NO_3)(H_2O)_{3.5}$	*Pnmm*	11.205	18.213	32.364
-	$(C_4H_{12}N)_{14}[(UO_2)_{10}(SeO_4)_{17}(H_2O)]$	*I*2*mm*	10.886	29.532	47.439

* LUS = **L**amellar **U**ranyl **S**elenate

section of the sphere, i.e. a circle with the radius of <T-O>. Using some simple calculations, we obtain that the surface area of a metal tetrahedron should be within the range of 7.1 to 9.1 Å^2. These values are significantly smaller than the calculated surface area of the uranyl pentagonal bipyramid. Therefore, the charge density of 2D uranyl substructures should be significantly smaller than the charge density of layered metal phosphate units. Let us consider some examples.

The structure of LUS-1 (Table 2) consists of $[(UO_2)(SeO_4)_2(H_2O)]^{2-}$ sheets shown in Fig. 6a. The surface area per one $[(UO_2)(SeO_4)_2(H_2O)]$ formula unit is 89.204 Å^2, which provides charge density of the sheet as **CD** = –2 / 89.204 = –0.0224 *e*Å^{-2}.

Feng et al. [28] reported a series of lamellar aluminophosphates with general formula $[Al_{13}(PO_4)_{18}H][NH_3(CH_2)_nNH_3]_7(H_2O)_8$ (*n* = 9-12). The surface area of the $[Al_{13}(PO_4)_{18}H]^{14-}$ sheet is 237.2 Å^2, which results in **CD** = –14 / 237.2 = –0.0590 *e*Å^{-2}.

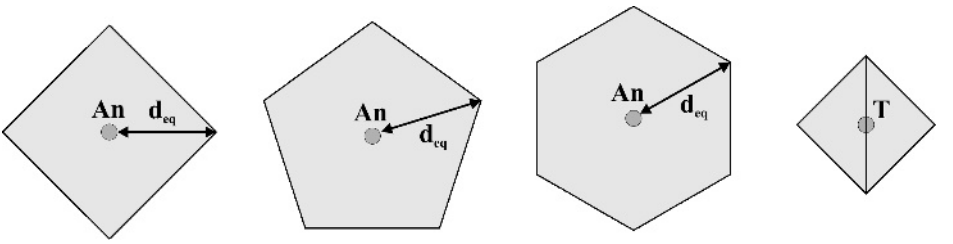

Fig. 5. Maximal surface area of uranyl bipyramids (An) in comparison to the maximal surface area of PO_4 tetrahedra in metal phosphates (T).

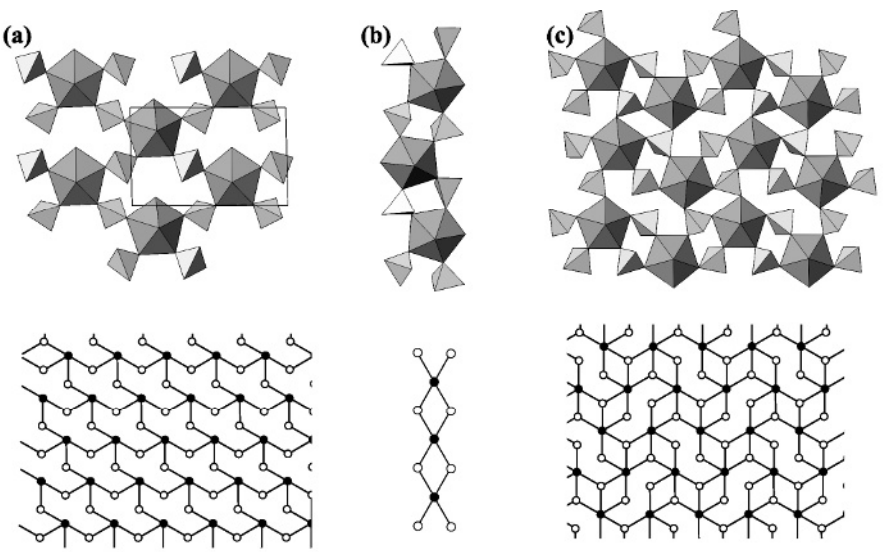

Fig. 6. Uranyl selenate units observed in the structures of organic-inorganic nanocomposite compounds: (a) LUS-1; (b) LUS-2 and LUS-4; (c) LUS-3 and LUS-5. Below polyhedral diagrams black-and-white graphs describing topology of structural units are given.

According to Maggard and Boyle [26], the charge densities of layered vanadate units $[V_xO_y]^{m-}$ vary from –0.0362 to –0.0493 eÅ^{-2}. The charge density of the gallophosphate layer in the structure of MIL-35, $[NH_3(CH_2)_{12}NH_3][Ga_4(PO_4)_4F_4]$ [30], is equal to –0.0756 eÅ^{-2}.

These examples demonstrate clearly that charge densities of uranyl-based sheets are in general smaller than charge densities of metal phosphate and vanadate units in lamellar compounds. However, the very existence of nanocomposite vanadates and metal phosphates means that the charge-density matching principle in these compounds is observed. Then how does it work for

uranyl nanocomposites? There are several possible solutions and two of them are realized in uranyl selenates.

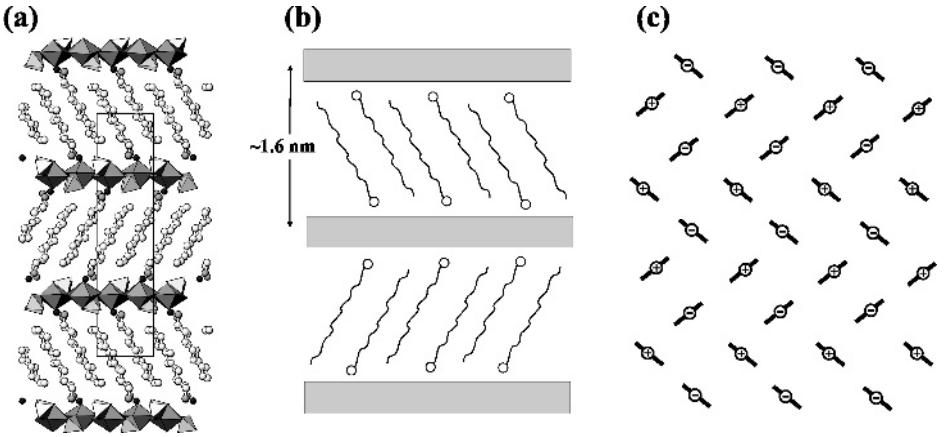

Fig. 7. Structure of LUS-1 (a), its schematic representation (b), and orientation of octylamine molecules within the organic nanolayer (c; "+" and "-" signs correspond to the orientations of amine headgroups "up" and "down", respectively).

4.2. Structures with tail interdigitation (long-chain monoamine structures)

The structure of LUS-1 is shown in Fig. 7. It is based upon the $[(UO_2)(SeO_4)_2(H_2O)]^{2-}$ sheets consisting of corner-sharing uranyl pentagonal bipyramids and selenate tetrahedra (Fig. 6a). The sheets alternate with the arrays of protonated octylamine molecules, $[CH_3(CH_2)_7NH_3]^+$, stacked in such a way that amine headgroups are oriented towards either overlying or underlying uranyl selenate sheets (see scheme in Fig. 7b). The tails of the octylamine cations interdigitate, so that the charge-density matching principle is observed. The inclination angle of the monoamine chain relative to the plane of the inorganic sheet, θ, is about 61°. Figure 3c shows the packing scheme of chains within the organic nanolayer (~1.5 nm thick). As shown above, the charge density of the uranyl selenate sheet is equal to –0.0224 eÅ^{-2}. The relative stability of the structure (it loses water under atmospheric conditions) indicates that the charge-density matching principle is observed, i.e. charge density of the organic surface is about –0.022 eÅ^{-2}.

4.3. Diamine-templated structures

In contrast to monoamines, long-chain diamines have amine headgroups on both sides of the chains. If the molecules are packed in the same way as in the structure of LUS-1, the charge density of the organic surface should be exactly

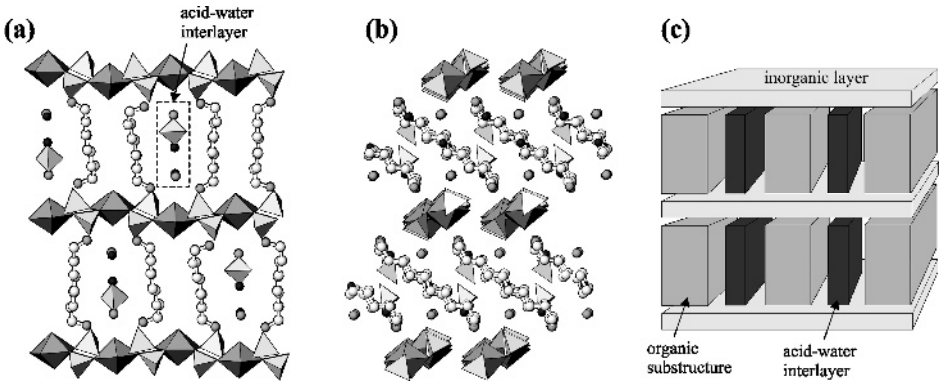

Fig. 8. Structure of LUS-5 projected along two mutually perpendicular directions along the uranyl selenate sheet (a, b) and schematic representation of its structural principle.

two times higher than that in LUS-1, i.e. it should be equal to –0.04-0.06 eÅ^{-2}. However, it appears that the charge density at the organic side of the interface can be adjusted by means of the packing mode and inclination angle θ. Thus, in the structure of MIL-35, **CD** = –0.0756 eÅ^{-2}, whereas, in lamellar aluminophosphates, it is around –0.06 eÅ^{-2}. In any case, it is at least two times higher than the charge density of typical uranyl selenate sheets.

The charge-density matching principle is observed by incorporation of acid-water interlayers into the organic substructure. Fig. 8 shows the structure of LUS-5 (Table 2) that contains the inorganic uranyl selenate sheets of hydrogen-bonded $[(UO_2)(SeO_4)_2(H_2O)]^{2-}$ chains shown in Fig. 7b. The charge density of the uranyl selenate sheet is –0.0217 eÅ^{-2}. The inorganic sheets are separated by organic nanolayers. The nanolayers are modified by incorporation of additional disordered $[H_2SeO_4]$ groups and H_2O molecules that form slices parallel to the orientations of protonated dodecanediamine molecules, $[NH_3(CH_2)_{12}NH_3]^{2+}$. The structural role of the acid-water interlayers is to modify organic substructure in order to satisfy the charge-density matching principle. The same behavior has been observed for the structures of LUS-3, 4, and 5. In the structures of LUS-3 and -4, the inorganic sheet is a 2D $[(UO_2)(SeO_4)_2]^{2-}$ sheet shown in Fig. 7c, whereas the structure of LUS-5 contains uranyl selenate chains similar to those observed in LUS-2.

A totally different situation of interplay between organic and inorganic substructures has been observed in the structure of $(H_3O)_2[C_{12}H_{30}N_2]_3[(UO_2)_4(SeO_4)_8]$ $(H_2O)_5$ [18] (Fig. 9). The inorganic substructure consists of the UO_7 bipyramids and SeO_4^{2-} tetrahedra that share corners to form $[(UO_2)(SeO_4)_2]^{2-}$ sheets depicted in Fig. 10. The sheets are parallel to (001) and are strongly undulated along the c axis. The undulation vector is parallel to [010] and equals to b =24.804 Å.

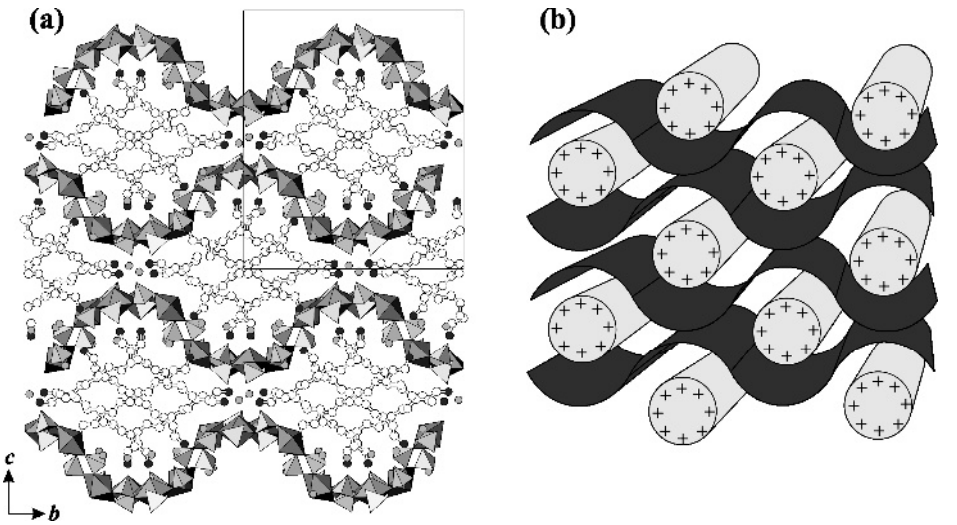

Fig. 9. Crystal structure of $(H_3O)_2[C_{12}H_{30}N_2]_3[(UO_2)_4(SeO_4)_8]\ (H_2O)_5$ (a) and a scheme of its construction (b: inorganic layers are dark, organic micelles are light).

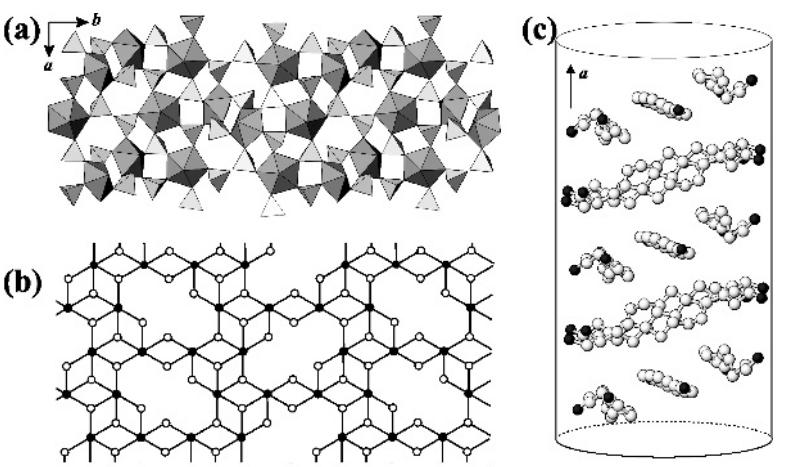

Fig. 10. The $[(UO_2)(SeO_4)_2]^{2-}$ sheet in the structure of $(H_3O)_2[C_{12}H_{30}N_2]_3[(UO_2)_4(SeO_4)_8]\ (H_2O)_5$ (a), its nodal representation (U and Se polyhedra are symbolized by black and white circles, respectively) (b), and organization of 1,12-dodecanediamine molecules into a micelle (c)

The undulation amplitude is about 25 Å. The undulations in the adjacent sheets have an anti-phase character so the large eliptical channels are created along the *a* axis.

The organic substructure consists of micelles of protonated 1,12-dodecanediamine molecules oriented parallel to the *a* axis. The micelles occupy channels created by the packing of the $[(UO_2)(SeO_4)_2]^{2-}$ sheets. The scheme of assembly of the 1,12-dodecanediamine chain molecules within the micelle is shown in Figure 5c. The molecules are arranged into sublayers approximately parallel to (-102). The planes of these sublayers are not perpendicular to the micelle axis but form an angle of about 60°. In each layer, there are three $[C_{12}H_{30}N_2]^{2+}$ molecules that are parallel to each other. The molecules in the adjacent layers are at a 30° angle relative to each other, and this results in the elliptical form of the perpendicular section of the micelle. The lateral dimensions of the micelle are about 20×24 Å, i.e. are at the level of nanometers. The interactions between organic and inorganic substructures involve N···O hydrogen bonds to oxygen atoms of uranyl ions and terminal oxygen atoms of selenate tetrahedra.

The protonated amine molecules with long-chain structure are known to form cylindrical micelles in aqueous solutions that involves self-assembly governed by competing hydrophobic/hydrophillic interactions. The flexible inorganic complexes present in the reaction mixture could then form around cylindrical micelles to produce an inorganic structure that reflects the cylindrical form of the micelles. In the case of $(H_3O)_2[C_{12}H_{30}N_2]_3[(UO_2)_4(SeO_4)_8](H_2O)_5$, the inorganic structure forms a strongly undulated sheet, although structures with highly porous uranyl selenate nanotubules have also been observed (see above). This indicates the possibility of preparation of uranium oxosalt mesostructures if larger organic moieties (e.g., block copolymers) are involved in the synthesis procedure.

5. Conclusions

Actinide peroxide nanospheres [3] and uranyl selenate nanotubules [4,5] represent the first examples of nanoscale structures in actinide compounds. It is noteworthy that, very frequently, formation of nanostructures corresponds to organic-inorganic composites with clearly defined interfacial interactions. To describe the character of these interactions, one can use the charge-density matching concept with some modifications related to the basic chemical properties of actinides.

Most of the reported nanostructured actinide compounds considered here have been obtained under soft synthesis conditions (room-temperature crystallization from aqueous solutions). Most of these compounds are soluble and it is rather hard to foresee any practical application of them. However, findings reported here demonstrate the possibility of nanoscale fabrication for actinides in higher oxidation states. For instance, we expect that a whole new range of uranium-based nanotubular and nanocomposite materials can be

synthesized. One possible application of these materials is the utilization of depleted uranium, hundreds of thousands of tons of which are now stored by nuclear countries such as the U.S. and Russia.

References

1. C.N.R. Rao, A.K. Cheetham, J. Mater. Chem. 11 (2001) 2887.
2. C.N.R. Rao, A. Govindaraj, Nanotubes and Nanowires, RSC Publishing, Cambridge, 2005.
3. P.C. Burns, K.-A. Hughes Kubatko, G. Sigmon, B.J. Fryer, J.E. Gagnon, M.R. Antonio, L. Soderholm, Angew. Chem. Int. Ed. 44 (2005) 2135.
4. S.V. Krivovichev, V. Kahlenberg, R. Kaindl, E. Mersdorf, I.G. Tananaev, B.F. Myasoedov, Angew. Chem. Int. Ed. 44 (2005) 1134.
5. S.V. Krivovichev, V. Kahlenberg, R. Kaindl, E. Mersdorf, I.G. Tananaev, B.F. Myasoedov, J. Amer. Chem. Soc. 127 (2005) 1072.
6. Th. Albrecht-Schmitt, Angew. Chem. Int. Ed. 44 (2005) 4836.
7. P.C. Burns, M.L. Miller, R.C. Ewing, Can. Mineral. 34 (1996) 845.
8. P.C. Burns, R.C. Ewing, F.C. Hawthorne, Can. Mineral. 35 (1997) 1551.
9. A. Muller, F. Peters, M.T. Pope, D. Gatteschi, Chem. Rev. 98 (1998) 239.
10. A.F. Hebard, M.J. Rosseinsky, R.C. Haddon, D.W. Murphy, S.H. Glarum, T.T.M. Palstra, A.P. Ramirez, A.R. Kortan, Nature 350 (1991) 600.
11. C.L. Hill, in: Applications of Coordination Chemistry, Ed.: M. Ward, Comprehensive Coordination Chemistry-II: From Biology to Nanotechnology, Elsevier: Oxford 2003. Vol. 4. pp. 679-759.
12. J.F. Banfield, H. Zhang, Rev. Mineral. Geochem. 44 (2001) 1.
13. P.C. Burns, Rev. Mineral. 38 (1999) 23.
14. S. Iijima, Nature 354 (1991) 56.
15. G.R. Patzke, F. Krumeich, R. Nesper, Angew. Chem. Int. Ed. 41 (2002) 2446.
16. L. Krush-Elbaum, D.M. Newns, H. Zeng, V. Derycke, J.Z. Sun, R. Sandstrom, Nature 431 (2004) 672.
17. S.V. Krivovichev, V.N. Yakovenchuk, T. Armbruster, N. Döbelin, P. Pattison, H.-P. Weber, W. Depmeier, Amer. Mineral. 89 (2004) 1561.
18. S.V. Krivovichev, P.C. Burns, J. Solid State Chem. 170 (2003) 106.
19. S.V. Krivovichev, V. Kahlenberg, J. Alloys Compds 389 (2005) 55.
20. S.V. Krivovichev, V. Kahlenberg, Z. Anorg. Allg. Chem. 630 (2004) 2736.
21. S.V. Krivovichev, P.C. Burns, Radiochem. 46 (2004) 408.
22. S.V. Krivovichev, P.C. Burns, Z. Kristallogr. 218 (2003) 683.
23. S.V. Krivovichev, P.C. Burns, Z. Kristallogr. 218 (2003) 725.
24. S.V. Krivovichev, V. Kahlenberg, Z. Anorg. Allg. Chem. 631 (2005) 739.
25. A. Monnier, F. Schuth, Q. Huo, D. Kumar, D. Margolese, R.S. Maxwell, G.D. Stucky, M. Krishnamurty, P. Petroff, A. Firouz, M. Janicke, B.F. Chmelka, Science 261 (1993) 1299.
26. P.A. Maggard, P.D. Boyle, Inorg. Chem. 42 (2003) 4250.
27. J.E. Haskouri, M. Roca, S. Cabrera, J. Alamo, A. Beltrán-Porter, D. Beltrán-Porter, M. Dolores Marcos, P. Amorós, Chem. Mater. 11 (1999) 1446.
28. P. Feng, X. Bu, G.D. Stucky, Inorg. Chem. 39 (2000) 2.
29. S.H. Tolbert, C.C. Landry, G.D. Stucky, B.F. Chmelka, P. Norby, J.C. Hanson, A. Monnier, Chem. Mater. 13 (2001) 2247.
30. C. Sassoye, T. Loiseau, G. Férey, J. Fluor. Chem. 107 (2001) 187.

Structural Chemistry of Inorganic Actinide Compounds
S.V. Krivovichev, P.C. Burns & I.G. Tananaev (Editors)

Chapter 13

Actinide host phases as radioactive waste forms

Sergey V. Yudintsev,[a] Sergey V. Stefanovsky,[b] Rodney C. Ewing[c]

[a]*Institute of Geology of Ore Deposits, Mineralogy, Petrography and Geochemistry RAS, Staromonetny lane 35, Moscow 119017 RUSSIA*
[b]*United Ecology, Technology, and Research Center on RAW Management and Environmental Remediation (SIA Radon), 7th Rostovskii lane 2/14, Moscow 119121 RUSSIA*
[c]*University of Michigan, Ann Arbor, MI 48109 USA*

1. Introduction

There are three significant types of actinide-containing materials generated by the nuclear fuel cycle that contain high levels of radioactivity: 1.) spent nuclear fuel (SNF) related to the production of fissile material for weapons, 2.) SNF from commercial nuclear reactors, 3.) liquid high-level waste (HLW) derived during the reprocessing of SNF [1]. Unreacted fuel constituents (^{235,238}U) make up approximately 96% of total mass of SNF. A major fraction of activity of SNF comes from fission product (FP) elements with mass numbers from 85 to 106 and from 125-147 (Kr, Sr, Y, Zr, Tc, Ru, Y, Sb, Cs, Ba, Ce, Pm, etc.), unreacted fuel (U), "minor" actinides (Np, Pu, Am, Cm), and activated products (H, C, Al, Na, Mn, Fe, Co). FPs consist of about 200 isotopes of approximately 40 elements from Zn to Gd. The yield of individual radionuclides ranges between 10^{-4} % to several percent (a yield of 1% corresponds to production of 1 atom of daughter isotope per 100 events of nuclear decay of ^{235}U or ^{239}Pu). The fraction of individual radionuclides in SNF varies depending on the type of reactor, burn-up and cooling time. From point of view of radiobiological risk the following groups of radionuclides are important:

- Short-lived FPs which are almost completely decayed to stable isotopes after a cooling of SNF for some tens of years: Rb, Y, Mo, Ru, Rh, Ag, Sb, Te, Xe, Ba, La, Ce, Pr, Nd, Pm. Their amount in total is ~26 kg per metric tone (MT) of SNF or 65 wt.% of the total FPs amount;

- FPs with high specific activity: mainly ^{90}Sr and ^{137}Cs; their total content is up to 6 kg per 1 MT of SNF (about 15 wt.% of total FPs);
- Long-lived FPs with low specific activity: Zr, Tc, Pd, Sn, I (about 8 kg per 1 MT of SNF or about 20 wt.% of total FPs);
- Actinides (Np, Pu, Am, Cm) and their daughter products which are less than 1 wt.% and dominated by Pu;
- Unreacted constituents: ^{238}U – 98.9 wt.% and ^{235}U – 1.1 wt.% of total.

The nuclear fuel cycle (NFC) mass balance for a pressurized water reactor (PWR) nuclear power plant (NPP) with electric power generation of 1 GW per year may be represented as follows [2]: 37 MT of enriched uranium (3.0 at.% ^{235}U) after burn-up generates 3.1 GW thermal, 1 GW electric energy and yields about 330 kg of plutonium (^{239}Pu, ^{240}Pu, ^{241}Pu), ~20 kg of minor actinides (^{237}Np, ^{241}Am, ^{243}Am, ^{244}Cm), 1,500 kg of FPs (^{85}Kr, ^{90}Sr, ^{93}Zr, ^{99}Tc, ^{125}Sb, ^{126}Sn, ^{129}I, ^{135,137}Cs) and the remainder is 35.7 MT of uranium (1.1 at.% of ^{235}U). There are two principal strategies for handling SNF [3]. Some countries consider SNF as a waste to be disposed (the open NFC). In the other countries SNF is considered to be a valuable product that is reprocessed for the recovery of plutonium and uranium for re-use in power generation (the closed NFC). In some countries a decision with respect to SNF has not yet been made. SNF has been reprocessed at radiochemical plants in France, United Kingdom, Russia, Japan, and India. In the USA, three plants with total capacity of 2,100 MT per year have been constructed and operated, but all closed in the 1970-1980s. SNF reprocessing generates great volumes of high- (HLW), intermediate- (ILW) and low-level wastes (LLW). Among these HLW is the most dangerous. HLW is a complex mixture of unreacted fuel constituents (U), actinides, fission (FP), and corrosion (CP) products, and processing contaminants. In the Russia liquid HLW in amount of 30,000 m^3 and activity of 350 millions Curies (Ci) are now stored at the “Mayak” site (South Urals) and the Mining & Chemical Combine (Siberia) [3]. In the USA, liquid HLW in amount of 380,000 m^3 with total activity of 960 million Ci are stored in large tanks at the Hanford, Washington and Savannah River, South Carolina, and as a solid calcine in metal silos at Idaho National Engineering Laboratory [1]. More than 99% of total activity is due to FPs and activated CPs having relatively short half-lives (less than 50 years – Table I). After 500 years of storage, the fraction of these radionuclides will be reduced significantly and the major contribution to total activity will be due to ^{151}Sm, ^{238}Pu, and ^{241}Am. Major fractions of the activity are due to ^{239}Pu and ^{240}Pu at approximately 50,000 years. Because of long half-lives and radiotoxicities, transuranic actinides: ^{237}Np, ^{239,240}Pu, ^{241,243}Am are considered to be the most dangerous [4]; thus, these actinides must be incorporated into durable host phases that prevent or much delay their release to environment.

Table I. Major HLW radionuclides.

Major FPs and CPs (β- and γ-emitters)		TRU elements (α-emitters)	
radionuclides	$T_{1/2}$, years	Radionuclides	$T_{1/2}$, years
^{90}Sr	29	^{237}Np	2.1×10^{6}
^{93}Zr	1.5×10^{6}	^{238}Pu	89.9
^{99}Tc	2.1×10^{5}	^{239}Pu	2.4×10^{4}
^{126}Sn	10^{5}	^{240}Pu	6.5×10^{3}
^{129}I	1.7×10^{7}	^{241}Pu	14
^{137}Cs	30	^{242}Pu	3.78×10^{5}
^{147}Pm	2.6	^{241}Am	433
^{151}Sm	93	^{242}Am	152
^{154}Eu	16	^{243}Am	7.3×10^{3}
^{54}Mn	0.87	^{243}Cm	28
^{59}Ni	7.5×10^{4}	^{244}Cm	17.9
^{60}Co	5.3	^{245}Cm	8.5×10^{3}
^{63}Ni	96	^{246}Cm	4.76×10^{3}

2. Actinide-bearing waste streams

The typical content of actinides in the SNF is about 10 kg per 1 MT or ~1 wt.% [2,5]. Among them ^{238}Pu + ^{239}Pu - ~ 90-93%, ^{237}Np - ~5.0-6.7%, ^{241}Am + ^{243}Am - ~1.3%, ^{242}Cm + ^{244}Cm - ~0.3% of total for the SNF from LWR; and ^{238}Pu + ^{239}Pu - ~85-95%, ^{237}Np - ~3-5%, ^{241}Am + ^{243}Am - ~1.5%, ^{242}Cm + ^{244}Cm - ~0.4% of total for the SNF from PWR. Actinides are the most dangerous HLW constituents from point of view of radiotoxicity and have the longest half-lives; thus, requiring storage for periods of up to 500,000 years.

So, it is expedient to separate them from the HLW that may be vitrified and incorporate these actinides into crystalline matrices (nuclear waste forms) or fabricate them into solid targets for transmutation in nuclear reactors or accelerators. There are a variety of processes for processing and partitioning the actinides - TRUEX (USA, Japan, Russia), DIAMEX (USA, Japan, EEC), TRPO (PRC), SANEX (USA, EEC, PRC), are under development [6]. The basic process in these technologies is extraction (or precipitation) of actinides from HLW solutions using special reagents. These methods provide for the separation of a high-actinide fraction or joint extraction of actinides, rare earths, and zirconium. The proportion of elemental concentrations in typical fractions is (in wt.%): actinides – 10-15, rare earths – 60-65, zirconium – 20-25 [7].

Actinides include U, Np, Pu, Am and traces of Cm. Among the lanthanides Nd, Ce, La, and Pr are the major constituents.
Since 1995, the disposition of "excess" plutonium from dismantled nuclear weapons has been under consideration. To date about 1,800 metric tons of plutonium have been created around the world [8]. Approximately 300 MT are held in weapons programs, 200 MT have been separated from commercially generated SNF, mostly in the United Kingdom and France and are destined for fabrication as a mixed-oxide fuel of Pu and U, and over 1,300 MT remain in spent nuclear fuel stored at nuclear power plants in 36 countries. Approximately 70 to 80 MT of new plutonium, generally left in the SNF, is added to the global inventory each year. In addition to Pu and U, minor actinides - ^{237}Np, ^{241}Am + ^{243}Am, and ^{244}Cm are generated in reactors, and global production rates are 3.4, 2.7, and 0.35 MT per year, respectively. Up to recent time the preferred strategy was the immobilization of the actinides in chemically durable and radiation resistant crystalline matrices. Since 2003, greater attention is being given to the conversion of excess plutonium into a MOX fuel, to be burned in nuclear reactors. The conversion process, however, will generate actinide (Am/Cm)-bearing waste. There are some other types of actinide-containing wastes, for example actinide-containing electrorefiner salts from the pyrochemical reprocessing of SNF [9,10].

3. Major requirements for actinide waste forms

Waste forms for long-lived radionuclides must satisfy the following requirements:
High chemical durability;
High radiation resistance;
Long-term stability;
Maximum waste volume reduction factor;
Strong mechanical integrity;
Appropriate thermal conductivity (for HLW forms);
Appropriate viscosity and electric resistivity (for materials produced by electric melting);
Homogeneous distribution of radionuclides (especially if fissile materials are present);
Compatibility with geological environment;
Simple, reliable and safe production technology;
Maximum security in order to prevent diversion fissile material, particularly Pu.

No single waste form satisfies completely all of these requirements. However, the key requirements are a high isomorphic capacity of host phase with respect to actinide (with neutron absorbers as necessary), high chemical durability -

especially at elevated temperatures, and high radiation resistance (in particular to alpha-decay from the actinides). A number of waste form ceramics can meet these criteria.

4. Determination of durability and radiation resistance of HLW forms

Chemical durability. There are approximately ten procedures used to test chemical durability, and each has numerous variations. They are generally of two types: *i*.) static (without or with limited replacement of the leachant) and *ii*.) dynamic (with continuous circulation or regular replacement of the leachant). The tests developed in Materials Characterization Center at Pacific Northwest National Laboratory [11,12] are the most often used, especially MCC-1 test. In this test the sample is placed into a Teflon container. The surface area to solution volume (SA/V) ratio is held constant at 10 m^{-1}. Three reference temperatures (40, 70, and 90 ^{0}C) and leachants (deionized water, silicate / carbonate and brine solutions) for a variety of test periods (for example 3, 7 or 28 days) are recommended. Site-specific leachants or actual samples of underground repository water may be used. The MCC-2 static high-temperature test is very similar to MCC-1, but leaching is performed at higher temperatures – 110, 150, and 190 ^{0}C in steel capsules with a removable thick-walled Teflon liner. MCC-3 solubility test differs from MCC-1 in leaching of powdered (particle sizes of 149-175 μm and <45 μm) rather than monolithic sample at a ratio of leachant volume to specimen mass of 10 ± 0.1 mL/g. The MCC-4 low-flowrate and single pass flow through (SPFT) dynamic tests are performed at three reference temperatures (40, 70 and 90 ^{0}C) and flow rates (0.1, 0.01 and 0.001 mL/min) using the same leachants as in the MCC-1 test. In the Product Consistency Test (PCT) powder (-100 – +200 mesh or 75-150 μm) in amount of 10 g is immersed in 100 mL distilled water and heated in a sealed vessel for 7 days following by measurement of pH and elemental concentrations in the leachate [13]. The normalized elemental leach rate in the tests is calculated as:

$$NL_i = (C_i - C_o) / [f_i (S/V) t], \quad (1)$$

where C_i-C_o is a difference between concentration of the element in solution after and before the test, g/m^3; f_i is a mass fraction of the element in the specimen; S is a surface area, m^2; V is volume of solution, m^3; and t is leaching time, days. For the radioactive specimens leach rate is calculated as:

$$R_i = a_i / (A_i S t_n), \quad (2)$$

where a_i is activity of the radionuclide in solution, Bq; A_i is activity of the radionuclide in sample, Bq/g; S is surface area, m^2; t is leaching time, days.

Radiation response. The structure and chemical composition of waste form will be changed in time due to radioactive decay. In order to study the effect of radiation on properties of waste forms three procedures are used [14]. The first

one is based on a study of (U,Th)-bearing minerals – natural analogues of actinide waste forms. In the second method, synthetic samples are doped with short-lived actinide isotopes, normally ^{238}Pu or ^{244}Cm with half-lives of 87.8 years and 18.1 years, respectively. The third method is irradiation of the specimen with neutrons or charged particles (ions, protons or electrons).

The first method is used for the waste forms for which there are radioactive (U,Th)-bearing minerals (e.g., pyrochlore, zirconolite, monazite, zircon) that are structurally and chemically very similar to the waste form of interest [14-18 and so on]. Also, we can still learn a great deal from minerals that do not contain actinides, e.g. baddelyite and tazheranite for zirconia, natural garnets and murataites and so on. Data resulting from actinide-doping experiments is the most useful, as this an accelerated study of the phenomenon of interest; however, such experiments are difficult because of the radioactivity and require special facilities that often to do have the full range of necessary analytical techniques available. Irradiation with heavy charged particles (Cs^+, Pb^+, Au^+) or noble gas ions (He^{2+}, Ne^+, Ar^+, Kr^+, Xe^+) does not have the disadvantages of the previous two techniques, but the sample geometry (a higher surface area to volume ratio) and the dose rate are very different from that experienced by the actual waste form over extended periods. The ion beam technique can be used to simulates the effects of both alpha particles and nuclear recoil in a wide variety of solids under controlled temperature conditions. The irradiated specimen is non-radioactive and high irradiation doses are accumulated in a short time (some tens of minutes). Structural damage may be observed during irradiation (in-situ) using transmission electron microscopy and radiation effects may be observed simultaneously in all the phases compose a specimen in a single run. To compare the doses resulting from different types of radiation equivalent values in displacements per atom (dpa) units may be calculated. To convert the α-dose per unit mass to dpa:

$$Dose\ (dpa) = N_d \times (D \times M) / (N_f \times N_A), \quad (3)$$

where N_d is average number of atomic displacements per single α-decay event; D = accumulated α-dose; M = molar mass of the compound; N_f = number of atoms in the compound; and N_A = Avogadro's number. The value of N_d is assumed to be 1500. Special computer codes, TRIM and SRIM, have been developed to estimate N_d and to recalculate irradiation doses from heavy ions to dpa values [19,20]. Heavy ion irradiation produces radiation damage at a dose rate many orders of magnitude higher than that, which will be experienced by the actual waste form. To prove that data on ion irradiation may be applied to evaluation of radiation damage in waste forms a comparative study of radiation effects in natural (U,Th)-bearing zircons, in synthetic ^{238}Pu-doped phase, and heavy-ion irradiated zircons has been completed [1,14]. Values of critical amorphization doses due to ion-irradiation and alpha decay in synthetic phases

were found to be similar. Thus the ion-irradiation method was recognized to be quite correct to study radiation effects in the actinide host phases. The same results were obtained at comparison of radiation damages in Cm-doped Gd-titanate pyrochlore and ion irradiated pyrochlore [21]. There is also a large literature on the use of natural glasses as analogues for vitreous HLW [22-24, and so on].

Additional requirements to high level and actinide waste forms are due to transportation to repository and long-term storage. From this point of view such properties as density, porosity, thermal and temperature conductivity, tensile, flexural and compressive strength, Young's and bulk modules, and microhardness are measured [24]. For the waste forms whose production via melting is suggested some properties of their melts (viscosity, electric resistivity, surface tension) are also important.

5. Types and design of the HLW and actinide waste forms

Research of waste forms was being carried out since the middle of 1950s when problem of safe disposal of HLW was first concerned a serious issue. There are four major types of waste forms: vitreous (glassy), glass-crystalline, crystalline (ceramic), and composite [24]. Glass-type materials have been suggested as suitable for HLW as well as for high-actinide waste streams [25] due to the capability of their random network to accommodate ions with variable charges and radii. Other advantages of glass waste forms include: demonstrated production technology with high-levels of radioactivity (transferred from electric melting of industrial glasses) and an acceptable level of chemical durability. In the United States, HLW have been vitrified at West Valley, New York and Savannah River Site in South Carolina. A vitrification plant is under construction at Hanford, Washington.

Crystalline waste forms utilize the waste stream composition (+ additives) to synthesize phases that either incorporate the radionuclides into the crystalline structure on at the atomic scale or to encapsulate radioactive phases into an inert matrix, such as TiO_2. Although ceramic waste forms have been under development since the early 1970s, there was a significant increase in the interest in using ceramic waste forms with the development of the Ti-based, multiphase assemblage, Synroc [24,26,27]. Because Synroc was developed as an alternative to borosilicate glass for HLW, its phase composition was tailored to ensure the incorporation of all of the HLW constituents among crystalline phases (e.g., zirconolite, hollandite, perovskite, alloy). This crystal-chemical of designing the waste form has been applied to the design of actinide-bearing waste [8,28,29].

Glass-ceramics combine the properties of vitreous and ceramic waste forms. The content of crystalline phases may be varied from ~20 to 90 vol.%. These

phases may selectively incorporate certain elements (e.g., actinides), while vitreous matrix serves as a second protective barrier. An attractive aspect of glass-ceramics is that they may be produced using conventional vitrification technologies.

Composite materials are mechanical dispersions of radioactive solids, for instance crystalline or vitreous radioactive phases in metal matrix [24], glass-encapsulated Ca-phosphate based ceramics [30]; glass-bonded sodalite [31,32]; glass-ceramics for plutonium waste immobilization [33] and so on.

Actinides are the most troublesome and hazardous HLW constituents due to long half-lives and toxicity. Most of actinides have multiple oxidation states: U, Pu – III, IV, V, VI; Np – IV, V; Am, Cm – III, IV. Th exists in the tetravalent state only. At high temperature (1200-1500 ^{o}C) corresponding to conditions of the actinide waste forms fabrication tri- and tetravalent actinides states are the most typical [34]. In these forms they are close to $REE^{3+/4+}$, Zr^{4+}, and Ca^{2+} in their properties and are able to incorporate actinides into these phases. The possible exception is uranium for which U^{6+} and U^{5+} ions are present in vitreous waste forms [35,36].

Many types of matrices for the immobilization of HLW are under consideration now [27,37-40]. There are comprehensive reviews on their properties [7,8,24,41-43] and numerous papers in journals and conference proceedings. Analysis of these data and the latest authors' results are the basis for writing of this chapter.

6. Production of the HLW and actinide waste forms

Vitrification technology for production of waste forms is the most developed and is only presently utilized at an industrial scale. Currently actual HLW from SNF reprocessing is being vitrified with production of borosilicate glass in France and UK using an inductively-heated (200-300 kHz) metallic (Inconel-690) melter [44,45]. Replacement of the induction-heated metallic melter by a cold-crucible melter is being considered [46]. In the USA and Russia Joule-heated ceramic melters are implemented for HLW vitrification in borosilicate or phosphate [24,47-50] glasses. By the end of 2000 the total amount of vitrified radioactive waste in the world was about 10 000 MT [43].

Ceramic technologies have not yet been implemented on an industrial scale. Lab-scale samples are produced by hot-pressing, sintering or melting technologies. The most widely applicable method is cold pressing and sintering (CPS). Mixtures of milled or especially prepared (by co-precipitation from solutions, sol-gel synthesis, spray calcinations, mechanical activation) powders are compacted in pellets under a pressure of 10-300 MPa, kept at sintering temperature (1000-1500 ^{0}C) for 3-50 hours, and cooled to room temperature by specified regime [24,27,42]. This method was suggested as a basis for

development of excess weapons Pu immobilization technology at the Lawrence Livermore National Laboratory, USA [51]. This process involves mixing of Pu oxide and a neutron absorber (Gd_2O_3 or HfO_2) with additives (TiO_2, ZrO_2, CaO, Al_2O_3) and cold-pressing of the powder at 14-21 MPa in 300 g pucks followed by heat treatment and a 4-h exposure to 1300 ºC, and cooling for 14 h in a turned-off furnace [52]. The final product (259 g "pucks", diameter = 6.9 cm, thickness = 1.6 cm) has a density of 4.46 g/cm^3 (95% of theoretical density).

An alternative route for ceramic production is hot uniaxial or isostatic pressing of precursors [27]. The demonstration plant for Synroc fabrication based on hot uniaxial pressing in bellows containers was designed at the Australian Nuclear Science and Technology Organization (ANSTO). Synroc powder is heated to 1150-1200 ºC and pressed at 14-21 MPa into "pancakes", which can be stacked on top of one another in the disposal canister. To improve product quality, a special precursor is prepared using wet milling or sol-gel techniques.

The newest method suggested for ceramic waste forms production is the inductive cold crucible melting, ICCM [53,54]. The cold crucible is a vessel fabricated from water-cooled Cu or stainless steel pipes, energized from a high frequency generator operated within the range of ~200 kHz to ~13 MHz. The melt is heated by an electromagnetic field penetrating through the gaps between the crucible pipes. A special feature of the cold crucible is formation of an intermediate layer ("skull") between the melt and the cold-crucible pipes. This protects the cold-crucible walls from corrosion due to interaction with the melt and provides the following advantages relative to other melters: longer lifetime; higher achievable process temperature; no contact between melt, refractories and electrodes; smaller overall dimensions; and higher specific productivity because of the active hydrodynamic regime. A number of polyphase ceramics based on zirconolite, pyrochlore, murataite, as well as glass-ceramics have been produced by this method using laboratory- and bench-scale facilities.

Novel ceramic production method, developed mainly in Russia, is the self-sustaining synthesis (SSS). This process is based on redox reactions in oxide-metal mixtures, where the oxidizer is the oxide of a multivalent element in its highest oxidation state (MoO_3, WO_3, Fe_2O_3), peroxide (CaO_2) or nitrate, and the metallic reducing agent (Ti, Zr, Al). Inert components used to produce the ceramic matrix are Ca, Ti, Zr, or calcine. An exothermic reaction is initiated in a local zone of batch mixture and then, the burning process is self-sustained up to formation of ceramic or glass-ceramic. The SSS procedure was applied to production of zirconolite- and pyrochlore-based ceramics [55,56].

However, all the ceramic technologies were tested on lab- or bench-scale basis in inactive variants and their suitability to actual HLW and actinide waste processing has not yet been demonstrated.

7. Vitreous actinide waste forms

First glass-based matrices for immobilization of the alpha-contaminated wastes were developed in the 1970s [57,58]. Solubility of the actinides in borosilicate glasses was limited and decreases with increasing atomic number and decreasing ionic radius at the same valence [34]. Solubilities of ThO_2, NpO_2, Np_2O_5, and PuO_2 in a sodium trisilicate glass are (in wt.%) ~18, ~12, ~29, and ~8 wt.%, respectively [34]. Maximum PuO_2 and AmO_2 concentrations in complex borosilicate glasses were found to be about 2 wt.% [59]. Due to low PuO_2 and AmO_2 solubility in conventional borosilicate glasses special compositions of the glasses for Pu/Am-bearing waste were designed. The alkali-tin-silicate, ATS [25,60] and lanthanide-borosilicate, LaBS [61,62] are said to dissolve up to 7-11 wt.% PuO_2 without segregation of PuO_2 (Table II). Actually, they did not carefully look for possible segregation PuO_2 in the glass. Higher Pu solubility may be due to modification of the glass network caused by the incorporation of larger-sized lanthanide cations. The melting temperature of the ATS glass is the same as of conventional borosilicate waste glasses (~1100 ^{0}C); whereas, the melting point for the LaBS glass is higher (~1400 ^{0}C). For waste streams with a high Pu-content, a glass produced from mixture of basalt and calcium tetraborate has been proposed [63]. This glass may contain of 5 to 6 wt.% PuO_2. The LaBS-type glasses were developed for immobilization of the (Am,Cm)-containing Savannah River Plant waste. They are obtained by melting a 25SrABS frit (33.7 wt.% SiO_2, 25 wt.% La_2O_3, 24.9 wt.% Al_2O_3, 13.5 wt.% B_2O_3, 2.9 wt.% SrO) and lanthanide and actinide oxides in amount of 20 to 50 wt.%. Liquidus temperatures of these glasses range between 1153 ^{0}C and 1405 ^{0}C, and the phases segregated in them are Al_2O_3 (at Ln_2O_3 content less than 43 wt.%), Al- and REE-silicates [64].

LaBS glasses are durable in water solutions, as compared with conventional borosilicate glasses [40]. A study of interaction between the LaBS glass and water has shown that this glass is by 50 times more durable than borosilicate glass [65]. REE-Pu silicates were found on the hydrothermally altered glass surface [40,66]. Incorporation of Pu into these phases may reduce its mobility, although these alteration products remain a possible source of colloid particles that may be transported in ground water. Nevertheless, the best borosilicate LaBS glasses have higher leach rates than titanate ceramics by a factor of several hundred [40]. Glasses may also devitrify with time depending on the thermal history. Because of these concerns for the long-term chemical durability of glass compositions, there have been active programs to develop durable, crystalline waste forms.

Table II. Chemical composition (wt.%) of glasses for Pu immobilization.

Oxides	ATS [25]	LaBS [40]	LaBS [61]	LaBS [62]
SiO_2	41.4	24.3	34.6	17.4
B_2O_3	12.0	9.7	5.1	9.9
Al_2O_3	2.3	17.9	9.0	17.8
ZrO_2	5.3	5.5 (HfO_2)	0.1	0.8
La_2O_3	-	6.8	9.3	$\Sigma Ln_2O_3 = 30.0$
Ce_2O_3	-	-	-	
Nd_2O_3	-	6.9	-	
Sm_2O_3	-	-	18.4	
Gd_2O_3	3.2	10.8	-	
SrO	-	2.1	-	3.6
AnO_2	11.4 (Pu)	10.0 (Pu)	6.9 (Pu)	20.0 (Th)
PbO	-	-	13.0	-
BaO	-	-	3.8	-
Li_2O	4.0	-	-	-
Na_2O	9.2	-	-	-
K_2O	5.2	-	-	-
Cs_2O	0.7	-	-	-
TiO_2	2.0	-	-	-
SnO_2	2.5	-	-	-
UO_3	-	3.0	-	-
Others	-	3.0	-	-
Total	99.2	100.0	100.2	99.5

8. Crystalline actinide waste forms

During the past ten years, there has been considerable research devoted to the development of crystalline waste forms for actinide immobilization [7,8,24,27, 28,39,40,67,68,41-43,69]. Many of the phases are based on studies of minerals that contain Th and U, such as pyrochlore [16-18], zirconolite [70,71], zircon [1,72], monazite [73], britholite [74]. Based on their degrees of alteration, most of the minerals are considered to have an acceptable chemical durability. In addition, closely related mineral structures, such as murataite and garnet, which do not contain U or Th have been synthesized with actinides [29,75,76].

Multiphase ceramics. Ceramic matrices were initially designed for the immobilization of non-partitioned HLW from SNF reprocessing and considered

as an alternative to borosilicate glass. The most well-known among them are tailored ceramics and Synroc [24,26,77]. Due to the low actinide content in the HLW, most of the attention was focused on the incorporation of FPs, CPs, and some processing contaminants (Na, S). Several varieties of Synroc-type ceramics were developed for immobilization of various HLW streams. An early version, Synroc-A, contained hollandite, zirconolite, perovskite, and aluminosilicate phases: leucite, kalsilite, and Ba-feldspar [26]. Later, in order to improve the retention of cesium, the silicate phases were excluded and a basic formulation, Synroc-B, consisted only of titanates. Synroc-C (Synroc-B + 20 wt.% HLW calcine) was investigated in more detail and is a titanate ceramic composed of mainly hollandite (~30 wt.%), zirconolite (~30 wt.%), perovskite (~20 wt.%), minor rutile, Magneli phases (TiO_{2-x}), Ca-Al-titanates, metallic alloy and phosphate (~5 wt.%). Hollandite, $Ba_x(Al,Ti)_{2x}Ti_{8-2x}O_{16}$, is the host phase for Cs and CPs (iron group elements), zirconolite is the host phase for actinides, REEs, and Zr, whilst perovskite accommodates Sr, trivalent REEs and actinides. The metallic alloy is composed of Tc, Mo, Ru, Rh, Pd, S, Se. Traces of phosphates and sulfates enter a phosphate phase. Among the Synroc formulations pyrochlore-rich Synroc-F developed for conditioning and disposal of SNF without reprocessing [27] and Synroc-FA suggested for immobilization of liquid HLW from reprocessing of SNF of heavy water CANDU reactor [78] are of the greatest interest. These varieties are composed of major pyrochlore $CaUTi_2O_7$ (up to 90%) and minor hollandite and rutile, as well as uraninite and perovskite (Synroc-FA).

All Synroc varieties demonstrate high leach resistance at elevated temperatures with respect to distilled water and brines [24]. Leach rates of ^{239}Pu and ^{241}Am from Synroc-C ceramics (MCC-1 test) doped with (wt.%) 1.14-1.3% ^{237}Np; 0,62-0.76% ^{239}Pu, and 0,005-0.007% ^{241}Am were found to be 5×10^{-6} – 3×10^{-5} g/($m^2\times$day) [79-82]. The leach rate for ^{237}Np was higher by order of magnitude from the ceramic prepared under reducing and by two orders of magnitude from the ceramic prepared under oxidizing conditions.

Based on the leaching data [40,69,83] as well as data on radiation resistance of fast neutron irradiated [84-85] and actinide-doped Synrocs [86-88], as well as individual synthetic phases and their natural analogues study [14-18,89-91] zirconolite- and pyrochlore-based ceramics have been proposed for immobilization of excess plutonium and the other actinides. Moreover, additional phases, which were not part of the Synroc formulation, have been considered because of their chemical durability and radiation resistance (e.g., murataite, zircon, garnet, monazite, britholite). Of particular interest are the zirconate pyrochlores, many of which are extremely radiation resistant [8,92].

Zirconolite-based ceramics. Zirconolite, ideally $CaZrTi_2O_7$, is a major actinide host phase in the Synroc-type ceramics. Study of natural and synthetic samples

have deomonstrated its high isomorphic capacity with respect to actinides and REEs. Zirconolite solid solution may incorporate up to (in wt.%) 27% UO_2, 24% PuO_2 or NpO_2, 20% ThO_2, 29% REE_2O_3 (mainly light and middle – Nd_2O_3, Sm_2O_3), 14% Nb_2O_5, 7% Al_2O_3, 5% MnO, 4% FeO, 5% MgO, 1% SrO, and Na_2O [93-97]. Depending on their oxidation states, actinides and REEs enter either the Zr-sites (Ce^{4+}, U^{4+}, Np^{4+}, Pu^{4+}) or the Ca-sites (Np^{4+}, $Pu^{3+/4+}$, REE^{3+}). keeping order to maintain charge neutrality, charge compensating substitutions ($Me^{2+/3+}$) are required. The capability of REE^{3+} to substitute for Ca^{2+} with simultaneous replacement of Ti^{4+} ions by Fe^{3+}or Al^{3+} increases with decrease of the ionic radius of the REE. For the middle and heavy REEs Ca-free zirconolites $REEZrTiAlO_7$ are known [98,99]. Ca-free zirconolites, $An^{4+}ZrTiMe^{2+}O_7$, have not yet been synthesized. Incorporation of tetravalent actinides into the Zr-site in the amount of 0.2-0.3 atoms per formula units (apfu) transforms the zirconolite structure to the pyrochlore structure [93,96,100,101]. Investigation of isomorphic exchanges with actinides and REEs in zirconolites has shown that the fraction of Ce^{4+} and Pu^{4+} reduces from 70-100% when the synthesis is in air to ~0% in a reducing or inert atmosphere (H_2/N_2, Ar). Np is different from Ce and Pu in that Np^{4+} is always predominant [68,102,103].

Leach rates (MCC-1 and MCC-2 procedures) of major waste elements, in g/(m^2×day), were found to be 10^{-1} - 10^{-2} for Ca, 10^{-2} - 10^{-3} for Ba, 10^{-3} - 10^{-4} for Nd, 10^{-4} - 10^{-5} for U, ~10^{-2} for Al, 10^{-6} for Ti, 10^{-7} for Zr [68] and ~10^{-4}-10^{-5} for Pu [104-105]. Zirconolite is chemically the most durable among all of the Synroc phases [106,107]. Interaction with water at 150 ^{0}C forms titanium oxides and hydroxides (anatase, brookite) on the surface of hollandite and perovskite grains in 1-7 days; whereas, the surfaces of the zirconolite grains remain unaltered. Zirconolite is stable in alkali and acid solutions at temperatures of up to 250 ^{0}C and pressures of 50 MPa, which correspond to disposal conditions in deep boreholes [108]. Alteration becomes substantial in acid solutions [109], as well as at temperatures higher 250 ^{0}C [110].

The effect of ^{244}Cm decay on stability of the zirconolite has been studied [111]. A dose of 2×10^{18} α-events/g produces isolated amorphous domains the retain the monoclinic structure. The sample became amorphous at a dose of 5x10^{18} α-events/g or 0.5 dpa. For the natural zirconolites critical amorphization doses are of 1 to 6 dpa [15,17]. The difference in dose for amorphization between the actinide-doping experiment results and observations of natural minerals are due the thermal recovery of the structure of minerals over geological periods [17,71]. Zirconolite-based waste forms may be produced through melting-crystallization or by solid state sintering. Ceramics produced by melting (ICCM) have by 1-2 orders of magnitude larger grain sizes, as compared with samples fabricated by sintering route (Figure 1).

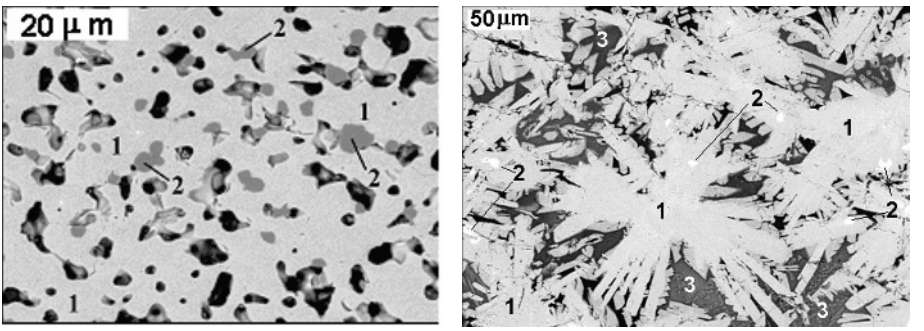

Figure 1. SEM-images of the ceramics produced by CPS at 1500 ^{0}C, left: 1 – zirconolite, 2 – perovskite, and melting in the ICCM, right: 1 – zirconolite, 2 – (Zr, Gd) oxide, 3 – glass + rutile.

Pyrochlore-based ceramics. Pyrochlore, $A_2B_2O_{7-x}$, (*Fd3m*, Z = 8) has a fluorite-derived structure for which the unit cell edge has doubled due to cation ordering. One-eighth of the oxygens has been removed, and the anion vacancies are ordered. The missing anion causes the original cubic coordination on the B-site to an octahedral coordination. Oxygen anions are positioned at the vertices of the octahedra and occupy six vertices of cubic coordination polyhedron (A-site). Two other vertices are occupied with "X" anions. $(A^{3+})_2(B^{4+})_2O_7$ compounds have the pyrochlore structure if the R_A:R_B ratio is between 1.46 and 1.80 (R_A and R_B are ionic radii in the A and B sites) [112]. This constraint determines the range of possible pyrochlore compositions that can be considered as appropriate actinide hosts. There are more than 500 compositions with the pyrochlore structure, a number of which contain actinides [8,113,114]. Different formulations have been designed for immobilization of actinides, including Synroc F and FA varieties, and a pyrochlore-rich ceramic for excess weapons plutonium [27,40,51,52]. The latter contains about 40 wt.% of oxides of actinides (Pu+U) and neutron absorbers (Gd, Hf) which provide for control of criticality, as they have high cross-sections for neutrons. Numerous samples doped with surrogates (Ce, U, Th) and actual Pu have been prepared by the CPS method. The Ce-doped sample is composed of major pyrochlore (84-90 vol.%) and minor perovskite and rutile [83]. The Pu-bearing ceramic with composition (wt.%): 9.9 – 10.0 CaO, 35.8 – 36 TiO_2, 9.6 – 10.6 HfO_2, 23.7 UO_2, 8.0 Gd_2O_3, and 11.9 PuO_2 [40,51,52] consists of major pyrochlore, minor brannerite $(U,Pu)Ti_2O_6$, rutile, zirconolite, and rare U-Pu-dioxide grains (Table III). Pu is predominantly tetravalent whilst up to 30% of Ce in the ceramic is in trivalent state resulting in the formation of perovskite [83,115,116].

Table III. Compositions (wt.%) and formula units (fu) of phases in the Pu-bearing ceramic.

Oxides/Ions	Pyrochlore		Zirconolite		Brannerite		Rutile	
	wt.%	fu	wt.%	fu	Wt.%	fu	wt.%	fu
CaO / Ca^{2+}	10.5	0.91	8.9	0.73	1.0	0.07	-	-
UO_2 / U^{4+}	24.3	0.43	7.6	0.13	35.4	0.55	2.9	0.01
PuO_2 / Pu^{4+}	13.3	0.24	6.7	0.11	14.1	0.22	-	-
Gd_2O_3 / Gd^{3+}	8.2	0.22	5.7	0.15	4.9	0.11	-	-
HfO_2 / Hf^{4+}	11.6	0.27	37.7	0.83	7.0	0.14	18.9	0.08
TiO_2 / Ti^{4+}	31.7	1.91	31.4	1.82	37.0	1.94	77.8	0.90
Al_2O_3 / Al^{3+}	0.4	0.04	2.0	0.18	0.6	0.05	0.4	0.01

Corrosion of the Pu-doped pyrochlore-based ceramics is by incongruent dissolution and segregation of secondary phases [40]. Leach rates in 1-year PCT-B tests were found to be (in g/(m^2×day) Ca – 10^{-2}, Gd – 10^{-3}, Pu – 10^{-4}, Zr - <10^{-5}. The leach rate of Pu is reduced by one order of magnitude – from 10^{-4} g/(m^2 day) in short tests (1 to 7 days) to 10^{-5} g/(m^2×day) after 112-324 days of interaction with water [105]. Introduction of 8 to 15 wt.% of oxides of typical contaminants (F, Cl, Na, Mg, K, Na, Si, Al, Ga, Mo, W, etc.) yielded extra glass, perovskite, and Ca-Al-Ti phase instead of brannerite [117]. This does not affect or even improve the chemical durability with respect to actinides.

Melted (U,Pu)-bearing ceramics are composed of major pyrochlore and minor brannerite and rutile. Their grain size is from 20 to 200 microns which is one or two orders of magnitude larger than in ceramics produced by sintering. Leach rates (7-day MCC-3 test at 90 ^{0}C) of Ti, Zr, U, and Pu were found to be (2 - 6)×10^{-5} g/(m^2×day) [118,119].

Fluorite and pyrochlore structure zirconates. Zirconia-based systems with oxides of lanthanides and tri- and tetravalent actinides may form fluorite-structure types (*Fm3m*) of (REE,An)-stabilized zirconia, $(Zr,An^{3+/4+},REE)O_{2-x}$, or pyrochlore structure-types (REE,An)-zirconates, $(An^{3+},REE)_2Zr_2O_{7-x}$, depending on chemical composition and synthesis conditions [112,120,121]. The Zr-based phases have excellent chemical and radiation stability; hence, they are particularly promising matrices for the immobilization of long-lived actinide wastes, such as excess weapons plutonium and Am/Cm residues [8, 122-126]. As an example, pyrochlore in series $Gd_2Ti_{2-x}Zr_xO_7$ with $x \geq 1.8$ could not amorphized, even at 25 K at doses of up to 5 displacements per atom (dpa). For the fluorite structure-types, radiation-induced amorphization cannot be achieved under ion-irradiation at room temperature, even at doses corresponding to 200 dpa, and at 20 K to a dose of 25 dpa. Irradiation with I^+ and Sr^+ up to 300 dpa produced defect clusters in Y-stabilized zirconia, but did not cause

amorphization. Amorphization was achieved after irradiation with Cs^+ at room temperature at dose of 1×10^{21} ions/m^2, or 330 dpa [127].

In the series $Gd_2Ti_{2-x}Zr_xO_7$, the minimum Gd-leach rate observed (SPFT test, pH=2, 90 ^{0}C) was 1.33×10^{-4} g/($m^2\times$day) at x = 0.75 [128]. Leach rates of Gd from the end-members with x = 0 and x = 1 were 1.57×10^{-2} and 6.26×10^{-3} g/($m^2\times$day), respectively, for unannealed samples under steady-state leaching conditions. Ion irradiation using 2 MeV Au^{2+} ions to a fluence of 5 ions nm^{-2} did not affect the leach rates for the samples with x = 0.75 and x = 1, but increased the leach rate for gadolinium titanate (x = 0) by ~10 times. The leach rate of Np for cubic oxide $(Zr,Np,Y)O_{2-x}$ containing of 20 to 40 mol.% NpO_2 is lower than 10^{-5} g/($m^2\times$day) (84-day MCC-2 test at 150 ^{0}C in a distilled water), two orders of magnitude lower than from Synroc-C and four orders of magnitude lower than that of a typical borosilicate glass [124].

Zirconate pyrochlores have a low isomorphic capacity with respect tetravalent actinides. However the amount of isomorphic substitution can be increased by coupled substitution of Ca, according to the scheme: $2REE^{3+} = An^{4+} + Ca^{2+}$. Production of single phase ceramic can be attained only for actinide waste streams with rather simple chemical compositions. In the case of a complex waste stream composition, extra phases occur [129]. Finally, zirconate matrices require high temperatures for their synthesis. In order to prepare REE-zirconates from oxide mixtures, sintering at 1500-1600 ^{0}C for about 50 hours is required [130]. Even synthesis from a sol-gel precursor still requires sintering at 1200 ^{0}C for 12 hours, crushing of the pellets, repeated sintering at 1500 ^{0}C for 30 hours, and finally hot pressing at 1600 ^{0}C for 2 hours at 200 MPa did not yield a single phase $Gd_2Zr_2O_7$ ceramic [128]. Significant acceleration of the formation rates of the phases is achieved by use of a mechanically pre-activated oxide mixture [131]. This reduces the sintering time to 3-6 hours at 1500 ^{0}C. Samples with the composition (wt.%) 7.1 La_2O_3, 14.0 Ce_2O_3, 6.8 Pr_6O_{11}, 22.2 Nd_2O_3, 4.1 Sm_2O_3, 2.0 EuO, 0.9 Gd_2O_3, 3.2 UO_2, 39.7 ZrO_2, consistent with the elemental ratio in the REE/actinide fraction of HLW, were composed of the only a pyrochlore phase (Figure 2).

Murataite-based ceramics. Natural murataite is an isometric oxide with an ideal formula: $A_6B_{12}C_4TX_{40-x}$ (A = Y, Na, Ca, Mn; B = Ti, Fe; C = Fe, Ti; T = Zn; X = O, F), $F\bar{4}3m$. The unit cell edge (a = 14.89 Å, Z = 4) is triple that of the fluorite unit cell. The structure contains four cation sites: eight-coordinated $A^{[8]}$, octahedral $B^{[6]}$, trigonal bipyramid $C^{[5]}$, and tetrahedral $T^{[4]}$ [132]. A synthetic murataite-like phase with composition, wt.%: 0.7 Na_2O; 9.3 Al_2O_3; 7.8 CaO; 32.1 TiO_2; 7.8 MnO; 23.4 FeO; 1.0 REE_2O_3; 13.2 ZrO_2 and 3.3 UO_2 was firstly found in Synroc-D developed for immobilization of Savannah River Plant defense waste [133,134].

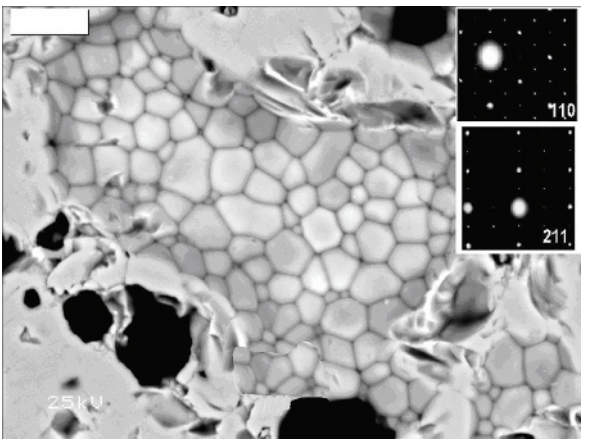

Figure 2. SEM-image of zirconate pyrochlore produced from activated mixture. Black – pores, insets – SAED patterns from the (110)* and (211)* planes of the lattice. Scale bar is 10 microns.

This fluorite-derived structure showed the characteristic tripling of the isometric cell edge, as compared with the fundamental fluorite unit cell. Due to the rather low uranium and REEs content of the murataite, relative to co-existing zirconolite (13.3 wt.% UO_2 and 3.2 wt.% REE_2O_3), murataite was not considered as potential host for actinides and REEs. Later, murataite was found in a Synroc-type ceramic used for the Russian plant "Mayak" waste surrogate [54]. This phase was only ~5 vol.% of the sample, but contained up to 40% of the total uranium in the sample. Uranium concentration in the cores of grains (about 10 wt.%) was higher than in the rim by one order of magnitude. The U-depleted edge of the grains potentially provide an additional barrier to release due to the lower leach rate and reduced damage caused by alpha-decay events at the rim. The zoned distribution of actinides and REEs in the murataite was found to be typical of ceramics produced via the melting route, especially using ICCM. For ceramics produced by the solid state synthesis (CPS) the waste element distributions were more uniform.

Because of these observations, there has been additional study of murataite as a potential actinide waste form. Numerous murataite-based ceramics have been synthesized. Most of the effort was focused on a basic formulation (wt.%): 55 TiO_2, 10 MnO, 10 CaO, 5 Al_2O_3, 5 Fe_2O_3, 5 ZrO_2, 10 REE / actinide oxides. The ceramics were doped with Ce, Pr, Nd, Sm, Eu, Gd, Tb, Dy, Yb, Y, U, Th, Np, and Pu. Actinide waste stream compositions were simulated by adjusting the elemental proportions of REE / actinide fraction of separated liquid HLW. These compositions were produced via melting and sintering routes [18,75]. In all of the ceramics murataite was the predominant phase. Rutile, crichtonite,

perovskite, pyrochlore were present in smaller proportions, typically lower than 15-20 vol.% in their total abundances. Problems with production of single phase murataite ceramic occur because of features of crystal structure and related complex isomorphic exchange mechanisms in the murataite structure. Moreover, the ceramics commonly contain different murataite polytypes with five-, eight-, and three-fold multiples of the fluorite unit cell [18,75,135-137].
Unlike the structure of the natural mineral, where the $T^{[4]}$ sites are occupied by small cations (Zn^{2+}), in the synthetic analogue the $T^{[4]}$ sites are empty and manganese is present rather than zinc. Urusov et al. [138] have suggested that pyrochlore (double multiples of the fluorite cell) and murataite (a triple multiple, M3) are the end-members of a common polysomatic series. The other members of this series consist of pyrochlore (Py) and murataite (M) modules: M+Py+M (murataite-M8), M+Py (murataite-M5), and Py+M+Py (murataite-M7). The pyrochlore formula can be written as $A_2B_2O_{7-x}$ and the M3-murataite formula is $A_2B_6C_2O_{20-x}$.The formulae of the phases with five- (M5), seven- (M7) and eight-fold (M8) multiples of the fluorite unit cell may be represented by $A_5B_8C_2O_{27-x}$, $A_7B_{10}C_2O_{34-x}$, and $A_8B_{14}C_4O_{47-x}$, respectively. Depending on composition of ceramics various members of the series are predominant [75,136]. Actinides and REE contents are reduced according to the sequence: Py > M7 > M5 > M8 > M3 and the content of Al and Fe increases (Table IV).
High actinide, REEs, and CPs contents are typical of the M5 phase, and this makes the M5-muratiate a promising matrix for immobilization of a complex waste stream. Zoned murataite grains are composed of M5 murataite in the core, M8 in intermediate zone, and M3 (murataite itself) at the edge (Figure 3).

Table IV. Composition of the phases in ceramics with 10 wt.% ThO_2 or UO_2.

Oxides	Th-doped					U-doped				
	M5	M8	M3	P	C	M5	M8	M3	C	Pf/I
Al_2O_3	2.7	4.3	7.9	0.6	3.7	1.2	4.1	7.0	3.7	0.5
CaO	11.2	10.9	9.5	21.9	4.2	10.7	11.2	10.9	0.4	0.9
TiO_2	52.2	54.8	55.6	48.6	71.2	45.4	53.7	57.4	68.1	51.9
MnO	8.5	9.2	10.9	1.0	7.4	7.1	8.8	10.6	13.3	26.3
Fe_2O_3	3.0	3.6	7.2	0.6	8.4	2.1	3.5	5.7	16.1	19.7
ZrO_2	9.7	6.5	2.1	(-)	1.3	12.2	7.0	3.1	(-)	(-)
AnO_2	12.6	10.9	5.1	24.1	2.7	21.5	11.3	4.6	(-)	(-)

M5, M8, M3 – phases with five-, eight-, and three-fold fluorite unit cell, P – perovskite, Pf/I – pyrophanite/ilmenite, C – crichtonite, (-) - below detection limit.

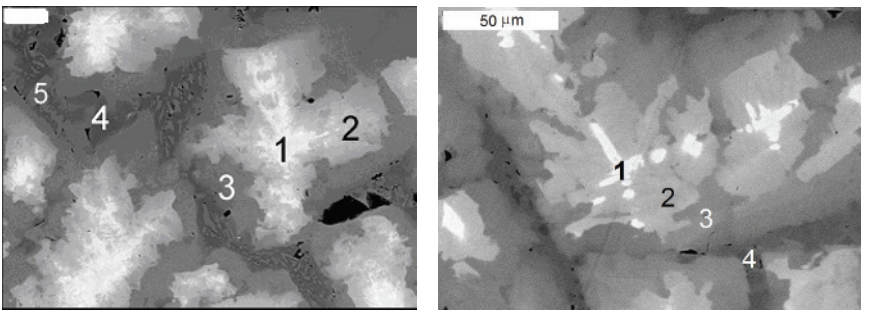

Figure 3. SEM-images of the U- (left) and Pu-doped (right) murataite ceramics. 1 – 3 – murataite-structure phases (1 - M5, 2 - M8, and 3 - M3), 4 – crichtonite, 5 – pyrophanite / ilmenite. Scale bars are 20 (left) and 50 (right) microns.

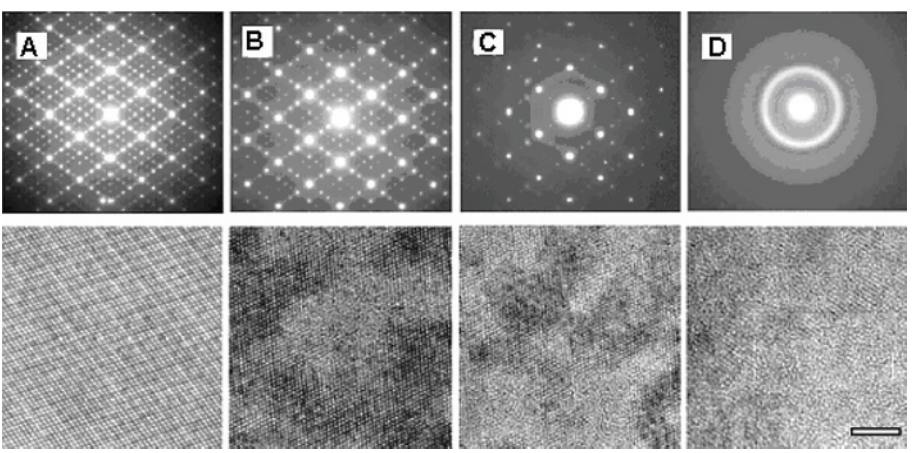

Figure 4. SAED patterns (upper) and HRTEM images (lower) of the M8 phase before (A) and after irradiation with 1 MeV Kr^{2+} at room temperature to doses: (B) 4.38×10^{17} ions/m^2; (C) 9.39×10^{17} ions/m^2; (D) 1.56×10^{18} ions/m^2. Scale bar is equal to 3 nm, data from [140].

Radiation resistance of murataite was studied using 1 MeV Kr^{2+} ions [139,140]. With the increasing of ion dose, the murataite superlattice shows a disordering (Figure 4) until it is completely amorphous. Diffraction spots from the murataite superlattice decrease in intensity relative to the maxima from the fluorite sublattice. With an increase in dose, the superlattice spots disappear. At a dose of $(0.9\text{-}1.0)\times10^{18}$ ions/m^2, the sample has the fluorite structure (Figure 4C). Eventually, the structure amorphized at doses of $(1.75\text{-}1.85)\times10^{18}$ ions/m^2 for the initial M8 and M5 type phases or at about 0.2 dpa.

The same changes in the SAED pattern are apparent at 600 ^{0}C, but at this temperature the critical amorphization dose, D_c, is markedly higher (about 0.8 dpa). This is due to annealing of radiation damage at elevated temperature. At temperatures higher than T_c, thermal annealing dominates over the damage accumulation process, and the sample cannot be amorphized. For the murataite phases examined, T_c ranges between 650 and 750 ^{0}C.

Leach rates of U, Np, and Pu from murataite ceramics (MCC-1 test at 25 ^{0}C) were found to be 10^{-6}-10^{-5} g/(m^2×day). For ceramic with 10 wt.% ^{239}Pu and 0.1 wt.% ^{241}Am, leach rates at 90 ^{0}C were reduced from 10^{-3} g/(m^2×day) after 3-7 days of contact with water to 10^{-4}-10^{-5} g/(m^2×day) after 63 days [141].

Perovskite-based ceramics. Perovskite, nominally $CaTiO_3$ (*Pnma*), has low solubility limits for U^{4+}, Pu^{4+} (Table V), but perovskite-structure phases form solid-solutions with REE-aluminates and ferrites, in particular $GdAlO_3$ [142]. Pu^{3+}, Am^{3+}, and Cm^{3+} substitute for Ca^{2+} by coupled substitution of Al^{3+} for Ti^{4+} in order to maintain charge balance. This finally leads to the end-member composition, $AnAlO_3$, which has a different structure ($PuAlO_3$: *Amm2*, JCPDS 43-1094). Perovskite-type matrices are considered for waste streams that consist of Am and Cm. The trivalent actinides are incorporated into $LnAlO_3$ or $LnFeO_3$ [143]. Leach rates of ^{90}Sr, ^{147}Pm, ^{238}Pu, and ^{241}Am from perovskite at 95 ^{0}C ceramics measured using Soxhlet test are approximately 10^{-4} g/(m^2×day), the leach rate of ^{238}U is higher by about two orders of magnitude [143-145]. Natural perovskites are normally crystalline; no amorphization is evident in minerals with accumulated doses up to 2.6×10^{18} α-decays/g [15]. Significant damage has been observed in perovskite containing ~6 wt% ThO_2 and with an accumulated dose of $\sim1\times10^{19}$ α-decays/g [15,17,146]. Perovskite was amorphized after irradiation with 1.5 MeV Kr^+ ions to a dose of $\sim1.8\times10^{19}$ ions/m^2. The critical dose for amorphization, D_c, at room temperature for perovskite is higher than for zirconolite by a factor of 2-4 [147,148].

Table V. Number of actinide atoms in the formula units of indicated phases [155].

Phase	Ideal formula	U4+	Pu4+	Pu3+	Hf4+	Gd3+
monazite	$REEPO_4$	0.5	0.25	1	< 0.01	1
zircon	$ZrSiO_4$	1	1	0.1	1	<0.1
pyrochlore	$REE_2Ti_2O_7$	1	1	2	0.3	2
zirconolite	$CaZrTi_2O_7$	0.7	0.7	-	1	1.4
sphene	$CaTiSiO_5$	0.02-0.05	0.02	0.05	0.5	0.3
britholite	$Ca_2REE_8(SiO_4)_6O_2$	0.5	0.05	-	< 0.1	8
perovskite	$CaTiO_3$	> 0.1	0.1-0.13	1	1	1

Garnet-structure ferrites. Garnet, ideally $^{VIII}A_3{}^{VI}B_2[TO_4]_3$, is isometric (*Ia*3*d*) with a structure built of TO_4 tetrahedra and BO_6 octahedra linked by shared vertices that form AO_8 dodecahedra. The A-sites accommodate divalent (Ca, Mn, Fe) and trivalent (Y, REE) elements. The B-site may contain various di-, tri- (Fe, Al, Ga, Cr, Mn, In, Sc, Co), tetra- (Zr, Ti, Sn, Ru) and even pentavalent elements (Nb, Ta, Sb). The T-sites are filled with tetravalent (Si, Ge, Sn) but may be also occupied by trivalent (Al, Ga, Fe) and pentavalent (P, V, As) elements. Synthetic garnets form multicomponent solid solutions that provide opportunities for incorporating of HLW elements into the structure [149].
The garnet-based actinide waste forms have no minerals analogues because natural garnets have very low U, Th (<1 wt.%), and REE contents (<3 wt.%). There are REE-Al-Ga garnets capable of incorporating up to 4-6 wt.% UO_2 and PuO_2 [150,151]. From the crystal-chemical perspective, incorporation of tri- and tetravalent actinide elements in the A-site is favored when the B- and T-sites contain large, low-valence cations. The largest of the trivalent ions capable of entering both of these sites simultaneously is Fe^{3+}. Ferrites have the largest dimensions for the FeO_6 octahedra and FeO_4 tetrahedra and the largest AO_8 site. In the garnets $(Ca_2Ce)(ZrFe)Fe_3O_{12}$, $(Ca_2Th)(ZrFe)Fe_3O_{12}$, $(Ca_2Ce)Zr_2Fe_3O_{12}$ Th^{4+} or Ce^{4+} occupy of one-third of the A-sites [152]. The radii of Np^{4+} (0.98 Å) and U^{4+} (1.00 Å) are between those of Th^{4+} (1.05 Å) and Ce^{4+} (0.97 Å), so it is expected that ferrite garnets will possess high isomorphic capacity with respect to all tetravalent actinides. Compositional variations have a strong effect on the isomorphic capacity of the garnet structure for actinides. Partial substitution of Si for Fe (0.6 atom per formula unit, apfu) reduces ThO_2 content from 15 wt.% to 3-6 wt.% [29,76]. Incorporation of 1.7 apfu Al, instead of Fe, reduces the Th solubility in the garnet structure to a lesser extent - from 15 wt.% to 7 wt.%. Excess ThO_2 produces thorianite (Figure 5). Temperature variations between 1200 ^{0}C and 1400 ^{0}C do not affect phase composition of garnet-based ceramics.

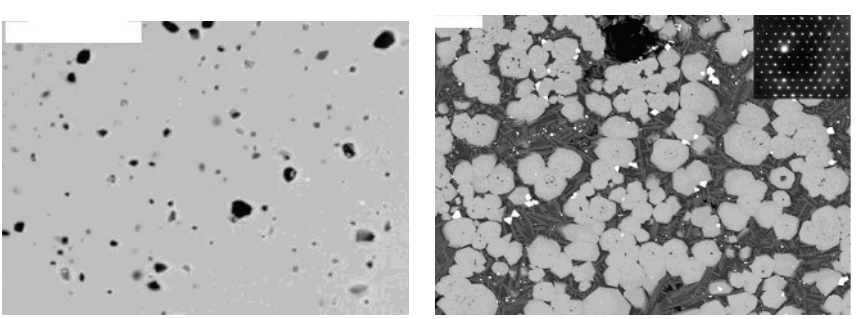

Figure 5. SEM-images of the garnet-based ceramics produced by cold pressing - sintering (left) and melting (right). Gray – garnet, dark-gray – hibonite, white – ThO_2, black – pores. Inset – SAED pattern from the (111)* plane of the garnet lattice. Scale bars are equal to 50 microns.

Corrosion tests (MCC-2, water or 0.01 M HCl at 150 ^{0}C) were performed for ceramics with compositions $Ca_{1.5}GdTh_{0.5}ZrFeFe_3O_{12}$ and $Ca_{2.5}Ce_{0.5}Zr_2Fe_3O_{12}$. The first sample consists of a single phase, the second one contains minor perovskite-structure calcium zirconate. Leach rates in water ranged between 3×10^{-5} g/(m$^2\times$day) for Gd and ~10^{-6} g/(m$^2\times$day) for Ce and Th [153]. In acid solution, the leach rates of Gd and Th increased to ~10^{-3} g/(m$^2\times$day). Cerium is the most leachable element (0.2 g/(m$^2\times$day). The increase in Ce leach rate in the acid solution is most probably due to reduction of Ce^{4+} to Ce^{3+}. Radiation response of the garnet-structure ferrites is comparable to that of titanate pyrochlore and murataite. The D_c value for the ferrite garnet irradiated with heavy ions was found to be 0.2 dpa at 25 ^{0}C [154]. Thus ferrite garnets are able to simultaneously accommodate actinides, REEs, and iron group elements and may be considered as one of the perspective matrices for immobilization of actinide waste streams with complex compositions.

Phosphates. Three major phosphate phases have been as potential actinide host phases: monazite, Th-phosphate-diphosphate, and kosnarite, a Na-Zr-phosphate (NZP). Monazite $LREEPO_4$ (LREE = Ln…Gd) and brabantite $CaTh(PO_4)_2$ or $Ca_{0.5}Th_{0.5}PO_4$ are monoclinic (*P2$_1$/n*), consisting of chains in which each $REEO_9$ polyhedron is linked with five PO_4 tetrahedra. Major coupled substition scheme is $2LREE^{3+} = Ca^{2+} + An^{4+}$. The limits for U^{4+}, Pu^{4+}, Pu^{3+} and Gd^{3+} incorporation in synthetic monazites were found to be 0.5, 0.25, 1 and 1 apfu [155]. Monazite ceramics are produced by sintering at 1250-1400 ^{0}C [156]. The leach rate of U from a monazite ceramic doped with 20 wt.% Savannah River defense waste (28-day MCC-1 test in distilled water at 90 ^{0}C) was found to be ~2×10^{-3} g/(m$^2\times$day), exceeding the chemical durability of B-Si glass by 1000 times [24]. Numerous EPR, Mössbauer and optical absorption investigations have been performed to prove that waste elements occupy specific crystallographic sites in the structure [24]. Am and Cm exist in trivalent form, U and Pu are tetravalent, and Np may be present as Np(III), Np(IV), and Np(V). Lanthanides are trivalent. Therefore, tri- and tetravalent actinides and REEs, as well as divalent Mn and traces of trivalent Fe, enter nine-coordinated sites. Due the isomorphic capacity of the monazite structure is limited, monazite is probably best used as a host phase for Am and Cm waste not contaminated by significant amounts of other waste stream elements. The leach rate of Am (7-day MCC-1 test, water, 90 ^{0}C) was one order of magnitude lower: 2.3×10^{-4} g/(m$^2\times$day) [157]. Monazite exhibits retrograde (decreasing with temperature) solubility from 70 to 300 ^{0}C in acid solutions and from 150 to 300 ^{0}C in neutral solutions [158]. Natural monazites contain of up to 27 wt.% ThO_2+UO_2. Despite the high actinide content and age they have remained crystalline. Amorphization was not observed even at a dose of 1.7×10^{20} α-events/g (14.2 dpa) [73]. $LuPO_4$ doped with 1 wt.% ^{244}Cm was not amorphized after 18 years at a dose of 1.5×10^{19} α-

events/g (1.3 dpa) corresponding to storage of matrix with 1 wt.% ^{239}Pu for 230,000 years [159]. Burakov et al. [160] found that (La,^{238}Pu)PO_4 monazite remained crystalline at dose $1.2x10^{25}$ α-events/m^3 (~0.3 dpa) but $PuPO_4$ phase became amorphous at a dose of $0.4x10^{25}$ α-events/m^3 or 0.12 dpa. Response of the REE orthophosphates with monazite and xenotime structures to accelerated ion bombardment was studied [161]. It was found that $LaPO_4$ is the least susceptible and $LuPO_4$ is the most susceptible phase to radiation damage. Monazite is readily amorphized under ion-irradiation: the D_c and T_c values for natural monazite are 0.15 dpa and 428 K [162]. For synthetic compounds irradiated with 800 keV Kr^{2+} ions, D_c values at 0 K ranged between 0.31 and 0.39 dpa [163]. Monazite cannot be amorphized under irradiation with 800 keV Kr^{2+} ions at T > 175 ^{0}C [164].

Thorium phosphate-diphosphate $Th_4(PO_4)_4P_2O_7$ (TPD, *Pcam*) is an actinide host phase due to its very high chemical durability and radiation stability [165-167]. TPD is synthesized by drying of thorium nitrate and phosphorus acid or ammonium phosphate solution, cold pressing at 300-800 MPa, and sintering of pellets at 1100-1250 ^{0}C for 10-30 hours. Th^{4+} in the TPD structure may be replaced by other tetravalent actinides but its isomorphic capacity is reduced with decreasing cationic radii in the following sequence: $U^{4+} > Np^{4+} > Pu^{4+}$. Solubility limits for these cations are 75 at.% (48 wt.%), 52 at.% (33 wt.%), and 41 at.% (26 wt.%) [165,168,169]. Zr^{4+} does not enter the TPD structure due to large difference in the radii of Th^{4+} and Zr^{4+}. Solubility of trivalent actinides and REEs is limited by ~0.1 mol.%. At higher contents of actinides and REE, two-phase ceramics composed of additional monazite or xenotime phases are produced. A TPD/monazite ceramic has been suggested for incorporation of both tetra- (U^{4+}, Np^{4+}, Pu^{4+}) and trivalent (Pu^{3+}, Am^{3+}, Cm^{3+}) actinides [170].

Irradiation of TPD with γ-rays, α-particles and accelerated ions was performed, as well as actinide-doping experiments (25 wt.% Pu) reached a total dose of $2.6x10^{16}$ α-events/g [165]. The TPD radiation response was similar to that of monazite. Leach rates of REEs and actinides (MCC-3, 25-90 ^{0}C) were found to be 10^{-6}-10^{-8} g/(m^2×day) [165,167]. These values are 2 to 3 orders of magnitude lower than of zirconolite, pyrochlore, and Synroc. Leach rates remain low, ~10^{-5} g/(m^2×day) even in acid solutions 0.1M $HClO_4$. Nevertheless, the presence of engineered barriers in the repository (e.g., a benthonite buffer) leads to decomposition of the TPD ceramic, yielding apatite and thorianite due to instability of the TPD phase in the Ca-bearing alkaline solutions [171].

Sodium-zirconium orthophosphate, $NaZr_2(PO_4)_3$ has a structure that is $R\,\bar{3}c$-D_3^6d (Z=6). The general formula is $M^IM_2^{II}(M^{III}O_4)_3$, where the M^I sites are occupied by mono-, di- and trivalent elements. Octahedrally coordinated M^{II} sites are filled with tri-, tetra-, and pentavalent elements; whereas, tetrahedrally coordinated M^{III} sites are normally occupied by P^{5+} ions, but may contain As^{5+},

Si^{4+} [172]. The NZP ceramics are believed to be capable of accommodating a wide variety of waste elements due to high isomorphic capacity of the kosnarite-type phases with respect to ions of I to V group elements [173]. The NZP structure is capable of accommodating up to 20 wt.% PW-4b simulated calcine [174]. NZP ceramics may be produced at relatively low temperatures (800-1000 ^{0}C). They have high chemical durability [175-176] and radiation resistance [177]. However, it has been shown that minor additives of iron group elements makes the NZP structure unstable, reducing its symmetry to monoclinic (*C2/c*) with formation of the monazite structure [178,179]. The same effect was observed when Na^+ substitutes in the Zr-site [174].

Silicates and titanosilicates. Britholite $(Ca,REE)_{10}(SiO_4)_6O_2$, zircon $ZrSiO_4$, and sphene $CaTiSiO_5$ occur in nature. These minerals contain U and Th and are chemically durable under most geological conditions. For this reason, they are considered as potential actinide host phases. The britholite structure consists of two types (CN=9 and CN=7) of Ca-O and REE-O polyhedra linked by PO_4 or SiO_4 tetrahedra. The ideal formula is $^{IX-VII}A_{10}{}^{IV}B_6O_{24}X_2$ (*P6$_3$/m*, Z=1), «A» = Ca, REE, Th, Al, Fe, Mn, Mg, Na, K; «B» = Si, P, B, F, Al; «X» = O, OH, F [180]. Contents of U^{4+} and Pu^{4+} in phase $Ca_{4-x}(REE,An)_{6+x}(SiO_4)_{6-y}(PO_4)_yO_2$ achieve 0.5 and 0.05 apfu. Solubility limits for Gd^{3+} and Hf^{4+} are estimated to be 8 and <0.1 apfu (Table V). The radiation response of synthetic britholite depends on type of irradiation and temperature [181]. For heavy-ion irradiated (1 MeV Kr^{2+}, 1.5 MeV Xe^+) samples, the D_c values at 25 ^{0}C were found to be 0.2-0.4 dpa and the T_c was determined to be 880-1010 K. Similar values were obtained for ^{244}Cm-doped britholite [14]. The D_c values for naturally-occurred britholites are higher and reach >1 dpa [18].

Zircon, $ZrSiO_4$, is tetragonal (*I4$_1$amd*, *Z*=4). The structure consists of chains of ZrO_8 dodecahedra parallel to the "c" axis and joined by isolated, alternating SiO_4 tetrahedra. Because of the presence of U and Th in natural zircon, as well as its high chemical durability, and the fact that pure actinide end-members may be synthesized, e.g., $PuSiO_4$, several workers have suggested that zircon would be a good actinide waste form [1,14,182]. Specific interest in zircon was enhanced because of its occurrence in the Chernobyl "lavas" as an important actinide host phase where the U-concentration reached 6-12 at.% [183].

The dissolution rate of zircon in water (Soxhlet tests) decreases from 4.1×10^{-4} at 250 ^{0}C to 4.6×10^{-5} g/(m$^2\times$day) at 90 ^{0}C [184]. Synthetic ceramics doped with of 6 to 10 wt.% Pu were produced [185]. Leach rates of Pu (MCC-1, 90 ^{0}C) were found to be 7×10^{-3} (sample with 6 wt.% Pu) and 0.2 g/(m$^2\times$day). In the sample with 10 wt.% Pu, extra PuO_2 was also present. Zircon is amorphized at a dose of ~10^{19} α-events/g or 0.6 dpa [72,186,187] and exhibits significant volume expansion (by 18-20%). This leads to microcracking [188] and an increase of the leach rate. Zircon has a rather low capacity with respect to trivalent actinides

and REEs (Table V). This restricts its possible application for immobilization of the compositionally complex actinide waste streams.
Sphene (or titanite), $CaTiSiO_5$, is monoclinic (*C2/c*). In the natural mineral Ca^{2+} is replaced by Na^{+}, Ce^{3+}, La^{3+}, Y^{3+}; Ti^{4+} is replaced by Fe^{3+}, Al^{3+}, Nb^{5+}, and OH^{-} and F^{-} may substitute for O^{2-} ions. Minor Mn^{2+}, Mg^{2+}, Cr^{3+}, Sn^{4+}, U^{4+}, Th^{4+} may be also present. In the synthetic phases maximum Gd and U contents were found to be 21.5 wt.% and 9.3 wt.% or 0.25 and 0.07 apfu [189]. These are comparable with data [155] where the solubilities of Gd^{3+} and U^{4+} were determined as 0.3 and 0.02-0.05 apfu. Close solubility limits are typical of Pu (Table V). Incorporation of Gd and U into the structure occurs in accordance with substitution schemes: $2Ca^{2+} = Gd^{3+} + Na^{+}$; $Ca^{2+} + Ti^{4+} = Gd^{3+} + Al^{3+}$; $Ca^{2+} + 2Ti^{4+} = U^{4+} + 2Al^{3+}$. High contents of actinides and REEs stabilize titanates and silicate with pyrochlore, perrierite, and britholite structures [24,189].

9. Glass-ceramic actinide waste forms

Compositions of actinide-bearing glasses can be selected such that on annealing actinide-bearing phases are produced. The volume fraction of the actinide-bearing phases range between 10 and 80 vol.%. Heat-treatment of glass is usually completed in two stages: nucleation followed by crystal growth. These materials may be also produced by spontaneous crystallization from a melt during cooling ("mineral-like materials" – [190]).
Zirconolite glass-ceramics. The batch with both simplified [191-193] and close to actual target compositions (wt.%) 40.6-43.2 SiO_2; 12.0-12.7 Al_2O_3; 19.6-20.9 CaO; 12.5-13.3 TiO_2; 8.5-9.0 ZrO_2; 0-6.0 Nd_2O_3; 0.9-1.0 Na_2O [194] and 40.2-49.7 SiO_2; 5.6-11.0 Al_2O_3; 24.3-25.8 CaO; 10.8-17.5 TiO_2; 0-8.2 ZrO_2; 0-4.9 HfO_2; 1.2-1.3 Ln_2O_3 (Ln = Nd, Ce, Eu, Gd, Yb) и 0.9-1.1 Na_2O [195] were melted in a Pt crucibles at 1550-1650 ^{0}C for 10 hours and quenched. The glass produced was heat-treated for 2 hours at 810 ^{0}C in order to create nucleation centers and at 1050-1200 ^{0}C for 2 hours to enhance crystal growth. Zirconolite in the amount of 10 to 20 vol.% was found to be the only crystalline phase. Pu-bearing zirconolite-based glass-ceramics were produced by hot-pressing of calcines at 1220-1320 ^{0}C. Pu partitioning into zirconolite over glass in excess of 100:1 has been achieved. The leach rate of Pu (28 day MCC-1 test) was found to be ~10^{-5} g/(m^2×day) [196].
Sphene-based glass ceramics. These ceramics are composed of titanite as the major crystalline phase (other minor phases may be present) and interstitial Na-Al-Si glass. Importantly, thermodynamic calculations indicate that titanite is stable in the Ca-Na-Cl brines, typically encountered in the Canadian Shield. Furthermore, analyses of natural specimens indicate that the titanite structure is able to accommodate ACTs, REEs, Na, Mn, Sr, Ba in the Ca-site, and Fe and

other transition metals in the Ti-site. Both crystalline and metamict natural titanites are chemically durable, and the interstitial aluminosilicate glass also appears to be chemically durable. Sphene is the only or predominant phase formed by partial devitrification of the glasses with compositions in the range, in mol.%: 4.6-9.5 Na_2O, 3.1-7.1 Al_2O_3, 10.7-20.5 CaO, 10.7-22.1 TiO_2, 49.6-63.9 SiO_2. Optimal content of the HLW elements is 15 wt.%. Glass-ceramics are produced by melting at 1300-1400 ºC, followed by cooling and thermal treatment (annealing) at 950-1050 ºC for 1 hour or more to induce crystallization. The resulting titanite concentrates REEs and corrosion products; whereas, Cs^+ and U^{6+} remain in the vitreous phase. The Sr^{2+} ions are equally partitioned between titanite and the glass. Leach rates of major waste elements (Cs, Sr, U, La) are intermediate between those of borosilicate glass and Synroc. This glass-ceramic demonstrated acceptable radiation stability and good mechanical integrity [24].

Glass-ceramics for defense HLW and excess plutonium immobilization. Glass-ceramic matrices containing of 40 to 70 wt.% HLW oxides, including 15-25 wt.% PuO_2 have been developed [197,198]. A mixture of waste calcine, PuO_2, and glass additives (wt.%): 70.3 SiO_2, 12.8 Na_2O, 6.2 Li_2O, 8.5 B_2O_3, 2.1 CuO and Sm_2O_3 and TiO_2 were melted at 1050-1450 ^{0}C for 4 hours. The temperature was then reduced to 550-700 ^{0}C to crystallize the glass. As a result, zirconia and zirconolite formed, both of which incorporate almost all the Pu. The leach rate of Pu from the glass-ceramic is 1.2×10^{-3} g/($m^2\times$day). Pyrochlore-based glass-ceramics have also been produced by hot-pressing, but data on Pu leach rates are not available [199,200]. Glass-ceramic with a fluorite structure plutonium zirconate as a target phase having Pu leach rate (PCT-A test) at a level of 10^{-5} to 10^{-6} g/($m^2\times$day) has also been developed [197].

The main advantage of glass-ceramic waste forms is the possibility of using melting for their production. One of the most attractive technologies is the ICCM, which may be applied to production of Synroc-glass materials, containing Synroc phases (zirconolite, perovskite) distributed in glass [201,202] and combining properties of both Synroc and glass waste forms.

10. Conclusion

An effective strategy for dealing with HLW is to partition the short-lived fission product elements from the long-lived actinides, creating separate waste streams. Once there are two waste streams, the properties and durability of the waste form can be designed to a level appropriate to the toxicity and time required for isolation from the environment. With such a strategy the fission product elements may be incorporated into a borosilicate glass; the actinides into more durable crystalline ceramics. Although special glass compositions may be

developed for actinide incorporation, their long-term durability is less easily assured, particularly on the time scales required for actinide immobilization and confinement.

Synroc-type titanate ceramics are the most well known and researched among the crystalline ceramic alternatives. Synroc is produced by hot-pressing at 1050-1200 ^{0}C under a pressure of 10-100 MPa in an inert or reducing atmosphere. For actinide wastes (e.g., excess weapons plutonium, actinide/REE fraction of HLW) matrices based on oxides with fluorite-derived structures (fianite, pyrochlore, murataite, zirconolite), aluminoferrite garnets, phosphates (monazite, Th phosphate-diphosphate, kosnarite), and silicates (zircon, britholite, sphene) show considerable promise. The phases with fluorite-derived structure have high isomorphic capacity with respect to actinides and REEs, some compositions are "resistant" to radiation-induced amorphization, forming instead a disordered defect fluorite structure, and the Ti- and Zr- based compositions have low leach rates for the actinides. A major advantage is that a number of these structure-types, e.g., murataite, can accommodate rather complicated compositions, e.g., high Fe-concentrations, and hence may find wide application for a variety of actinide-bearing waste streams. Typical polyphase waste forms include titanate ceramics composed of pyrochlore + murataite, zirconolite + murataite, and ferrite garnets.

At present, research groups around the world are developing and characterizing new matrices for the new types of actinide-bearing residues and waste streams that will result from advanced fuel cycles. These include the actinide-containing residues from the processing of SNF from fast-neutron reactors, from "dry" pyroelectrochemical reprocessing of SNF, as well as due to development of materials for transmutation of minor actinides using inert matrix fuels or as targets for accelerator-driven transmutation. The final selection of any waste form should depend on its ability to incorporate the radionuclides of interest, its chemical durability, response to a radiation-field, and physical properties, as well as the time required for isolation to protect the environment. With the anticipated expansion of nuclear power production, the development of new fuel cycles, and increasing demands for safe disposal of radioactive waste, the need for new and better waste forms should only increase.

Acknowledgements

The research was supported by the Russian Foundation for Basic Research (projects 05-05-64005, 05-05-08000, 05-03-08024), and the United States Department of Energy, Office of Basic Energy Sciences (RUC2-20009-MO-04). The authors are grateful to colleagues from the Russian Academy of Sciences (M. Lapina, A. Mokhov, B. Nikonov, B. Omelianenko, S. Perevalov,

A. Sivtsov, V. Urusov, T. Yudintseva), SIA “Radon” (O. Kirjanova, T. Lashtchenova, N. Mikhailenko, A. Ptashkin), VNIINM (Yu. Matyunin), and Michigan University (J. Lian, S. Utsunomiya and L.M. Wang) for their contributions to the research summarized in the chapter. R.C. Ewing acknowledges several decades of collaboration with Bill Weber (PNNL) and Werner Lutze (Catholic University) that have provided many of the results and much of the insight that are included in this chapter.

References

1. R.C. Ewing, Proc. Natl. Acad. Sci. USA 96 (1999) 3432.
2. R.H. Flowers, L.E.J. Roberts, F.R.S. Tymons, Phil. Trans. R. Soc. Lond. A319 (1986) 5.
3. End Points for Spent Nuclear Fuel and High-Level Radioactive Waste in Russia and the United States, The National Academies Press, Washington, DC, 2003.
4. R.C. Ewing, Environmental Impact of the Nuclear Fuel Cycle, in Energy, Waste and the Environment: a Geochemical Perspective, Eds. R. Giere and P. Stille, The Geological Society of London, London, 2004.
5. A.V. Ochkin, N.S. Babaev, E.P. Magomedbekov, Introduction to Radioecology, IzdAT, Moscow, 2003 (in Russian).
6. Actinide and fission product partitioning and transmutation. Sixth information exchange meeting. OECD NEA, France, 2000.
7. C.G. Sombret, The Geol. Disposal of High Level Wastes, Theoph. Public., Athens, 1987.
8. R.C. Ewing, W.J. Weber, J. Lian, J. Appl. Phys. 95 (2004) 5949.
9. W. Sinkler, T.P. O’Holleran, S.M. Frank, M.K. Richmann, S.G. Johnson, Mater. Res. Soc. Symp. Proc. 608 (2000) 423.
10. Pyrochemical Separations in Nuclear Applications. OECD NEA, France, 2004.
11. Nuclear Waste Materials Handbook (Test Methods). Report DOE/TIC-11400, DOE Technical Information Center, Washington, DC, 1981.
12. Chemical Durability and Related Properties of Solidified High-Level Waste Forms. Technical Reports Series N257, IAEA, Vienna, 1985.
13. Standard Test Methods for Determining Chemical Durability of Nuclear Waste Glasses: The Product Consistency Test (PCT), Standard C1285-94, ASTM, 1994.
14. R.C. Ewing, W.J. Weber, F.W. Clinard Jr., Progress in Nuclear Energy 29 (1995) 63.
15. W. Sinclair, A.E. Ringwood, Geochem. J. 15 (1981) 229.
16. G.R. Lumpkin, B.C. Chakoumakos, R.C. Ewing, Amer. Mineral. 71 (1986) 569.
17. G.R. Lumpkin, J. Nucl. Mater. 289 (2001) 136.
18. N.P. Laverov, S.V. Yudintsev, T.S. Yudintseva, S.V. Stefanovsky, R.C. Ewing, J. Lian, S. Utsunomiya, L.M. Wang, Geology of Ore Deposits 45 (2003) 423.
19. J.F. Ziegler, J.P. Biersack, U. Littmark, The Stopping and Range of Ions in Solids, Pergamon Press, NY, 1985.
20. R.C. Ewing, A. Meldrum, L.M. Wang, S.X. Wang, in Reviews in Mineralogy & Geochemistry, Eds. S.A.T. Redfern and M.A. Carpenter, 39 (2000) 319.
21. W.J. Weber, R.C. Ewing, Science 289 (2000) 2051.
22. R.C. Ewing, in Scientific Basis for Nuclear Waste Management, Ed. G. McCarthy, Plenum Press, NY, 1979.
23. J.L. Crovisier, T. Advocat, J.L. Dussossoy, J. Nucl. Mater. 321 (2003) 91.
24. Radioactive Waste Forms for the Future, Eds: W. Lutze and R.C. Ewing, Elsevier Sci. Publ., Amsterdam, 1988.

25. J.K. Bates, A.J.G. Ellison, J.W. Emery, J.C. Hoh, Mater. Res. Soc. Symp. Proc. 412 (1996) 57.
26. A.E. Ringwood, Austral. Nat. Univ. Press, Canberra (1978) 64.
27. A.E. Ringwood, Miner. Magaz. 49 (1985) 159.
28. P.E. Fielding, T.J. White, J. Mater. Res. 2 (1987) 387.
29. S.V. Yudintsev, Geol. Ore Deposits 45 (2003) 172.
30. I.W. Donald, B.L. Metcalfe, R.S. Greedharee, Mater. Res. Soc. Symp. Proc. 713 (2002) 287.
31. W. Sinkler, T.P. O'Holleran, S.M. Frank, M.K. Richmann, S.G. Johnson, Mater. Res. Soc. Symp. Proc. 608 (2000) 423.
32. L.R. Morss, M.L. Stanley, C.D. Tatko, W.L. Ebert, Mater. Res. Soc. Symp. Proc. 608 (2000) 733.
33. W.L. Gong, W. Lutze, R.C. Ewing, J. Nucl. Mater. 278 (2000) 77.
34. B.W. Veal, J.N. Mundy, D.J. Lam, in Handbook of the Physics and Chemistry of Actinides, Eds. A.J. Freeman and G.H. Lander, 1987.
35. D.G. Karraker, J. Amer. Ceram. Soc. 65 (1982) 53.
36. H.D. Schreiber, G.B. Balazs, Phys. Chem. Glasses. 23 (1982) 139.
37. L.L. Hench, D.E. Clark , J.Campbell . Nuclear and Chemical Waste Management. 5 (1984) 149.
38. W. Lutze, R.C. Ewing, Ceramic Transactions 61 (1995) 357.
39. I.W. Donald, B.L. Metcalfe, R.N.J. Taylor, J. Mater. Sci. 32 (1997) 5851.
40. D.M. Strachan, A.J. Bakel, E.C. Buck, D.B. Chamberlain, J.A. Fortner, C.J. Mertz, S.F. Wolf, W.F. Bourcier, B.B. Ebbinghaus, H.F. Shaw, R.A. Van Konynenburg, B.P. McGrail, J.D. Vienna, J.C. Marra, D.K. Peeler, Waste Management '98 Conf. Proc., Laser Options Inc., Tucson, AZ, 1998.
41. I. Muller, W.J. Weber, E.R. Vance, G. Wicks, D. Karraker, in Advances in Plutonium Chemistry 1967-2000, Ed. D. Hoffman, American Nuclear Society (2002) 260.
42. S.V. Stefanovsky, S.V. Yudintsev, R.Gieré, G.R. Lumpkin, in Energy, Waste, and the Environment: A Geochemical Perspective, Eds. R. Gieré and P. Stille, Geological Society. London. Special Publications N236, 2004.
43. W.E. Lee. M.I. Ojovan, M.C. Stennett, N.C. Hyatt, Adv. Appl. Ceram. 105 (2006) 3.
44. H. Masson, J.-L. Desvaux, E. Pluche, P. Roux, Waste Management '99 Conf. Proc., Laser Options Inc., Tucson, AZ, 1999.
45. V. Petitjean, C. Fillet, R. Boen, C. Veyer, T. Flament, Waste Management '02 Conf. Proc., Laser Options Inc., Tucson, AZ, 2002.
46. S.L. Marra, R.J. O'Driscoll, T.L. Fellinger, J.M. Ray, P.M. Patel, J.E. Occhipinti, Waste Management'99 Conf. Proc., Laser Options Inc., Tucson, AZ, 1999.
47. R.A. Palmer, A.J. Misercola, Waste Management '03 Conf. Proc., Laser Options, Inc., Tucson, AZ, 2003.
48. Glass as a Waste Form and Vitrification Technology, Natnl. Acad. Press, Washington, D.C., 1996.
49. Yu.V. Glagolenko, E.G. Dzekun, S.I. Rovnyi, Issues of Radiat. Safety, 2 (1997) 3 (in Russian).
50. E. Warnecke, in Conditioning of Radioactive Operational & Decommissioning Wastes, KONTEC '97, 1997.
51. B.B. Ebbinghause, C. Cicero-Herman, L. Gray, H.F. Shaw, Plutonium immobilization project: baseline formulation, UCRL-ID-133089, Lawrence Livermore National Laboratory, Livermore, CA, 1999.
52. W. Brummond, G. Armantrout, Waste Management '98 Conf. Proc., Laser Options, Inc., Tucson, AZ, 1998.

53. I.A. Sobolev, S.V. Stefanovsky, F.A. Lifanov, Mater. Res. Soc. Symp. Proc. 353 (1995) 833.
54. I.A. Sobolev, S.V. Stefanovsky, S.V. Ioudintsev, B.S. Nikonov, B.I. Omelianenko, A.V. Mokhov, Mater. Res. Soc. Symp. Proc. 465 (1997) 363.
55. A.Yu. Postnikov, E.V. Levakov, P.I. Gavrilov, E.M. Glagovsky, A.V. Kuprin, Phys. Chem. Mater. Treatment 5 (2001) 58 (in Russian).
56. E.M. Glagovskii, S.V. Yudintsev, A.V. Kuprin, L.P. Pelevin, E.E. Konovalov, V.I. Velichkin, B.F. Myasoedov, Radiochemistry 43 (2001) 632.
57. M.J. Kupfer, W.W. Schulz, C.W. Hobbick, J.E. Mendel, American Institute of Chemical Engineering Symposia, Series 72, 1976.
58. C.R. Palmer, G.B. Mellinger, J.M. Rusin, Management of Alpha-Contaminated Wastes, IAEA, Vienna, 1981.
59. P.G. Eller, G.D. Jarvinen, J.D. Purson, R.A. Penneman, R.R. Ryan, F.W. Lytle, Radiochim. Acta, 39 (1985) 17.
60. D.B. Chamberlain, J.M. Hanchar, J.W. Emery, J.C. Hoh, S.F. Wolf, R.J. Finch, J.K. Bates, A.J.G. Ellison, D.B. Dingwell, Mater. Res. Soc. Symp. Proc. 465 (1997) 1229.
61. N.E. Bibler, W.G. Ramsey, T.F. Meaker, J.M. Pareizs, Mater. Res. Soc. Symp. Proc. 412 (1996) 65.
62. M.G. Mesko, T.F. Meaker, W.G. Ramsey, J.C. Marra, D.K. Peeler, Mater. Res. Soc. Symp. Proc. 465 (1997) 105.
63. Yu.I. Matyunin, Immobilization of of excess weapons plutonium in Russia: a review of LLNL contract work, UCRL-ID-143486, Lawrence Livermore National Laboratory, Livermore, CA, 2001.
64. B.J. Riley, J.D. Vienna, M.J. Schweiger, Mater. Res. Soc. Symp. Proc. 608 (2000) 677.
65. D.K. Peeler, T.F. Meaker, I.A. Reamer, Proc. 3-rd Top. Meet. DOE Spent Nucl. Fuel and Fiss. Mater. Managem, American Nuclear Society, 1998.
66. J.A. Fortner, C.J. Mertz, A.J. Bakel, R.J. Finch, D.B. Chamberlain, Mater. Res. Soc. Symp. Proc. 608 (2000) 739.
67. E.R. Vance, Mater. Res. Soc. Bulletin 19 (1994) 28
68. E.R. Vance, B.D. Begg, R.A. Day, C.J. Ball, Mater. Res. Soc. Symp. Proc. 353 (1995) 767.
69. D.M. Strachan, R.D. Scheele, E.C. Buck, J.P. Icenhower, A.E. Kozelisky, R.L. Sell, R.J. Elovich, W.C. Buchmiller, J. Nucl. Mater. 345 (2005) 109-135.
70. W. Sinclair, A.E. Ringwood, Geochem. J. 15 (1981) 229.
71. G.R. Lumpkin, K.L. Smith, M.G. Blacford, R. Giere, C.T. Williams, Mater. Res. Soc. Symp. Proc. 506 (1998) 215.
72. T. Murakami, B.C. Chakoumakos, R.C. Ewing, G.R. Lumpkin, W.J. Weber, Amer. Mineral. 76 (1991) 1510.
73. A.M. Seydoux-Guillaume, R. Wirth, A. Deutsch, U. Scharer, Geoch. Cosmoch. Acta 68 (2004) 2517.
74. W.L. Gong, L.M. Wang, R.C. Ewing, L.F. Chen, W. Lutze, Mater. Res. Soc. Symp. Proc. 465 (1997) 649.
75. O.I. Kirjanova, S.V. Stefanovsky, S.V. Yudintsev, Mater. Res. Soc. Symp. Proc. 757 (2003) 297.
76. T.S. Yudintseva, Geol. Ore Deposits 47 (2005) 403.
77. G.J. McCarthy, Nucl. Techn. 32 (1977) 92.
78. A.G. Solomah, T.S. Sridhar, S.C. Jones, Advances in Ceramics 20 (1986) 259.
79. K.P. Hart, E.R. Vance, R. Stanojevic, R.A. Day, Mater. Res. Soc. Symp. Proc. 556 (1999) 173.
80. A. Jostsons, E.R. Vance, D.J. Mercer, V.M. Oversby, Mater. Res. Soc. Symp. Proc. 353 (1995) 775.

81. K.L. Smith, M.G. Blackford, G.R. Lumpkin, K.P. Hart, B.J. Robinson, Mater. Res. Soc. Symp. Proc. 412 (1996) 313.
82. K.L. Smith, G.R. Lumpkin, M.G. Blackford, M. Hambley, R.A. Day, K.P. Hart, A. Jostsons, Mater. Res. Soc. Symp. Proc. 465 (1997) 1267.
83. J.P. Icenhower, D.M. Strachan, B.P. McGrail, R.D. Scheele, E.A. Rodriguez, J.L. Steele, V.L. Legore, Amer. Mineral. 91 (2006) 39.
84. K.D. Reeve, J.L. Woolfrey, J. Aust. Ceram. Soc. 16 (1980) 10.
85. J.L. Woolfrey, K.D. Reeve, D.J. Cassidy, J. Nucl. Mater. 108&109 (1982) 739.
86. K.A. Boult , J.T. Dalton , J.P. Evans, A.R. Hall, A.J. Inns, J.A.C. Marples, E.L. Paige, The Preparation of Fully-Active Synroc and Its Radiation Stability. Final Report AERE R13318, 1988.
87. H. Mitamura, S. Matsumoto, T. Miyazaki, T. White, K. Nukaga, Y. Tagashi, T. Sagawa, S. Tashiro, D.M.Levins, A. Kikuchi, J. Amer. Ceram. Soc. 73 (1990) 3433.
88. H. Mitamura, S. Matsumoto, K.P. Hart, T. Miyazaki, E.R. Vance, Y. Tamura, Y. Togashi, T. White, J. Amer. Ceram. Soc. 75 (1992) 392.
89. J.W. Wald, W.J. Weber, Advances in Ceramics 8 (1984) 71.
90. F.W. Clinard Jr., Amer. Ceram. Soc. Bull., 65 (1986) 1181.
91. W.J. Weber, R.C. Ewing, Mater. Res. Soc. Symp. Proc. 713 (2002) 443.
92. S.X. Wang, B.D. Begg, L.M. Wang, R.C. Ewing, W.J. Weber, K.V.G. Kutty, J. Mater. Res. 14 (1999) 4470.
93. S.E. Kesson, W.J. Sinclair, A.E. Ringwood, Nucl. Chem. Waste Manag. 4 (1983) 259.
94. G.R. Lumpkin, K.P. Hart, P.J. McGlinn, T.E. Payne, Radiochim. Acta 66/67 (1994) 595.
95. N.P. Laverov, B.I. Omelianenko, S.V. Yudintsev, B.S. Nikonov, Geol. Ore Deposits 38 (1996) 387.
96. E.R. Vance, C.J. Ball, R.A. Day, K.L. Smith, M.G. Blackford, B.D. Begg, P.J. Angel, J. Alloy Comp. 213/214 (1994) 406.
97. R. Giere, C.T. Williams, G.R. Lumpkin, Schweiz. Mineral. Petrogr. Mitt. 78 (1998) 433.
98. S.V. Stefanovsky, A.Y. Troole, M.I. Lapina, B.S. Nikonov, A.V. Sivtsov, S.V. Yudintsev, Mater. Res. Soc. Symp. Proc. 713 (2002) 345.
99. S.V. Stefanovsky, S.V. Chizhevskaya, A.S. Mironov, O.I. Kirjanova, S.V. Yudintsev, Advanced Materials 6 (2003) 61 (in Russian).
100. T.J. White, Amer. Miner. 69 (1984) 1156.
101. H. Xu, Y. Wang, P. Zhao, W.L. Borcier, R. Van Konenburg, H.F. Shaw, Mater. Res. Soc. Symp. Proc. 757 (2003) 235.
102. B.D. Begg, E.R. Vance, R.A. Day, M. Hambley, S.D. Conradson, Mater. Res. Soc. Symp. Proc. 465 (1997) 325.
103. B.D. Begg, E.R. Vance, G.R. Lumpkin, Mater. Res. Soc. Symp. Proc. 506 (1998) 79.
104. K.P. Hart , E.R. Vance, M.E.A. Stewart, J. Weir, M.L. Carter, M. Hambley, A. Brownscombe, R.A. Day, S. Leung, C.J. Ball, B.B. Ebbinghaus, L. Gray, T. Kan, Mater. Res. Soc. Symp. Proc. 506 (1998) 161.
105. K.P. Hart, Y. Zhang, E. Loi, Z. Aly, M.W. Stewart, A. Brownscombe, B.B. Ebbinghaus, W. Bourcier, Mater. Res. Soc. Symp. Proc. 608 (2000) 353.
106. P.J. McGlinn, K.P. Hart, E.H. Loi, E.R. Vance, Mater. Res. Soc. Symp. Proc. 353 (1995) 847.
107. G.R. Lumpkin, K.L. Smith, M.G. Blacford, Mater. Res. Soc. Symp. Proc. 353 (1995) 855.
108. J. Malmström, E. Reusser, R. Giere, G.R. Lumpkin, M. Duggelin, D. Mathys, R. Guggenheim, Mater. Res. Soc. Symp. Proc. 556 (1999) 165.
109. Z. Zhang, H. Li, E.R. Vance, T. McLeod, N. Scales, Mater. Res. Soc. Symp. Proc. 824 (2004) 293.
110. R. Giere, J. Malmström, E. Reusser, G.R. Lumpkin, M. Düggelin, D. Mathys, R. Guggenheim, D. Günther, Mater. Res. Soc. Symp. Proc. 663 (2001).

111. W.J. Weber, J.W. Wald, Hj. Matzke, J. Nucl. Mater. 138 (1986) 196.
112. P.E. Raison, R.G. Haire, T. Sato, T. Ogawa, Mater. Res. Soc. Symp. Proc. 556 (1998) 3.
113. B.C. Chakoumakos, R.C. Ewing, Mater. Res. Soc. Proc. 44 (1985) 641.
114. N.P. Laverov, S.V. Yudintsev, S.V. Stefanovsky, Y.N. Jang, R.C. Ewing, Mater. Res. Soc. Symp. Proc. 713 (2002) 337.
115. J.A.Fortner, A.J.Kropf, A.J.Bakel et al. Mat. Res. Soc. Symp. Proc. 608. (2000) 401.
116. Yu.A. Teterin, S.V. Stefanovski, S.V. Yudintsev, G.N. Bek-Uzarov, A.Yu. Teterin, K.I. Maslakov, I.O. Utkin, Russ. J. Inorg. Chem. 49 (2004) 87.
117. A.J. Bakel, V.N. Zyryanov, C.J. Mertz, E.C. Buck,, D.B. Chamberlain, Mater. Res. Soc. Symp. Proc. 556 (1999) 181.
118. I.A. Sobolev, B.F. Myasoedov, S.V. Stefanovsky, S.V. Yudintsev, Y.M. Kulyako. Radiochem. 43 (2001) 113 (in Russian).
119. S.V. Stefanovsky, S.V. Yudintsev, B.S. Nikonov, M.I. Lapina, A.S. Aloy, Mater. Res. Soc. Symp. Proc. 663 (2001) 315.
120. T. Moriga, A. Yoshiasa, F. Kanamaru, K. Koto, M. Yoshimura, S. Somiya, Solid State Ionics 31 (1989) 319.
121. M.J.D. Rushton, R.W. Grimes, C.R. Stanek, S. Owens, J. Mater. Res. 19 (2004) 1603.
122. W.L. Gong, W. Lutze, R.C. Ewing, Mater. Res. Soc. Symp. Proc. 556 (1999) 63.
123. W.L. Gong, W. Lutze, R.C. Ewing, J. Nucl. Mater. 277 (2000) 239.
124. H. Kinoshita, K. Kuramoto, M. Uno, S. Yamanaka, H. Mitamura, T. Banba, Mater. Res. Soc. Symp. Proc. 608 (2000) 393.
125. B.E.Burakov, E.B.Anderson, M.V.Zamoryanskaya, M.A. Yagovkina, E.V. Nikolaeva, Mater. Res. Soc. Symp. Proc. 713 (2002) 333.
126. J. Lian, L.M. Wang, J. Chen, R.C. Ewing, K.V.C. Kutty, Mater. Res. Soc. Symp. Proc. 713 (2002) 507.
127. L.M. Wang, S. Zhu, S.X. Wang, R.C. Ewing, Mater. Res. Soc. Symp. Proc. 663 (2001) 293.
128. J.P. Icenhower, W.J. Weber, N.J. Hess, S. Thevuthasen, B.D. Begg , B.P. McGrail, E.A. Rodriguez, J.L. Steele, K.N. Geiszler, Mater. Res. Soc. Symp. Proc. 757 (2003) 227.
129. M.W.A. Stewart, B.D. Begg, E.R. Vance, K. Finnie, H. Li, G.R. Lumpkin, K.L. Smith, W.J. Weber, S. Thevuthasan, Mater. Res. Soc. Symp. Proc. 713 (2002) 311.
130. N.P. Laverov, S.V. Yudintsev, M.P. Lapina, S.V. Stefanovsky, S.C. Chae, R.C. Ewing, Mater. Res. Soc. Symp. Proc. 757 (2003) 321.
131. S.V. Stefanovsky, O.I. Kirjanova, S.V. Chizhevskaya, S.V. Yudintsev, B.S. Nikonov, Waste Management '03 Conf. Proc., Laser Options Inc., Tucson, AZ, 2003.
132. T.S. Ercit, F.C. Hawthorne, Canad. Miner. 33 (1995) 1223.
133. P.E.D. Morgan, F.J. Ryerson, J. Mat. Sci. Lett. 1 (1982) 351.
134. F.J. Ryerson, J. Amer. Ceram. Soc. 67 (1984) 75.
135. N.P. Laverov, S.V. Yudintsev, A.I. Gorshkov, A.V. Sivtsov, M.I. Lapina, Dokl. Russ. Acad. Sci. 363 (1998) 540 (in Russian).
136. N.P. Laverov, S.V. Yudintsev, B.I. Omelianenko, B.S. Nikonov, S.V. Stefanovsky, Geol. Ore Deposits 41 (1999) 99.
137. S.V. Stefanovsky, S.V. Yudintsev, B.S. Nikonov, B.I. Omelianenko, A.G. Ptashkin, Mater. Res. Soc. Symp. Proc. 506 (1999) 121.
138. V.S. Urusov, N.I. Organova, O.V. Karimova, S.V. Yudintsev, S.V. Stefanovsky, Dokl. Russ. Acad. Sci. 401 (2005) 226 (in Russian).
139. J. Lian, S.V. Yudintsev, S.V. Stefanovsky, O.I. Kirjanova, R.C. Ewing. Mat. Res. Soc. Symp. Proc. 713 (2002) 455.
140. J. Lian, L.M. Wang, R.C. Ewing, S.V. Yudintsev, S.V. Stefanovsky, J. Appl. Phys. 97 (2005) 113536.

141. S.A. Perevalov, S.V. Stefanovsky, S.V. Yudintsev, A.V. Mokhov, A.G. Ptashkin, Migration '05 Proc. (2005) 49.
142. E.R. Vance, R.A. Day, Z. Zhang, B.D. Begg, C.J. Ball, M.G. Blackford, J. Solid State Chem. 124 (1996) 77.
143. A.V. Ochkin, S.V. Chizhevskaya, N.E. Archakova (Cherniavskaya), A.O. Merkushkin, I.A. Petukhova, N.S. Mikhailenko, S.V. Stefanovsky, Mater. Res. Soc. Symp. Proc. 757 (2003) 303.
144. S.V. Chizhevskaya, N.E. Cherniavskaya, A.V. Ochkin, A.M. Chekmarev, S.V. Stefanovsky, Mater. Res. Soc. Symp. Proc. 663 (2001) 367.
145. N.S. Mikhailenko, A.V. Ochkin, S.V. Stefanovsky, O.I. Kirjanova, Mater. Res. Soc. Symp. Proc. 807 (2004) 327.
146. G.R. Lumpkin, M. Colella, K.L. Smith, R.H. Mitchell, A.O. Larsen, Mater. Res. Soc. Symp. Proc. 506 (1998) 207.
147. T.J. White, R.C. Ewing, L.M. Wang, J.S. Forrester, C. Montross, Mater. Res. Soc. Proc, 353 (1995) 1413.
148. K.L. Smith, N.J. Zaluzec, G.R. Lumpkin, Mater. Res. Soc. Symp. Proc. 506 (1998) 931.
149. S. Geller, Zeits. Kristallogr. 125 (1967) 1.
150. B.E. Burakov, E.B. Anderson, D.A. Knecht, M.A. Zamoryanskaya, E.E. Strykanova, M.A. Yagovkina, Mater. Res. Soc. Symp. Proc. 556 (1999) 55.
151. B.E. Burakov, E.B. Anderson, M.A. Zamoryanskaya, M.A. Petrova, Mater. Res. Soc. Symp. Proc. 608 (2000) 419.
152. J. Ito, C. Frondel, Amer. Mineral. 52 (1967) 773.
153. S.V. Yudintsev, A.A. Osherova, A.V. Dubinin, A.V. Zotov, S.V. Stefanovsky, Mater. Res. Soc. Symp. Proc. 824 (2004) 287.
154. S. Utsunomiya, L.M. Wang, S. Yudintsev, R.C. Ewing, J. Nucl. Mater. 303 (2002) 177.
155. E.R. Vance, M.L. Carter, B.D. Begg, R.A. Day, S.H.F. Leung, Mater. Res. Soc. Symp. Proc. 608 (2000) 431.
156. O. Terra, N. Clavier, N. Dacheux, R. Podor, New J. Chem. 27 (2003) 957.
157. A.S. Aloy, E.N. Kovarskaya, T.I. Koltsova, Immobilization of excess weapons plutonium in Russia: a review of LLNL contract work, UCRL-ID-149341, Lawrence Livermore National Laboratory, Livermore, CA, 2002 (in Russian).
158. F. Poitrasson, E. Oelkers, J. Schott, J.M. Montel, Geoch. Cosmoch. Acta 68 (2004) 2207.
159. G.K. Liu, J.S. Luo, S.T. Li, C.-K. Loong, M.M. Abraham, J.V. Beitz, J.K. Bates, L.A. Boatner, Mater. Res. Soc. Symp. Proc. 506 (1998) 921.
160. B.E. Burakov, M.A. Yagovkina, V.M. Garbuzov, A.A. Kitsay, V.A. Zirlin, Mater. Res. Soc. Symp. Proc. 824 (2004) 219.
161. K.B. Helean, A. Navrotsky, J. Lian, R.C. Mater. Res. Soc. Symp. Proc. 824 (2004) 279.
162. A. Meldrum, L.A. Boatner, R.C. Ewing, Phys. Rev. B. 56 (1997) 13805.
163. A. Meldrum, L.A. Boatner, W.J. Weber, R.C. Ewing, Geoch. Cosmoch. Acta. 62 (1998) 2509.
164. A. Meldrum, L.M. Wang, R.C. Ewing, Nucl. Instr. Meth. Res. B. 116 (1996) 220.
165. M. Genet, N. Dacheux, A.C. Thomas, B. Chassigneux, E. Pichot, V. Brandel, Waste Management '99 Conf. Proc., Laser Options Inc., Tucson, AZ, 1999.
166. A.C. Thomas, N. Dacheux, P. Le Coustumer, V. Brandel, M. Genet, J. Nucl. Mater. 295 (2001) 249.
167. A.C. Robisson, N. Dacheux, J. Aupiais, J. Nucl. Mater. 306 (2002) 134.
168. N. Dacheux, R. Podor, V. Brandel, M. Genet, J. Nucl. Mater. 252 (1998) 179.
169. N. Dacheux, A.C. Thomas, V. Brandel, M. Genet, J. Nucl. Mater. 257 (1998) 108.
170. N. Clavier, N. Dacheux, R. Podor, P. Le Cousumer, Mater. Res. Soc. Symp. Proc. 802 (2004).
171. B. Goffe, E. Janots, F. Brunet, C.C.R. Poinssot, Geoscience 334 (2002) 1047.

172. L.O. Hagman, P. Kierkegaard, Acta. Chem. Scand. 22 (1968) 1822.
173. B.E. Scheetz, D.K. Agrawal, E. Breval, R. Roy, Waste Manag. 14 (1994) 489.
174. H.T. Hawkins, B.E. Scheetz, G.D. Guthrie, Mater. Res. Soc. Symp. Proc. 465 (1997) 387.
175. M. Ishida, K. Kikuchi, T. Yanagi, R. Terai, Nucl. Chem. Waste Manag. 6 (1986) 127.
176. A.I. Orlova, V.N. Zyryanov, O.V. Egor'kova, V.T. Demarin, Radiochem. 38 (1996) 22 (in Russian).
177. A.I. Orlova, Yu.F. Volkov, R.F. Melkaya, L.Yu. Masterova, I.A. Kulikov, V.A. Alferov, Radiochem. 36 (1994) 295 (in Russian).
178. A.I. Troole, S.V. Stefanovsky, L.D. Bogomolova, Mater. Res. Soc. Symp. Proc. 556 (1999) 99.
179. A. Troole, S. Stefanovsky, Mater. Res. Soc. Symp. Proc. 713 (2002) 359.
180. J. Ito, Amer. Mineral. 53 (1968) 890.
181. S. Utsunomiya, S. Yudintsev, L.M. Wang, R.C. Ewing, J. Nucl. Mater. 322 (2003) 180.
182. B.E. Burakov, Proc. Saf. Waste'93 2 (1993) 19.
183. E.B. Anderson, B.E. Burakov, E.M. Pazukhin, Radiochim. Acta 60 (1993) 149.
184. R.C. Ewing, Can. Mineral. 39 (2001) 697.
185. E.V. Nikolaeva, B.E. Burakov, Mater. Res. Soc. Symp. Proc. 713 (2003) 429.
186. W.J. Weber, R.C. Ewing, L.M. Wang, J. Mater. Res 9 (1994) 688.
187. W.J. Weber, R.C. Ewing, A. Meldrum, J. Nucl. Mater. 250 (1997) 147.
188. B.C. Chakoumakos, T. Murakami, G.R. Lumpkin, R.C. Ewing, Science 236 (1987) 1556.
189. S.V.Stefanovsky, S.V.Yudintsev, B.S.Nikonov et al. Mat. Res. Soc. Symp. Proc. 608 (2000) 455.
190. V.I. Vlasov, O.L. Kedrovsky, A.S. Nikiforov, A.S. Polyakov, I.Y. Shishtchitz, in: Back End of the Nuclear Fuel Cycle: Strategies and Options, Vienna, IAEA, (1987) 109.
191. T. Advocat, C. Fillet, J. Marillet, G. Leturcq, J.M. Boubals, A. Bonnetier, Mater. Res. Soc. Symp. Proc. 506 (1998) 55.
192. T. Advocat, P.J. McGlinn, C. Fillet, G. Leturcq, S. Schuller, A. Bonnetier, K.P. Hart, Mater. Res. Soc. Symp. Proc. 663 (2001) 277.
193. P.J. McGlinn, T. Advocat, E. Loi, G. Leturcq, J.P. Mestre, Mater. Res. Soc. Symp. Proc. 663 (2001) 249.
194. P. Loiseau, D. Caurant, N. Baffier, C. Fillet, Mater. Res. Soc. Symp. Proc. 663 (2001).
195. P. Loiseau, D. Caurant, I. Bardez, O. Majerus, N. Baffer, C. Fillet, Mater. Res. Soc. Symp. Proc. 757 (2003) 281.
196. R.A. Day, S. Moricca, M.W.A. Stewart, B.D. Begg, E.R. Maddrell, C.R. Scales, N. Gawthorpe. ICEM'05 Proc. (2005) ID 1136.
197. T.P. O'Holleran, S.G. Johnson, P.C. Kong, B.A. Staples, Waste Management'98 Conf. Proc., Laser Options Inc., Tucson, AZ, 1998.
198. D.A. Knecht, K. Vinjamuri, S.V. Raman, B.A. Staples, J.D. Grandy, S. Johnson, T.P. O'Holleran, S. Frank, Waste Management'98 Conf. Proc., Laser Options Inc., Tucson, AZ, 1998.
199. A.A. Digeos, J.A. Valdez, K.E. Sickafus, S. Atiq, R.W. Grimes, A.R.J. Boccaccini, Nucl. Mater. 38 (2003) 1597.
200. A.R. Boccaccini, S. Atiq, R.W. Grimes, Adv. Eng. Mater. 5 (2003) 501.
201. E.R. Vance, R.A. Day, M.L. Carter, A.A. Jostsons, Mater. Res. Soc. Symp. Proc. 412 (1996) 289.
202. T.N. Lashtchenova, S.V. Stefanovsky, Proc. XVIII International Congress on Glass, Eds:.K. Choudhary, N.T. Huff, and C.H. Drummond III, San Francisco, CA, USA (1998).

Subject Index

*f = and following pages